

UNIVERSITE TOULOUSE III – PAUL SABATIER
U.F.R Physique, Chimie, Automatique

THESE

pour obtenir le grade de

DOCTEUR DE L'UNIVERSITE TOULOUSE III

Discipline : Astrophysique

présentée et soutenue

par

Nicolas LODIEU

le 07 Juillet 2004

**Recherche d'étoiles de faible masse et de naines brunes:
Voisinage solaire et amas d'âge intermédiaire Alpha Per et Collinder 359**

JURY

Prof. Dr. Peter von Ballmoos
Prof. Dr. Mark McCaughrean
Dr. Emmanuel Caux
Prof. Dr. Pavel Kroupa
Prof. Dr. Eduardo Martín
Dr. Thierry Montmerle

Président du jury
Directeur de thèse
Directeur de thèse
Rapporteur
Rapporteur
Examinateur

AUTEUR : Nicolas Lodieu

TITRE : Recherche d'étoiles de faible masse et de naines brunes :
Voisinage solaire et amas d'âge intermédiaire Alpha Per et Collinder 359

DIRECTEURS DE THESE : Dr. Emmanuel Caux & Prof. Dr. Mark McCaughrean

DATE ET LIEU DE LA SOUTENANCE : Le 07 Juillet 2004 à 10h30
Salle de Conférences, CESR
9, Avenue du Colonel Roche
31400 Toulouse

RESUME EN FRANCAIS

Nous décrivons les résultats de cartographies d'étoiles de faible masse et de naines brunes à la fois agées et proches appartenant au champ ainsi que jeunes et éloignées dans des amas d'étoiles.

Premièrement, nous présentons les résultats d'une étude à mouvement propre dédiée aux objets froids et proches du Soleil. Nous avons découvert de nombreuses naines ultra-froides à moins de 50 parsecs ainsi que la naine brune binaire la plus proche.

Deuxièmement, nous étudions la fonction de masse sous-stellaire dans les amas ouverts jeunes. Une cartographie proche infrarouge d'une région de 0.7 degré carré dans Alpha Per a révélé de nouveaux membres stellaires et sous-stellaires. Une cartographie visible d'une région de 1.6 degré carré dans Collinder 359 a extrait de nouveaux membres de masses inférieures à une masse solaire, révisant l'âge et la distance de l'amas. Sa fonction de masse croît dans le domaine sous-stellaire avec une pente inférieure à celles estimées pour les Pléiades.

MOTS-CLES

Naines brunes, étoiles de faible masse
Fonction de luminosité, fonction de masse
Voisinage solaire
Amas ouverts individuels : Alpha Per et Collinder 359
Techniques : photométrie, spectroscopie
Techniques : visible, proche infrarouge

DISCIPLINE ADMINISTRATIVE : Astrophysique

ADRESSE DU LABORATOIRE : Astrophysikalisches Institut Potsdam
An der Sternwarte 16
D-14 482 Potsdam
Allemagne

*A mes parents
pour leur soutien*

Remerciements

Toute ma gratitude revient à ma famille sans qui cette thèse n'aurait pu aboutir. Un immense MERCI pour votre soutien pendant ces trois ans et dix mois qui furent si éprouvants. Sans les multiples conseils et encouragements de mes parents, Josette et Jean-Pierre, mes désespoirs et désillusions auraient eu raison de ma passion pour l'astronomie. Je vous dédie cette thèse car vous le méritez amplement. Mes grands-parents maternels et paternels ont toujours su raviver mon énergie suite à une longue semaine me rappelant que leurs problèmes de santé étaient bien plus grave que mes petits soucis quotidiens. Et je n'oublie pas les multiples échanges d'e-mails que j'ai eus avec mon oncle, ma tante et mon cousin. Merci à Robert pour la relecture et les corrections des parties françaises.

Je souhaite aussi remercier la famille Behrendt, Ursula, Hans et Christoph (sans oublier Eva !) pour leur gentillesse et leur aide ainsi que l'amour qu'il porte à ma région. Merci à Christoph pour les multiples excursions à Berlin pendant les week-ends. Les visites de chaque quartier et les explications historiques furent très profitables. Et puis, les visites de Cottbus, Dresde, et Brandenburg. Merci à Hans et Ursula pour les nombreuses invitations, les bons petits plats avec les produits du marché, leurs encouragements et les nombreuses discussions.

Je me souviens parfaitement du jour où Emmanuel Caux, mon responsable de DEA à cette époque, mentionna l'offre de thèse existante à Potsdam. Je travaillais avec Alain Klotz dans son bureau et Emmanuel jeta sur la table la feuille contenant l'offre de thèse. Après de longs jours de reflexion et me rappelant le fameux proverbe "Qui ne tente rien n'a rien !", j'ai finalement envoyé ma candidature. Suite à plusieurs échanges de courriers électroniques avec Hans Zinnecker et Mark McCaughean ainsi qu'un entretien 'live' à Grenoble avec Hans, la position me fut attribuée. Je dois ici remercier Emmanuel et Hans de m'avoir offert l'opportunité de vivre cette expérience unique. L'un de mes rêves était d'aller en Allemagne et je l'ai réalisé. Ce ne fut malheureusement pas un conte de fée mais plutôt un cauchemar Je pourrais en effet écrire un roman basé sur les diverses expériences vécues pendant ces quatre années à Potsdam. Je ne souhaite cependant pas entrer dans les détails puisque ce chapitre s'intitule remerciements !

Tout ne fut heureusement pas négatif et cela grâce à la gentillesse et la bonne humeur de certaines personnes. Tout d'abord, j'exprime ma gratitude à un voisin et collègue, Christian Fendt (et sa famille) pour sa sympathie et son aide à la fois dans le travail et dans la vie. Ensuite, Mara Salvato pour sa bonne humeur qui fut d'une aide merveilleuse lors des deux premières années. Merci aussi à Ralf-Dieter Scholz, le monsieur "Proper Motion" de l'AIP, pour les nombreuses discussions scientifiques variées. J'exprime ma reconnaissance à Jérôme Bouvier et David Barrado y Navascués pour leurs conseils scientifiques et le temps passé à écrire les lettres de référence qui ont toutes échouées à ce jour.

Quelques remerciements supplémentaires en vrac. Merci aux membres du groupe “Star and Planet Formation” de l’institut et, en particulier, Ralf Klessen pour essayer de maintenir une réunion de groupe très mal en point à son arrivée. Merci aux autres étudiants qui ont partagé le “student office” pendant ces quelques années, les anciens comme les nouveaux. Morten Andersen pour corriger mon anglais et ses éternelles critiques, Tanya Urrutia pour son indestructible bonne humeur, et Stefan Schmeja pour son aide à toute épreuve avec IDL et L^AT_EX. Je n’oublie évidemment pas Jens Rodmann et Mirko Krumpe pour leur amitié. Un petit coucou à mes partenaires de tennis de table, devenus adversaires le temps d’une partie, Karl-Heinz Böning et Milan Zboril pour ne citer que les plus acidus. Idéal pour oublier momentanément le travail. Herzlichen Dank an Super Mario (Mario Dionies) pour résoudre les bugs de mon ordinateur ainsi que Michael Fiebiger pour les multiples backups, devenus fréquents suite au crash du disque dur de mon ordinateur. Et enfin, pour n’oublier personne, Herzlichen Dank an alle Mitarbeiter des AIPs. Pour finir, merci à mon mentor, Jean-Marie Féret, pour son support pendant l’écriture du nouveau chapitre de thèse.

Je n’oublie pas les membres du réseau européen qui en ont bavé pour réduire les données du Canada France Hawaii. Merci Jérôme pour nous avoir rendu la vie si dure ! Je remercie le réseau de la commission européenne, ‘The Formation and Evolution of Young Stellar Clusters’ (HPRN-CT-2000-00155) pour avoir, d’une part financé ma thèse et, d’autre part, de m’avoir donné l’opportunité de vivre une expérience unique.

Je remercie Peter von Ballmoos d’avoir accepté la présidence de mon jury de thèse. Un grand merci à Eduardo Martín et Pavel Kroupa d’avoir accepté le rôle ingrat de rapporteurs et à Thierry Montmerle d’avoir fait le déplacement pour assister à ma soutenance de thèse. Un hommage particulier à mes deux directeurs de thèse, Mark McCaughrean et Emmanuel Caux, pour m’avoir accompagné pendant ces quatre longues années. Merci à tous d’avoir fait le déplacement à Toulouse et de m’avoir consacré un peu de votre temps si précieux.

This work has made use of a large number of data products and I would like to mention them here. I have used the SuperCOSMOS Sky Surveys, i.e. digitized data obtained from scans of UKST and ESO Schmidt plates. Schmidt plates. This research has also made use of data products from the Two Micron All Sky Survey, which is a joint project of the University of Massachusetts and the Infrared Processing and Analysis Center, funded by the National Aeronautics and Space Administration and the National Science Foundation. DENIS is the result of a joint effort involving human and financial contributions of several Institutes mostly located in Europe. I have made use of the VizieR and Simbad catalogue access tools, Centre de Données astronomiques de Strasbourg.

Le 24 Mai 2004
Nicolas

Contents

Remerciements	i
Contents	iii
List of figures	vii
List of tables	ix
List of acronyms	xi
Version française	xiii
Introduction	xiii
F-1 Théorie et observation des naines brunes	xv
F-1.1 Présentation théorique des naines brunes	xv
F-1.2 Présentation observationnelle des naines brunes	xvii
F-2 Recherche d'étoiles de faible masse et de naines brunes par mouvement propre dans le ciel austral	xviii
F-3 Nouveaux membres stellaires et sous-stellaires dans α Per	xxi
F-4 L'amas ouvert jeune Collinder 359	xxiii
F-5 Futurs plans pour vérifier l'appartenance de candidats à un amas ouvert	xxiv
Conclusions et perspectives	xxv
Nouveau chapitre de thèse	xxix
1) Cadre général et enjeux de la thèse	xxx
2) Coût du projet	xxxii
3) Déroulement et gestion du projet	xxxiii
4) Compétences, savoir-faire, qualités professionnelles et personnelles	xxxiv
5) Résultats et impact de la thèse	xxxvi
6) Pistes professionnelles identifiées	xxxvi
Introduction	1
1 A theoretical and observational overview of brown dwarfs	3
1.1 The Initial Mass Function	4
1.1.1 Definitions	4
1.1.2 The mass-luminosity relation	5
1.1.3 Observational determinations of the IMF	6

1.2	The formation of brown dwarfs	9
1.2.1	The theory of brown dwarf formation	9
Turbulence		9
Irradiated pre-stellar cores		9
Disk instabilities		9
Ejection mechanism		10
Formation in circumstellar disks		11
1.2.2	Observational constraints on the formation of brown dwarfs	11
1.2.3	Conclusions on the formation of brown dwarfs	12
1.3	The physics of brown dwarfs	13
1.3.1	The evolution of luminosity	13
1.3.2	The evolution of temperature	14
1.3.3	The evolution of radius	16
1.3.4	The influence of metallicity	16
1.3.5	Deuterium and lithium burning in brown dwarfs	16
1.3.6	Atmosphere models of low-mass stars and brown dwarfs	17
1.4	Characterisation of M, L, and T dwarfs	19
1.4.1	Spectroscopy of M dwarfs	19
1.4.2	Spectroscopy of L dwarfs	20
1.4.3	Spectroscopy of T dwarfs	24
1.5	Different kinds of searches for brown dwarfs	27
1.5.1	Brown dwarfs as companions	27
Radial velocity surveys		28
Microlensing		29
Brown dwarf companions to low-mass stars		30
Brown dwarf binaries		31
Conclusions to the frequency of brown dwarfs as companions		32
1.5.2	The field brown dwarfs	34
The Two Micron All-Sky Survey		34
The DEep Near-Infrared Survey		35
The Sloan Digital Sky Survey		35
Proper motion surveys		36
Serendipitous discoveries		38
1.5.3	Brown dwarfs in star-forming regions	39
1.5.4	Brown dwarfs in young open clusters	43
2	Proper motion survey for nearby low-mass stars and brown dwarfs in the southern sky	47
2.1	The sample	48
2.2	Observations	49
2.3	Data reduction	50
2.3.1	Optical imaging	50
2.3.2	Near-infrared imaging	50
2.3.3	Optical spectroscopy	51
2.3.4	Near-infrared spectroscopy	52
2.4	General results of the proper motion survey	52

2.5	Subdwarfs in the solar neighbourhood	57
2.6	An active M8.5 dwarf wide companion to a M4/DA binary	59
2.7	Two M dwarfs within 10 pc	61
2.8	Three new ultracool dwarfs in the solar neighbourhood	63
2.9	ε Indi Ba,Bb: the nearest binary brown dwarf	65
2.10	Conclusions on the proper motion survey and outlook	69
3	New low-mass stars and brown dwarfs in the α Per cluster	71
3.1	Known members of the α Per cluster	74
3.2	The age determination of the α Per cluster	76
3.3	The wide-field optical survey of the α Per cluster	79
3.4	The luminosity and mass functions of the α Per cluster	81
3.4.1	The cluster luminosity function	81
3.4.2	The cluster mass function	82
3.5	The near-infrared survey of the α Per cluster	83
3.5.1	Observations	84
3.5.2	Data reduction	85
3.5.3	Astrometry of the near-infrared images	85
3.5.4	Optical-infrared catalogue	87
3.5.5	Colour-magnitude diagram	88
3.5.6	Colour-colour diagram	90
3.6	Optical spectroscopy of cluster member candidates	95
3.6.1	Spectroscopic observations	96
3.6.2	Data reduction	96
3.6.3	Analysis of the optical spectra	100
3.7	Comparison of the α Per IMF with other open clusters	104
3.8	Conclusions on α Per and future plans	104
4	The intermediate-age open cluster Collinder 359	107
4.1	The CFHT Key Programme	108
4.1.1	Description of the CFHT Key Programme	108
4.1.2	The choice of the optical filters	108
4.1.3	Aims of the CFHT Key Programme	109
4.1.4	Selection of the pre-main-sequence open clusters	110
4.2	Literature on the open cluster Collinder 359	110
4.3	The wide-field optical survey of Collinder 359	114
4.3.1	The CFH12K wide-field optical observations	114
4.3.2	The data reduction of the wide-field optical images	115
4.3.3	The extraction of the photometry	118
4.3.4	The optical colour-magnitude diagram for Collinder 359	125
4.3.5	Selection of cluster member candidates	125
4.4	Near-infrared follow-up of optically-selected candidates	131
4.4.1	Cross-correlation with the 2MASS database	131
4.4.2	The CFHT K -band follow-up	132
4.4.3	Data reduction of the CFHT near-infrared images	133
4.4.4	Analysis of the CFHT observations	135

4.4.5	Contamination of the optical sample	137
4.5	The luminosity function of Collinder 359	139
4.5.1	The existence of the cluster	140
4.5.2	The age of the cluster	140
4.5.3	The distance of the cluster	143
4.5.4	The cluster luminosity function	144
4.6	The mass function of Collinder 359	146
4.6.1	The mass-magnitude relation	146
4.6.2	The cluster mass function	148
4.6.3	Uncertainties on the cluster mass function	150
4.6.4	Comparison with other young clusters	151
4.7	Conclusions of the survey in Collinder 359 and perspectives	153
5	Outlook and future work for cluster membership	155
5.1	Full coverage of a cluster	155
5.2	Proper motion	157
5.3	Near-infrared imaging of cluster member candidates	158
5.4	Optical spectroscopy of cluster member candidates	159
5.4.1	Spectral classification	159
5.4.2	Chromospheric activity	160
5.4.3	Surface gravity	160
5.4.4	Lithium depletion boundary	161
5.4.5	Rotational velocities	161
5.4.6	Radial velocities	161
5.4.7	Planned spectroscopic observations in Collinder 359	162
5.5	Near-infrared spectroscopy of cluster member candidates	163
5.6	X-ray surveys of open clusters	163
5.7	Binarity of cluster members	164
5.8	Variability of cluster members	165
Conclusions and perspectives		167
Bibliography		171
Appendices		191
A	Spectroscopy for southern sky proper motion objects	193
B	Table of cluster members in the open cluster Collinder 359	205
C	Finding charts for candidate members of Collinder 359	231
D	List of my publications	233

List of Figures

1.1	Comparison of IMF from the literature	7
1.2	Evolution of the luminosity and the effective temperature of a brown dwarf	15
1.3	Spectroscopy of M dwarfs	20
1.4	Spectroscopy of L dwarfs	21
1.5	Spectroscopy of T dwarfs	25
1.6	Separation and mass ratio distributions for G, M, and ultracool dwarfs	33
1.7	Comparison of mass function estimates in star-forming regions	40
1.8	Comparison of mass function estimates in the Pleiades and α Per open clusters . .	44
2.1	Spectrum of the latest nearby objects in our proper motion survey	53
2.2	Distribution of the photometric distances of the proper motion objects	55
2.3	$H\alpha$ equivalent widths versus spectral type	56
2.4	Gravity features equivalent widths versus spectral type	56
2.5	Optical spectroscopy of subdwarfs found in the proper motion survey	58
2.6	Optical spectroscopy of the M8.5 active dwarf, APMPM J2354–3316C	60
2.7	Spectrum of two late-M dwarfs within 10 pc	62
2.8	Optical and near-infrared spectroscopy of three ultracool dwarfs: SSSPM0109 (M8.5), SSSPM2310 (M9.5), and SSSPM0219 (L1).	64
2.9	Original spectrum of the ε Indi B system	66
2.10	NACO broad-band near-IR adaptive optics images of ε Indi Ba,Bb	67
2.11	H -band spectra of ε Indi Ba and ε Indi Bb	68
3.1	Location of the KPNO/MOSA fields-of-view in the α Per cluster	74
3.2	Location of known α Per members in the (ra, dec) frame	77
3.3	Colour-magnitude ($I_c, I_c - R_c$) for α Per	80
3.4	Luminosity function of the α Per cluster	81
3.5	Mass function of the α Per cluster	83
3.6	Completeness limits of the near-infrared wide-field survey	86
3.7	Matching of the optical and near-infrared catalogues	88
3.8	Colour-magnitude ($K', I_c - K'$) of the 0.7 deg ² area in α Per	89
3.9	Zoom of the colour-magnitude ($K', I_c - K'$)	91
3.10	Colour-colour (($I_c - K'$),($R - I$) _c) of the 0.7 deg ² area in α Per	92
3.11	Zoom of the colour-colour ($I_c - K'$,($R - I$) _c)	93
3.12	Optical spectroscopy of cluster member candidates in α Per	99
3.13	$H\alpha$ equivalent widths versus spectral type	101
3.14	Gravity features equivalent widths versus spectral type	102

4.1	Location of the Collinder 359 cluster in the constellation of Ophiuchus	111
4.2	Location of the CFH12K fields-of-view in the cluster	114
4.3	Background, psf, and residual images created by SExtractor	119
4.4	I magnitude offsets between the CFHT short, medium, and long exposures	123
4.5	Offsets between the CFHT and DENIS I magnitudes	124
4.6	Colour-magnitude diagram ($I, I-z$) for Collinder 359	126
4.7	Distribution of the probable member candidates in Collinder 359	130
4.8	($I, I-K$) diagram for the optically-selected cluster member candidates	136
4.9	($I-z, I-K$) colour-magnitude diagram for the cluster member candidates	139
4.10	Vector point diagrams for Collinder 359	141
4.11	Age determination of the supergiants, Alpha Per and 67 Oph	142
4.12	Vector point diagram and colour-magnitude diagram for proper motion candidates	144
4.13	Luminosity function for Collinder 359 for an age of 80 Myr and a distance of 500 pc	145
4.14	Mass functions for Collinder 359 for different age and distances	149
4.15	Comparison of the Collinder 359 mass function with other open clusters	152
A.1	Consistency of the optical spectral indices with spectral type	201
A.2	Low-resolution spectroscopy of proper motions objects earlier than M5.0	202
A.3	Low-resolution spectroscopy of proper motions objects spanning M5.5–M8.5 .	203
A.4	Near-infrared spectroscopy of 26 proper motion objects	204
C.1	Finding chart for cluster member candidates in Collinder 359 (Field A CCD00 top)	232

List of Tables

1.1	Determination of substellar IMF in open clusters and in star-forming regions	8
1.2	Spectral indices for optical classification of M and L dwarfs	23
1.3	Near-infrared spectral indices for the classification of L dwarfs	24
1.4	Near-infrared spectral indices for the classification of T dwarfs	26
1.5	Low-mass stellar and brown dwarf companions to K, G, M, and L dwarfs	31
1.6	List of all brown dwarf binaries discovered to date and their parameters	32
2.1	Characteristics of the six subdwarfs found in the proper motion survey	57
2.2	Astrometry and photometry of two M dwarfs and 3 ultracool dwarfs	61
3.1	Optical fields-of-view observed in α Per along with near-infrared follow-up	78
3.2	New infrared-selected cluster candidates in α Per	94
3.3	Spectroscopic data of α Per member candidates	97
4.1	Regions observed within the framework of the CFHT Key Programme	108
4.2	Latest status of the bright stars in Collinder 359 (before 2000)	112
4.3	Observing logs of Collinder 359	115
4.4	Offsets between the I and z short exposure images	117
4.5	Offsets between the I and z medium exposure images	117
4.6	Offsets between the I and z long exposure images	117
4.7	Colour shifts between individual chip for the short exposures	121
4.8	Colour shifts between individual chip for the medium exposures	121
4.9	Colour shifts between individual chip for the long exposures	122
4.10	List of candidates in Collinder 359 for different (distance, age) combinations	128
4.11	List of cluster member candidates observed in the K -band	133
4.12	List of standard stars observed within the framework of the CFHTIR follow-up .	134
4.13	Values for the luminosity function and mass function in Collinder 359	147
4.14	Dependence of the power law index α with distance and age	149
A.1	Names, coordinates, and proper motions of all proper motion objects	195
A.2	Names, magnitudes, spectral types, and distances of all proper motion objects . .	197
A.3	Spectral indices and spectral types of proper motion objects	199
B.1	All optically-selected cluster member candidates in Collinder 359	206

List of acronyms

2MASS	2 Micron All-Sky Survey
ACS	Advanced Camera for Surveys on the <i>Hubble Space Telescope</i>
APM	Automatic Plate Measuring
ARICNS	Astronomisches Rechnen Institut Heidelberg Data Base for Nearby Stars
AU	Astronomical Units
CCD	Charge Coupled Device
CDS	Centre de Données Astronomiques de Strasbourg
CONICA	High Resolution Infrared Camera and Spectrograph on the Very Large Telescope
DARWIN	The Infrared Space Interferometry Mission
DENIS	DEep Near-Infrared Survey
DOLORES	Device Optimized for the LOw RESolution on the Telescopio Nazionale di Galileo
EC-RTN	European Commission Research Training Network
EFOSC2	ESO Faint Object Spectrograph and Camera (v.2) on the ESO 3.6-m telescope
EROS	Expérience pour la Recherche d'Objets Sombres
ESO	European Southern Observatory
FORS	FOocal Reducer/low dispersion Spectrograph on the Very Large Telescope
GSC	Guide Star Catalogue
HST	Hubble Space Telescope
IAU	International Astronomical Union
IDL	Interactive Data Language
IMF	Initial Mass Function
IPAC	Infrared Processing and Analysis Center
ISAAC	Infrared Spectrometer And Array Camera on the Very Large Telescope
ISO	Infrared Space Observatory
KPNO	Kitt Peak National Observatory
LHS	Luyten Catalogue of Stars with Proper Motions Exceeding 0.5"/yr Annually
LRIS	Low-Resolution Imaging Spectrograph on the Keck 10-m telescope on Mauna Kea
MMT	Multiple Mirror Telescope on Mount Hopkins, Arizona
MOA	Microlensing Observations in Astrophysics
MOSA	MOSAIC Imager on the Kitt Peak National Observatory 4-m telescope
MPS	Microlensing Planet Search
NAOS	Nasmyth Adaptive Optics System on the ESO Very Large Telescope on Paranal, Chile
JWST	James Webb Space Telescope
NLTT	New Luyten Catalogue of Stars with Proper Motions larger than Two-Tenths of an Arcsec
NTT	New Technology Telescope on La Silla, Chile

OGLE	Optical Gravitational Lensing Experiment
PLANET	Probing Lensing Anomalies NETwork
PSF	Point Spread Function
RAVE	RAdial Velocity Experiment on the 1.2-m UKST of the Anglo-Australian Observatory
ROSAT	Röntgen Satellite
SDSS	Sloan Digital Sky Survey
SED	Spectral Energy Distribution
SofI	Son of Isaac on the New Technology Telescope
TNG	Telescopio Nazionale di Galileo on La Palma, Canary Islands
TPF	Terrestrial Planet Finder
UCAC	USNO CCD Astrograph Catalog
UKIDSS	UKIRT Infrared Deep Sky Surveys
UKST	United Kingdom Schmidt Telescope of the Anglo-Australian Observatory
USNO	United States Naval Observatory
VISTA	Visible Infrared Survey Telescope for Astronomy on Paranal, Chile
VLT	Very Large Telescope, on Paranal, Chile
WHT	William Herschel Telescope, on La Palma, Canary Islands
WIRCam	Wide-field InfraRed Camera for CFHT
WYFFOS	Wide Field Fibre Optical Spectrograph on the 4.2-m William Herschel Telescope
ZAMS	Zero-Age Main-Sequence

Version française

Introduction

Les étoiles, quelle que soit leur masse, naissent de la fragmentation des nuages moléculaires et de l'effondrement gravitationnel des fragments formés. Les étoiles, définies comme des objets dont la masse excède 0.072 fois la masse du Soleil, après une phase de contraction, passent la grande majorité de leur vie sur la "séquence principale". Elles sont alors en équilibre hydrostatique car l'énergie produite par la fusion nucléaire empêche l'effondrement gravitationnel de l'étoile.

En revanche, les objets de métallicité solaire dont la masse est inférieure à 0.072 masse solaire n'atteindront jamais des températures et des pressions centrales suffisantes pour déclencher la fusion de l'hydrogène. Ces objets sont appelés naines brunes. Leur luminosité est très faible et décroît inexorablement au cours du temps, ce qui rend leur détection difficile. En conséquence, les naines brunes sont restées indétectables pendant les trente années qui ont suivi leur prédition théorique. L'avènement des grands télescopes, des détecteurs à grand champ et des cartographies du ciel à grande échelle a permis la découverte de centaines de naines brunes isolées dans le voisinage solaire, en tant que compagnons d'étoiles de faible masse, mais aussi dans les amas ouverts et les régions de formation d'étoiles.

Le nombre d'étoiles formées par unité de masse est appelé la fonction initiale de masse (Initial Mass Function, IMF). Cette grandeur a été définie dans l'étude pionnière de Salpeter en 1955. L'IMF a été étudiée lors des dernières décennies dans plusieurs régions du ciel et sur un grand intervalle de masse afin d'examiner sa dépendance avec l'âge et l'environnement. En effet, la forme de l'IMF pour les faibles et les fortes masses est importante car elle permet de contraindre les processus de formation des étoiles. C'est malheureusement dans ces régions du spectre de masse que les données sont le plus difficile à interpréter car, d'une part, les étoiles massives sont rares et possèdent une courte durée de vie et, d'autre part, les étoiles de faible masse et les naines brunes sont peu lumineuses et difficiles à détecter.

Les amas ouverts et les régions de formation d'étoiles sont généralement de taille modeste et représentent une population de même âge et de même métallicité située à la même distance du Soleil. Par conséquent, de nombreuses études se sont concentrées sur ces régions pour tenter de déterminer s'il existait un changement de pente près de la transition étoile-naine brune. Comme, de plus, les étoiles de faible masse et les naines brunes sont intrinsèquement plus lumineuses quand elles sont jeunes, leur détection est plus aisée dans les amas jeunes comme les Pléiades, α Per, le Trapèze d'Orion, IC348 et σ Orionis que dans le voisinage solaire. Les diverses études menées dans ces amas indiquent que l'IMF croît rapidement des étoiles de grande masse aux étoiles de masse solaire, elle croît ensuite plus lentement pour atteindre un maximum vers 0.1–0.2,masse

solaire avant de décliner dans le domaine sous-stellaire.

Un autre volet de l'étude de l'IMF concerne la recherche de sa variation avec les conditions physiques régnant dans le lieu de formation. Par exemple, une cartographie à grand champ menée récemment dans le nuage du Taureau a révélé un déficit de naines brunes dans cette région de faible densité par rapport aux études effectuées dans IC348 et le Trapèze d'Orion. Cette différence suggère qu'il existe une variation de l'IMF avec les propriétés physiques de l'environnement.

Cette thèse a pour but d'approfondir l'étude de l'IMF, particulièrement pour les étoiles de faible masse et les naines brunes, et ses variations avec l'environnement. Pour cela, les résultats de trois cartographies indépendantes, dédiés à la recherche d'étoiles de faible masse et de naines brunes dans le voisinage solaire et dans deux amas d'étoiles jeunes, α Per et Collinder 359, sont détaillés dans ce manuscrit.

Le chapitre 1 offre un aperçu des connaissances actuelles sur les naines brunes, à la fois théoriques et observationnelles. La physique des naines brunes est décrite et les divers mécanismes de formation récemment proposés passés en revue. La définition de l'IMF est donnée et son importance dans le domaine sous-stellaires abordée. La partie observationnelle fait un point sur les caractéristiques photométriques et spectroscopiques des naines ultra-froides découvertes au cours des dix dernières années. Enfin, les déterminations de l'IMF sous-stellaire dans les amas jeunes et les régions de formation d'étoiles sont analysées.

Le chapitre 2 présente les résultats photométriques et spectroscopiques d'un échantillon de candidats du voisinage solaire sélectionnés sur la base de leur grand mouvement propre et de leur couleur. Ces objets sont en majorité des naines M situées à moins de 50 parsecs du Soleil. Les résultats généraux de l'étude sont décrits et une attention particulière est portée sur certains objets singuliers.

Le chapitre 3 présente les résultats d'une cartographie dans le proche infrarouge d'une région de 0.7 degré carré dans α Per, un amas analogue aux Pléiades. De nouveaux candidats stellaires et sous-stellaires ont été extraits des diagrammes couleur-magnitude et couleur-couleur, combinant des données photométriques dans les domaines visible et proche infrarouge. Les données spectroscopiques dans le domaine visible d'une trentaine de candidats, sélectionnés par leur propriétés photométriques, sont analysées pour vérifier leur appartenance à l'amas.

Le chapitre 4 est dédié à l'étude d'un amas pré-séquence principale peu étudié par le passé, Collinder 359. Une cartographie dans le domaine visible de 1.6 degré carré dans Collinder 359 a permis d'extraire des candidats membres de l'amas dont les masses sont comprises entre 1.3 et 0.04 masse solaire. Les données photométriques dans le proche infrarouge des candidats, à partir du catalogue 2MASS et d'observations faites au CFHT, sont également analysées. Les résultats de cette cartographie visible, combinée à l'étude du mouvement propre de l'amas, ont permis de préciser l'âge de l'amas ainsi que sa distance. D'autre part, nous avons montré que la fonction de masse de Collinder 359 présente une pente plus faible que celles estimées pour les Pléiades et α Per.

Le chapitre 5 présente la marche à suivre pour extraire une liste de membres d'amas ouverts. Les principaux critères permettant de distinguer les objets pré-séquence principale des étoiles du champ, tels que le mouvement propre, la photométrie et la spectroscopie dans les domaines visible et infrarouge et les observations en rayons X, sont passés en revue. Les futures observations et

perspectives pour les amas α Per et Collinder 359 sont également abordées et placées dans un contexte plus large.

Le chapitre Conclusions et Perspectives présente le bilan de ce travail de thèse et décrit les observations et études à mener dans le futur au regard des résultats obtenus avec celles analysées dans ce manuscrit.

F-1 Théorie et observation des naines brunes

Kumar (1963) a été le premier à prédire l'existence d'objets dont la masse est inférieure à 0.08 masse solaire. Hayashi & Nakano (1963) ont également contribué à la compréhension de ces objets de faible luminosité, appelés à l'origine "naines noires". Cette dénomination était cependant déjà utilisée pour les naines blanches très âgées. En conséquence, Tarter (1976) a proposé le terme de "naines brunes" du fait de la complexité de leur atmosphère, dénomination rapidement acceptée par les astronomes.

L'optimisation des équations d'état et la meilleure connaissance de l'atmosphère des naines brunes ont permis de localiser avec précision la limite étoile-naine brune à 0.072 masse solaire. Les données spectroscopiques acquises au cours des dernières années montrent que les naines brunes ne sont pas de couleur brune mais de couleur violette. Cette couleur s'explique par la présence de sodium deutéré dans l'atmosphère, qui supprime les couleurs vertes. Comme les raies de cette molécule sont en absorption, la couleur des naines brunes correspond à la couleur complémentaire du mélange des longueurs d'ondes émergentes.

F-1.1 Présentation théorique des naines brunes

Les étoiles sont des sphères de gaz composées à 73 % d'hydrogène, 25 % d'hélium et 2 % de métaux (pourcentages donnés en masse). Les étoiles restent en équilibre hydrostatique une grande partie de leur vie car l'énergie produite par les réactions nucléaires en empêche son effondrement gravitationnel. En revanche, les naines brunes de métallicité solaire, dont la masse est inférieure à 0.072 masse solaire, n'atteindront jamais des températures et des pressions centrales suffisantes pour transformer l'hydrogène en hélium. Les objets sous-stellaires dont la masse est supérieure à 0.013 masse solaire brûlent le deutérium selon la réaction $p + d \rightarrow \gamma + {}^3\text{He}$. Les naines brunes plus massives que 0.065 masse solaire brûlent leur lithium pendant une courte période de leur vie et de manière instable selon les réactions $p + {}^7\text{Li} \rightarrow 2\alpha$ et $p + {}^6\text{Li} \rightarrow \alpha + {}^3\text{He}$.

Les coeurs de naines brunes représentent un mélange d'hydrogène et d'hélium moléculaire. L'atmosphère des naines brunes est principalement composée d'hydrogène, d'hélium, de carbone, d'oxygène et d'azote. Leur distribution spectrale d'énergie est fortement influencée par des bandes moléculaires de vapeur d'eau et de méthane, des raies d'absorption d'alcalins neutres et de métaux hydrogénés ainsi que par la présence de grains de poussière.

L'équilibre entre l'énergie nucléaire et l'effondrement gravitationnel conduit à la stabilisation de la luminosité, de la température effective et du rayon d'une étoile après quelques millions d'années. Au contraire, la luminosité et la température effective des naines brunes diminuent inexorablement avec le temps (Figure 1.2). Par exemple, la luminosité d'une naine brune de 0.03 masse solaire décroît de 10^{-2} L_\odot à $6 \times 10^{-6} \text{ L}_\odot$ entre un million et un milliard d'années. De même, sa température décroît de 2800 à 900 Kelvins. Le rayon des naines brunes décroît avec

l’âge à une masse donnée puis atteint un plateau pour des âges supérieurs à un milliard d’années. Par exemple, le rayon d’une naine brune de 0.03 masse solaire passe de 4.3 fois celui de Jupiter à une fois celui de Jupiter entre un million et un milliard d’années. Par ailleurs, le rayon croît avec la masse pour les naines brunes plus jeunes que 100 millions d’années puis la relation s’inverse ce qui rend les objets sous-stellaires peu massifs plus larges.

Les étoiles sont issues de l’effondrement gravitationnel de fragments d’un nuage moléculaire. Plusieurs phases évolutives se succèdent pendant lesquelles la matière circumstellaire est progressivement accrétée par l’objet central. Son évolution est ensuite décrite par une phase pré-séquence principale avant d’amorcer la fusion de l’hydrogène.

L’extension du mécanisme de formation d’étoiles aux naines brunes pose deux problèmes. Premièrement, l’effondrement gravitationnel d’un nuage moléculaire intervient lorsque sa masse excède celle de Jeans. Les observations montrent cependant que cette masse de Jeans est typiquement dix fois supérieure à la masse des naines brunes. Deuxièmement, la phase d’accrétion doit être interrompue à un moment donné pour empêcher l’objet central de devenir une étoile.

En conséquence, plusieurs mécanismes ont récemment été proposés pour expliquer la formation des naines brunes comme par exemple:

1. Extension du scénario de fragmentation des nuages moléculaires par gravo-turbulence aux naines brunes (Mac Low & Klessen 2004).
2. Irradiation de coeurs pré-stellaires par des étoiles massives appartenant aux associations OB (Whitworth & Zinnecker 2003; communication personnelle).
3. Instabilités gravitationnelles de disques pré-stellaires jeunes et massifs (Watkins et al. 1998a, 1998b; Boss 1998, 2000, 2001; Li 2002).
4. Ejection de la composante la moins massive de systèmes multiples jeunes (Reipurth & Clarke 2001; Bate et al. 2002; Sterzik & Durisen 2003).
5. Formation au sein d’un disque circumstellaire comme les planètes géantes de notre Système Solaire (Papaloizou & Terquem 2001; Armitage & Bonnell 2002).

L’étude de la forme de l’IMF sur un grand intervalle de masse est primordiale pour comprendre le ou les processus de formation d’étoiles. Un second aspect de l’IMF concerne sa dépendance avec les conditions physiques et le temps. L’étude de l’IMF sous-stellaire dans diverses régions de formation d’étoiles est donc importante pour mieux comprendre l’origine des naines brunes.

L’IMF est définie comme étant le nombre d’étoiles n par unité de volume dans un intervalle de masse m , $m+dm$:

$$\xi(m) = \frac{dn}{dM} = \frac{1}{m(\ln 10)} \frac{dn}{d \log m} \quad \text{étoiles pc}^{-3} M_{\odot}$$

Les approximations les plus utilisées pour représenter l’IMF sont des lois de puissance dont les index x et α sont liés par la relation $x = \alpha - 1$.

$$\xi(m) = m^{-\alpha} \quad \text{et} \quad \xi(\log m) = m^{-x}$$

L'IMF a été étudiée sur un grand intervalle de masse et les plus récentes estimations suggèrent les valeurs $\alpha = 2.7$ pour les étoiles plus massives qu'une masse solaire, $\alpha = 2.2$ entre 1.0 et 0.5 masse solaire et $\alpha = 1.3$ dans l'intervalle 0.5–0.08 masse solaire (Kroupa 2002; Figure 1.1). Les multiples études de l'IMF sous-stellaire dans les amas jeunes convergent vers un index $\alpha = 0.5$ –1.0 en dessous de 0.5 masse solaire (e.g. Bouvier et al. 1998; Figure 1.8).

F-1.2 Présentation observationnelle des naines brunes

Après de multiples efforts dédiés à la recherche d'objets sous-stellaires pendant les trente années qui ont suivi leur prédition théorique, les deux premières naines brunes irréfutables, Gl229B et Teide 1, ont été annoncées en 1995: la première orbitant une naine M (Nakajima et al. 1995) et la seconde dans l'amas des Pléiades (Rebolo et al. 1995). Peu de temps après ces deux découvertes, plusieurs centaines de naines ultra-froides (types spectraux $> M7$) ont été trouvées en moins d'une décennie grâce à l'avènement des cartographies à grande échelle et de larges télescopes. Ces objets ont été découverts isolés dans le voisinage solaire, en tant que compagnons d'étoiles, dans les amas ouverts jeunes et dans les régions de formation d'étoiles.

Plus de 250 naines L et 50 naines T isolées dans le voisinage solaire ont été découvertes par les cartographies à grande échelle comme 2MASS (e.g. Kirkpatrick et al. 2000), DENIS (e.g. Delfosse et al. 1999) et SLOAN (e.g. Leggett et al. 2000). Les études à mouvement propre ont aussi contribué à leur recensement dans le voisinage solaire (Ruiz et al. 1997; Cruz & Reid 2002; Lépine et al. 2002; Scholz et al. 2000). Notre contribution dans ce domaine est détaillée dans le chapitre 2.

Ces découvertes ont poussé les astronomes à compléter le système de classification de Harvard en vigueur par deux nouvelles classes. Leurs caractéristiques photométriques et spectroscopiques des objets appartenant aux classes L et T sont décrites ci-dessous:

1. Les naines L sont des objets plus froids que les naines M, dont les températures sont comprises entre 2200 et 1300 Kelvins. Plus d'un tiers des naines L sont sous-stellaires d'après les modèles théoriques actuels (Baraffe et al. 1998). La disparition des bandes de TiO et VO combinée avec l'apparition de raies d'absorption de métaux hydrogénés et d'alcalins neutres augmentent le flux dans le proche infrarouge (Figure 1.4). La classification dans le visible représente une extension de celle des naines M (Martín 1997; Martín et al. 1999b; Kirkpatrick et al. 1999b). Une classification est aussi disponible dans le proche infrarouge (Table 1.3). La plupart des naines L ont été découvertes par les cartographies 2MASS (Kirkpatrick et al. 2000) et SDSS (Fan et al. 2000). Nous avons aussi découvert plusieurs naines L lors de notre étude à mouvement propre dans le ciel austral (Chapitre 2).
2. Les naines T sont des objets plus froids que les naines L et sont toutes des naines brunes. Leurs températures sont inférieures à 1300 Kelvins. Le flux émergent atteint un maximum vers $1 \mu\text{m}$ du fait de la présence de vapeur d'eau et de méthane dans leur atmosphère. La présence de grains de poussière réduit considérablement le flux dans les domaines visible et proche infrarouge (Figure 1.5). Leur classification est définie dans le proche infrarouge à partir des systèmes développés par Geballe et al. (2002) et Burgasser et al. (2002) (Table 1.4). Les cartographies à grande échelle comme 2MASS (Burgasser et al., 1999, 2000a, 2000b, 2002, 2003b, 2003c) et SDSS (Strauss et al. 1999; Tsvetanov et al. 2000; Leggett et al. 2000; Geballe et al. 2002) ont découvert la majorité de ces objets. Notre contribution

est illustrée dans le chapitre 2 par la découverte de la naine T binaire la plus proche du Soleil (Scholz et al. 2003; McCaughrean et al. 2004).

De nombreuses naines brunes orbitant des étoiles de faible masse ont été récemment trouvées. Les cartographies de vitesse radiale (e.g. Mayor et al. 1992) ont conclu que les naines brunes sont peu fréquentes (0.5 %) à faible séparation (≤ 3 unités astronomiques) autour d'étoiles comparables à notre Soleil. Les récentes imageries à haute résolution menées avec l'optique adaptative au sol (Close et al. 2003; McCaughrean et al. 2004) et le télescope spatial *Hubble* (Reid et al. 2001b; Bouy et al. 2003; Gizis et al. 2003; Burgasser et al. 2003b) ont découvert plusieurs naines brunes orbitant des étoiles de faible masse (Table 1.5) de même que des naines brunes binaires (Table 1.6).

La fréquence des systèmes binaires de faible masse, estimée à 10–15 % est cependant inférieure à celles des naines G ($57 \pm 9\%$; Duquennoy & Mayor 1991) et des naines M ($42 \pm 9\%$; Fischer & Marcy 1992). Par ailleurs, la distribution des séparations et des rapports de masse (Figure 1.6) diffèrent notablement de celle des étoiles de type solaire (Duquennoy & Mayor 1991) et de celle des naines M (Fischer & Marcy 1992). Les naines brunes binaires possèdent de très faibles séparations de l'ordre de 4–8 unités astronomiques et semblent favoriser les systèmes d'égale masse.

Des centaines de naines brunes ont également été découvertes dans les amas ouverts jeunes et dans les régions de formation d'étoiles. Les résultats des estimations de l'IMF dans le domaine sous-stellaire ont conclu:

1. La pente α des Pléiades se situe entre 0.5 et 1.0 dans l'intervalle de masse 0.5–0.03 masse solaire (Bouvier et al. 1998; Martín et al. 1998; Tej et al. 2002; Dobbie et al. 2002; Moraux et al. 2003) en accord avec le résultat obtenu dans α Per (0.59; Barrado y Navascués et al. 2002; Figure 1.8).
2. L'IMF a été estimée dans le domaine sous-stellaire pour les régions suivantes (Figure 1.7): le Trapèze d'Orion (Muench et al. 2002), σ Orionis (Béjar et al. 2001), IC348 (Luhman et al. 2003b), le Taureau (Briceño et al. 2002), ρ Ophiucus (Luhman et al. 2000), et Caméléon (Comerón et al. 2000). La fonction de masse du Taureau fait apparaître une carence de naines brunes par rapport aux autres régions qui suggère une possible variation de l'IMF avec l'environnement.

Notre contribution dans ce domaine est détaillée dans les chapitres 3 et 4, dédiés aux amas ouverts jeunes α Per et Collinder 359.

F-2 Recherche d'étoiles de faible masse et de naines brunes par mouvement propre dans le ciel austral

Une recherche d'objets à grand mouvement propre a été initiée dans le ciel austral pour des déclinaisons inférieures à -33° par Scholz et al. (2000). Les données photométriques, disponibles dans les filtres B_J et R , sont issues de plaques photographiques. Les magnitudes limites respectives sont approximativement $B_J = 22.5$ mag et $R = 21$ mag. Deux époques, séparées par une quinzaine d'années sont disponibles, permettant la détection d'objets dont le mouvement propre est compris entre 0.3 et 1.0 secondes d'arc par an. La méthode initiale a révélé des naines blanches

ainsi que des naines de type K et M dans le voisinage solaire. Cette technique a ensuite évolué vers la recherche d'objets de faible masse et de naines brunes proches du Soleil.

Le chapitre 2 présente les résultats photométriques et spectroscopiques pour un échantillon de 70 objets sélectionnés pour leur large mouvement propre et leur couleur semblable à celle d'étoiles de faible masse (Table A.1). Les données spectroscopiques dans le domaine visible (6000–10000 Å) des candidats sélectionnés ont été obtenues avec différents télescopes et instruments comme VLT/FORS1 et ESO 3.6-m/EFOSC2 (Figures 2.1, A.2, A.3). Les données spectroscopiques dans le domaine infrarouge (1.0–2.5 μ m) ont été acquises avec les instruments ISAAC et SofI montés respectivement sur les télescopes VLT et NTT (Figure A.4). La résolution des spectres dans le domaine visible et infrarouge est identique pour l'ensemble de l'échantillon, de l'ordre de $R = 600$.

Ce travail est le fruit d'une collaboration au sein du groupe "Star and Planet Formation" de l'AIP entre Ralf-Dieter Scholz, Mark McCaughrean et moi-même. Les résultats présentés dans ce chapitre ont été publiés dans plusieurs articles:

1. Lodieu, Scholz, & McCaughrean (2002b) a reporté la découverte de trois naines L dans le voisinage solaire.
2. McCaughrean, Scholz, & Lodieu (2002b) a trouvé deux naines M tardives à moins de 10 pc.
3. Scholz, Lodieu, Ibata et al. (2004) a présenté la découverte d'une naine M active orbitant un système binaire situé à environ 20 parsecs.
4. Scholz, McCaughrean, Lodieu, & Kuhlbrodt (2003) et McCaughrean et al. (2004) ont découvert la naine brune binaire la plus proche du Soleil, ε Indi Ba/Bb.
5. Une publication est en préparation pour présenter l'ensemble des résultats exposés dans ce chapitre (Lodieu et al. 2004)

Les principaux résultats de cette étude sont détaillés ci-après. Nous avons attribué un type spectral à chacun des 70 candidats sélectionnés selon les systèmes de classification développés par Martín et al. (1999b) et Kirkpatrick et al. (1999b). Nous avons calculé plusieurs indices spectraux mesurant la force des bandes moléculaires et des raies d'absorption par rapport au continuum voisin. Les spectres ont également été comparés à ceux de naines M et L dites standards, dont le type spectral est connu avec une grande précision. Les types spectraux dérivés par ces deux méthodes sont en bon accord et donnés dans la Table A.1.

Nous avons répertorié 6 sous-naines, 10 naines M de type spectral inférieur à M5, 47 naines M tardives (M5.5–M9.5), 4 naines L et une naine T binaire. Tous ces objets sont situés à moins de 50 parsecs (Figure 2.2).

Parmi les 52 étoiles dont un spectre a été obtenu dans le domaine visible, plus de la moitié présentent une émission en H α à 6563 Å. Dix huit d'entre elles possèdent des largeurs équivalentes supérieures à 5 Å, certaines atteignant 15 Å (Figure 2.3). Les étoiles les plus actives ont des types spectraux M7–M8, en accord avec des résultats antérieurs (Hawley et al. 1996; Gizis et al. 2000).

Nous avons également mesuré le flux contenu dans les raies d'absorption des doublets du potassium (K I) et du sodium (Na I) respectivement situés à 7665/7699 Å et 8183/8195 Å. Les largeurs équivalentes de ces doublets, qui sont sensibles à la gravité d'un objet, atteignent aussi un maximum pour des étoiles de type spectral M7–M8 (Figure 2.4).

Parmi l'échantillon de naines ultra-froides découvertes au cours de notre étude, plusieurs objets intéressants ont fait l'objet d'une publication et méritent une attention particulière:

1. Six sous-naines à grand mouvement propre, dont la métallicité est inférieure à celle du Soleil ($[Fe/H]$ compris entre -1.0 et -2.0), ont été découvertes dans notre échantillon. Deux objets ont été classifiés sous-naines ($[Fe/H] = -1.0$) et quatre autres extrêmes sous-naines ($[Fe/H] = -2.0$) grâce aux indices spectraux définis par [Gizis \(1997\)](#) et leurs spectres dans le domaine visible (Figure 2.5). Les distances sont comprises entre 40 et 350 parsecs et les masses estimées entre 0.08 et 0.15 masse solaire (Table 2.1), d'après les modèles théoriques de [Baraffe et al. \(1997\)](#).
2. Deux naines M tardives ont été trouvées à moins de 10 parsecs ([McCaughrean, Scholz, & Lodieu 2002b](#)) grâce à leur mouvement propre supérieur à 0.3 secondes d'arc par an. Les spectres de ces deux objets, obtenus dans le domaine visible, suggèrent des types spectraux respectifs M7.5 et M8 (Figure 2.7 et Table 2.2). [Cruz et al. \(2003\)](#) a récemment déduit un type spectral M7 pour les deux objets, confirmant une distance inférieure à 10 parsecs.
3. Trois naines L ont été découvertes dans le voisinage solaire grâce au catalogue à grande échelle SuperCOSMOS Sky Surveys ([Lodieu, Scholz, & McCaughrean 2002b](#)). Nous avons assigné à SSSPM J0109–5101, SSSPM J2310–1759 et SSSPM J0219–1939 des types spectraux respectifs M8.5, M9.5, et L1 (Table 2.2), d'après les spectres obtenus à la fois dans le domaine visible et proche infrarouge (Figure 2.7). Les distances ont été estimées entre 30 et 40 parsecs par comparaison avec des naines ultra-froides qui possèdent une parallaxe trigonométrique.
4. Nous avons découvert la naine T la plus brillante et la plus proche du Soleil, ε Indi B. [Scholz et al. \(2003\)](#) annonça une naine T à 3.626 parsecs, orbitant l'étoile ε Indi A à une distance d'environ 1500 unités astronomiques. Nous avons assigné à ce nouvel objet un type spectral T2.5 suite à l'acquisition de son spectre dans le domaine infrarouge (Figure 2.9). L'imagerie à haute résolution obtenue avec l'optique adaptative du VLT a montré que ε Indi B est en fait une binaire dont les deux composantes sont séparées par 2.65 unités astronomiques à la distance du système (Figure 2.10). La spectroscopie acquise dans le domaine infrarouge en bande H nous a permis d'assigner des types spectraux respectifs T1 et T6 à ε Indi Ba et ε Indi Bb (Figure 2.11), d'après les systèmes de classification définis par [Burgasser et al. \(2002\)](#) et [Geballe et al. \(2002\)](#). Les masses de chaque composante sont estimées à 47 ± 10 et 28 ± 7 masses de Jupiter et les températures effectives de $\sim 1300 \pm 40$ et $\sim 900 \pm 20$ Kelvins ([McCaughrean et al. 2004](#)).
5. Une naine M tardive, APMPM J2354–3316C, a été découverte par [Scholz et al. \(2003\)](#) orbitant un système composé d'une naine M4 et d'une naine blanche. Cet objet possède un mouvement propre identique à celui du système, dont la distance photométrique est estimée à 21 parsecs (catalogue ARICNS). Nous avons obtenu deux spectres de ce compagnon dans le domaine visible à deux époques différentes (3 October 1999 et 25 November 2001). La différence entre ces deux spectres est frappante (Figure 2.6). D'une part, le second spectre présente une large raie d'émission en $H\alpha$ de largeur équivalente égale à 61.4 ± 5.0 Å et, d'autre part, un large continuum dans le bleu ($\lambda \leq 7500$ Å) est observé. Ces caractéristiques sont également observées dans le spectre de LHS 2397a ([Bessell 1991](#)). Une image haute résolution de cet objet a révélé un compagnon sous-stellaire à moins de 4

unités astronomiques (Freed et al. 2003), susceptible d'expliquer la présence de H α et du continuum dans le bleu.

F-3 Nouveaux membres stellaires et sous-stellaires dans α Per

Les premières sections du chapitre 3 font le point des connaissances acquises sur α Per, un amas ouvert analogue aux Pléiades. Son mouvement propre ($\mu_\alpha = 23$ et $\mu_\delta = -25$ millièmes de secondes d'arc par an respectivement en ascension droite et en déclinaison) combiné à la photométrie optique a établi une liste de membres appartenant à l'amas les moins massives ayant un type spectral égal à M5 (Heckmann et al. 1956; Stauffer et al. 1985, 1989b; Prosser 1992, 1994). De nombreuses observations en rayons X ont été menées dans cet amas et ont permis la découverte de nouveaux membres (Randich et al. 1996; Prosser et al. 1996a). Le test du lithium, proposé par Rebolo et al. (1992), a été récemment appliqué à α Per par Stauffer et al. (1999). Son âge a été estimé à 90 ± 10 millions d'années, deux fois la valeur déterminée par le turn-off de la séquence principale (e.g. Mermilliod 1981).

Une cartographie profonde dans le domaine visible de 4.5 degrés carrés dans α Per a extrait environ 100 nouveaux candidats dont les masses sont comprises entre 0.3 et 0.035 masse solaire (Barrado y Navascués et al. 2002). Ces candidats ont été classifiés sur la base de leur photométrie visible et infrarouge comme suit: 54 membres probables, 12 membres possibles et 26 objets rejetés. La liste de candidats probables de l'amas a été utilisée pour déduire la fonction de luminosité de α Per (Figure 3.4; Barrado y Navascués et al. 2002). Sa fonction de luminosité a été transformée en fonction de masse par l'intermédiaire de plusieurs modèles théoriques dont celui de Baraffe et al. (1998). La fonction de masse a été reproduite par une loi de puissance de pente $\alpha = 0.59 \pm 0.05$ sur l'intervalle de masse 0.35–0.035 masse solaire (Figure 3.5; Barrado y Navascués et al. 2002).

Ce travail sur α Per est le fruit d'une collaboration entre Mark McCaughrean (Potsdam), Jérôme Bouvier (Grenoble), David Barrado y Navascués (Madrid) John Stauffer (Pasadena) et moi-même. Une partie des résultats présentés dans ce chapitre a été publiée dans plusieurs articles:

1. Barrado y Navascués et al. (2002) où la photométrie infrarouge présentée dans ce chapitre a été utilisée pour séparer les membres de l'amas des objets du champ.
2. Lodieu et al. (2003) a énoncé les résultats de la cartographie proche infrarouge d'une région de 0.7 degré carré dans α Per (conférence proceedings).
3. Lodieu et al. (2004, en préparation) sera dédié à la cartographie proche infrarouge exposée dans ce chapitre.

Le chapitre 3 présente les résultats d'une cartographie proche infrarouge faite avec le filtre K' à $2.12\text{ }\mu\text{m}$ d'une surface totale de 0.7 degré carré dans α Per (Figure 3.1 et Table 3.1). Les observations ont été obtenues avec la caméra infrarouge grand champ, Omega-Prime, montée sur le télescope de 3.5-m à l'observatoire de Calar Alto en Espagne. La réduction des données comporte toutes les étapes usuelles pour des images proche infrarouge: soustraction d'un fond de ciel, division par une carte de champ plat et moyenne de toutes les images. Le flux de chaque étoile a été estimé à l'intérieur d'un cercle dont le rayon est de l'ordre de la largeur à mi-hauteur

du profil de l'étoile. Les calibrations photométrique et astrométrique ont été obtenues à l'aide du catalogue à grande échelle 2MASS.

Un total de 22129 sources a été extrait de la corrélation des catalogues visible et infrarouge. La sélection d'objets à gauche des isochrones NextGen (Baraffe et al. 1998) dans le diagramme couleur-magnitude ($K', I_c - K'$) a extrait 103 nouveaux candidats en assumant une distance de 182 parsecs et un âge de 90 millions d'années pour α Per (Figure 3.9 et Table 3.2). La localisation de ces nouveaux candidats dans le diagramme couleur-couleur ($(I_c - K'), (R - I)_c$) a démontré que près de 70 % sont des géantes qui contaminent notre échantillon (Figure 3.11). La moitié des candidats restant ont été précédemment classifiés comme candidats probables de α Per par Barrado y Navascués et al. (2002). Les 16 candidats restants sont de nouveaux membres probables de α Per dont les magnitudes en bande I comprises entre 15.5 et 21.0 (Figure 3.9 et Table 3.2). La sélection de candidats entre les isochrones NextGen (Baraffe et al. 1998) et Dusty (Chabrier et al. 2000b) a permis d'extraire 3 nouvelles naines brunes comme membres possibles de l'amas (Table 3.2). Tous ces nouveaux candidats nécessitent cependant l'obtention d'un spectre dans le domaine visible afin de vérifier leur appartenance à l'amas.

Nous avons également analysé les spectres visibles (5800–8800 Å) de 29 candidats dans α Per extraits par Barrado y Navascués et al. (2002). L'échantillon contient 24 membres probables, 1 membre possible et 4 objets n'appartenant pas à l'amas. La spectroscopie, de résolution modérée ($R \sim 2000$), a été obtenue avec le spectrographe Twin sur le télescope de 3.5-m à Calar Alto. La réduction des données spectroscopiques comporte les étapes suivantes: soustraction d'un fond de ciel, division par une carte de champ plat, élimination des rayons cosmiques, extraction d'un spectre unidimensionnel, et enfin calibration en longueur d'onde et en flux grâce à l'observation dans les mêmes conditions d'étoiles spectrophotométriques.

Nous avons assigné à chaque objet un type spectral selon les systèmes de classification définis par Martín et al. (1999b) et Kirkpatrick et al. (1999b). Chaque spectre a également été comparé à des étoiles dont le type spectral est connu à une sous-classe près. Tous les candidats probables ont des flux, des types spectraux, des raies d'émission H α (largeur équivalente comprise entre 4.0 et 15.0 Å) et des indices de gravité confirmant leur appartenance à α Per. Le membre possible et les candidats non membres de α Per, dont un spectre a été obtenu dans le domaine visible, sont définitivement exclus car leurs caractéristiques diffèrent de celles d'étoiles jeunes. Nous avons également acquis un spectre visible pour quatre candidats sélectionnés au cours de notre étude. Leurs flux et leurs types spectraux sont cependant incohérents comparés à ceux des membres de l'amas.

Nous avons obtenu un spectre dans le domaine visible pour tous les candidats probables extraits par Barrado y Navascués et al. (2002) dont les masses sont comprises entre 0.4 et 0.12 masses solaires. La pente de la fonction de masse (0.59; Barrado y Navascués et al. 2002), basée uniquement sur les données photométriques visible et proche infrarouge, est désormais confirmée par notre spectroscopie sur l'intervalle de masse 0.4–0.12 masse solaire.

Le travail présenté dans ce chapitre démontre l'efficacité des cartographies menées dans le domaine visible, suivies d'une photométrie dans le proche infrarouge pour distinguer les membres d'un amas ouvert jeune des étoiles de champ. En revanche, la sélection basée uniquement sur un diagramme couleur-magnitude en bandes I et K n'apparaît pas optimale du fait de la large contamination par les étoiles géantes. Deux filtres en bande visible sont préférables pour optimiser l'extraction d'objets pré-séquence principale. Les cartographies restent cependant très efficaces

dans les régions de formation d'étoiles comme le Trapèze d'Orion (Hillenbrand 1997) ou le Serpens (Lodieu et al. 2002a).

F-4 L'amas ouvert jeune Collinder 359

Le chapitre 4 est dédié à l'amas ouvert pré-séquence principale Collinder 359. Cet amas a été observé dans le cadre d'un large programme mené avec la caméra CFH12K du télescope Canada-France-Hawaii. Ce projet a été supporté par le réseau européen “The Formation and Evolution of Young Stellar Clusters” pour examiner la dépendance de la fonction de masse stellaire et sous-stellaire avec l'âge et l'environnement. Quatre amas ouverts pré-séquence principale, dont Collinder 359, quatre régions de formation d'étoiles et les Hyades ont été observés pendant les 30 nuits attribuées à ce projet (Table 4.1). Les résultats présentés dans ce chapitre sont le fruit d'une collaboration entre plusieurs membres d'instituts appartenant au réseau européen. Les résultats relatifs à Collinder 359 feront partie intégrante d'une publication dans un proche avenir.

Collinder 359 est un amas pré-séquence principale situé autour de l'étoile supergéante 67 Oph dans la constellation du Serpentaire (Melotte 1915; Collinder 1931). Sa distance est estimée à 250 parsecs (Ruciński 1987; Loktin & Beshenov 2001) mais de récentes estimations ont revu cette distance à la hausse 650 parsecs; Kharchenko et al. 2004, communication personnelle). Son âge est estimé à 30 millions d'années (Wielen 1971; Kharchenko et al. 2004). Une recherche dans la littérature montre que cet amas jeune a été peu étudié par le passé, évoquant de larges incertitudes liées à sa distance et à son âge. Par ailleurs, une poignée de membres est connue, tous plus brillants que $V = 10$ mag, dont l'appartenance est incertaine (Table 4.2 et Figure 4.2).

Une surface totale de 1.6 degrés carrés a été observée en bande I et z avec la caméra grand champ du télescope CFH (Figure 4.2 et Table 4.3). Trois séries d'observations de 2, 30 et 300 secondes ont été acquises afin de sonder le plus grand intervalle de masse possible. La limite de saturation intervient autour de $I = 12$. Les limites de complétude et de détection sont $I \sim z \sim 22$ et 24. La réduction des données et l'extraction de la photométrie dans le domaine visible ont été achevées avec SExtractor (voir sections 4.3.2 et 4.3.3 pour plus de détails).

Tous les objets situés à gauche des isochrones NextGen (Baraffe et al. 1998) et Dusty (Chabrier et al. 2000b) dans le diagramme couleur-magnitude ($I, I-z$) (Figure 4.6) ont été sélectionnés comme candidats membres de l'amas en assumant une distance de 650 parsecs et un âge de 80 millions d'années. Cette procédure a extrait un total de 1033 candidats dont les magnitudes, comprises entre $I = 12$ et 22.5, correspondent à des masses situées entre 1.3 et 0.040 masses solaires. (Table B.1, Appendix B). La photométrie dans le domaine infrarouge (JHK), disponible pour tous les candidats plus brillants que $I = 17$, a permis d'éliminer certains objets sur la base de leur couleur $I-K$ (Figure 4.8). Nous avons également présenté la photométrie en bande K' , obtenue avec la caméra infrarouge du télescope CFH pour 39 candidats supplémentaires, dont la magnitude est comprise entre $I = 17$ et $I = 22$, afin d'examiner la contamination vers les faibles masses.

Nous avons exploré les incertitudes liées à la distance et l'âge de Collinder 359 en combinant notre photométrie dans le domaine visible avec le catalogue UCAC2 (USNO CCD Astrograph Catalog) qui fournit le mouvement propre d'étoiles dont la déclinaison est inférieure à $+40^\circ$ (Zacharias et al. 2003). Nous avons tout d'abord démontré que l'existence de l'amas est non équivoque. Le diagramme à mouvement propre (Figure 4.10) fait apparaître la présence de deux groupes d'étoiles. Le premier caractérise les étoiles de champ et le second, localisé à $(0.0, -8.5)$

millisecondes d'arc par an, traduit la présence de Collinder 359. Nous avons ensuite estimé l'âge de l'amas entre 50 et 90 millions d'années en comparant la position de 67 Oph aux isochrones de métallicité solaire qui inclue un overshoot modéré (Figure 4.11). Nous avons enfin déduit une distance de 500 ± 100 parsecs. La position diagramme couleur-magnitude ($I, I-z$) des candidats sélectionnés sur la base de leur mouvement propre et leur photométrie (Figure 4.12) est bien reproduite par les isochrones NextGen (Baraffe et al. 1998) à 80 millions d'années et déplacées à une distance de 500 parsecs.

Considérant une distance de 500 parsecs et un âge de 80 millions d'années pour Collinder 359, nous avons dérivé ses fonctions de luminosité et de masse. La fonction de luminosité (Figure 4.13 et Table 4.13), tracée à partir des candidats sélectionnés par le biais de leur photométrie dans les domaines visible et infrarouge, est caractérisée par:

- Un maximum à $I = 12.5-13.0$ qui correspond à une masse solaire. Une contamination importante par les naines de champ est attendue dans cet intervalle de magnitude. Le déclin de la fonction de luminosité autour de $I = 12$ est la conséquence de notre limite de saturation.
- Un creux autour de $I = 15-16$ qui correspond à 0.6 masse solaire. Son authenticité est à vérifier après l'obtention de la spectroscopie des étoiles brillantes, nécessaires pour éliminer les contaminants.
- Un maximum vers $I = 17.0$ ($M \sim 0.3$ masse solaire) est détecté, comparable à celui observé dans les Pléiades (Jameson et al. 2002) et α Per (Barrado y Navascués et al. 2002) par exemple. La magnitude absolue de ce maximum diffère cependant d'un amas à l'autre.
- Un creux à $I = 20.0-20.5$ ($M \sim 0.07$ masse solaire) dû à la carence de naines M7–M8 observée à la fois dans le voisinage solaire (Reid & Cruz 2002) et les amas ouverts comme les Pléiades (Jameson et al. 2002), IC 2391 (Barrado y Navascués et al. 2001a), σ Orionis (Béjar et al. 2001), le Trapèze d'Orion (Lucas & Roche 2000), et IC348 (Luhman 1999).

Pour transformer la fonction de luminosité en fonction de masse, nous avons utilisé les modèles théoriques NextGen (Baraffe et al. 1998) et Dusty (Chabrier et al. 2000b). Ces isochrones couvrent notre domaine de masse, incluent le traitement des grains de poussière pour des températures effectives inférieures à 2500 K et ont été fréquemment utilisés pour examiner la fonction de masse d'amas ouverts jeunes et les systèmes binaires (White et al. 1999).

La fonction de masse de Collinder 359 présente un creux à 0.07 masse solaire dû à la carence de naines M7–M8 observée dans le voisinage solaire et les amas ouverts (Figure 4.14 et Table 4.13). La forme et la pente de la fonction de masse sont peu sensibles à l'âge et la distance de l'amas. Nous avons estimé la pente α de la fonction de masse, exprimée en $\frac{dN}{dM} \propto M^{-\alpha}$, à 0.3 ± 0.2 . Cette détermination apparaît plus faible que les estimations dans l'amas des Pléiades (0.5–1.0; Bouvier et al. 1998; Martín et al. 1998; Dobbie et al. 2002; Tej et al. 2002) ou α Per (0.59 ± 0.05 ; Barrado y Navascués et al. 2002).

F-5 Futurs plans pour vérifier l'appartenance de candidats à un amas ouvert

Les cartographies dans le domaine visible et proche infrarouge de Collinder 359 et α Per ainsi que les futures observations photométriques et spectroscopiques dans ces régions sont décrites

dans le chapitre 5 et étendues à d'autres amas jeunes. Les diverses observations nécessaires pour extraire une liste de candidats appartenant à un amas ouvert sont passées en revue.

Premièrement, l'étude d'un amas ouvert dans son ensemble est primordiale pour examiner son évolution dynamique. Seuls les amas des Pléiades, σ Orionis et IC348 ont fait l'objet d'une étude statistique conduisant à l'estimation de l'IMF sur la totalité de l'amas (Tej et al. 2002). Les catalogues à grande échelle comme 2MASS, le Guide Star Catalog ou encore le SuperCOSMOS Sky Surveys fournissent les photométries dans le domaine visible et proche infrarouge de même que le mouvement propre d'un grand nombre d'étoiles appartenant aux amas ouverts.

Deuxièmement, la sélection de candidats membres d'un amas par mouvement propre est une technique très efficace, déjà appliquée aux Pléiades (Hambly et al. 1999) et à α Per (Heckmann et al. 1956) par exemple. Les catalogues à grande échelle sont à nouveau d'une grande utilité pour une étude préliminaire des amas ouverts dont le mouvement propre diffère de celui des étoiles de champ. Dans le cas contraire, l'extraction de candidats est uniquement basée sur la photométrie.

Troisièmement, le suivi dans le domaine infrarouge des candidats sélectionnés pour leur photométrie visible est abordé. Les catalogues 2MASS ou DENIS ont été fréquemment utilisés pour obtenir les magnitudes dans le proche infrarouge de candidats appartenant aux amas ouverts et aux régions de formation d'étoiles. Nous avons abondamment tiré profit de ces catalogues dans le cadre des études de α Per et Collinder 359 pour les candidats plus brillants que $K = 14.5$. Les objets les plus faibles nécessitent des observations supplémentaires plus profondes comme celles acquises avec la caméra infrarouge du télescope CFH dans le cadre de l'étude relative à Collinder 359.

Quatrièmement, la spectroscopie visible des candidats photométriques, étape essentielle dans l'étude d'un amas ouvert, fournit des critères supplémentaires permettant de distinguer les membres d'un amas par rapport aux étoiles du champ. Ces critères sont: le type spectral, la gravité, l'activité chromosphérique, l'abondance en lithium et les vitesses radiales et rotationnelles. Des observations spectroscopiques sont prévues en juin 2004 pour tous les candidats plus brillants que $I = 19$ dans Collinder 359 afin de poursuivre notre étude de l'amas et vérifier la forme de la sa fonction de masse.

Cinquièmement, la comparaison des spectres des candidats dans le domaine proche infrarouge avec les récents modèles d'atmosphère développés pour les naines ultra-froides par Allard et al. (2001) fournit une estimation de leur gravité et de leur température effective.

Enfin, l'obtention d'une liste de membres authentiques dans les amas ouverts jeunes permettra d'entreprendre des observations supplémentaires à long terme comme par exemple:

1. Etude de l'émission des membres en rayons X pour étudier l'activité en fonction de la masse.
2. Imagerie à haute résolution pour étudier la fraction de binaires en fonction de la masse.
3. Etude de la variabilité à court et long termes pour mieux comprendre l'atmosphère des étoiles de faible masse et des naines brunes.

Conclusions et perspectives

Nous avons présenté dans cette thèse les résultats de recherches d'étoiles de faible masse et de

naines brunes dans le voisinage solaire et dans deux amas ouverts jeunes, α Per et Collinder 359. Les perspectives relatives à ces trois études sont détaillées ci-dessous.

La sélection d'objets à grand mouvement propre dans le ciel austral à partir de plaques photographiques a révélé un grand nombre de naines ultra-froides situées à moins de 50 parsecs. La spectroscopie dans les domaines visible et proche infrarouge de 70 candidats nous a permis de répertorier 6 sous-naines, 10 naines M de types spectraux inférieurs à M5, 48 naines M tardives, 4 naines L et une naine T binaire. Certains de ces objets offrent de nouvelles opportunités:

1. Les deux naines M tardives situées à 8.0 et 6.4 parsecs représentent une importante addition au sein de l'échantillon de 10 parsecs. Elles constituent également d'excellentes cibles pour la recherche de compagnons de faible masse par imagerie à haute résolution et pour les missions futures dédiées à l'exploration de planètes extrasolaires comme TPF ou DARWIN.
2. Le spectre visible de la naine M8.5 active découverte orbitant le système composé d'une naine M et d'une naine blanche ressemble fortement à celui de LHS2397a. Une imagerie à haute résolution avec l'optique adaptative au sol ou avec le télescope spatial *Hubble* est nécessaire pour vérifier la présence d'un compagnon sous-stellaire à proche séparation.
3. La découverte de la naine T binaire la plus proche du Soleil offre une opportunité unique de tester les isochrones théoriques dans le domaine sous-stellaire. L'éclat de cette binaire va permettre l'obtention d'une spectroscopie haute résolution de bonne qualité pour chaque composante sur un grand intervalle en longueur d'onde. La faible séparation des deux composantes est adéquate pour déterminer les masses individuelles d'ici une quinzaine d'années.

Le chapitre 3 a présenté les résultats d'une cartographie à grand champ dans le domaine proche infrarouge de l'amas ouvert jeune α Per. De nouveaux membres stellaires de l'amas ont été découverts ainsi que quatre naines brunes sélectionnées à partir des données photométriques. Un spectre visible de chaque nouveau candidat est cependant nécessaire pour vérifier leur appartenance à l'amas. Pour étendre la couverture dans α Per et révéler de nouveaux membres dans le domaine sous-stellaire, plusieurs projets sont envisageables, comme:

1. Une cartographie en bande z de l'amas en supplément de celle en bandes R et I afin de démasquer de nouvelles naines brunes (avec MEGACAM par exemple).
2. Etendre la cartographie R , I , et z à la partie de l'amas non étudiée jusqu'à présent pour dévoiler de nouveaux membres et déduire l'IMF sur la totalité de l'amas α Per.
3. Un programme d'imagerie à haute résolution au sol (optique adaptative) ou dans l'espace (*Hubble*) pour étudier la dépendance de la binarité en fonction de la masse.

Le chapitre 4, dédié à Collinder 359, constitue une première étape dans l'étude de cet amas quasi inconnu précédemment. La sélection des membres de l'amas à partir des données photométriques visible et proche infrarouge a révélé 1033 candidats dont les masses sont comprises entre 1.3 et 0.040 masse solaire pour une distance de 650 parsecs et un âge de 80 millions d'années. Afin de vérifier l'affiliation de ces candidats à l'amas, deux périodes d'observations dédiées à Collinder 359 auront lieu en juin 2004.

1. Une imagerie dans le proche infrarouge des 250 candidats restants dont la magnitude I est comprise entre 17 et 20 pour éliminer les étoiles de champ contaminant notre échantillon. Un total de 8 nuits d'observations a été octroyé à ce projet en juin 2004, dont 4 nuits avec l'instrument MAGIC sur le 2.2-m à Calar Alto et 4 nuits avec la caméra infrarouge du CFH.
2. Une spectroscopie dans le domaine visible à basse résolution des candidats sélectionnés à partir des données photométriques afin de vérifier leur appartenance à l'amas. Six nuits ont été octroyées à ce projet en juin 2004 avec le spectrographe multi-fibre AF2/WYFFOS monté sur le télescope William Herschel. Trois nuits supplémentaires ont été spécialement accordées à la spectroscopie visible des candidats dans Collinder 359 avec le spectrographe DOLORES sur le Telescopio Nazionale di Galileo.

L'amas Collinder 359 a été l'un des quatre amas pré-séquence principale cartographié dans le cadre du programme destiné à examiner les possibles variations de l'IMF avec l'environnement et l'âge. Dès que nous avons obtenu un spectre visible pour tous les candidats sélectionnés sur la base de leur photométrie, plusieurs projets à long terme sont envisageables afin d'étudier les propriétés des étoiles et des naines brunes dans les amas d'étoiles jeunes:

- Etendre la cartographie (I, z) à la partie centrale de l'amas (dans un rayon de un degré) pour déduire l'IMF sur la totalité de l'amas. L'instrument MEGACAM offre un grand champ (un degré carré), idéal pour cartographier Collinder 359.
- Observations des membres de l'amas en rayons X pour étudier l'activité chromosphérique et coronale en fonction de la masse.
- Imagerie à haute résolution des membres de l'amas pour examiner la binarité en fonction de la masse.
- Suivi des variabilités photométriques à court et long termes des membres de l'amas pour en étudier la dépendance avec la masse.

Les amas d'étoiles jeunes ont trois avantages importants: tout d'abord, une évolution dynamique minimale, ensuite une absence de gaz provenant du nuage moléculaire originel, et enfin, un grand intervalle en masse. Les amas ouverts répertoriés dans l'Open Cluster Database ont des distances et des âges incertains uniquement basés sur quelques étoiles brillantes. Les mouvements propres combinés avec la photométrie dans les domaines visible et/ou infrarouge fournis par les catalogues à grande échelle permettront d'affiner ces deux paramètres essentiels avant d'entreprendre des cartographies visibles profondes dédiées à la recherche de naines brunes sur une zone limitée de l'amas.

Les incertitudes actuelles sur la pente de l'IMF sont trop larges pour déterminer le nombre d'étoiles formées par unité de temps dans un amas et fournir d'importants diagnostics sur la naissance et l'évolution des étoiles et des naines brunes appartenant à notre Galaxie. La cible idéale pour adresser ces questions serait un amas pré-séquence principale (10–50 millions d'années) proche ($d \leq 500$ parsecs) situé à haute latitude galactique et possédant un mouvement propre qui diffère de celui des étoiles du champ pour réduire leur contamination.

Le volet essentiel relatif à l'étude de l'IMF concerne sa dépendance avec les conditions physiques du lieu de formation, de l'âge et de la métallicité. Cette question était au cœur du large programme mené avec le télescope CFH et initié par notre réseau européen. Nous espérons apporter quelques réponses à cette question fondamentale suite aux résultats des données spectroscopiques obtenues dans les amas pré-séquence principale et des régions de formation d'étoiles. Les futures missions spatiales comme le JWST, successeur de *Hubble*, permettront d'élargir le concept de notre étude sur deux aspects fondamentaux. Premièrement, les objets de masse planétaire deviendront accessibles dans les amas proches pour examiner le rôle de la limite de fragmentation sur l'IMF. Deuxièmement, le recensement de naines brunes dans des amas ouverts plus distants apportera des indications sur l'influence de la métallicité sur l'évolution de ces objets.

Il y a moins de dix ans, la quête d'objets sous-stellaires était ravivée par la découverte des deux premières naines brunes. Notre connaissance de ces objets, situés à la frontière entre les étoiles et les planètes, a nettement progressé grâce à la découverte de centaines de naines brunes dans le voisinage solaire, en tant que compagnons d'étoiles et dans les amas jeunes. Les moyens d'observations actuels semblent en mesure d'apporter une réponse à divers sujets sensibles au cours des dix prochaines années. Premièrement, l'émergence de binaires de faible masse va rapidement permettre la détermination de la masse dynamique d'une naine brune afin de tester les isochrones théoriques dans le domaine sous-stellaire. Deuxièmement, les futurs projets comme SIRTF et ALMA sont en mesure d'estimer la dimension et la masse des disques autour des naines brunes pour mieux comprendre leur mécanisme de formation. Enfin, les cartographies profondes menées au sein de régions dont les conditions physiques sont différentes apporteront, à long terme, une réponse à la question de l'universalité de l'IMF.

Nouveau chapitre de thèse

Titre de la thèse :	Recherche d'étoiles de faible masse et de naines brunes : Voisinage solaire et dans les amas d'âge intermédiaire α Per et Collinder 359
Prénom et nom du doctorant :	Nicolas Lodieu
Ecole doctorale :	Sciences de l'Univers, de l'Environnement et de l'Espace
Directeurs de thèse :	Emmanuel Caux & Mark McCaughean
Nom du mentor :	Jean-Marie Fétrot
Date probable de soutenance :	Juillet 2004

Résumé de thèse :

Nous décrivons les résultats de cartographies d'étoiles de faible masse et de naines brunes à la fois agées et proches appartenant au champ ainsi que jeunes et éloignées dans des amas d'étoiles.

Premièrement, nous présentons les résultats d'une étude à mouvement propre dédiée aux objets froids et proches du Soleil. Nous avons découvert de nombreuses naines ultra-froides à moins de 50 pc ainsi que la naine brune binaire la plus proche.

Deuxièmement, nous étudions la fonction de masse sous-stellaire dans les amas ouverts jeunes. Une cartographie proche infrarouge d'une région de 0.7 deg^2 d'un amas analogue aux Pléiades, α Per, a révélé de nouveaux membres stellaires et sous-stellaires. Une cartographie visible d'une région de 1.6 deg^2 dans Collinder 359 a extrait de nouveaux membres de masses inférieures à une masse solaire, révisant l'âge et la distance de l'amas. Sa fonction de masse croît dans le domaine sous-stellaire avec une pente inférieure à celles estimées pour les Pléiades.

1) Cadre général et enjeux de la thèse

J'ai effectué ma thèse au sein de l'AIP (Astrophysikalisches Institut Potsdam) situé sur la butte de Babelsberg à environ 30 km au sud-ouest de Berlin. L'institut est composé de deux branches scientifiques. Premièrement, la physique stellaire et la magnétohydrodynamique et deuxièmement, la physique extragalactique et la cosmologie. Le groupe "formation d'étoiles", auquel j'appartiens, fait partie de la seconde branche. Un laboratoire d'instrumentation est aussi présent au sein de l'AIP. Les sections non-scientifiques incluent la bibliothèque, la maintenance informatique et l'administration avec une division pour le personnel et la finance.

Le groupe "formation d'étoiles", dirigé par Hans Zinnecker, est constitué de douze membres, dont six étrangers :

- 4 astronomes permanents
- 1 Emmy-Noether Fellow
- 3 post-doctorants dont 1 financé par la communauté européenne et 2 par le Centre Spatial Allemand (DLR)
- 4 thésards dont 2 financés par Emmy-Noether, 1 par le DLR et moi-même par la commission européenne

Comprendre la formation des étoiles est un but important de l'astronomie moderne. Les étoiles sont, d'une part, les constituants élémentaires des galaxies, et, d'autre part, les sites de formation des planètes. D'un côté, la compréhension de la formation d'étoiles massives est essentielle pour améliorer les modèles de galaxies. D'un autre côté, la formation des planètes et des systèmes planétaires est un produit dérivé de la formation d'étoiles de faible masse (c'est-à-dire plus faible que le Soleil). Les disques entourant les étoiles pendant leur phase pré-stellaire sont les sites de formation des planètes géantes et telluriques comme celles de notre Système Solaire.

Notre groupe travaille aux deux extrêmes de la formation d'étoiles. Une partie des études se porte sur les étoiles massives appartenant à des amas jeunes et une autre sur la détection et l'imagerie de disques stellaires dans des régions de formation d'étoiles. Par ailleurs, notre groupe est composé de théoriciens qui s'attachent à comprendre les processus physiques impliqués dans la formation d'étoiles et d'observateurs qui souhaitent en établir les règles empiriques.

Ma contribution au sein du groupe est double et concerne la recherche de naines brunes. Par définition, les naines brunes, communément appelées "étoiles ratées", ont des masses comprises

entre 0.075 et 0.013 fois la masse de notre Soleil. La densité et la température au centre de ces objets sont trop faibles pour déclencher la fusion de l'hydrogène qui constitue l'empreinte d'une étoile. Le premier but est de répertorier les objets proches de notre Soleil, importants pour la recherche de vie extrasolaire. Le second but concerne l'investigation de la fonction de masse des amas d'étoiles jeunes, c'est-à-dire le nombre d'étoiles par unité de masse formées à la naissance de l'amas, afin d'étudier ses variations environnementales et temporelles.

Les techniques utilisées lors de ma thèse pour découvrir les naines brunes dans le voisinage solaire et les amas d'étoiles sont multiples. Tout d'abord, l'observation de plaques photographiques à deux époques différentes pour détecter le mouvement d'un objet. Plus un objet est proche du Soleil, plus son mouvement dans le ciel est grand. Ensuite, la photométrie dans le visible et le proche infrarouge pour détecter les objets de faible masse. Moins un objet est massif, plus il est froid et plus il émet à grandes longueurs d'onde. Enfin, la spectroscopie permet de classifier l'objet et de déterminer la composition de son atmosphère.

Mon principal outil de travail est l'ordinateur. Les systèmes d'exploitation utilisés sont Unix ou Linux de même que des logiciels de traitement d'images, de réduction de données. Les messages électroniques (E-mails) sont fréquemment utilisés pour communiquer à distance, préparer un article scientifique ou une demande de temps d'observation. L'accès à Internet pour la disponibilité des sites astronomiques constitue une source incommensurable d'informations. Certains sites sont abondamment consultés comme le Centre de Données Astronomiques de Strasbourg, l'Astrophysics Data System pour obtenir les articles scientifiques récents, ou encore l'Open Cluster Database pour récupérer les données concernant les amas d'étoiles. La conférence scientifique est un autre moyen bénéfique aux échanges d'idées. Ces conférences réunissent plusieurs dizaines à plusieurs centaines d'astronomes suivant le sujet traité. Des présentations orales et des sessions posters en constituent l'essentiel pour communiquer les derniers résultats et partager les idées. La publication et transmission des résultats scientifiques se font exclusivement en anglais sauf dans le cadre de certaines publications nationales.

Le télescope est un autre outil de travail essentiel à l'astronome. Outre les télescopes qui appartiennent à un institut privé, les nuits allouées par les observatoires internationaux (Observatoire Sud-Européen, Kitt Peak Observatory, Gemini Observatory, etc...) sont sujettes à la compétition internationale. Par exemple, dans le cadre de l'Observatoire Sud-Européen, deux dates limites (avril et octobre) sont fixées pour soumettre des demandes de temps. Un comité scientifique juge chaque application afin d'allouer un certain nombre de nuits aux meilleures d'entre elles. Les observations se font alors soit au télescope soit par l'intermédiaire des astronomes résidant au Chili. Ce processus est également valable pour les autres observatoires internationaux.

Notre groupe est à la tête d'un réseau européen qui regroupe sept équipes européennes (voir ci-dessous). Deux écoles ou conférences sont organisées annuellement pour réunir ses membres afin d'aborder les dernières avancées scientifiques et stimuler la collaboration entre instituts. Cette expérience fut très enrichissante au niveau humain mais plutôt décevante au niveau collaboration car les astronomes ont tendance à négliger le travail en équipe. Outre le réseau européen, il n'existe pas de véritables relations entre instituts, mais des relations entre membres de divers instituts par le biais de projets en commun. Le nombre de collaborateurs augmente avec l'expérience. Dans mon cas, j'ai collaboré avec Jérôme Bouvier et son groupe à l'Observatoire de Grenoble du fait de nos intérêts communs, à savoir l'étude de la fonction de masse dans les amas d'étoiles jeunes. Cette collaboration fut élargie à l'ensemble du réseau européen suite à l'aboutissement d'un large

programme d'observations au cours de la dernière année. Outre les collaborations au sein du réseau européen, j'ai collaboré avec David Barrado y Navascués de Madrid et John Stauffer de Pasadena aux Etats-Unis dans le cadre de mon étude de l'amas de Persée. J'ai aussi gardé d'étroits contacts avec mon ancien responsable de stage de DEA à Toulouse. J'ai aussi beaucoup travaillé avec Ralf-Dieter Scholz à l'AIP dans le cadre de la recherche de naines brunes dans le voisinage solaire.

A l'opposé des collaborations, il y a la forte concurrence au niveau national et international. Du fait de mon intégration au sein du réseau européen, j'ai peu ressenti cette concurrence. Cependant, un collaborateur sur un projet peut aussi être un concurrent sur un autre projet. Par exemple, mon collaborateur espagnol est impliqué dans la recherche de naines brunes dans d'autres amas d'étoiles.

Notre groupe fut en concurrence à maintes reprises avec plusieurs équipes américaines dans le cadre de mon projet sur la détection de naines brunes proches du Soleil. Une petite anecdote pour illustrer cette compétition. Nous avons découvert la naine brune la plus proche du Soleil il y a environ un an. Suite à cette découverte, nous avons obtenu du temps d'observations sur des télescopes européens pour étudier cet objet en détails. Pendant les six mois qui séparent l'acceptation de la demande de temps et les observations, une équipe américaine a observé "notre" objet avec le télescope en question et a découvert un compagnon. Cette attitude est contraire à la déontologie et est interdite par le guide conduite de l'observatoire . En conséquence, nous avons obtenu la primeur de la découverte et publié les résultats.

2) Coût du projet

Mon financement provient du Fifth Framework Programme (FP5) de la Commission Européenne. Le réseau européen, auquel j'appartiens, est intitulé "The Formation and Evolution of Young Stellar Clusters" et regroupe sept équipes de six pays différents :

1. Astrophysikalisches Institut Potsdam, Allemagne
2. Osservatorio Astrofisico di Arcetri, Florence, Italie
3. Institute of Astronomy, Cambridge, Angleterre
4. Department of Astronomy and Astrophysics, Cardiff, Pays de Galles
5. Laboratoire d'Astrophysique de l'Observatoire de Grenoble, France
6. Observatório Astronómico de Lisboa, Lisbonne, Portugal
7. Commissariat à l'Energie Atomique, Saclay, France

Le budget total du réseau européen est de 1.4 MEuros distribué de manière équitable entre les sept équipes. Le nombre total de personnes impliquées est de 70, en incluant les sept post-doctorants (un par équipe) et les trois thésards employés par le réseau. Le financement dédié à la formation des jeunes chercheurs correspond à 283 semaines de salaire. Notre institut est financé à hauteur de 250 kEuros par le réseau ce qui inclue un poste de thésard plus un post-doctorant.

Mon salaire net mensuel est d'environ 900 à 950 Euros pour 40 heures de travail (20 heures pour l'institut et 20 heures pour ma thèse). L'institut débourse 21 kEuros pour payer mon salaire sur une année. Le coût des missions s'est élevé à environ 4 700 Euros en 2002, 3 000 Euros en 2003, et 1 400 Euros en 2004 (conférences et visites dans d'autres instituts incluses). Il faut y ajouter les observations aux télescopes. Ce montant varie en fonction des années et dépend du taux du succès des applications soumises. Le financement de ces observations provient généralement de

la fondation de recherche allemande (DFG). Par exemple, une nuit d'observations sur un télescope de 3.5-m à Calar Alto (Espagne) s'élève à 10 kEuros, à La Silla (Chili) à 15 kEuros. Une nuit d'observations sur un télescope de 8-m à Paranal (Chili) s'élève à 50-60 kEuros

Le coût du matériel (ordinateurs, cd-rom, fournitures en tout genre) s'élève à environ 3 kEuros par an. Le budget administratif de l'institut s'élève à 150 kEuros (3 personnes), soit environ 2 kEuros par chercheur. Le coût de l'infrastructure n'est pas déterminé précisément et n'est donc pas disponible.

3) Déroulement et gestion du projet

J'ai géré mon travail et conduis mon projet de manière autonome. Dans mon domaine de recherche, chaque personne est indépendante et décide de ses projets selon ses idées et buts scientifiques. Lors de mon arrivée à Potsdam, le sujet suivant, plutôt vague, était défini ainsi : "l'étude de la fonction de masse d'amas ouverts jeunes". Plusieurs types de données astronomiques étaient disponibles afin de s'entraîner avant d'embrayer sur un sujet plus précis.

Premièrement, j'ai réduis les données concernant la recherche d'objets proches du Soleil obtenues par deux membres du groupe "formation d'étoiles" de l'AIP. Suite aux résultats préliminaires, nous avons soumis des demandes de temps aux télescopes européens. Ces demandes de temps, bi-annuelles et à dates fixes, sont ouvertes à la concurrence internationale. Nos efforts furent malheureusement vains et le projet resta en suspens pendant un an. Les demandes ultérieures furent couronnées de succès, avec à la clé, la découverte d'objets intéressants et plusieurs publications. La découverte de la naine brune la plus proche du Soleil déboucha sur deux publications dans des journaux spécialisés et plusieurs articles dans des revues à grand public. En résumé, ce projet démarra tardivement mais fonctionne désormais à plein régime.

Deuxièmement, j'ai disposé de données sur l'amas de Persée dès mon arrivée à l'AIP. Par ailleurs, je suis immédiatement parti observer en Espagne. Les bonnes conditions météorologiques (3 nuits claires sur 4) ont fourni de nouvelles données que j'ai analysées dans la foulée. Ce projet, fruit d'une collaboration entre plusieurs chercheurs en Allemagne, France, Espagne et Etats-Unis, fut donc couronné de succès. Aucun article ne fut cependant publié du fait de la lenteur des collaborateurs.

Un large programme d'observations fut octroyé à notre réseau européen au cours de la dernière année de thèse. La quantité de données récoltées déclencha une étroite collaboration au sein des différentes équipes ainsi que la mise en oeuvre de stratégies communes pour mener à bien ce projet. Les premiers résultats sont apparents, l'un d'eux étant inclus dans ma thèse, et plusieurs publications sont attendues l'année prochaine.

Je souhaite maintenant mettre en avant deux facteurs à risque important que j'ai expérimentés pendant ma thèse.

Le premier concerne le crash du disque dur de l'ordinateur et, par conséquent, la perte des données analysées. La stratégie de mise en place pour éviter cet incident dramatique fut traitée comme suit. Tout d'abord, une sauvegarde régulière sur cd-rom des fichiers les plus importants comme les programmes d'analyse de données. Ensuite, une méthode de sauvegarde à trois ordinateurs basée sur le principe suivant : étudiant 1 sauvegarde sur ordinateur 2, étudiant 2 sauvegarde sur ordinateur 3, et étudiant 3 sauvegarde sur ordinateur 1. Par conséquent, si un ordinateur tombe en panne, les données sont sauvegardées sur un second.

Le deuxième facteur à risque concerne les conditions météorologiques rencontrées lors d'observations astronomiques. Autant nous pouvons apporter une solution à une panne d'ordinateur autant nous sommes impuissants devant les aléas climatiques. Une façon d'éviter la bérézina totale est de multiplier les demandes de temps sur divers télescopes (dans la mesure du possible) afin d'augmenter le taux de succès lors des observations.

Les publications scientifiques dans des articles spécialisés (*Monthly Notices of the Royal Astronomical Society*, *Astrophysical Journal*, *Astronomy & Astrophysics*, etc...) constituent l'aboutissement d'un travail d'équipe à court, moyen, et long termes. Les observations et, en particulier, les résultats sont généralement dévoilés lors des publications. Ensuite, les données et résultats deviennent publics et sont utilisables par n'importe quel chercheur. Les articles font référence à des travaux antérieurs et les citations doivent y apparaître de façon à mettre en avant les auteurs de ces travaux.

Les réunions au sein du groupe "Formation d'étoiles" sont hebdomadaires et réunissent tous les membres (dans la mesure du possible) le mardi vers 13h. Les discussions sont variées, comme par exemple (la liste n'est bien sûr pas exhaustive) :

1. Les conférences importantes, qui va où et quand ?
2. Les projets associés aux demandes de temps d'observations (bi-annuels)
3. Les invités, leur durée de séjour et leur but
4. Les discussions de récents articles ou résumé de conférences
5. Les avancées scientifiques au sein du groupe
6. Les problèmes administratifs

Les discussions avec mon responsable de thèse en Allemagne furent beaucoup plus espacées dans le temps que les réunions de groupe. En conséquence, j'ai géré mon projet seul, ce qui, en fait, correspondait à l'attente de mon responsable. Quant à mon responsable de thèse à Toulouse, les contacts furent téléphoniques. Il n'est venu à Potsdam qu'une seule fois en 4 ans. Son implication dans mon travail scientifique fut moindre que celle de mon responsable en Allemagne. En revanche, lorsqu'il est question de déplacement (visites dans un autre institut, conférences, observations, etc...), une signature du responsable de thèse (ou de groupe) est obligatoire. Les dépenses d'un thésard sont, en effet, gérées par les membres permanents de l'institut.

4) Compétences, savoir-faire, qualités professionnelles et personnelles

Mon domaine d'expertise scientifique concerne la formation d'étoiles de faible masse et des naines brunes et la physique qui y est associée. En tant qu'astronome amateur, je possède également des connaissances de base sur une variété de sujets couverts par l'astronomie. J'ai développé pendant ma thèse des connaissances nécessaires à la réduction de données photométriques et spectroscopiques dans le domaine visible et infrarouge. Le domaine visible est la partie du spectre électromagnétique accessible à notre oeil contrairement à l'infrarouge qui est à plus courtes fréquences. La photométrie permet de mesurer la quantité de lumière émise par une étoile à différentes fréquences afin d'estimer sa température. La spectrométrie, qui étudie la composition chimique

de l'atmosphère des étoiles, permet de les classifier et d'estimer leurs températures. Ces deux méthodes sont complémentaires et nécessaires à l'identification d'étoiles de faible masse.

Les données astronomiques qui constituent l'essentiel de ma thèse furent obtenues grâce à divers télescopes de pointe situés sur des observatoires en Espagne, au Chili ou à Hawaii. Leurs utilisations nécessitent plusieurs étapes. Tout d'abord, un projet précis, adapté à l'instrument et au télescope, est défini. Ensuite, les objets, les temps d'exposition et autres paramètres indispensables à l'optimisation de la nuit d'observation sont sélectionnés. Enfin vient l'analyse des données obtenues. Une méthode standard de réduction d'images existe pour la photométrie et la spectroscopie. En revanche, chaque type de données reste unique et nécessite un traitement spécifique. Un travail d'analyse et de synthèse différent dans chaque cas constitue la force du doctorant. Ce travail implique divers logiciels de traitement d'images (Midas ou IRAF) et de programmation (Fortran, Idl, SuperMongo). L'analyse des données exige une recherche dans la littérature pour comparer les résultats. La publication des résultats nécessite l'utilisation de logiciels de traitement de texte pour les publications (Latex, Word, Excel) et de présentation comme Powerpoint ou StarOffice lors de colloques. L'ordinateur apparaît donc comme le compagnon indispensable de l'astronome.

La langue principale des chercheurs est l'anglais. Une connaissance parfaite de la langue de Shakespeare est obligatoire pour publier par écrit ou présenter oralement ses travaux. J'ai également communiqué en allemand sachant que j'ai vécu près de 4 ans à Potsdam. Un minimum est nécessaire pour la vie de tous les jours (supermarché, docteur, pharmacie, ...). De plus, les termes techniques liés à l'ordinateur (panne ou installation d'un logiciel) ou administratifs (inscription à la mairie, contrat appartement) furent très utiles pour faire face aux contingences quotidiennes.

Trois types d'organisation sont nécessaires dans mon domaine de recherche : un travail à court, moyen et long termes. L'organisation à court terme correspond au travail de la semaine. Avant chaque début de semaine, un plan de travail est tracé avec une grille d'importance pour chaque chose à accomplir. Par exemple, une heure est consacrée en fin de semaine pour résumer le travail de la semaine, les nouvelles idées et sauvegarder les fichiers importants. Par ailleurs, notre réunion de groupe hebdomadaire constitue le lieu de présentation de nos avancées scientifiques. L'organisation à moyen terme concerne la préparation d'une présentation (orale ou poster) dans le cadre d'une conférence par exemple. Tout d'abord vient l'inscription, ensuite la réservation d'un vol (en allemand pour communiquer avec l'agence de voyage attitrée à l'institut) puis la réservation de l'hôtel et, enfin, la participation. Le sujet doit mûrir à l'avance, puis exige une préparation minutieuse afin d'optimiser la qualité de la présentation. L'organisation à long terme concerne principalement les demandes de temps d'observations. Deux fois par an et par télescope, nous, les astronomes, sommes invités à soumettre nos demandes. Les résultats de la sélection apparaissent environ six mois après, et les observations neuf mois après. En conséquence, une préparation du projet se fait sur un an. Ensuite, s'ajoutent des préparations à plus court terme comme les observations en elles-mêmes. Un minimum d'adaptabilité est exigé, en particulier, lorsque la date limite de soumission est à minuit. Je suis resté à plusieurs reprises très tard le soir en attente des dernières corrections des collaborateurs. Le second exemple traite de la recherche d'un post-doctorant, commencée plus de six mois avant la fin de mon contrat. Les offres d'emplois ont des dates aléatoires qui ne correspondent pas précisément à la fin de ma thèse.

L'organisation du matériel et des fichiers sauvegardés sur l'ordinateur est très importante. Le principe de base consiste à retrouver rapidement l'article, l'image, ou le fichier dont on a be-

soin à l'instant T. Les tâches d'un étudiant concernent principalement son travail scientifique. Les tâches administratives sont mineures et représentent une infime partie du temps. Par exemple, avant et après un voyage (observations ou conférence), un formulaire est à remplir et à signer par le responsable de groupe afin d'obtenir remboursement des frais. Ces tâches administratives sont principalement l'affaire des responsables de groupe.

5) Résultats et impact de la thèse

L'incidence de ma thèse (et de l'astronomie en général) sur l'économie et la société est minime. L'astrophysique est une science qui fait rêver les gens mais sans modifier leur vie quotidienne comme peut le faire la médecine par exemple. L'incidence sur le laboratoire est également faible. En revanche, ma thèse a un impact au niveau du groupe. Tout d'abord, l'institut est mis en avant à travers les articles que je publie et mes présentations orales lors de conférences. Par ailleurs, le réseau européen a développé et renforcé la collaboration entre les membres des sept instituts impliqués dans les projets communs. Ce fort lien scientifique n'existe pas préalablement et chaque personne a apporté quelque chose aux autres au travers des réunions organisées par le réseau.

L'impact de ma thèse sur mon domaine de recherche est double. En premier lieu, la découverte d'objets très proches du Soleil s'inscrit dans un cadre général qui vise à détecter toutes les étoiles contenues dans une sphère centrée sur le Soleil. Cette approche est un complément des recherches menées par d'autres groupes au niveau international. En second lieu, l'étude d'un amas d'étoiles jeunes peu étudié par le passé a démontré que les instruments et méthodes utilisées sont adéquats pour ce genre d'études. Cette analyse sera élargie à un grand nombre d'amas dans un avenir proche.

6) Pistes professionnelles identifiées

La continuité logique de ma thèse est un post-doctorat en astrophysique. Les thésards français partent généralement à l'étranger pour une ou plusieurs années de post-doctorat puis postulent pour un poste permanent en France. Mon cas est donc particulier puisque j'ai effectué ma thèse à l'étranger tout en étant inscrit à l'Université de Toulouse. A l'heure où j'écris ce document, j'ai envoyé sept candidatures pour un post-doctorat qui ont échoué et quatre autres sont en préparation. L'une d'entre elles concerne précisément le sujet de ma thèse et le financement provient de l'institut d'astrophysique des Iles Canaries. Plusieurs types de post-doctorat sont envisageables. La première possibilité est un post-doc 100 % dédié à la recherche ; la seconde est un poste en tant qu'assistant d'un télescope dans un observatoire c'est-à-dire 50 % du temps est passé à encadrer les observateurs et le reste est destiné à sa propre recherche. L'Observatoire Sud-Européen, l'Observatoire Canada-France-Hawaii, le Groupe Isaac Newton et autres observatoires renouvellent régulièrement leurs membres. N'ayant pas obtenu de réponse positive aux deux premiers observatoires, je vais soumettre ma candidature au troisième.

Un débouché supplémentaire est une orientation vers des industries ou groupes liés à l'espace et la construction de satellite comme l'ESA, Astrium, Alstom ou le CNES. Ces entreprises ont besoin de personnel qualifié, pas seulement ingénieurs, pour définir le projet scientifique en amont de la construction du satellite. Bien que n'étant pas qualifié pour l'élaboration en soi du satellite, je peux apporter mes connaissances astronomiques et mon expérience dans la réduction des données.

L'espace et les missions spatiales constituent, à mon avis, un débouché industriel pour les thésards en astronomie. L'expérience développée en informatique appliquée à la science peut également s'avérer utile dans le domaine spatial.

Deux autres possibilités envisageables sont liées aux connaissances acquises pendant mon expérience de 4 ans à l'étranger. La première concerne le journalisme scientifique. De nombreuses revues à grand public ou plus spécialisées comme Ciel et Espace, l'Astronomie, Pour la Science relatent les dernières avancées astronomiques ou scientifiques. Nos connaissances scientifiques alliées aux qualités de rédaction développées au travers des publications dans des journaux spécialisés pourraient intéresser les rédacteurs en chef de telles revues. La seconde possibilité est interprète. Pendant quatre ans, j'ai développé des qualités linguistiques (anglais + allemand) qui deviennent indispensables dans de nombreuses circonstances, en particulier en vue de l'élargissement de l'Europe. Bien que ces métiers ne soient pas intimement liés à ma thèse sur les naines brunes, un stage d'apprentissage de quelques mois de mise à niveau est à envisager et aisément du fait de l'adaptabilité du doctorant.

Introduction

The gravitational collapse and fragmentation of molecular clouds form stars over a large range of masses. Stars spend most of their lifetime on the so-called main-sequence in hydrostatic equilibrium, as the nuclear fusion energy supports the star against gravitational collapse. However, objects with masses lower than $0.072 M_{\odot}$ at solar metallicity will never reach core temperatures and pressures high enough to fuse hydrogen. Hence, these objects, termed “brown dwarfs”, cool off inexorably as they age and reach very low luminosities, hampering their detection. As a consequence, brown dwarfs remained elusive for some 30 years after their first theoretical prediction. The advent of wide-field arrays, all-sky surveys, and large telescopes have now led to the discovery of hundreds of brown dwarfs as isolated objects in the solar neighbourhood, as companions to low-mass stars, in young open clusters, and in star-forming regions.

The number of stars per unit of mass, known as the Initial Mass Function (hereafter IMF), is of prime importance in understanding star formation processes. Following the pioneering study by Salpeter in 1955, the stellar IMF has been investigated during the last decades in various environments and over a wide mass range to look into its possible dependence on time and place.

Many questions were, however, raised regarding the shape of the IMF at the high-mass and low-mass ends. On the one hand, high-mass stars are not so numerous and have extremely short lifetimes. On the other hand, low-mass stars and brown dwarfs are faint and difficult to detect.

To address some of the crucial issues including a possible turn-over in the IMF at the hydrogen burning limit, young open clusters and star-forming regions have been extensively targeted as they represent a coeval population of stars of similar metallicity at a given distance within a small area in the sky. Brown dwarfs are amenable for detailed analysis in young clusters because they are intrinsically brighter when younger. Most studies carried out in the Pleiades, α Per, Trapezium Cluster, IC348, and σ Orionis indicate that the mass function rises from high-mass down to a solar mass, more slowly down to a maximum around $0.1\text{--}0.2 M_{\odot}$ before declining into the substellar regime. A recent wide-field survey conducted in the low-density Taurus region revealed a dearth of brown dwarfs, suggesting that the IMF might indeed vary with the environment.

Three independent surveys are discussed in this thesis, aimed at finding brown dwarfs in the solar neighbourhood and in young open clusters to contribute to the understanding of the low-mass end of the mass function. First, we describe a search for nearby old low-mass stars and brown dwarfs using proper motion as the primary selection criterion. Second, we present a wide-field near-infrared survey of α Per, a Pleiades analogue cluster. Finally, we report an optical survey of a pre-main-sequence cluster, Collinder 359, along with infrared follow-up observations.

Chapter 1 reviews the current theoretical and observational knowledge on brown dwarfs and the recent mass function determinations in various regions. Then, we present the alternative for-

mation mechanisms proposed to account for brown dwarfs. Afterwards, we describe the evolution of substellar objects as well as the composition of their atmospheres. Finally, we discuss the different kinds of searches conducted in different environments to uncover brown dwarf as companions to low-mass stars, as isolated objects, in star-forming regions, and in young open clusters.

Chapter 2 deals with a proper motion survey in the southern sky, aimed at finding the closest and coolest neighbours to the Sun. Our approach is complementary to the methods employed by all-sky surveys such as 2MASS, where colour was the primary selection criterion used to reveal nearby brown dwarfs. Our targets were selected from overlapping regions of archival photographic plates available in three optical filters and taken at different epochs. We present the outcome of optical and near-infrared spectroscopic follow-up observations of low-mass stellar and brown dwarf candidates with an emphasis on some interesting objects.

Chapter 3 focuses on α Per, a Pleiades-like cluster, which is among the four closest and youngest open clusters. We first review previous proper motion, photometric, and spectroscopic surveys dedicated to the search for cluster members. Then, we emphasise recent breakthroughs regarding the age of the cluster and the mass function determination from $0.3 M_{\odot}$ down into the substellar regime. Thereafter, we present the results of a wide-field near-infrared survey of a 0.7 square degree area in α Per initiated to uncover new young low-mass stars and brown dwarfs belonging to the cluster. Finally, we discuss the membership of previous cluster members and new infrared-selected candidates on the basis of moderate-resolution optical spectroscopy.

Chapter 4 is dedicated to the pre-main-sequence cluster Collinder 359 observed within the framework of a wide-field optical imaging survey of young open clusters to investigate the possible dependence of the low-mass stellar and substellar mass function on time and environment. We first report the current knowledge of the cluster and put it into a wider context. We then present the wide-field optical observations of a 1.6 square degree in Collinder 359 carried out in the I and z filters down to a completeness limit of $0.040 M_{\odot}$. We have selected cluster member candidates from their location in the optical ($I, I-z$) colour-magnitude diagram and have used near-infrared photometry as a further criterion to disentangle cluster candidates from contaminating field objects. We also discuss the age and distance of Collinder 359 based on the optical survey and other data available for the cluster. Finally, we derive luminosity and mass functions for Collinder 359 down into the substellar regime and compare it to other estimates in open clusters.

Chapter 5 discusses the perspectives regarding the α Per and Collinder 359 open clusters. We also put the photometric surveys of α Per and Collinder 359 into a wider context for subsequent extension to other young open clusters. We describe the various follow-up observations of cluster member candidates, including proper motion, optical and near-infrared photometry with subsequent spectroscopy, X-ray surveys, binarity, as well as variability monitoring.

Chapter 1

A theoretical and observational overview of brown dwarfs

Stars are large spheres of gas composed of $\sim 73\%$ of hydrogen in mass, $\sim 25\%$ of helium, and about 2% of metals, elements with atomic number larger than two like oxygen, nitrogen, carbon or iron. The core temperature and pressure are high enough to convert hydrogen into helium by the proton-proton cycle of nuclear reaction yielding sufficient energy to prevent the star from gravitational collapse. The increased number of helium atoms yields a decrease of the central pressure and temperature. The inner region is thus compressed under the gravitational pressure which dominates the nuclear pressure. This increase in density generates higher temperatures, making nuclear reactions more efficient. The consequence of this feedback cycle is that a star such as the Sun spend most of its lifetime on the main-sequence.

The most important parameter of a star is its mass because it determines its luminosity, effective temperature, radius, and lifetime. The distribution of stars with mass, known as the Initial Mass Function (hereafter IMF), is therefore of prime importance to understand star formation processes, including the conversion of interstellar matter into stars and back again. A major issue regarding the IMF concerns its universality, i.e. whether the IMF is constant in time, place, and metallicity.

When a solar-metallicity star reaches a mass below $0.072 M_{\odot}$ (Baraffe et al. 1998), the core temperature and pressure are too low to burn hydrogen stably. Objects below this mass were originally termed “black dwarfs” because the low-luminosity would hamper their detection (Kumar 1963). The name black dwarfs was also suggested for extremely old white dwarfs, but both types of objects were undetected at that time. Tarter (1976) proposed the name “brown dwarfs” because the atmospheres dominated by molecules would be difficult to understand. This denomination was quickly adopted by astronomers. However, the true colour of a brown dwarf is not brown but purple. Indeed, deuterated sodium (Na D) absorption lines are prominent in substellar objects, suppressing green wavelengths. Therefore, a mixture of red colour from a blackbody and colour from the absorption lines of Na D appear most likely, yielding a magenta colour in the optical.

After 30 years of unfruitful searches, the first unambiguous brown dwarfs were announced independently around a nearby M2 dwarf, Gl229B (Nakajima et al. 1995) and in the Pleiades, Teide 1 (Rebolo et al. 1995). Substellar objects are now routinely uncovered as companions to low-mass stars (e.g. Bouy et al. 2003), as isolated field objects (e.g. Kirkpatrick et al. 2000), as members of young open clusters (e.g. Bouvier et al. 1998), and in star-forming regions (e.g. Hillenbrand 1997). Many recent studies in young clusters have focused on the shape of the substellar IMF to investigate a possible dependence on time and environment.

This chapter reviews the current observational and theoretical knowledge on brown dwarfs and recent determinations of the substellar mass functions. This chapter is organised as follows. We define the Initial Mass Function in § 1.1 and review its determinations in the field, in young open clusters, and in star-forming regions. In § 1.2, we discuss the formation mechanisms proposed to explain the existence of brown dwarfs along with the current observational constraints. We present the physics of substellar objects in § 1.3, including the evolution of luminosity, effective temperature, and radius with time and briefly describe the composition of their atmospheres. We describe the spectral classification of ultracool dwarfs (spectral types $\geq M8$) as well as their photometric and spectroscopic characteristics in § 1.4. Finally, we give in § 1.5 an overview of the different ways to look for brown dwarfs: radial velocity, microlensing, proper motion, as companions to nearby low-mass stars, as isolated field objects, in young open clusters, and in star-forming regions.

1.1 The Initial Mass Function

1.1.1 Definitions

The stellar Initial Mass Function, $\xi(\log m)$, was defined by Salpeter (1955) as the number of stars N in a volume of space V per logarithmic mass interval $d \log m$:

$$\xi(\log m) = \frac{dN/dV}{d \log m} = \frac{dn}{d \log m} \quad \text{stars pc}^{-3} M_{\odot}$$

where $n = N/V$ represent the stellar number-density and m the mass.

Scalo (1986) defined the mass spectrum, $\xi(m)$, as the number density distribution of stars per unit mass bin. The mass spectrum, whose definition is given below, is linked to the logarithmic mass function by:

$$\xi(m) = \frac{dn}{dM} = \frac{1}{m (\ln 10)} \xi(\log m) \quad \text{stars pc}^{-3} M_{\odot}$$

The most commonly used approximations for the logarithmic and linear IMFs are power laws of index x and α , respectively:

$$\xi(\log m) = m^{-x} \quad \text{and} \quad \xi(m) = m^{-\alpha}$$

The x and α indices are related by the relation $x = \alpha - 1$.

The Initial Mass Function represents the distribution of stars with mass which were born together. However, as stars more massive than the Sun evolve off the main-sequence within the age of the Galactic disk, the present distribution of stars above $1 M_{\odot}$ differs from the primordial distribution. For stars with masses below about $0.8 M_{\odot}$, the initial mass function is well approximated by the present-day mass function.

Many studies have investigated the IMF over a large mass range in the solar neighbourhood and in young clusters. A brief overview of these estimates is given in § 1.1.3 with an emphasis on the substellar IMF. The results quoted throughout this work for the IMF derived from the observed

luminosity function will refer to the mass spectrum (unless otherwise stated) i. e. $\frac{dN}{dM} \propto M^{-\alpha}$, where α represents the slope of the power law.

1.1.2 The mass-luminosity relation

The observed quantity is the luminosity function and not the mass function. A mass-luminosity relation is required to transform the observed parameters such as fluxes and colours into physical parameters, including masses and effective temperatures. On the one hand, the mass-luminosity relation can be obtained from various evolutionary models down into the substellar regime as described below. On the other hand, a mass-luminosity relation can be derived from the observations of nearby stars with accurate trigonometric parallaxes. However, this approach is hampered by several difficulties, including the small statistics of stars with known masses and the limited depth of parallax programs. At a given age τ , the relation between the luminosity function, $\frac{dn}{dM_\lambda(m)}$, and the mass function, $\frac{dn}{dM}$, is as follows:

$$\frac{dn}{dM}(m)_\tau = \left(\frac{dn}{dM_\lambda(m)} \right) \times \left(\frac{dM_\lambda(m)}{dm} \right)_\tau$$

where $\frac{dM_\lambda(m)}{dm}$ represents the mass-luminosity relation. $M_\lambda(m)$ denotes the absolute magnitude in a given filter centred on the wavelength λ .

Two different ways exist to transform the luminosity function into a mass function. The first method involves the modelling of the luminosity function at a given wavelength to derive its mass function. The second method involves multi-colour photometry, spectroscopy, and proper motions to place each individual object in a Hertzsprung-Russell diagram in order to estimate their mass. The latter approach, which will be used in this work, requires a huge amount of telescope time. Both techniques suffer from uncertainties, including the large contamination by field stars at the low-mass end, the effect of reddening, and the uncertainties in pre-main-sequence isochrones. The most frequently used sets of isochrones to convert magnitudes into masses in young clusters are listed below:

- Palla & Stahler (1993) computed pre-main-sequence evolutionary tracks for stars in the 1.0–7.0 M_\odot mass range. The objects originated from protostars accreting from molecular clouds and were followed up to an age of 100 Myr.
- D'Antona & Mazzitelli (1994) computed pre-main-sequence evolutionary tracks for objects younger than 100 Myr over the 2.5–0.015 M_\odot mass range, assuming hydrostatic equilibrium, no mass accretion, and no mass loss.
- Burrows et al. (1997) generated non-gray solar-metallicity models predicting the colours, spectral energy distributions, and evolution of brown dwarfs and extrasolar giant planets down to 0.3 M_{Jup} from 1 Myr to 10 Gyr.
- Baraffe et al. (1998) generated non-gray solar metallicity pre-main-sequence isochrones for low-mass stars down to the substellar regime (1.4–0.020 M_\odot) spanning 1 Myr–1 Gyr in age (NextGen models). These models have been extended to 0.001 M_\odot (Dusty models; Chabrier et al. 2000b) and include the treatment of grain formation in the equation of state and in the opacity. A third set of models, the Cond models (Chabrier et al. 2000b), consider the settling of refractory species, hence eliminating their role in the opacity.

- Siess et al. (2000) presented new pre-main-sequence evolutionary tracks from 0.1 to $7.0 M_{\odot}$ at four different metallicities ($Z = 0.01–0.04$), including solar metallicity.

1.1.3 Observational determinations of the IMF

The pioneering study of the IMF by Salpeter (1955) yielded a slope with an index α equal to 2.35 between 0.4 and $10 M_{\odot}$, when expressed as the mass spectrum (Figure 1.1). Miller & Scalo (1979) and Scalo (1986) extended the IMF in the subsolar regime and approximated the mass spectrum by a three segment power law with α equal to 1.4, 2.5, and 3.3 in the mass ranges $0.1 \leq M \leq 1 M_{\odot}$, $1 \leq M \leq 10 M_{\odot}$, and $M \geq 10 M_{\odot}$, respectively (Figure 1.1). Scalo (1986) updated the determination of the mass function by Miller & Scalo (1979) using the luminosity function taking into account the latest star-count surveys in the solar neighbourhood (Wielen, Jahreiß, & Krüger 1983) and deep photometric surveys (Reid & Gilmore 1982). However, the low-mass end of the luminosity function considered by Scalo (1986) is now outdated because, on the one hand, its mass-luminosity relation is inconsistent with current stellar models, and, on the other hand, the luminosity function is not corrected for binarity.

Since the extensive study of the mass function by Scalo (1986), several breakthroughs occurred regarding the luminosity function determination. First, several deep photometric surveys were conducted along different lines of sight, yielding similar results on the shape of the luminosity function at faint magnitudes (e.g. Tinney et al., 1993). Second, progress in the modelling of the scatter observed in colour-magnitude diagrams were achieved (Kroupa, Tout, & Gilmore 1993). Third, the mass-magnitude relation was better constrained observationally to fainter magnitudes and explained theoretically (Kroupa, Tout, & Gilmore 1990). Finally, surveys dedicated to the multiplicity of field G, K, and M dwarfs (Duquennoy & Mayor 1991; Fischer & Marcy 1992) helped constraining the binary properties of nearby stars, and, thus their influence on the mass function determination.

Using the latest set of data available in the solar neighbourhood and in young clusters, Kroupa, Tout, & Gilmore (1993) extended the IMF to the hydrogen-burning limit. They represented the mass function (Figure 1.1) by a three segment power law with $\alpha = 2.7$ for stars more massive than $1 M_{\odot}$, $\alpha = 2.2$ from 0.5 to $1.0 M_{\odot}$, and $\alpha = 0.7–1.85$ in the $0.08–0.5 M_{\odot}$ mass range with a best estimate of 1.3 (Kroupa 2002). The latter estimate is in agreement with the Salpeter's estimate between 0.5 and $1 M_{\odot}$, and also above $1 M_{\odot}$.

The IMF is fairly well constrained in the $1.0–0.1 M_{\odot}$ mass range but uncertainties remain at the high and low-mass ends. For stars more massive than $15 M_{\odot}$, several complications affect the determination of the IMF, including the difficulty of spectral classification, the uncertainties on the kinematics, and the unresolved binary companions. On the low-mass end, the recent determinations of the IMF across the hydrogen-burning limit are briefly quoted below, suggesting a power law index of $\alpha = 0.5–1.0$ in the $0.5–0.03 M_{\odot}$ mass range.

Reid et al. (1999) approximated the mass function of stars within 8 parsecs by a power law with an index α ranging from 1.0 to 2.0 with a mean value of 1.3 in the $0.1–1.0 M_{\odot}$ mass range. This result was superseded by a more recent work, yielding a index of about 1.3, in agreement with the former study, as well as a change in slope in the range $0.7–1.1 M_{\odot}$ (Reid et al. 2002a). This latest estimate of the nearby mass function essentially verifies the results of Kroupa et al. (1993), yielding a consensus on the field-star mass function. Uncertainties remain nevertheless large with regard to the choice of the mass-luminosity relation for the 8-pc sample which constitute a mixture

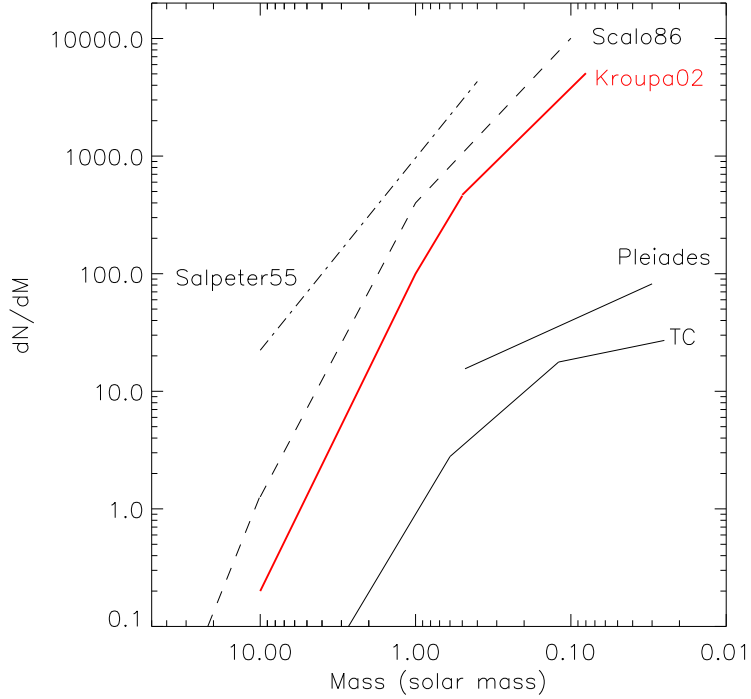


Figure 1.1: Comparison of IMF from the literature, including the pioneering estimate by Salpeter (1955; dashed-dotted line), the studies by Scalo (1986; dashed line) and Kroupa (2002; solid line). The derived mass functions for the Pleiades (Moraux et al. 2003) and the Trapezium Cluster (Muench et al. 2002) are overplotted as solid lines for comparison purposes. The different estimates are offset along the y-axis for clarity.

of stars at different ages and distances.

The advent of sensitive and wide-field optical and infrared detectors led to the discovery of a large number of substellar objects in young open clusters and in star-forming regions. In Table 1.1, we list the recent substellar IMF determinations obtained in the Pleiades (Bouvier et al. 1998; Martín et al. 1998; Tej et al. 2002; Dobbie et al. 2002; Moraux et al. 2003), α Per (Barrado y Navascués et al. 2002), σ Orionis (Béjar et al. 2001), IC348 clusters (Najita et al. 2000; Tej et al. 2002; Luhman et al. 2003b), in the Taurus cloud (Briceño et al. 2002; Luhman et al. 2003a), and in the Trapezium Cluster (McCaughrean et al. 2002a; Hillenbrand & Carpenter 2000; Luhman et al. 2000; Muench et al. 2002).

One should nevertheless keep in mind that the measured mass function will not be the same as the true IMF for several reasons. First, unresolved multiple systems will high faint companions which are not corrected for in the mass function (Kroupa 2001). The binary population evolves with time through disruption of multiple systems occurring at early ages (Kroupa 2002). In addition, the derivation of an IMF from high-mass stars down to the substellar regime is a difficult task due to dynamical evolution leading to the loss of massive and low-mass stars (Kroupa 2002). Finally, gas expulsion during the earliest times of an embedded cluster leads to violent evolution

which might affect the shape of the IMF (Kroupa et al. 2001).

To summarise, the current knowledge on the substellar IMF suggests a power law index in the range 0.5–1.0 for a large number of open clusters and star-forming regions (Table 1.1). The recent study in the low-density Taurus cloud, however, indicates a dearth of brown dwarfs compared to the Trapezium Cluster and IC348 (Briceño et al. 2002; Luhman et al. 2003a). The derived mass function peaks around $0.8 M_{\odot}$ and $0.1\text{--}0.2 M_{\odot}$ in Taurus and IC348, respectively, followed by a decline into the substellar regime when expressed in logarithmic units (Figure 1.7).

This difference might indicate a possible variation of the IMF with environment. This point is important to address the issue of the formation of brown dwarfs. Based on hydrodynamical simulations, Delgado-Donate et al. (2004) concluded that the substellar IMF is more sensitive to initial conditions than the stellar mass function, hence providing a possible explanation for the dearth of brown dwarfs observed in Taurus compared to the Trapezium Cluster. Kroupa & Bouvier (2003a) conducted N-body simulations and favoured the ejection from multiple systems to explain the variability of the substellar population between low-mass and massive star-forming regions. Those results support the conclusions from surveys dedicated to the binarity of field brown dwarfs (Burgasser et al. 2003b; Close et al. 2003; Bouy et al. 2003).

Table 1.1: The substellar IMF determinations in young open clusters and in star-forming regions. The estimates of the slope of the IMF, expressed as the mass spectrum ($\frac{dN}{dM} \propto M^{-\alpha}$), are provided for the Pleiades, α Per, σ Orionis, and IC348 clusters, the Taurus region, and Trapezium Cluster (TC). The mass range where the mass function is valid is given in solar mass (M_{\odot}). The value of α is not given for Taurus and IC348 because the authors did not attempt to fit the mass functions given in logarithmic scale. In Figure 1.7, we compare both estimates along with the determinations in the Trapezium Cluster and in σ Orionis.

Cluster	Age Myr	Distance parsecs	Mass range M_{\odot}	Mass spectrum Slope α	References
Pleiades	125 ± 8	130	0.25–0.040	1.00 ± 0.50	Martín et al. 1998
			0.40–0.040	0.60 ± 0.15	Bouvier et al. 1998
			0.50–0.055	0.50 ± 0.20	Tej et al. 2002
			0.60–0.030	0.80	Dobbie et al. 2002
			0.48–0.030	0.60 ± 0.11	Moraux et al. 2003
α Per	90 ± 10	182	0.30–0.035	0.59 ± 0.05	Barrado y Navascués et al. 2002
			0.20–0.013	0.80 ± 0.40	Béjar et al. 2001
σ Ori	3–8	352	0.30–0.030		Luhman et al. 2003b
			0.50–0.035	0.70 ± 0.20	Tej et al. 2002
			0.22–0.015	0.50	Najita et al. 2000
IC348	1–3	315	0.30–0.035		Briceño et al. 2002
			0.15–0.020	0.43	Hillenbrand & Carpenter 2000
			0.56–0.035	0.70	Luhman et al. 2000
			0.60–0.120	1.15	Muench et al. 2002
Taurus	1–2	140	0.12–0.025	0.27	Muench et al. 2002
TC	≤ 1	450			

1.2 The formation of brown dwarfs

Molecular clouds fragment into smaller entities which collapse once they exceed the thermal Jeans mass. The minimum mass reached by fragmentation is approximately $0.007 M_{\odot}$ under high density medium (Hoyle 1953; Rees 1976; Low & Lynden-Bell 1976). This lower mass limit is achieved when the collapse becomes optically-thick that is when the central object cannot radiate its heat away and is unable to fragment further. The subsequent accretion of the surrounding material on the central object leads to the formation of stars of different masses.

As a consequence, the formation mechanism of brown dwarfs appear controversial for two aspects. First, the critical mass a volume of space must contain before it will collapse under the force of its own gravity, called the Jeans mass, is typically an order of magnitude higher than the mass of a brown dwarf. Second, the central object should stop accreting in order not to reach the hydrogen-burning limit. We will briefly describe below mechanisms which have emerged over the last years to explain the existence of brown dwarfs as companions to stars, as isolated objects, and in young clusters.

1.2.1 The theory of brown dwarf formation

Turbulence

In this scenario, stars form from turbulent fragmentation of molecular clouds (for a review on this topic, refer to Mac Low & Klessen 2004). On the one hand, supersonic turbulence will prevent the collapse of large scale structures. On the other hand, the enhancement of density fluctuations on small scales will provoke their collapse. At later stages, the gravity takes over. This picture can be extended to lower masses, including substellar masses, assuming large enough density fluctuations (Klessen 2001; Padoan & Nordlund 2002).

Irradiated pre-stellar cores

A mechanism proposed by Whitworth & Zinnecker (2003; personal communication) suggests that brown dwarfs may be prestellar cores whose outer layers were eroded by the ionising radiation from OB stars. This process, obviously only possible in OB associations, requires large fluxes of ionising photons, high densities of hydrogen, and small isothermal sound speed, according to the model.

Disk instabilities

Gravitational instabilities of self gravitating protostellar disks might be responsible for the formation of brown dwarfs (Boss 1998, 2000; Li 2002). The inclusion of strong magnetic fields in the disk, responsible for an efficient cooling, can reduce the classical opacity-limit fragmentation (Low & Lynden-Bell 1976) by a factor of 10 to produce fragments with masses less than a Jupiter mass (Boss 2001).

The formation mechanism of brown dwarfs might be induced by star-disk (Boffin et al. 1998) and disc-disc encounters (Watkins et al. 1998a, 1998b; Lin et al. 1998) occurring at early stages with the presence of massive disks.

Star-disk interactions tend to truncate the disk and trigger its fragmentation to produce new stars, many of them ending up into multiple systems. For disk-disk interactions, the evolution

of the system is dominated by the fragmentation of the disk to produce twice or three times as many companions to the original stars as star-disk encounters. In coplanar disk-disk encounters, the disk material between the two interacting stars is swept into a shock layer that fragments to produce new objects, including brown dwarfs (Watkins et al. 1998a). Non-coplanar encounters trigger gravitational instabilities in the disk, which then fragment to form new companions (Watkins et al. 1998b).

In recent hydrodynamical calculation by Bate, Bonnell, & Bromm (2002), three quarters of brown dwarfs formed via fragmentation of gravitationally unstable disks, followed by a subsequent ejection from multiple systems.

Ejection mechanism

The dynamical ejection of the least massive component in multiple systems can account for brown dwarfs as well and is necessary to stop the accretion phase during the formation process (McDonald & Clarke 1993; Reipurth & Clarke 2001). This scenario suggests that brown dwarfs stopped accreting gas from the molecular cloud due to an early ejection from a multiple system (Reipurth & Clarke 2001), in agreement with the conclusions drawn from the hydrodynamical simulation by Bate et al. (2002) where all brown dwarfs are ejected, independent of their formation mechanism.

Delgado-Donate et al. (2003) and Sterzik & Durisen (2003) conducted modelling of the decay of non-hierarchical N-body systems to investigate the properties of each individual object after completion of the decay. The main results of these simulations, in terms of multiplicity, mass ratio and binary separation distributions of low-mass stars and brown dwarfs, can be summarised as follows:

1. Brown dwarfs are preferentially companions to low-mass stars. Pure binary brown dwarfs are predicted to be rare by the N-body simulations. If brown dwarfs are seen as companions, the primary is often a binary. The latter prediction await for observational tests. The simulation by Bate et al. (2002) formed at most one binary brown dwarf with a separation smaller than 10 AU, indicating that binary brown dwarfs should be less frequent than 5 %. This prevision contradicts recent observations suggesting a lower limit of about 10 % (Burgasser et al. 2003b; Close et al. 2003; Bouy et al. 2003). However, the present comparison of theoretical predictions and observations is hampered by small statistics.
2. The mass ratio distribution of brown dwarfs is predicted to be flat with rare extreme mass ratios, in agreement with current observations. Low-mass and brown dwarf binaries have separations smaller than 16 AU with a peak in the distribution around 4-8 AU (Burgasser et al. 2003b; Close et al. 2003; Bouy et al. 2003).
3. Velocity dispersions should be typically of a few km s^{-1} . Brown dwarfs would tend to exhibit slightly higher velocities than their stellar counterparts. This fact represents a potential explanation for the lack of low-mass stars and brown dwarfs in open clusters older than 200 Myr, in agreement with recent dynamical evolution simulations by de la Fuente Marcos & de la Fuente Marcos (2000).

Formation in circumstellar disks

Straddling the realms of stars and planets, brown dwarfs might also form within a circumstellar disk as the giant planets of our Solar System. The formation of planets in circumstellar disks is a longer process than the disk instabilities discussed earlier because the rocky core needs time to grow by accretion and become a planet. To test this scenario, Papaloizou & Terquem (2001) implemented simulations of dynamical interactions of $5 \leq N \leq 100$ planetary-mass objects within 100 AU of a solar mass star on a time-scale of about 100 orbits. At the end of the simulation, at most three planetary mass objects remained bound to the central star, the remainder objects being ejected. As those simulations do not impose an lower limit on the mass, the ejected objects could contribute to the population of planetary-mass objects uncovered in the Trapezium Cluster (Lucas & Roche 2000) and σ Orionis (Zapatero Osorio et al. 2000).

Radial velocity searches have noticed a lack of tight (≤ 3 AU) brown dwarf companion to solar-type stars at odds with the one hundred extrasolar planets discovered to date. Motivated by this ‘brown dwarf desert’, Armitage & Bonnell (2002) envisioned a scenario where brown dwarfs migrate either inwards or outwards, depending on the initial separation. For example, a $0.040 M_{\odot}$ brown dwarf would migrate inwards and merge into the central star in a few Myr if the initial orbital radius is smaller than 5 AU. For radii larger than 10 AU, where the disk is expanding, outwards migration occurs and pushes brown dwarfs out to radii of about 100 AU. As a consequence, the model predicts a reduction by a factor of 5 to 10 of tight brown dwarf companions to solar mass stars older than a few Myr, explaining thus the observed ‘brown dwarf desert’.

1.2.2 Observational constraints on the formation of brown dwarfs

To address the issue regarding the formation of brown dwarfs and constrain the proposed mechanisms (§ 1.2.1), several surveys have recently been carried out to search for disks around young brown dwarfs in various environments. The presence of disks around substellar objects will imply a star-like formation scenario. Truncated disks will favour the ejection model described by Reipurth & Clarke (2001) whereas the absence of disks will suggest a planet-like formation mechanism followed by dynamical ejection. Planets can nevertheless have their own disks from which their moon systems form due to the angular momentum of the accreting material.

The direct evidence for disks around young low-mass stars and brown dwarfs has been found using five different techniques described below:

1. Near-infrared (J at $1.25 \mu\text{m}$, H at $1.65 \mu\text{m}$, and K at $2.2 \mu\text{m}$) excess of selected members were reported in the Trapezium Cluster (McCaughrean & O’Dell 1996; Hillenbrand et al. 1998; Muench et al. 2002), ρ Ophiuchus (Wilking et al. 1999; Cushing et al. 2000), IC348 (Luhman 1999), and σ Orionis (Oliveira et al. 2002) based on their location in the ($J-H, H-K$) colour-colour diagram. The disk frequency around brown dwarfs appears lower in the σ Orionis cluster ($6 \pm 4\%$; Oliveira et al. 2002) than in the Trapezium Cluster ($65 \pm 15\%$; Muench et al. 2002), suggesting a disk lifetime lower than few Myr.
2. High-resolution spectroscopy for a large sample of spectroscopically confirmed low-mass stellar and brown dwarf members in a variety of star-forming regions, including Taurus, IC348, ρ Ophiuchus, and Upper Scorpius, showed that all of the targets exhibit moderate to strong asymmetric $\text{H}\alpha$ emission lines (Jayawardhana et al. 2002, 2003b; Muzerolle

et al. 2003; White & Basri 2003). Some objects also exhibit emission features such as OI (8446 Å), CaII (8662 Å), and HeI (6678 Å), characteristic of accretion in classical TTauri stars. Furthermore, the fraction of accretors tends to decrease with increasing age. In addition, the inferred accretion rates are lower than in TTauri stars by at least one order of magnitude and range from $10^{-9} M_{\odot} \text{ yr}^{-1}$ to $10^{-12} M_{\odot} \text{ yr}^{-1}$ (Muzerolle et al. 2003), suggesting the mass of the disk scales with the mass of the central object. Finally, Barrado y Navascués & Martín (2003) have reported similar timescales of accretion for low-mass stars and brown dwarfs.

3. Two extensive and complementary L'-band at $3.8 \mu\text{m}$ surveys were conducted in various star-forming regions and associations (ρ Oph, IC348, Chameleon I, Taurus, Upper Scorpius, σ Orionis, and TW Hydrae) to search for disk around pre-main-sequence objects with spectral types later than M5 (Liu, Najita, & Tokunaga 2003; Jayawardhana et al. 2003a). The L'-band offers two advantages compared to near-infrared (*JHK*) filters. First, the emission from the brown dwarf photosphere is lower at $3.8 \mu\text{m}$ than below $2.5 \mu\text{m}$ and, second, the dust sublimes at temperatures hotter than 1000 K. Those studies concluded that a large number of young low-mass stars and brown dwarfs harbour infrared $K-L'$ excesses correlated with strong H α emission, indicating a common formation mechanism for stars and brown dwarfs. The disk frequency decreases with increasing age, supporting the idea that disks do not survive longer than 10 Myr.
4. The first evidence for disks around young brown dwarfs were made in the mid-infrared with ISO (Infrared Space Observatory) measurements in ρ Ophiuchus (Bontemps et al. 2001) and in Chameleon I (Comerón et al. 2000; Persi et al. 2000). The spectral energy distributions of brown dwarfs in both regions were successfully fit by optically-thick flared disk models (Natta et al. 2002) with a possible extension to the planetary-mass regime (Testi et al. 2002), suggesting a common formation mechanism for stars and substellar mass objects. Mid-infrared ground-based measurements failed, however, to detect the silicate feature around $10 \mu\text{m}$ (Apai et al. 2002) predicted by flared disk models (Natta & Testi 2001), indicating that an optically-thick flat disk model might be sufficient to explain the observed fluxes. The mid-infrared spectral energy distribution of nearby old brown dwarfs was satisfactorily reproduced by a blackbody at the temperature of the photosphere, confirming the dissipation of disks within few hundred Myr.
5. The first dust continuum emission associated with young brown dwarfs belonging to the Taurus cloud and the IC348 cluster were reported by Klein et al. (2003). Upper limits of the quantity of dust were inferred around Pleiades and old field brown dwarfs and amounts for few Earth and Moon masses, respectively. Those detections suggest that planets might form around brown dwarfs. The presence of circumstellar dust around young brown dwarfs along with the discovery of binary brown dwarfs (Burgasser et al. 2003b; Close et al. 2003; Bouy et al. 2003) exclude the fragmentation of disks as major formation mechanism of brown dwarfs.

1.2.3 Conclusions on the formation of brown dwarfs

Several mechanisms have recently emerged to explain the existence of brown dwarfs, including turbulence, erosion of pre-stellar cores, protostellar disk instabilities with subsequent fragmenta-

tion and collapse, dynamical ejection from multiple systems, and in circumstellar disks. Current observations conducted in the infrared have concluded that a large fraction of brown dwarfs are surrounded by disks within the first Myr of their life as stars are. However, the L' -band and mid-infrared measurements below $15\ \mu\text{m}$ are only capable to probe the inner radii (\leq few AU) of disks around brown dwarfs.

The planet-type formation for brown dwarfs seems to be ruled out by the present observations. The ejection model proposed by Reipurth & Clarke (2001) predicts truncated circumstellar disks of a few AU in size, in agreement with the current infrared studies and N-body simulations (Kroupa & Bouvier 2003a). These results suggest that brown dwarfs and stars share a common formation mechanism. The recent observations of binary brown dwarfs (see Section 1.5.1; Burgasser et al. 2003b; Close et al. 2003; Bouy et al. 2003) and N-body simulations by Kroupa et al. (2003) suggest that brown dwarfs do not form with the same properties as stars because their binary properties do not represent a natural extension of those seen in stars. These results tend to favour the ejection mechanism proposed by Reipurth & Clarke (2001). Regarding the turbulence scenario of star formation, it remains plausible as both stellar and substellar can be formed without additional mechanism.

The next step is to determine disk sizes and masses from the (sub)millimetre wavelengths to shed light on the formation mechanism(s) of brown dwarfs. The expected fluxes from disks around young brown dwarfs are within the capabilities of future instrumentation, including the Atacama Large Millimeter Array (ALMA).

1.3 The physics of brown dwarfs

Current observations suggest that stars and brown dwarfs share a common formation mechanism (§ 1.2). How about the physics? Stars are large spheres of gas where the nuclear fusion compensates the gravitational energy, yielding a relationship $R \propto M^{0.6}$ between the mass (M) and the radius (R). As the electron degeneracy pressure becomes more and more important at the low-mass end of the main-sequence, the evolution of a brown dwarf is not dominated by thermonuclear processes. As a consequence, brown dwarfs cool off inexorably as they age.

This section is structured as follows. First, we describe the evolution of luminosity (§ 1.3.1), effective temperature (§ 1.3.2), and radius (§ 1.3.3) with age. Second, we discuss the influence of metallicity on the luminosity, temperature, and mass (§ 1.3.4). Then, we present the role of deuterium and lithium burning in brown dwarfs (§ 1.3.4). Finally, we give a brief overview of the composition of brown dwarf atmospheres (§ 1.3.6).

1.3.1 The evolution of luminosity

The top panel in Figure 1.2 depicts the evolution of luminosity of substellar mass objects ranging from $0.3\ M_{\text{Jup}}$ to $0.2\ M_{\odot}$ (Burrows et al. 2001)¹. Objects with masses below the deuterium burning limit at $0.013\ M_{\odot}$ are plotted in red, brown dwarfs from 0.013 to $0.075\ M_{\odot}$ in green, and stars in blue.

The separation between stars and brown dwarfs occurs only at age older than 1 Gyr. Indeed, stars stabilise at a given luminosity when the nuclear burning in the core compensates the loss

¹ $1\ M_{\odot} = 1047\ M_{\text{Jup}}$

of photons at the surface. To the contrary, brown dwarfs will never reach core temperatures and pressures high enough to ignite hydrogen. Only brown dwarfs more massive than $0.065 M_{\odot}$ will burn hydrogen briefly, but not stably.

The late-time (≥ 1 Gyr) evolution of luminosity of substellar objects can be approximated by the Equation 1.1 (Burrows et al. 2001):

$$L \sim 4 \times 10^{-5} L_{\odot} \left(\frac{10^9 \text{yr}}{t} \right)^{1.3} \left(\frac{M}{0.05 M_{\odot}} \right)^{2.64} \left(\frac{\kappa_R}{10^{-2} \text{cm}^2 \text{gm}^{-1}} \right)^{0.35} \quad (1.1)$$

where κ_R is an average atmospheric Rosseland opacity. The luminosity of a solar-metallicity star at the hydrogen burning limit is $6 \times 10^{-5} L_{\odot}$. According to Figure 1.2, the luminosity² of a $0.030 M_{\odot}$ object is approximately $10^{-2} L_{\odot}$ at 1 Myr falling down to $6 \times 10^{-6} L_{\odot}$ at 1 Gyr. This quick computation demonstrates why the detection of old brown dwarfs is limited to the Solar Neighbourhood whereas young substellar objects are uncovered in more distant open clusters and star-forming regions.

For comparison, the luminosity of main-sequence low-mass stars is approximately independent of age and is a weaker function of mass than for brown dwarfs as shown in Equation 1.2:

$$L_{star} \sim 10^{-3} L_{\odot} \left(\frac{M}{0.1 M_{\odot}} \right)^{2.2} \quad (1.2)$$

1.3.2 The evolution of temperature

The bottom panel in Figure 1.2 depicts the evolution of the effective temperatures of substellar mass objects spanning $0.3 M_{\text{Jup}} - 0.2 M_{\odot}$ in mass (Burrows et al. 2001).

If the mass is high enough, the thermonuclear power equals the total luminosity allowing the surface and core temperatures to stabilise, yielding a core temperature of about 3×10^6 K at the hydrogen-burning limit. However, the core of brown dwarfs will not achieve temperatures sufficient enough to balance nuclear burning and photon losses. Their core temperatures rise with age, reach a peak before falling down again. The peak of the core temperature is mass dependent and is given below:

$$T_c \sim 2 \times 10^6 \text{ K} \left(\frac{M}{0.05 M_{\odot}} \right)^{4/3}$$

The late-time evolution of the effective temperature of brown dwarfs is reproduced by the power-law given in Equation 1.3 (Burrows et al. 2001). The effective temperature is of prime importance in the classification schemes for brown dwarfs (Section 1.4).

$$T_{\text{eff}} \sim 1550 \text{ K} \left(\frac{10^9 \text{yr}}{t} \right)^{0.32} \left(\frac{M}{0.05 M_{\odot}} \right)^{0.83} \left(\frac{\kappa_R}{10^{-2} \text{cm}^2 \text{gm}^{-1}} \right)^{0.088} \quad (1.3)$$

According to Figure 1.2, a $0.030 M_{\odot}$ mass brown dwarf has effective temperatures of approximately 2800 K and 900 K at 1 Myr and 1 Gyr, respectively.

²A calculator for brown dwarfs is available on Burrows's homepage: <http://zenith.as.arizona.edu/~burrows/>

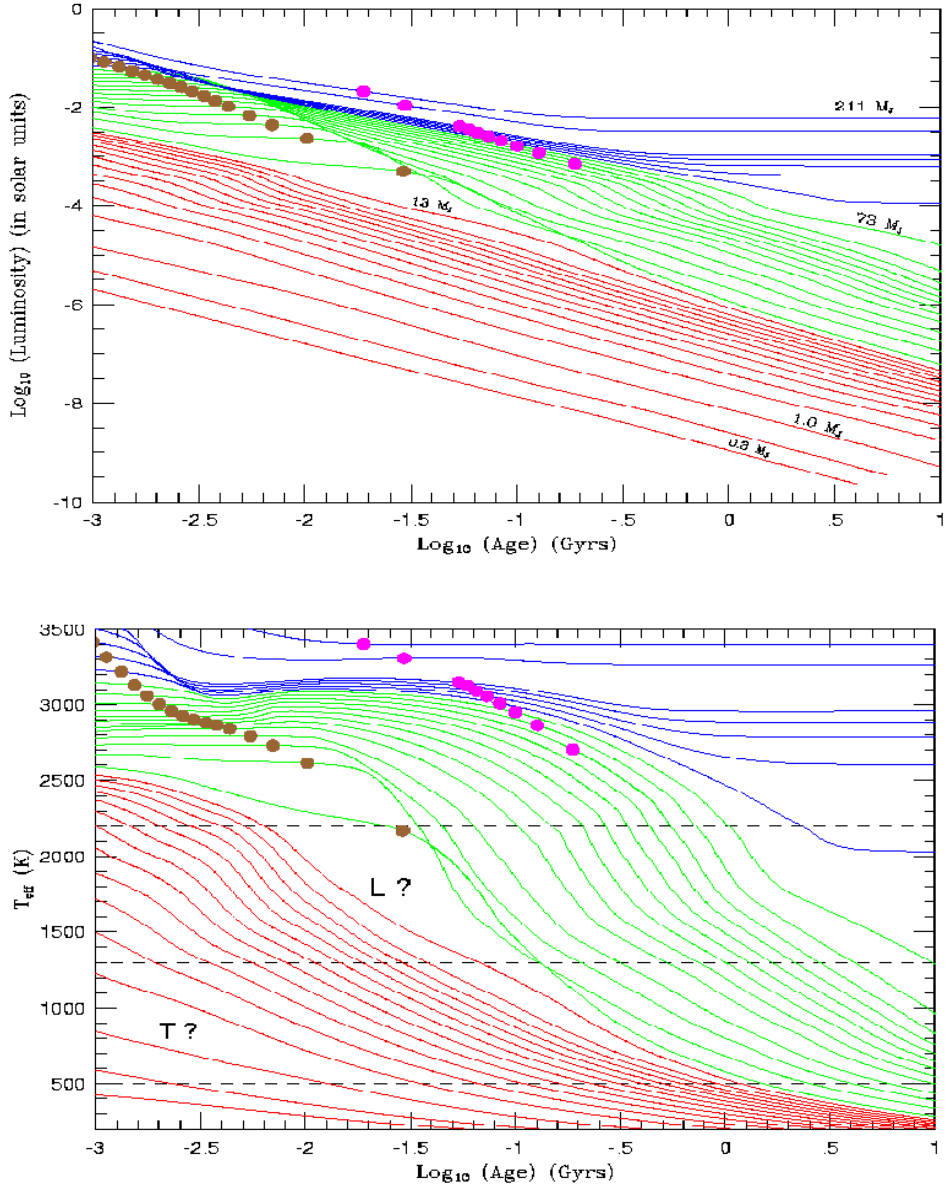


Figure 1.2: These figures, extracted from Burrows et al. (2001), depict the evolution of luminosity (top panel) and effective temperature (bottom panel) versus age of isolated solar-metallicity red dwarfs and substellar-mass objects. The stars are shown in blue, brown dwarfs above $0.013 M_{\odot}$ in green, and brown dwarfs below $0.013 M_{\odot}$ in red. The masses of objects portrayed are $0.3, 0.5, 1.0, 2.0, 3.0, 4., 5.0, 6.0, 7.0, 8.0, 9.0, 10.0, 11.0, 12.0, 13.0$, and $15.0 M_{J_{\text{up}}}$ and $0.02, 0.025, 0.03, 0.035, 0.04, 0.05, 0.06, 0.065, 0.07, 0.075, 0.08, 0.085, 0.09, 0.095, 0.1, 0.15$, and $0.2 M_{\odot}$. For a given object, the gold and magenta dots mark when 50 % of the deuterium and lithium have burned, respectively.

1.3.3 The evolution of radius

The radius decreases with age for a given mass and reaches a plateau at ages older than about 1 Gyr. For very low-mass stars, the radius increases with mass as $R \propto M^{0.6}$ but is roughly independent of age while on the main-sequence. However, the radius increases with mass for brown dwarfs younger than 100 Myr and decreases at later times. As a consequence of the competition in the equation of state between the Coulomb and the electron degeneracy, the radii of old substellar objects are independent of mass to within 30 % with the least massive ones having larger radii. Indeed, the Coulomb degeneracy yields a radius-mass relation of $R \propto M^{1/3}$ whereas the electron degeneracy (two electrons cannot occupy similar states according to the Pauli Exclusion Principle) gives $R \propto M^{-1/3}$. A more thorough analysis of the mass-radius dependence yields a relation of $R \propto M^{-1/8}$ (Chabrier & Baraffe 2000).

The radius of old substellar objects can be approximated by Equation 1.4 given below (Burrows et al. 2001).

$$R \sim 6.7 \times 10^4 \text{ km} \left(\frac{10^5}{g} \right)^{0.18} \left(\frac{T_{\text{eff}}}{1000 \text{ K}} \right)^{0.11} \quad (1.4)$$

As an example, a $0.030 M_{\odot}$ mass brown dwarf has a radius of $4.3 R_{\text{Jup}}$ and $1.0 R_{\text{Jup}}$ at 1 Myr and 1 Gyr, respectively.

1.3.4 The influence of metallicity

The properties of stars and brown dwarfs are a function of the helium fraction ($Y_{\alpha} \sim 0.25$ –0.28), the metallicity, and the opacity of the clouds in the atmosphere. Larger helium fraction, larger metallicities and larger opacities produce lower central temperature and decrease the energy from the surface, yielding more compact objects with lower masses.

The mass of a star at the hydrogen-burning limit is a function of metallicity with values between 0.070 and $0.092 M_{\odot}$ at solar and zero metallicity, respectively. Moreover, the luminosity of a star at the stellar/substellar boundary increases from 6×10^{-5} to $6 \times 10^{-3} L_{\odot}$ and its effective temperature by a factor of two from 1700 K to 3600 K with decreasing metallicity.

On the observational side, a solar-metallicity star at the hydrogen-burning limit has absolute magnitudes of $M_V = 19.5$, $M_R = 18.0$, and $M_K = 11.5$ compared to 12.8, 12.0, and 11.1 at zero-metallicity. The similarity in the K -band magnitudes is a consequence of collision-induced absorption by H_2 which suppresses the flux longwards of $2.0 \mu\text{m}$. Subdwarfs (or low-metallicity dwarfs with $[\text{Fe}/\text{H}]$ between –2.0 to –1.0) are, thus, intrinsically more luminous than normal dwarfs.

1.3.5 Deuterium and lithium burning in brown dwarfs

Substellar objects do not generate sufficient thermonuclear power to reach the hydrogen-burning limit but the most massive ones can have partial or temporary nuclear phases.

Objects more massive than $0.013 M_{\odot}$ will burn deuterium via the $p + d \rightarrow \gamma + {}^3\text{He}$ reaction. The evolution of the deuterium fraction versus age shows that all brown dwarfs more massive than $0.015 M_{\odot}$ have burned their deuterium within 30 Myr. This limit corresponds to $T_{\text{eff}} \sim 2000 \text{ K}$, spectral types around L0–L2, and luminosity of $10^{-3} L_{\odot}$.

Stars more massive than approximately $0.3 M_{\odot}$ are composed of a convective outer layer and a radiative core. Lithium is mixed in the convective part of the star but is unable to reach the central part due to the radiative region, implying that lithium is retained. On the contrary, low-mass stars ($\lesssim 0.3 M_{\odot}$) are fully convective. As a consequence, lithium can reach the central core of the star and be destroyed if the temperature is high enough.

In the substellar regime, brown dwarfs more massive than $0.065 M_{\odot}$ and older than 300 Myr will totally deplete their lithium, while substellar objects younger than 30 Myr will retain it all. Brown dwarfs more massive than $0.065 M_{\odot}$ with an age range between 30 and 300 Myr will burn lithium isotopes via the $p + {}^6Li \rightarrow \alpha + {}^3He$ and $p + {}^7Li \rightarrow 2\alpha$ reactions. This theoretical prediction translates into an observational boundary, known as the lithium depletion boundary, between objects which exhibit lithium in absorption and those which do not. Indeed, above a given magnitude, lithium will not be spectroscopically observable because depleted, while below this magnitude limit, the lithium absorption line will appear in the spectra at 6708 \AA . This lithium depletion boundary technique, called the lithium test (Rebolo et al. 1992), was successfully applied to date open clusters, including the Pleiades (Stauffer et al. 1998), α Per (Stauffer et al. 1999), IC2391 (Barrado y Navascués et al. 2001a), and NGC 2547 (Oliveira et al. 2003).

1.3.6 Atmosphere models of low-mass stars and brown dwarfs

The main species near and above solar metallicity brown dwarf photospheres are hydrogen, helium, oxygen, carbon, and nitrogen. Strong molecular bands, absorption features, and dust are responsible for the shape and the observed spectral energy distributions of brown dwarfs. We will briefly discuss below the composition of brown dwarf atmospheres and the theoretical atmospheric models available to reproduce the emerged spectra.

- ◊ Hydrogen is predominantly in the form of H_2 and is as abundant as 90 % in brown dwarf atmospheres. Its abundance enables the presence of light hydrides (H_2O , CH_4 , NH_3 , and H_2S) as well as heavier ones, including FeH , CrH , CaH , and MgH .
- ◊ Helium is the second most abundant ($\sim 9\%$) species after hydrogen. Helium is not observed in brown dwarfs because it is chemically and spectroscopically inert.
- ◊ Oxygen is predominantly in the form of water (H_2O) and carbon monoxide (CO) but abundant enough to form of oxides, including Al_2O_3 (alumina), TiO , and VO . Titanium oxide (TiO) and vanadium oxide (VO) are responsible for the shape of M dwarf spectra but disappear at temperatures lower than $\sim 2100 \text{ K}$ and $\sim 1800 \text{ K}$, respectively, by condensing out or forming condensable species such as perovskite ($CaTiO_3$).
- ◊ Carbon is in the form of carbon monoxide (CO) at high temperatures and low pressure and of methane (CH_4) at low temperature and high pressures. Thus, CO is dominant in M dwarfs and CH_4 in T dwarfs and Jovian planets. The transition from CO to CH_4 is governed by the equation $CH_4 + H_2O \rightleftharpoons CO + 3H_2$, and occurs around 1100 K (Fegley & Lodders 1996). Carbon monoxide has been detected at $4.5\text{--}5.0 \mu\text{m}$ in Gl229B (Noll et al. 1997) whereas methane was observed at $3.3 \mu\text{m}$ in field dwarfs as early as L5, suggesting that vertical mixing play an important role in brown dwarf atmospheres (Saumon et al. 2000).
- ◊ The dominant form of nitrogen in brown dwarf atmospheres is NH_3 (ammonia) at low temperatures and N_2 at high temperatures. The transition from N_2 to NH_3 occurs at $600\text{--}700 \text{ K}$

and is governed by the equation $\text{N}_2 + 3 \text{H}_2 \rightleftharpoons \text{NH}_3$. Molecular nitrogen is invisible in the near-infrared but ammonia has already been detected in Gl229B (Noll et al. 1997), proof that vertical mixing is important (Saumon et al. 2000).

- ◊ Neutral alkalis like Na, K, Li, Cs, and Rb are less refractory than Ti, V, Ca, Si, Al, Fe, and Mg and survive in abundance in substellar atmospheres at temperatures around 1000–1500 K because of the condensation of other species. For example, lithium forms into LiCl below ~ 1400 K, making it undetectable in the optical spectra of T dwarfs.
- ◊ Metallic hydrides as FeH and CrH are present in late-M dwarfs, L dwarfs, and in M subdwarfs. CrH persists down to ~ 1500 K whereas FeH disappears below ~ 2000 – 2200 K after condensating on grains.
- ◊ Magnesium and silicium are more abundant than calcium and aluminium and form Mg/Si/O compounds, including Mg_2SiO_4 (forsterite) and MgSiO_3 (entstatite), which rain out around temperatures in the range 1800–2500 K.

Two simple cases of atmospheric models can broadly reproduce the spectral energy distributions of L and T dwarfs (see § 1.4 for a definition) over the 0.6–5.0 μm wavelength range.

- The Dusty models consider an atmosphere where the dust is uniformly mixed. These models reproduce the red optical-to-infrared and infrared colours of L dwarfs because the emerged photons are absorbed by the dust and re-emitted at longer wavelengths.
- The Cond models deal with an atmosphere where the dust has entirely settled down. These models reproduce the red optical-to-infrared and blue infrared colours of T dwarfs because the dust is located in the optically-thick region and photons are not reprocessed.

These two extreme cases of models are, however, unable to reproduce the overall spectral energy distributions of L/T transition objects (e.g. Leggett et al. 2000). The presence of clouds as those seen on Jupiter are introduced to explain the colours and spectra of L/T transition brown dwarfs.

Allard et al. (2001) proposed the “Settl” models as intermediate phase to the Dusty and Cond models, where refractory species are depleted and rain out.

Tsuji (2002) introduced the presence of a cloud in the atmosphere characterised by fixed particle sizes and constant temperatures at the bottom and the top.

Ackerman & Marley (2001) introduced the f_{rain} parameter, defined as the ratio between the sedimentation velocity and the convective velocity. A small value of f_{rain} corresponds to little sedimentation and dense clouds with vertical extent. The spectra of L/T transition objects were best reproduced by $f_{rain} = 3$ after varying this parameter from 0.1 to 10.

The L/T transition is nevertheless very sudden and still poorly understood. Cloud models, which allow to reproduce the observations, might still be in error. Possibilities of holes in the clouds, optically-thin regions with higher outward flux transmission, as well as other mechanisms should be included and tested in future atmospheric models.

To summarise, the actual atmosphere models broadly reproduce the spectral energy distributions of low-mass stars and brown dwarfs. Despite the improvement in the modelling of the atmospheres, several issues remain to be quantified, including the treatment of grain condensation,

the location of dust clouds, the molecular line lists for water and methane, the non-equilibrium chemistry, and the interplay between processes such as sedimentation and condensation. A large number of objects in the L/T transition with full wavelength coverage (0.4–5.0 μm) and high quality spectroscopy are mandatory to narrow down the uncertainties mentioned above.

1.4 Characterisation of M, L, and T dwarfs

The first release of the 2MASS database (Kirkpatrick et al. 1997), covering roughly 1 % of the whole sky, led to the discovery of several objects redder than late-M dwarfs with spectra comparable to the cool companion to the white dwarf GD165, GD165B (Becklin & Zuckerman 1988). Discoveries of cooler objects with strong methane bands and spectral features resembling those seen in the infrared spectrum of Gl229B (Oppenheimer et al. 1995) followed quickly (Burgasser et al. 1999; Strauss et al. 1999; Cuby et al. 1999).

The large number of objects cooler than the latest M dwarfs triggered the definition of two new spectral classes in addition to the Harvard Spectral classification scheme in use to classify stars (Morgan et al. 1943). Martín (1997) and Kirkpatrick et al. (1999b) proposed the letter “L” for the class of objects cooler than M dwarfs, with GD165B as a benchmark. The discovery of L dwarfs originates from the first analysis of the DENIS database (Delfosse et al. 1997) and the spectroscopic follow-up reported by Martín (1997). The classification was improved by Kirkpatrick et al. (1999b) using the discoveries from the 2MASS survey. Objects belonging to the same class as Gl229B were named “T” dwarfs and are sometimes dubbed “methane” dwarfs (Kirkpatrick et al. 1999b).

A further class of objects (the “Y” dwarfs) cooler than T dwarfs with strong ammonia absorption bands in the near or mid-infrared, characteristic of effective temperature cooler than 700 K could be expected in the near future (Burrows et al. 2001).

We will describe, in this section, the main characteristics of field M (§ 1.4.1), L (§ 1.4.2), and T (§ 1.4.3) dwarfs, including optical and near-infrared colours as well as major spectral features.

1.4.1 Spectroscopy of M dwarfs

The original MKK classification scheme defined a list of standards stars for each subclass from O stars to a spectral type of M2 (Morgan et al. 1943) with a subsequent extension to M5 (Johnson & Morgan 1953). Boeshaar (1976) extended this classification to a spectral type of M6.5 based on new later type dwarfs found in the meantime. The large number of late-M dwarfs discovered in the 1990s yielded a well-defined classification scheme for M dwarfs (Kirkpatrick et al. 1991; Kirkpatrick et al. 1999b; Martín et al. 1999b)

Optical spectra of M dwarfs (Figure 1.3) are characterised by strong oxide bands including TiO at 6320–6500 Å, 6600–6800 Å, 7050–7250 Å, 7590–7680 Å, 7670–7860 Å, 8430–8450 Å, and 8860–8940 Å and VO at 7330–7530 Å, 7850–7970 Å, and 8520–8670 Å. The atomic K I and Na I doublets at 7665/7699 Å and 8183/8195 Å, respectively, are strong as well. The H α emission line at 6563 Å, which represents a measure of chromospheric activity in M dwarfs, reaches a peak at around M6–M7 in spectral type and drops significantly towards later types (Hawley et al. 1996). The lithium absorption line at 6708 Å is detected in some late-M dwarfs like LP944-20 (Tinney 1998), placing constraints on the age and mass of these objects. The detection of

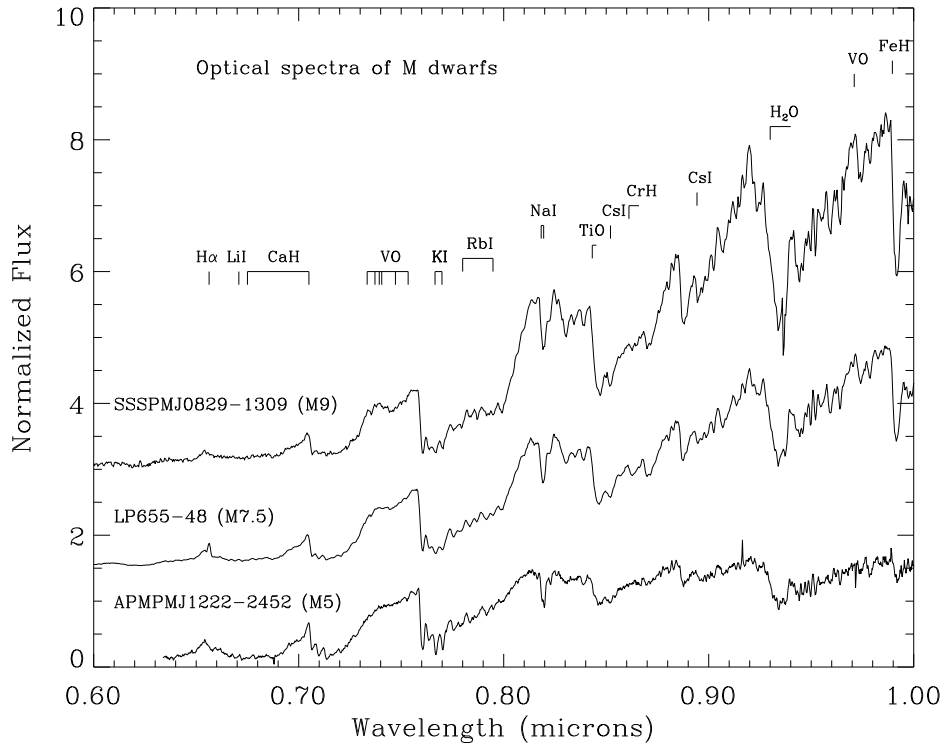


Figure 1.3: Examples of optical spectra (0.6–1.0 μm) of M dwarfs, along with the main molecular features and atomic lines. From top to bottom, the M dwarfs are SSSPM J0829-1309 (M9), LP655-48 (M7.5; McCaughean et al. 2002b), and APMPM J1222-2452 (M5) taken from our sample of proper motion objects in the Southern Sky. Optical spectra are normalised at 7500 Å and offset in intensity for clarity.

lithium in absorption at 6708 Å implies a mass less than $0.065 M_{\odot}$ and ages older than 300 Myr (Rebolo et al. 1992). The amount of lithium and the luminosity of the object provide an estimate of its mass and age (Figure 1.2).

Near-infrared spectra of M dwarfs exhibit strong H_2O , CO (2.3 μm), and FeH (1.2 μm) features as well as strong atomic lines, including KI and NaI at 1.25 and 1.51 μm , respectively.

The optical spectral classification of M dwarfs is based on spectral indices (Table 1.2) defined by Kirkpatrick et al. (1991), Kirkpatrick et al. (1999b), and Martín et al. (1999b). A complementary method useful for spectral classification is the direct comparison with template objects i.e. whose spectral type is well-determined for internal consistency.

1.4.2 Spectroscopy of L dwarfs

L dwarfs are characterised by redder optical colours ($R-I \geq 2.2$), redder optical-to-infrared colours ($I-J \geq 3.0$), and redder infrared colours ($J-K \geq 1.2$; $0.7 \leq J-H \leq 1.5$; $0.4 \leq H-K \leq 1.0$) than M dwarfs. A large scatter in colours is nevertheless observed among L dwarfs (Leggett

et al. 2000; Hawley et al. 2002). A complete list of L dwarfs with infrared magnitudes and optical spectra is available at Kirkpatrick's webpage³. Most of them are extracted from the 2MASS (e.g. Kirkpatrick et al. 2000) and SDSS (e.g. Geballe et al. 2002).

The effective temperatures of field L dwarfs range from 1300–1500 K to 2000–2200 K and their luminosities from 4×10^{-4} to $3 \times 10^{-5} L_\odot$ (Basri et al. 2000; Leggett et al. 2000). Typical uncertainties on these parameters are on the order of 15 % mostly due to uncertainties on the age of nearby ultracool dwarfs. L dwarfs represent a mixture of stars and brown dwarfs with the ones later than L5 being unambiguously substellar as theoretical models predict effective temperatures of 1700 K for a star at the hydrogen-burning limit. The detection of lithium in absorption in the optical spectrum of a L dwarf places the object in the substellar regime but not sufficient as the most massive brown dwarfs will burn hydrogen for a short period of time. As a consequence, the status of L dwarfs remain uncertain but more than one third of L dwarfs are expected to brown dwarfs (Kirkpatrick et al. 1999b). The derived density of field L dwarfs in the solar neighbourhood is estimated to $2\text{--}8 \times 10^{-3} \text{ pc}^{-3}$ (Kirkpatrick et al. 2000) compared to $2 \times 10^{-2} \text{ pc}^{-3}$ for stars in the $0.1\text{--}1.0 M_\odot$ mass range.

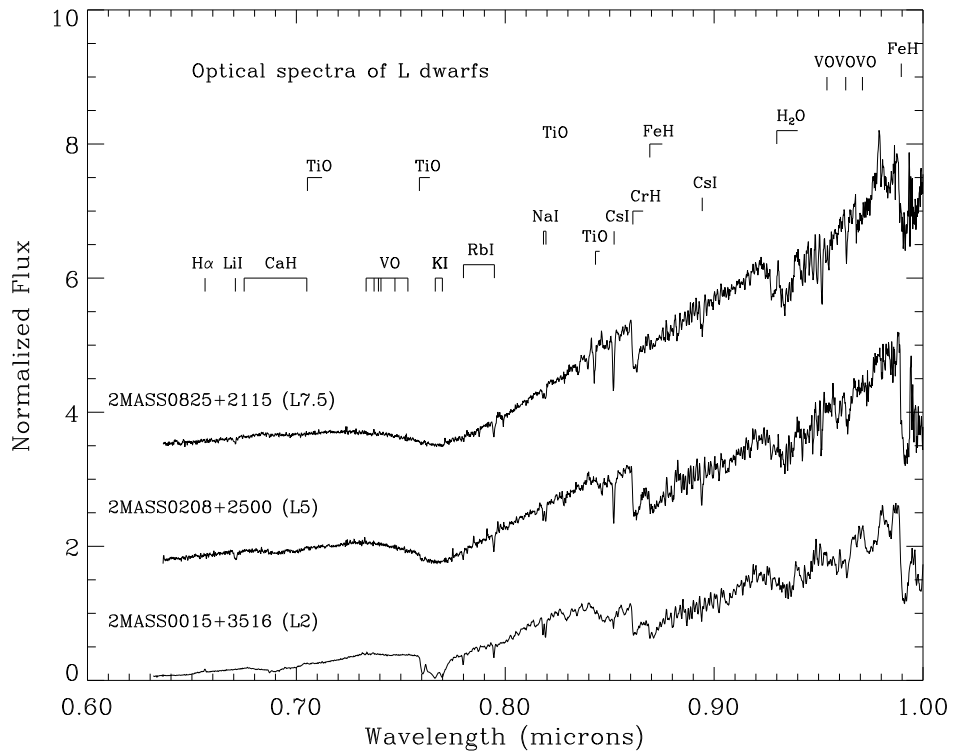


Figure 1.4: Examples of optical spectra ($0.6\text{--}1.0 \mu\text{m}$) of L dwarfs along with the main molecular features and atomic lines. From top to bottom, the L dwarfs are 2MASS0825+2115 (L7.5), 2MASS0208+2500 (L5), and 2MASS0015+3516 (L2) from Kirkpatrick et al. (2000). Optical spectra are normalised at 8250 \AA and offset in intensity for clarity.

³<http://spider.ipac.caltech.edu/staff/davy/ARCHIVE/>

The TiO and VO absorption bands, responsible for the shape of M dwarfs, disappear at lower temperatures and vanish completely by mid-L. Optical spectra of L dwarfs (Figure 1.4) are characterised by metallic hydrides such as CrH (8611 and 9969 Å), and FeH (8692 and 9896 Å), and neutral alkalis, including NaI (8183/8195 Å), KI (7665/7699 Å), RbI (7800 and 7948 Å), CsI (8521 and 8943 Å), and lithium at 6708 Å. Hydride metals, CrH and FeH, are strong around mid-L and weaken towards late types. Ground state alkali of CsI and RbI strengthen towards late types because molecules condense out in the atmosphere diminishing the veiling of atomic lines. Overall, the spectra of L dwarfs are best reproduced by the so-called “Dusty” atmosphere models of Allard et al. (2001).

The optical classification scheme of L dwarfs is based on spectral indices defined by the ratio of the summed flux in a region containing a line or a band of interest divided by the flux in a nearby continuum region. Two schemes were independently proposed by Kirkpatrick et al. (1999b) and Martín et al. (1999b).

The Kirkpatrick scheme is based on several spectral ratios which characterise the strength of oxides, metallic hydrides, and neutral alkali, as well as on comparison with template spectra of well-defined standards.

The Martín scheme relies on the so-called PC3 spectral index and on spectrum synthesis of high-resolution profiles developed by Basri et al. (2000).

There is a slight difference between both schemes particularly at low temperatures. The community tends more often to use the Kirkpatrick et al. (1999b) scheme although the PC3 index remains a good spectral type discriminant for M dwarfs and early-L dwarfs (Figure A.1 in Appendix A). Meanwhile, some authors have defined new spectral indices or adapted existent ones to their spectral resolution and/or signal-to-noise (e.g. Lépine et al. 2003b).

Table 1.2 lists the most reliable spectral indices for the spectral classification of M and L dwarfs, according to our own experience (see Chapter 2 for more details). We suggest the following “recipe” to classify M and L dwarfs in the optical with an uncertainty of half a subclass or better:

- Compute the VO-a index from Kirkpatrick et al. (1999b).
- Compute the TiO5 index from Reid et al. (1995).
- Compute the PC3 index from Martín et al. (1999b).
- Take the average of the spectral types derived from each spectral index.
- Compare the spectrum to M dwarf templates preferentially observed with the same telescope/instrument configuration as the science targets.
- Average the results obtained from both methods. If a difference larger than one subclass is found, the direct comparison with spectral templates should be favoured.

Spectral indices trace the strength of an absorption band or a spectral feature. Each wavelength of a spectrum is associated with a flux value. Those values contained in the numerator and denominator wavelength ranges are summed or averaged, according to the definition. The ratio of the two results is then computed, yielding a value for the spectral index. The output is then compared to tabulated numbers quoted in the papers where the indices are defined.

Table 1.2: Spectral indices taken from Martín et al. (1999b; hereafter M99), Reid et al. (1995; hereafter R95), and Kirkpatrick et al. (1999b; hereafter K99) for optical classification of M and L dwarfs. The different values of the flux available in the wavelength range for the numerator and denominator are summed or averaged (depending on the definition). The output of the ratio provides a value for the spectral index. This result should then be compared to values tabulated in the original papers.

Index	Numerator (Å)	Denominator (Å)	Feature	Ref
PC3	8230–8270	7540–7580	Pseudo-continuum	M99
TiO5	7126–7135	7042–7046	TiO λ 7053Å	R95
VO-a	Sum of 7350–7370 and 7550–7570	7430–7470	VO $\lambda \sim$ 7434Å	K99
CrH-a	8580–8600	8621–8641	CrH λ 8611Å	K99
Rb-b	Av of 7922.6–7932.6 and 7962.6–7972.6	7942.6–7952.6	Rb I λ 7947.6Å	K99
TiO-b	8400–8415	8435–8470	TiO λ 8432Å	K99
Cs-a	Av of 8496.1–8506.1 and 8536.1–8546.1	8516.1–8526.1	Cs I λ 8521.1Å	K99
VO-b	Sum of 7860–7880 and 8080–8100	7960–8000	VO $\lambda \sim$ 7912Å	K99

Near-infrared spectra of L dwarfs are dominated by water absorption bands at $\sim 0.95\text{ }\mu\text{m}$, $\sim 1.15\text{ }\mu\text{m}$, $1.35\text{--}1.50\text{ }\mu\text{m}$, $1.75\text{--}2.05\text{ }\mu\text{m}$, and longwards of $2.3\text{ }\mu\text{m}$, as well as by the CO band head at $2.3\text{ }\mu\text{m}$. Strong molecular bands of FeH around $1\text{ }\mu\text{m}$ and a prominent KI doublet at $1.25\text{ }\mu\text{m}$ in the *J*-band are present as well.

Several attempts have been made to provide a near-infrared classification scheme for L dwarfs in agreement with the optical scheme(s) presented above. We will briefly mention below the various indices and their applicability (Table 1.3):

- Tokunaga & Kobayashi (1999) defined two indices, K1 and K2 (Table 1.3) based on high-resolution *K*-band spectroscopy and narrow-band photometry. No clear relationship could be inferred due to the small number of objects under study. More recently, Geballe et al. (2002) concluded that these indices could be used to distinguish M, L, and T dwarfs.
- Based on very low-resolution ($R \sim 50\text{--}100$) near-infrared ($0.85\text{--}2.5\text{ }\mu\text{m}$) spectra of 26 L dwarfs with optically-determined spectral types, Testi et al. (2001) defined indices (Table 1.3) in agreement with the optical classification scheme from Kirkpatrick et al. (1999b). However, those spectral indices appear highly dependent on the instrument setup and might yield different classification at higher spectral resolution. Nevertheless, this approach remains appealing for faint brown dwarf candidates in star-forming regions invisible at optical wavelength due to the high extinction.
- Reid et al. (2001a) proposed four water-vapour indices well-correlated with the optical scheme from Kirkpatrick et al. (1999b) according to a sample of 14 L dwarfs with full $1.0\text{--}2.5\text{ }\mu\text{m}$ coverage. The best calibration with spectral type is provided by the index H_2O^B (Table 1.3) which measures the depth of absorption in the redward wing of the $1.4\text{ }\mu\text{m}$ steam band.
- Geballe et al. (2002) defined three water vapour indices and two methane indices to classify T dwarfs and extended the scheme to L dwarfs. The water vapour index at $1.5\text{ }\mu\text{m}$ is suitable for classification across the entire L-T sequence and in agreement with the optical

scheme from Kirkpatrick et al. (1999b). The CH₄ 2.2 μm and H₂O 1.5 μm spectral indices are efficient ways of classifying the L/T transition objects.

Table 1.3: Near-infrared spectral indices proposed by Tokunaga & Kobayashi (1999; TK99), Testi et al. (2001; T01), Reid et al. (2001a; R01), and Geballe et al. (2002; G02) to extend the optical classification scheme from Kirkpatrick et al. (1999b). Only the best discriminants for spectral classification are given in the case of Reid et al. (2001a) and Geballe et al. (2002).

Index	Numerator (μm)	Denominator (μm)	Ref
K1	$\langle 2.10 - 2.18 \rangle - \langle 1.96 - 2.04 \rangle$	$0.5 \times (\langle 2.10 - 2.18 \rangle + \langle 1.96 - 2.04 \rangle)$	TK99
K2	$\langle 2.20 - 2.28 \rangle - \langle 2.10 - 2.18 \rangle$	$0.5 \times (\langle 2.20 - 2.28 \rangle + \langle 2.10 - 2.18 \rangle)$	TK99
sHJ	$\langle 1.265 - 1.305 \rangle - \langle 1.60 - 1.70 \rangle$	$0.5 \times (\langle 1.265 - 1.305 \rangle + \langle 1.60 - 1.70 \rangle)$	T01
sKJ	$\langle 1.265 - 1.305 \rangle - \langle 2.12 - 2.16 \rangle$	$0.5 \times (\langle 1.265 - 1.305 \rangle + \langle 2.12 - 2.16 \rangle)$	T01
sH ₂ O ^J	$\langle 1.265 - 1.305 \rangle - \langle 1.09 - 1.13 \rangle$	$0.5 \times (\langle 1.265 - 1.305 \rangle + \langle 1.09 - 1.13 \rangle)$	T01
sH ₂ O ^{H1}	$\langle 1.60 - 1.70 \rangle - \langle 1.45 - 1.48 \rangle$	$0.5 \times (\langle 1.60 - 1.70 \rangle + \langle 1.45 - 1.48 \rangle)$	T01
sH ₂ O ^{H2}	$\langle 1.60 - 1.70 \rangle - \langle 1.77 - 1.81 \rangle$	$0.5 \times (\langle 1.60 - 1.70 \rangle + \langle 1.77 - 1.81 \rangle)$	T01
sH ₂ O ^K	$\langle 2.12 - 2.16 \rangle - \langle 1.96 - 1.99 \rangle$	$0.5 \times (\langle 2.12 - 2.16 \rangle + \langle 1.96 - 1.99 \rangle)$	T01
H ₂ O ^B	Average of 1.47–1.49	Average of 1.59–1.61	R01
H ₂ O 1.5 μm	Sum of 1.46–1.48	Sum of 1.57–1.59	G02
CH ₄ 2.2 μm	Sum of 2.08–2.12	Sum of 2.215–2.255	G02

1.4.3 Spectroscopy of T dwarfs

T dwarfs or methane dwarfs, objects cooler than L dwarfs, are all brown dwarfs have effective temperatures below 1300 K. Most of them were discovered among the SDSS (Strauss et al. 1999; Tsvetanov et al. 2000; Leggett et al. 2000; Geballe et al. 2002) and the 2MASS (Burgasser et al., 1999, 2000a, 2000b, 2002, 2003b, 2003c) surveys. The remainder were found as companions (Els et al. 2001), in deep fields (Liu et al. 2002b; Cuby et al. 1999), and in proper motion surveys (Scholz et al. 2003; McCaughean et al. 2004). A list of T dwarf discoveries with magnitudes, spectral types, and references is available on Burgasser’s webpage⁴. There are currently 50 T dwarfs known (May 2004).

T dwarfs exhibit very red optical colours, redder than L dwarfs, making them often invisible in the *R* filter and sometimes in the *I* filter. The optical-to-infrared colours are very red ($R-J \geq 9.0$; Golimowski et al. 1998) with an increase towards later types.

Contrary to the optical colours, however, the infrared colours are bluer than L dwarfs and decrease towards later types due to:

- Methane absorption in the *H* and *K* bands
- Strong water vapour bands depressing the flux in the *K* band
- H₂ pressure-induced absorption lines increasing the opacity longwards of 2.0 μm

Infrared colours of T dwarfs are provided here as an indication: $-0.5 \leq J-H \leq 0.9$, $-0.9 \leq J-K \leq 1.4$, and $1.5 \leq K-L' \leq 2.5$. A large scatter is observed in infrared colours particularly towards

⁴<http://www.astro.ucla.edu/~adam/homepage/research/tdwarf>

later types (Hawley et al. 2002). Furthermore, colours and magnitudes are strongly dependent on the filter systems used, with variations up to 30 % (Hawley et al. 2002; Stephens & Leggett 2004). A transformation between filter systems is required prior to any comparison.

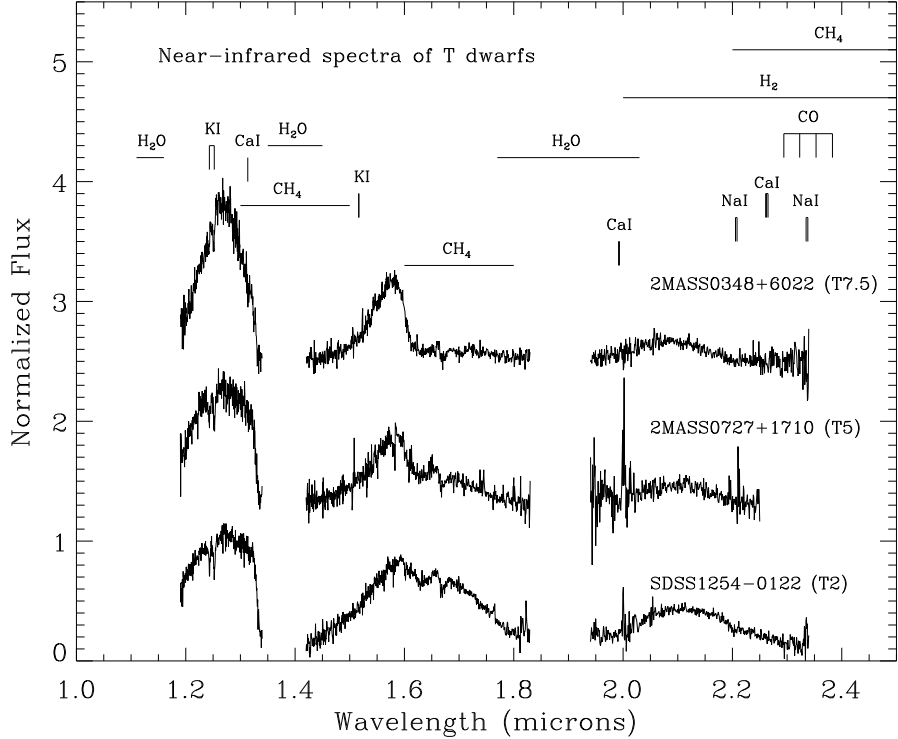


Figure 1.5: Examples of near-infrared ($1.0\text{--}2.5\,\mu\text{m}$) spectra of T dwarfs along with the main molecular features and atomic lines. From top to bottom, the T dwarfs are 2MASS0348+6022 (T7.5; Burgasser et al. 2003c) 2MASS0727+1710 (T5; Burgasser et al. 2002), and SDSS1254–0122 (T2; Burgasser et al. 2002). Near-infrared spectra, available on Burgasser’s webpage, are normalised at $1.28\,\mu\text{m}$ and offset for clarity.

Optical spectra of T dwarfs exhibit less striking features than M and L dwarfs. Pressure-broadened Na I at $5890/5895\,\text{\AA}$ and K I at $7665/7699\,\text{\AA}$ resonance doublets are responsible for the shape of T dwarf shortwards of $8000\,\text{\AA}$. Strong neutral alkali absorption lines of Cs I (8521 and $8943\,\text{\AA}$) and Rb I (7800 and $7948\,\text{\AA}$) and strong H₂O band at $9250\,\text{\AA}$ are present as well. Metallic hydrides such as FeH at $8692\,\text{\AA}$ and CrH at $8611\,\text{\AA}$ and $9969\,\text{\AA}$ are present in early-T dwarfs and vanish at mid-T.

Contrary to L dwarfs, no accurate optical classification scheme is available for T dwarfs due to their faintness at those wavelengths and their red colours. Optical spectra, even obtained with the largest telescopes, are often noisy, hampering the definition of spectral indices.

Near-infrared spectra (Figure 1.5) are mostly shaped by strong water ($1.11\text{--}1.6\,\mu\text{m}$, $1.35\text{--}1.45\,\mu\text{m}$, and $1.77\text{--}2.03\,\mu\text{m}$) and methane ($1.30\text{--}1.50\,\mu\text{m}$, $1.60\text{--}1.80\,\mu\text{m}$, and $2.20\text{--}2.50\,\mu\text{m}$) bands.

Strong KI doublets at 1.17, 1.25, and 1.45 μm as well as the NaI doublet at 2.21 μm are also present. The CO band at 2.3 μm is detected in early T dwarfs but disappear at later types. Finer features of the metallic hydride FeH are seen at 1.19, 1.21, and 1.237 μm . Finally, the collision-induced H₂ exhibit no distinct band head but suppresses the flux longwards of 2.0 μm . Methane and carbon monoxide have been detected at 3.3 μm and 4.7 μm in L dwarfs and in Gl229B, respectively (Noll et al. 1997) and are attributed to vertical mixing in the upper atmospheres (Saumon et al. 2000).

Table 1.4: Near-infrared spectral indices for the classification of T dwarfs as defined by Burgasser et al. (2002; B02) and Geballe et al. (2002; G02).

Index	Numerator (μm)	Denominator (μm)	Feature	Ref
H ₂ O-A	Average of F _{1.12–1.17}	Average of F _{1.25–1.28}	1.15 μm H ₂ O/CH ₄	B02
H ₂ O 1.2 μm	Sum of F _{1.26–1.29}	Sum of F _{1.13–1.16}	1.12 μm H ₂ O	G02
H ₂ O-B	Average of F _{1.505–1.525}	Average of F _{1.575–1.595}	1.4 μm H ₂ O	B02
H ₂ O 1.5 μm	Sum of F _{1.57–1.59}	Sum of F _{1.46–1.48}	1.5 μm H ₂ O	G02
H ₂ O-C	Average of F _{2.00–2.04}	Average of F _{2.09–2.13}	1.9 μm H ₂ O	B02
H ₂ O 2.0 μm	Average of F _{2.09–2.11}	Average of F _{1.975–1.995}	1.9 μm H ₂ O	B02
CH ₄ -A	Average of F _{1.295–1.325}	Average of F _{1.25–1.28}	1.3 μm CH ₄	B02
CH ₄ -B	Average of F _{1.64–1.70}	Average of F _{1.575–1.595}	1.6 μm CH ₄	B02
CH ₄ 1.6 μm	Sum of F _{1.56–1.60}	Sum of F _{1.635–1.675}	1.6 μm CH ₄	G02
CH ₄ -C	Average of F _{2.225–2.275}	Average of F _{2.09–2.13}	2.2 μm CH ₄	B02
CH ₄ 2.2 μm	Sum of F _{2.08–2.12}	Sum of F _{2.215–2.255}	2.2 μm CH ₄	G02
H/J	Average of F _{1.50–1.75}	Average of F _{1.20–1.325}	NIR colour	B02
K/J	Average of F _{2.00–2.30}	Average of F _{1.20–1.325}	NIR colour	B02
K/H	Average of F _{2.00–2.30}	Average of F _{1.50–1.75}	NIR colour	B02
CO	Average of F _{2.325–2.375}	Average of F _{2.09–2.13}	2.3 μm CO	B02

Two near-infrared classification schemes have been proposed by Burgasser et al. (2002) and Geballe et al. (2002) based on the 2MASS and SDSS samples, respectively. The near-infrared classification schemes of T dwarfs are generally more accurate than for L dwarfs due to much wider observed ranges in spectral indices. To first order, T dwarfs can be classified by direct inspection, noting the strengthening of methane absorption at 1.6–1.7 μm and 2.2 μm towards later types.

To quantify the classification, Burgasser et al. (2002) defined several indices (Table 1.4) to measure the strength of water, methane and carbon monoxide features. These regions have been chosen to sample the peak of the *J*, *H*, and *K* broad-band filters and the associated pseudo-continuum. Additional spectral indices have been defined to probe the near-infrared colours at 1.25, 1.6, and 2.1 μm .

Geballe et al. (2002) independently proposed three water spectral indices at 1.2, 1.5, and 2.0 μm and two methane spectral indices at 1.6 and 2.2 μm (Table 1.4). The advantage of Geballe et al. (2002) classification is the extension towards L dwarfs. For example, the water index at 1.5 μm and the methane index at 2.2 μm are sufficiently monotonic through the L-T sequences to classify both types of objects.

The recipe to classify T dwarfs consists of measuring all indices listed in Table 1.4 and then comparing the results to the standard values given in Burgasser et al. (2002) and Geballe et al. (2002). After rejecting the lowest and highest results, the values are averaged, yielding spectral

types accurate to half a subclass or better. Additional measurements of template T dwarfs observed with the same instrument setup as the science target would refine the spectral classification.

A project is underway for a joint classification scheme in the spirit of the MK scheme. The main goals are the following (Burgasser et al. 2003a):

- Define T dwarf standards for each subclass from T0 to T8. These standards must be single, bright, and accessible from both hemispheres.
- Obtain uniform spectral coverage for each standard.
- Define optimal spectral indices, useful over broad range of resolution that avoid contaminating telluric absorption features.

Analysis of the gravity-dependence of spectral features, including collision-induced H₂, is a future goal to allow differentiation between young and old T dwarfs to the field and in open clusters, respectively.

1.5 Different kinds of searches for brown dwarfs

The theoretical prediction of the existence of objects unable to fuse hydrogen in their cores led astronomers to improve their search methods and probe the sky at greater depths.

The advent of infrared detectors, wide-field capabilities at optical and infrared wavelengths and adaptive optics facilities has triggered discoveries of numerous brown dwarfs in various environments. Discoveries of brown dwarfs as companions to solar-like stars, low-mass stars, and substellar objects are reported in § 1.5.1. Large-scale and proper motion survey contributions are presented in § 1.5.2. Searches for young brown dwarfs in star-forming regions and in open clusters are highlighted in § 1.5.3 and in § 1.5.4, respectively.

1.5.1 Brown dwarfs as companions

The confirmation of brown dwarfs is mostly based on the detection of the lithium absorption line at 6708 Å, on the low-luminosities and cool temperatures. To date, no direct dynamical mass measurement of a brown dwarf has been reported. The observation of a full orbit of the low-mass binary Gl569Bab with adaptive optics by Lane et al. (2001) provided an accurate estimate of the total mass of the system. The secondary is incontrovertibly substellar whereas the primary is either a low-mass star or a brown dwarf depending on the age. The detection of brown dwarfs as companions to stars and brown dwarfs is of prime importance to investigate several aspects of star formation, including:

1. Mass ratios provide a constraint to the formation mechanism(s) of low-mass stars and brown dwarfs
2. Correct the Initial Mass Function for binarity.
3. Study the binary frequency as a function of mass in the field and in open clusters
4. Dynamical masses would allow us to test evolutionary tracks at different ages

A variety of surveys have been undertaken to unveil brown dwarfs around objects covering a large range in mass from solar-type stars to the recently defined T class. Different methods are employed to probe certain zones around field dwarfs. The close orbits within few astronomical units are the realms of radial velocity searches. Separations of 1 to 10 AU are probed by speckle imaging. Coronagraphic surveys are best suited to investigate companions with separations between 10 and 100 AU. Wider companions (> 100 AU) are most efficiently searched with wide-field surveys. This section summarises the current knowledge of the frequency of brown dwarf companions to solar-type stars and low-mass stars.

Radial velocity surveys

The presence of a companion around a star can be inferred by the perturbation it engenders in the radial velocity of the star. This constitutes the hallmark of the radial velocity surveys started about 25 years ago to unveil extrasolar planets around solar analogues.

The first extrasolar planet was discovered a pulsar by Wolszczan & Frail (1992). The first extrasolar planet orbiting a solar-type star was discovered around 51 Peg by Mayor & Queloz (1995), the same year as the first unambiguous brown dwarfs. Prior to this discovery, planetary companions were detected around the pulsars PSR1829–10 (Bailes et al. 1991) and PSR1257+12 (Wolszczan & Frail 1992). Hundreds of F, G, K, and M dwarfs have now been surveyed by radial velocity programs with sensitivities reaching few metres per seconds (Mayor et al. 1992; Marcy & Butler 1992; McMillan et al. 1994; Cochran & Hatzes 1994).

To date, more than hundred extrasolar planets have been uncovered by Doppler measurements⁵ within 3 AU of their parent stars and masses as low as the mass of Jupiter (Butler et al. 2003). About five percent of the surveyed solar-type stars harbour one or multiple planets with a wide range of eccentricities and periods. The analysis of 164 nearby solar-type stars by Duquennoy & Mayor (1991) indicates that about 13 % of G dwarfs have stellar companions within the same separation limit.

The distribution of masses of extrasolar planets around solar like stars is peaked at low masses ($1\text{--}2 M_{\text{Jup}}$) with a decreasing power law towards larger masses (see Figure 17 in Vogt et al. 2000 for example). Radial velocity surveys are *not* biased against the discovery of brown dwarfs (defined here as object more massive than $13 M_{\text{Jup}}$) as their perturbation on the parent stars is stronger than planets. This observed lack of brown dwarf companions at low separation around solar-type stars is suggestive of the existence of a “brown dwarf desert”. The $\sin i$ uncertainty on the measurement of the mass does not affect the shape of the distribution of objects as a function of mass because the probability to see a brown dwarf at small inclination is negligible, according to numerous simulations (Queloz 2002).

A radial velocity survey of about 1000 stars with a precision of 0.5 km s^{-1} implemented by Latham et al. (1989) announced the first brown dwarf candidate among 20 radial velocity standards. The object, HD114762, stood out of the sample with a lower limit of 11 Jupiter masses. The current status of this object remain controversial due to the uncertainties on the inclination (Halbwachs et al. 2000).

To date, a dozen brown dwarf candidates extracted from radial velocity programs have been reported. Mayor et al. (1992) found nine stars with possible substellar companions from a survey of 540 nearby F and G dwarfs. Mazeh et al. (1996) investigated low-amplitude radial velocity

⁵<http://www.obspm.fr/encycl/cat1.html>

variations of three stars belonging to the original list of radial velocity standards. Tokovinin et al. (1994) merged radial velocity observations accomplished independently with two spectrometers to infer a mass of $60 M_{Jup}$ for one companion. However, the orbital inclinations from the *Hipparcos* satellite concluded that most of them are simply stellar companions (Halbwachs et al. 2000). Seven objects are definitely rejected as brown dwarf companions, one is accepted with a low confidence level, and the remainder require additional studies to assess their substellarity.

Three additional brown dwarfs, with masses ($m \sin i$) ranging from 13 to $18 M_{Jup}$, have been reported around HD168443 (Marcy et al. 1999), HD162020, and HD202206 (Udry et al. 2002). These three candidates remain, to date, the sole bona-fide substellar companions found by Doppler measurements. It is worth mentioning that HD168443 is a system composed of an extrasolar planet/brown dwarf pair orbiting the nearby high proper motion K dwarf, Gl 86A (Els et al. 2001).

To summarise, the present set of data drawn from radial velocity surveys indicates that less than 0.5 % of solar-type stars harbour close brown dwarf companions (Marcy & Butler 2000; Zucker & Mazeh 2001). The extension of this brown dwarf desert at wide separation is ruled out by current observations, suggesting a frequency comparable to stellar companions despite the large uncertainties ($18 \pm 14\%$; Gizis et al. 2001a).

Microlensing

The main principle of microlensing, originally suggested by Paczynski (1986), is the following: when the “lens” is aligned with a distant bright star, it bends and distorts the light of the background object, yielding an enhancement of flux on a short timescale. Several types of lenses are possible, including compacts objects in external galaxies or disk objects in our Galaxy such as normal stars, brown dwarfs and planets.

Various collaborative efforts are under way to unveil extrasolar planets and brown dwarfs. Among them are the MACHO project, the Optical Gravitational Lensing Experiment (OGLE), the Expérience pour la Recherche d’Objets Sombres (EROS), Microlensing Observations in Astrophysics (MOA), Microlensing Follow-up Network (MicroFUN), the Microlensing Planet Search (MPS), and Probing Lensing Anomalies Network (PLANET).

The search for brown dwarfs through microlensing is just starting. Three possible candidates have been recently reported but the uncertainties on the mass determination remain large and additional observations are obviously required to further constrain the nature of the lens.

1. Alcock et al. (2001) observed a microlensing event in the Large Magellanic Clouds with the *Hubble Space Telescope*, yielding a mass estimate between 0.03 and $0.10 M_{\odot}$. Optical spectroscopy of the lens suggests however a mass larger than $0.09 M_{\odot}$, placing the object above the hydrogen-burning limit.
2. Smith et al. (2003) inferred a mass of $M \sim 0.050^{+0.016}_{-0.011} M_{\odot}$ for a bright microlensing event observed towards the Galactic bulge by the OGLE project. If verified, the lens would be a brown dwarf located at a distance of 6.5 kpc.
3. A recent microlensing event toward M31 was announced by An et al. (2004). The lens is a binary system located either in the disk of M31 or in the halos of the Milky Way or M31. The secondary is either a brown dwarf or a low-mass star depending on the distance of the system.

Brown dwarf companions to low-mass stars

The first brown dwarf companion candidate was found around a white dwarf, GD165 (Becklin & Zuckerman 1988). This object is now recognised as a template for the newly-defined L class and is likely a brown dwarf (Kirkpatrick et al. 1999a). The first T dwarf, Gl229B, was discovered orbiting an early-M dwarf (Nakajima et al. 1995). Those discoveries have triggered a large number of high-resolution imaging surveys conducted with the *Hubble Space Telescope* and adaptive optics systems on the world's largest telescopes to uncover new brown dwarf companions to low-mass stars. A brief overview is provided below and in Table 1.5.

The most complete population available to date to investigate the binary frequency of low-mass stellar and substellar companions are the 5- and 8-pc samples. Several programs have been dedicated to the closest neighbours to the Sun to unveil companions over different separation ranges. Henry & McCarthy (1990) failed to detect new brown dwarfs at separations closer than 10 AU from a systematic search around M dwarfs within 5 parsecs using infrared speckle interferometry. Simons, Henry, & Kirkpatrick (1996) investigated separations between 100 and 1400 AU around 63 systems within 8 pc and $\delta \geq -25^\circ$. Second-epoch observations supplemented the previous search with proper motion as primary criterion but did not uncover new low-mass companions (Hinz et al. 2002). High-resolution imaging of 23 nearby dwarfs within 13 pc carried out with the *Hubble Space Telescope* failed to detect any companion at separations between 1 and 50 AU (Schroeder et al. 2000). Similarly, a coronagraphic survey of 107 nearby star systems probing separations ranging from 40 to 100 AU turned up no new brown dwarf companions (Oppenheimer et al. 2001). It sounds likely that all stellar companions to nearby dwarfs have now been detected by the extensive programs implemented over several decades (Reid & Gizis 1997a).

New low-mass stars and brown dwarf companions have been detected around K (Gizis, Kirkpatrick, & Wilson 2001b), G (Potter et al. 2002; Goto et al. 2002; Liu et al. 2002a), M (Rebolo et al. 1998; Goldman et al. 1999; Martín et al. 2000b; Lane et al. 2001; Close et al. 2002a; Freed et al. 2003), and L dwarfs (Martín et al. 1999a; Koerner et al. 1999). Table 1.5 lists those discoveries along with their parameters, including spectral types of the primary and secondary (when a spectrum was obtained), distance and age of the system, as well as the separation in astronomical units. The secondary of these systems is either a low-mass star or a brown dwarf depending on the age of the system. The separation and mass ratio distributions of ultracool dwarfs are plotted in Figure 1.6.

Large samples of ultracool dwarfs with spectral types ranging from M8 to T8 have been recently implemented to improve statistics in order to investigate the binary frequency of substellar mass objects to very low-mass stars and brown dwarfs.

Reid et al. (2001b) reported the discovery of four binary systems out of 20 L dwarfs observed with the *Hubble Space Telescope*. The low-mass binaries have separations spanning 2–8 AU with near equal-masses. However, one object did exhibit a much fainter companion, suggesting a mass ratio (q_1/q_2) as low as 0.8.

A sample of 10 T dwarfs observed by Burgasser et al. (2003b) unveiled two binary systems. As for the previous study by Reid et al. (2001b), both systems are tight binaries within 4 AU with near equal-brightness ratios.

A survey of 39 late-M dwarfs with spectral types later than M8 revealed nine binary systems (Close et al. 2002a, 2002b, 2003). The large majority of primaries are low-mass stars with spectral types M8–L0.5 and the secondaries are either stellar or substellar depending on the and distance.

Table 1.5: List of low-mass stellar and brown dwarf companions to stars. Note that Gl569B and HD130948 orbit normal stars and were resolved as binary systems. The remaining low-mass stellar and brown dwarf companions to ultracool dwarfs found in the course of recent high-resolution imaging surveys (Reid et al. 2001b; Close et al. 2002b; Burgasser et al. 2003b; Gizis et al. 2003; Close et al. 2003; Bouy et al. 2003) are given in Table 4 in Close et al. (2003) with their estimated parameters (separation, spectral types, masses and periods).

References: (1) Rebolo et al. 1998 (2) Martín et al. 1999a (3) Goldman et al. 1999 (4) Martín et al. 2000b (5) Burgasser et al. 2000a (6) Lane et al. 2001 (7) Gizis et al. 2001b (8) Potter et al. 2002 (9) Goto et al. 2002 (10) Liu et al. 2002a (11) Close et al. 2002a (12) Freed et al. 2003.

Name	SpT Primary	Distance pc	Age system Gyr	Separation AU	Characteristics Secondary	Refs
G196-3	M2.5	21	~ 0.1	~ 300	BD Lithium	1
LHS102	M3.5	9.6	~ 1	~ 200	BD or VLM	3
Gl569ABa/Bb	M2	9.8	< 1	50 and 1	M8.5/M9.0	4,6
GD570ABCD	K4	5.9	2–10	1525	T8; BD	5
GJ1048	K2	21.2	≤ 1	250	L1	7
HD130948ABa/Bb	G2	18	<0.8	50 and 2.4	L2–L4/L2–L4	8,9
15 Sge	G1	17.7	1–3	14	L2–L6	10
2MASS J1426316+155701	M8.5	18.8	0.5–7.5	2.92	L1–L3	11
LHS2397a	M8	14.3	2–12	2.96	L7.5	12

The main conclusions are similar to previous surveys. Two systems exhibit, however, fainter companions suggestive of low-mass ratios (e.g. Freed et al. 2003).

The largest sample of ultracool dwarfs studied to date explored 134 objects (Bouy et al. 2003), including 20 L dwarfs (Reid et al. 2001b), 84 M and L dwarfs (Gizis et al. 2003), and 30 new objects. Except one target associated with a G dwarf in a triple system, 25 out of the 133 ultracool dwarfs turned out to be binaries. This statistically significant study suggests a binary fraction around 10 % among field dwarfs within 25 pc. The main conclusions drawn by these recent surveys are discussed in the conclusions of this section.

Brown dwarf binaries

Brown dwarf binaries are of prime importance to test evolutionary tracks in the substellar regime. Close binaries are most suitable to obtain dynamical masses over a short timescale. However, the number of known field brown dwarf binaries is low and most of them do not have a resolved spectrum. Note that PPI15 is the only spectroscopic binary (Basri & Martín 1999b) and is a member of the Pleiades open cluster.

All genuine brown dwarf binaries discovered to date are listed in Table 1.6 along with their estimated physical parameters, including distances, spectral types, separation, mass ratio, and period. Only three systems have accurate distances, namely 2MASSW 1146345+223053, DENIS-PJ 0205.4–1159, and ε Indi B.

Few other objects are suggested as possible binary brown dwarfs, including Gl569Ba/Bb (Martín et al. 2000b; Kenworthy et al. 2001; Lane et al. 2001), HD130948B/C (Potter et al. 2002;

Table 1.6: List of brown dwarf binaries discovered to date in the field and in the Pleiades along with the estimated physical parameters. The distance of the system is given in parsecs, the separation in astronomical units (AU), the spectral types, the mass ratio (q parameter), and the period in years.

References: (1) Martín et al. 1999a (2) Koerner et al. 1999 (3) Reid et al. 2001b (4) Burgasser et al. 2003b (5) Gizis et al. 2003 (6) Bouy et al. 2003 (7) McCaughrean et al. 2004. (8) Martín et al. 2003.

Name	Distance pc	Sep AU	SpT	Mass ratio q	Period yr	Refs
2MASSs 0850359+105716	27.7	4.4	L6/??	0.75	43	3,6
2MASSW 0920122+351742	20.8	1.6	L6.5/??	1.0	16	3,6
2MASSW 1146345+223053	26.2	7.6	L3/??	1.0	70	2,3
2MASS 1225–2739AB	11.2	3.0	T6/T8	0.7–0.8	25–40	4
2MASS1239272+551537	21.3	4.0	L5/L5	1.0	30	5,6
2MASS 1534–2952AB	16.5	1.0	T5/T5	1.0	4–6.5	4
2MASS1728114+394859	20.4	3.4	L7/early T	0.8	30	5,6
2MASS2101154+175658	23.2	4.0	L7.5/L8	1.0	42	5,6
DENIS-PJ 0205.4–1159	18.0	9.2	L7/L7	1.0	??	2
DENIS-PJ 1228.2–1547	18.1	5.0	L5/??	1.0	35	1,2
ε Indi B	3.626	2.65	T1/T6	0.6	15	7
CFHT-PI-12	125	7.75	—	0.7	76	8
IPMBD25	125	11.75	—	0.62	126	8
IPMBD29	125	7.25	—	0.84	68	8

Goto et al. 2002), 2MASSW 0746425+200032 (Reid et al. 2001b), and 2MASS1426316+155701 (Close et al. 2002a). The masses remain uncertain due to the lack of lithium in absorption and uncertainties on the age and/or distance. As a consequence, the primary is a very low-mass star or a brown dwarf and the secondary a brown dwarf.

Conclusions to the frequency of brown dwarfs as companions

The main results of programs dedicated to the search for substellar companions to very low-mass stars and brown dwarfs can be summarised as follows:

1. A few brown dwarf companions have been detected within 3 AU around main-sequence stars by radial velocity surveys, yielding a binary frequency less than 0.5 % and suggestive of a “brown desert” at these separations. A dearth of brown dwarfs at wide separations (> 1000 AU) is not apparent around main-sequence (F–M0) stars (Gizis et al. 2001a) with a frequency of 18 ± 14 %. Studies dedicated to intermediate separations are barely under way. The binary frequency of ultracool field dwarfs lies around 10–15 % in contrast with 57 ± 9 % for G dwarfs (Duquennoy & Mayor 1991) and 42 ± 9 % for M dwarfs (Fischer & Marcy 1992). The frequency of binary brown dwarfs of at most 5 % predicted by recent simulations (Bate et al. 2002; Delgado-Donate et al. 2003) is lower than the observed values.
2. Very low-mass and brown dwarf binaries have separations smaller than 16 AU with a peak in the distribution occurring around 4–8 AU (Left panel in Figure 1.6). Similarly, surveys in the Hyades (Reid & Gizis 1997b) and in the Pleiades (Martín et al. 2000a) produced no

brown dwarf companions with separations larger than 14 and 27 AU, respectively. These results are at odds with the distribution of companions around M dwarfs. Firstly, about 40 % of M dwarf multiple systems within 8 pc have separations greater than 10 AU (Reid & Gizis 1997a). Secondly, 50 % of M0–M6 dwarfs have separations between 10 and 10^4 AU (Fischer & Marcy 1992). Furthermore, the distribution of separation of G and M dwarfs is much broader with a maximum from 3 to 30 AU (Fischer & Marcy 1992; Duquennoy & Mayor 1991). Current techniques are sensitive to wide low-mass stellar and substellar companions but suffer from observational biases towards spectroscopic binaries.

3. Low-mass binaries in the field tend to favour equal-mass systems with mass ratios larger than 0.8 (Right panel in Figure 1.6). The lowest mass ratio is the ε Indi B system with $q \sim 0.6$ (McCaughrean et al. 2004). This might simply reflect the lack of sensitivity to companions fainter than the primary by more than 4 mag. These results are in agreement with the peak at equal-mass systems noticed in the 8-pc sample (Reid & Gizis 1997a) but are at odds with the flatter distributions of G dwarfs which peaks around $q = 0.2$ (Duquennoy & Mayor 1991). Dynamical simulations of small clusters predict a flat mass ratio distribution of brown dwarfs with a rarity of extreme ratios (Delgado-Donate et al. 2003; Sterzik & Durisen 2003) in agreement with current observations.

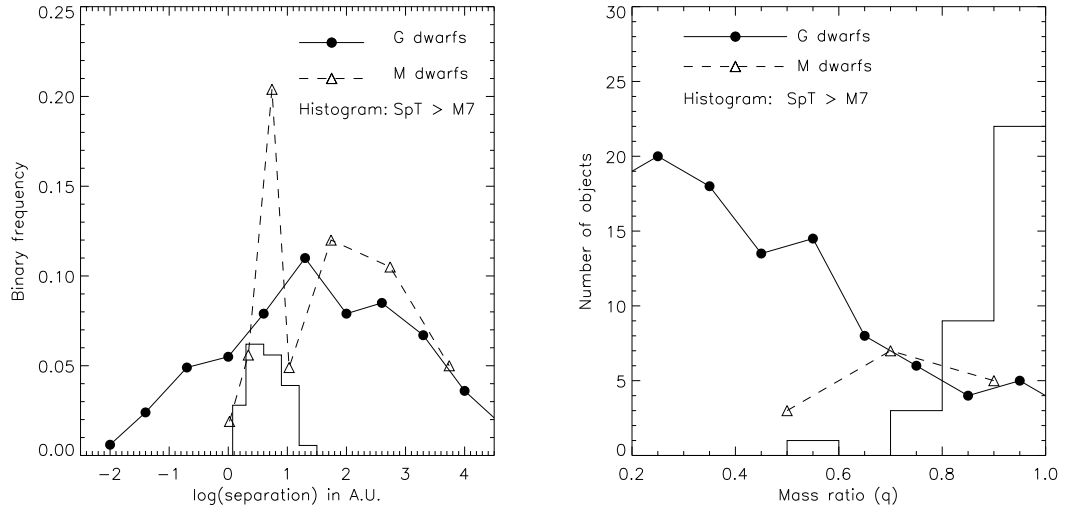


Figure 1.6: Distribution of separation (left panel) and mass ratio (right panel) for G dwarfs (solid line; Duquennoy & Mayor 1991), M dwarfs (dashed line; Fischer & Marcy 1992), and ultracool dwarfs (histogram; see text for all references). We have found a total of 34 binary systems out of 178 ultracool field dwarfs observed with high-resolution imaging from the ground and from space. The binaries found in the Pleiades by Martín et al. (2003) are not plotted as they represent a younger subsample. The errors on the measurements are Poisson errors (not included).

1.5.2 The field brown dwarfs

Over 250 L dwarfs and about 50 T dwarfs have been discovered in the field over the last five years, most of them by three large-area sky surveys, namely the Two Micron All-Sky Survey (hereafter 2MASS), the DEep Near-Infrared Survey (hereafter DENIS), and the Sloan Digital Sky Survey (hereafter SDSS).

The 2MASS (§ 1.5.2), DENIS (§ 1.5.2), and SDSS (§ 1.5.2) surveys, their selection criteria to unearth new L and T dwarfs, and their main discoveries are described. Proper motion surveys aiming at finding ultracool dwarfs in the solar neighbourhood are highlighted in § 1.5.2. Finally, some serendipitous discoveries of L and T dwarfs are presented in § 1.5.2.

The Two Micron All-Sky Survey

The Two Micron All-Sky Survey (<http://ipac.caltech.edu>), project led by the University of Massachusetts, provides full sky coverage in the near-infrared J (1.25 μm), H (1.65 μm), and K_s (2.15 μm) broad-band filters (Skrutskie et al. 1997). The survey was conducted with twin 1.3-m telescopes each equipped with a three-channel 256 \times 256 pixel NICMOS3 camera observing simultaneously in J , H , and K_s . The pixel scale was 2'', yielding a 8.5' \times 8.5' field-of-view. Six frames of 1.3 seconds each were obtained for each individual field on the sky, yielding a total integration time of 7.8 seconds. The nominal survey completeness limit was $J = 15.8$, $H = 15.1$, $K_s = 14.3$ with signal-to-noise of 10 at high galactic latitudes.

The selection method to find nearby L dwarfs was rather crude but highly efficient. All candidates with $J - K_s$ colour redder than 1.2 mag were followed-up spectroscopically with the Keck/LRIS spectrograph to ensure sufficient signal-to-noise. Over 150 nearby L dwarfs were found in the 2MASS database (Kirkpatrick et al. 1999b; Kirkpatrick et al. 2000; Cruz et al. 2003), yielding accurate spectral type classification at optical wavelengths shortwards of 1 μm (Kirkpatrick et al. 1999b).

The CorMASS project aims at low-resolution ($R \sim 300$) spectroscopy of all red ($J - K_s \geq 1.2$) and bright ($K_s \leq 13.0$) to extend the optical classification scheme to the near-infrared (Wilson et al. 2003).

About half of the T dwarfs were discovered in the 2MASS database (Burgasser et al. 1999, 2000a, 2000b, 2002, 2003b, 2003c). Several colour cuts, including $J \leq 16.0$, $J - H \leq 0.4$, and $H - K_s \leq 0.3$ or $J \leq 16.0$, $J - H \leq 0.4$, and $H - K_s \geq 0.3$ were applied to find field T dwarfs in the 2MASS database. Targets were selected to have galactic latitudes above 15° and to avoid the Magellanic Cloud and 47 Tuc regions. Proper motions and optical counterparts present in the Digital Sky Surveys were removed from the initial sample, yielding a small pool of bona-fide T dwarf candidates for near-infrared spectroscopic follow-up.

The 2MASS project is a powerful tool to detect brown dwarfs in the field as well as in open clusters. Several studies made use of the 2MASS database to confirm membership status of cluster candidates in the Pleiades (Tej et al. 2002), in Taurus (Briceño et al. 2002), in MBM12 (Luhman 2001), in α Per (Barrado y Navascués et al. 2002) and to study disk fractions in star-forming regions, including σ Ori (Oliveira et al. 2002).

On the theoretical side, the 2MASS database was used to refine atmosphere models and derive effective temperature scales for ultracool dwarfs (Schweitzer et al. 2001).

The DEep Near-Infrared Survey

The DEep Near-Infrared Survey (<http://www-denis.iap.fr/>) was conducted with the ESO 1-m telescope at La Silla with a three-channel camera in the Gunn-*I* (0.82 μm), *J* (1.25 μm), *K_s* (2.15 μm) filters, covering the whole Southern Sky from -90° to $+2.5^\circ$ (Epchtein et al. 1997). Two NICMOS3 arrays with 256×256 pixels and a pixel size of $3''$ were used in the *J* and *K_s* channels whereas a 1024×1024 Tektronix CCD detector with $1''$ pixel scale was used for the *I* channel. The resulting field-of-view was $12'$. The sky was scanned in step and stare mode along 30 degree strips at constant right ascension with integration time of 10 seconds. The approximate 3σ limits of the survey were $I = 18.5$, $J = 16.5$, $K_s = 13.5$.

The selection criterion to find low-luminosity objects in the field was two-fold (Delfosse et al. 1997, 1999):

- Objects redder than $I-J$ colour of 2.5 mag.
- Objects with *J* and *K* detections and no optical counterpart.

No systematic spectroscopic follow-up was implemented as for 2MASS, yielding a smaller number of L dwarf discoveries. Nonetheless, the DENIS “Mini-Survey” revealed about 20 objects later than M8, including 3 L dwarfs (Delfosse et al. 1999), with optical and near-infrared spectroscopic assessment (Tinney et al. 1998; Delfosse et al. 1999). High-resolution spectroscopy of the 3 L dwarfs placed one object, DENIS-PJ 1228.2–1547, as the first discovered field brown dwarf with Kelu 1 (Ruiz et al. 1997), after detection of lithium absorption at 6708 Å (Martín et al. 1997; Tinney et al. 1997).

The Sloan Digital Sky Survey

The Sloan Digital Sky Survey (<http://sdss.org>) has surveyed over 10000 deg^2 (one fourth of the celestial sphere) of the high galactic latitude sky, centred approximatively on the North Galactic Pole, with a dedicated 2.5-m telescope at the Apache Point Observatory (York et al. 2000). The SDSS project imaged the sky in 5 filters (*u*, *g*, *r*, *i*, and *z*), covering the 0.4 – $1.0 \mu\text{m}$ wavelength range (Fukugita et al. 1996).

The imaging array was a mosaic of thirty 2048×2048 CCDs with $0.396''/\text{pix}$ providing a total field-of-view of $2.5^\circ \times 13'$. The effective integration time was 54.1 seconds per filters per print on sky. The expected completeness limits (5σ detection limit) of the survey were $u \sim 22.3$, $g \sim 23.3$, $r \sim 23.1$, $i \sim 22.3$, and $z \sim 20.8$, assuming a full-width-half-maximum of $1''$ and an airmass of 1.4. Photometric calibration was obtained with a small auxiliary telescope at the same site. Different types of objects were followed-up spectroscopically with a dedicated SDSS twin fibre-fed spectrograph. Fibres were $3''$ in diameter and provided wavelength coverage from 3800 to 9200 Å at $R \sim 1800$.

The SDSS commissioning data revealed about 20 L dwarfs reported in Fan et al. (2000) and Schneider et al. (2002). The selection criteria to find L dwarfs in the SDSS survey are:

1. Objects redder than $i-z \geq 1.6$ and $r-i \geq 1.8$.
2. $i-z \geq 1.6$ and 2σ detection in *i* and/or detection in the 2MASS catalogue for objects undetected in the *r* images.

The search for T dwarfs in the SDSS data took into account the faintness and the red optical colours of these objects, considering the following search criteria:

1. Detection above 3σ in i and detection twice in the z filter with 2MASS counterpart.
2. Detection only in the z -band required $z \leq 19.0$.

A dozen T dwarfs were discovered in the SDSS commissioning data (Strauss et al. 1999; Tsvetanov et al. 2000), including the first L/T transition objects (Leggett et al. 2000). Geballe et al. (2002) developed a near-infrared classification scheme for ultracool dwarfs from M to T, according to the SDSS discoveries (Table 1.4).

Proper motion surveys

The knowledge of the solar neighbourhood, defined as the volume of space within 25 pc, was largely established by photographic proper motion surveys prior to the advent of large-area digital sky surveys. Despite the large number of ultracool dwarfs unearthed by the 2MASS, DENIS, and SDSS surveys, the census of the solar vicinity is incomplete at the faint end by 30 % within 10 pc (Henry et al. 1997) and about twice this value within 25 pc (Henry et al. 2002). Trigonometric parallaxes represent the best way to measure distances but proper motions remain a good distance discriminant when the spectral type of the object is known.

The most extensive proper motion databases available to date are two catalogues compiled by Luyten based mainly on data obtained with the 1.2-m Palomar Oschin Schmidt telescope and published more than twenty years ago:

1. The Luyten Catalogue of Stars with Proper Motions Exceeding $0.5''/\text{yr}$ Annually (hereafter LHS; Luyten 1979) lists about 3600 stars with $\mu \geq 0.500''/\text{yr}$ and hundreds of stars with proper motions spanning $0.235\text{--}0.500''/\text{yr}$.
2. The New Luyten Catalogue of Stars with Proper Motions larger than Two-Tenths of an Arcsecond (hereafter NLTT; Luyten 1980) represents a compilation of 58,845 stars with proper motions larger than $0.18''/\text{yr}$.

Two epochs were obtained with positions accurate to a few arcseconds. Magnitudes measured in two photographic passbands m_{pg} and m_r , corresponding roughly to the current photometric B and R_{Kron} , respectively, were accurate to about 0.5 mag. The faintest stars catalogued have $m_r \sim 19$ and $m_{pg} \sim 20.5$, respectively.

South of $\delta \leq -33^\circ$, both the LHS and the NLTT catalogues were extended using data from the Bruce Proper Motion survey conducted with the 0.65-m Bruce refractor beginning of the 20th century. Although the Bruce survey extended to proper motions down to $0.1''/\text{yr}$, only stars brighter than $m_{pg} \sim 15.5$ were catalogued with a blue magnitude but no colour information. The search for low-luminosity objects in the south is, thus, highly hampered by the bright detection limit of the Bruce catalogue. New faint proper motion objects down to $m_r = 19.5$ and south of $\delta < -5^\circ$ were extracted by Wroblewski & Torres (1989, 1992, 1994, 1995, 1996, 1997, 1998) and Wroblewski & Costa (1999, 2000, 2001).

To improve the census of the solar neighbourhood and characterise the luminosity and mass functions across the stellar/substellar boundary, several proper motion surveys have recently been implemented both in the Northern and Southern hemispheres. We will briefly highlight the results

of the surveys which contributed to the discovery of low-mass stars and brown dwarfs in the solar vicinity, including our own Southern Sky proper motion survey for nearby red dwarfs presented in details in Chapter 2.

- Reid & Cruz (2002), Reid, Kilkenny, & Cruz (2002b), and Cruz & Reid (2002) presented a series of papers aiming at finding low-mass stars and brown dwarfs within 20 pc. By cross-correlating the NLTT catalogue with an early release of the 2MASS database for galactic latitudes higher than 10° , the authors discovered over 100 new ultracool dwarfs based on their location in the $(m_r, m_r - K_s)$ colour-magnitude diagram. Although photometric distances are subject to large uncertainties due to errors on photometric measurements or binarity, these results demonstrate clearly the incompleteness of the solar neighbourhood, especially at the low-luminosity end.

More recently, Cruz et al. (2003) initiated a volume-limited ($d \leq 20$ pc) survey of nearby M7–L6 dwarfs over the whole sky entirely based on the 2MASS survey. Moderate-resolution ($R \sim 3000$) optical (6000–10000 Å) spectroscopy provided spectral types and photometric distances for each individual object, yielding the discovery of 39 new L dwarfs. A bright ($K_s = 9.1$) M8.5 dwarf at 6 pc with a proper motion of $0.759''/\text{yr}$ was uncovered within the framework of this search (Reid et al. 2003).

- Lépine, Shara, & Rich (2002) conducted a systematic search for high proper-motion stars ($0.5 \leq \mu \leq 2.0''/\text{yr}$) at low-galactic latitudes ($|b| \leq 20^\circ$) using the Digital Sky Survey database. The same procedure was recently extended to galactic latitudes above 25° (Lépine, Rich, & Shara 2003a). Most of the high proper motion ($0.5 \leq \mu \leq 2.0''/\text{yr}$) stars listed in Luyten's catalogues were recovered and new objects brighter than 20.0 mag were discovered. The search method was based on the SUPERBLINK software developed by the authors to recover high proper motion stars in an automatic way after scaling, shifting, rotating, and subtracting the POSS I and POSS II photographic plates. This tool was specifically optimised to work on relatively crowded fields and to improve the detection of proper motion stars affected by a bright neighbour.

Optical spectroscopy of numerous new high proper motion stars revealed white dwarfs, M dwarfs, metal-poor dwarfs (Lépine, Rich, & Shara 2003b) as well as:

1. A high proper motion ($\mu = 2.38''/\text{yr}$) faint ($V = 19.3$) M8.5 dwarf at 14 pc (Lépine, Shara, & Rich 2002).
 2. A bright ($K_s \sim 10.9$) L1 brown dwarf at 10 pc confirmed by the detection of lithium at 6708 Å (Salim et al. 2003).
 3. An early-L subdwarf (Lépine, Rich, & Shara 2003a).
- The Calán-ESO Proper Motion Catalogue contains 542 stars with proper motions larger than $0.2''/\text{yr}$ identified on $5^\circ \times 5^\circ$ ESO red plates taken ~ 10 yr apart (Ruiz et al. 2001). The field selection was random but avoided the high galactic latitude regions with declinations ranging from $\delta = -40^\circ$ to $\delta = -25^\circ$. The two hours integration time yielded photographic magnitudes m_r spanning 7.5–19.5 mag. This proper motion survey, originally aiming at the identification of cool white dwarfs in the solar neighbourhood, led to the discovery of the first field brown dwarf, Kelu-1 (Ruiz, Leggett, & Allard 1997).
 - The Liverpool-Edinburgh catalogue (Pokorny, Jones, & Hambly 2003) is a compilation of about 6200 stars at the South Galactic Cap, with proper motions exceeding $0.18''/\text{yr}$ and

$R=9.0\text{--}19.5$ mag. Interesting objects were selected from the reduced proper motion and colour-colour diagrams for spectroscopic follow-up observations but no new subdwarfs or brown dwarfs have been announced to date.

- A new high proper motion survey was conducted in the Southern Sky south of $\delta \leq -33^\circ$ based on $6^\circ \times 6^\circ$ photographic plates obtained with the UKST telescope and measurements made with the APM machine at Cambridge (Scholz et al. 2000). The initial search was based on measurements in two passbands (B_J and R) at two epochs separated by ~ 15 years for $\delta \leq -20^\circ$. Typical limiting magnitudes are $B_J \sim 22.5$ and $R \sim 21$, with an uncertainty of ~ 0.25 mag. Search radii of 60 to 90 arcsec were used to recover large proper motions (typically $0.3\text{--}1.0''/\text{yr}$).

The pilot survey (Scholz et al. 2000) extracted about 100 new high proper motion objects down to $R \sim 20.0$ over thousand square degrees between 0^h and 7^h in right ascension and -63° and -32° in declination, respectively. This sample included new white dwarfs as well as K and M dwarfs. This survey was later extended by Scholz using the SuperCOSMOS Sky Survey and 2MASS catalogues over the entire southern sky at four different epochs. The new approach, detailed in Chapter 2, led to the discovery of:

1. Six subdwarfs (Chapter 2).
2. Numerous M dwarfs within 50 parsecs (Chapter 2).
3. Two M dwarfs within 10 parsecs (McCaughrean, Scholz, & Lodieu 2002b).
4. Three ultracool dwarfs (Lodieu, Scholz, & McCaughrean 2002b).
5. The closest binary brown dwarf and brightest T dwarf to the Sun, ε Indi Ba/Bb (Scholz et al. 2003; McCaughrean et al. 2004).

Serendipitous discoveries

Besides the large-scale sky surveys which revealed a large number of ultracool dwarfs and the proper motion surveys dedicated to the search for nearby stars, a small number of L and T dwarfs were unearthed during unrelated surveys. Among them, we would like to emphasise the following discoveries:

- Cuby et al. (1999) reported the discovery of a late-T dwarf in the course of a deep survey carried out with the SofI and SUSI instruments mounted on the NTT. The NTT Deep Field covered an area of $2.3' \times 2.3'$ in the B , V , and r filters down to magnitude limits of 27.2, 27.0, and 26.7, respectively. A $5' \times 5'$ field-of-view was observed as well in the J and K_s filters down to magnitude limits of 24.6 and 22.8, respectively. This new T dwarf has $J = 20.15$ and $K_s = 20.3$ and a low-resolution near-infrared spectrum comparable to Gl229B.
- Liu et al. (2002b) presented the discovery of a faint ($I = 23.6$, $J = 18.2$) T dwarf within the framework of the Institute for Astronomy Deep Survey. This survey used the prime-focus imager Suprime-Cam on the Subaru 8.2-m telescope to cover a total area of 2.5 square degrees in the R , I , and z' filters down to 27.1, 26.5, and 25.5, respectively. Optical and infrared colours with additional near-infrared spectroscopy yielded a spectral type of T3–T4 and a photometric distance of 45 ± 9 pc (Liu et al. 2002b).

- As the result of a spectroscopic search for distant AGB stars, Kendall et al. (2003) announced the discovery of seven unknown L dwarfs. All seven objects were very faint on the I -band photographic plates with magnitudes ranging from 17.0 to 20.0 mag. The objects were assigned spectral types between L0.5 and L5 from direct comparison with template L dwarfs.
- Thorstensen & Kirkpatrick (2003) recently discovered a bright ($K_s = 11.3$) L3.5 dwarf within the framework of a parallax program for a sample of cataclysmic binaries. This new L dwarf, 2MASS J0700+3157, has a well determined parallax of 82 ± 2 mas, and constitutes a new addition to the catalogue of nearby stars (Gliese & Jahreiss 1995). It also represents an important addition to the small sample of L and T dwarfs with accurate distances.

1.5.3 Brown dwarfs in star-forming regions

In § 1.5.2, we have described different kinds of searches dedicated to the improvement of the census of stars and brown dwarfs in the solar neighbourhood. The ultimate goal is to derive the luminosity and mass functions of a volume-limited sample of objects. However, the determination of the field IMF is hampered by major drawbacks, including:

- Parallaxes are required for each individual star to infer their masses. The most reliable mass function estimate is currently available for the 5- and 8-pc samples although the incompleteness might be as high as 30 %, particularly towards low-mass stars (Henry et al. 1997).
- Ages are generally unknown and a mean value of the order of 1 Gyr is assumed for nearby objects to infer the mass. The possible time variations occurring in the star formation rate are lost in this process.
- Large incompleteness exists for high-mass stars because of their rarity in the solar neighbourhood and their short lifetimes.
- The incompleteness towards low-mass stars and brown dwarfs is significant due to their faintness (Henry et al. 1997). The recent discovery of the ε Indi Ba/Bb system at 3.626 pc (Chapter 2) provides one counterexample.

To alleviate many of those issues, several studies have focused on embedded clusters and star-forming regions because they represent an equidistant sample of stars with a similar chemical composition within a limited area on the sky. The advantages (+) and drawbacks (−) compared to the solar vicinity are the following:

- + Very low-mass stars and brown dwarfs are brighter when younger at a given distance, making their detection easier in star-forming regions than in the field (Figure 1.2).
- + Small contamination by field stars and background giants due to the presence of dust and the compactness of embedded clusters.
- + Dynamical evolution is obviously low at young ages although the birth of young clusters might go through phases of violent gas expulsion affecting the shape of the IMF (Kroupa et al. 2001). High-mass stars will not have evolved off the main-sequence yet and low-mass stars are retained within the cluster core. The IMF can, therefore, be derived from high-mass stars down to the deuterium burning limit and below.

- Star-forming regions are heavily embedded in their molecular cloud hampering optical observations.
- Large uncertainties are expected on evolutionary tracks at very young ages due to unknown initial conditions (Baraffe et al. 2002).
- The timescale to form stars represents an appreciable fraction of the cluster age. The star formation process is still on-going so that the mass function is a lower limit of the IMF.

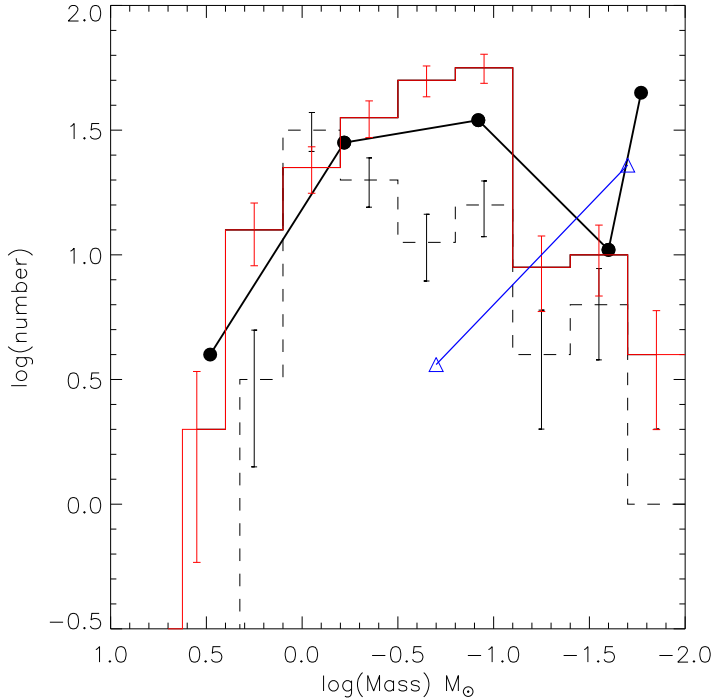


Figure 1.7: Comparison of substellar mass functions in logarithmic scale (Salpeter definition) for the Taurus cloud (dashed histogram; Briceño et al. 2002; Luhman et al. 2003a), the IC348 cluster (solid histogram; Luhman et al. 2003b), the Trapezium Cluster (filled circles with solid line; Muñch et al. 2002), and σ Orionis (open triangles with solid line; Béjar et al. 2001). Possible explanations for the difference in the mass function between Taurus and the Trapezium Cluster are discussed in Section 1.1.3

Bearing in mind those caveats, an emphasis on the recent mass function determinations will follow along with a brief description of the most studied young clusters, including the Trapezium Cluster, σ Orionis, IC348, Taurus, ρ Ophiuchus, and Chameleon (Figure 1.7). Additional star-forming regions have been targeted to uncover low-mass stars and substellar objects but no mass functions were published to date. It includes Lupus (Nakajima et al. 2000), R Corona Australis (Comerón et al. 2002), Upper Scorpius (Martín et al. 2004), NGC1333 (Aspin et al. 1994), and Serpens (Lodieu et al. 2002a). Wilking et al. (2004) have recently set an upper limit of $\alpha \leq 1.6$

on the mass spectrum for NGC1333 across the hydrogen burning limit based on a spectroscopic sample of 25 brown dwarf candidates.

- The Trapezium Cluster lies within the central region of the Orion Nebula Cluster and is the most extensively studied young cluster. The cluster is young (~ 1 Myr), nearby (450 pc), rich and dense ($\sim 10^4$ pc $^{-3}$) and harbours a wide range of stellar masses from $50 M_{\odot}$ to few Jupiter masses. Furthermore, its location in front of molecular cloud minimises the background contamination, making objects with a small extinction likely members.

Multiple surveys at various wavelengths have been conducted in the region, including proper motion (Jones & Walker 1988), optical images from the ground (Herbig & Terndrup 1986) and from space (Luhman et al. 2000), infrared surveys (McCaughrean & Stauffer 1994) complemented by spectroscopy (Hillenbrand 1997; Lucas et al. 2001) to infer masses and ages for each individual member.

Hillenbrand (1997) inferred a IMF which peaks at about $0.2 M_{\odot}$ and declines towards lower masses. The extension of this work to the substellar regime confirmed the previous conclusions (Luhman et al. 2000; Slesnick et al. 2004). Muench et al. (2002) reported a similar IMF from B stars down to the deuterium-burning limit by modelling the infrared luminosity function (Table 1.1 and filled circles with solid line in Figure 1.7).

- The σ Orionis cluster, located around the O9.5 star of the same name, belongs to the Orion OB 1b association. The X-ray detection of a high concentration of sources around the star σ Ori by ROSAT (Walter et al. 1994) triggered deep optical surveys dedicated to the low-mass component of the cluster. The cluster is 1–8 Myr old (Béjar et al. 1999), located at 352 pc according to *Hipparcos* (Perryman et al. 1997), and suffers from little reddening (Lee 1968).

A deep optical (R , I , and Z) survey of a ~ 850 arcmin 2 area in the cluster with additional near-infrared photometry revealed numerous low-mass stars, brown dwarfs (Béjar et al. 1999), and planetary-mass objects (Zapatero Osorio et al. 2000). Many objects have been spectroscopically confirmed over a large mass range in the optical (Barrado y Navascués et al. 2001b) and in the near-infrared (Martín et al. 2001). The cluster mass function, derived from low-mass stars ($0.2 M_{\odot}$) down to the deuterium-burning limit, indicates a rising slope with an index $\alpha = 0.8 \pm 0.4$ (Béjar et al. 2001), when expressed as the mass spectrum (Table 1.1 and open triangle with solid line in Figure 1.7).

- IC 348 is located on the northeast end of the Perseus molecular cloud complex. The cluster is young (1–3 Myr), relatively nearby ($d \sim 315$ pc), rich (about 400 members), compact ($D \sim 20'$) with low extinction ($< A_V > = 0\text{--}5$ mag). IC348 has been extensively targeted in the past to extract cluster members via proper motion (Fredrick 1956), H α emission (Herbig 1998), infrared luminosity functions (Lada & Lada 1995), and optical colour-magnitude diagrams (Herbig 1998; Luhman 1999).

Tej et al. (2002) recently derived a cluster mass function from all-sky catalogues over the whole cluster area and inferred a power law with an index $\alpha = 0.8 \pm 0.2$. Luhman et al. (2003b) assigned spectral types, effective temperatures, and masses for a large number of members within the central $42' \times 28'$ area in the cluster to construct an extinction-limited sample ($A_V \leq 4$) from B stars to late-M dwarfs. The cluster mass function rises from high-mass stars down to $1 M_{\odot}$, rises more slowly to peak at $0.1\text{--}0.2 M_{\odot}$, and declines towards the substellar regime in logarithmic scale (Table 1.1 and histogram with solid line in Fig-

ure 1.7). The IMF derived from the modelling of the luminosity function of a 20.5 arcmin² region confirmed those results (Muench et al. 2003).

- Taurus is a young (1–2 Myr), nearby ($d \sim 140$ pc), low-density ($n \sim 1\text{--}10 \text{ pc}^{-3}$) star-forming region located above the galactic plane ($b \sim 20^\circ$). The total extent of the Taurus region on the sky is about 100 deg². However, 60 % of the pre-main-sequence stars are concentrated in six groups with an average radius of about one parsec (25' on the sky).

Combining previous studies (Briceño et al. 1998; Luhman 2000) with a new optical and near-infrared wide-field survey of 8.4 square degrees in Taurus, Briceño et al. (2002) selected an extinction-limited ($A_V \leq 4$) sample of spectroscopically confirmed members down to $20 M_{\text{Jup}}$. Luminosities, effective temperatures, and masses were inferred for each individual member based on their location in the H-R diagram. Briceño et al. (2002) and Luhman et al. (2003a) concluded that the Taurus IMF peaks at about $0.8 M_{\odot}$ and declines more sharply than the Trapezium Cluster towards low-mass and high-mass stars, yielding a deficit of brown dwarfs and stars more massive than $1 M_{\odot}$ in logarithmic scale (Table 1.1 and histogram with dashed line in Figure 1.7).

- The ρ Ophiuchus dark cloud contains a young (< 1 Myr), nearby ($d = 160$ pc), and compact ($D = 20'$) population of low-mass stars. The region has been extensively targeted in the near-infrared (e.g. Rieke & Rieke 1990), in the mid-infrared (e.g. Bontemps et al. 2001), and in the X-rays (Vuong et al. 2003) due to large extinction (A_V up to 50 mag) hampering optical observations. Near-infrared spectroscopy is available for a large number of low-mass stars, including possible brown dwarfs (e.g. Greene & Lada 1996).

Luhman & Rieke (1999) inferred a complete IMF down to $\sim 0.08 M_{\odot}$ from a compilation of new spectroscopic data and previous surveys. They concluded that the IMF for the studied region in ρ Oph matches that of Miller & Scalo (1979) at masses above $0.4 M_{\odot}$ and slowly declines to the hydrogen-burning limit, in agreement with a flat IMF found by Comerón et al. (1993). These results are consistent with logarithmic IMF determinations in the Trapezium Cluster and IC348 using similar methods to infer luminosities and masses for cluster members (Luhman et al. 2000).

- Chameleon is a young (1–2 Myr) and nearby ($d \sim 160$ pc) star-forming region with an angular size of about 3 square degrees (Boulanger et al. 1998) composed of several clouds (Wichmann et al. 1998). The relatively high galactic latitude and moderate extinction makes the region amenable to unveil brown dwarfs with X-ray (Neuhäuser & Comerón 1998), near-infrared (Cambresy et al. 1998), and mid-infrared (Persi et al. 2000) observations.

A deep H α survey combined with near-infrared imaging of a 300 arcmin² area in the most obscured region of the Chameleon cloud revealed 22 members less massive than $1 M_{\odot}$ (Comerón et al. 1999; Comerón et al. 2000). The derived mass function, although affected by small statistics, is in agreement with estimates in other star-forming regions (Comerón et al. 2000). A wide-field near-infrared survey of about one square degree in Chameleon has extracted an additional set of about 100 members spanning $K = 12\text{--}16$ mag, on the basis of their colour excess (Gómez & Kenyon 2001). Similarly, photometry from the DENIS survey has extracted new members, including possible brown dwarfs (Vuong et al. 2001).

1.5.4 Brown dwarfs in young open clusters

In the previous section, we have focussed on star-forming regions and embedded clusters to indicate the advantages compared to the solar neighbourhood. We will emphasise here the significant advantages (+) and drawbacks (−) of young open clusters (50–200 Myr) compared to the field and star-forming regions:

- + Open clusters are equidistant, coeval sample of stars with a similar chemical composition within a limited area on the sky as star-forming regions.
- + Brown dwarfs are brighter at young ages. They are obviously brighter in star-forming regions than in open clusters but the distance comes into play as well.
- + Mass segregation and evaporation of the less massive components affects clusters older than ~ 200 Myr, not of interest within the framework of this thesis.
- Larger distances than nearby stars implies a lower sensitivity to low-mass stars. This effect is often compensated by the youth of open clusters.
- Contamination by field stars is the biggest disadvantage of open clusters particularly at the faint end, yielding large incompleteness in the substellar regime.
- Incompleteness in the high-mass regime because of the short lifetime of high-mass stars. This point and the previous one constitute arguments in favour of the studies directed towards star-forming regions and massive clusters.

Most of the surveys have concentrated on nearby and young open clusters to investigate the substellar mass function. Only four open clusters younger than 200 Myr are closer than 200 pc: the Pleiades, α Per, IC2602, and IC2391. We will emphasise below the Pleiades and α Per clusters for which substellar mass function estimates are available (Figure 1.8).

The Pleiades open cluster is by far the best studied open cluster and the ideal place to reveal very low-mass stars and brown dwarfs. As a consequence, Rebolo et al. (1995) unearthed the first cluster brown dwarf, Teide 1, followed by many others over the last few years (e.g. Bouvier et al. 1998 and references therein). The reasons for the large number of surveys targeting the Pleiades are the following:

1. The Pleiades is a rich cluster with approximately 1200 known members.
2. The cluster is relatively nearby with a distance estimated to ~ 130 pc. The isochrone fitting estimate ($d = 128$ pc; Pinsonneault et al. 1998) has been recently confirmed by the orbital solution of a double-lined eclipsing binary ($d = 132$ pc; Munari et al. 2004) compared to the *Hipparcos* distance ($d = 119$ pc; van Leeuwen 1999).
3. The cluster proper motion is $\mu_\alpha = +19$ mas/yr and $\mu_\delta = -43$ mas/yr (Jones 1973) with a radial velocity of 5.9 kms^{-1} (Rosvick, Mermilliod, & Mayor 1992). The motion of the cluster is large enough to disentangle members from field stars.
4. The cluster is relatively compact with the majority of members located within 2.5° of the cluster centre (Pinfield et al. 1998).

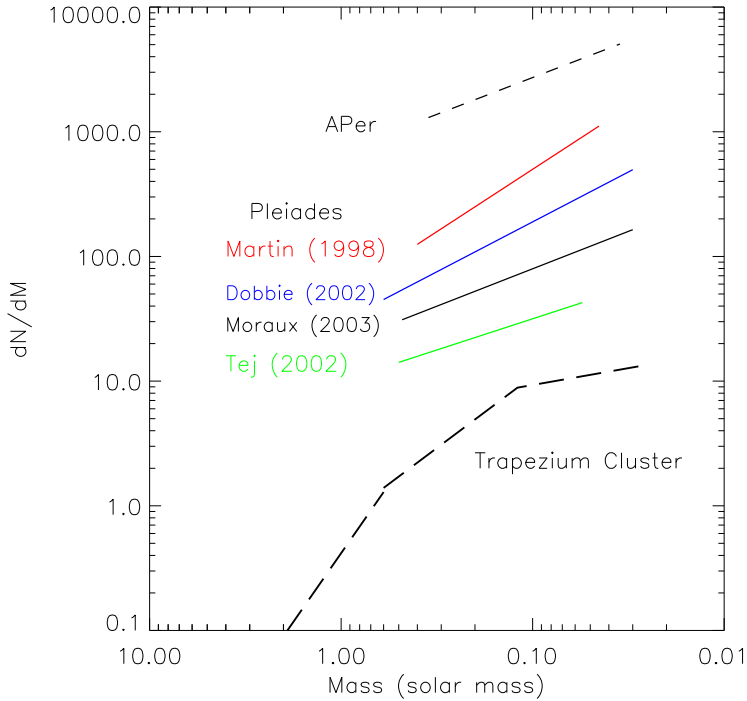


Figure 1.8: Comparison of substellar mass functions, plotted as the mass spectrum, for the Pleiades (Bouvier et al. 1998; Martín et al. 1998; Tej et al. 2002; Dobbie et al. 2002; Moraux et al. 2003), and α Per (Barrado y Navascués et al. 2002) clusters. The mass function estimated by Muench et al. (2002) for the Trapezium Cluster is included for comparison purposes. The different estimates are offset along the y-axis for clarity.

5. The cluster is relatively young. The upper main-sequence turn-off fitting yielded an age of 70 Myr while the lithium test derived an age of 125 Myr (Stauffer et al. 1998).
6. Extinction and reddening towards the cluster are generally uniform ($A_V = 0.12$) and the relatively high galactic latitude ($b = -24^\circ$) reduces the contamination by background objects.

Proper motion studies using multi-epoch photographic plates revealed cluster members down to the hydrogen-burning limit with no significant contamination by background objects (Hambly et al. 1993; Meusinger et al. 1996; Hambly et al. 1999). The search for brown dwarfs in the Pleiades was mainly based on deep optical surveys over small areas on the sky (Bouvier et al. 1998; Zapatero Osorio et al. 1997b; Pinfield et al. 2000) with subsequent near-infrared imaging to weed out contaminating objects (Zapatero Osorio et al. 1997a; Dobbie et al. 2002).

Additional spectroscopic criteria, including $H\alpha$ in emission, lithium in absorption, gravity, radial and rotational velocities have strengthened the membership (Basri et al. 1996; Martín et al. 1996). The large proper motion of the cluster relative to field stars allowed Moraux et al. (2001) to confirm brown dwarf candidates as members over a time baseline of five years.

The numerous surveys quoted below converged towards comparable estimates of the Pleiades mass spectrum (Figure 1.8 and Table 1.1) across the stellar/substellar boundary.

- Martín et al. (1998) derived $\alpha = 1.0 \pm 0.5$ in the $0.40\text{--}0.045 M_{\odot}$ mass range based on a deep survey initiated by Zapatero Osorio et al. (1997b).
- Tej et al. (2002) estimated $\alpha = 0.5 \pm 0.2$ between 0.50 and $0.055 M_{\odot}$ based on a pure statistical approach involving 2MASS and GSC databases.
- Dobbie et al. (2002) inferred $\alpha = 0.8 \pm 0.2$ based on a deep optical photometric survey down to $0.040 M_{\odot}$.
- Moraux et al. (2003) found $\alpha = 0.6 \pm 0.11$ over the $0.48\text{--}0.03 M_{\odot}$ mass range from a complementary deep (I, Z) imaging program to the (R, I) survey by Bouvier et al. (1998).

The α Per cluster is the second best studied open cluster after the Pleiades. Although α Per might be as rich as the Pleiades, the membership list is less complete than the Pleiades for the following reasons:

1. α Per has a small proper motion not well separated from field stars. Hence, proper motion surveys were less frequent and more subject to contamination than in the Pleiades.
2. The cluster is located at low galactic latitude ($b = -7^{\circ}$ versus $b = -24^{\circ}$ for the Pleiades), increasing the contamination by reddened background giants and field stars.
3. α Per is further away than the Pleiades (180 pc versus 130 pc). However, the cluster is younger than its Pleiades counterpart (90 Myr versus 125 Myr), yielding a comparable location of the lithium depletion boundary $I \sim 18.0$.

The reddening to the cluster is low ($A_V = 0.30$) although some spatial variations are seen across the cluster (Prosser 1994). Proper motion studies based on Schmidt plates have provided a large list of probable cluster members (Heckmann et al. 1956; Stauffer et al. 1985; Stauffer et al. 1989b). Colour selection and spectroscopic follow-up were, however, necessary to ascertain the membership of selected candidates due to the small proper motion and low galactic latitude of the cluster (Prosser, 1992, 1994). Surveys conducted in X-rays confirmed the membership of known cluster members (Randich et al. 1996; Prosser et al. 1996b) and unearthed new candidates later assessed as members via photometry and spectroscopy (Prosser & Randich 1998, Prosser et al. 1998).

Recently, Stauffer et al. (1999) applied the lithium test (Rebolo et al. 1992) and inferred an age of 90 ± 10 Myr for the α Per cluster, value twice as large as the upper main-sequence turn-off age (50 Myr). Combining optical and near-infrared imaging, Barrado y Navascués et al. (2002) extracted a list of new cluster members down to $35 M_{Jup}$. The cluster mass function was well approximated by a power law of index $\alpha = 0.59 \pm 0.05$ over the $0.3\text{--}0.05$ mass range, in agreement with the Pleiades estimates (Figure 1.8 and Table 1.1). Additional information on the cluster is provided in Chapter 3.

Other open clusters have been surveyed in details but no mass function estimate has been made available to date. The mass function for the 150–200 Myr old open cluster M35 was derived down to the hydrogen-burning limit (Barrado y Navascués et al. 2001) due to its larger distance ($d \sim 900$ pc). Among open clusters, pre-main-sequence ones are of prime interests, including NGC2547 (20–40 Myr and ~ 400 pc), IC2391 (30–50 Myr and 150 pc), and IC2602 (~ 30 Myr and 150 pc). The large number of cluster members in IC2391 and IC2602 originate from X-rays

surveys with subsequent photometric and spectroscopic assessments. The age of IC2391 was recently derived from the lithium test, yielding a value of 53 Myr (Barrado y Navascués et al. 2001a), larger than the turn-off main-sequence estimate (30 Myr).

The main conclusions of the studies directed towards young open clusters and star-forming regions suggest that the IMF keeps rising in the substellar regime. However, the recent survey conducted in the Taurus cloud indicate a possible variation of the mass function with the environment.

The work presented in this thesis will focus on the search for low-mass stars and brown dwarfs in the solar neighbourhood and in open clusters. Chapter 2 presents the results of a proper motion survey carried out in the southern sky to unearth the closest and coolest neighbours to the Sun. Chapter 3 and Chapter 4 concentrate on the substellar IMF in two young open clusters. In Chapter 3, we will report a near-infrared wide-field survey of the α Per cluster in addition to the recent mass function determination published by Barrado y Navascués et al. (2002). In Chapter 4, we will describe the results of a deep wide-field optical survey with near-infrared follow-up observations of the pre-main-sequence open cluster Collinder 359.

Chapter 2

Proper motion survey for nearby low-mass stars and brown dwarfs in the southern sky

Aiming at finding the closest neighbours to the Sun, a new high proper motion survey was initiated in the southern sky for declinations below -33° by Scholz et al. (2000) using $6^\circ \times 6^\circ$ photographic plates from the United Kingdom Schmidt Telescope (UKST) and measurements made with the Automatic Plate Measuring (APM) machine at Cambridge. The approach was initially based on measurements of UKST photographic plates in two passbands (B_J and R) at epochs separated by about 15 years. Typical limiting magnitudes from the photographic plates are $B_J \sim 22.5$ mag and $R \sim 21$ mag. Search radii of 60 to 90 arcsec were used to recover typical proper motions of $0.3\text{--}1.0''/\text{yr}$ depending on the epoch difference. The pilot survey revealed about 100 new high proper motion stars over thousand square degrees between 0^h and 7^h in right ascension and from -63° to -32° in declination, including white dwarfs as well as K and M dwarfs. More recently, this proper motion survey has focused on the search for low-mass stars and brown dwarfs in the solar neighbourhood.

This chapter, dedicated to the recent results of the search for red high proper motion stars, is organised as follows. In § 2.1, we present the sample of about 70 very red high proper motion targets selected as brown dwarf candidates. In § 2.2, we describe the observations and give an overview of the various telescope/instrument configurations used for imaging and spectroscopic follow-up observations. In § 2.3, we detail the data reduction of the optical and near-infrared photometry and spectroscopy. General results of the proper motion survey are given in § 2.4. Interesting objects discovered within the framework of the survey are highlighted in the following sections, including some subdwarfs (§ 2.5), an active M8.5 as a wide companion of a M4/DA binary (§ 2.6), two M dwarfs within 10 parsecs (§ 2.7), three ultracool dwarfs in the solar neighbourhood (§ 2.8), and the nearest binary brown dwarf, ε Indi Ba,Bb (§ 2.9). Conclusions and future plans are presented in § 2.10.

The discoveries presented in this chapter are described in more details in several published papers, including:

1. Lodieu, Scholz, & McCaughrean (2002b) reported three L dwarfs in the solar neighbourhood although two of them were subsequently classified as M dwarfs.
2. McCaughrean, Scholz, & Lodieu (2002b) discovered two M dwarfs within 10 parsecs.
3. Scholz, Lodieu, Ibata et al. (2004) related the discovery of an active M dwarf as a wide companion to a binary system.

4. Scholz, McCaughrean, Lodieu, & Kuhlbrodt (2003) reported the discovery of ε Indi B resolved later into a binary system by McCaughrean et al. (2004).
5. A paper on the general results of the entire proper motion survey is currently in preparation (Lodieu et al. 2004).

The results presented in this chapter constitute the outcome of a team work (mainly R.-D. Scholz, M. J. McCaughrean, and myself). We will use “we” and not “I” to describe this work throughout the whole chapter. Nevertheless, I would like to stress that the sample selection was conducted by Ralf-Dieter Scholz. My contribution consisted in reducing and analysing optical and near-infrared imaging and spectroscopic data obtained for the whole sample of objects. The data reduction of the adaptive optics data obtained for the ε Indi B system was carried out by Mark McCaughrean.

2.1 The sample

The proper motion survey described here aims at finding brown dwarfs in the solar neighbourhood among selected red high proper motion objects. A first set of follow-up imaging and spectroscopic data for red proper motion objects was obtained in 1999 with the FORS1 and ISAAC instruments on the ESO Very Large Telescope at Paranal, Chile. At this time, the preliminary sample revealed *only* early and late-M dwarfs as well as cool white dwarfs (Scholz et al. 2002). The high proper motion survey was extended later by Ralf-Dieter Scholz using the SuperCOSMOS Sky Surveys (hereafter SSS) database¹, covering the whole southern sky from -90° to $+2.5^\circ$ in three passbands (B_J , R , and I) and at four different epochs. We should stress here that the sample is neither magnitude nor volume-limited. The intrinsic limit of our survey is given by the flux limit of the photographic plates. The objects are randomly selected on the basis of their large proper motions and optical and/or optical-to-infrared colours for spectroscopic follow-up observations. Candidates have generally proper motions larger than $0.3''/\text{yr}$. The colour selection of the candidates did vary according to the type of objects we aimed at finding. The search procedure to find nearby low-mass stars and brown dwarf candidates evolved with time for the following reasons:

1. With time and experience, the colours cuts have been improved to uncover later type dwarfs. As an example, most of the L dwarfs turned out to be undetected in the B_J passband.
2. The full southern sky I -band database from the UK Schmidt Telescope was released at the SuperCOSMOS Sky Surveys web page.
3. The Two Micron All-Sky Survey became fully available and enabled colour selections based on optical-to-infrared and infrared colours.

Combining various approaches and different selection criteria, several samples of proper motion objects selected as brown dwarf candidates have been extracted. The original or ‘preliminary’ sample contained objects mostly selected on the basis of their B_J-R colours. At that time, most objects were lacking I -band and infrared measurements as the SSS and 2MASS databases were not yet fully released. The remaining samples take into account proper motion *and* colour as selection criteria.

¹<http://www-wfau.roe.ac.uk/sss/>

We describe here the sample of red proper motion objects selected by Ralf-Dieter Scholz as brown dwarf candidates for spectroscopic follow-up in the optical and/or in the near-infrared. The sample contains 6 subdwarfs, 10 early-M dwarfs ($\leq M5$), 47 late-M dwarfs (M5.5–M9.5), four L dwarfs, and the nearest binary brown dwarf, ε Indi Ba,Bb. The photometric and spectroscopic results are given in Table A.1 in Appendix A. The optical (6000–10000 Å) spectra are shown in Figures 2.1 and 2.5, and Figures A.2 and A.3 in Appendix A. Near-infrared (1.0–2.5 μm) spectra are displayed in Figure A.4 in Appendix A. Some template objects with well-known spectral types have been added for comparison purposes, including Kelu 1 (L2.0; Ruiz et al. 1997), BRI B0021–0214 (M9.5; Irwin, McMahon, & Reid 1991), and LP944-20 (M9.5; Tinney 1998).

2.2 Observations

Optical and near-infrared photometry and spectroscopy were obtained with several telescopes and instruments in service and visitor modes². The observations as well as the characteristics of each instrument are briefly described below.

- Optical imaging was obtained for a ‘preliminary’ sample of selected red proper motion objects with VLT/FORS1 in service mode (grey time and seeing $\leq 0.8''$). The aim was to derive more accurate magnitudes and colours than the SSS photometry and observe the objects lacking I -band measurements.

FORS1 is a focal reducer multi-mode instrument mounted on the UT1 on the VLT. The camera is equipped with a 2048×2048 pixel TK thinned CCD chip. The pixel size is $24 \mu\text{m}$, corresponding to a spatial resolution of 0.20 arcsec, yielding a field of view of $6.8' \times 6.8'$. A series of three dithered positions in the R_{Bessell} and I_{Bessell} broad-band filters, exposed 10 and 5 sec, respectively, were obtained for all the objects among the ‘preliminary’ sample. Standard stars were observed during the night to calibrate the magnitudes of our target.

- Near-infrared imaging was obtained in service mode (seeing $\leq 0.8''$) with the ISAAC camera on the VLT for the ‘preliminary’ sample during the same observing periods as the optical imaging. As the 2 Micron All-Sky Survey is now fully released, newly selected proper motions objects have generally infrared counterparts.

The near-infrared camera ISAAC is equipped with a HAWAII 1024×1024 pixel array (Moorwood & Spyromilio 1997) optimised in the 1.0–2.5 μm range with a pixel size of $0.147''$, yielding a field of view of $2.5' \times 2.5'$. A series of five dithered positions, exposed two seconds, was obtained in three broad-band filters (J_s , H , K_s) to subtract the sky background. Standard stars were observed during the night to calibrate the magnitudes of our target.

- Optical spectroscopy was obtained by Ralf-Dieter Scholz and myself with EFOSC2 mounted on the ESO 3.6-m telescope at La Silla in November 2001 and December 2002. The camera uses a 2048×2048 pixel Loral/Lesser CCD with a pixel size of $0.157''$, yielding a useful field-of-view of $5.2' \times 5.2'$. A 1 arcsec slit was used for spectroscopy with Grism 12 covering 6000–10000 Å at a resolution of $R \sim 600$. Up to three spectra shifted along the slit by ~ 100 pixels were obtained for each target depending on the brightness of the object. An internal quartz lamp flat field was taken just after the spectrum in order to remove efficiently

²ESO programmes 63.L-0634, 65.L-0689, 68.C-0664, and 70.C-0568

the fringing above 8000 Å. Arc lamps were obtained before and after the night to achieve the wavelength calibration. Spectrophotometric standards were also observed to calibrate our targets in flux.

- Near-infrared spectroscopy was obtained with SofI (Son of ISAAC) mounted on the New Technology Telescope (hereafter NTT) at La Silla in November 2001 by Ralf-Dieter Scholz and myself. The near-infrared camera/spectrograph SofI is equipped with a 1024×1024 pixel HgCdTe HAWAII array (Moorwood & Spyromilio 1997) with a pixel size of $0.294''$ for the Large Field Objective used for spectroscopy. A 1 arcsec slit was used for both the blue ($0.95\text{--}1.64\,\mu\text{m}$) and the red ($1.53\text{--}2.52\,\mu\text{m}$) gratings, yielding a resolution of $R \sim 600$. Three positions along the slit shifted by ~ 100 pixels were taken to remove the background. Arc lamps were obtained before and after the night to achieve wavelength calibration. Featureless spectroscopic standards (typically F5–F8) were measured within one degree on the sky to remove telluric absorption.

2.3 Data reduction

The data reduction in the optical and in the near-infrared imaging and spectroscopic modes was conducted by myself using IRAF in a similar manner for each telescope/instrument configuration. A quick overview is presented below.

2.3.1 Optical imaging

The data reduction of the optical imaging consisted in subtracting bias and dividing each individual science frame by the dome flat-field. Subsequent aperture photometry in $R_{Bessell}$ and $I_{Bessell}$ filters was computed with the APPHOT package in IRAF on each individual frame. Errors on the magnitudes are estimated from the differences between the three measurements. The measured magnitudes were then corrected for the extinction at Paranal and for exposure time following the equation given below.

$$m_{\text{instrumental}} = (m_{\text{measured}}) - (\text{Extinction} \times \text{Airmass}) + (2.5 \times \log(\text{ExpTime}))$$

The typical extinction coefficients at Paranal are 0.13 and 0.09 in $R_{Bessell}$ and $I_{Bessell}$, respectively (as listed in the ESO web page). The same procedure was applied to the standard stars observed on the same nights and the aperture kept constant for photometry. The derived zero points were then applied to the targets. No colour equation was used in the computation of the magnitudes.

2.3.2 Near-infrared imaging

The data reduction of the near-infrared imaging differs from the optical due to the higher sky background and was achieved as follows. Differential flat-fields (lights on – off) were taken before or after each night of observations and averaged to create a mean flat-field frame. To subtract the background on each science frame, the four remaining exposures were averaged to create a sky image. The raw image was then sky-subtracted and flat-fielded. The same procedure was applied to the standard stars. Subsequent aperture photometry was computed with the APPHOT package

in IRAF on each individual frame in the J_s , H , and K_s filters. The measured magnitudes were corrected for extinction and exposure times according to the equation given above. The mean extinction coefficients at Paranal are 0.11, 0.07, and 0.06 in J , H , and K_s , respectively. A mean zero point, obtained from several measurements of standard stars observed throughout the night, were applied to the instrumental magnitudes.

2.3.3 Optical spectroscopy

The data reduction of the optical spectroscopy was carried out within the IRAF environment (packages *onedspec* and *twodspec*) and consisted in several steps detailed below.

1. Ten bias frames, taken before the night, were averaged by rejecting the lowest and highest values of each individual pixel. The resulting mean bias is then subtracting from the raw science image.
2. A mean flat field was created by averaging five dome flats with a minmax rejection. This procedure is adapted for the VLT/FORS1 spectroscopy. However, the presence of fringing redward of 8000 Å in the ESO 3.6-m/EFOSC2 data required the observations of an internal flat field immediately after the first spectrum of each target to remove the fringing efficiently. A response function was created to correct for the wavelength dependence of the flat-field using a high-order polynomial along the dispersion axis (task *response*).
3. The bias-corrected science frame was then divided by the normalised polynomial fit of the flat-field.
4. The location of the aperture, the size, and the background level were estimated interactively (task *apsum*). The aperture varies from few pixels up to 10 or so depending on the brightness of the source. The trace of the spectrum was fit throughout the entire spectrum by a cubic spline function, yielding the extraction of a one-dimensional spectrum.
5. The He and Ar lines were marked in arc lamp spectra and identified (task *identify*) to create a linear fit of the wavelength as a function of the pixel number. The two-dimensional curvature of the arc spectra was also taken into account by the task. Reference tables containing the accurate positions were available within IRAF for cross-correlation with the observed arc lamps.
6. The dispersion solution was assigned to the science target according to the linear fit of the wavelength as a function of the pixel number (task *dispcor*). The starting and ending wavelength as well as the wavelength per pixel and the number of pixels were output and should obviously correspond to the parameters listed in the user manual of the instrument.
7. The final step was the flux calibration of the science spectrum (task *calibrate*) expressed in $\text{erg cm}^{-2} \text{s}^{-1} \text{\AA}^{-1}$. This procedure requires observations of spectrophotometric standard stars whose data reduction was identical to the science targets. Two more steps were, however, required to correct for the non-uniform response of the detector over the whole wavelength range. The number of counts for each standard star were integrated over bandpasses (typically 20–50 Å) to tabulate the flux according to the number of counts at a given wavelength (task *standard*). A mean sensitivity function was extracted from several standard star observations to calibrate in flux the science spectrum (task *sensfunc*).

The calibrated spectra were normalised at 7500 Å. No removal of the telluric absorption has been applied. Optical (6000–10000 Å) spectra of the coolest objects discovered within the framework of the proper motion survey are shown in Figure 2.1. Optical spectra of M dwarfs are displayed in Figure A.2 and A.3 in Appendix A. Spectra of subdwarfs are displayed in Figure 2.5.

2.3.4 Near-infrared spectroscopy

The data reduction of the near-infrared spectroscopy conducted with VLT/ISAAC and NTT/SofI was different from the optical procedure due to the higher and variable sky background at infrared wavelength. A minimum of three spectra shifted along the slit by ~ 100 pixels was obtained to remove the sky background. Featureless standards were observed at a similar airmass to remove the telluric absorptions present in the spectra of the targets.

The initial phase of the data reduction required the subtraction of the sky background. The procedure is similar to the infrared imaging as spectra were combined by pairs and averaged. We subtracted the combined spectra from the remainder spectrum and subsequently divided by the response function of the flat-field. We extracted a one-dimensional spectrum and applied the wavelength calibration in a similar manner as for the optical spectra. The whole near-infrared range was covered with three gratings for ISAAC in J (1.1–1.4 μm), H (1.42–1.82 μm), and K_s (1.82–2.50 μm). A slightly larger wavelength range was covered with the blue (0.95–1.64 μm) and red (1.53–2.52 μm) gratings using the SofI instrument. We repeated the same data reduction procedure for each filter.

Then, we averaged the three individual wavelength-calibrated spectra and divided them by the averaged spectrum of the featureless standard observed just before or after the science frame at a similar airmass to get rid off the telluric absorptions. We multiplied the resulting spectrum by the blackbody spectrum of a template with the same spectral type as the standard, smoothed to the resolution of the target spectra. To achieve this step, we have used stellar spectra of O to M dwarfs (Pickles 1998) covering 1150–25000 Å available at the ESO webpage³. Those template spectra were degraded to the resolution of our observations by a simple smoothing operation. Hence, near-infrared spectra are not flux-calibrated because the standard stars are not *spectrophotometric* standards, contrary to optical spectra. This step can, nevertheless, be achieved by comparing the spectra to the near-infrared JHK magnitudes when available.

Near-infrared (1.0–2.5 μm) spectra of our targets, normalised at 1.25 μm , are displayed in Figure A.4 in Appendix A.

2.4 General results of the proper motion survey

The primary selection criteria of the bona-fide brown dwarf candidates was their significant proper motion. The optical and/or the infrared colours of the selected objects provided a rough classification of the target. However, spectroscopy was mandatory to classify accurately the objects and estimate their distance. Altogether, optical and/or near-infrared spectroscopy was obtained for about 70 objects using a variety of telescopes and instruments. The spectral classification of the selected red proper motion objects is based on the schemes defined by Martín et al.

³<http://www.eso.org/instruments/isaac/lib/>

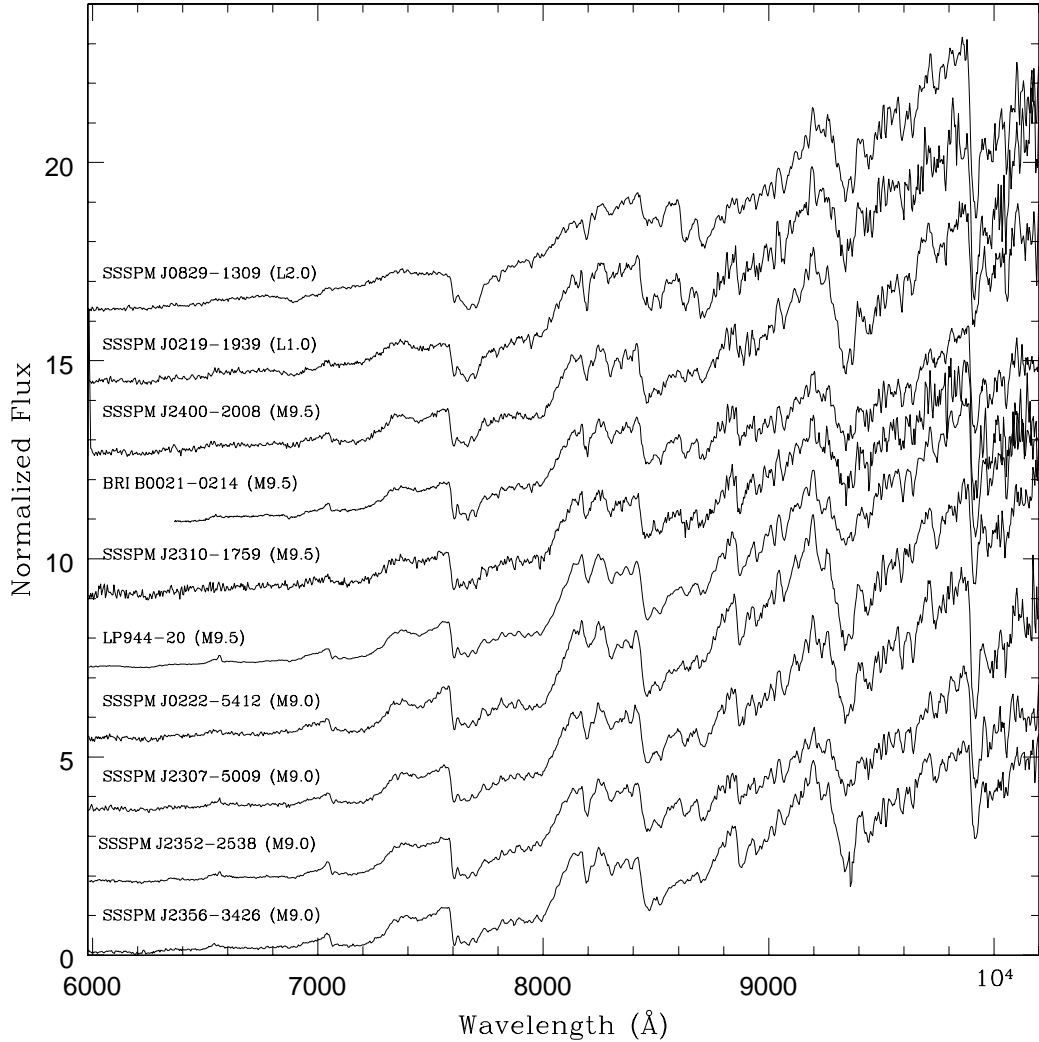


Figure 2.1: Optical (6000–10000 Å) spectra of the latest (M9–L2) nearby objects found in the course of our southern sky proper motion survey. Spectra of SSSPM J2356–3426 (M9.0), SSSPM J2352–2538 (M9.0), SSSPM J2307–5009 (M9.0), SSSPM J0222–5412 (M9.0), SSSPM J2310–1759 (M9.5), and SSSPM J2400–2008 (M9.5), SSSPM J0219–1939 (L1.0), and SSSPM J0829–1309 (L2.0; Scholz & Meusinger 2002). Two template M dwarfs, LP944-20 (M9.5) and BRI B0021–0214 (M9.5), are also shown for comparison. Spectral types are accurate to half a subclass. Telluric features have not been removed from the spectra. An arbitrary constant has been added to the spectra for clarity.

(1999b) and Kirkpatrick et al. (1999b).

We have applied the recipe described in Section 1.4.2 in Chapter 1 to assign spectral types, with uncertainties of half a subclass or better. A brief summary is given here. We have computed the VO-a (Table 1.2; Kirkpatrick et al. 1999b), TiO5 (Table 1.2; Reid et al. 1995), and PC3 (Table 1.2; Martín et al. 1999b) and took the average of the three values. Then, we have determined the spectral type of our targets by comparing the spectrum with the spectrum of a M dwarf template observed with the same telescope/instrument configuration. Finally, we have averaged the results obtained independently by both methods.

Spectral indices versus spectral types are displayed in Figure A.1 in Appendix A. Those graphs clearly demonstrate that some dispersion exists for the TiO5 and VO-a indices. However, the PC3 index correlates very well and appears as the most accurate spectral index for our sample of M and L dwarfs.

The spectral classification of near-infrared spectra relied on templates with well-determined optical spectral types available on Sandy Leggett's web page. As the spectral classification is more accurately defined in the optical, we have favoured the optical spectral typing to the infrared one when the target was observed at both wavelengths.

The sample of proper motion objects presented in this chapter includes 6 subdwarfs, 10 M dwarfs with spectral types earlier than M5, 47 late-M dwarfs, four L dwarfs, and the nearest binary brown dwarf discovered to date. Table A.1 in Appendix A lists 67 red proper motion objects with their coordinates (in J2000), epochs, and proper motions in mas/yr. The optical and near-infrared magnitudes for all targets are provided in Table A.2 in Appendix A. The values of spectral indices and the derived spectral types are given in Table A.3 in Appendix A. Optical spectra of the latest ultracool dwarfs (M9–L2) found in the survey are displayed in Figure 2.1. Spectra of early and late-M dwarfs are shown in Figure A.2 and Figure A.3 in Appendix A, respectively. Near-infrared (1.0–2.5 μm) spectra are displayed in Figure A.4 in Appendix A.

We have estimated the photometric distances of the proper motion objects within our sample using the $I - J$ colours versus spectral types relation given in Dahn et al. (2002). Those relations are based on late-type dwarfs with parallax measurements and valid in the spectral range M6.5–L8. Due to differences observed in the I filter definition (central wavelength and width), more accurate distance estimates are obtained with the absolute J magnitude versus spectral type relationship given below (Dahn et al. 2002):

$$M_J = 8.38 + 0.341 \times \text{SpT}$$

where SpT = 7 for spectral type M7 up to 18 for spectral type L8, with a dispersion of 0.25 mag. Apparent J magnitudes are available from the 2MASS database for all proper motion objects. For objects with earlier spectral types, we have used the primary standards listed in Kirkpatrick et al. (1991). The histogram of the distance distribution of our sample of proper motion objects is displayed in Figure 2.2. The shaded area includes all objects later than spectral type of M6.5. Figure 2.2 shows that most of the objects ($\sim 95\%$) are located within 50 parsecs of the Sun.

Uncertainties on the photometric distances are given in Table A.2 in Appendix A. We have used the dispersion value of 0.25 mag given in Dahn et al. (2002) and considered an upper limit on the error of the 2MASS J -band magnitudes of 0.1 mag. The major uncertainties on the photometric distances are, on the one hand, the uncertainty on the spectral type determination (generally

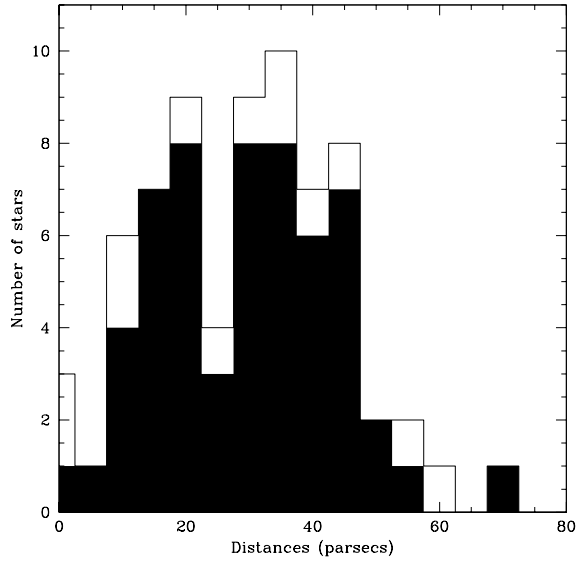


Figure 2.2: Distribution of the photometric distances (in pc) of the proper motion objects found in the course of our survey in the southern sky. Distances and their uncertainties are listed in Table A.2 in Appendix A. The shaded area indicates the stars with spectral types later than M6.5 with photometric distances derived from the absolute magnitude-spectral type relation from Dahn et al. (2002). For spectral types earlier than M6, we have used the primary standards from Kirkpatrick et al. (1991). This graph shows that most of the objects are within 50 pc of the Sun.

better than half a subclass) and, on the other hand, the uncertainty on the luminosity of the standard stars. As a consequence, these photometric parallaxes are not a linear function of decreasing mass. The cosmic scatter due to inhomogeneous sample of objects in terms of metallicity, age, and spin (Kroupa et al. 1993) is negligible compared to the uncertainties quoted above.

Out of 52 proper motion objects observed spectroscopically in the optical, more than half of them exhibit H α in emission (Figure 2.3). The chromospheric activity is very high in some objects, with equivalent widths up to 15 Å. Among the active objects, 18 exhibit equivalent widths larger than 5 Å. The peak of H α emission occurs around spectral types M7–M8, in agreement with previous studies of nearby stars (Hawley et al. 1996; Gizis et al. 2000). Nevertheless, about 10 objects with earlier spectral types (M4–M5) exhibit large equivalent widths. It is known that there is a strong connection between rotation and chromospheric activity for in K to mid-M dwarfs but this trend is less clear for later type dwarfs (Mohanty & Basri 2003).

We have also investigated the distribution of the equivalent widths of two gravity-sensitive doublets, K I at 7665/7699 Å and Na I at 8183/8195 Å as a function of spectral type (Figure 2.4 and Table A.3). The K I doublet is resolved at the resolution of the spectra but the Na I doublet is not. Figure 2.4 shows that the K I equivalent widths are rather constant with spectral type whereas the Na I peak around spectral type M8. These results should be considered as trends due to the limited statistics but will be compared with spectroscopic results obtained for low-mass stars and

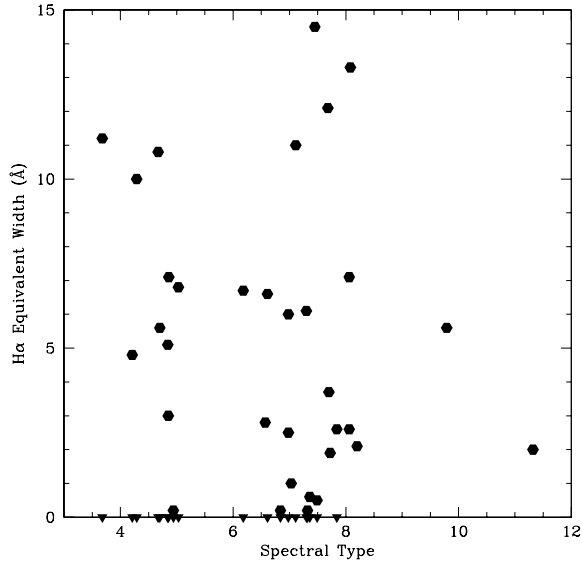


Figure 2.3: H α equivalent widths (in Å) versus spectral type (4 \equiv M4, 5 \equiv M5, 10 \equiv L0, etc ...) for all proper motion objects observed spectroscopically in the optical. Filled triangles indicate objects with no H α detection at the resolution of the spectra.

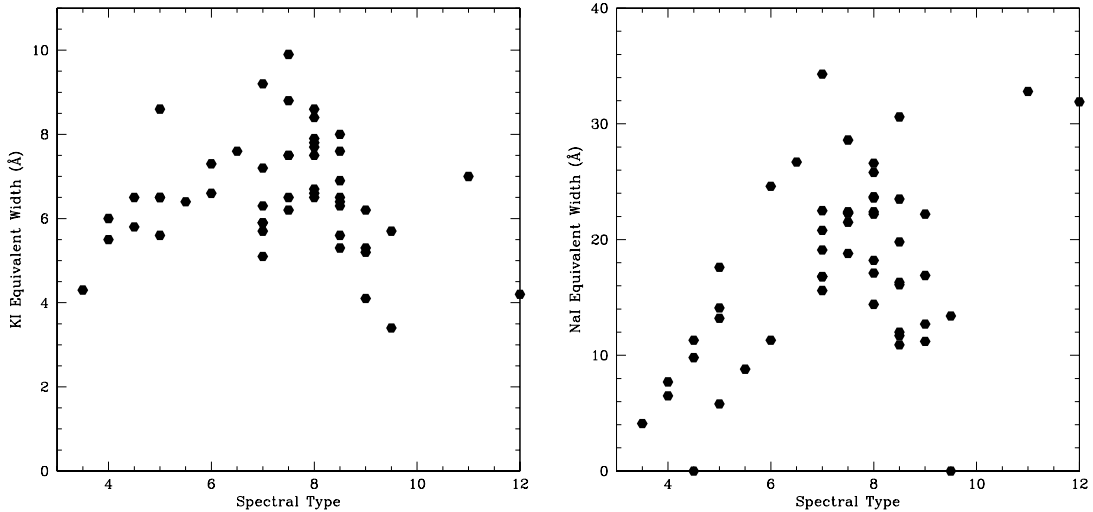


Figure 2.4: Gravity feature equivalent widths (in Å) versus spectral type (4 \equiv M4, 5 \equiv M5, 10 \equiv L0, etc ...) for all red proper motion objects except the subdwarfs and the objects observed only in the near-infrared. The K I doublet at 7665/7699 Å is shown in the left panel whereas the Na I doublet at 8183/8195 Å is in the right panel.

brown dwarfs belonging to the α Per cluster (Chapter 3).

2.5 Subdwarfs in the solar neighbourhood

Six subdwarfs have been identified among our sample of red proper motion objects. The subdwarfs are listed in Table 2.1 along with their coordinates, spectral types, heliocentric velocities, estimated masses and distances.

The spectral classification of lower metallicity objects ([Fe/H] between -2.0 and -1.0) than normal dwarfs was undertaken by Reid et al. (1995) and later on extended by Gizis (1997). As described in the latter paper, three steps, involving TiO and CaH band strengths measurements, are required to pin down the spectral type. All objects considered in this section (Figure 2.5 and Table 2.1) fulfil the cutoffs criteria defined by Equations 4–6 given in Gizis (1997).

Table 2.1: The six subdwarfs found within the framework of the proper motion survey in the southern sky. Names, coordinates (in J2000), spectral types with an uncertainty of half a subclass, heliocentric radial velocities (in km/s), estimated masses in solar masses from Baraffe et al. (1997), and distances in parsecs are listed. Errors on the masses take into account the uncertainties on the magnitudes and metallicity.

Target	R.A. (J2000)	Dec (J2000)	SpT	V_{HeI} (km/s)	$M (M_\odot)$	d (pc)
LP815-21	20:28:04.52	-18:18:57.5	esdM0.0	+122 \pm 20	0.200 \pm 0.100	325 \pm 15
LP614-35	12:07:51.63	-00:52:32.0	esdM0.5	+288 \pm 20	0.110 \pm 0.020	103 \pm 15
CE 352	13:40:38.77	-30:32:02.7	esdM3.0	-66 \pm 20	0.100 \pm 0.020	151 \pm 15
LP 314-67	09:48:05.16	+26:24:18.9	sdM3.5	+214 \pm 20	0.110 \pm 0.020	151 \pm 15
SSSPM J0500–5406	05:00:15.77	-54:06:27.3	esdM6.0	+247 \pm 20	0.090 \pm 0.020	60 \pm 15
SSSPM J1930–4311	19:29:40.99	-43:10:36.8	sdM5.5	—	0.085 \pm 0.020	44 \pm 15

From the indices, three objects, namely LP614-35, CE 352, and SSSPM J0500–5406, are unambiguously classified as extreme subdwarfs with spectral types esdM0.5, esdM3.0, and esdM6.0, respectively, with an accuracy of half a subclass. The latter, SSSPM J0500–5406, is among the coolest extreme subdwarfs found to date. This object is as cool as LHS 1826 (esdM6.0; Gizis & Reid 1997) but warmer than APMPM J0559–2903 (esdM7.0; Schweitzer et al. 1999). The sample of late-M subdwarfs has recently been extended by the discovery of the first two L subdwarfs (Burgasser et al. 2003c; Lépine et al. 2003a).

Concerning LP815-21, this object lies in the boundary region between subdwarfs and extreme subdwarfs (cf. Figure 1 in Gizis 1997). A direct comparison with the spectrum of LHS489 (esdM0.0; Gizis 1997) allowed us to classify it as a esdM0.0 due to the similarity of their spectra.

Another uncertain object, LP314-67, appears ambiguous. Spectral indices defined by Gizis (1997) classify this object either as a subdwarf or an extreme subdwarf or both. Direct comparison with template subdwarfs and extreme subdwarfs from Gizis (1997) solved the ambiguity, yielding a spectral type of sdM3.5.

Finally, despite the low signal-to-noise spectrum of SSSPM J1930–4311, the classification as a subdwarf of spectral type sdM5.5 \pm 1.0 could be established.

We have detected spectral line shifts in the Ca II lines at 8542 and 8662 Å in all objects except SSSPM J1930–4311, where the signal-to-noise of the spectrum was too low. The wave-

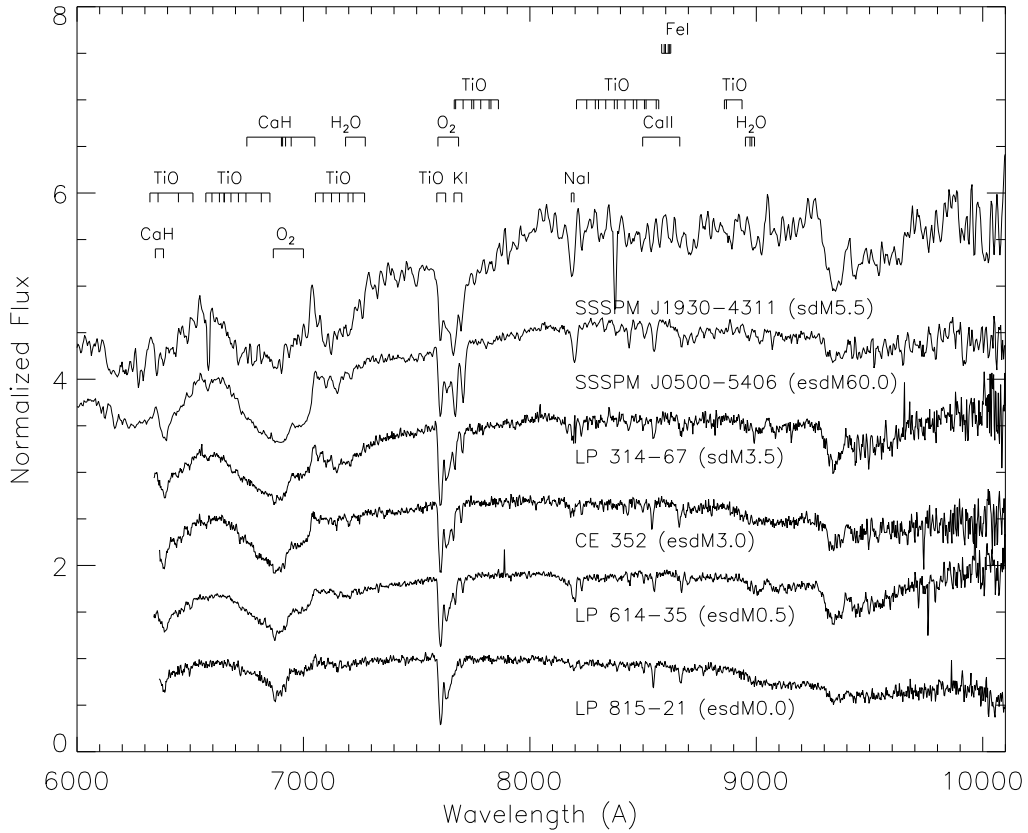


Figure 2.5: Spectra of six subdwarfs and extreme subdwarfs found among the proper motion objects observed with VLT/FORS1 and ESO 3.6m/EFOSC2. From bottom to top are LP 815-21, LP 614-35, CE 352, LP 314-67, SSSPM J0500–5406, and SSSPM J1930–4311 classified as esdM0.0, esdM0.5, esdM3.0, sdM3.5, esdM6.0, and sdM5.5, respectively, based on the scheme described in Gizis (1997). Major absorption bands are overplotted. An arbitrary constant has been added to each spectrum for clarity.

length shifts indicate that those objects have a radial velocity component. The computed shifts of $+3.5$, $+8.0$, -2.5 , $+6.5$, and $+7.0 \pm 0.5 \text{ Å}$, correspond to heliocentric radial velocities of $+122$, $+288$, -66 , $+214$, and $+247 \pm 20 \text{ km/s}$ for LP815-21, LP614-35, CE 352, LP314-67, SSSPM J0500–5406, respectively (Table 2.1).

The metallicity of subdwarfs and extreme subdwarfs, defined here as the iron to hydrogen ratio, is estimated as $[\text{Fe}/\text{H}] = -1.2 \pm 0.3$ and $[\text{Fe}/\text{H}] = -2.0 \pm 0.5$, respectively. The enhancement of the oxygen to iron ratio originating from the production of oxygen in type II supernovae is taking into account in the computation of the metallicity (Baraffe et al. 1997). Hence, we have computed the physical parameters of all subdwarfs (Table 2.1), including distance and mass, according to the evolutionary models from Baraffe et al. (1997) at an age of 10 Gyr. The errors on the masses include uncertainties on the magnitudes as well as uncertainties on the metallicity.

2.6 An active M8.5 dwarf wide companion to a M4/DA binary

We have recently discovered an active late-M dwarf as a wide companion to a M4/DA binary system within the framework of our proper motion program (Scholz et al. 2004).

APMPM J2354–3316C was first detected in the UKST B_J and R plates with a subsequent detection in the R and I bands from SuperCOSMOS Sky Surveys at different epochs. We have selected this object as a field brown dwarf candidate based on its large proper motion (about $0.5''$) and red optical colour ($R-I \sim 2.7$). Later, we identified it as a common proper motion to an already known binary, consisting of a mid-M dwarf (LHS4039) and a white dwarf (LHS4040). The pair was originally discovered by Luyten (1979) during his Bruce proper motion survey and a recent spectral classification by Oswalt, Hintzen, & Luyten (1988) assigned spectral types of dM4 and DA5+ to LHS4039 and LHS4040, respectively. The photometric distance of the pair is estimated to 21 pc in the ARICNS database for nearby stars⁴. The triple system is the first M4/white dwarf pair complemented by a late-M dwarf component, all three being widely separated and suited for detailed follow-up observations.

Two optical spectra of APMPM J2354–3316C were obtained on 3 October 1999 with the EFOSC2 camera mounted on the 3.6-m telescope at La Silla. One spectrum was taken with the grism#1 covering the wavelength range 3200–10900 Å. The spectrum of the object was typical of a late-M dwarf and considered as a possible brown dwarf. Hence, a second higher resolution spectrum ($R \sim 600$), exposed 900 sec, was observed during the same observing run with the grism#12, covering 6000–10000 Å (thin line in Figure 2.6). The data reduction for the second spectrum was standard and is described in § 2.3. The PC3 index defined by Martín et al. (1999b) yielded a spectral type of M8.7 while the VO-a index from Kirkpatrick et al. (1999b) gave M8.3. A direct comparison with template spectra (M7.5–M9.5) from Kirkpatrick et al. (1999b) as well as with late-M dwarfs from other proper motion objects observed with the same telescope configuration led to a spectral type of M8.5, with an uncertainty of half a subclass. Comparing the JHK_s magnitudes from 2MASS and the absolute magnitudes of two M8.5 dwarfs given by Dahn et al. (2002), we have derived a spectroscopic distance of 19.5 pc, in good agreement with the ARICNS estimate.

We observed APMPM J2354–3316C with low-resolution ($R = 600$) spectroscopy in the near-infrared (0.9–2.5 μm) on 25 November 2001 with the camera SofI mounted on the NTT at La Silla. The data reduction of the near-infrared spectrum was identical to the other targets and is described in § 2.3. The comparison with infrared spectra available on Leggett’s web page yielded a spectral type of M8, with an uncertainty of half a subclass, consistent with the optical classification. However, since the optical classification scheme is more accurately defined, we have assigned a spectral type of $M8.5 \pm 0.5$ to APMPM J2354–3316C. The near-infrared classification of M8.0 would place the object at a distance of 25 pc by comparison with four M8 dwarfs listed in Dahn et al. (2002).

We obtained a new low-resolution optical spectrum of APMPM J2354–3316C on 8 December 2002 with the same telescope/instrument configuration as the previous optical spectrum (EFOSC2; grism#12). The data reduction was also identical for both spectra. Both calibrated spectra are overplotted in the upper part of Figure 2.6. The spectrum taken in October 1999 is shown as a thin

⁴<http://www.ari.uni-heidelberg.de/aricns/>

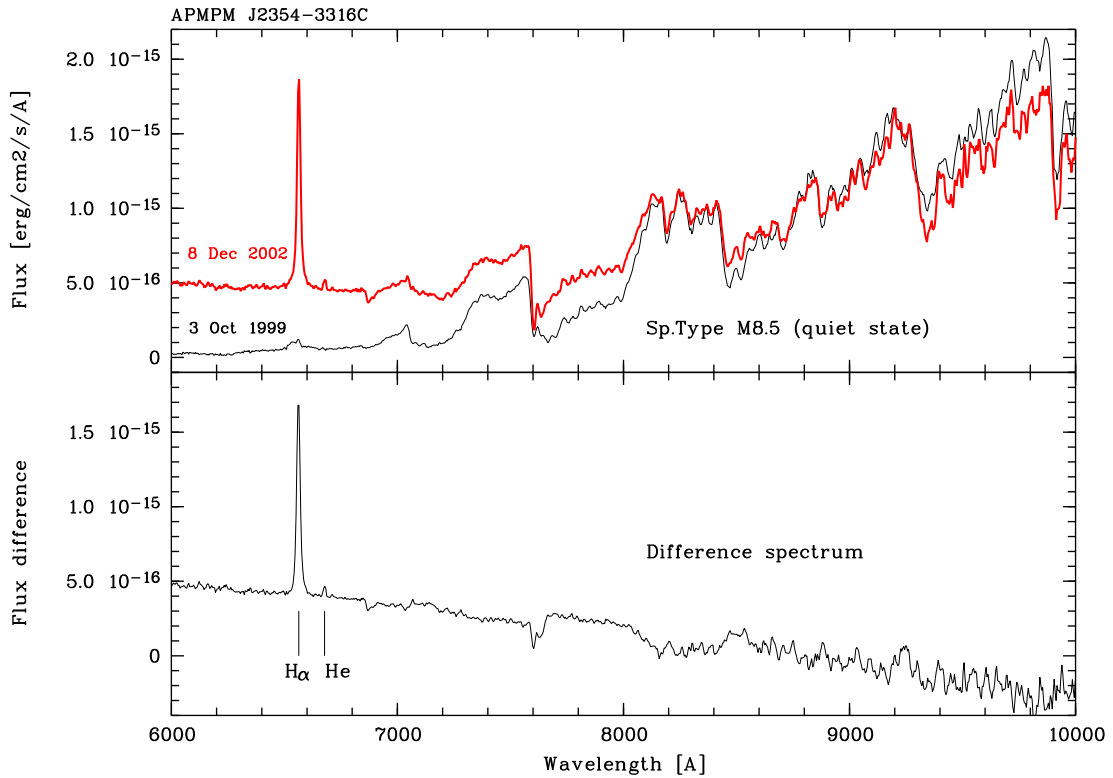


Figure 2.6: *Top:* Flux calibrated spectra of APMPM J2354–3316C in quiet state (thin line) from 1999 and with strong H_{α} emission in 2002 (thick line). *Bottom:* The difference spectrum, which is a perfect blue veiling continuum plus H_{α} at 6563.8 Å and HeI at 6678.1 Å in emission, with equivalent widths of 61.4 ± 5.0 Å and 2.3 ± 0.5 Å, respectively. From Scholz et al. (2004).

line whereas the 2002 spectrum is displayed as a thick line. The lower part of Figure 2.6 shows the result after subtracting the spectrum obtained in 1999 from the 2002 spectrum.

The difference between the two spectra of the same object, taken with the same instrumental set-up, is striking. Not only does the recent spectrum exhibit a large H_{α} emission line, but a very strong blue continuum is also present, making the optical colour of the object bluer in the active state. Many other late-M dwarfs were observed during that night and none of them exhibit such a blue continuum. Furthermore, a look at the raw image immediately revealed a peculiar behaviour below 7500 Å, excluding an incorrect data reduction. Unfortunately, we are lacking another optical spectrum of APMPM J2354–3316C during that night (and the observing run) so that the duration in time of the event is unknown. Note that APMPM J2354–3316C has also been targeted in X-rays but no excess was detected at the position of the object on 13 December 2001, suggesting an inactive state at that time.

The flare spectrum of APMPM J2354–3316C exhibit strong H_{α} at 6563 Å and He I at 6678 Å emission lines as well (Figure 2.6), with equivalent widths of 61.4 ± 5.0 Å and 2.5 ± 0.5 Å, respectively. The flux contained in the H_{α} emission line during the flare spectrum was 2.8×10^{-14} erg cm⁻² s⁻¹ whereas the flux in the quiescent state was 5.0×10^{-16} erg cm⁻² s⁻¹. Assuming a distance of 21 pc, the H_{α} luminosity $L_{H_{\alpha}}$ is of about 1.5×10^{27} erg s⁻¹ during the flare and about a factor 60 less in quiescence. Using absolute bolometric magnitudes of two

M8.5 dwarfs given in Dahn et al. (2002), we have derived a mean bolometric luminosity of $L_{bol} = 1.1 \times 10^{30}$ erg s $^{-1}$.

The blue continuum seen in the flare spectrum of APMPM J2354–3316C is steeper by a factor of two compared to the continuum detected in the M9.5 dwarf 2MASSW J0149+29 (Liebert et al. 1999). However, the resulting L_{H_α}/L_{bol} ratios in the flare and quiescent states are comparable for both objects (1.4×10^{-3} versus 2.5×10^{-3} and 2.4×10^{-5} versus 2.5×10^{-5}). A comparable flare spectrum was noticed in the nearby M8 dwarf, LHS 2397a (Bessell 1991), recently resolved as a binary system with a tight brown dwarf companion at a separation of approximately 3 AU (Freed et al. 2003). We speculate that APMPM J2354–3316C could be orbited thus by a tight brown dwarf. If it turns out that APMPM J2354–3316C is similar to LHS 2397a, the triple system discussed here would actually be a quadruple system with two wide binaries at a separation of 2200 AU, constituted of a M4/white dwarf and a M8.5/brown dwarf, respectively.

2.7 Two M dwarfs within 10 pc

McCaughrean, Scholz, & Lodieu (2002b) reported the discovery of two bright ($K_s \sim 9.5$ mag) late-M dwarfs of spectral types M7.5 and M8 within 10 pc with proper motions larger than 0.30"/yr.

To find these nearby red dwarfs in the southern sky, we selected all 2MASS objects without optical counterpart in the USNO-A2 catalogue but a counterpart within 60" in the NLTT catalogue as bona-fide candidates. After applying a colour selection such as $m_r - K_s \geq 6.0$, two objects, namely LP775-31 and LP655-48, stood out from the remaining short list. The full astrometric and photometric data for LP775-31 and LP655-48 are provided in Table 2.2. Note that LP655-48 was identified with a bright X-ray source (1RXS J044022.8–053020; Voges et al. 1999). Other late-type M dwarfs with comparable brightness include the brown dwarf LP944-20 (Tinney 1998), the M9 dwarf DENISP J104814.7–395606 reported by Delfosse et al. (2001), and 2MASSI J1835379+325954 at 6 pc recently discovered by Reid et al. (2003).

Table 2.2: Astrometry and photometry from SSS and 2MASS for two M dwarfs within 10 pc (LP775-31 and LP655-48), SSSPM J0109–5101 (M8.5), SSSPM J2310–1759 (M9.5), and SSSPM J0219–1939 (L1) found in our proper motion survey.

Name	α, δ	Epoch	$\mu_\alpha \cos \delta$	μ_δ	R	I	J	H	K_s
	(J2000)		mas/yr	mas/yr	(SSS)		(2MASS)		
LP775-31	04 35 16.14 –16 06 57.5	1998.9	+160 ± 4	+305 ± 4	16.35	12.36	10.40	9.78	9.34
LP655-48	04 40 23.33 –05 30 07.9	2001.8	+335 ± 2	+131 ± 2	16.50	13.17	10.68	9.99	9.56
SSSPM0219	02 19 28.03 –19 38 41.0	1999.9	+194 ± 4	-173 ± 06	20.13	17.46	14.09	13.30	12.83
SSSPM2310	23 10 18.53 –17 59 09.4	1998.1	+24 ± 17	-246 ± 13	20.52	17.67	14.40	13.58	13.01
SSSPM0109	01 09 01.29 –51 00 51.1	1990.8	+207 ± 4	+94 ± 11	18.21	14.80	12.23	11.54	11.09

We obtained optical spectroscopy (6000–10000 Å) of LP775-31 and LP655-48 with the EFOSC2 camera mounted on the ESO 3.6-m telescope. The normalised spectra are displayed in Figure 2.7 along with those of LP944-20 (M9) and the M7 dwarf 2MASS 095229–192431 (Gizis et al. 2000) for comparison purposes.

We assigned spectral types of M7.5 and M8 to LP655-48 and LP775-31, respectively, with an uncertainty of half a subclass. Spectral indices, including the PC3 (Martín et al. 1999b), TiO5

(Reid et al. 1995), and VO-a (Kirkpatrick et al. 1999b) led to similar results. The spectral indices found for the comparison objects (2MASS 095229–192431 and LP944-20) are in good agreement with published values as well.

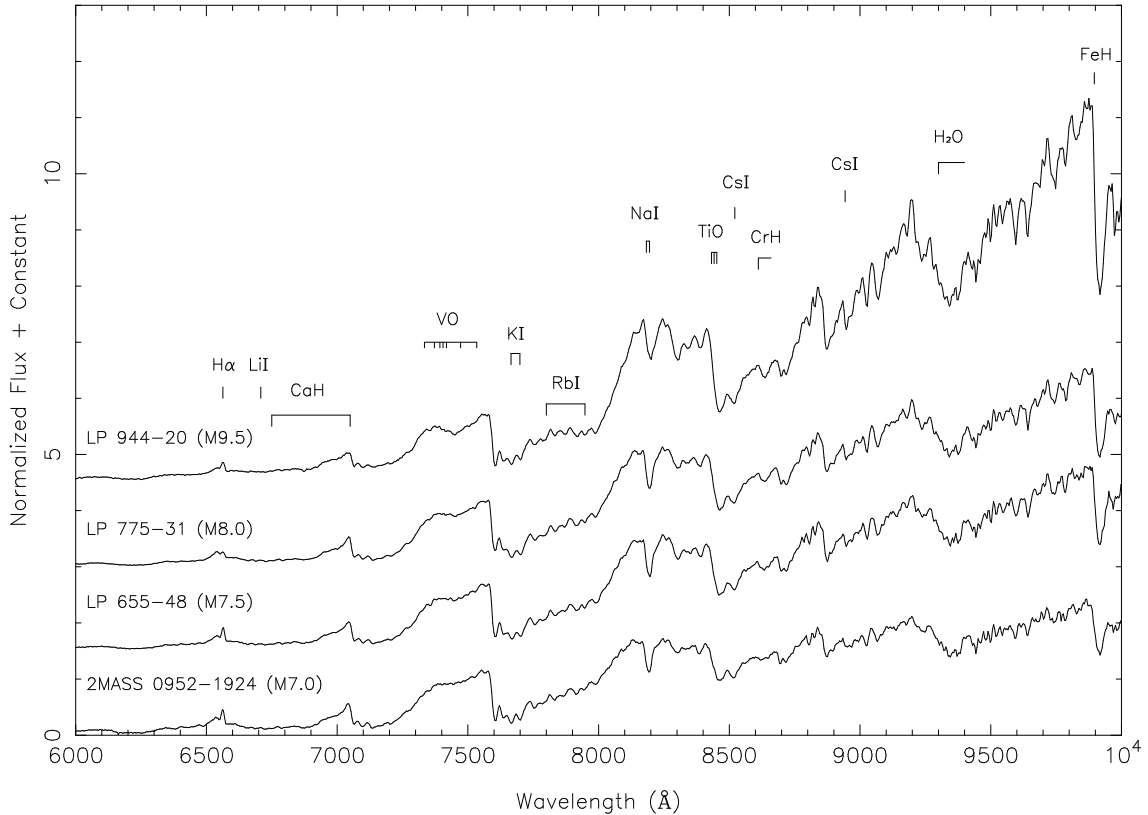


Figure 2.7: ESO 3.6-m/EFOSC2 spectra of LP775-31 and LP655-48 (McCaughrean et al. 2002b), compared with those of LP944-20, a known brown dwarf (Tinney 1998), and the M7.0 dwarf 2MASS J0952219–192431 (Gizis et al. 2000). The location of typical features of late-M dwarfs are labelled, including metal oxide and hydride absorption bands, atomic absorption lines, lithium absorption, and H α emission. An arbitrary constant has been used to separate the spectra.

Independently, Cruz & Reid (2002) classified both stars as M6 dwarfs, while Cruz et al. (2003) revised the spectral types and assigned M7 to both objects. The direct spectroscopic evidence presented in Figure 2.7 favours later spectral types.

Based on the absolute magnitudes of known objects with the same spectral types, we have derived distances of 8.0 ± 1.6 pc and 6.4 ± 1.4 pc for LP655-48 and LP775-31, respectively. If the spectral types estimated by Cruz & Reid (2002) are correct, the distances will be roughly twice as large for both objects. Those assigned by Cruz et al. (2003) would yield distances within 10 pc, confirming our findings.

Further observations are needed to check the binarity of those objects and obtain trigonometric parallaxes. If distances within 10 pc are confirmed, LP655-48 and LP775-31 would represent new

benchmark dwarfs allowing detailed follow-up observations and search for planetary companions with future missions such as DARWIN and/or TPF.

2.8 Three new ultracool dwarfs in the solar neighbourhood

Lodieu et al. (2002b) reported the discovery of three L dwarfs in the solar vicinity within 30 parsecs. We found the three objects by combining B_J , R , and I measurements from the UKST plates and R -band data from ESO Schmidt plates within the framework of a search for objects with typical proper motions of 0.15–0.20 $''$ /yr on plates with 15–20 years epoch differences.

The basic search strategy consisted at looking for objects on a given plate which were not matched with a corresponding object in a different passband to within a nominal search radius of 3 arcsec. This process was repeated for each available photographic plate at a given location on the sky. Then, we compared the reduced catalogues of unmatched objects to look for possible counterparts out to a search radius of 1 arcmin. We identified as proper motion candidates only objects picked up at least three times along a straight line. Further positional information, including the 2MASS database, was added to refine these detections.

As all three objects were discovered in the SuperCOSMOS Sky Surveys data, we named them as follows: SSSPM J0219–1939 (hereafter SSSPM0219), SSSPM J2310–1759 (hereafter SSSPM2310), and SSSPM J0109–5101 (hereafter SSSPM0109). A full astrometric and photometric information for SSSPM0219, SSSPM2310, and SSSPM0109 is given in Table 2.2.

We obtained low-resolution ($R \sim 600$) optical (6000–10000 Å) spectra of SSSPM0219 and SSSPM2310 with ESO 3.6-m/EFOSC2 and near-infrared (0.9–2.5 μ m) spectra for all three objects with NTT/SofI in December 2001 (Figure 2.8). Optical spectra were normalised at 7500 Å and near-infrared spectra were adjusted to the optical spectra around 9700 Å thanks to the overlapping region between the EFOSC2 and SofI data. The observing procedure and data reduction were standard and are described in § 2.2 and § 2.3, respectively.

The spectral classification for SSSPM0219 and SSSPM2310 was based on optical spectral indices defined by Kirkpatrick et al. (1999b) and Martín et al. (1999b) whereas the classification of SSSPM0109 was entirely based on the near-infrared spectral indices defined by Tokunaga & Kobayashi (1999), Testi et al. (2001), Reid et al. (2001a), and Geballe et al. (2002). Lodieu et al. (2002b) published spectral types of L1, L2, and L2 for SSSPM2310, SSSPM0219, and SSSPM0109, respectively.

However, in the meantime, we have obtained an optical spectrum for SSSPM0109 as well as for M and L dwarf templates with known spectral types using the same instrument setup. The sample of template objects includes LP944-20 (M9.5), BRI0021-0214 (M9.5), and Kelu-1 (L2). Unfortunately, it is now apparent that the published classifications were in error and we revise here the spectral types of SSSPM0109, SSSPM2310, and SSSPM0219 to M8.5, M9.5, and L1, respectively, with an uncertainty of half a subclass. We have noticed a significant discrepancy between the optical and the near-infrared classification for SSSPM0109. Possible reasons for the difference might be:

1. Tokunaga & Kobayashi (1999) defined two spectral indices K1 and K2 (see Table 1.3) based on higher resolution spectroscopy than our data and on narrow-band photometry.

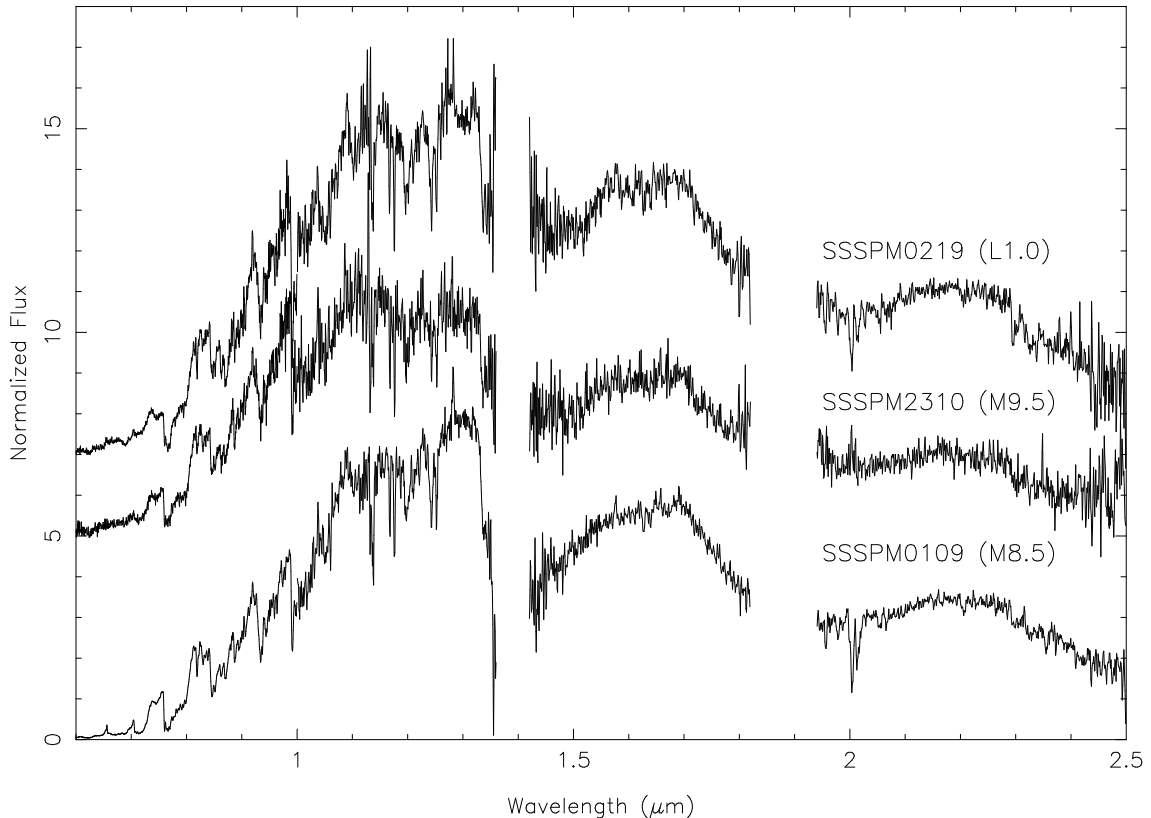


Figure 2.8: Low-resolution ($R \sim 600$) optical (6000–10000 Å) and near-infrared (1.0–2.5 μm) spectra of SSSPM0109 (M8.5), SSSPM2310 (M9.5), and SSSPM0219 (L1) obtained with ESO 3.6-m/EFOSC2 and NTT/SofI, respectively. Spectra are normalised at 7500 Å. Regions of strong telluric absorption around 1.4 and 1.9 μm have been removed for clarity. An arbitrary constant has been added in intensity to separate each spectrum.

2. Spectral indices defined by Testi et al. (2001) appear efficient only at very low-resolution ($R=50$ –100).
3. Geballe et al. (2002) has recently concluded that the water steam index at 1.5 μm is a good spectral type discriminant across the L-T sequences but its values exhibit large dispersion for M8–L2 dwarfs.

Based on trigonometric parallaxes of late-M and early-L dwarfs and on spectral type/absolute J magnitude relationships proposed by Dahn et al. (2002), we have inferred distances of 37 ± 7 pc, 35 ± 1 pc, and 30 ± 16 pc for SSSPM0109, SSSPM2310, and SSSPM0219, respectively. We have derived tangential velocities of 43 ± 10 km/s, 51 ± 2 km/s, and 93 ± 50 km/s for SSSPM0109, SSSPM2310, and SSSPM0219, respectively. The errors are large, particularly for SSSPM0219 as they originate from two different estimates. On the one hand, distances are derived from the spectral types and, on the other hand, from the $I - J$ colours. Measurements were in good agreement for SSSPM0109 and SSSPM2310, but discrepant for SSSPM0219.

From the optical and infrared colours, SSSPM0219 is actually bluer SSSPM2310 although classified as later type. It might either be the effect of a close companion or the result of the dispersion in optical-to-infrared and infrared colours of L dwarfs (Hawley et al. 2002). The published I magnitudes are photographic magnitudes, and, thus, subject to large uncertainties.

Thus, these objects are not L dwarfs within 30 pc as claimed in Lodieu et al. (2002b) but ultracool dwarfs likely between 30 and 40 pc. Their radial velocities are consistent with the kinematics of disk stars.

We have recently included those objects in a sample of ~ 15 ultracool M8.5–L2 dwarfs for high-resolution ($R \sim 16000$ at 6000 \AA) spectroscopy (5750–7310 \AA) with VLT/FORS2 to search for lithium at 6708 \AA . We have also included the well-known M9.5 brown dwarf, LP944-20, as a template since lithium was previously detected via echelle spectroscopy using ESO 3.6-m/CES spectrograph (Tinney & Reid 1998). The data are now in hand and await analysis. The detection of lithium in objects later than M8 would place an upper limit on their mass and add constraints to their ages.

2.9 ε Indi Ba,Bb: the nearest binary brown dwarf

Scholz, McCaughean, Lodieu, & Kuhlbrodt (2003) announced the discovery of a bright ($K_s \sim 11.2$ mag) T2.5 dwarf at 3.626 pc from the Sun, as a common proper motion ($4.7''/\text{yr}$) companion (projected physical separation ~ 1500 AU) to the nearby K5V star ε Indi A (HD209100).

We used the UKST B_J , R , and I plates as well as the ESO R plates as starting point for the selection procedure. We selected all objects brighter than $I = 17$ with no counterpart within 6 arcsec on the UKST B_J and ESO R photographic plates. ε Indi B was among the candidates but had a UKST R plate counterpart. Visual inspection of the finding charts revealed that the R detection was associated with the diffraction spike of a bright star, namely ε Indi A. Furthermore, on an overlapping I plate with an epoch difference of just two years, the object had clearly shifted, yielding a large proper motion of $4.7''/\text{yr}$ identical to one of ε Indi A. Thus, we ‘discovered’ ε Indi B just 7 arcmin away on the sky (corresponding to a physical separation of 1459 AU) from ε Indi A. The red optical and blue near-infrared colours of ε Indi B immediately suggested that the object belongs to the newly-defined T class (Kirkpatrick et al. 1999b).

A few days later on the night of 16–17 November 2002, Bjoern Kuhlbrodt obtained a near-infrared spectrum of ε Indi B with the SofI instrument mounted on the NTT. Three spectra of ε Indi B, shifted by about 100 pixels, were taken along with a standard star at a similar airmass. The data reduction was standard for near-infrared spectroscopy and is described in § 2.3. The final normalised spectrum (0.9 – $2.5 \mu\text{m}$) is displayed in Figure 2.9 along with the location of prominent water and methane absorption bands.

We assigned a spectral type of $T2.5 \pm 0.5$, according to the near-infrared indices defined by Burgasser et al. (2002) and Geballe et al. (2002) and direct comparison with T dwarf templates available at Burgasser and Leggett’s⁵ web pages.

ε Indi A is among the 20 nearest systems to the Sun and has an accurate *Hipparcos* parallax measurement, yielding a distance of 3.626 ± 0.010 pc. Based on rotational properties of ε Indi A,

⁵[ftp://ftp.jach.hawaii.edu/pub/ukirt/skl/dT.spectra/](http://ftp.jach.hawaii.edu/pub/ukirt/skl/dT.spectra/)

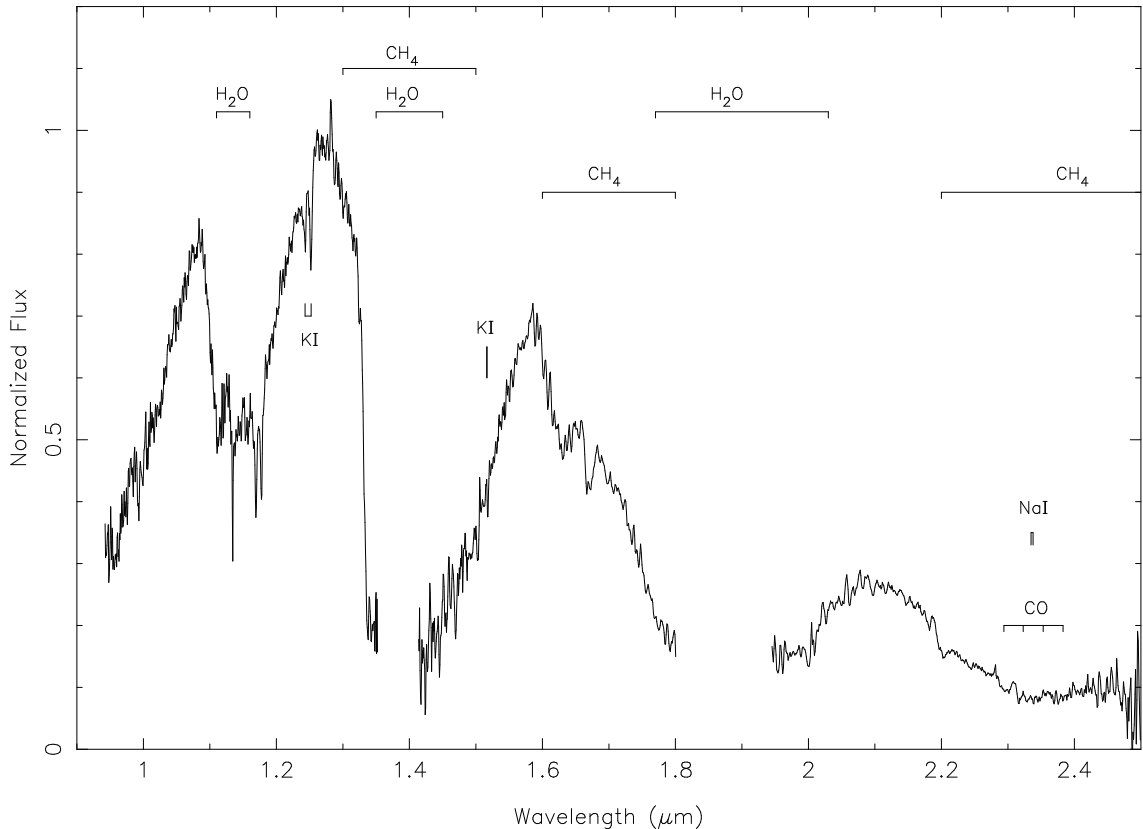


Figure 2.9: Original near-infrared spectrum of ε Indi B obtained with NTT/SofI from Scholz et al. (2003). Regions of strong telluric absorption around 1.4 and $1.9 \mu\text{m}$ have been removed for clarity. The locations of prominent H_2O and CH_4 absorption bands in the atmosphere of ε Indi B are indicated. Also labelled are the KI at $1.25 \mu\text{m}$ and tentative detections of KI doublet at $1.52 \mu\text{m}$ and the NaI doublet at $2.33 \mu\text{m}$.

Lachaume et al. (1999) inferred a mean value for the age of $1.3^{+0.7}_{-0.5}$ Gyr. Hence, we derived the following physical parameters for ε Indi B:

$$\begin{aligned}
 T_{\text{eff}} &= 1270 \text{ K} \\
 \log(L/L_{\odot}) &= -4.67 \\
 R &= 0.097 R_{\odot} \\
 M &= 40-60 M_{\text{Jup}}
 \end{aligned}$$

Following our discovery, we submitted a *Hubble Space Telescope* (HST) proposal to search for a possible (planetary) companion, as well as a VLT proposal for a detailed photometric and spectroscopy study, including adaptive optics, of this new benchmark T dwarf. The HST proposal was rejected⁶ and the VLT proposal was granted 20h service mode observing time in spring 2004.

⁶Comments from the HST Time Allocation Committee were: Strengths: This seems to be the possibility to find a planet companion to a brown dwarf. Use of the HST/ACS is well justified. Weaknesses: Very expensive to look

Meanwhile, commissioning of a new differential methane imaging system on NAOS/CONICA mounted on the VLT took place and ε Indi B was chosen as a reference by Laird Close and collaborators. And, surprise! ε Indi B was resolved into a binary system with a separation of approximately $0.7''$. Following the recognition of the binary, a collaboration started between us and the observers. Few days later, observers at the Gemini Observatory resolved ε Indi B into a binary and announced their discovery in the IAU circular n° 8188 on 27th August 2003 (Volk et al. 2003). A quick look into the ESO Archive revealed that the companion was already detectable in short, 0.6 arcsec FWHM seeing VLT/FORS1 acquisition images obtained within the framework of a polarimetric program for brown dwarfs carried out in June 2003⁷. The binary nature of ε Indi B was however not noticed at that time. Due to its large proper motion, both components of ε Indi B moved by 0.8 arcsec in two months, confirming their physical association.

Immediately after the VLT discovery, we conducted adaptive optics observations with the infrared wavefront sensing capability of the NAOS/CONICA system. Despite the natural seeing of $0.5''$ FWHM, we obtained sharp (0.08 arcsec in the K_s band) near-infrared images of the ε Indi B binary T dwarf. The field-of-view of the S27 NACO camera is 27.7×27.7 arcsec with an image scale of 27.07 ± 0.05 milliarcsec per pixel. The total integration time in each filter was 90 seconds. No other source than the ε Indi Ba,Bb system was detected in the field-of-view (Figure 2.10). The mean separation of both components is 0.732 ± 0.002 arcsec, corresponding to a projected physical separation of 2.65 ± 0.01 AU at the distance of the system.

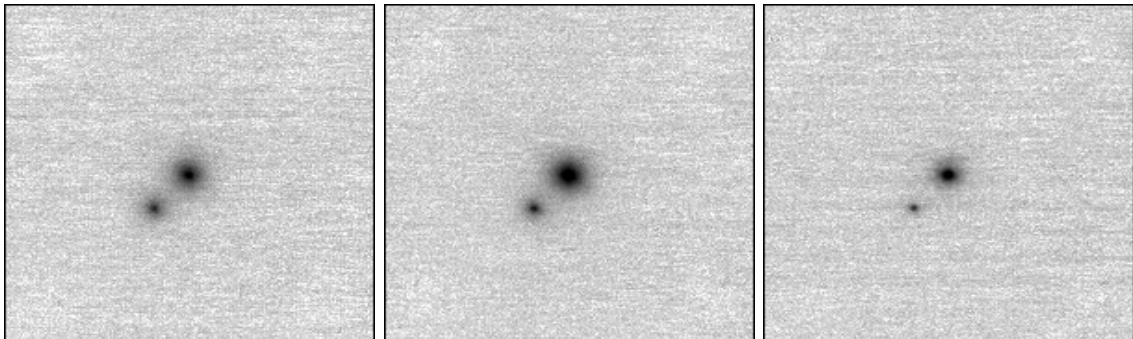


Figure 2.10: NACO broad-band near-IR adaptive optics images of the ε Indi Ba,Bb system, with J , H , and K_s from left to right (McCaughrean et al. 2004). Each image is a 5.4×5.4 arcsec (19.6×19.6 AU at 3.626 pc) subsection of the full 27.7×27.7 arcsec NACO S27 camera field-of-view. The angular resolutions are ~ 116 , 100, and 84 mas FWHM at J , H , and K_s , respectively. North is up, East left: ε Indi Bb is the fainter source to the south-east. The intensities are displayed logarithmically. No other sources are detected in any filter across the whole NACO field-of-view.

We also obtained moderate-resolution ($R \sim 1000$) H -band spectroscopy for both components with the NAOS/CONICA long-slit mode, covering $1.5\text{--}1.85 \mu\text{m}$, with a total on-source integration time of 24 minutes. Observations of a nearby G2V star (HD209552) were made shortly afterwards to measure the telluric absorption. Tungsten-illuminated spectral dome flats were also

for something that might not be there. If nothing is found in first 4 orbits, how will the remaining 8 orbits be used? Observations in 3 epochs are unnecessary, two would do.

⁷Polarimetric programme 72.C-0575(A) for brown dwarfs from Ménard, Delfosse, & Monin

taken with the same configuration at the end of the night. The resulting H -band spectra for both components along with the major water and methane absorption bands are shown in Figure 2.11. We assigned spectral types of T1 and T6 to ϵ Indi Ba and ϵ Indi Bb, respectively, according to the spectral indices from Burgasser et al. (2002) and Geballe et al. (2002).

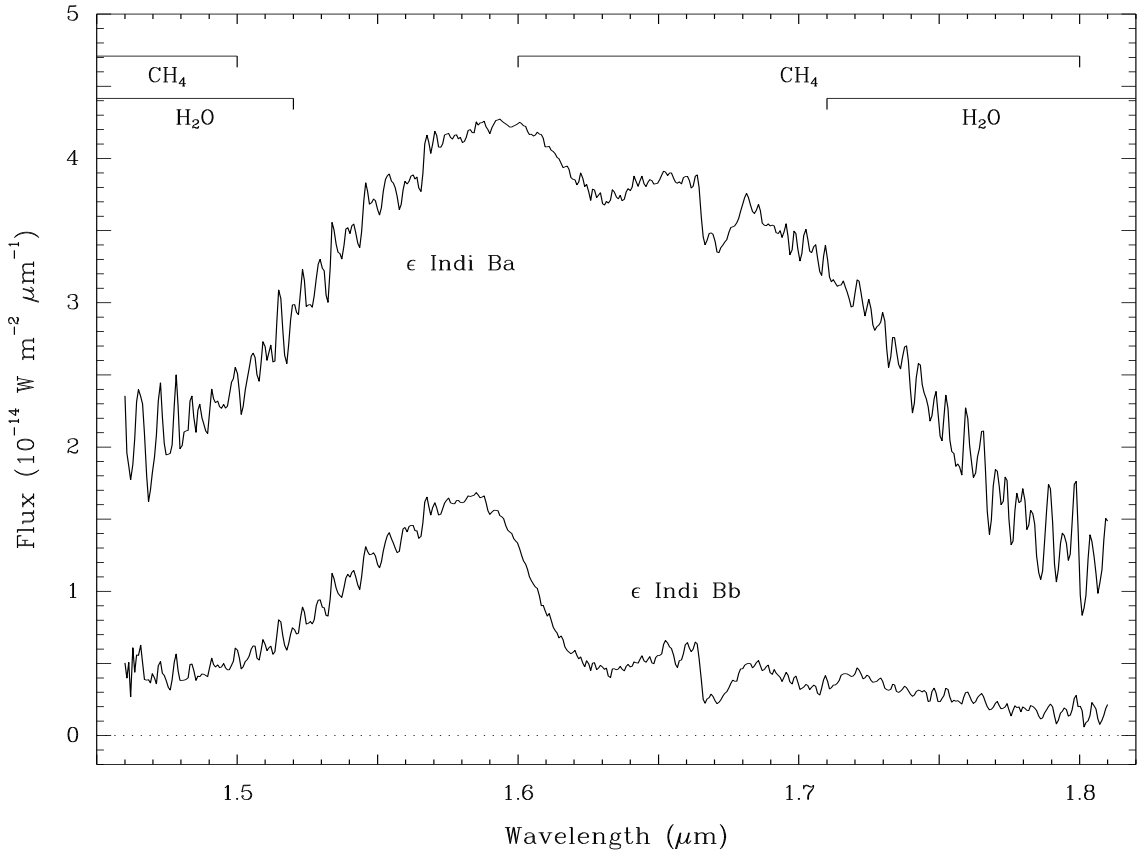


Figure 2.11: H band spectra of ϵ Indi Ba and ϵ Indi Bb from McCaughean et al. (2004). The spectral resolution is $\sim 17 \text{ \AA}$ FWHM, yielding $R \sim 1000$. Flux calibration was made by convolving the spectrum of ϵ Indi Bb with the 2MASS H filter profile and assuming a 2MASS magnitude of $H = 11.51$. The excellent signal-to-noise of the spectra is seen in the relatively smooth $1.58\text{--}1.62 \mu\text{m}$ range; the ‘ripples’ shortward of $1.56 \mu\text{m}$ and longward of $1.72 \mu\text{m}$ are real features, predominantly due to H_2O and CH_4 but also possibly in part due to FeH. The deep double CH_4 absorption trough seen in both sources at $1.67 \mu\text{m}$ is also seen in the T6 dwarf Gl 229 B (Geballe et al 1996), as is the adjacent absorption feature at $1.658 \mu\text{m}$ seen in ϵ Indi Bb.

The physical parameters of both components, ϵ Indi Ba and ϵ Indi Bb, can be estimated by combining individual magnitudes and spectral types with the accurate distance of 3.626 pc and the mean age value of 1.3 Gyr for ϵ Indi A. We have employed the evolutionary models from Baraffe et al. (1998) to derive the physical parameters listed below. The parameters of ϵ Indi A are given as well for comparison purposes. Uncertainties in the effective temperatures are $\pm 40 \text{ K}$ and $\pm 20 \text{ K}$ for ϵ Indi Ba and ϵ Indi Bb. Uncertainties on the masses are $10 \text{ M}_{\text{Jup}}$ and 7 M_{Jup} for ϵ Indi Ba and

ε Indi Bb and are dominated by the age uncertainty. A cumulative error of about 20 % affects the determination of the luminosity due to uncertainties in T dwarf bolometric correction.

- ε Indi A (K5V) $T_{\text{eff}} = 4200 \text{ K}$ $R = 0.72 R_{\odot}$ $\log(L/L_{\odot}) = -0.16$ $M = 0.63 M_{\odot}$
- ε Indi Ba (T1V) $T_{\text{eff}} = 1276 \text{ K}$ $R = 0.091 R_{\odot}$ $\log(L/L_{\odot}) = -4.71$ $M = 47 M_{\text{Jup}}$
- ε Indi Bb (T6V) $T_{\text{eff}} = 854 \text{ K}$ $R = 0.096 R_{\odot}$ $\log(L/L_{\odot}) = -5.35$ $M = 28 M_{\text{Jup}}$

To conclude on this very interesting object(s), we would like to mention that photometric and spectroscopic data of the ε Indi Ba,Bb system obtained with FORS2 and ISAAC on the VLT in the wavelength range $0.6\text{--}5.0 \mu\text{m}$ are now in hand and await analysis. Accurate *JHKLM* photometry will be extracted for both components as well as a good signal-to-noise moderate-resolution spectrum from 1.0 to $5.0 \mu\text{m}$.

Few mid-infrared data are available for T dwarfs to date and, in particular, good quality spectra longwards of $3.0 \mu\text{m}$. On the one hand, ε Indi Ba is a transition object where refractory species are depleted and rain out in the atmosphere to form clouds as in Jupiter. On the other hand, ε Indi Bb has an atmosphere where the dust has entirely settled out. The modelling of the spectral energy distribution of each T dwarf component represents a major challenge to the understanding of brown dwarf atmospheres. Moreover, the detection of the methane band at $3.3 \mu\text{m}$ in both components will add constraints to the understanding the vertical mixing involved in brown dwarf atmospheres. To date, the only modelling of the $3.3 \mu\text{m}$ methane band relies on a poor signal-to-noise spectrum of the T6 dwarf, Gl229B (Saumon et al. 2000).

The other interesting advantage of the ε Indi B system is the opportunity to derive dynamical masses for the system within a few years, according to the relatively short orbit of approximately 15 years. Finally, the ultimate goal will be to obtain the individual masses, independently of the evolutionary models in order to test their reliability. The ε Indi B system is currently the only binary brown dwarf with accurate spectral classification and mass estimates for both components.

Because the ε Indi B system is close, bright, and has a short orbit, it will become, to my opinion, one of the most extensive studied system in the coming years and provide vital clues for understanding the atmospheres, formation, and evolution of brown dwarfs.

2.10 Conclusions on the proper motion survey and outlook

We have presented in this chapter the photometric and spectroscopic results of an on-going proper motion survey in the southern sky focusing on the search for low-mass stars and brown dwarfs in the solar neighbourhood. Optical and near-infrared spectroscopy has revealed a variety of objects within 50 parsecs, including 6 subdwarfs, 57 M dwarfs, four L dwarfs, and the closest binary T dwarf to date, ε Indi Ba,Bb. New red proper motion selected as brown dwarf candidates have been already observed spectroscopically in the optical and await analysis.

Future possible observations of some interesting objects, presented in this chapter, have already been obtained or are foreseen.

- High-resolution ($R \sim 20000$) spectroscopy of ultracool dwarfs (M8.5–L2) belonging to our sample of proper motion objects to detect the lithium absorption line at 6708 \AA . The detection of lithium in the atmosphere of these nearby objects will set an upper limit on their mass and constrain their age. This program has already been granted time at the VLT and spectra of about 15 objects are now in hand.

- High signal-to-noise optical and infrared photometry ($VRIJHKLM$) as well as moderate-resolution spectroscopy (0.6–5.0 μm) of each component of the ε Indi B system to constrain atmospheric models of brown dwarfs. The near-infrared data have been already obtained with VLT/ISAAC and await analysis.
- The determination of the parameters of the orbit of the ε Indi B system will provide the total mass of the system. Several epochs have been observed with the adaptive optics system on the VLT. The ultimate aim is to determine dynamically the individual masses of each component to test evolutionary models in the substellar regime. This can be achieved by measuring the orbital-motion induced radial velocity variations in one of the component.
- High spatial resolution imaging from space with *Hubble* or from the ground with VLT/NACO for example to verify the presence of a tight brown dwarf companion to the M8.5 active dwarf APMPM J2354–3316C. Such a discovery would provide an explanation for the observed peculiar spectrum.
- Adaptive optics imaging of the two nearby late-M dwarfs within 10 parsecs to search for possible brown dwarf or planetary companions.

The work presented in this chapter represents a first step in the characterisation of brown dwarfs. However, large uncertainties remain regarding the age and the distance of nearby objects. As brown dwarfs cool off with age, the ideal place to unearth brown dwarfs at a given distance and with a homogeneous age are young open stellar clusters. We will present in the following chapters the latest results of a near-infrared wide-field survey in the α Per cluster (Chapter 3) as well as a detailed optical and near-infrared photometric study of the pre-main-sequence cluster Collinder 359 (Chapter 4).

Chapter 3

New low-mass stars and brown dwarfs in the α Per cluster

Chapter 2 focused on the search for low-mass stars and brown dwarfs in the solar neighbourhood. Although nearby and generally amenable to detailed studies, large uncertainties remain concerning their mass estimates due to the poor age determination and the lack of trigonometric parallaxes. Therefore, the determination of the local IMF down into the substellar regime is hampered by several issues given below:

1. Accurate distance measurements are required to infer masses. However, the sample of stars with trigonometric parallaxes from the astrometric satellite *Hipparcos* is complete down to $V \lesssim 8$. A small number of fainter nearby objects have well-determined distances as well but the sample is by far incomplete. A large programme has been recently initiated in order to provide trigonometric parallaxes for objects straddling the stellar/substellar limit (Dahn et al. 2002). This survey is essential for improving the galactic field star luminosity function in the low-mass and brown dwarf regimes.
2. Nearby objects span a wide range in age from few millions years for co-moving groups and young associations to billions of years for the coolest and oldest neighbours.
3. High-mass stars are rare and almost nonexistent in the solar neighbourhood due to their short lifetimes.
4. Numerous low-mass stars and brown dwarfs have now been detected in the solar vicinity over the last past years. However, their faintness renders their detection difficult as they cool off with age. Hence, the number density of low-mass stars and brown dwarfs is expected to be largely incomplete as emphasised by Henry et al. (1997).

The determination of a meaningful IMF for galactic field stars requires a volume-limited sample of objects with known age and spectral types over a large mass range. However, the incompleteness is approximately 30 % within 5 pc and double within 8 pc (Henry et al. 1997). The recent discovery of the ε Indi Ba/Bb system (Scholz et al. 2003; McCaughean et al. 2004) at 3.626 pc provide a striking example.

To alleviate some of the issues mentioned above, many recent surveys have concentrated on young open clusters (30–200 Myr) to unearth very-low-mass stars and brown dwarfs. Indeed, open stellar clusters are good places for such quest as they represent equidistant and coeval populations of stars of similar chemical composition within a relatively small volume of space. Some caveats nevertheless remain, including the dearth of high-mass stars and issues regarding the incompleteness towards low-mass stars caused by the contamination by background objects. The best targets

are, hence, the youngest open clusters. However, *only* four open clusters are within 200 pc and younger than 200 Myr. A brief description of each cluster is given below:

- The Pleiades ($\alpha = 03^\circ 46.6^m$, $\delta = -24^\circ 4'$) is, by far, the best studied open cluster for low-mass stars and brown dwarfs. The cluster is rich (about 1200 members), nearby (~ 130 pc), young (~ 120 Myr), relatively compact, located at high galactic latitude ($b = -24^\circ$) with a metallicity estimated to be solar (Boesgaard & Friel 1990). The extinction is low ($A_V = 0.12$ mag) and generally uniform. The large proper motion ($\mu_\alpha \cos \delta \sim +25$ mas/yr and $\mu_\delta \sim -45$ mas/yr) allows membership assessment of photometrically-selected candidates over a time scale of few years (Moraux et al. 2001). Many proper motion and photometric surveys have focused on the Pleiades, yielding the discovery of the first young brown dwarf, Teide 1 (Rebolo et al. 1995). Since that time, many brown dwarf candidates have been proposed and some confirmed spectroscopically (Martín et al. 1996; Stauffer et al. 1998). The cluster mass function over a large mass range ($10\text{--}30 M_\odot$) was well approximated by a lognormal distribution of index 1.7 and a peak around $0.25 M_\odot$ (Chabrier 2003).
- IC2391 ($\alpha = 08^\circ 40.2^m$, $\delta = -53^\circ 04'$) is a close (~ 150 pc) and young (~ 30 Myr) open cluster with solar metallicity (Randich et al. 2001). The extinction towards the cluster is rather low ($E(B-V) = 0.06$). Except for the brightest components of the cluster ($V \leq 11$), proper motion studies are hampered by the lack of bright members and the low galactic latitude of the cluster ($b = -6.9^\circ$). Most of the cluster members (about 100 members) have been selected in X-rays with the *ROSAT* satellite (Patten & Pavlovsky 1999) and their membership assessed with optical photometry and/or spectroscopy (Stauffer et al. 1989a). The estimated age of 30 Myr, derived from the upper main-sequence turn-off fitting, was recently revised to 53 ± 5 Myr from the lithium test (Barrado y Navascués et al. 1999). The lithium depletion boundary was found at $R-I = 1.91$ and $M(I) = 10.25$ mag, corresponding to a mass of $\sim 0.12 M_\odot$, assuming a distance modulus of 5.95 and an age of 53 Myr. New brown dwarf candidates have also been extracted from a deep *R* and *I*-band survey with infrared follow-up (Barrado y Navascués et al. 2001) but no cluster mass function has been derived to date.
- IC2602 ($\alpha = 10^\circ 43^m$, $\delta = -64^\circ 24'$) is similar to IC2391 in terms of distance ($d = 150$ pc), age (30 Myr), and metallicity. The cluster is located around the B0Vp star θ Carinae ($b = -4.9^\circ$) in a region of low extinction ($E(B-V) = 0.04$). The proper motion of the cluster is estimated to $\mu_\alpha \cos \delta \sim -9$ mas/yr and $\mu_\delta \sim +3.5$ mas/yr. This is the least studied cluster among the four cluster within 200 pc and younger than 200 Myr. The largest membership list (about 100 members) was established by Randich et al. (1995) through an X-ray study conducted with the *ROSAT* satellite. Photometric and spectroscopic follow-up confirmed most candidates as genuine cluster members (Prosser et al. 1996a). No cluster mass function is available at present.
- The α Per cluster ($\alpha = 03^\circ 50^m$, $\delta = 49^\circ 00'$) has been well studied, though less than the Pleiades due to its smaller proper motion ($\mu_\alpha \cos \delta \sim +23$ mas/yr and $\mu_\delta \sim -25$ mas/yr) and lower galactic latitude ($b = -7^\circ$). The cluster is located north-east of the F5V supergiant Alpha Persei at a distance of about 180 pc and solar metallicity (Boesgaard & Friel 1990). The extinction towards the cluster was estimated to be $A_V = 0.30$ mag with possible spatial variations. Several proper motions, photometric and spectroscopic surveys have

revealed about 400 members in α Per (Prosser 1994). The cluster was also extensively studied in the X-rays, yielding new member candidates based on *ROSAT* observations (Randich et al. 1996; Prosser et al. 1996b). The lithium test applied to the cluster yielded an age of 90 ± 10 Myr (Stauffer et al. 1999). The cluster mass function is well approximated by a power law with an index $\alpha = 0.59 \pm 0.05$ in the $0.30\text{--}0.035 M_{\odot}$ mass range (Barrado y Navascués et al. 2002). We will provide more details about those surveys in the next sections (§ 3.1–3.4) and emphasise our contribution to the α Per cluster in § 3.5 and § 3.6.

The present chapter is dedicated to a comprehensive study of the young open cluster α Per carried out within the framework of our collaboration. The α Per cluster is richer than IC2391 and IC2602 but probably less rich than the Pleiades. The cluster presently has about 400 catalogued members compared to about 1200 for the Pleiades. However, the cluster member list of α Per is much less complete than the Pleiades for three major reasons:

1. The number of deep optical and/or proper motion surveys implemented in α Per is smaller than in the Pleiades.
2. The cluster mean proper motion is not well separated from field stars.
3. α Per is located at lower galactic latitude than the Pleiades.

This chapter is organised as follows. In § 3.2, we review results from surveys dedicated to the search for low-mass cluster members in α Per. In § 3.2, we report the recent determination of the age of the cluster by the “lithium test” (Stauffer et al. 1999). In § 3.3, we describe the main results of the optical wide-field survey in the α Per cluster carried out within our collaboration (Barrado y Navascués et al. 2002), including the determination of the luminosity function (§ 3.4.1) and the mass function (§ 3.4.2). In § 3.5, we describe the selection of new cluster member candidates including new brown dwarfs from a near-infrared survey of a 0.70 square degree area in the cluster. Optical spectroscopic follow-up of a subsample of selected cluster member candidates is presented in § 3.6. We compare the updated α Per mass function to the field and Pleiades-like open clusters in § 3.7. Conclusions and future work are discussed in § 3.8.

The results presented in this chapter have been (or will be) published in several papers, including:

1. Barrado y Navascués, Bouvier, Stauffer, Lodieu, & McCaughrean (2002) where I have provided infrared photometry of faint optically-selected cluster members.
2. Lodieu, McCaughrean, Bouvier, Barrado y Navascués, & Stauffer (2003) published the major results of the near-infrared wide-field survey described in § 3.5 in the IAU211 conference proceedings.
3. The new results related to the near-infrared wide-field survey will be part of a forthcoming paper (Lodieu et al. 2004, in preparation). This part of the work has been essentially done by myself.

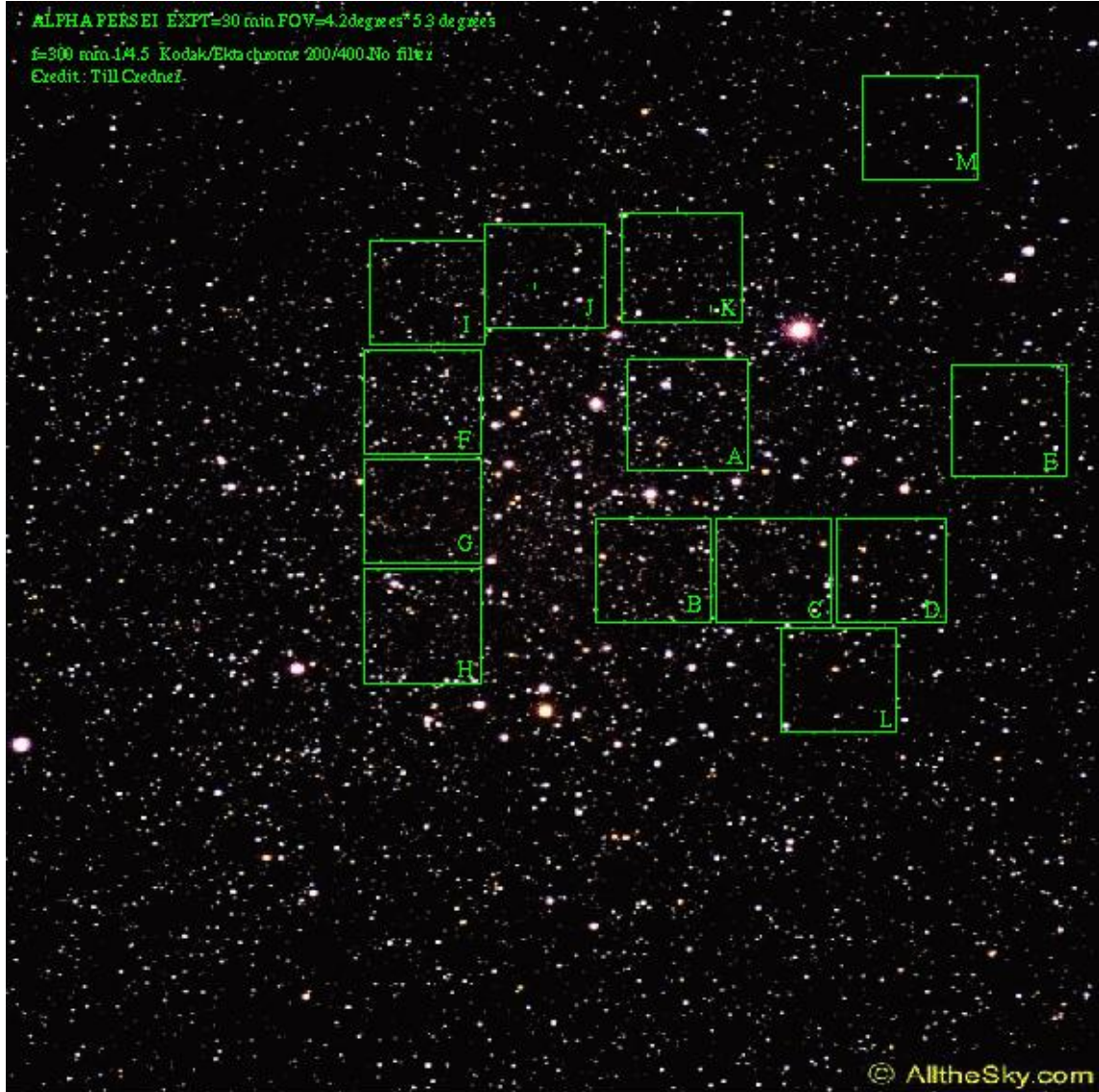


Figure 3.1: Image of a $4.2^\circ \times 5.3^\circ$ towards the α Per cluster. North is at the top and East to the left. A concentration of stars is seen south-east of the brightest star in the image, the F5 supergiant Alpha Persei. The green squares represent the 13 KPNO/MOSA fields-of-view ($35.4' \times 35.4'$) observed in the R_c and I_c bands down to a completeness limit of 21.9 and 20.75, respectively.
Copyright: T. Credner & S. Kohle, AlltheSky.com

3.1 Known members of the α Per cluster

The α Per cluster is clearly seen on photographic plates as a concentration of stars south-east of the F5 supergiant Alpha Persei, whose membership of the cluster is estimated to 97 % probability (de Zeeuw et al. 1999). Figure 3.1 is a $4.2^\circ \times 5.3^\circ$ image taken towards the α Per cluster.

Several authors, including Heckmann, Stauffer, Prosser and collaborators, have extensively

studied the bright components and low-mass members of the α Per cluster. The membership assessment made use of proper motion, multi-band photometry, optical spectroscopy for H α and lithium detection, as well as radial and rotational velocities. We will briefly summarise previous surveys designed to identify low-mass members in the α Per cluster.

1. Heckmann, Dieckvoss, & Kox (1956) obtained proper motions for stars brighter than a V magnitude of 12.0 in the vicinity of α Per. Slightly more than 10 % of the 1400 stars surveyed within the field-of-view were identified as probable cluster members. Those members were termed by HE (as Heckmann) followed by three digits starting with one. UBV photometry of those ~ 150 new members was obtained by Mitchell (1960), providing reddening and distance estimates as well as criteria to reject non members.
2. Stauffer et al. (1985) surveyed a $1.2^\circ \times 1.2^\circ$ area of the α Per cluster and obtained proper motion for 4000 stars down to $V \sim 16.0$ mag. Proper motion, VRI photometry, H α emission, radial and rotational velocities were used as main criteria to select about 90 new low-mass cluster members. Those new G, K, and M cluster dwarfs with high rotational velocities roughly span the $0.5\text{--}1.2 M_\odot$ mass range, assuming a distance of 165 pc and an age of 50 Myr. These objects were termed by AP as in ‘Alpha Per’ followed by three digits starting with one.
3. Stauffer, Hartmann, & Jones (1989b) identified new low-mass members over a 2.5 square degree region in α Per based on proper motion, $BVRI$ photometry, and subsequent spectroscopy. The percentage of cluster members compared to the total number of stars along the line of sight drops to few percents from $V = 10$ to $V = 15$ mag due to the low galactic latitude of α Per. In total, Stauffer et al. (1985, 1989b) confirmed the membership of 30 HE members and 50 AP stars and identified new members down to $V \sim 16.0$ mag.
4. Prosser (1992) carried out an extensive membership survey of a $6^\circ \times 6^\circ$ whole Palomar photographic plate in the α Per cluster. About 130 new cluster members among a sample of proper motion candidates were extracted down to $V \sim 19.0$ mag, using additional photometric and spectroscopic information. Spectral types were also provided for some candidates brighter than $V = 17$ mag, corresponding to a spectral type of M4. The spatial distribution of the new members (filled circles) is shown in Figure 3.2. This study provided a revised age for the cluster to 80 Myr based on isochrone fitting with no significant age spread. The mean reddening was estimated to $E(V-I) = 0.18$, consistent with previous determinations although some spatial variations across the cluster were reported.
5. In an attempt to search for low-mass members in the α Per cluster, Prosser (1994) obtained new CCD images of a ~ 0.8 square degree area in the cluster in the V and I bands down to $V \sim 22.0$ mag. Contrary to former surveys, no first epoch was available at these faint magnitudes. About new 30 new cluster member candidates were solely selected on the basis of their location in the $(V, V-I)$ colour-magnitude diagram. Low-dispersion spectroscopy obtained for some of the new candidates, confirming the cluster membership of eight objects and classified three others as non-members.
6. A raster scan and pointed X-ray observations were obtained towards the α Per cluster with the *ROSAT* satellite in the soft (0.1–0.4 keV) and hard (0.4–2.0 keV) bands.

The raster scan covered ~ 10 deg 2 in α Per with an exposure time of 10 ksec, yielding limiting sensitivity of $L_X \sim 10^{29}$ erg sec $^{-1}$ (Randich et al. 1996). Out of ~ 160 X-ray detections, 89 were associated with previously selected cluster members. More than 80 % of the F, G, and K dwarfs and ~ 50 % of the M dwarfs belonging to the cluster were detected.

The *ROSAT* pointing observations (Prosser et al. 1996b), exposed 22–25 ksec, covered a slightly smaller area (three pointings ~ 50 arcmin in radius) than the raster scan but achieved higher sensitivities. About 80 X-ray sources, including 40 common to the raster scan, were associated with an optical counterpart from previous proper motion surveys. All the K dwarfs and a high number of M dwarfs belonging to the cluster were detected by the pointing observations. However, both surveys revealed about 200 sources with no optical counterparts. Photometry along with low- and high-dispersion spectroscopy classified about 40 X-ray sources as probable new cluster members (Prosser & Randich 1998; Prosser et al. 1998). A detailed analysis of the X-ray properties of the F, G, K, and M cluster dwarfs detected with *ROSAT* led to the following results:

- (i) The X-ray luminosity peaks at G dwarfs and then declines towards M dwarfs, suggesting that the dynamo activity efficiency decreases towards low-mass stars.
- (ii) Rotational velocities are correlated with the X-ray luminosity. Fast rotators with velocities larger than 15 km s^{-1} have larger X-ray luminosities than slow rotators.
- (iii) The mean X-ray luminosity of F and G stars in α Per is larger than in their Pleiades counterparts whereas no difference is found for K and M dwarfs. This result indicates that F and G stars are spinning down faster in α Per than in the Pleiades.

Due to the low galactic latitude ($b = -7^\circ$) of the α Per cluster, it was quickly recognised that proper motion and photometry alone would fail to eliminate all non-members. Radial and rotational velocities as well as spectroscopic features, including H α in emission at 6563 Å and lithium in absorption at 6708 Å provide additional criteria suggestive of cluster membership. Hence, a full analysis of membership in α Per requires large amount of observing time as well as a variety of measurements and analysis. We will now review recent improvements achieved within the framework of our collaboration on the α Per cluster.

3.2 The age determination of the α Per cluster

The age determination of open clusters originates traditionally from isochrone fitting of the upper main-sequence and giant branch. However, this method is generally hampered by the small number of stars evolving off the main-sequence, their photometric uncertainties, their unknown binary status, and the difficulties in modelling the amount of mixing of hydrogen-rich matter into the convective core (“convective core overshoot”). Depending on the amount of overshoot (no overshoot versus strong overshoot), the age of open clusters can vary by a factor of two (Mermilliod 1981; Mazzei & Pigatto 1988).

Recently, a new method, the “lithium test” was proposed to estimate the age of open clusters (Rebolo et al. 1992). The idea is that for low-mass stars, lithium is quickly destroyed and, therefore, unobservable in their spectra. On the contrary, brown dwarfs preserve their lithium content because the central temperature is not sufficient to fuse hydrogen. The lithium depletion

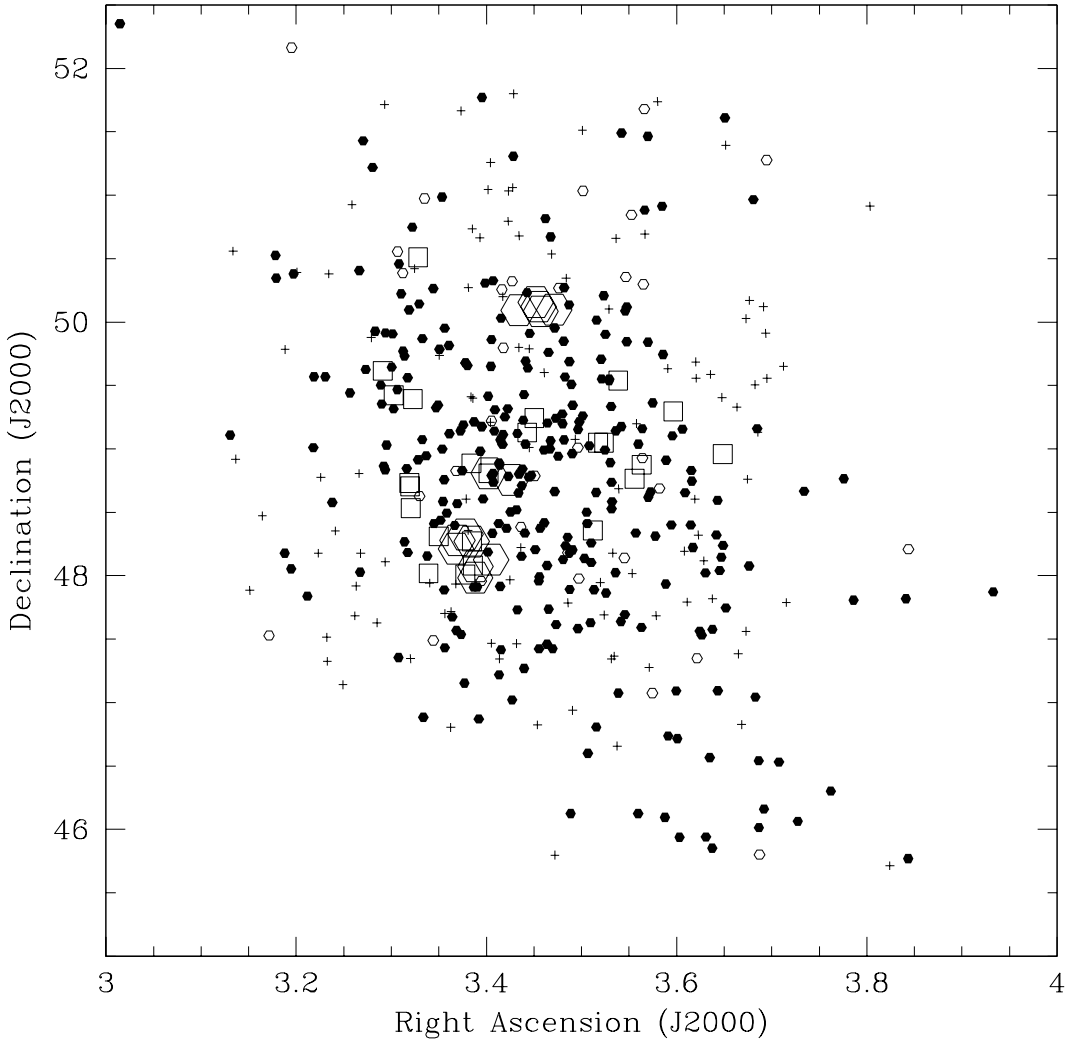


Figure 3.2: Location of known α Per members in the (ra, dec) frame. Filled circles, open circles, and crosses are the probable, possible members, and non-members, respectively, based on surveys dedicated to low-mass members in α Per. Open squares are spectroscopically confirmed cluster members from Stauffer et al. (1999). Large open hexagons are new infrared-selected candidates from our wide-field survey (Section 3.5)

boundary, the point where lithium has been depleted by a factor of 100, is expected to be sharp with no lithium for objects above the limit and cosmic abundance essentially for objects below the boundary. Furthermore, as stars are fully convective in the mass range of interest, the surface lithium abundance reflects directly the core abundance, yielding smaller uncertainties than the “convective core overshoot” determination. The mixing theory in the atmospheres of low-mass stars remains none the less poorly constrained. Applied successfully to the Pleiades, the value of

the age increased by a factor of two from 70 Myr to 125 Myr (Stauffer et al. 1998). A similar result holds for the young open cluster IC 2391 with an age of 35 Myr derived from upper main-sequence fitting and 53 Myr inferred from the lithium test (Barrado y Navascués et al. 1999).

The lithium test was recently applied to the α Per cluster based on a 6 deg^2 optical survey in the R_c and I_c broad-band filters (Stauffer et al. 1999). A few bona-fide cluster member candidates were identified in a limited magnitude range ($16.25 \leq I \leq 18.75$) to seek for lithium absorption at 6708 \AA and subsequently infer the lithium depletion boundary. The selection procedure yielded 27 bona-fide member candidates redder than the Zero-Age Main Sequence (hereafter ZAMS; Leggett 1992), shifted to the distance of the cluster ($d = 176\text{ pc}$; Pinsonneault et al. 1998) in the $(I_c, R_c - I_c)$ colour-magnitude diagram. The bad agreement between the theoretical isochrones and the sequence of cluster members originates from the difference between the ZAMS of old field dwarfs and the isochrones drawn for pre-main-sequence stars. In addition, models do not predict accurate optical colours due to the incompleteness of the current opacity line lists. Low- and high-resolution spectroscopy were carried out with the Low-Resolution Imaging Spectrograph (LRIS) on Keck II telescope for 14 and 11 candidates, respectively. Among the probable and possible member candidates, five objects did exhibit lithium in absorption whereas nine others did not, yielding a sharp determination in $(R_c - I_c)$ colour and more uncertain value of the I_c magnitude.

Table 3.1: Field centres observed in the α Per cluster with CCD Mosaic Imager on the KPNO-4m telescope. Each image has a $35.4' \times 35.4'$ field-of-view with a spatial scale of $0.26''$. Right ascension and declination are given in J2000. The five optical fields followed-up in the K' -band using Omega-Prime on the Calar Alto 3.5-m telescope are indicated with the respective observing dates, exposure times, surveyed area, and limiting magnitudes. I observed fields E, K, and L in the near-infrared whereas Thomas Stanke observed the A and C fields.

Field	R.A. (J2000.0)	DEC	Near-infrared follow-up			
			Obs. Date	ExpT	Area	K'_{lim}
A	03:27:10.00	49:24:00.0	04–06 Dec 98	20 min	$580''^2$	17.5
B	03:28:00.00	48:42:00.0				
C	03:24:50.00	48:42:00.0	06 Dec 98	20 min	$280''^2$	17.5
D	03:21:40.00	48:42:00.0				
E	03:19:35.00	49:27:00.0	14 Dec 00	20 min	$560''^2$	15.5
F	03:33:45.00	49:35:00.0				
G	03:33:45.00	49:04:00.0				
H	03:33:45.00	48:34:00.0				
I	03:33:45.00	50:06:00.0				
J	03:30:30.00	50:09:00.0				
K	03:27:00.00	50:13:00.0	11–12 Dec 00	20 min	$560''^2$	17.5
L	03:23:10.00	48:11:00.0	11–12 Dec 00	20 min	$560''^2$	17.5
M	03:21:00.00	50:48:00.0				

The adopted values for the lithium depletion boundary were $R_c - I_c = 2.12$ and $I_c = 17.70 \pm 0.15$ mag. Assuming a distance modulus of 6.23, and applying the NextGen isochrones from Baraffe et al. (1998), Stauffer et al. (1999) derived an age of 90 ± 10 Myr for α Per, twice larger than the

50 Myr value from the turn-off main-sequence fitting. The lithium depletion boundary based on the K -band photometry was estimated to be at $M_K \sim 8.3$ mag and $(I_c - K) \sim 3.07$, though with larger uncertainties. Note that comparison with other evolutionary tracks (D'Antona & Mazzitelli 1994; Burrows et al. 1997) led to similar values of the age within the uncertainties. **We will adopt the age of 90 ± 10 Myr for subsequent analysis of the α Per cluster unless otherwise stated.** We note that Basri & Martín (1999b) derived an age between 65 and 75 Myr from the detection of the lithium absorption line in a handful of objects.

3.3 The wide-field optical survey of the α Per cluster

The aim of Stauffer et al. (1999) was to locate the lithium depletion boundary in α Per to derive the cluster age. No attempt was made to select a complete sample of low-mass stars and brown dwarf member candidates and derive the cluster mass function. Nevertheless, Stauffer et al. (1999) obtained spectroscopy for a subsample of objects, including two brown dwarf candidates.

Meanwhile, a new wide-field optical survey was conducted with the KPNO/MOSA detector and covered ~ 4.5 square degrees in the α Per cluster to unearth new low-mass stars and brown dwarfs over the largest possible area in the cluster. The MOSA (Mosaic Imager) detector mounted on the Kitt Peak 4-m telescope is a 8192×8192 pixels CCD array with a spatial scale of $0.26''/\text{pixel}$, yielding a $35.4' \times 35.4'$ field-of-view. Thirteen fields-of-view (see Table 3.1 and Figure 3.1 for coordinates and locations in the cluster) were observed, reaching detection and completeness limits of $R_c \sim 25.5$ and 21.9 mag, and $I_c \sim 22.5$ and 20.75 mag, respectively (Barrado y Navascués et al. 2002).

A sample of 94 cluster member candidates was extracted from 260 000 detections in the 4.5 deg^2 surveyed area based on their location in the optical $(I_c, R_c - I_c)$ colour-magnitude diagram (Figure 3.3). All objects located to the right of the empirical Zero-Age Main-Sequence (Leggett 1992) shifted to the distance of α Per were classified as candidate cluster members. The gap between field stars and cluster candidates is detectable (Figure 3.3) although not as sharp as in the Pleiades (Bouvier et al. 1998). Indeed, a higher contamination by field stars and background giants is expected, as α Per is located at lower galactic latitude than the Pleiades ($b = -7^\circ$ versus $b = -24^\circ$).

To estimate the contamination by field stars, Barrado y Navascués et al. (2002) obtained near-infrared photometry in the K' -band for most of the optically-selected candidates, in the J -band for 24 of them, and in the H -band for a handful of objects, using Omega-Prime and Omega-Cass cameras on the 3.5-m telescope and the MAGIC camera on the 2.2-m telescope at Calar Alto. The membership status of the optically-selected cluster member candidates was assessed by comparing the location of the objects to the NextGen (Baraffe et al. 1998), Dusty, and Cond (Chabrier et al. 2000b) isochrones in various colour-magnitude diagrams. Objects located to the right of the isochrones in all the diagrams were classified as probable members whereas those to the left were rejected as cluster members. The candidates were classified as follows:

- 54 ($\sim 60\%$) as probable members
- 12 ($\sim 12\%$) as possible members
- 26 ($\sim 28\%$) as non-members

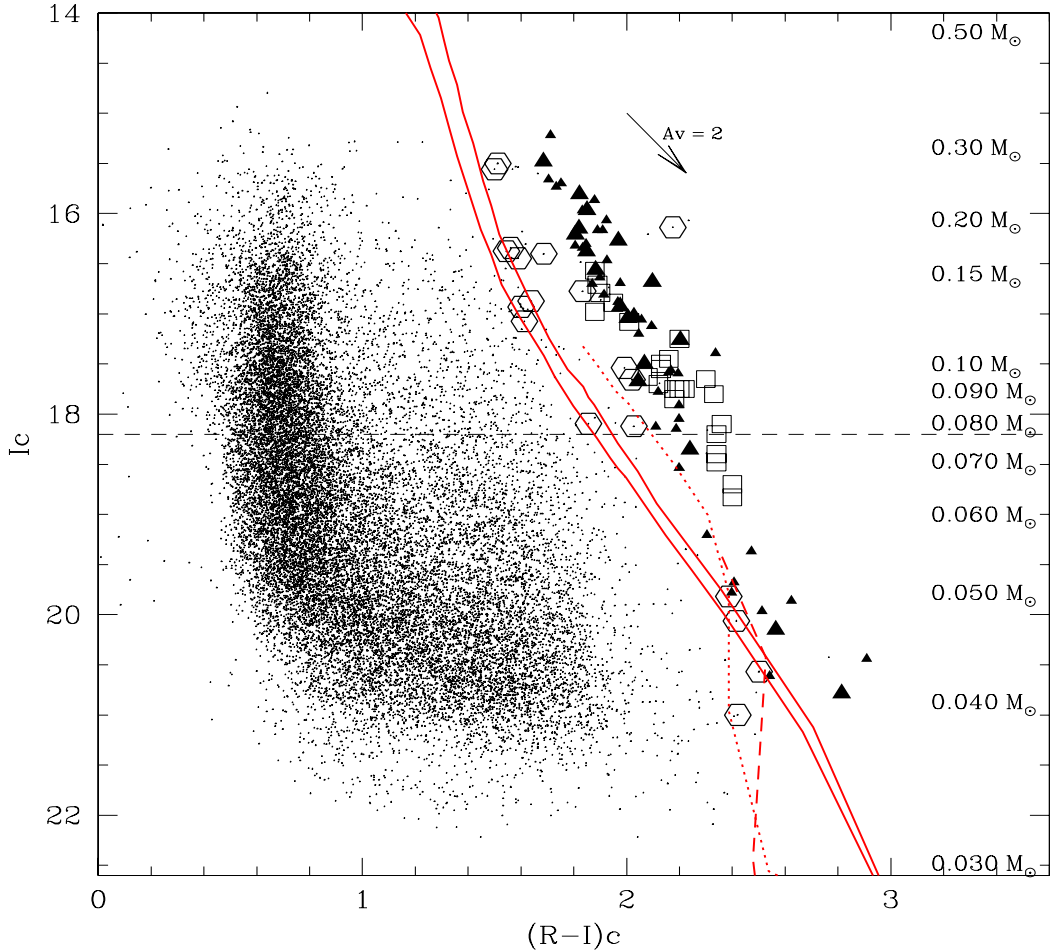


Figure 3.3: Colour-magnitude ($I_c, I_c - R_c$) for all optical detections within the 0.70 square degree area followed-up in the near-infrared with the Omega-Prime camera. Large filled triangles are probable candidates from Barrado y Navascués et al. (2002) recovered in our optical-infrared selection whereas small filled triangles were not recovered. Open hexagons are the new infrared-selected cluster member candidates. Large open hexagons indicate the new candidates to the right of the NextGen 100 Myr isochrones in the optical-to-infrared colour-magnitude diagram. Open squares are spectroscopically confirmed cluster members from Stauffer et al. (1999). Also overplotted are the NextGen (Baraffe et al. 1998) isochrones for 50 and 100 Myr (solid lines), the Cond (dotted line) and Dusty (dashed line) 100 Myr isochrones (Chabrier et al. 2000b), assuming a distance of 182 pc. A reddening vector for $A_V = 2$ is also included for comparison purpose. The horizontal dashed line at $I_c = 18.2$ indicates the stellar/substellar boundary at $0.075 M_\odot$, assuming a distance of 182 pc and an age of 90 Myr for the cluster (Stauffer et al. 1999). The mass scale is indicated on the right side of the plot. The discrepancy between isochrones and cluster candidates might originate from the uncertainties on the current opacity line lists.

Thus, the contamination by field stars lies in the range 28–40 %, estimate slightly larger than in the Pleiades (Bouvier et al. 1998; Martín et al. 2000a; Moraux et al. 2001). Based on this sample of approximately 100 objects, Barrado y Navascués et al. (2002) derived luminosity and mass functions for α Per in the 0.30 – $0.05\,\text{M}_\odot$ mass range. The influence of the contamination and the age on the shape of the mass function was analysed as well.

3.4 The luminosity and mass functions of the α Per cluster

3.4.1 The cluster luminosity function

Barrado y Navascués et al. (2002) derived the luminosity function for very low-mass stars and brown dwarfs in α Per according to the sample of probable and possible cluster members (dashed line with filled circles in Figure 3.4). The completeness and detection limits of $I_c = 19.5$ and 22.5 mag translate into masses of $0.050\,\text{M}_\odot$ and $0.035\,\text{M}_\odot$, respectively, assuming a distance of $176\,\text{pc}$ and an age of $90\,\text{Myr}$ for the α Per cluster. The luminosity function is displayed in Figure 3.4. The solid and dashed lines with filled circles show the cluster luminosity function before and after rejection of non-members, respectively. The solid line with open circles represent the number of stars per magnitude bin for a sample of field stars with an arbitrary shift of -0.2 mag in the $R-I$ colour compared to cluster members.

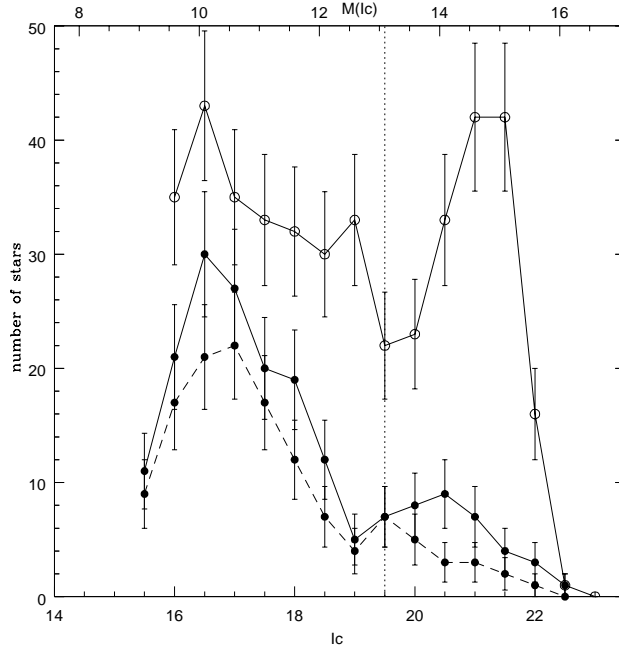


Figure 3.4: Luminosity function (number of stars per bin of magnitudes) of the α Per cluster before and after rejecting the non-members (solid and dashed line with filled circles, respectively). The distance modulus is 6.22 , corresponding to a distance of $176\,\text{pc}$. Apparent and absolute magnitudes are plotted on the lower and upper abscissae, respectively. The upper solid line with open circles was derived for a comparison sample of field stars. From Barrado y Navascués et al. (2002).

Compared to a control field luminosity function, the cluster luminosity function (Figure 3.4) exhibits several features detailed below:

1. A peak at $M_I = 10$, detected in the luminosity function of the control field and in other open clusters, including the Pleiades (Zapatero Osorio et al. 1997c). This peak was, however, located at $M_I = 11$ mag in NGC 2516 (Jeffries et al. 2001) and at $M_I = 9$ mag in M35 (Barrado y Navascués et al. 2001), suggesting that the location of this feature is not universal in clusters 100–200 Myr old and might be age dependent. This maximum might correspond to the H₂-convection peak identified by (Kroupa et al. 1990, 1993) in the luminosity function of nearby field stars.
2. A gap was detected at $M_I \sim 12.5$ mag, corresponding to $0.055 M_{\odot}$ and spectral types ranging from M6 to M8. This feature was already apparent at same spectral type in other clusters at different ages, including σ Orionis (Béjar et al. 2001), the Trapezium Cluster (Lucas & Roche 2000), IC348 (Luhman 1999), the Pleiades (Jameson et al. 2002), and IC 2391 (Barrado y Navascués et al. 2001a). Jameson et al. (2002) suggested that the formation of large dust grains at those specific temperatures could be responsible for this feature although it might result from the formation mechanism of low-mass objects.
3. A second peak at $M_I = 14.5$ mag was detected in the cluster luminosity function but not in the control field. This feature was, however, below the completeness limit of the survey and should be interpreted with caution.

3.4.2 The cluster mass function

Barrado y Navascués et al. (2002) transformed the α Per luminosity function into a cluster mass function (Figure 3.5 using the NextGen models from Baraffe et al. (1998)). The conversion of the luminosity function into a mass function requires a mass-magnitude relation extracted from evolutionary tracks. The choice of a particular set of isochrones had, however, little influence on the shape and the slope of the mass function (Barrado y Navascués et al. 2002). The influence of the age on the mass function was studied as well: no variation on the slope and the shape of the cluster mass function was obvious (Barrado y Navascués et al. 2002). Varying the age shifts only the mass of the objects towards higher and lower masses when older and younger, respectively. Moreover, the cluster mass function derived with the different kind of membership selection criteria exhibits little difference as shown in Figure 3.5. The influence of binaries on the shape and the slope of the mass function is not considered in this study although it can affect the power law index by up to 0.5 (Kroupa 2001).

The most probable mass function in the α Per cluster is displayed as a thick solid line in Figure 3.5. Two estimates of the Pleiades mass function from Bouvier et al. (1998; $\alpha = 0.56$) and Zapatero Osorio (2002, personal communication; $\alpha = 0.75$) are displayed in Figure 3.5 as well. The slope of the α Per mass function in the 0.30 – $0.035 M_{\odot}$ mass range was approximated by a power law with an index $\alpha = 0.59 \pm 0.05$ for comparison with other mass function estimates in open clusters (Barrado y Navascués et al. 2002). The shape of the mass function might, however, reflect some physics intrinsic to stars. A drop is detected at $0.055 M_{\odot}$ in the cluster mass function. A second drop at $0.035 M_{\odot}$ is also detected but is uncertain as it is located below the completeness limit of the survey.

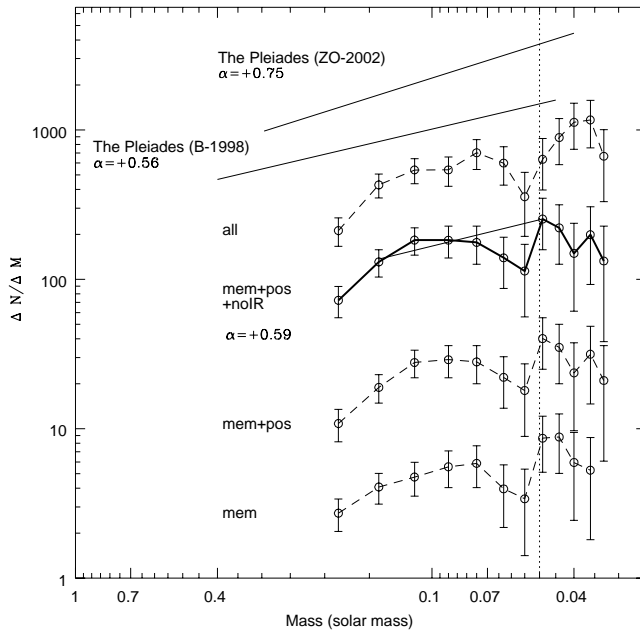


Figure 3.5: Mass functions of the α Per cluster, illustrating the effect of contamination by field stars. These mass functions were derived using a 80 Myr isochrone (Baraffe et al. 1998). From top to bottom, mass functions are displayed for all members, all members except the non-members, probable and possible members, and finally for only probable members. The most probable mass function is shown as a thick line. A linear fit to this mass function is also included, with a power law index of $\alpha = 0.59 \pm 0.05$ when expressed as a power spectrum. For comparison, the Pleiades mass function, by Bouvier et al. (1998), valid between 0.40 and $0.045 M_{\odot}$, and by Zapatero Osorio (2002, personal communication), derived in the 0.3 – $0.040 M_{\odot}$ mass range are included. Figure taken from Barrado y Navascués et al. (2002).

In summary, **the α Per mass function (Figure 3.5) is similar to the various estimates of the Pleiades mass function over the same mass range** (Bouvier et al. 1998 inferred $\alpha = 0.6$; Dobbie et al. 2002 derived $\alpha = 0.8$; and Tej et al. 2002 found $\alpha = 0.5$).

3.5 The near-infrared survey of the α Per cluster

The main purpose of the K' -band follow-up survey was to detect new cluster member candidates, including lower mass brown dwarfs down to the deuterium burning limit around $0.013 M_{\odot}$ when combined with the wide-field optical observations presented in § 3.3.

We present in this section a near-infrared (K' -band) survey of 0.70 square degree area in the α Per open cluster conducted with the Omega-Prime camera mounted on the Calar Alto 3.5-m telescope. The completeness limit of the near-infrared survey is deep enough to probe the substellar regime down to the deuterium burning limit. According to the Dusty isochrones from Baraffe et al. (1998), a $20 M_{Jup}$ object in the α Per cluster has a $(I-K)$ colour of about 9.0 and

$K = 18.1$, assuming an age of 90 Myr and a distance of 182 pc. We have chosen a compromise for the cluster distance between the *Hipparcos* estimate ($d = 190$ pc; Robichon et al. 1999) and the main-sequence fitting ($d = 176$ pc; Pinsonneault et al. 1998). The latter estimate was used by Barrado y Navascués et al. (2002) to infer the cluster luminosity and mass functions.

This section is structured as follows. First, the near-infrared observations carried out with Omega-Prime are presented in § 3.5.1. Second, the data reduction and the extraction of the photometry are described in § 3.5.2. Third, the astrometry of the near-infrared fields is detailed in § 3.5.3. Finally, the optical-infrared catalogue is provided in § 3.5.4 and new cluster member candidates are extracted from the colour-magnitude (§ 3.5.5) and colour-colour (§ 3.5.6) diagrams, respectively.

3.5.1 Observations

Five of the optical fields, observed in the R_c and I_c bands with the KPNO/MOSA detector (Table 3.1), were followed-up in the near-infrared (K' -band at $2.12\ \mu\text{m}$) using the wide-field camera Omega-Prime mounted on the Calar Alto 3.5-m telescope. Omega-Prime has a 1024×1024 pixel HAWAII detector with a spatial scale of $0.396''/\text{pixel}$, yielding a $6.7' \times 6.7'$ field-of-view (Bizenberger et al. 1998). At the time of the observations, Omega-Prime had the largest field-of-view among infrared detectors at Calar Alto¹. The near-infrared observations presented in this section were carried out at two different epochs (Table 3.1) and cover a total area of 0.70 square degree in the α Per cluster. This area represents only about half of the total area covered by the five KPNO/MOSA fields-of-view despite the large field-of-view of the Omega-Prime camera.

The first set of data was obtained on 4–6 December 1998 under good seeing ($\sim 1''$) but non-photometric conditions. Mosaics of 3×3 and 4×4 Omega-Prime fields-of-view were obtained for the A and C optical fields, respectively. The second set of data was obtained two years later on 11–14 December 2000. Two 4×4 mosaics in the K and L fields were obtained during the first three nights under variable seeing (between $1''$ and $1.4''$) and non-photometric conditions. The field E was observed during the last night under poor weather conditions (and bad seeing) and is, therefore, shallower than the other fields (Table 3.1).

Twenty exposures of 1 min each dithered by less than $40''$ around the centre of each field were obtained to subtract the sky background and keep a good signal-to-noise ratio over the largest area possible. Series of five differential (lights on–off) dome flat fields were taken before and after each night of observations, as well as series of ten dark frames with exposure times similar to those of the targets. Several standard stars were selected from the near-infrared catalogue of Northern Hemisphere standard stars by Hunt et al. (1998), some stars being common to the Faint Standard catalogue (Landolt 1992) to estimate the zero-points throughout the night. A five-dither pattern was observed for each individual standard star. The observed standards were FS1, FS16 and FS17, FS23, FS31, FS32, FS33, and AS15 over the four nights with FS16 and FS17 taken on three different nights to cross-check the zero points. The centre of the K field in α Per, taken on the first night, was observed again during the remainder nights for internal calibration.

¹This instrument has now been superseded by Omega2000, a $15.4' \times 15.4'$ camera with a spatial scale of $0.3''/\text{pixel}$ on the Calar Alto 3.5-m telescope

3.5.2 Data reduction

The observing procedure and the data reduction method were accomplished in a similar manner for both sets of data and carried out within the IRAF environment (package *digiphot*).

- The flat-field exposures were averaged using a minmax rejection algorithm i.e. the lowest and highest values were rejected and the remainder averaged.
- Each on-source frame was sky-subtracted using the median of the remaining dithered images and divided by the averaged flat field.
- The individual images were averaged to create a 20 min-exposure image. The final images were trimmed to keep the central part with the total exposure time of 20 minutes and reject the edges with lower signal-to-noise. Due to the dithering pattern, roughly 100 pixels were trimmed in both x and y coordinates, resulting in a final 6×6 square arcmin usable field-of-view.

We adjusted the full-width-half-maximum, the sky level and the detection threshold for source detection in the field, providing (x,y) coordinates and photometry for each individual object. To optimise the photometry, we have applied an aperture similar to the FWHM to each detection. The flux of few relatively bright and isolated stars was measured for different aperture sizes (from 1 to 4 times the FWHM) to compute the aperture correction. The sky was estimated from a $3 \times$ FWHM-wide annulus at a radius of $4 \times$ FWHM from the centre of the star. Then, we have corrected the resulting magnitudes for extinction and zero points using the 2MASS K_s photometry available for some patches in the α Per cluster. The zero points differ for each individual Omega-Prime field-of-view caused by the non-photometric conditions and the zero-points derived from the standard stars were different at a level higher than the accuracy of 0.1 mag. No obvious colour term was seen between the K' and the K_s broad band filters.

The completeness limit of each field, defined as the magnitude where the histogram of the number of stars per bin of magnitude stops increasing, is listed in Table 3.1 and displayed in Figure 3.6. Galactic models (Annie Robin personal communication) predict a rising luminosity function up to $K \sim 21.0$ (lower right panel in Figure 3.6). Therefore, the magnitude at which the observed luminosity drops is likely the completeness limit of the survey and not a feature intrinsic of the field luminosity function as it happen three magnitudes brighter than the model predictions. A similar approach was applied by Barrado y Navascués et al. (2002) to estimate the completeness limits of the optical wide-field survey in α Per.

3.5.3 Astrometry of the near-infrared images

Accurate astrometry in the near-infrared was necessary to cross-correlate our infrared survey with the previous optical data (Barrado y Navascués et al. 2002). The astrometry of the near-infrared images was carried out with IRAF (package *imcoord* including the tasks *ccxymatch*, *cemap*, *ccsetwcs*, and *cctrans*).

The astrometry of the K' -band images was done by matching the observed K' coordinates (x,y) and the equatorial (ra,dec) coordinates from the USNO-A2 catalogue (Monet et al. 1998) for relatively bright stars located in the Omega-Prime field-of-view. The USNO-A2 catalogue was

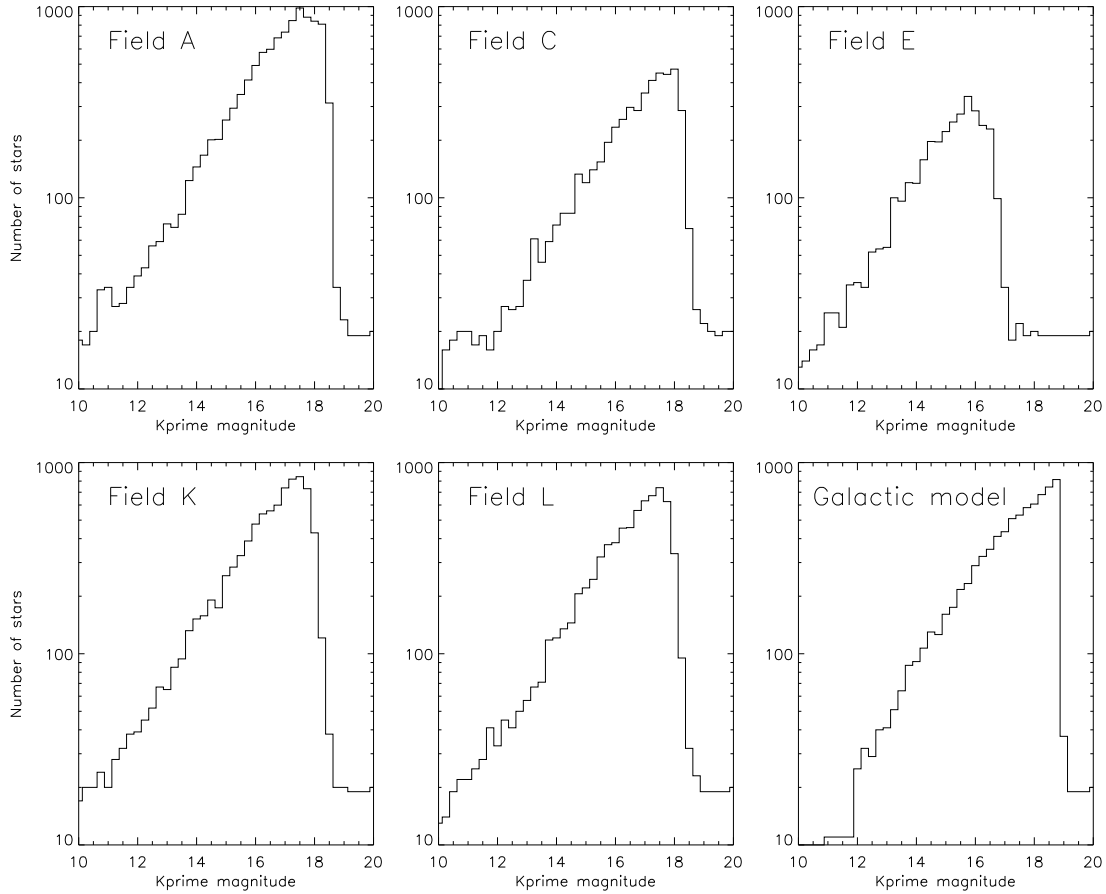


Figure 3.6: Completeness limits of the near-infrared wide-field survey. An histogram of the number of stars versus magnitude is shown for each individual optical field with K' -band observations. The completeness limits are 17.5 for fields A, C, K, and L and 15.5 for field E. The galactic model along the line of sight of the α Per cluster is displayed in the bottom right panel with an arbitrary cut at $K' = 19.0$ mag (Annie Robin, personal communication).

preferred to the Guide Star Catalogue (STScI, 2001) due to the better sky coverage and higher number of stars available in the α Per cluster.

We have, first, matched the pixel (x,y) coordinates to the celestial (ra,dec) coordinates of three reference stars chosen in the Omega-Prime field-of-view. The three stars were chosen to form a triangle which covers the largest area possible in the Omega-Prime frame. The reference stars should obviously not be aligned to provide a good first guess of the plate solution.

We have, then, extracted a plate solution from the three reference stars and refined it with stars common to the USNO database and the Omega-Prime image (typically 50 to 100 stars), yielding accuracy of order $0.1\text{--}0.2''$ in right ascension and declination.

Finally, we have updated the header of the fits file with the second-order polynomial fit for the plate solution, providing a file with pixel and celestial coordinates as well as photometry for each

individual source.

To check the validity of the plate solution, the science frames were displayed with the Skycat software and the USNO-A2 catalogue detections overplotted. The visualisation is straightforward since any discrepancy between the position of the USNO-A2 detections and the objects on the Omega-Prime images was immediately noticed.

3.5.4 Optical-infrared catalogue

As discussed extensively in Barrado y Navascués et al. (2002), near-infrared (JHK) follow-up observations of optically-selected cluster member candidates constitute good means to reject contaminating objects based on their location in various optical-infrared colour-magnitude diagrams. The infrared data were either extracted from the 2MASS database or obtained with Omega-Prime and Omega Cass on the Calar Alto 3.5-m telescope during various observing runs. Three subsamples were extracted and classified as follows:

- 54 are probable candidates
- 12 possible candidates
- 26 were rejected as cluster members

Some optically-selected cluster members were, however, lacking near-infrared information or had only upper limits. Furthermore, with a limiting magnitude of $K_s = 14.3$, the 2MASS survey provided near-infrared magnitudes only for objects at or above the stellar/substellar boundary in α Per. To estimate the contamination in the brown dwarf regime, deeper observations were therefore required. At the time of the observations, the full 2MASS database was not released, creating patches within the α Per cluster with no infrared data at all. Finally, another aim of the wide-field infrared survey was to uncover lower mass brown dwarfs down to the deuterium burning limit. Indeed, we have expected to find a near-infrared counterpart to faint object in the I_c -band (and no R_c measurement) in order to unveil new cluster brown dwarfs.

The cross-correlation of the optical (R_c and I_c) and near-infrared (K') catalogues was not straightforward. The matching radius was first increased to inspect the evolution of the number of matched objects with radii ranging from 0.1 to $10''$. The number of matches increased steeply up to $2\text{--}3''$ and then kept rising slowly. To optimise the cross-correlation and avoid the loss of good candidates, we have estimated the dispersion in right ascension and declination between the optical and the near-infrared catalogues. The best gaussian fits to the distributions have sigma values of $0.372''$ and $0.193''$ for the right ascension and declination, respectively (Figure 3.7). The difference observed in the dispersion between both directions comes from the $\cos(\delta)$ not applied to the right ascension, especially at high declinations ($\delta = 48\text{--}50^\circ$ for α Per). We have cross-correlated the near-infrared (K') and the optical (R_c and I_c) catalogues with matching radii of four times the dispersion values quoted above. Hence, we have missed only one or two objects among the 22,000 matches in the 0.70 square degree area surveyed in α Per.

The final catalogue is available upon request and will be available at the CDS website² after publication of the results of the infrared survey in α Per. The final catalogue contains 22,129

²<http://vizier.u-strasbg.fr/cgi-bin/VizieR>

entries with the right ascension and declination (in J2000), and the optical and near-infrared magnitudes. We will use this catalogue to extract the new cluster members in α Per and we will refer to these objects as new infrared-selected candidates as opposed to the optical members extracted by Barrado y Navascués et al. (2002). The selection procedure of the new candidates is described in the forthcoming sections.

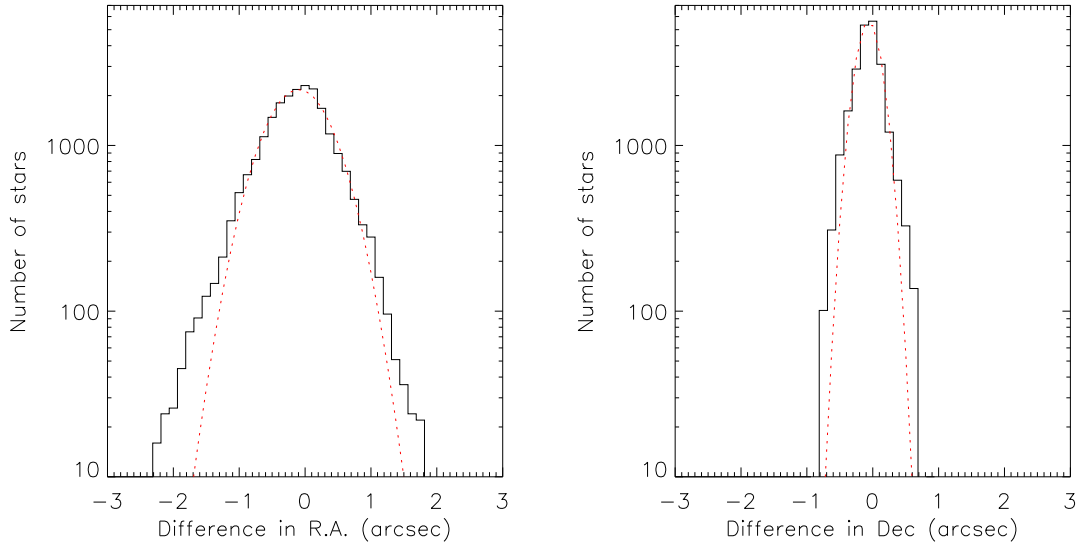


Figure 3.7: Determination of the matching radii in right ascension and declination for the cross-correlation of the optical and near-infrared catalogues of α Per. The left and right panel shows the number of stars versus the difference between the optical and the near-infrared coordinates in right ascension and declination, respectively. The histograms are shown for a matching radius of $10.0''$. The dotted curves represent the best gaussian fits to the distributions.

3.5.5 Colour-magnitude diagram

A colour-magnitude diagram represents the observational counterpart of the Hertzsprung-Russell diagram. The magnitudes on the y-axis correspond to the luminosities whereas the observed colours on the x-axis reflect the temperatures of the objects. Young cluster members will exhibit redder colours than their field counterparts and, therefore, occupy the right side of the plot.

The optical-to-infrared colour-magnitude diagram ($K', I_c - K'$) is displayed in Figure 3.8. All sources detected within the 0.70 square degree area surveyed in the cluster are drawn as black dots. Overplotted are the NextGen isochrones (solid lines) for 50 and 100 Myr (Baraffe et al. 1998), the Dusty (dashed line), and Cond (dotted line) isochrones for 100 Myr (Chabrier et al. 2000b), assuming an age of 182 pc for the cluster. A reddening vector for $A_V = 2$ is also included for comparison purpose.

Three sequences are clearly visible in the ($K', I_c - K'$) colour-magnitude diagram (Figure 3.8). The blue side of the diagram with $K \leq 18$ mag is populated by F and G dwarfs from the Galactic

thin disk, while fainter objects are F and G dwarfs belonging to the thick disk. Later-type K and M dwarfs populate the red side of the diagram. The bulk of objects seen on the right hand side below the isochrones with a $I_c - K'$ colour of approximately 4 are mainly reddened background giants.

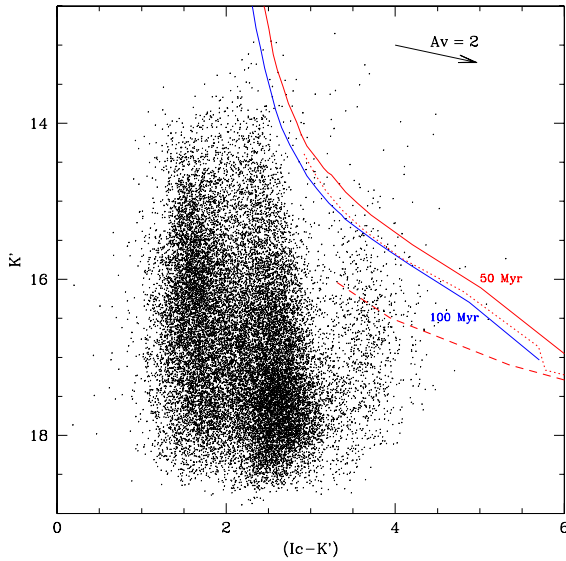


Figure 3.8: Colour-magnitude ($K', I_c - K'$). More than 22,000 detections over the 0.70 sq. deg. area surveyed in the α Per cluster are plotted as black dots. Also overplotted are the NextGen (solid lines) isochrones for 50 and 100 Myr (Baraffe et al. 1998), and Dusty (dashed line) 100 Myr isochrones (Chabrier et al. 2000b), assuming a distance of 182 pc for the cluster. A reddening vector for $A_V = 2$ is also included for comparison purposes.

We have selected new member candidates from the optical-infrared survey of 0.70 square degree area in α Per by extracting objects falling to the right of the NextGen and Dusty 100 Myr isochrones (Figure 3.8 and Figure 3.9). As a first step, we have extracted all objects falling to the right of the NextGen 100 Myr isochrones over the whole magnitude range and assumed a distance of 182 pc for α Per. The total number of newly infrared-selected member candidates is 103 out of 22,129 detections in the 0.70 square degree surveyed area. Figure 3.9 provides a close-up region of the $(K', I_c - K')$ colour-magnitude diagram where the new infrared-selected candidates are located. Those new cluster member candidates are represented by large hexagons and listed in the bottom panel of Table 3.2. We have also overplotted the optically-selected probable (filled triangles) and possible (open triangles) cluster member candidates from Barrado y Navascués et al. (2002) for comparison.

We have cross-correlated the new infrared-selected candidates with the recent release of the 2MASS database in order to provide additional J and H magnitudes. The K' magnitude from the wide-field survey and the K_s magnitudes from 2MASS are in good agreement. Analysis of the location of new candidates in various colour-magnitude diagrams confirmed their status as new probable cluster members, except for AP415 which appears redder in the optical ($I_c, R_c - I_c$) colour-magnitude diagram (Figure 3.3). This discrepancy might arise from a possible companion.

Further analysis of the membership status of the new cluster candidates will be pursued in the next section (§ 3.5.6).

In an attempt to estimate the influence of the distance on the candidate selection, we have repeated the procedure assuming distances of 176 pc and 190 pc, respectively. The number of infrared-selected candidates did vary as follows: 90 and 119 candidates were extracted for a distance of 176 and 190 pc, respectively. The additional objects found for a distance of 190 pc compared to 182 pc are included in Figure 3.9.

However, the NextGen isochrones do not include the modelling of dust in ultracool dwarfs. Several surveys in the field and in open clusters concluded that the spectral energy distributions of very low-mass stars and brown dwarfs are shaped by the presence of dust in their atmospheres.

We have, therefore, selected all objects located in the area delineated by the Dusty (masses below $50 M_{\text{Jup}}$ or T_{eff} below 2500 K) and the NextGen 100 Myr isochrones. Galactic models predict that those objects are mostly distant reddened giants but we would expect some cluster members hidden in this region of the colour-magnitude diagram. The number of selected objects are 269, 310, 333, assuming distances of 176, 182, and 190 pc, respectively. These numbers do not include the candidates selected based on the NextGen isochrones. All selection procedures assumed a mean extinction of 0.3 mag (Barrado y Navascués et al. 2002). The number of genuine cluster member candidates extracted from each selection method is given in the next section.

3.5.6 Colour-colour diagram

The colour-colour diagram is of prime importance to distinguish probable cluster member candidates from distant background giants. The photometry available in three broad-band filters (R_c , I_c , K') provides a colour-colour diagram $((I_c-K'),(R-I)_c)$ to further assess the membership of the infrared-selected candidates (Figure 3.10). The giant branch is clearly visible and centred approximately on $(R-I)_c \sim 1$ and $I_c-K' \sim 4$. Figure 3.10 displays all detections in the 0.7 square degree area surveyed in the α Per cluster (black dots) along with the NextGen 50 and 100 Myr isochrones (solid lines; Baraffe et al. 1998).

The initial selection of new cluster members using the NextGen 100 Myr isochrones at a distance of 182 pc for α Per extracted a total of 103 new infrared-selected candidates.

Among those new candidates, more than two-thirds of them (70 %) turned out to be reddened background giants (diagonal crosses on Figure 3.9 and Figure 3.11) rather than low-mass brown dwarf candidates, according to their location in the $((I_c-K'),(R-I)_c)$ colour-colour diagram. This contamination is caused by the ability of the K' -band to probe larger distances through highly extincted regions towards the Galactic plane, as it is the case for α Per.

The remaining infrared-selected candidates, which lie to the right of the NextGen 100 Myr isochrones in the colour-colour diagram, stay probable cluster member candidates. However, about half of these candidates (16 out of 30) were already extracted by the optical survey as probable members, thus, confirming their genuine membership. The shift in colour observed between the candidates and the isochrones originates from the selection procedure of these candidates and the uncertainties of the opacity line lists. We have recovered more than 50 % (18 out of 31) of the probable cluster members from Barrado y Navascués et al. (2002) (filled triangles in Figure 3.11 and upper panel in Table 3.2), distributed over the area surveyed in the near-infrared as follows.

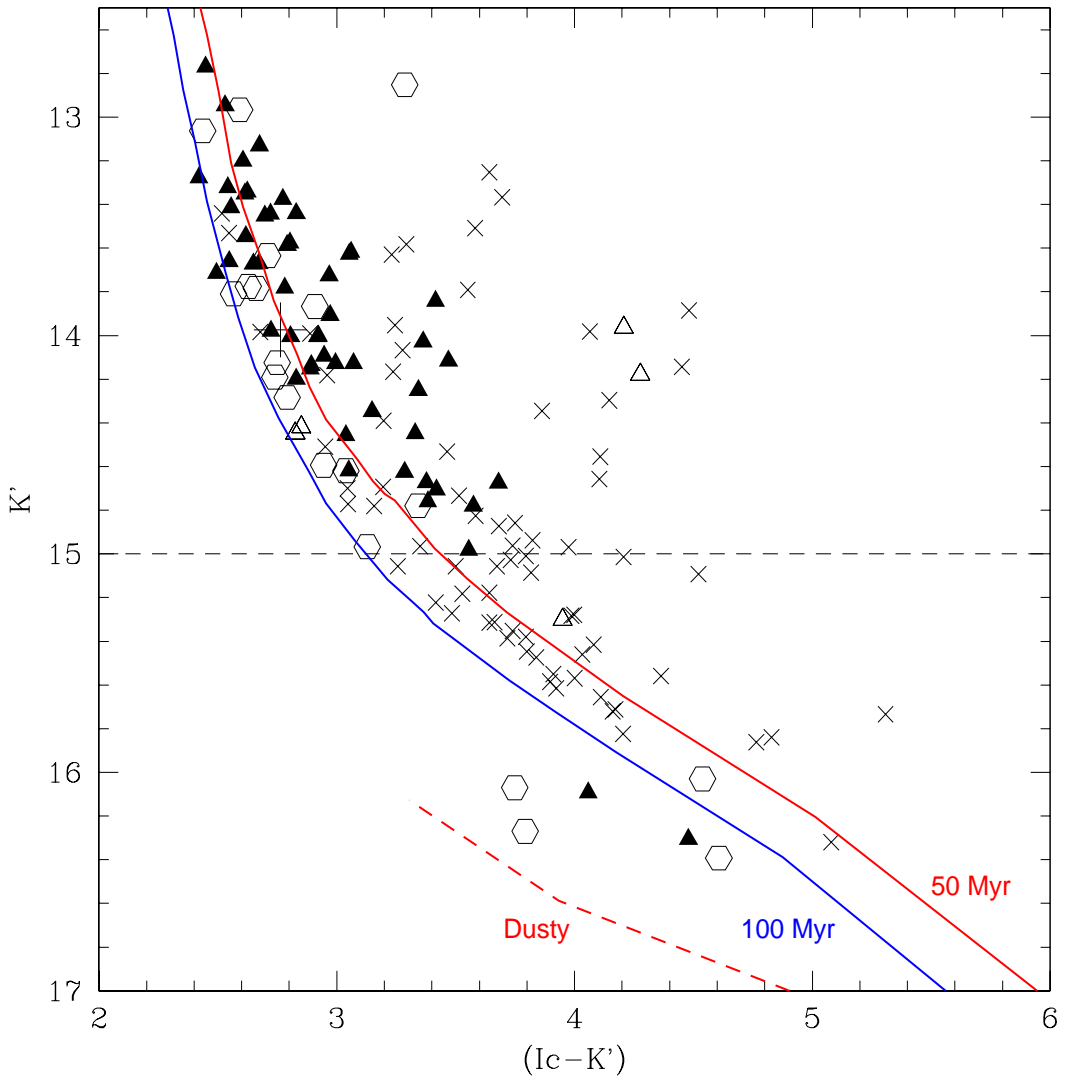


Figure 3.9: Colour-magnitude ($K', I_c - K'$) diagram showing the location of the new infrared-selected member candidates. Also overplotted are the NextGen (solid lines) isochrones for 50 and 100 Myr (Baraffe et al. 1998) and the Dusty (dashed line) 100 Myr isochrones (Chabrier et al. 2000b), assuming a distance of 182 pc for the cluster. Filled and open triangles are probable and possible cluster member candidates extracted by the optical survey described in Barrado y Navascués et al. (2002). Open hexagons are new infrared-selected cluster member candidates from our optical-infrared survey. The two selection methods are clearly apparent. The diagonal crosses indicate the distant background giants. The horizontal dashed line represents the stellar/substellar boundary at $M_K = 8.7$ mag ($M_I = 11.8$ mag) assuming a distance of 182 pc for the cluster.

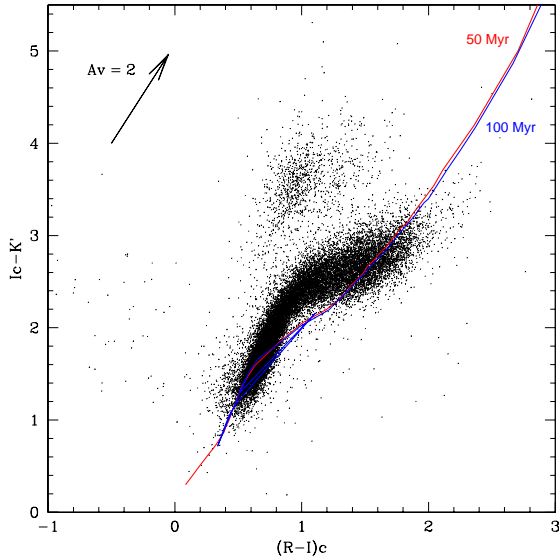


Figure 3.10: Colour-colour $((I_c - K'), (R - I)_c)$. All 22,129 detections are plotted as black dots. Also overplotted are the NextGen (solid lines) isochrones for 50 and 100 Myr (Baraffe et al. 1998), age bracketing the one estimated for α Persei, assuming a distance of 182 pc. The giant branch is well populated in this diagram $((R - I)_c \sim 1$ and $I_c - K' \sim 4$), due to the low galactic latitude of the α Per cluster. A reddening vector for $A_V = 2$ is also included for comparison purpose.

- Three probable cluster members out of four in the field A
- Three out of six in field C
- Two out of three in field E
- Five out of seven in field K
- Five out of eleven in field L

The remaining 14 objects are new infrared-selected probable member candidates not extracted as such by the optical survey (open hexagons in Figure 3.11 and lower panel in Table 3.2). One of these new member candidates (AP426) has R_c , I_c , and K' magnitudes below the hydrogen-burning limit, indicating a probable brown dwarf cluster member. Another candidate (AP425) straddles the stellar/substellar boundary and is possibly a brown dwarf. Finally, AP424 lies close to the lithium depletion boundary estimated by Stauffer et al. (1999).

Moreover, one object, previously classified as a non-member by Barrado y Navascués et al. (2002), was included in our sample as well (large cross in Figure 3.11).

As mentioned earlier (§ 3.5.5), our selection of new cluster members in α Per to the right of the NextGen 100 Myr isochrones extracted 90 and 119 candidates for distances of 176 and 190 pc, respectively. How does the number of infrared-selected cluster member candidates and/or giants depend on the assumed distance?

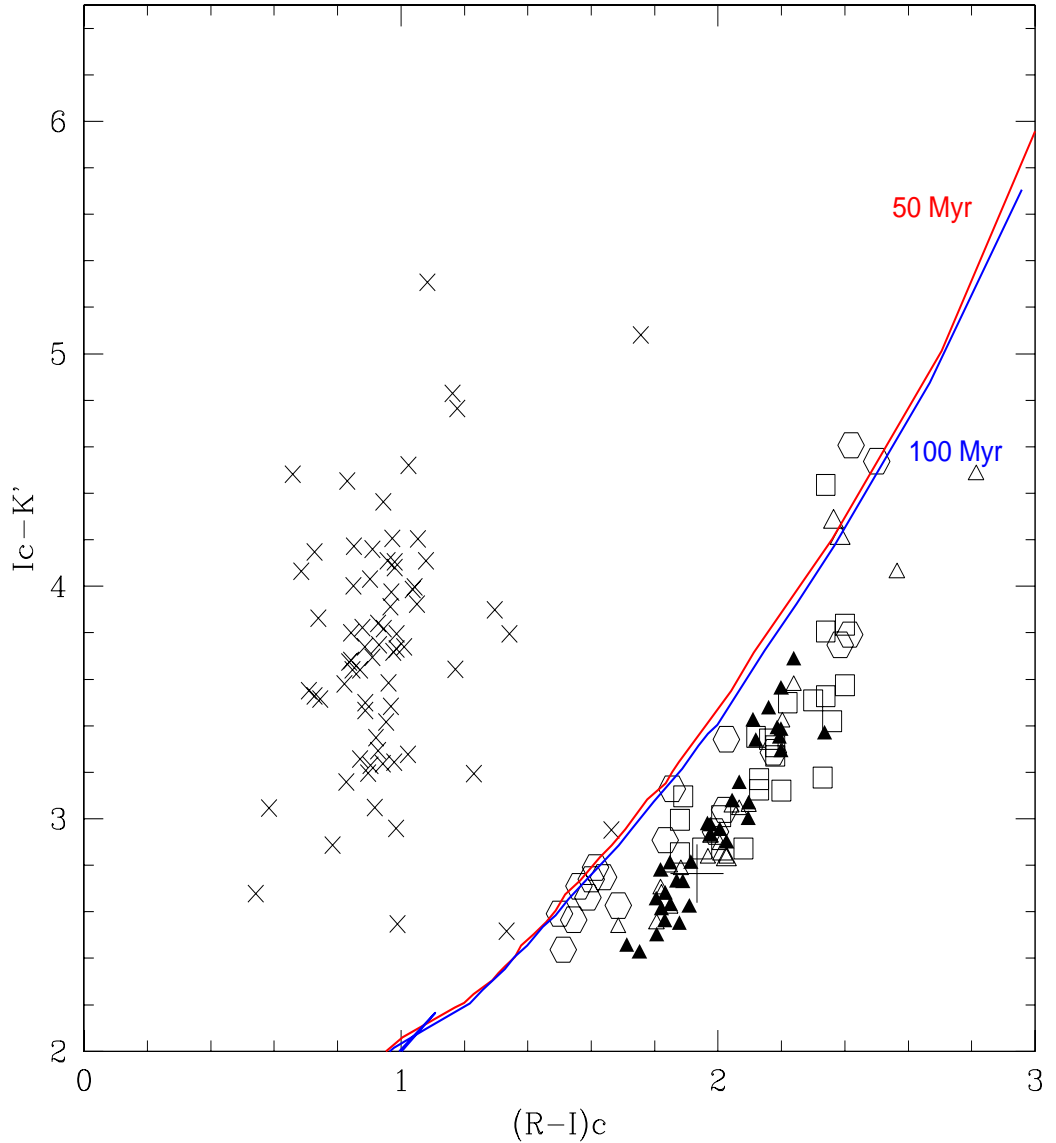


Figure 3.11: Colour-colour diagram $((I_c - K'), (R - I)_c)$. Also overplotted are NextGen (Baraffe et al. 1998) isochrones for 50 and 100 Myr, age bracketing the one estimated for the cluster. Filled and open triangles are probable and possible cluster member candidates extracted by the optical survey described in Barrado y Navascués et al. (2002). Open squares are spectroscopically confirmed members of α Per from Stauffer et al. (1999). Open hexagons are new infrared-selected cluster member candidates from our optical-infrared survey. The diagonal crosses indicate the distant background giants rejected as cluster member. The discrepancy between isochrones and cluster candidates might originate from the uncertainties on the current opacity line lists.

Table 3.2: List of the new member candidates of the α Per cluster selected from the optical-to-infrared survey (Section 3.5). The names, coordinates in J2000, and R_c , I_c , the 2MASS J , H , and K_s magnitudes and K' magnitudes from our near-infrared observations as well as the colours of each object are quoted. The upper part of the table provide the list of optically-selected member candidates found independently in the optical-to-infrared survey whereas the lower part lists the new infrared-selected probable candidates. Among them, four new objects are brown dwarf candidate members. The numbering of the new candidate members follows the one described in Barrado y Navascués et al. (2002) and stars at AP413.

Name	R.A.	Dec	R_c	I_c	J	H	K_s	K'	$(R-I)_c$	(I_c-K')
Optically-selected cluster member candidates										
AP329	03:23:56.36	+48:09:21.1	17.16	15.48	13.88	13.31	13.04	12.95	1.69	2.53
AP332	03:25:16.91	+48:36:09.3	17.63	15.80	14.06	13.43	13.19	13.13	1.82	2.67
AP334	03:22:45.51	+48:21:33.4	17.82	15.96	14.25	13.66	13.34	13.35	1.85	2.61
AP339	03:26:33.28	+50:07:41.9	17.97	16.15	14.35	13.76	13.40	13.45	1.82	2.70
AP343	03:23:48.49	+48:36:43.3	18.01	16.21	14.62	14.07	13.72	13.66	1.81	2.55
AP344	03:26:52.11	+50:00:32.8	18.24	16.27	14.33	13.69	13.39	13.44	1.97	2.83
AP309	03:22:40.69	+48:00:33.8	18.23	16.38	14.49	13.88	13.58	13.59	1.85	2.79
AP349	03:26:48.01	+50:02:15.7	18.45	16.56	14.62	14.04	13.73	13.78	1.88	2.78
AP353	03:24:48.69	+48:49:47.3	18.78	16.68	14.61	14.00	13.65	13.63	2.10	3.05
AP364	03:20:39.19	+49:32:06.2	18.90	16.92	15.00	14.41	14.03	14.00	1.98	2.92
AP365	03:28:22.98	+49:11:24.3	19.06	17.03	15.02	14.33	14.15	14.20	2.03	2.83
AP366	03:26:35.49	+49:15:44.2	19.05	17.04	15.12	14.54	14.22	14.15	2.00	2.89
AP369	03:26:45.11	+50:25:06.7	19.46	17.26	14.88	14.26	13.88	13.84	2.20	3.42
AP311	03:23:08.70	+48:04:50.7	19.56	17.50	15.44	14.71	14.32	14.46	2.07	3.04
AP370	03:27:01.00	+49:14:41.2	19.71	17.67	15.61	14.94	14.50	14.62	2.04	3.05
AP305	03:19:21.62	+49:23:31.1	20.59	18.36	15.81	14.96	14.64	14.78	2.24	3.57
AP399	03:25:48.55	+50:01:00.8	22.71	20.15	—	—	—	16.09	2.56	4.06
AP406	03:23:09.86	+48:16:30.0	23.60	20.78	—	—	—	16.31	2.81	4.48
New infrared-selected cluster member candidates(NextGen isochrones)										
AP413	03:24:17.75	+48:07:36.0	17.01	15.50	14.03	13.34	13.05	13.06	1.51	2.44
AP414	03:22:05.17	+48:12:46.1	17.06	15.56	14.00	13.26	13.05	12.97	1.50	2.59
AP415	03:25:32.89	+48:45:21.4	18.31	16.14	13.75	13.06	12.82	12.85	2.17	3.29
AP416	03:28:16.33	+50:05:51.6	17.91	16.34	14.57	13.91	13.63	13.63	1.56	2.71
AP417	03:22:40.50	+48:19:35.0	18.09	16.40	14.80	14.09	13.83	13.78	1.69	2.63
AP418	03:26:02.06	+50:05:34.7	18.04	16.45	14.68	14.06	13.71	13.78	1.59	2.66
AP419	03:23:18.80	+48:04:25.4	18.61	16.77	14.75	14.07	13.77	13.87	1.83	2.91
AP420	03:27:17.27	+50:07:19.8	18.51	16.87	15.12	14.41	14.13	14.12	1.64	2.75
AP421	03:22:09.83	+48:16:43.8	18.53	16.93	15.30	14.66	14.28	14.19	1.60	2.74
AP422	03:23:17.96	+47:59:01.7	18.69	17.07	15.31	14.54	14.20	14.28	1.61	2.79
AP423	03:24:08.12	+48:48:30.0	19.53	17.54	15.50	15.03	14.44	14.59	1.99	2.94
AP424	03:23:04.86	+48:16:11.3	19.68	17.66	14.61	15.15	14.61	14.62	2.02	3.04
AP425	03:27:07.06	+50:09:22.7	20.15	18.12	15.75	15.00	14.77	14.78	2.03	3.34
AP426	03:26:16.24	+50:18:43.3	23.07	20.57	—	—	—	16.03	2.50	4.54
AP427	03:23:59.92	+48:08:00.5	17.92	16.38	14.84	14.09	13.87	13.81	1.54	2.57
AP428	03:23:05.59	+48:09:00.7	19.95	18.10	16.12	15.07	14.76	14.97	1.85	3.13
New infrared-selected cluster member candidates(Dusty isochrones)										
AP429	03:27:30.59	+49:11:09.6	22.48	20.06	—	—	—	16.27	2.42	3.79
AP430	03:20:14.94	+49:31:46.6	23.42	21.00	—	—	—	16.39	2.42	4.61
AP331	03:24:06.45	+48:23:11.5	22.20	19.82	—	—	—	16.07	2.39	3.76

For a distance of 176 pc, the list of 90 candidates is divided as follows:

- 64 candidates (71 %) turned out to be giants.
- One object was previously classified as non-member by Barrado y Navascués et al. (2002).
- 15 candidates are common to the optical and near-infrared surveys.

- 10 are new infrared-selected candidates. The ‘missing’ new candidates compared to distance of 182 pc are AP421, AP422, AP423, and AP426, the latter being a possible cluster brown dwarf.

For a distance of 190 pc, the list of 119 candidates is divided as follows:

- 86 candidates (72 %) are classified as giants
- The same candidate classified as non-member by Barrado y Navascués et al. (2002).
- 16 objects are common candidates as for a distance of 182 pc
- 16 new candidates including two new ones, AP427 and AP428, represent our new infrared-selected candidates. AP428 is straddling the stellar/substellar boundary, indicating a possible brown dwarf member.

To summarise, the number of giants is approximately 70 % of all infrared-selected candidates. The number of new member candidates is 16, assuming the distance derived from isochrone fitting. However, all these new candidates are stellar components of the α Per cluster except, AP426.

To find new brown dwarf candidates in the cluster, we have examined the location in the colour-colour diagram of the objects selected to the right of the Dusty 100 Myr isochrone in the colour-magnitude diagram. Following the previous selection procedure, we could extract 5 new brown dwarf candidates, including the recovery two candidates from Barrado y Navascués et al. (2002). The latter two brown dwarfs, AP399 and AP406, were lacking near-infrared photometry. The numbering of the new candidates strictly follows the previous one and starts at AP439. The remainder objects, rejected as possible cluster members, are mostly distant reddened giants as anticipated by galactic models (not shown in Figure 3.11 to avoid overloading the plot).

One can now ask the following question: why were those new infrared-selected cluster member candidates missed in the optical selection? To address this issue, we have compared the location of the new candidates to previous members in the optical $(I_c, (R-I)_c)$ colour-magnitude diagram (Figure 3.3).

All the infrared-selected candidates located to the right of the NextGen isochrones in the $(K', I_c - K')$ colour-magnitude diagram also lie to the right of the NextGen isochrones in the $(I, R - I)$ colour-magnitude diagram. They define a bluer sequence than the probable members extracted by Barrado y Navascués et al. (2002) and remain, therefore, likely new cluster member candidates. Some objects follow the sequence defined by the probable candidates extracted by Barrado y Navascués et al. (2002). One object, AP415, lie above the sequence and might be either a contaminant or a binary belonging to the cluster (Figure 3.3). Optical spectroscopy is required to ascertain the membership of these new infrared-selected cluster members.

The new brown dwarf candidates follow the sequence defined by the probable candidates from Barrado y Navascués et al. (2002). The faintest new brown dwarf candidate, AP431, exhibit bluer optical colour which might reflect the settling of dust in the atmospheres of young substellar objects.

3.6 Optical spectroscopy of cluster member candidates

Due to the low galactic latitude of the α Per cluster, proper motion and photometry alone fail to eliminate all non-members. The membership of the new cluster member candidates extracted

by Barrado y Navascués et al. (2002) and our near-infrared wide-field survey are solely based on colour selection as no first epoch is available due to the faintness of the objects. To ascertain the membership of the photometrically-selected candidates in α Per, we were granted four observing nights in autumn 2002 to carry out moderate-resolution optical spectroscopy of the new candidates with the Twin spectrograph mounted on the Calar Alto 3.5-m telescope.

The spectroscopic observations are described in § 3.6.1. The data reduction is detailed § 3.6.2. The main results of the spectroscopy of the new cluster member candidates in α Per are presented in § 3.6.3.

3.6.1 Spectroscopic observations

Spectroscopic observations were conducted with the Twin spectrograph mounted on the Calar Alto 3.5-m telescope in October/November 2002 under variable weather conditions over the four night observing run.

The Twin CCD camera is a 2000×800 pixel detector with a spatial resolution of 0.5 \AA/pixel . The light entering the spectrograph is separated by a dichroic beam splitter which allows the user to obtain a blue and red spectrum of the target. We have obtained moderate-resolution ($R \sim 2000$) optical spectra of 33 selected member candidates using the T07 grating covering $5800\text{--}8800 \text{ \AA}$. Our sample of objects can be divided into four categories:

- 24 probable members (Barrado y Navascués et al. 2002)
- 1 possible member, AP350 (Barrado y Navascués et al. 2002)
- 4 non-members: AP327, AP336, AP338, and AP342 (Barrado y Navascués et al. 2002)
- Four new infrared-selected members: AP414, AP415, AP416, and AP418

We have observed most of the objects three times (Table 3.3), each exposure being shifted along the slit by approximately 100 pixels. Table 3.3 lists the 33 objects observed spectroscopically, their I_c magnitudes, the observing dates, the exposure times, as well as spectroscopic results which are detailed in the next section (§ 3.6.3). We have used two different slits ($1.5''$ and $2.1''$) depending on the seeing conditions. We have adjusted the exposure times taking into account the brightness of the object as well as the weather conditions. We have taken dome flat fields, dark frames and He–Ar arc lamps before the beginning of each night as well. We have observed spectrophotometric standard stars Feige 110 (Hamuy et al. 1992) and G191-B2B (Massey & Gronwall 1990) twice each during the night to flux calibrate the spectra. Meanwhile, we have observed some template objects with known spectral types with the same set-up to derive accurate spectral type classification and compare gravity-sensitive absorption features. The template objects and their spectral types are GJ251 (M3.5), LHS1417 (M4.0), LHS0168 (M5.0), LHS1326 (M6.0), LHS0248 (M6.5), bracketing our cluster targets in spectral types.

3.6.2 Data reduction

The data reduction was entirely accomplished within the IRAF environment (package *twodspec* and *onedspec*). Each step of the procedure used to extract a one-dimensional optical spectrum is described below. The dispersion axis of the spectra obtained with the Twin spectrograph are along the lines and the blue wavelength are the end of the x-axis.

Table 3.3: List of all 33 objects observed with the red channel of the T07 grating on the Twin spectrograph at the Calar Alto 3.5-m telescope. Names, coordinates (in J2000), I_c magnitudes, observing date and exposure times, equivalent widths for H α at 6563 Å, equivalent widths for the KI and NaI doublets at 7665/7699 Å and 8183/8195 Å, respectively, are included in the table. Values obtained for three spectral indices, TiO5 (Reid et al. 1995), VO-a (Kirkpatrick et al. 1999b), and PC3 (Martín et al. 1999b) are given in columns 10, 11, and 12, respectively. Former and new membership status as well as the spectral types with an uncertainty of half a subclass are provided in columns 13 and 14. The objects are in decreasing order of I_c magnitude.

Target	R.A.	Dec	I_c	Obs. Date	ExpT	H α	KI	NaI	TiO5	VO-a	PC3	Member	Sp. Type
AP327	03:20:31.74	49:39:59.6	15.06	01 Nov 02	3 × 600 s	—	—	—	0.985 (M***)	1.984 (M***)	1.109 (M***)	N → N	Giant
AP329	03:23:56.34	48:09:21.0	15.48	31 Oct 02	1 × 1800 s	-6.5	2.0/1.3	2.1/2.4	0.390 (M4.0)	2.001 (M4.8)	1.236 (M4.7)	Y+ → Y	M4.5 ± 0.5
AP414	03:22:05.21	48:12:46.0	15.56	03 Nov 02	3 × 600 s	—	1.9/1.7	0.4/1.2	0.518 (M2.6)	1.950 (M4.2)	1.086 (M3.7)	N	M3.5 ± 0.5
AP330	03:34:15.60	49:58:48.0	15.66	31 Oct 02	2 × 1800 s	-10.2	2.6/1.6	2.7/3.4	0.375 (M4.2)	1.975 (M4.5)	1.240 (M4.7)	Y+ → Y	M4.5 ± 0.5
AP283	03:24:38.78	48:17:17.1	15.70	10 Oct 02	2 × 1200 s	-4.2	2.3/1.6	2.4/2.8	0.386 (M4.0)	1.987 (M4.6)	1.232 (M4.7)	Y+ → Y	M4.5 ± 0.5
AP331	03:32:05.90	50:05:55.0	15.73	31 Oct 02	3 × 900 s	-7.9	2.2/2.6	2.7/1.8	0.341 (M4.5)	1.973 (M4.5)	1.299 (M5.1)	Y+ → Y	M4.5 ± 0.5
AP332	03:25:16.90	48:36:09.0	15.80	31 Oct 02	3 × 800 s	-8.2	2.8/1.9	3.3/2.5	0.319 (M4.8)	1.992 (M4.7)	1.307 (M5.2)	Y+ → Y	M4.5 ± 0.5
AP333	03:25:13.55	50:27:33.0	15.86	31 Oct 02	3 × 800 s	-5.7	3.2/2.7	2.7/3.4	0.380 (M4.1)	1.942 (M4.1)	1.316 (M5.2)	Y+ → Y	M4.5 ± 0.5
AP335	03:28:52.96	50:19:25.9	15.97	01 Nov 02	3 × 1500 s	-10.7	3.6/1.8	2.9/3.2	0.352 (M4.4)	1.994 (M4.7)	1.306 (M5.2)	Y+ → Y	M4.5 ± 0.5
AP336	03:31:55.30	49:08:31.0	16.04	01 Nov 02	3 × 600 s	—	—	—	0.972 (M***)	1.971 (M***)	1.088 (M***)	N → N	Giant
AP337	03:34:07.50	48:32:08.0	16.07	01 Nov 02	3 × 1200 s	-7.9	2.5/2.3	2.5/2.3	0.295 (M5.0)	2.006 (M4.8)	1.341 (M5.4)	Y+ → Y	M5.0 ± 0.5
AP338	03:24:52.65	48:46:12.8	16.07	02 Nov 02	3 × 600 s	—	—	—	0.964 (M***)	1.940 (M***)	0.953 (M***)	N → N	Giant
AP415	03:25:32.90	48:45:20.8	16.14	03 Nov 02	3 × 750 s	-1.1/2.0	1.1/0.8	0.520 (M2.6)	1.980 (M4.5)	1.030 (M3.2)	N	M3.5 ± 0.5	
AP339	03:26:33.24	50:07:41.7	16.15	01 Nov 02	3 × 1200 s	-6.5	2.6/1.6	3.6/3.3	0.337 (M4.6)	1.982 (M4.6)	1.340 (M5.4)	Y+ → Y	M5.0 ± 0.5
AP340	03:21:34.85	48:16:28.7	16.16	01 Nov 02	3 × 900 s	-3.8	5.4/4.6	3.6/4.3	0.276 (M5.2)	2.018 (M4.9)	1.390 (M5.7)	Y+ → Y	M5.0 ± 0.5
AP341	03:31:03.39	50:24:41.6	16.16	01 Nov 02	3 × 750 s	-10.7	3.1/2.1	3.0/3.0	0.276 (M5.2)	1.997 (M4.7)	1.376 (M5.6)	Y+ → Y	M5.0 ± 0.5
AP344	03:26:52.00	50:00:33.0	16.27	01 Nov 02	3 × 600 s	-10.6	3.4/2.3	3.1/3.1	0.254 (M5.5)	2.030 (M5.1)	1.392 (M5.7)	Y+ → Y	M5.5 ± 0.5
AP345	03:33:45.80	50:08:53.0	16.30	01 Nov 02	3 × 600 s	-9.9	2.4/1.5	2.7/3.2	0.313 (M4.8)	1.995 (M4.7)	1.372 (M5.6)	Y+ → Y	M5.0 ± 0.5
AP346	03:21:30.06	48:49:23.2	16.32	01 Nov 02	3 × 600 s	-8.3	2.7/2.1	2.5/3.5	0.327 (M4.7)	1.981 (M4.5)	1.381 (M5.6)	Y+ → Y	M5.0 ± 0.5
AP416	03:28:16.28	50:05:51.7	16.34	02 Nov 02	3 × 1200 s	-4.8	0.9/1.0	2.3/2.3	0.520 (M2.6)	1.989 (M4.6)	1.048 (M3.4)	N	M3.5 ± 0.5
AP347	03:31:33.77	49:52:02.1	16.34	01 Nov 02	3 × 600 s	-6.9	3.1/1.9	3.0/3.0	0.288 (M5.1)	1.962 (M4.4)	1.368 (M5.6)	Y+ → Y	M5.0 ± 0.5
AP342	03:25:39.24	48:45:21.1	16.34	02 Nov 02	3 × 600 s	—	—	—	0.958 (M***)	1.998 (M***)	1.043 (M***)	N → N	Giant
AP309	03:22:40.65	48:00:33.6	16.38	01 Nov 02	3 × 600 s	-4.9	2.1/1.5	2.3/1.6	0.345 (M4.5)	2.021 (M5.0)	1.336 (M5.4)	Y+ → Y	M5.0 ± 0.5
AP418	03:26:02.08	50:05:34.5	16.45	03 Nov 02	2 × 750 s	—	—	—	0.979 (M***)	1.971 (M***)	0.871 (M***)	N	Giant
AP349	03:26:47.90	50:02:16.0	16.56	02 Nov 02	3 × 1200 s	-9.6	2.4/2.2	3.3/3.4	0.293 (M5.0)	1.986 (M4.6)	1.373 (M5.6)	Y+ → Y	M5.5 ± 0.5
AP350	03:32:06.80	49:25:23.0	16.57	03 Nov 02	1 × 750 s	—	—	—	1.017 (M***)	1.996 (M***)	0.913 (M***)	Y? → N	Giant
AP351	03:28:47.80	50:02:01.0	16.64	02 Nov 02	3 × 1200 s	-7.6	2.5/2.1	3.5/3.7	0.295 (M5.0)	2.041 (M5.2)	1.322 (M5.3)	Y+ → Y	M5.0 ± 0.5
AP353	03:24:48.66	48:49:47.0	16.68	02 Nov 02	3 × 1200 s	-9.2	3.6/2.9	3.0/3.1	0.228 (M5.7)	2.061 (M5.4)	1.476 (M6.2)	Y+ → Y	M6.0 ± 0.5
AP354	03:27:31.64	48:53:23.3	16.69	02 Nov 02	3 × 1200 s	-11.1	3.4/2.6	2.9/3.2	0.224 (M5.8)	2.069 (M5.5)	1.458 (M6.1)	Y+ → Y	M6.0 ± 0.5
AP355	03:22:33.15	48:47:00.3	16.70	02 Nov 02	3 × 1200 s	-9.2	2.9/2.7	3.3/3.7	0.297 (M5.0)	2.005 (M4.8)	1.344 (M5.4)	Y+ → Y	M5.0 ± 0.5
AP363	03:24:00.33	47:55:29.7	16.88	02 Nov 02	3 × 1200 s	-14.9	3.1/2.0	3.7/4.1	0.288 (M5.1)	1.992 (M4.7)	1.400 (M5.8)	Y+ → Y	M5.5 ± 0.5
AP364	03:20:39.16	49:32:06.0	16.92	02 Nov 02	3 × 1200 s	-8.2	2.4/2.8	3.9/4.3	0.430 (M3.6)	2.028 (M5.0)	1.390 (M5.7)	Y+ → Y	M5.5 ± 0.5
AP366	03:26:35.50	49:15:43.8	17.04	02 Nov 02	3 × 1200 s	-10.5	3.4/2.3	3.1/3.1	0.244 (M5.6)	1.987 (M5.9)	1.417 (M5.9)	Y+ → Y	M6.0 ± 0.5

1. The first step consists in creating an averaged bias frame. Ten bias images were taken before the night and were averaged with a minmax rejection. The lowest and highest value of each pixel were, therefore, removed and the remainder averaged. The mean bias was then subtracted from the raw science image.
2. A large number of cosmic rays affected the longest exposures necessary to obtain sufficient signal-to-noise ratio for the faintest cluster member candidates. We have employed a program using the convolution with a Laplacian kernel (van Dokkum 2001)³ to remove cosmic rays because none of the IRAF task was found efficient in this respect.
3. We have averaged the five dome flat-fields taken before the beginning of the night with a minmax rejection. To correct for the wavelength dependence of the flat-field, we have fit a high-order polynomial along the dispersion axis of the flat-field. Then, we have divided the bias-corrected science frame by the normalised response function of the flat-field.
4. We have estimated the sky background around the spectrum by choosing two intervals to the left and to the right of the spectrum along the dispersion axis. The resulting image was a two-dimensional sky-subtracted spectrum of the object.
5. The centre of the spectrum, the width of the aperture, and the intervals for sky subtraction were chosen interactively until a satisfactory result was achieved. Finally, we have fit the trace of the spectrum by a cubic spline to extract the one-dimensional spectrum of the target.
6. A linear fit of the wavelength as a function of the pixel number was achieved by identifying helium and neon lines. For the Twin spectrograph, the blue wavelength corresponds to high number pixels. Three or four good lines were initially selected to obtain a first guess of the linear fit. The fit was refined using a larger number of lines with positions available in the IRAF database. Any discrepant line was deleted to optimise the fit.
7. The linear fit of the wavelength as a function of the pixel was then used to assign the dispersion solution to the science target. The starting and ending wavelengths as well as the wavelength per pixel were computed and should obviously match the parameters provided in the user manual of the instrument.
8. The flux calibration of the science spectrum required observations of spectrophotometric standard stars. The flux of the calibrated spectra is expressed in $\text{erg cm}^{-2} \text{s}^{-1} \text{\AA}^{-1}$. We have applied the same data reduction procedure to the standard stars and the science targets. However, two additional steps were required to correct for the non-uniform response of the detector over the whole wavelength range. First, the flux of the standard star was integrated over 50 Å-wide bandpasses and corrected for exposure time. Second, the sensitivity function of the detector as a function of wavelength was computed taking into account the extinction.

Then, we have applied the fit of the sensitivity function to the dispersion-corrected one-dimensional spectrum of the target. Finally, we converted the spectrum into an ascii file with flux versus wavelength for further analysis. We have normalised the spectra at 7500 Å. Figure 3.12 displays *only* the objects whose spectroscopic results confirmed their status of bona-fide cluster member candidates.

³<http://www.astro.yale.edu/dokkum/lacosmic/>

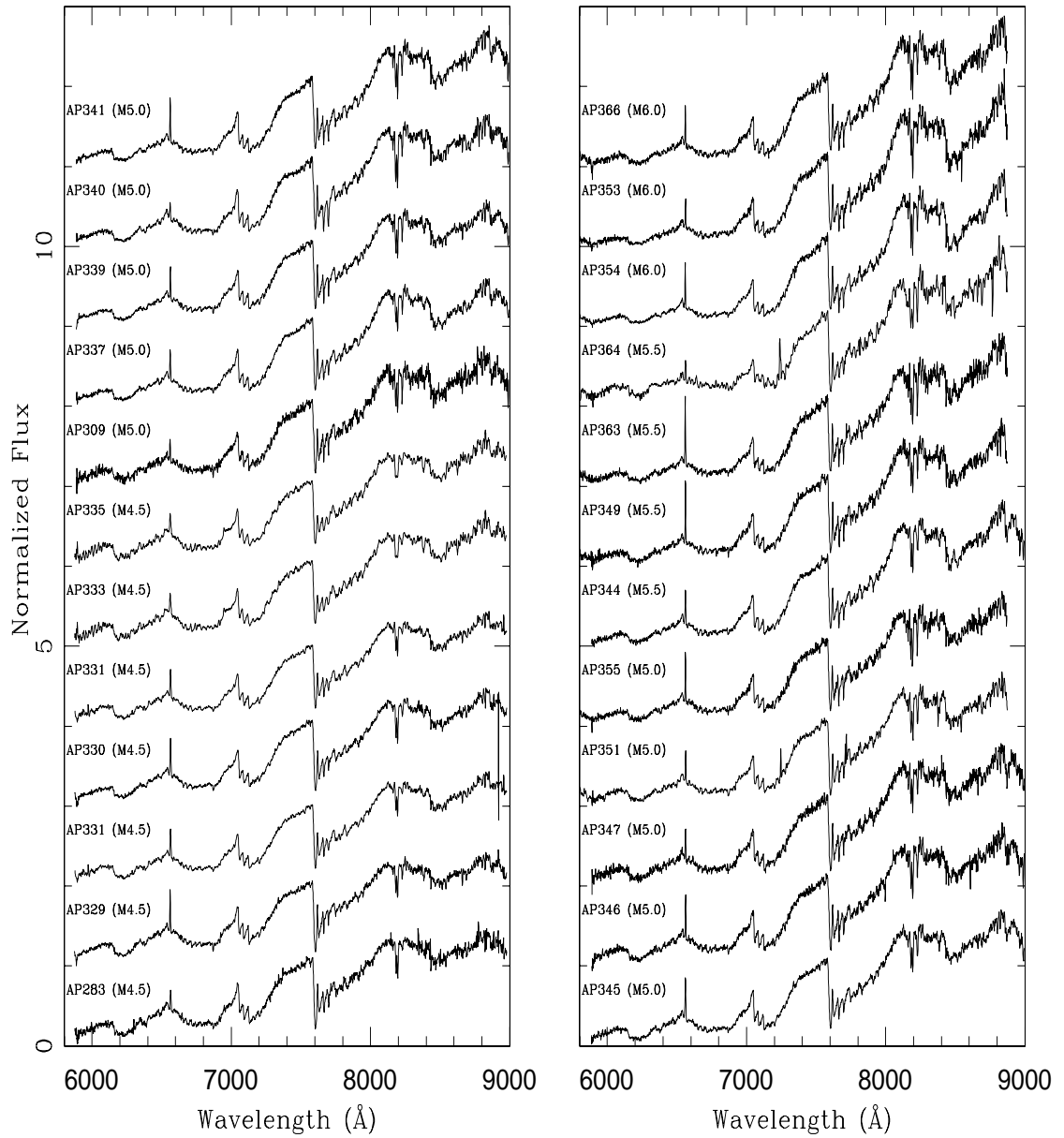


Figure 3.12: Spectra of the 24 objects listed in Table 3.3 apart from the giants classified as a non-member and the new infrared-selected objects. The spectral types quoted into brackets after the name of the target range from M4.5 to M6.0 with a typical uncertainty of order half a subclass. Typical features of M dwarfs are clearly seen on the spectra, including TiO and VO absorption broad bands. All targets exhibit H α in emission at 6563 Å. An arbitrary constant has been added to each spectrum for clarity.

3.6.3 Analysis of the optical spectra

We have observed spectroscopically a subsample of cluster member candidates in α Per containing 24 probable members, 1 possible member, and 4 non-members taken from the candidate list in Barrado y Navascués et al. (2002). The objects are listed in Table 3.3 along with their spectroscopic results. We have obtained optical (5800–8800 Å) spectroscopy with the Twin spectrograph of *all* probable members spanning $I = 15.0$ – 17.0 , but four. Among the remaining four objects, we have taken optical spectra of two of them with the Keck telescope. Additionally, we have also carried out optical spectroscopy of *all* probable members spanning $I = 17.0$ – 18.0 with Keck. We will focus here on the optical spectroscopy conducted with the Twin spectrograph, including the nine candidates (AP329, AP332, AP309, AP339, AP349, AP344, AP353, AP364, and AP366) common to the near-infrared survey.

We have assigned a spectral type to each individual confirmed member with an uncertainty of half a subclass, according to the M dwarf classification schemes defined by Kirkpatrick et al. (1999b) and Martín et al. (1999b). The spectra of the non-members are consistent with giant spectra, confirming that these objects do not belong to the cluster. The only possible member candidate observed in the sample exhibits a similar spectrum and was, therefore, rejected as cluster member.

We have applied the “recipe” presented in § 1.4 to classify each probable cluster member. We have computed spectral indices for each individual target (Table 3.3), including TiO5 (Reid et al. 1995), VO-a (Kirkpatrick et al. 1999b), and PC3 (Martín et al. 1999b)⁴.

The inferred spectral types from each index were generally consistent within a subclass. However, we have noticed some differences and favoured the direct comparison with spectral templates of well-known M dwarfs. The spectral indices quoted above were defined to classify field dwarfs which have larger gravity than young cluster members in α Per.

To derive a self-consistent classification and not rely solely on spectral indices, we have compared each individual target with spectra of template M dwarfs of similar spectral types, including 2MASS J2300189+121024, 2MASS J0244463+153531A&B, and 2MASS J0242252+134313 (Kirkpatrick et al. 1999b), as well as 2MASS J0435490+153720 (Gizis & Reid 1999), with spectral types M4.5, M5.0, M5.5, M6.5, and M6.0, respectively. In addition, due to possible differences in telescope/instrument configurations and detector sensitivities, we have observed comparison objects with known spectral types, including GJ251 (M3.0), LHS1417 (M4.0), LHS0168 (M5.0), LHS1326 (M6.0), and LHS0248 (M6.5) with the same instrument set-up. The three different spectral type estimates yielded consistent results with uncertainties of half a subclass (last column in Table 3.3 and Figure 3.12).

Finally, Table 3.3 shows that the brighter the cluster members are, the earlier is the spectral type. Furthermore, we have found the flux measured in the spectra of the targets consistent with the I_c magnitudes from the wide-field optical survey.

The objects displayed in Figure 3.12 span spectral types M4–M6, M6.5 being considered as the stellar/substellar border in young open clusters. All probable members in α Per, followed-up spectroscopically, are, therefore, stellar components of the cluster. According to the NextGen isochrones (Baraffe et al. 1998), the cluster members have masses ranging from $0.40\,\text{M}_\odot$ to $0.12\,\text{M}_\odot$, assuming a distance of 182 pc and an age of 90 Myr for α Per.

⁴The definition of the three spectral indices is given in Chapter 1 in Table 1.2

The H α emission line at 6563 Å constitutes a further criterion to ascertain the membership of the selected cluster candidates as it is a sign of youth. This feature is clearly detected in *all* 24 probable candidates from Barrado y Navascués et al. (2002) (Figure 3.12). The H α equivalent widths range from 4.0 to 15.0 Å and are consistent with previous measurements in α Per obtained by Zapatero Osorio et al. (1996), Prosser (1992, 1994), and Stauffer et al. (1999) in the M3–M6 spectral type range. However, the sample contains too few objects to probe the turnover around M3–M4 in α Per (Zapatero Osorio et al. 1996) caused by the transition from radiative to convective cores occurring at 0.3–0.2 M_{\odot} , regardless of the age (D’Antona & Mazzitelli 1994). This turnover was detected in the Pleiades cluster as well (Stauffer et al. 1994b; Hodgkin et al. 1995). Figure 3.13 shows H α equivalent widths versus spectral types for previous α Per members (open triangles) and from our spectroscopy (filled hexagons).

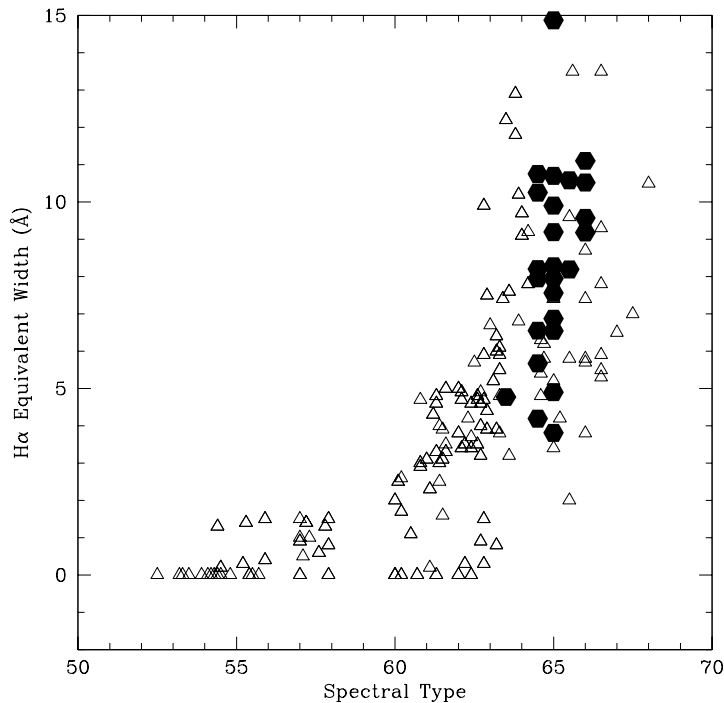


Figure 3.13: H α equivalent widths versus spectral type for all spectroscopically confirmed cluster members in the α Per cluster. Open triangles indicate members listed in Prosser (1992, 1994) and Stauffer et al. (1999). Our H α equivalent widths are indicated with filled hexagons and are consistent with measurements of cluster members with comparable spectral types. Values of 50, 60, and 70 given on the x-axis correspond to K0, M0, and L0 spectral types, respectively.

our sample of proper motion candidates (§ 2.4). Optical spectroscopy for field M dwarfs spanning M4–M6 shows that about half of them exhibit H α with equivalent widths as large as those detected in α Per members.

Moreover, H α equivalent widths measured in proper motion M4–M8 cluster members in the Pleiades is typically greater than 3 Å. Although arbitrary, the 3 Å value reflects the envelope of equivalent widths in the Pleiades (Hodgkin et al. 1995).

The detection of the H α emission line in all probable cluster member candidates as well as the arguments presented here add support to the belief that there are indeed members of the cluster.

To further constrain the membership of the photometrically-selected candidates, we have computed the strengths of gravity-sensitive features, including the K I and Na I doublets at 7665/7699 Å and 8183/8195 Å, respectively (task *splot* in IRAF; Table 3.3). Young pre-main-sequence candidates are younger than field dwarfs and should, therefore, exhibit lower gravity. The equivalent widths of the gravity features Na I and K I versus spectral types are shown in Figure 3.14 for all probable member candidates observed spectroscopically.

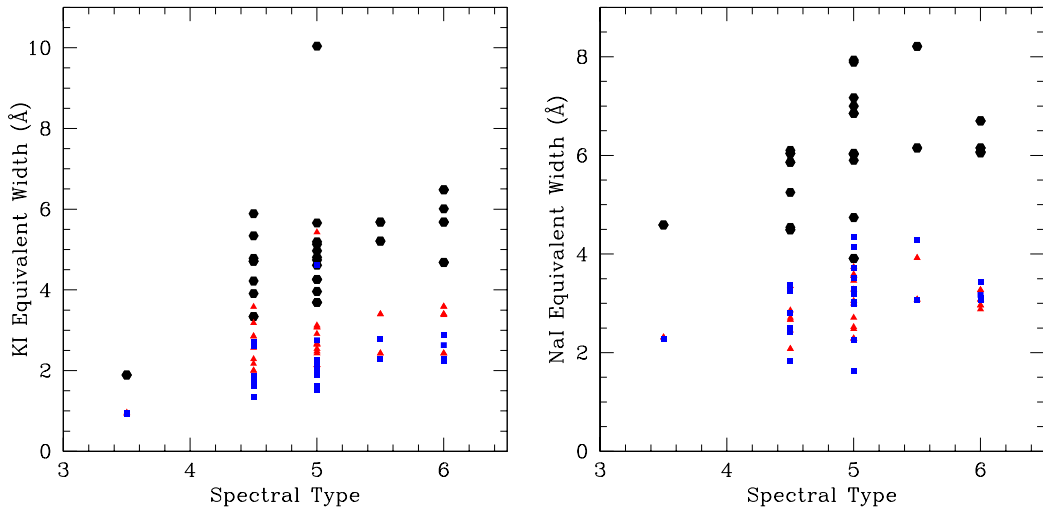


Figure 3.14: Equivalent widths (in Å) of gravity-sensitive absorption doublets (K I at 7665/7699 Å on the left panel and Na I at 8183/8195 Å on the right panel) for all spectroscopically confirmed cluster member in the α Per cluster. The hexagons indicate the sum of the equivalent widths of both lines whereas the triangles and the squares indicate the equivalent widths of the first and second line, respectively. Values of 3, 4, 5, and 6 on the x-axis correspond to spectral types of M3, M4, M5, and M6, respectively.

The equivalent width of the first absorption line of the K I doublet exhibit stronger equivalent widths than the second line while this trend is not obvious for the Na I doublet (Figure 2.4). Those measurements are comparable to results for the sample of field M dwarfs in the proper motion survey (Figure 2.4). The equivalent widths of the K I doublet in α Per are slightly smaller than for field M dwarfs of similar spectral types. Similarly, a difference in the Na I doublet equivalent widths between α Per and field dwarfs is observed when comparing Figure 2.4 and Figure 3.14

(note the difference in the Y-axis scale), indicative of a younger age. The differences are nevertheless small and might simply reflect the fact that the gravity difference in 100 Myr-old cluster members and old (1–5 Gyr) field dwarfs is less than 0.2 dex, according to the NextGen models (Baraffe et al. 1998). Our results regarding the equivalent widths of the Na I doublet are consistent with a total equivalent width of order 6 Å measured in the Pleiades (Martín et al. 1996). Our measurements are also larger than those in σ Orionis (Béjar et al. 1999).

As a whole, gravity measurements add support to the belief that those objects are genuine members of the α Per cluster.

The detection of the lithium absorption at 6708 Å is not expected as all candidates observed spectroscopically are stellar members of α Per.

We have obtained optical spectroscopy of a subsample of four infrared-selected member candidates in α Per (AP414, AP415, AP416, and AP418) to test the optical-to-infrared selection method presented in § 3.5. We have classified those objects according to their spectra as follows:

- One object (AP418) is clearly a non-member of the cluster due to its spectra exhibiting H α and NaID in absorption as well as a proper motion inconsistent with the α Per cluster.
- We rejected two other candidates, AP414 and AP415, as possible members due to the non-detection of the H α emission line and fluxes inconsistent with membership. They are likely contaminating field dwarfs with a spectral type of $M3.5 \pm 0.5$.
- The last object, AP416, exhibits H α although with an equivalent width weaker than those measured for the cluster members, but still consistent with previous studies in the α Per cluster (Figure 3.13). However, we would consider this object as a non-member because the spectral type ($M3.5$) is inconsistent with the measured I_c magnitude (Table 3.3).

To summarise, the fact that the four infrared-selected cluster member candidates in α Per are likely contaminating field dwarfs do not add strong support to the efficiency of the optical-to-infrared selection method in selecting cluster member candidates in a low galactic latitude open cluster as α Per.

The spectroscopy of the optically-selected candidates confirmed their membership. The probable candidates *all* exhibit H α and have fluxes consistent with their spectral types. The previously classified non-members are, indeed, non-members as is the only possible members observed spectroscopically. Hence, the optical survey and the additional near-infrared imaging appear as excellent discriminant between cluster members and contaminants.

On the contrary, the optical-infrared survey alone appears less adequate at selecting cluster members as the contamination among selected objects is higher than in the optical. The large majority of candidates selected from the ($K', I_c - K'$) colour-magnitude diagram are reddened background giants ($\sim 70\%$). Half of the remainder were previously considered as probable members while the rest awaits for spectroscopic follow-up observations. As a whole, the contamination lies in the range 70–85 %, twice larger than the optical selection (28–40 %; Barrado y Navascués et al. 2002). Despite the low statistics among infrared-selected cluster members with spectroscopic follow-up, none of the new candidates are bona-fide cluster members. We strongly emphasise the use of the K' -band as a tool to constrain the optical selection. However, one should be cautious using the optical-infrared ($K', I_c - K'$) colour-magnitude diagram as a prime and sole criterion to

extract cluster members, in agreement with the Pleiades surveys focusing on deep optical surveys (R , I , and Z) to search for very low-mass stars and brown dwarfs. This procedure avoids large optical-to-infrared colours such as $I-K$, where reddened field dwarfs and distant background giants exhibit similar colours as young pre-main sequence stars.

3.7 Comparison of the α Per IMF with other open clusters

The new results from the optical spectroscopy of all probable members spanning $I_c = 15.0 - 17.0$ have confirmed their cluster membership status. Thus, we are in a position to assert that the mass function derived for the probable cluster members in α Per (bottom IMF in Figure 3.5) is the true cluster mass function according to our spectroscopic study. Despite the small number of possible members and non-members followed-up spectroscopically (5 objects out 38 extracted by the optical survey), those objects exhibit spectra inconsistent with cluster membership. These results were expected with regard to objects classified as non-members but the question remained open for the possible members. To summarise, the slope of the α Per open cluster remains $\alpha = 0.59 \pm 0.05$ (when expressed as the mass spectrum) in the $0.30 - 0.05 M_\odot$ mass range where the photometric data are complete.

The Pleiades is the best studied young open cluster with a large number of photometrically-selected candidates being confirmed spectroscopically. Although most estimates of the index of the Pleiades mass function are not derived from a homogeneous and complete sample of spectroscopic members, power law indices (when expressed as the mass spectrum) agree within the uncertainties. Martín et al. (1998) derived $\alpha = 1.0 \pm 0.5$ in the $0.40 - 0.045 M_\odot$ mass range based on a deep survey initiated by Zapatero Osorio et al. (1997b). Tej et al. (2002) estimated $\alpha = 0.5 \pm 0.2$ from 0.50 to $0.055 M_\odot$ based on a pure statistical approach involving 2MASS and GSC databases. Dobbie et al. (2002) derived $\alpha = 0.8 \pm 0.2$ based on a deep optical photometric survey down to $0.040 M_\odot$. Finally, Moraux et al. (2003) inferred $\alpha = 0.60 \pm 0.11$ over the $0.48 - 0.03 M_\odot$ mass range from a deep (I , Z) survey complementing the (R , I) survey by Bouvier et al. (1998).

All the results from the Pleiades indicate an α index spanning $0.5 - 1.0$ between 0.5 and 0.030 solar masses, in close agreement with the α Per estimate. Similar results are found in the Trapezium Cluster (Muench et al. 2002), in IC348 (Luhman et al. 2000), and in σ Orionis (Béjar et al. 2001), suggesting that the shape of the mass function in this mass range holds from few Myr up to few hundreds of Myr.

3.8 Conclusions on α Per and future plans

We have carried out a wide-field near-infrared (K' -band) survey of a 0.70 square degree area in the α Per cluster. Combining the new infrared photometry with existing optical (R_c and I_c) imaging, we have extracted a total of 198 new cluster member candidates based on their location in the optical-to-infrared ($K', I_c - K'$) colour-magnitude diagram. However, the position of these new candidates in the colour-colour diagram revealed that about 80 % of them are contaminants, including reddened field dwarfs and a large number of background giants due to the low galactic latitude of the cluster. The optical ($I_c, (R-I)_c$) colour-magnitude diagram shows that the new infrared-selected candidates define a bluer sequence than previous probable members in α Per but remain bona-fide cluster members. Among the new candidates, we have unveiled four new brown

dwarf candidates.

Additional optical (5800–8800 Å) spectroscopy of four infrared-selected cluster member candidates has revealed that their spectral types and $H\alpha$ equivalent widths are inconsistent with cluster membership. About 40 new infrared-selected remain as probable cluster members, including 18 objects already classified as such by Barrado y Navascués et al. (2002). Their optical and optical-to-infrared colours are consistent with membership but spectroscopic confirmation is lacking.

We have also presented moderate-resolution ($R \sim 2000$) optical (5800–8800 Å) spectroscopy of 29 candidates extracted by Barrado y Navascués et al. (2002) with the Twin spectrograph mounted on the Calar Alto 3.5-m telescope. The sample contains twenty-four probable cluster member candidates, one possible member, and the remainder were classified as non-members. All probable members have spectral types, $H\alpha$ equivalent widths, and gravity measurements consistent with cluster membership. The other candidates are clearly non-members with respect to their spectra. All probable members spanning $I_c = 15.0$ –17.0 in α Per, but four, have been spectroscopically followed-up. Their spectral types range from M4 to M6 and their masses from 0.40 to $0.12 M_\odot$.

The α Per mass function is, therefore, well represented by the probable mass function derived by Barrado y Navascués et al. (2002) and approximated by a power law with a slope of 0.59 over the 0.30 – $0.05 M_\odot$ mass range, when expressed as the power spectrum. This mass function is confirmed down to $0.12 M_\odot$ with our results based on *photometric and spectroscopic* membership criteria.

The optical spectroscopy has demonstrated that the optical (R and I) photometry with near-infrared follow-up imaging constitutes a good discriminant between field stars and young cluster members. More recently, deep (I and Z) surveys have proven very efficient to detect lower mass brown dwarfs in open clusters due to the saturation of the R – I colours at late spectral types.

The near-infrared wide-field survey combined with existing optical photometry is hampered by higher contamination by background objects than purely optical surveys. A combination of optical and near-infrared imaging is nevertheless mandatory to disentangle cluster members from contaminants.

We would like to stress here some issues related to the future deep near-infrared surveys planned within the framework of the UKIDSS and CFHT consortia. Both surveys aim at surveying large area in well-known open clusters, including α Per. On the one hand, such deep surveys are required to supersede the 2MASS database and enable cross-correlation with faint objects unveiled in on-going deep optical surveys. On the other hand, these surveys would be optimised by including one (or two) optical filters to reveal less massive brown dwarfs in clusters. Near-infrared surveys remain, however, extremely efficient in star-forming regions where the high extinction hampers optical observations.

Chapter 4

The intermediate-age open cluster Collinder 359

Young open clusters are ideal regions to place good constraints on the time spread of star formation for two reasons. First, cluster members less massive than about $0.8 M_{\odot}$ are displaced well above the ZAMS, making their identification easier. Second, low-mass stars and brown dwarfs remain bound to the cluster due to the limited dynamical evolution.

To identify complete and homogeneous samples of young very low-mass stars and brown dwarfs in clusters over large areas, a Canada-France-Hawaii Key Programme was initiated within the framework of our EC Research Training Network to survey about 80 square degrees in the I and z filters down to completeness limits of 22.0 in star-forming regions, open clusters and in the Hyades. One part of the project focused on five pre-main-sequence open clusters, including IC 4665, NGC 2232, Collinder 70, Stephenson 1, and Collinder 359. The analysis of the optical images yielded several hundreds bona-fide member candidates in each cluster down into the substellar regime, some of them being already followed-up in the near-infrared to weed out contaminating objects.

This chapter, devoted to the pre-main-sequence open cluster Collinder 359, is organised as follows. The CFHT Key Programme is presented in § 4.1 along with the target list and the main goals. A literature review of the present knowledge of Collinder 359 is given in § 4.2. The wide-field optical (I, z) observations of a 1.6 square degree area in Collinder 359 are detailed in § 4.3.1. The data reduction of the optical images is detailed § 4.3.2 and the extraction of the photometry described in § 4.3.3. The optical ($I, I-z$) colour-magnitude diagram is drawn § 4.3.4 and the cluster member candidates selection procedure described in § 4.3.5. The near-infrared follow-up of the optically-selected cluster member candidates in Collinder 359 is presented in § 4.4. The cluster luminosity and mass functions are derived in § 4.5 and § 4.6, respectively, including a discussion on the uncertainties on the age and distance of the cluster. Conclusions of the study of Collinder 359 and future projects are presented in § 4.7.

The data reduction and analysis of the CFH12K results from a large collaboration involving several teams within the European Network. The work described in this chapter has been mostly done by myself and will part of a forthcoming paper. I will continue to use “we” and not “I” to describe the results on Collinder 359 and to keep with the general principle of this thesis.

4.1 The CFHT Key Programme

4.1.1 Description of the CFHT Key Programme

A Canada-France-Hawaii Telescope (hereafter CFHT) Key Programme (30 nights over 2 years) centred on wide-field optical imaging of young, intermediate-age, and older open clusters (Bouvier, PI) was carried out within the framework of the European Research Training Network “The Formation and Evolution of Young Stellar Clusters” (McCaughrean, coordinator) to examine the sensitivity of the low-mass stellar and substellar IMF to time and environment.

The survey was conducted with a large-CCD mosaic camera (CFH12K) in the I and z filters down to detection and completeness limits of $I = 24.0$ and 22.0 , respectively, covering a total of 80 square degrees in a variety of environment, from star-forming regions (Serpens, Taurus, Ophiuchus, and Perseus), to pre-main-sequence open clusters (IC 4665, Collinder 359, Steph 1, Collinder 70, and NGC 2232), to the older Hyades. All regions are listed in Table 4.1 along with their coordinates (J2000), ages in Myr, distances in parsecs and diameters. The area surveyed in the optical with the CFH12K camera (and MegaCam when usable) are given in the last column of Table 4.1.

Table 4.1: List of star-forming regions (SFR), pre-main-sequence open clusters (PMS), and older clusters (OC) targeted within the framework of the CFHT Key Programme. Right ascension and declination (in J2000) are given in columns 3 and 4, respectively. Ages, distances, and diameters are listed in columns 5–7 (Open Star Cluster database and Lyngå 1987). The area surveyed in each cluster with the CFH12K camera is provided in the last column.

	Target	R.A.	Dec	Age	Distance	Diameter	Surv. Area
SFR	Perseus	03:35:00	+30:00:00	≤ 3 Myr	300 pc	—	6.5 deg ²
	Taurus	04:30:00	+20:00:00	≤ 3 Myr	140 pc	—	7.8 deg ²
	Ophiuchus	16:00:00	-25:00:00	≤ 3 Myr	145 pc	—	6.5 deg ²
	Serpens	18:30:00	+01:00:00	≤ 3 Myr	260 pc	—	5.9 deg ²
PMS	Collinder 70	05:33:00	-01:00:00	10 Myr	387 pc	140'	4.0 deg ²
	NGC 2232	06:24:00	-04:00:00	53 Myr	324 pc	45'	4.0 deg ²
	IC 4665	17:43:00	+05:00:00	43 Myr	352 pc	70'	4.2 deg ²
	Collinder 359	17:58:00	+02:00:00	32 Myr	249 pc	240'	1.6 deg ²
	Stephenson 1	18:51:00	+37:00:00	53 Myr	390 pc	20'	0.65 deg ²
OC	Hyades	04:24:00	+14:45:00	600 Myr	46 pc	12 deg.	17.3 deg ²

4.1.2 The choice of the optical filters

We have chosen to carry out the wide-field optical observations in the I and z filters mainly to optimise the search for low-mass stars and brown dwarfs in young clusters. This choice was also motivated by the results of 6.4 deg² imaging survey of the Pleiades with the CFH12K in the I - and z -bands (Moraux et al. 2003) conducted with the same telescope/instrument configuration. New brown dwarf candidates of the cluster were revealed and the cluster mass function, derived

from the previous study in the Pleiades by Bouvier et al. (1998), extended to $30 M_{Jup}$.

1. The sky background in (I,z) passbands is dominated by OH emission and not by the moon. The observations of Collinder 359 were carried out with a lunar phase of about 50 %.
2. The $I-J$ colours get redder towards low-mass cluster members, providing a good discriminant to separate the cluster sequence from field stars (Zapatero Osorio et al. 2000). Hence, we expect a similar behaviour for the $I-z$ colours.
3. The $I-z$ colours were found to be a good discriminant to weed out field stars from low-mass cluster members in the Pleiades (Cossburn et al. 1997; Zapatero Osorio et al. 1999; Moraux et al. 2003). We expect a similar trend, perhaps enhanced for younger pre-main-sequence objects than the Pleiades due to the redder colours.
4. Young brown dwarfs get redder in $R-I$ colours implying very faint R magnitudes which greatly hamper the detection of the least massive components of the cluster. Much longer exposure times in the R filter than in I are, therefore, required to compensate for this effect. To the contrary, we have achieved similar completeness and detection limits of 24.0 and 22.0, respectively, both in I - and z -bands with comparable exposure times of 300 sec and 360 sec in I and z .

4.1.3 Aims of the CFHT Key Programme

The main goals of CFHT Key Programme was to address the most pressing issues:

- How do brown dwarfs form and at which rate?
- What is the mass distribution of low-mass stars and brown dwarfs?
- Is there a lower mass limit to the Initial Mass Function?
- Is the Initial Mass Function sensitive to the environment?
- How do substellar objects evolve with time?

As a second step after membership assessment of the photometrically-selected cluster candidates, this large programme will aim at studying the evolution and properties of stellar and substellar objects in various environments:

- Test the evolutionary tracks using 10–50 Myr old open clusters.
- Age and mass dependence of the coronal and chromospheric activity of very low-mass stars.
- Mass dependence of the lithium depletion in very low-mass stars and brown dwarfs.
- Distribution of rotation rates as a function of mass.
- Distribution of rotational velocities of very low-mass stars as a function of age.
- Disk frequency and their lifetime.
- Distribution of wide binaries as a function of mass.

4.1.4 Selection of the pre-main-sequence open clusters

The selection of the five pre-main-sequence open clusters made use of the Open Cluster Database¹. The following criteria were applied to select the most suitable open clusters to answer the present issues within the framework of the CFHT Key Programme.

- Clusters with an age between 10 and 50 Myr
- Clusters less distant than 500 pc to be able probe the substellar regime
- Northern Hemisphere open clusters observable with the CFHT at Mauna Kea, Hawai'i
- A lower limit of 10° in galactic latitude to avoid significant contamination

Besides well-known open clusters such as the Pleiades, α Per, IC2391, IC2602, among others, five pre-main-sequence clusters satisfied the criteria listed above. The clusters were IC 4665, Stephenson 1, Collinder 70, NGC 2232, and Collinder 359, the latter constitutes the core of this chapter whose results will be published in a forthcoming paper. The main characteristics of the five selected open clusters are provided in Table 4.1, including coordinates, age, distances, and estimated diameters.

4.2 Literature on the open cluster Collinder 359

Collinder 359 (=Melotte 186) was selected as a 30 Myr open cluster at a distance of 250 pc, from a search in the Open Star Cluster webpage. The cluster is located in the Ophiuchus constellation around the star 67 Oph (Figure 4.1). The equatorial and galactic coordinates (J2000) of the cluster centre are: ($18^{\text{h}}01^{\text{m}}06\text{s}$, $+02^\circ 54'$) and ($29.7, +12.5$), respectively.

Collinder 359 was relatively unstudied and very little literature is available about the cluster. No deep optical survey had been carried out around the cluster centre, although several papers mention the cluster in passing. However, one needs to be polyglot to deal with papers in different languages such as French, English, and Russian! I will review the current knowledge on this cluster by summarising the content of major articles.

- Collinder 359 (=Melotte 186) was first seen on the Franklin-Adams Charts Plates and classified as a coarse cluster by Melotte (1915) within the framework of his large catalogue of globular and open clusters. It was described it as *a large scattered group of bright stars around 67 Ophiuchi (= HD164353), covering an area of about 6 square degrees.*
- In a large catalogue of open clusters, Collinder (1931) described Collinder 359 as *a group of about 15 stars with no appreciable concentration on the sky and no well-defined outline.* Cluster stars appear brighter than the surrounding stars but no bright stars stand out from the others. The diameter of the cluster was estimated to $240'$ and dimensions of $5^\circ \times 3^\circ$ were mentioned. The cluster contains thirteen stars listed in Table 4.2 and shown as filled hexagons in Figure 4.2. Collinder (1931) provided the coordinates, V magnitudes, spectral types for all 13 stars and additional proper motion information when available. Isochrone fitting to the five early-B stars yielded photometric parallax of 0.0048 ($d = 209$ pc) while the

¹<http://www.seds.org/messier/open.html>

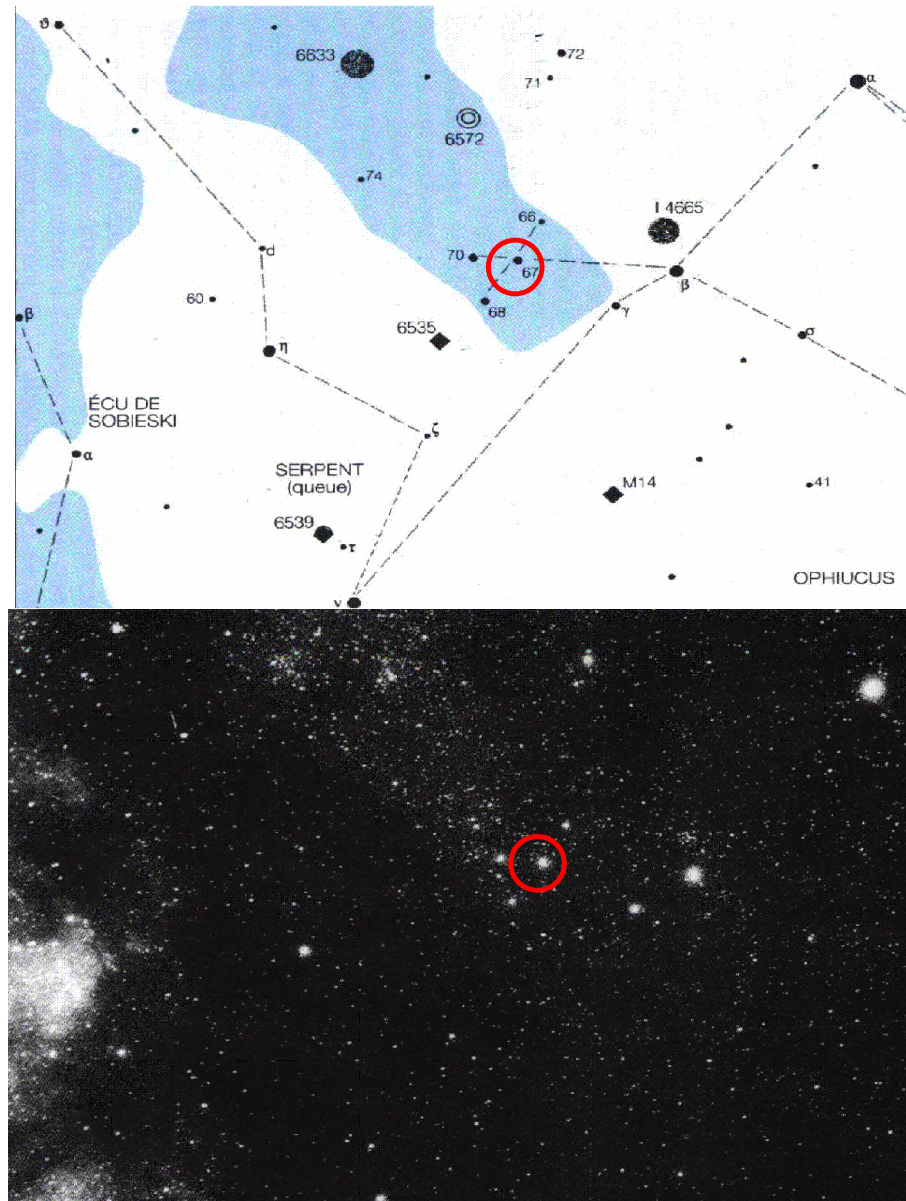


Figure 4.1: The upper panel is a schematic view of the location of the open cluster Collinder 359 (red circle) in the constellation of Ophiuchus, around the B5 supergiant, 67 Oph. The bright stars belonging to the constellation of Ophiuchus, Serpens and Scutum are marked with symbols representing their brightness. Other astronomical objects are indicated, including open clusters, globular clusters (diamonds), and planetary nebula (concentric circles). The lower panel is an image of the same region of the sky and at the same scale. *Courtesy: Astronomia.* For indication, the difference between α Oph and β Oph is about 2.1° and 8.0° in right ascension and declination, respectively. The difference between 67 Oph and 70 Oph is about 1.2° and $26'$ in right ascension and declination, respectively.

Table 4.2: This table lists the 13 bright stars within Collinder 359 as listed in Collinder (1931). Column 1 lists the running number of the member, column 2 gives the Henry Draper Catalogue number, columns 3 and 4 list the right ascension and the declination (in J2000), column 5 lists the spectral types Collinder (1931), columns 6, 7, and 8 lists the V magnitude and the $B-V$ and $U-B$ from Blanco et al. (1968), columns 9 and 10 list the $V-R$ and $R-I$, columns 11 and 12 list the proper motion of the object according to the SAO catalogue (1966). The membership of the object is given on the last column according to the discussion between Ruciński (1980) and Van't Veer (1980).

	HD	RA	Dec	SpT	V	$B-V$	$U-B$	$V-R$	$R-I$	μ_α	μ_δ	M?
1	166233	18 09 33.8	03 59 35	F2	5.72	+0.37	+0.02	0.22	0.21	+0.0360	-0.007	NM
2	168797	18 21 28.4	05 26 08	B5	6.16	-0.02	-0.64	0.00	0.01	+0.0105	-0.004	NM
3	164353	17 58 08.3	02 55 57	B5 Ib	3.96	+0.04	-0.63	0.06	0.03	-0.0015	-0.010	M
4	164352	18 00 41.7	03 08 57	B8	9.33	-0.01	-0.39	0.02	0.06	-0.0015	-0.002	M
5	164284	18 00 15.8	04 22 07	B3	4.70	-0.04	-0.86	0.10	0.08	+0.0000	-0.013	NM
6	164283	17 57 42.4	05 32 37	A0	9.10	+0.26	+0.19	0.16	0.21	+0.0075	-0.014	M
7	164096	17 59 34.6	02 30 16	A2	9.70	+0.20	+0.17	0.13	0.20	-0.0105	-0.006	M
8	164097	17 59 29.5	02 20 37	A2	8.54	+0.17	+0.15	0.12	0.15	-0.0060	+0.003	M
9	164432	18 00 52.8	06 16 05	B3	6.35	-0.08	-0.77	-0.01	-0.01	+0.0015	-0.003	M
10	164577	18 01 45.2	01 18 18	A2	4.43	+0.04	+0.05	0.04	0.01	+0.0090	-0.012	NM
11	165174	18 04 37.3	01 55 08	B3	6.14	-0.01	-0.98	0.03	0.03	-0.0045	-0.003	NM
12	163346	17 55 37.5	02 04 29	A3	6.78	+0.56	+0.36	0.37	0.40	-0.0030	+0.007	NM
13	161868	17 47 53.5	02 42 26	A0	3.74	+0.03	+0.14	0.01	0.00	-0.0240	-0.074	NM

fainter B8–A2 stars gave a mean parallax of 0.0035 ($d = 286$ pc). However, the membership of these objects was not well established as neither proper motion nor photometric studies were available in Collinder 359. One object, 67 Ophiuchi, is a supergiant member of the cluster with a spectral type of B5Ib (Humphreys 1970).

- Searching in the 1958 *General Catalogue of Variable Stars* based on open clusters catalogued by Collinder (1931), Trumpler (1930), and others, Sahade & Frieboes (1960) extracted 10 W UMa-type stars within three cluster radii. A few years later, Sahade & Berón Dàvila (1963) concluded that none of the eclipsing binaries within the cluster were probable members. In a total of 26 eclipsing variables, 12 objects were classified as possible members while the remainder were unlikely to be members of Collinder 359.
- Blanco et al. (1968) compiled a huge photoelectric catalogue of more than 20,000 stars in the Galaxy in the UBV broad-band filters based on measurements extracted from the literature. The 13 stars mentioned by Collinder (1931) are included in this catalogue. The UBV magnitudes given in Table 4.2 are averaged values of all measurements available for those stars from the literature.
- The only age estimate of the cluster originates from the work by Wielen (1971) and Abt & Cardona (1983). The former derived an age ranging from 20 to 50 Myr with a mean value of 30 Myr using isochrone fitting based on three-colour photometry available in large catalogues of open clusters (Becker & Fenkart 1971). Abt & Cardona (1983) studied the distribution of Ap stars in open clusters as a function of age. A trend of older clusters having a larger number of Ap stars was noticed. Abt & Cardona (1983) put an upper limit of 30 Myr on the age of Collinder 359, assuming that 67 Oph is a member of the cluster, in agreement with the former determination.

- Akhundova (1971)² selected member candidates in Collinder 359 based on their proper motions. Using the magnitude versus spectral type relationship, and after rejection of likely non-members, Akhundova (1971) derived a distance of 350 pc and estimated the absorption to $A_V = 1.4$ mag.
- A discussion took place between Ruciński (1980) and Van't-Veer (1980) regarding the existence of W UMa-type systems in Collinder 359. While Ruciński (1980) noted that most of the stars listed by Collinder (1931) might actually be field stars, Van't-Veer (1980) argued the contrary based on homogeneous conversion of spectral types into colours. Van't-Veer (1980) found consistent distance moduli estimates from the B3 and A0 group of stars based on the $(M_V, B-V)$ colour-magnitude diagram. A few years later, Ruciński (1987) confirmed the results of Van't-Veer (1980) and concluded that stars n° 3, 4, 6, 7, 8, and 9 (Table 4.2) are bona-fide cluster members based on $BVRI$ CCD photometry. A distance modulus of 8.2 mag (distance = 436 pc) was derived from the isochrone fitting of the possible members.
- The 5th edition of the Open Cluster Data Catalogue (Lyngå 1987)³ provides a distance of 200 pc and a diameter of 240' for Collinder 359. The former is based on the estimate from the Bochum-Strasbourg magnetic tape catalogue of open clusters. The latter is taken from the work of Collinder (1931). However, no age was mentioned for Collinder 359.
- Baumgardt et al. (2000) confirmed cluster members in Collinder 359 from photometry, radial velocity and *Hipparcos* measurements. A mean proper motion of 0.42 ± 0.47 mas/yr in right ascension and -7.86 ± 0.35 mas/yr in declination was estimated. Parallax measurements yielded distances ranging from 317 to 460 pc, in agreement with isochrone fitting (Ruciński 1987). The parallax measurement from the supergiant 67 Oph led to a distance of 435^{+220}_{-110} pc (Perryman et al. 1997), consistent with the study by Baumgardt et al. (2000). Of the 13 possible members (Collinder 1931), only two share a common proper motion (stars n° 3 and 9; Table 4.2). Three other *Hipparcos* stars may be additional cluster members while the remaining objects were excluded as members.
- *Hipparcos* trigonometric parallaxes of five stars in Collinder 359 were used to derive photometric and spectroscopic distances, yielding estimates between 260 to 280 pc (Loktin & Beshenov 2001)⁴ with typical errors of about 20 pc.
- Combining the *Hipparcos* and Tycho 2 catalogues, a list of about 100 possible cluster members were extracted by Kharchenko et al. (2004, personal communication)⁵ based on their location within the cluster area and their proper motions. The position of these objects in the $(V, B-V)$ colour-magnitude diagram yielded a distance of 650 pc from isochrone fitting. The core and corona radii of the cluster were estimated to 0.4 and 1.1 degree, respectively.

To summarise, the current knowledge of Collinder 359 based on the available literature suggests an age of 30 Myr and a distance between 200 pc and 650 pc with a mean value of approximately 400 pc.

²This paper is in Russian and is not available at the ADS webpage

³The full catalogue can be accessed through the Centre de Données astronomiques de Strasbourg

⁴The data of the five stars were lost after the death of one of the author (A.V. Loktin, personal communication)

⁵Nina Kharchenko and Anatoly Piskunov visited our group at the AIP for a few months and kindly provided me with their results on Collinder 359 prior to submission

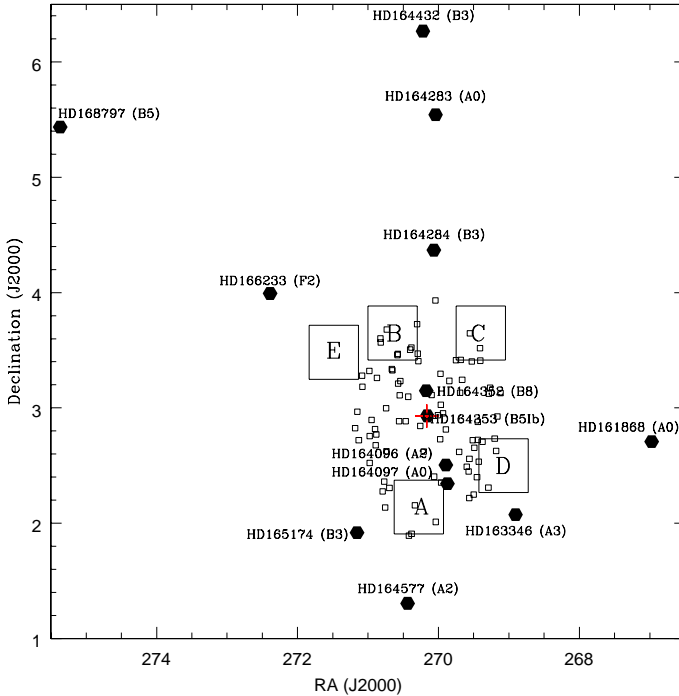


Figure 4.2: Location of the five CFH12K fields-of-view (A, B, C, D, and E) shown as boxes within the cluster area defined by the Open Cluster webpage. The 13 possible cluster members listed by Collinder (1931) are displayed as filled hexagons (Table 4.2). Their names and spectral types are provided as well. The open squares are the possible cluster members used for isochrone fitting by Kharchenko et al. (2004; personal communication), yielding a distance of 650 pc.

4.3 The wide-field optical survey of Collinder 359

We initiated a wide-field optical survey in the I and z filters down to a detection limit of 24.0 to study the very low-mass stars and brown dwarfs in the pre-main-sequence open cluster, Collinder 359.

4.3.1 The CFH12K wide-field optical observations

Five CFH12K frames were obtained on 18 and 20 June 2002 in Collinder 359 in the I and z filters, covering a total area of 1.6 square degrees in the cluster (Table 4.3). Figure 4.2 displays the location of the five CFH12K fields-of-view within the cluster area. Thirteen possible members as listed by Collinder (1931) (filled hexagons) are included as well. The CFH12K frames were chosen to avoid bright cluster members.

Fields A, B, C, and D were obtained on 18 June 2002 under photometric conditions with seeing ~ 0.8 arcsec. The remainder field, field E, was observed on 20 June 2002 under non-photometric conditions. The coordinates of the five CFH12K fields-of-view are provided in Table 4.3 along with the journal of the observations. Three sets of exposures were taken for each field-of-view:

short, medium, and long exposures with integration times of 2, 30, and about 900 seconds, respectively. The long exposures were exposed three times 300 and 360 seconds in the I and z filter, respectively, yielding detection limits of 24.0 in both passbands. Only one image was taken for the short and medium exposures, whereas three dithered positions were obtained for the long exposures, allowing rejection of bad pixels and removal of bad columns. The observations were scheduled in a queue mode so that the short, medium, and long exposures in the I -band were taken first, immediately followed by the short, medium, and long exposures in the z -band.

The CFH12K is a CCD mosaic camera dedicated to high-resolution wide-field imaging⁶. The camera comprises 12 chips of 4128×2080 pixels with a pixel scale of $0.206''$, yielding a field-of-view of $42' \times 28'$. Hence, no problem of undersampling was foreseen even during excellent conditions on Mauna Kea, which was the case for our observations. The cosmetic of the CFH12K mosaic was excellent with a total of 200 bad columns, most of them were concentrated on CCD05. The CCD06, CCD08, CCD09, CCD10, and CCD11 are entirely free of bad columns. The read-out time of the 12 chips was small (58 seconds). The camera has an excellent response in the red part of the spectrum as well, better than MegaCam, partly compensating for the smaller field-of-view.

Table 4.3: Coordinates of the five CFH12K fields-of-view along with the journal of observations obtained in the pre-main-sequence open cluster Collinder 359. The times of observations are given in UT and correspond to the beginning of the short exposures in the I -band.

Field	R.A. (J2000)	Dec (J2000)	Obs. Date	Time of obs. (UT)
A	18:01:06.60	+02:07:26.0	2002–06–18	08h19m15s
B	18:02:36.90	+03:37:52.7	2002–06–18	09h07m43s
C	17:57:36.90	+03:37:56.1	2002–06–18	09h56m07s
D	17:56:16.40	+02:29:46.4	2002–06–18	11h52m24s
E	18:05:55.70	+03:28:58.4	2002–06–20	12h29m20s

4.3.2 The data reduction of the wide-field optical images

The initial data reduction was provided by the Elixir pipeline and was mostly executed by David James at the CFHT Headquarters. Elixir is not a single program or package but a collection of programs, databases, and other tools related to the processing and evaluation of data obtained at the telescope. This pipeline includes bias subtraction, flat-fielding, correction for scattered light in the I and z bands, combining the dithered frames in case of long exposures, and astrometric solution provided in the header of the fits files. Standard stars were observed throughout the nights and were monitored constantly by the Elixir/Skyprobe tool to provide accurate zero-points.

The data reduction procedure to extract a catalogue of all objects from the reduced and stacked images processed by the pipeline was identical for each CFH12K field-of-view. The procedure presented in this paragraph is the result of intense discussions and close collaboration between the Grenoble, Potsdam, and Arcetri (EC network) teams to achieve a common and consistent data reduction for the wide-field optical images of the pre-main-sequence open clusters obtained within

⁶The camera is now superseded by MegaCam on the CFH 3.6-m telescope

the framework of the CFHT Key Programme. The major steps of the data reduction procedure are described below:

1. **Find the offsets between the I - and z - band images.** The telescope should theoretically point at the same position on the sky both in I - and z -bands as the coordinates provided by the user are identical for both filters. However, we have found shifts of order few pixels (2 to 5 pixels typically) between the I and z images. Three random stars were generally enough to correct for the differences in (x,y) coordinates between the I and z images. The task *imexamine* in IRAF was used to find the shifts. Tables 4.4, 4.5 and 4.6 provide the shifts (in integer pixels) of the z image relative to the I image. The CCD09 sometimes exhibits shifts larger than typically observed and affected fields A and C in the case of Collinder 359. The cause of this discrepancy is under investigation.
2. **Trim the I - and z - band images at [1:2048,1:4096].** Although not mandatory, the overscan regions in each chip in the I and z images were removed to avoid subsequent problem while running the extraction of the photometry with SExtractor. Indeed, some bright lines and columns affected the edges of the raw images, yielding overflow problems during the extraction of the photometry. Trimming was applied to both I and z images using the task *imcopy* in IRAF.
3. **Combine the I - and z - band images.** This step brings two advantages. First, the signal-to-noise ratio is increased by a factor of $\sqrt{2}$, allowing detection of fainter sources close to the detection limit ($I \sim z \sim 24.0$). Second, SExtractor has the ability to run the source detection on one image and extract the photometry on another image. Hence, the coordinates given in the final catalogues result from the combined (I,z) images whereas the photometry is extracted from the individual trimmed and shifted images. The astrometry of the faintest sources is thus more accurate than the astrometry from a single passband measurement.
4. **Run SExtractor and PSFEx.** Both packages were ran on each individual CCD of each CFH12K field-of-view for the short, medium, and long exposures in the I and z filters, respectively. A total of 180 (5 Fields \times 12 chips \times 3 exposures) catalogues were generated and contain coordinates (J2000), I and z magnitudes for each source, as well as other source parameters, including the ellipticity, FWHM, and quality of the photometry. A description of the parameters gathered in the final catalogues is given in the next section (§ 4.3.3).
5. **Apply zero points for photometric calibration.** To calibrate the photometry, the I and z magnitudes were corrected for the zero points listed on the Elixir webpage⁷. The CFH12K nominal zero points for the I - and z - bands are:

$$\begin{aligned} ZP(I) &= 26.184 \pm 0.023 \\ ZP(z) &= 25.329 \pm 0.031 \end{aligned}$$

These zero point values originates from the best quality set of standard stars observed with the CFH12K camera and collected over several years. However, we have applied a slight correction to the zero points to take into account the conditions of the night of the observations⁸. The corrections to the I and z filters were -0.0055 and +0.0575 for the first night

⁷<http://www.cfht.hawaii.edu/Instruments/Elixir/stds.2003.06.html>

⁸<http://www.cfht.hawaii.edu/cgi-bin/uncgi/elixir/skyprobe.pl?2002.06>

Table 4.4: Offsets (in integer pixels) between the I and z short exposure images.

CCD	Field A	Field B	Field C	Field D	Field E
00	(+5,+1)	(+4,+2)	(+4,+2)	(+3,+2)	(+3,-1)
01	(+4,+0)	(+3,+2)	(+4,+2)	(+3,+3)	(+2,-1)
02	(-2,+0)	(-3,+2)	(-4,+2)	(-3,+3)	(-2,-1)
03	(-3,+1)	(-2,+2)	(-2,+2)	(-3,+3)	(-1,-1)
04	(+1,+1)	(+2,+3)	(+1,+2)	(+2,+4)	(+0,+0)
05	(+1,+1)	(+2,+2)	(+1,+2)	(+1,+4)	(+0,-1)
06	(+4,-1)	(+4,+0)	(+4,+0)	(+4,-2)	(+3,+2)
07	(+4,+0)	(+3,-1)	(+4,+0)	(+4,-2)	(+3,+2)
08	(+3,+0)	(+3,-1)	(+3,-1)	(+3,-3)	(+2,+2)
09	(+2,+0)	(+2,-1)	(+2,-1)	(+2,-3)	(+1,+2)
10	(+0,+0)	(+1,-1)	(+1,-1)	(+1,-3)	(+1,+2)
11	(+1,-1)	(+1,-1)	(+1,-1)	(+1,-3)	(+0,+2)

Table 4.5: Offsets (in integer pixels) between the I and z medium exposure images.

CCD	Field A	Field B	Field C	Field D	Field E
00	(+5,+4)	(+4,+0)	(+4,+1)	(+4,+1)	(+3,+1)
01	(+4,+4)	(+3,+1)	(+4,+2)	(+4,+1)	(+3,+1)
02	(-3,+4)	(-3,+1)	(-3,+2)	(-3,+1)	(-2,+1)
03	(-3,+4)	(-2,+1)	(-3,+2)	(-3,+1)	(-2,+1)
04	(+2,+4)	(+1,+1)	(+1,+2)	(+2,+2)	(+1,+1)
05	(+2,+4)	(+1,+1)	(+1,+2)	(+2,+1)	(+1,+1)
06	(+4,-3)	(+4,+1)	(+4,+0)	(+4,+0)	(+3,+0)
07	(+4,-3)	(+3,+1)	(+4,-1)	(+4,+0)	(+3,+0)
08	(+3,-3)	(+2,+1)	(+3,-1)	(+3,-1)	(+2,+0)
09	(+2,-3)	(+2,+0)	(+2,-1)	(+3,-1)	(+2,+0)
10	(+2,-3)	(+1,+0)	(+1,-1)	(+2,-1)	(+1,+0)
11	(+1,-4)	(+1,+0)	(+2,-2)	(+2,-1)	(+1,+0)

Table 4.6: Offsets (in integer pixels) between the I and z long exposure images.

CCD	Field A	Field B	Field C	Field D	Field E
00	(+4,+1)	(+4,+1)	(+4,+1)	(+4,+0)	(+3,+0)
01	(+4,+2)	(+4,+1)	(+3,+1)	(+3,+0)	(+3,+0)
02	(-3,+2)	(-3,+1)	(-3,+1)	(-3,+0)	(-2,+0)
03	(-2,+2)	(-2,+2)	(-2,+2)	(-2,+0)	(-2,+0)
04	(+1,+2)	(+1,+2)	(+1,+1)	(+2,+1)	(+1,+0)
05	(+1,+2)	(+1,+2)	(+1,+1)	(+1,+1)	(+1,+0)
06	(+4,-1)	(+4,+0)	(+3,+0)	(+3,+1)	(+3,+0)
07	(+3,-1)	(+4,+0)	(+3,+0)	(+3,+0)	(+3,+1)
08	(+2,-1)	(+3,-1)	(+3,+0)	(+3,+0)	(+2,+0)
09	(+30,+29)	(+2,-1)	(-27,-30)	(+2,+0)	(+2,+0)
10	(+2,-1)	(+2,-1)	(+1,+0)	(+1,+0)	(+3,+1)
11	(+1,-2)	(+1,-2)	(+1,-1)	(+1,+0)	(+3,+0)

(18 June 2003) and -0.013 and +0.011 for the second night (20 June 2002), respectively. Those corrections to the zero points were computed from two standard stars bracketing the observations of fields A, B, C, and D on the 18 June 2002 whereas only one standard star was observed before the observations of field E. The Elixir/Skyprobe software indicated that the first night (18 June 2003) was photometric until 10h30 (UT) so that fields A, B, and C were observed under photometric conditions and good seeing conditions. However, the rest of the night was non-photometric with attenuation up to 0.1 mag, affecting the observations of field D. The Elixir/Skyprobe software indicated small variations of order of 0.050 mag during the observations of field E, taken on the second night (20 June 2002).

4.3.3 The extraction of the photometry

We have used the SExtractor software⁹ (Bertin & Arnouts 1996) to extract the photometry from the wide-field optical survey carried out with the CFH12K camera. However, although very efficient to distinguish stars from extended sources, SExtractor is only capable of aperture photometry. We have been kindly provided by the PSFEx package¹⁰ specially developed to extract PSF fitting photometry. We have favoured the PSF fitting to the aperture photometry because it provided more accurate photometric measurements for faint sources, which are, in our case, the cluster brown dwarf candidates.

The extraction of the photometry using the SExtractor and PSFEx packages was a three-step procedure. First, relatively bright stars (but not saturated!) were extracted with a reasonable detection threshold above the sky background. Next, a number of isolated objects suitable for point-spread function modelling were selected. A point-spread function was created for each individual chip and each exposure with the selected stars. However, one main drawback of the PSF modelling is the impossibility for the user to check interactively the reliability of the selected stars for the PSF computation. From our experience, the results were satisfactory though. Finally, SExtractor was run a second time, with the PSF created in the previous step, to detect all sources in the field-of-view and extract the photometry. The last step allowed us to cross-correlate the I and z catalogues through the *assoc_name* parameter keyword. The matching was done in pixel coordinates and not in celestial coordinates. The accuracy was better since the I and z images were previously shifted to the same pixel coordinate system.

To illustrate the procedure described above, the example of a script to run the SExtractor and PSFEx packages is given below.

1. **sex** imaI.fits -c default.sex -catalog_name psfI.cat -checkimage_name backgI.fits
2. **psfex** psfI.cat coll359I.psfex -checkimage_name psfI.fits
3. **sex** combIZ.fits,imaI.fits coll359I.sex -catalog_name catI.cat -checkimage_name resI.fits
4. **sex** imaZ.fits -c default.sex -catalog_name psfZ.cat -checkimage_name backgZ.fits
5. **psfex** psfZ.cat coll359Z.psfex -checkimage_name psfZ.fits

⁹<http://astroa.physics.metu.edu.tr/MANUALS/sextaror/>

¹⁰The PSFEx package is not freely available as the SExtractor package

```
6. sex combIZ.fits,imaZ.fits coll359Z.sex -catalog_name catIZ.cat -checkimage_name resZ.fits  
-assoc_name catI.cat
```

The input are the trimmed I , z , and combined (I, z) images referenced as imaI.fits, imaZ.fits, and combIZ.fits, respectively. The sex and psfex keywords written in bold letters correspond to the executables of the SExtractor and PSFEx packages, respectively. The words written in italics are the parameter keywords listed in the default.sex configuration file. We choose to assign the file names to the keywords *catalog_name* and *checkimage_name* on the command line to create a single configuration file template for all chips. However, these parameters can also be modified directly in the default.sex file.

The default.sex configuration file contains the main detection (threshold, deblending) and photometric (aperture size, zero points) parameters as well as header keywords, including the gain, and pixel size. The coll359I.sex and coll359Z.sex are copies of the default.sex configuration file for the I and z filters, respectively.

The output files from the whole procedure are the PSF, background, and residual images denoted as psfI.fits (psfZ.fits), backgI.fits (backgZ.fits), and resI.fits (resZ.fits) for the I (z) filters. The psfI.cat and psfZ.cat files are binary files containing the stars selected for the PSF modelling. The psfI.fits and psfZ.fits images represent the PSF of one chip of one CFH12K field-of-view. The background images correspond to the variation of the sky background across the whole chip. We adjusted the parameters in the default.sex configuration file with cautiousness to take into account the background variation around bright stars. The residual images represent the science frame after removal of all sources by the PSF taken from the psfI.fits and psfZ.fits files. Figure 4.3 shows the science frame corresponding to one CCD chip of one CFH12K field-of-view, as well as the corresponding PSF, background and residual images.

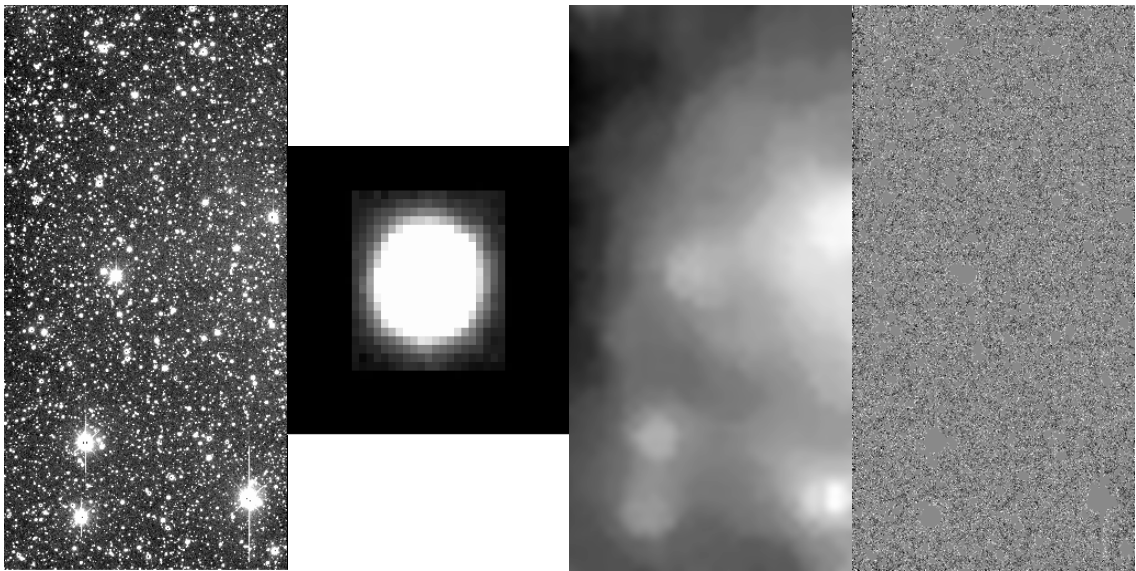


Figure 4.3: Output images from the extraction of the photometry using SExtractor and PSFEx. From left to right are shown the science frame corresponding to one CCD chip of one CFH12K field-of-view, the corresponding PSF, background and residual images after object subtraction.

The six steps described above were repeated for each CCD chip of the CFH12K in each field-of-view (A, B, C, D, and E) for all three exposures (short, medium, and long), generating a total of 180 catalogues. The final output catalogues contain the following parameters (bold font and capital letters) which we have selected to be of interest for our purposes:

- **ID** is the number of the object.
- **FLUX_PSF** is the flux contained within the PSF in counts.
- **FLUXERR_PSF** is the error on the flux contained within the PSF in counts.
- **MAG_PSF** is the magnitude derived from the psf fitting in mag.
- **MAGERR_PSF** is the error on the magnitude derived from PSF photometry. Up to now, no error estimate is provided.
- **MAG_APER** is the magnitude derived from aperture photometry (in mag).
- **MAGERR_APER** is the rms error vector on the magnitude derived from aperture photometry (in mag).
- **X_IMAGE** is the X position of the object.
- **Y_IMAGE** is the Y position of the object.
- **ALPHA_J2000** is the right ascension of the object in degrees (in J2000).
- **DELTA_J2000** is the declination of the object in degrees (in J2000).
- **ELONGATION** is the ratio of the profile rms along the ellipse axis.
- **ELLIPTICITY** is equal to (1–ELONGATION).
- **FWHM_IMAGE** is the full-width-half-maximum of the object or seeing if we take into account the pixel scale of the CFH12K camera (0.206"/pix). Values lower than 1 indicate bad pixels while large values correspond to extended sources. We have considered objects spanning 1–5 in FWHM for the subsequent analysis.
- **FLUX_RADIUS** is the flux contained in half of the FWHM.
- **FLAGS** are internal flags evaluating the quality of the photometry. They are multiple of 2 ranging from 0 to 64. A flag of 0 indicate good photometry. We have considered only objects with flag values lower than four.
- **VECTOR_ASSOC** is the associated parameter vector which adds two columns, namely the PSF magnitude in the *I*-band and its associated error.

Before discussing the colour-magnitude diagram and the selection of cluster member candidates, a number of “checks” were required to insure the validity of the output catalogues in terms of colour and photometry. If the photometric calibrations were perfect, all colour-magnitude diagrams of each individual chip and field-of-view of the CFH12K camera should be aligned on top of each other. However, we found colour shifts between individual chip, between fields-of-view, and between the short, medium, and long exposures for all three pre-main-sequence open clusters (IC4665, Steph 1, and Collinder 359) and for the Serpens observations. We have no explanation for the cause of these colour shifts. Note that we have corrected for the z -band scattered light. We describe below the procedure applied to correct for those colour shifts.

Table 4.7: Colour shifts between individual chip for each CFH12K field-of-view for the short exposures. The reference is the CCD 04. Negative and positive values indicate blue and red colour shifts of the colour-magnitude diagram, respectively.

CCD	Field A	Field B	Field C	Field D	Field E
00	-0.057	-0.035	-0.062	-0.057	-0.014
01	-0.055	-0.075	-0.061	-0.083	-0.024
02	-0.051	-0.075	-0.070	-0.076	-0.051
03	-0.054	-0.070	-0.037	-0.042	-0.028
04	+0.000	+0.000	+0.000	+0.000	+0.000
05	-0.010	+0.004	-0.017	+0.030	+0.012
06	-0.072	+0.030	+0.010	+0.004	+0.027
07	-0.103	-0.070	-0.023	-0.042	-0.019
08	-0.181	-0.110	-0.103	-0.094	-0.090
09	-0.137	-0.128	-0.129	-0.120	-0.081
10	-0.103	-0.122	-0.072	-0.061	-0.034
11	-0.077	-0.070	-0.057	-0.047	-0.040

Table 4.8: Colour shifts between individual chip for each CFH12K field-of-view for the medium exposures. The reference is the CCD 04. Negative and positive values indicate blue and red colour shifts of the colour-magnitude diagram, respectively.

CCD	Field A	Field B	Field C	Field D	Field E
00	-0.014	+0.023	-0.011	-0.002	-0.007
01	-0.026	-0.032	-0.049	-0.036	-0.029
02	-0.061	-0.044	-0.082	-0.039	-0.042
03	-0.013	-0.018	-0.012	-0.022	-0.014
04	+0.000	+0.000	+0.000	+0.000	+0.000
05	+0.040	+0.039	+0.038	+0.030	+0.022
06	+0.018	+0.023	+0.003	+0.023	+0.012
07	-0.051	-0.021	-0.020	-0.018	-0.016
08	-0.081	-0.070	-0.059	-0.074	-0.054
09	-0.090	-0.112	-0.090	-0.110	-0.086
10	-0.026	-0.035	-0.027	-0.035	-0.028
11	-0.021	-0.058	-0.027	-0.021	-0.024

Table 4.9: Colour shifts between individual chip for each CFH12K field-of-view for the long exposures. The reference is the CCD 04. Negative and positive values indicate blue and red colour shifts of the colour-magnitude diagram, respectively.

CCD	Field A	Field B	Field C	Field D	Field E
00	-0.006	+0.020	+0.000	+0.028	+0.023
01	-0.028	-0.025	-0.029	+0.002	+0.004
02	-0.050	-0.036	-0.055	-0.065	-0.021
03	-0.025	-0.030	-0.038	-0.035	+0.001
04	+0.000	+0.000	+0.000	+0.000	+0.000
05	+0.050	+0.038	+0.063	+0.030	+0.045
06	+0.006	-0.006	+0.036	+0.016	+0.063
07	-0.038	-0.019	-0.017	-0.006	+0.005
08	-0.069	-0.062	-0.064	-0.075	-0.041
09	-0.097	-0.076	-0.077	-0.092	-0.066
10	-0.023	-0.015	-0.006	-0.000	-0.010
11	-0.036	-0.029	-0.003	-0.019	+0.003

- **Interchip colour shifts** were detected in all CFH12K fields-of-view. For consistency in the data reduction of pre-main-sequence open clusters, the CCD04 was chosen as reference (the $I-z$ colour shift for this chip is always 0.0 mag). Tables 4.7, 4.8, and 4.9 list the shifts found for each individual chip in all five CFH12K field-of-view compared to CCD04 for the short, medium, and long exposures, respectively. Negative and positive values correspond to blue and red shifts in the $I-z$ colour to align properly all colour-magnitude diagrams with respect to CCD04. No clear trend was obvious for each individual chip besides that all of them need to be blue-shifted, except CCD05 and CCD06
- **Field-to-field colour shifts** were detected as well in all open cluster observations. Although fields A, B, and C were obtained on the same night and under photometric conditions, the $I-z$ colour did not align on top of each other. We choose field A as reference for the data in Collinder 359. We have applied colour shifts of +0.100, +0.010, +0.130, and +0.030 to the short exposures of fields B, C, D, and E, respectively, to align their colour-magnitude diagrams with respect to field A. We have applied colour shifts of -0.090, +0.010, -0.060, and -0.020 to the medium exposures and shifts of +0.030, +0.050, -0.010, and -0.020 to the long exposures of fields B, C, D, and E, respectively.
- **Exposure-to-exposure colour shifts** were detected as well in all CFH12K observations. After correcting for interchip and field-to-field discrepancies, we expected the colour-magnitude diagrams of the short, medium, and long exposures to align properly. However, $I-z$ colour shifts of -0.050, +0.030, and +0.020 for the short, medium, and long exposures, respectively, were still needed to correct for the difference.

After applying all colour shifts as described above, the $I-z$ colours are correct relative to a reference frame (in our case CCD04 of field A for short exposures) but the individual I and z magnitudes are in error by up to 0.10 mag, depending on the offset (Table 4.7, 4.8, and 4.9).

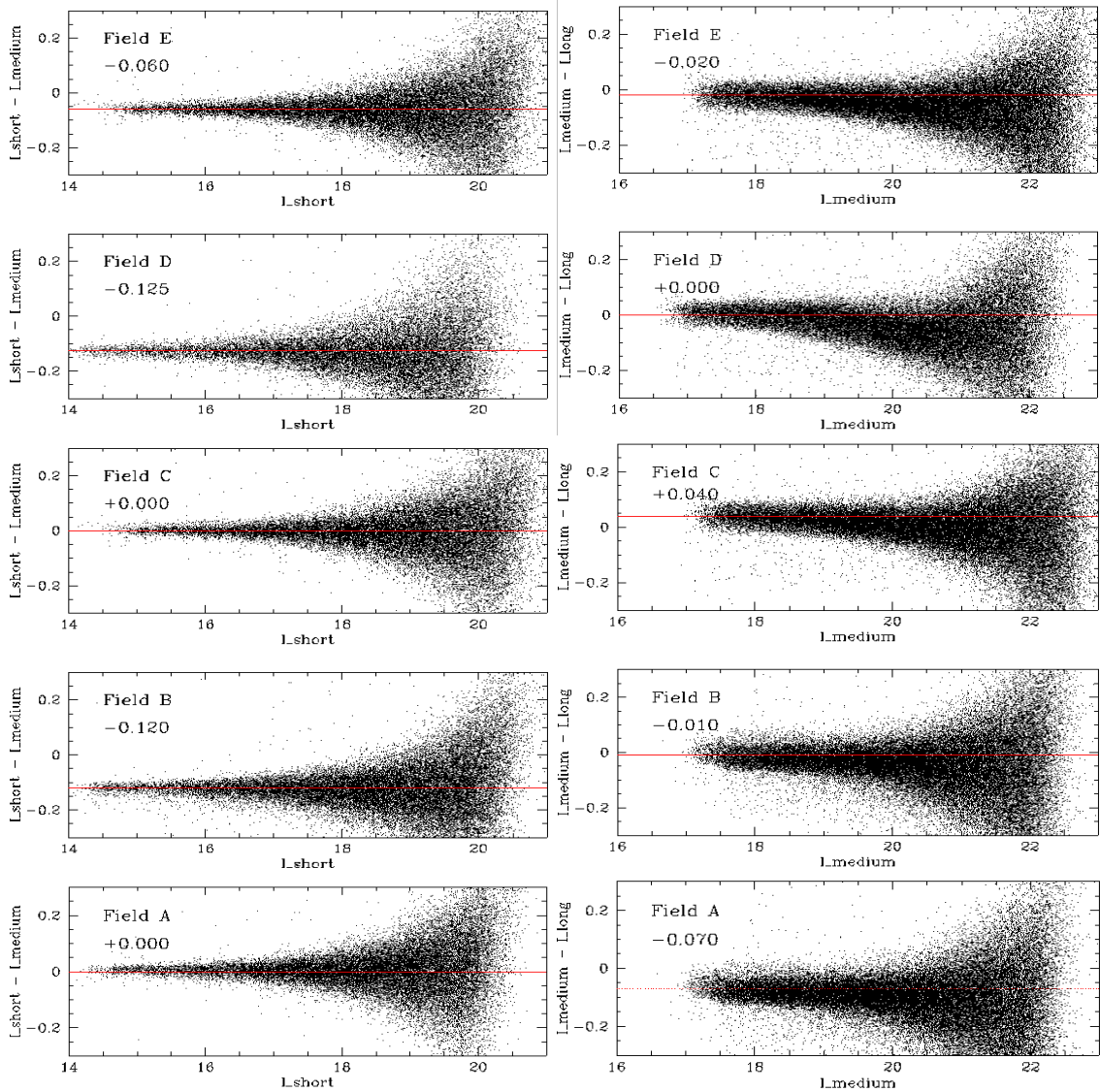


Figure 4.4: Differences in I magnitudes observed between the short and medium (left panels) and medium and long (right panels) exposures. From bottom to top are shown offsets for fields A, B, C, D, and E, respectively. Offsets are indicated in each panel and are represented by the lines.

This level of accuracy is certainly good enough for the selection of subsequent cluster member candidates.

To calibrate internally the I -band photometry, we have cross-correlated the short with medium and medium with long exposures for each individual field-of-view. Figure 4.4 displays the shift in I magnitude between the short and medium (left panel) and the medium and long (right panel) exposures, respectively. We have found offsets of +0.000, -0.120, +0.000, -0.125, and -0.060, between the short and medium exposures of fields A, B, C, D, and E, respectively. We have found

offsets of -0.070 , -0.010 , $+0.040$, $+0.000$, and -0.020 , between the medium and long exposures of fields A, B, C, D, and E, respectively. We could not calibrate the I magnitude between the five CFH12K fields-of-view since no overlapping region was available (Figure 4.2).

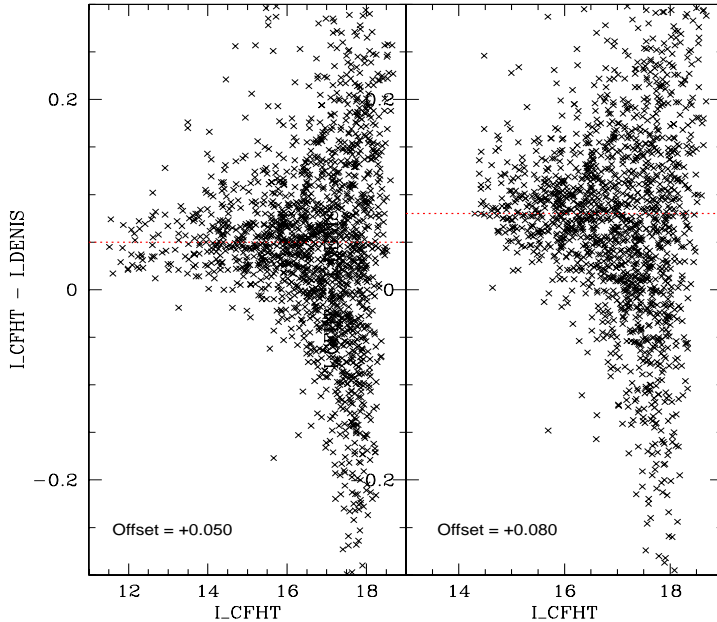


Figure 4.5: Offsets in I magnitudes between the CFHT and DENIS measurements for a $15' \times 6'$ overlapping area located in field A. Photometric shifts of $+0.050$ and $+0.080$ are found for the short (left panel) and medium (right panel) exposures, respectively. The same procedure was not possible with the long exposures since the detection of DENIS corresponds to the saturation limit of the CFH12K long exposures.

Comparison of the I magnitudes with measurements available in the literature for known cluster members was necessary to calibrate externally the I -band photometry. However, first, the CFH12K fields-of-view were chosen to avoid the bright components of the cluster (Figure 4.2), and, second, this cluster was fairly unstudied so that no known member is available in the surveyed area. Thus, we are not in a position to apply this method to the pre-main-sequence cluster Collinder 359. However, we have cross-correlated the final catalogue with the recent release of the DEep Near-Infrared Survey (Epchtein et al. 1997). The DENIS project is a deep astronomical survey of the Southern Sky in one optical band (I at $0.8\mu\text{m}$) and two near-infrared bands (J at $1.25\mu\text{m}$ and K at $2.16\mu\text{m}$) carried out with a one-meter telescope at La Silla (Chile). The whole Southern Sky is covered up to a declination of $+2^\circ$ down to $I = 18.5$, $J = 16.5$, $K_s = 13.5$. We could, therefore, extract a small overlapping region between the DENIS survey and the area covered by Field A. The right ascension and declination (J2000) of the $15' \times 6'$ overlapping area are:

$$\begin{array}{lclcl} 17:59:30 & \leq & \text{RA} & \leq & 18:02:30 \\ +01:54:00 & \leq & \text{Dec} & \leq & +02:00:00 \end{array}$$

The photometric offsets in the I magnitudes between the CFHT and DENIS measurements are +0.050 and +0.080 for short and medium exposures, respectively. Figure 4.5 shows the difference in I magnitudes between the CFHT and DENIS photometry versus the CFHT magnitudes for the short (left panel) and the medium (right panel) exposures, respectively. A similar procedure could not be applied to the long exposures because the DENIS detection limit corresponds to the saturation of the CFH12K long exposures ($I = 18.0\text{--}18.5$).

After both internal and external calibration of the photometry and colours, the final magnitudes given in the output catalogues are calibrated and the error on the I magnitudes should be of order 0.1 mag. However, no errors on the I and z magnitudes were computed by the PSFex software and we assume this uncertainty for the forthcoming analysis. The photometric errors could be extracted from overlapping regions but none is available in Collinder 359. The z magnitudes listed in the various tables throughout this chapter and in appendix are in error because the I magnitude was calibrated and colour shifts applied. However, the I –(I – z) values are correct within an uncertainty of 0.1 mag.

4.3.4 The optical colour-magnitude diagram for Collinder 359

The final ($I, I-z$) colour-magnitude diagram is presented on Figure 4.6. It includes all detections in the 1.6 square degree area surveyed in the pre-main-sequence open cluster Collinder 359. The detection and completeness (dashed line) limits of the survey are estimated to $I \sim z \sim 24.0$ and 22.0, respectively. To create the final colour-magnitude diagram, we have cross-correlated the short with medium and medium with long exposures to remove common detections and keep the best photometry. Hence, the photometry of the objects with $I \leq 15.0$, $15.0 \leq I \leq 19.0$, and $I \geq 19.0$ is extracted from the short, medium, and long exposures, respectively.

Overplotted on the colour-magnitude diagram are the NextGen (solid line; Baraffe et al. 1998), Dusty (dashed line; Chabrier et al. 2000b) and Cond (dotted line; Chabrier et al. 2000b) isochrones for 80 Myr, assuming a distance of 500 pc for the cluster (this distance is found to be the most likely; see § 4.5). The horizontal dashed line at $I \sim 20.0$ corresponds to the stellar/substellar boundary at $0.075 M_{\odot}$. The mass scale (in M_{\odot}) is indicated on the right-hand side of the plot and ranges from $1.3 M_{\odot}$ down to $0.030 M_{\odot}$. The large filled dots characterise all optically-selected cluster member candidates selected up to a distance of 650 pc for an age of 80 Myr to take into account the largest distance estimate from the literature (§ 4.2). The open triangles are cluster member candidates common to the Zacharias (2003) catalogue and consistent with the mean proper motion of the cluster. A reddening vector with $A_V = 1$ is indicated by an arrow for comparison purposes. We have considered the interstellar absorption law from Rieke & Lebofsky (1985), namely $A_I = 0.482$ for the I -band. As no estimate is available in the z band, we have assumed a linear fit between the interstellar absorption in the I and J bands ($A_J = 0.282$), yielding a value of $A_z = 0.382$.

4.3.5 Selection of cluster member candidates

The extraction of the cluster member candidates in open clusters generally consists in selecting objects located to the right of the ZAMS (Leggett 1992) shifted to the distance of the cluster. We have chosen the evolutionary models from the Lyon group to select cluster member candidates in Collinder 359. We have used the NextGen isochrones (solid line in Figure 4.6; Baraffe

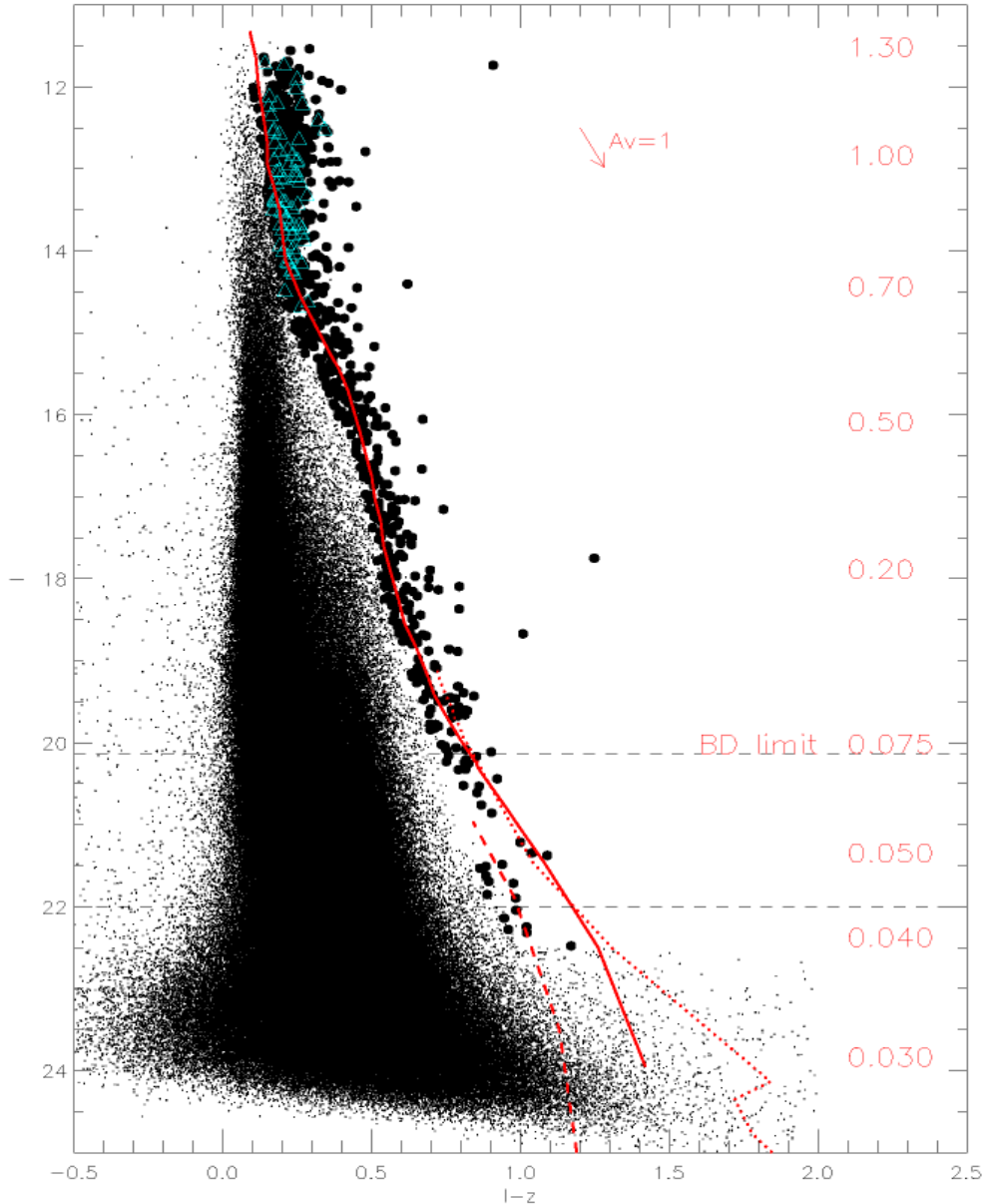


Figure 4.6: Colour-magnitude diagram ($I, I - z$) for the intermediate-age open cluster Collinder 359 over the full 1.6 deg^2 area surveyed by the CFH12K camera. The large filled dots are all optically-selected cluster member candidates spanning $1.30 - 0.04 M_{\odot}$. Overplotted are NextGen (solid line; Baraffe et al. 1998), the Dusty (dashed line; Chabrier et al. 2000b) and the Cond (dotted line; Chabrier et al. 2000b) isochrones for 80 Myr, assuming a distance of 500 pc for the cluster. The dashed line at $I \sim 20$ indicates the stellar/substellar boundary at $0.075 M_{\odot}$. The mass scale (in M_{\odot}) is given on the right side of the graph. A reddening vector of $A_V = 1$ is indicated for comparison purposes. The open triangles depict candidates with proper motion consistent with cluster membership.

et al. 1998) for effective temperatures higher than 2500 K (corresponding to masses of $0.050 M_{\odot}$ at the age and distance of the cluster) and the Dusty (dashed line in Figure 4.6; Chabrier et al. 2000b) isochrones for lower temperatures (and masses). We did not consider the Cond models (dotted line in Figure 4.6; Chabrier et al. 2000b) since the isochrone lie to the right of the Dusty isochrone. Consequently, objects located to the right of the Cond isochrones are to the right of the Dusty isochrones as well and, hence, remain bona-fide cluster member candidates.

We have considered three different values for the age of the cluster. First, an age of 30 Myr which corresponds to the value quoted in the Open Cluster Database. Next, an age of 50 Myr, and, finally, an age of 80 Myr to take into account uncertainties in the age determination of open clusters. There is, indeed, typically a factor of two between the age estimate from the turn-off main-sequence fitting (Mermilliod 1981) and the age determination based on the lithium test (Re-bolo et al. 1992). For example, the age of the Pleiades increased from 70 Myr to 125 Myr after applying the lithium test (Stauffer et al. 1998). Concerning α Per, the age increased from 50 Myr to 90 Myr (Stauffer et al. 1999; Chapter 3). Larger uncertainties are foreseen for unstudied open clusters such as Collinder 359.

The second uncertain parameter of Collinder 359 is the distance. From the literature search presented in § 4.2, distances range from 200 pc from the Open Cluster Database to 650 pc for the latest estimate by N. Kharchenko et al. (2004; personal communication). Early estimates of the distance by Collinder (1931) are within this interval. Isochrone fitting suggests a mean distance of 450 pc.

To take into account the uncertainties in the age and the distance of the cluster, we have selected *all* objects located to the right of the combined NextGen+Dusty isochrones (Baraffe et al. 1998; Chabrier et al. 2000b), shifted to distances from 250 pc to 650 pc by intervals of 50 pc and assuming three different ages (30, 50, and 80 Myr). This procedure has generated a total of 27 catalogues, each of them corresponding to a specific (distance, age) combination. The number of objects in each file is given in the Table 4.10 (§ 4.4.5). These files will be available on CDROMs upon request or in a webpage dedicated to Collinder 359. We have implemented the selection independently for the short, medium, and long exposures. Then, we have cross-correlated those catalogues to remove multiple detections and provide a list of cluster member candidates (Table B.1 in Appendix B). According to these conservative limits, we have certainly included the majority of true cluster members at the expense of a higher contamination.

We have examined each cluster member candidate by eye both in the I and z images to reject extended objects, blended sources, and detections affected by bad pixels or bad columns. Indeed, more than two-thirds of the objects located to the right of the evolutionary models were affected by bad pixels in one filter at least, or located on a bad column despite the good cosmetics of the CFH12K camera. The number of candidates, divided into short, medium, and long exposures (including the common ones), is as follows.

- 737 candidates extracted only in the short exposures
- 100 common candidates to the short and medium exposures
- 13 common candidates to the short, medium, and long exposures
- 102 candidates found only in the medium exposures

Table 4.10: Numbers of optically-selected candidates in Collinder 359 classified as probable (Y+), possible (Y?), and non-members (NM) for different (distance, age) combinations. Probable members are defined as objects located to the right of the NextGen+dusty isochrones, shifted at distances between 250 and 650 pc. Possible members are located between the NextGen+Dusty isochrones shifted at a given distance and the NextGen isochrone shifted at the distance of 650 pc. The non-members are bluer than the NextGen isochrone shifted at the distance of 650 pc. The assumed ages for the cluster are 30, 50, and 80 Myr. The fourth column indicates the number of objects located in the bright part of the diagram ($I = 12-15$) where the field contamination is expected to be high. The list includes the number of objects with infrared magnitudes from 2MASS and from our CFHT follow-up for the different (distance, age) combinations.

Distance (pc)	Age (Myr)	All	$I > 15$	Y+	Y?	NM	2MASS	CFHTIR
250	30	50	46	41	2	2	43	5
	50	100	96	88	2	2	87	4
	80	172	166	151	4	2	156	6
300	30	98	93	87	3	2	87	5
	50	182	173	156	7	2	159	10
	80	260	248	220	10	2	228	13
350	30	165	156	138	7	2	140	9
	50	264	252	221	10	2	228	13
	80	369	352	299	14	3	315	15
400	30	243	231	194	9	3	199	13
	50	350	336	294	12	2	303	14
	80	470	449	379	18	3	401	17
450	30	300	288	245	10	2	253	13
	50	455	437	370	15	3	387	16
	80	604	578	456	22	4	494	21
500	30	375	359	310	13	3	318	16
	50	551	528	436	19	4	458	19
	80	732	699	538	25	8	589	23
550	30	471	450	360	16	5	375	20
	50	656	627	505	24	5	538	21
	80	854	816	603	27	11	672	26
600	30	539	516	424	19	4	443	19
	50	777	743	580	25	9	624	24
	80	867	829	600	27	11	669	26
650	30	632	603	486	24	5	515	20
	50	862	824	620	25	13	681	27
	80	1033	991	665	27	15	733	30

- 29 common candidates to the medium and long exposures
- 52 candidates extracted only in the long exposures

After removal of all spurious detections, the final list of cluster members contains a total of 1033 candidates ranging from $I = 12.0$ to $I = 22.5$ over 1.6 deg^2 area surveyed in Collinder 359. From the colour-magnitude diagram ($I, I-z$), the large field contamination at magnitudes brighter than $I \sim 15$ is clearly visible. Out of the 1033 candidates, about 60 % of them lie in the range $I = 12\text{--}15$. The contamination at brighter magnitudes (and thus at high masses) originates from the merging between the cluster sequence and the sequence of field stars. As a consequence, the large majority of candidates extracted in this part of the colour-magnitude diagram are mostly contaminants. The subsequent luminosity function (§ 4.5) and mass function (§ 4.6) are therefore biased at high masses. Additional observations are required to estimate the level of contamination in this part of the diagram. For comparison, the number of objects found in the medium and long exposures is similar to the number of cluster candidates extracted from the (R, I) survey in α Per (Barrado y Navascués et al. 2002; Chapter 3).

All 1033 cluster member candidates are listed in Table B.1 in Appendix B with their coordinates, photometry and membership status. They are ordered by increasing right ascension. The details of the columns in Table B.1 are given in Appendix B. Additional parameters, including the pixel (x,y) coordinates, ellipticity, full-width-half-maximum of each candidate will also be available upon request. The range of ellipticities and FWHM for all candidates are, 0.001–0.389 and 1.6–3.5, respectively. Only one object has an ellipticity of 0.602 and a FWHM of 4.0, casting doubt about its membership. The distribution of the ellipticity shows that 95 % of the objects have an ellipticity smaller than 0.15. The majority of objects have full-width-half-maximum between 1.8 and 3.0, corresponding to a seeing varying approximately between 0.4 and 0.6 arcsec. The seeing values are better than those requested in the CFHT proposal (0.65–0.8 arcsec).

All tables corresponding to the various (distance, age) combinations will be saved on CDROMs. Only the whole sample of candidates is provided in Appendix B as paper version. Appendix C provides one example of finding charts for candidates candidates in Collinder 359. The remaining finding charts will be available on CDROMs or available on a dedicated webpage.

We are confident that we have extracted most of the cluster member candidates in Collinder 359. However, inherent uncertainties to the selection procedure remain. We have possibly missed some bona-fide cluster members for various reasons. First, 200 bad columns affect the CFH12K field-of-view and most especially the CCD05. The largest incompleteness is expected in this specific chip. Second, objects affected by bad pixels might actually be genuine cluster candidates but were rejected from the final list. Next, blended objects were removed from the candidate list because their photometry was affected. Finally, some bright stars might hide faint cluster members although the short exposures were obtained to partly address this issue.

Figure 4.7 shows the distribution of all probable (Y+) cluster member candidates in the five CFH12K fields-of-view for a distance of 500 pc and an age of 80 Myr. The number of selected candidates is much lower in fields B and D than in the other three fields. We have found 169, 63, 105, 33, and 182 candidates in the field A, B, C, D, E, respectively. This plot is independent of the completeness limit of our survey as it happens above $I = 22.5$ mag. Using strong constraints in the FWHM and ellipticity for all detections in each individual CFH12K field-of-view, we have investigated the number of detections within one CFHT12K field-of-view:

- 94233 ± 934 objects in field A

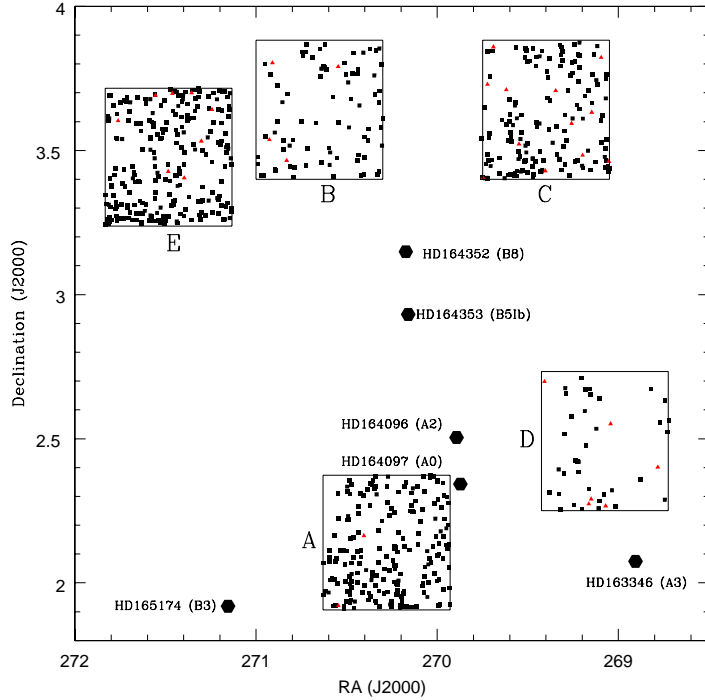


Figure 4.7: Distribution of the probable member candidates in the 1.6 square degree area in Collinder 359, assuming a mean distance of 500 pc and an age of 80 Myr. Six bright stars listed as cluster members by Collinder (1931) are included to facilitate the comparison with Figure 4.2.

- 118018 ± 812 objects in field B
- 99071 ± 467 objects in field C
- 81714 ± 331 objects in field D
- 111868 ± 506 objects in field E

The difference in density for cluster member candidates in Collinder 359 does not follow the difference in the total number of detections. The field D appear much less dense than the other fields. However, field B is as dense as field E in terms of detections but not with regard to the number of candidates. Fields A and C are comparable in density. The difference in density might result from a non-uniform extinction along the line of sight. Collinder 359 is located in the Aquila Rift, where CO maps indicate the presence of extinction (Dame et al. 2001).

It would be premature to explain this effect as a result of dynamical evolution within the cluster as optical spectroscopy and additional membership criteria are lacking. However, this issue certainly requires special attention in the near future and should be further investigated once the cluster sequence is better defined.

4.4 Near-infrared follow-up of optically-selected candidates

Collinder 359 is at a galactic latitude of $b = +12.5^\circ$, intermediate between α Per ($b = -7^\circ$) and the Pleiades ($b = -24^\circ$). Therefore, the sample of optically-selected cluster member candidates in Collinder 359 is inevitably contaminated by foreground and background objects. The possible sources of contamination are:

1. Galaxies
2. Reddened background giants
3. Field dwarfs

As special care was taken to remove extended objects from the cluster candidate list, the contamination by galaxies should be extremely small. Moreover, reddened background giants could be well rejected using an optical-to-infrared colour-colour diagram as described in the case of α Per (Section 3.5.6 and Figure 3.10). The last but not least, field dwarfs represent another source of contamination as they have similar optical colours as young cluster members. However, optical-to-infrared colour-magnitude diagrams such as $(I, I-J)$ or $(I, I-K)$ have proven their efficiency to weed out field dwarfs in σ Orionis (Zapatero Osorio et al. 2000), in the Pleiades (Zapatero Osorio et al. 1997a; Pinfield et al. 2000), in α Per (Barrado y Navascués et al. 2002), and in IC2391 (Barrado y Navascués et al. 2001a). Furthermore, the latest theoretical Dusty isochrones (Chabrier et al. 2000a) predict bluer $I-K$ colours for field dwarfs than young low-mass cluster members by 1.0 to 1.5 mag depending on the mass.

Near-infrared observations provide good means to weed out contaminating objects from the optical sample. This section is dedicated to the near-infrared follow-up of the optically-selected cluster member candidates in Collinder 359 extracted in the previous section. First, the list of cluster members was cross-correlated with the 2MASS all-sky survey database for objects brighter than $I = 17.0$ (§ 4.4.1). Next, near-infrared (K -band) follow-up observations, conducted with the Canada-France-Hawaii Telescope, for a sample of 39 cluster member candidates are described in § 4.4.2. The data reduction and analysis of the near-infrared images are presented in § 4.4.3 and § 4.4.4, respectively. The contamination of the optical sample is discussed in § 4.4.5.

The work presented in this section was done in collaboration with members from the Arcetri, Grenoble, and Potsdam teams, within the framework of the CFHT Key Programme and EC network. David James and Jérôme Bouvier carried out the observations at CFHT in visitor mode and Jérôme Bouvier reduced the infrared data. Willem-Jan de Wit, David James and I extracted the infrared photometry of the cluster member candidates in the IC4665, Steph 1, and Collinder 359 pre-main-sequence open clusters, respectively.

4.4.1 Cross-correlation with the 2MASS database

To estimate the contamination towards bright member candidates in Collinder 359, we have cross-correlated the sample of optically-selected cluster member candidate with the 2MASS survey. Information concerning the 2MASS all-sky survey and the catalogue products can be found in Beichman et al. (1998) as well as on the 2MASS webpage¹¹. A short overview of the 2MASS project is given in Chapter 1 (§ 1.5.2). Due to its completeness limit of $K_s = 14.3$, the 2MASS

¹¹<http://www.ipac.caltech.edu/2mass/releases/second/doc/>

database provides infrared counterparts in J , H , and K_s for most of the optically-selected cluster candidates brighter than $I = 17.0$. For objects fainter than $K_s = 14.3$, the uncertainty on the magnitude become larger than 0.1 mag and additional near-infrared observations are required to establish membership.

Among 805 cluster member candidates brighter than 17.0 in the I -band, 772 of them have a 2MASS counterpart within a radius of $2''$, with K_s magnitudes brighter than 14.3, and errors on the J , H , and K_s magnitudes smaller than 0.1 mag. These criteria did not allow the identification of 33 cluster member candidates in Collinder 359. Those objects have a 2MASS counterpart but either at larger radii (2 to $3''$) or K_s magnitudes fainter than 14.3 or uncertainties larger than 0.1 mag. We have therefore not taken into account their 2MASS magnitudes.

A radius of $2''$ is adapted to the selected cluster members as we examined those objects not to be blended with other stars in the field. For comparison, we used radii of about 1.5 and $1''$ to cross-correlate the optical and near-infrared catalogues in α Per (Sect 3.5.4). As only 33 objects were not identified during the matching, our sample of cluster member candidates with near-infrared counterparts in Collinder 359 is complete to 96 %. The subsample of cluster member candidates with 2MASS counterparts is displayed as plus symbols in Figure 4.8.

4.4.2 The CFHT K -band follow-up

Near-infrared (K' -band) observations of 39 optically-selected cluster member candidates were carried out with the infrared camera (CFHTIR) mounted on the Canada-France-Hawaii 3.6-m telescope on 10–12 July 2003 (Table 4.11). The observations were conducted by David James. The conditions were non-photometric over the three night observing run and the seeing around 0.5–0.7 arcsec. A second observing run was granted in November 2003 with the same infrared camera on CFHT. The observer was Jérôme Bouvier. The conditions were highly non-photometric and none of the five observed fields in Collinder 359 was usable to achieve the photometric accuracy better than 0.1 mag.

The CFHTIR infrared camera has a 1024×1024 pixel HAWAII detector with a spatial scale of $0.204''/\text{pixel}$ yielding a $3.5' \times 3.5'$ field-of-view. Five dithered frames (offset by ~ 50 pixels) were obtained for each target, each frame being a co-add of 7 or 8 images exposed 8 seconds, yielding a total exposure time on the order of 5 minutes. All observations were pointed observations as the candidates are randomly distributed over large areas. By chance, two or more objects were sometimes within one CFHTIR field-of-view. In total, we have observed K' -band photometry of 39 candidates in Collinder 359, spanning $I = 17.0\text{--}22.0$ to probe the contamination across the stellar/substellar boundary in the cluster. The error on the K -mag is better than 0.1 mag (see column 7 in Table 4.11).

Many CFHTIR fields contain bright cluster members as well but those are generally saturated. Hence, we retained the 2MASS photometry for the objects brighter than $I = 17.0$. Several standard stars (AS30, AS31, AS33; Table 4.12; Hunt et al. 1998) were observed throughout the nights to calibrate the zero-points. the achieved accuracy is on the order of 0.02 mag. Series of dome flat-fields (light on and off) were taken before the beginning of the night to correct pixel-to-pixel variations.

Table 4.11 lists the 39 optically-selected cluster member candidates followed-up in the K' -band with the CFHTIR camera. Two objects, brighter than $I = 17.0$, are among the objects whose 2MASS magnitudes were rejected. Columns 1 and 2 list the identification number of the target

Table 4.11: List of optically-selected cluster member candidates in Collinder 359 with infrared follow-up obtained with the CFHTIR camera. The objects are sorted by decreasing I magnitudes. Column 1 provide the name according to the IAU convention, starting with Coll359 J and followed by the coordinates. Columns 2 and 3 give the field and the CCD where the object is located. Columns 4, 5, and 6 lists the I , z magnitudes, and $I-z$ colour, respectively. Columns 7 and 8 gives the K' magnitude along with its associated error and the $I-K'$ colour. Column 9 gives the membership status based on the optical-to-infrared colour-magnitude diagram.

Coll359 J ...	Field	ID	I	z	$I - z$	$K' \pm \text{err}K'$	$I - K'$	Memb?
180432+031617	E06	250	14.800	14.490	0.310	13.328 ± 0.003	1.472	Y?
180511+032221	E07	2225	16.667	16.159	0.508	14.325 ± 0.005	2.342	Y+
180553+033510	E02	2089	17.044	16.551	0.493	14.743 ± 0.006	2.301	Y+
180009+022152	A00	153	17.246	16.689	0.557	14.842 ± 0.007	2.404	Y+
180045+020257	A08	2038	17.465	16.932	0.533	14.913 ± 9.999	2.552	Y+
180000+022159	A00	95	17.484	16.843	0.641	14.934 ± 0.007	2.550	Y?
180548+033619	E02	1774	17.548	16.902	0.646	15.008 ± 0.008	2.540	Y?
175743+032953	C09	1239	17.600	17.048	0.552	15.055 ± 0.008	2.545	Y+
180343+033137	B11	3969	17.720	17.106	0.614	15.033 ± 0.007	2.687	Y?
180032+020711	A07	2501	17.752	17.148	0.604	15.438 ± 0.009	2.314	Y?
180551+031550	E08	439	17.778	17.076	0.702	15.471 ± 0.011	2.307	Y?
175852+033359	C11	1971	17.857	17.164	0.693	15.158 ± 0.009	2.699	Y?
175458+021734	D06	271	17.997	17.267	0.730	15.026 ± 0.007	2.971	Y?
180147+032650	B07	565	17.998	17.306	0.692	15.651 ± 0.010	2.347	Y+
175728+033036	C08	1509	18.140	17.482	0.658	15.315 ± 0.008	2.825	Y?
180520+032123	E07	4232	18.166	17.555	0.611	15.605 ± 0.011	2.561	Y?
180351+032945	B11	2938	18.234	17.675	0.559	15.615 ± 0.010	2.619	Y+
175725+033117	C08	1676	18.442	17.679	0.763	15.744 ± 0.011	2.698	Y?
180004+022210	A00	201	18.674	17.666	1.008	14.895 ± 0.007	3.779	Y+
180549+031530	E08	523	18.945	18.236	0.709	16.355 ± 0.019	2.590	Y?
180022+021436	A01	3978	19.007	18.161	0.846	15.657 ± 0.011	3.350	Y?
180554+031521	E08	418	19.260	18.515	0.745	16.720 ± 0.024	2.540	NM
180657+034026	E05	2197	19.336	18.348	0.988	16.962 ± 0.024	2.374	NM
175506+021710	D06	576	19.556	18.609	0.947	15.874 ± 0.011	3.682	Y?
180516+032036	E07	3671	19.630	18.948	0.682	17.069 ± 0.025	2.561	NM
180439+033421	E00	8531	20.020	19.232	0.788	17.787 ± 0.042	2.233	NM
180342+033213	B11	7730	20.257	19.432	0.825	16.793 ± 0.022	3.464	Y+
180656+033222	E05	10305	21.026	19.694	1.332	17.982 ± 0.055	3.044	NM
180305+035059	B03	1155	21.857	20.918	0.939	18.852 ± 0.067	3.005	NM
180702+033219	E05	10242	22.175	21.052	1.123	18.308 ± 0.093	3.867	Y?

according to IAU conventions. The CFH12K field and CCD number where the candidate is located are given in columns 2 and 3, respectively. The I , z , K' magnitudes and the $I-z$ and $I-K'$ colours are provided in columns 4–8. The membership status of the cluster member candidates in Collinder 359 is updated in the last column of Table 4.11. The Y+, Y?, and NM abbreviations refer to objects classified as probable, possible members and non-members, respectively.

4.4.3 Data reduction of the CFHT near-infrared images

Five dithered frames, offset by about 50 pixels ($\sim 10''$) were obtained for each science target. Each science frame is a sum of images, that is one FITS file saved on disk contains several images

Table 4.12: List of standard stars observed within the framework of the CFHTIR follow-up of selected cluster member candidates in three pre-main-sequence open clusters on 10–12 July 2003. Note that only standard stars bracketing the observations in Collinder 359 are listed. The remainder show similar zero-points converging to a mean value of $ZP = 22.90 \pm 0.02$.

Name	RA	DEC	Time	ExpT	Airm	K_{Hunt}	K'_{instr}	ZPs
10 June 2003								
AS30-0	16:40:41.6	+36:21:13	06h17	3.0 sec	1.112	13.141	15.255	22.886
AS30-1	16:40:41.6	+36:21:13	06h17	3.0 sec	1.112	12.175	14.155	23.020
AS31-0	17:44:06.8	-00:24:58	06h23	5.0 sec	1.335	12.048	14.144	22.904
AS31-1	17:44:06.2	-00:24:22	06h23	5.0 sec	1.335	12.476	14.614	22.862
AS33-0	18:27:13.6	+04:03:10	10h50	3.0 sec	1.100	11.739	13.826	22.913
AS33-2	18:27:12.4	+04:02:16	10h50	3.0 sec	1.100	13.168	15.286	22.882
AS33-0	18:27:13.6	+04:03:10	10h55	3.0 sec	1.100	11.739	13.826	22.913
AS33-2	18:27:12.4	+04:02:16	10h55	3.0 sec	1.100	13.168	15.336	22.832
11 June 2003								
AS30-0	16:40:41.6	+36:21:13	05h54	3.0 sec	1.145	13.141	15.309	22.832
AS30-1	16:40:41.6	+36:21:13	05h54	3.0 sec	1.145	12.175	14.189	22.987
AS31-0	17:44:06.8	-00:24:58	06h22	3.0 sec	1.324	12.048	14.160	22.888
AS31-1	17:44:06.2	-00:24:22	06h22	3.0 sec	1.324	12.476	14.620	22.856
AS33-0	18:27:13.6	+04:03:10	07h48	3.0 sec	1.149	11.739	13.822	22.917
AS33-2	18:27:12.4	+04:02:16	07h48	3.0 sec	1.149	13.168	15.292	22.876
AS31-0	17:44:06.8	-00:24:58	10h29	3.0 sec	1.182	12.048	14.185	22.863
AS31-1	17:44:06.2	-00:24:22	10h29	3.0 sec	1.182	12.476	14.610	22.866
12 June 2003								
AS30-0	16:40:41.6	+36:21:13	05h51	3.0 sec	1.142	13.141	15.243	22.898
AS30-1	16:40:41.6	+36:21:13	05h51	3.0 sec	1.142	12.175	14.173	23.002
AS31-0	17:44:06.8	-00:24:58	05h57	3.0 sec	1.425	12.048	14.233	22.815
AS31-1	17:44:06.2	-00:24:22	05h57	3.0 sec	1.425	12.476	14.633	22.843
AS33-0	18:27:13.6	+04:03:10	11h00	3.0 sec	1.130	11.739	13.844	22.895
AS33-2	18:27:12.4	+04:02:16	11h00	3.0 sec	1.130	13.168	15.343	22.824

(in this specific case 7 or 8) which were co-added to construct the final image. The data reduction was relatively standard for near-infrared observations and was carried out by Jérôme Bouvier. However, due to non-photometric conditions, we have tested three different methods to estimate the sky and achieve the best possible photometric accuracy. A brief outline is provided below:

1. **Method 1: “standard”:** The sky was estimated by taking the median of the five dithered science field frames. As only 5 dithered frames were available to compute the sky, the final sky subtracted science images did exhibit “negative stars” in the background. These “negative stars” affect the real “stars” themselves and will flaw the photometry. Thus, we rejected this approach.
2. **Method 2: “supersky”:** To get rid off the “negative stars”, a median images of 11 successive science frames with minmax rejection was used to create a “supersky”. The science

exposures corrected for the “supersky” nevertheless exhibit a non-uniform (low-level) background. The photometry will be correct as long as the sky is estimated locally around the stars. This method yields the highest signal-to-noise ratio as more frames were used to estimate the sky.

3. **Method 3: “skynorm”:** To get “nice-looking” images without “negative stars” and a uniform background, the sky was estimated from the five frames after having renormalised all of them to the same value. The median average of the normalised science image is a more meaningful sky estimate and do exhibit neither “negative stars” nor non-uniform background even during non-photometric conditions. The photometry measured on these images will also be correct, though probably lower signal-to-noise than method 2, because fewer frames (only five) were used to estimate the sky.

After estimating correctly the sky background, each science frame was sky-subtracted and flat-fielded. The flat-field is the difference between averaged flat fields observed lamp on and lamp off. Aperture photometry was done by myself within the IRAF environment and is described below.

The measured magnitudes were corrected for extinction and exposure time according to the equation below in order to obtain instrumental magnitudes.

$$m_{\text{instrumental}} = m_{\text{measured}} - \text{Extinction} \times \text{Airmass} + 2.5 \times \log(\text{ExpTime})$$

The airmass correction for CFHT on Mauna Kea was assumed to be 0.07 mag/airmass. The airmass and exposure time keywords were directly read from the header of the fits files. Zero-points from the various standards observed throughout the nights were applied to the instrumental magnitudes of the cluster member candidates to derive the final magnitudes. A list of standard stars along with their instrumental magnitudes as well as the derived zero-points is provided in Table 4.12. The mean zero-point for all three nights was $ZP = 22.90 \pm 0.02$ but variable during a night.

However, due to the non-photometry conditions encountered during the observing run, a cross-correlation with the 2MASS database was implemented to check the reliability of the photometric calibration. The task *daofind* was used to detect all sources on the science frames. The full-width-half-maximum, the sky level and the detection threshold were adjusted for each frame to detect all sources. The photometry was then computed with the task *phot*. An aperture on the order of the FWHM was chosen. The flux of few relatively bright and isolated stars was measured for different aperture sizes (from 1 to 4 times the FWHM) to compute the aperture correction. Each individual frame was astrometrically calibrated following the procedure described in Section 3.5.3. Then, we have cross-correlated the CFHTIR sources with the 2MASS database to compare both photometry. The differences in K magnitudes were in agreement with the zero-points derived from the standard stars within 0.05 mag.

The final calibrated magnitudes of the optically-selected cluster candidates in Collinder 359 are listed in Table 4.11 and displayed as filled circles in Figure 4.8.

4.4.4 Analysis of the CFHT observations

We have obtained near-infrared (K' -band) photometry for 39 optically-selected cluster member candidates in Collinder 359 (Table 4.11 and Figure 4.8). Those candidates span $I = 17.0\text{--}22.0$

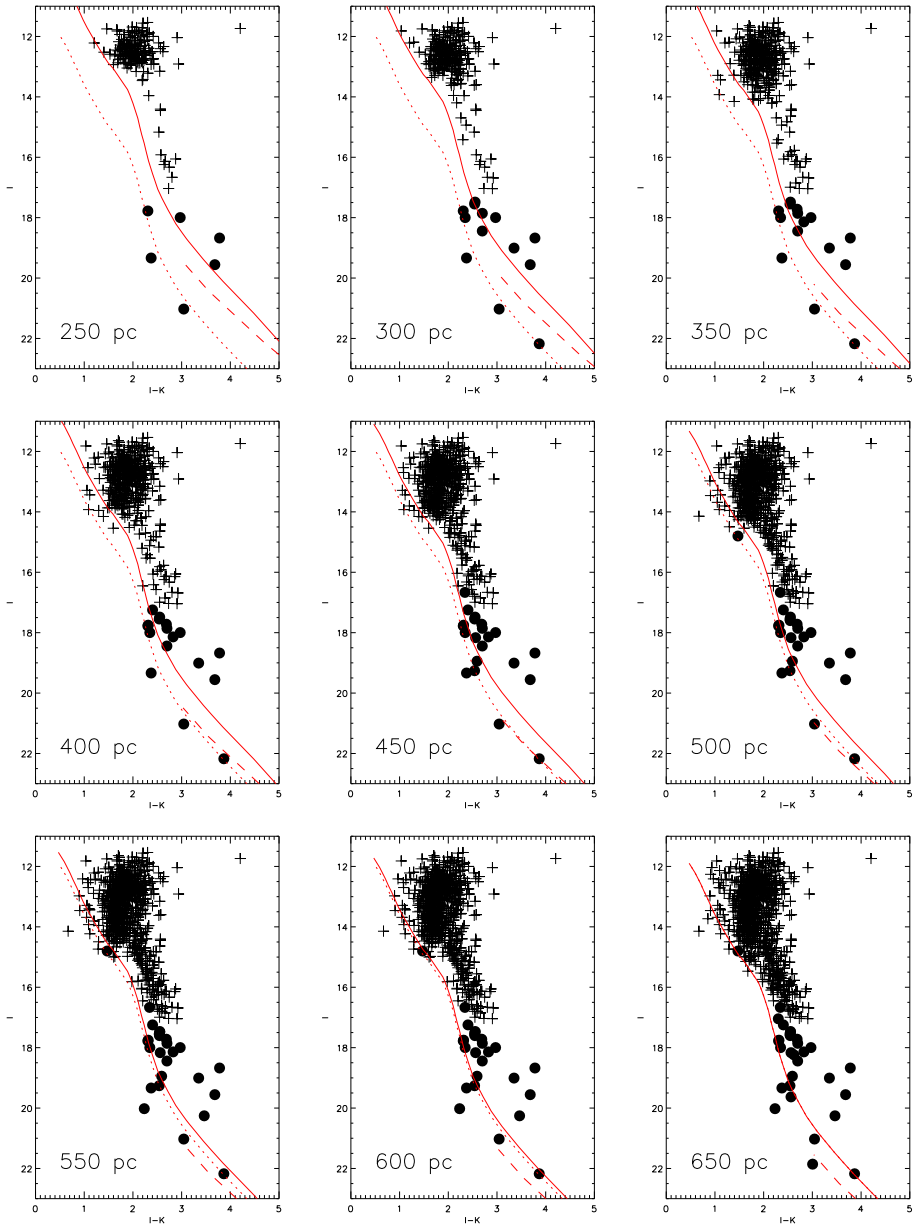


Figure 4.8: We plot in the $(I, I-K)$ colour-magnitude diagrams the cluster member candidates located to the right of the NextGen+Dusty isochrones in the $(I, I-z)$ diagram, shifted at distances ranging from 250 to 650 pc by intervals of 50 pc at an age of 80 Myr. The infrared photometry comes from the 2MASS catalogue from objects brighter than $I = 17$ (plus symbols) and from our CFHTIR follow-up observations for fainter objects (filled circles). Overplotted are the NextGen (solid lines) and Dusty (dashed lines) isochrones shifted at the distance indicated at the bottom left corner as well as the NextGen isochrone shifted at a distance of 650 pc (dotted line). Probable members ($Y+$) are objects located to the right of the isochrones shifted at the distance indicated in the diagrams. Possible members ($Y?$) are located to the right of the isochrones shifted at the indicated distance and the isochrone at 650 pc. The objects bluer than the isochrone shifted at 650 pc are rejected as cluster members.

mag and were specifically followed-up to probe the contamination across the hydrogen-burning limit as well as in the brown dwarf regime in pre-main-sequence open clusters. Two objects are brighter and one fainter than those limits. The brightest one, for which K' photometry has been obtained is added to the list of objects with 2MASS counterparts. The position of these candidates in the $(I, I-K)$ colour-magnitude diagram will add a further criterion to weed out contaminating objects from the list of cluster members. For example, at a given luminosity, a $0.04 M_{\odot}$ brown dwarf at 30 Myr has a $I-K$ colour of 3.8, while a $0.1 M_{\odot}$ star at 1 Gyr has a colour of 3.2 (Baraffe et al. 1998).

Figure 4.8 displays in optical-infrared ($I, I-K$) colour-magnitude diagrams the candidates selected to the right of the NextGen+Dusty isochrones in the $(I, I-z)$ diagram. Each diagram corresponds to a given distance, ranging from 250 to 650 pc by intervals of 50 pc. The infrared photometry was extracted from the 2MASS database for candidates brighter than $I = 17$ (plus symbols in Figure 4.8; Section 4.4.1). The fainter candidates have K' -band photometry from our CFHTIR follow-up observations (filled circles in Figure 4.8; Section 4.4.2). According to the location of the optically-selected cluster member candidates in the $(I, I-K)$ diagram and assuming an age of 80 Myr, three samples have been defined as follows:

1. Probable members (Y+): these objects lie to the right of the NextGen+dusty isochrones (solid and dashed lines), shifted at the distance indicated in the lower left corner in the diagram (distances ranging from 250 to 650 pc). Their optical and optical-to-infrared colours are consistent with cluster membership.
2. Possible members (Y?): these candidates are located between the NextGen+Dusty isochrones (solid and dashed lines) at the distance indicated in the diagram and the NextGen isochrone shifted at the distance of 650 pc (dotted line).
3. Non-members (NM): these objects are bluer than the NextGen isochrone shifted at the distance of 650 pc. They are rejected as cluster members.

Table 4.10 summarises the number of optical detections (all), probable (Y+) and possible (Y?) members, and non-members (NM) as well as the number of candidates with infrared photometry from 2MASS and from our CFHTIR observations for the various (distance, age) combinations. The membership of each individual object observed with CFHT is also given in the last column in Table B.1 in Appendix B. Out of 39 candidates observed with the CFHTIR camera, 8 remain probable candidates (Y+), 14 are possible members (Y?), and the remainder are classified as non-members (NM). For comparison purposes, we provide the number of objects present in the magnitude range $I = 12-15$, where the contamination is extremely high.

4.4.5 Contamination of the optical sample

The aim of this section is to estimate the contamination among the optically-selected cluster member candidates in Collinder 359. Combining the optical and optical-to-infrared colour-magnitude diagrams, most of the candidates brighter than $I = 17.0$ remain probable candidates. Indeed, 9 out of 805 are rejected as cluster members and 15 more are classified as possible members. Hence, the contamination appears to be on the order of 1–3 %. However, from the $(I, I-K)$ colour-magnitude diagrams (Figure 4.8), we can assess that the estimate above is a strict lower limit to the true contamination. A large bulk of stars brighter than $I = 15$ mag are likely very

red field stars contaminating the optical sample as discussed before. Ultimately, low-resolution spectroscopy will add further constraints to distinguish field stars from cluster members. The cluster sequence appears more pronounced for magnitudes fainter than about 15 and extends to fainter magnitudes. However, from the colour-magnitude diagrams, this sequence is less and less well-defined towards fainter magnitudes simply because near-infrared follow-up observations are lacking for the large majority (90 %) of candidates (only 39 were followed-up out of 359).

In Figure 4.9, we display the $(I-z, I-K)$ colour-colour diagram of the optically-selected cluster member candidates with infrared magnitudes. The K magnitudes refer to K_s for objects with 2MASS counterparts ($I \leq 17.0$ mag) and to K' for fainter objects followed-up with the CFHTIR camera. The 50 % transmission edges of the K_s filter¹² lie at $2.31\,\mu\text{m}$ and $1.97\,\mu\text{m}$ whereas it is located at $2.0\,\mu\text{m}$ and $2.30\,\mu\text{m}$ for the K' filter¹³. The difference between both filters becomes important shortwards of $2.1\,\mu\text{m}$ as the K_s filter is narrower than the K' filter to minimise the contribution from the Earth atmosphere. We will consider here that the choice of the filter has little influence on the magnitude as no colour term was found in the course of our infrared study in α Per. As a consequence, the $(I-K)$ colour and the membership assessment are not strongly affected by the difference in filters. However, this is likely to play a role for large optical-to-infrared colours.

In Figure 4.9, the solid line indicates the NextGen 50 Myr isochrone for masses larger than $0.1\,\text{M}_\odot$ and the Dusty 50 Myr isochrone for lower masses. The hook at $I-z \sim 0.65$ and $I-K \sim 2.5$ corresponds to $0.1\,\text{M}_\odot$ and reflects the difference in magnitudes derived from the NextGen and Dusty models. The NextGen model predicts an absolute I magnitude of 10.33 and whereas the Dusty model predicts $I = 10.51$ mag for a $0.1\,\text{M}_\odot$ star.

The $(I-z, I-K)$ colour-colour diagram (Figure 4.9) does not provide any additional useful criterion for membership assessment. No clear cluster sequence emerges from this diagram due to, on the one hand, the large contamination at small $(I-K)$ colour (plus symbols), and, on the other hand, the small number of objects with infrared magnitudes below $I = 17$ mag (filled circles). We nevertheless notice that the contamination originates mostly from field stars rather than giants, contrary to the results found in our study of α Per (Chapter 3).

To summarise, the optical selection method appears rather efficient at extracting cluster member candidates in Collinder 359 from the large number of contaminating objects detected in the CFH12K wide-field images. Infrared K' -band photometry was used to weed out contaminating field dwarfs at magnitudes fainter than about $I = 15$. for the bulk of objects brighter than this boundary, the optical-to-infrared colours are not sufficient to estimate the level of contamination. Additional near-infrared photometry of the remainder ~ 300 faint candidates is required to further analyse the contamination at and below the stellar/substellar boundary. A total of 8 nights was granted for K -band imaging in June 2004, divided into 4 nights with the 2.2-m telescope at Calar Alto and 4 nights with the CFHT 3.6-m telescope. Also time for low-resolution optical spectroscopy was granted with the TNG/DOLORES and WHT/AF2/WYFFOS spectrographs to assign spectral types to the optically-selected cluster member candidates in Collinder 359 and ascertain membership.

¹²http://www.ipac.caltech.edu/2mass/releases/allsky/doc/sec6_4a.tbl3.html

¹³<http://www.cfht.hawaii.edu/Instruments/Filters/curves/cfh5338.dat>

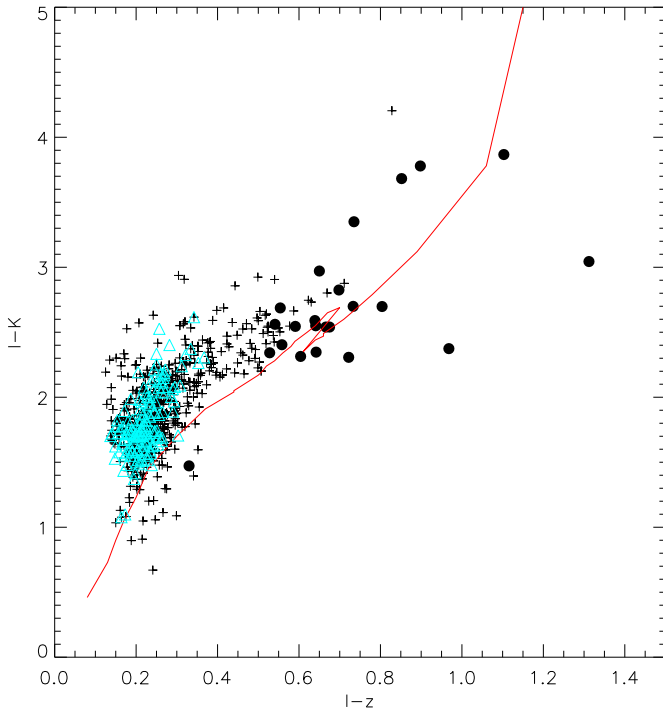


Figure 4.9: $(I-z, I-K)$ colour-colour diagram for the cluster member candidates in Collinder 359 with infrared magnitudes. The photometry is derived from the 2MASS database for objects brighter than $I \leq 17$ mag (plus symbols) and from the CFHTIR follow-up obtained in July 2003 for fainter objects (filled circles). The open triangles indicate candidates with proper motion (UCAC2; Zacharias et al. 2003) consistent with cluster membership. The solid line corresponds to the NextGen 50 Myr isochrone for masses above $0.1 M_{\odot}$ and the Dusty 50 Myr isochrone for lower masses. The hook reflects the difference in magnitudes predicted by the NextGen and Dusty isochrones for a $0.1 M_{\odot}$. Most of the contaminants are likely field dwarfs and not background giants seen along the line of sight of the cluster.

4.5 The luminosity function of Collinder 359

As discussed earlier, the age and distance estimates for Collinder 359 are poorly constrained. Collinder 359 has not been studied extensively to date and the wide-field optical survey presented in this thesis is the first of this kind for the cluster. Thus, we would like to address in this section three major issues regarding the cluster, which are of prime importance in inferring its luminosity function.

1. Can we confirm the existence of the cluster?
2. What is the age of the cluster?
3. What is the distance of the cluster?

4.5.1 The existence of the cluster

According to the available literature on Collinder 359, a handful of objects belong to the cluster, we are confronted to the following question: can we confirm the existence of the cluster? Optical images of the region around 67 Oph do not show an obvious clustering as for the Pleiades as reported by Melotte (1915) and Collinder (1931). Despite the intermediate galactic latitude ($b = +12.5^\circ$) of Collinder 359 between the α Per and the Pleiades clusters, the gap between field stars and cluster members is not evident in the $(I, I-z)$ colour-magnitude diagram (Figure 4.6). Furthermore, no clear cluster sequence stands out in this diagram to infer the presence of a cluster.

To address this issue, we have used proper motion information from the second release of the on-going USNO CCD Astrograph Catalog (hereafter UCAC2) project. Another source of proper motions for the cluster is the SuperCOSMOS Sky Survey database. However, plates north of $+2^\circ$ in declination are being processed and scanned at the moment and will be available only in summer 2004 over the entire cluster area (N. Hambly, personal communication).

The UCAC2 is a high density and highly accurate astrometric catalogue of over 48 million stars covering the sky from -90° to $+40^\circ$ in declination (Zacharias et al. 2003). The observed positional errors are about 20 mas for stars brighter than 14 mag and of order 70 mas for stars down to 17.0 mag. The photometry is provided in a non-standard filter located between the V and R filters. The magnitudes suffer from large uncertainties up to 0.3 mag but are not of interest within the framework of this study. We have extracted from the UCAC2 database the coordinates (J2000) and proper motions for all objects within one degree in radius from the cluster centre (RA = $18^{\text{h}}02^{\text{m}}$ and Dec = $+02^\circ 54'$) to the faintest magnitude available.

Figure 4.10 displays the vector point diagrams (proper motion in right ascension versus proper motion in declination) for all stars within one degree in radius from the cluster centre for magnitude brighter than 10.0, 11.0, 12.0, and 13.0, respectively. Two clustering of stars emerge from vector point diagrams where objects brighter than 12.0 mag are included. Two peaks are seen as well when plotting the number of stars as a function of declination. The first group of stars has no significant proper motion and denotes field stars whereas the second exhibits a shift in declination and corresponds to the cluster. The proper motion of the cluster is approximately 0.0 mas/yr and -8.5 mas/yr in right ascension and declination, respectively. The latter values are consistent with the proper motion of the star 67 Oph (*Hipparcos*; Perryman et al. 1997) and the various cluster motion estimates (Collinder 1931; Kharchenko et al. 2004). The separation between field stars and cluster members is hampered at fainter magnitudes by higher contamination so that both groups of stars become indistinguishable.

Based on the vector point diagrams with proper motion measurements for bright objects, **we conclude that the cluster exists and has a mean proper motion of approximately $(0.0, -8.5)$ mas/yr in right ascension and declination, respectively.**

4.5.2 The age of the cluster

Next, we attempt to derive an age for Collinder 359 using our wide-field optical survey and estimate the associated uncertainties. We have followed the approach applied to the α Per cluster by Stauffer et al. (2003). By comparing the location of the star α Persei (filled square in Figure 4.11) in the colour-magnitude diagram ($M_V, B-V$) with theoretical solar metallicity isochrones including moderate overshoot (Girardi et al. 2002), Stauffer et al. (2003) inferred an age of about 50 Myr

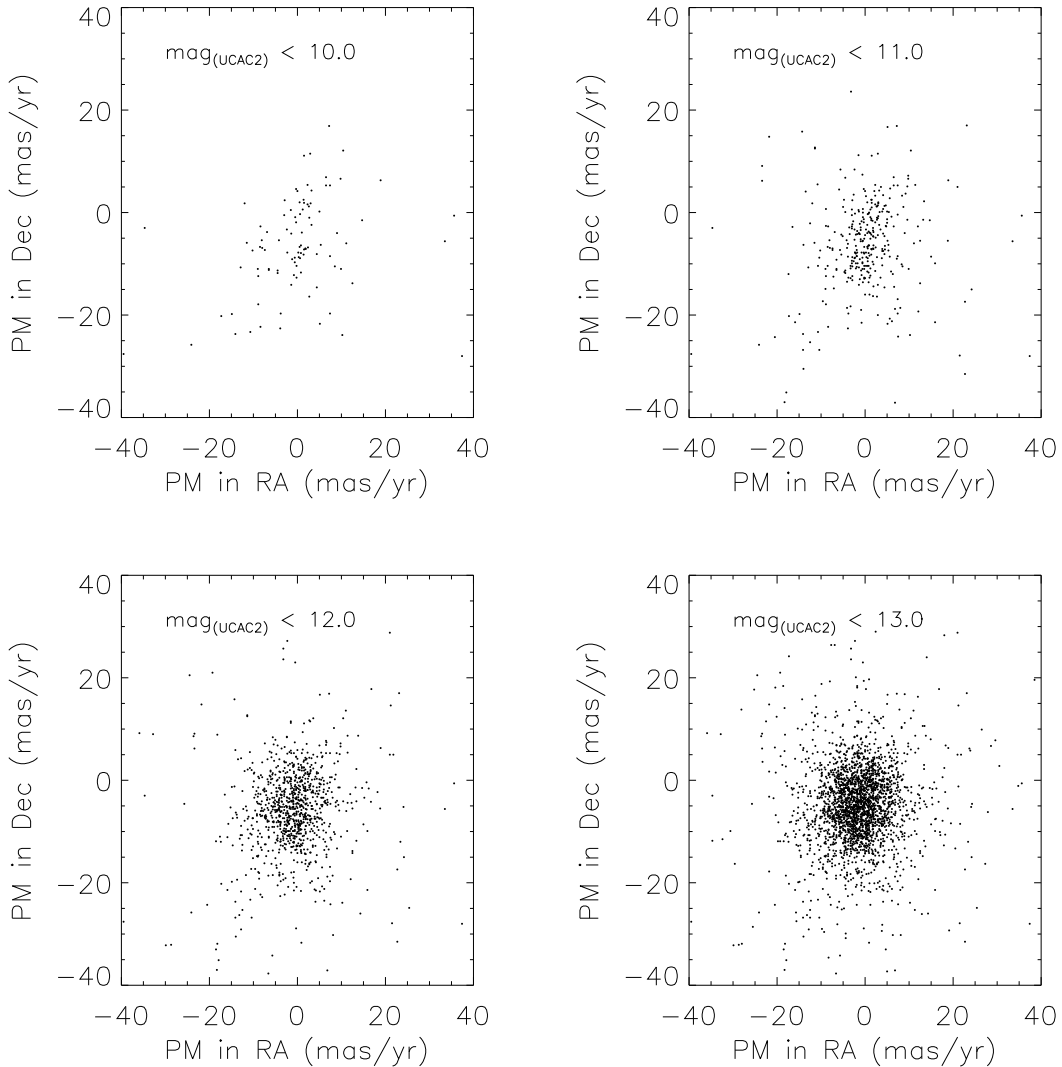


Figure 4.10: Vector point diagrams for all stars located within one degree in radius from the cluster centre for magnitudes brighter than 10, 11, 12, and 13 from left to right, respectively. The proper motions (accurate to 6 mas/yr) are taken from the USNO CCD Astrograph Catalog (Zacharias et al. 2003). Two groups of stars are clearly separated for magnitudes brighter than 12.0. The first is located at (0,0), and the second at approximately (0.0, -8.5) mas/yr in right ascension and declination, respectively. For fainter stars, both groups of stars are merged because of higher field star contamination.

for α Per (solid line in Figure 4.11). We should keep in mind here that the lithium test applied to the α Per cluster yielded a value twice larger than the turn-off main-sequence method (90 Myr versus 50 Myr; Stauffer et al. 1999).

Collinder 359 is located around the B5 supergiant, 67 Oph (filled hexagon in Figure 4.11), which is considered as a member of the cluster with a probability of 75 % and over 95 % by Baumgardt et al. (2000) and Kharchenko et al. (2004, personal communication), respectively. The Hipparcos parallax of 67 Oph is 2.30 ± 0.77 mas/yr and its proper motion 0.41 and -8.22 mas/yr in right ascension and declination, respectively (Perryman et al. 1997).

Assuming a mean apparent magnitude of $V = 3.97 \pm 0.02$ and a mean distance of 435^{+220}_{-110} pc (Perryman et al. 1997), we have derived an absolute magnitude of $M_V = -4.22^{+0.63}_{-0.89}$. The vertical line crossing the hexagon in Figure 4.11 represents the uncertainty on the parallax estimate of 67 Oph. The best positional fit of 67 Oph in the $(M_V, B-V)$ colour-magnitude diagram is obtained for an age of 60 Myr (between the solid and dotted lines in Figure 4.11), with an uncertainty of 20 Myr (extent of the vertical line). Our age estimate is twice as large as the 30 Myr age from

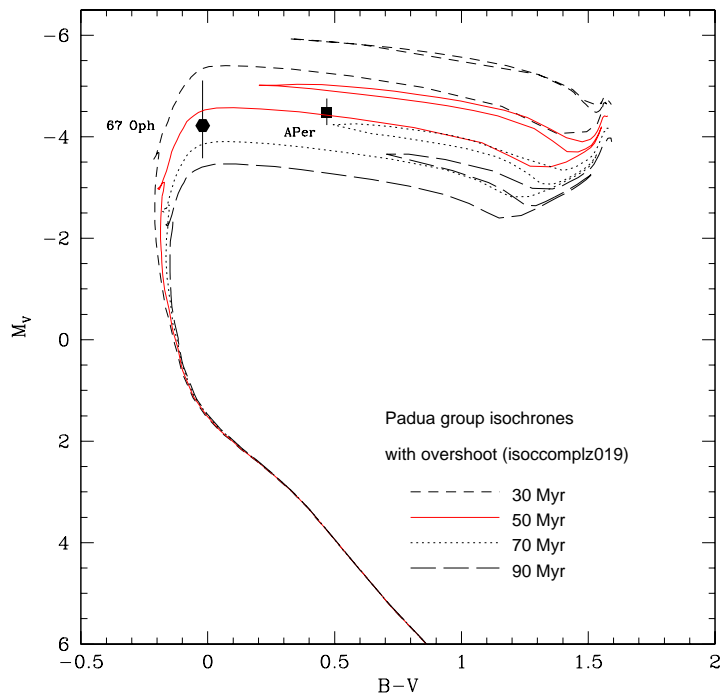


Figure 4.11: $(M_V, B-V)$ colour-magnitude diagram. The position of the F5 supergiant Alpha Per (filled square) and the B5 supergiant 67 Oph (filled hexagon) are indicated. Overplotted are the solar metallicity evolutionary models with moderate overshoot from the Padua group (Girardi et al. 2002) for 30 Myr (dashed line), 50 Myr (solid line), 70 Myr (dotted line), and 90 Myr (long dashed line). The vertical line crossing the solid hexagon represent the errors on the *Hipparcos* parallax measurement for 67 Oph (Perryman et al. 1997). The best fit is obtained for ages of 50 Myr and 60 Myr for the α Per and Collinder 359 clusters, respectively.

Wielen (1971) but comparable to the main-sequence turn-off age of the α Per cluster. Considering the increase in age from 50 Myr to 90 Myr for α Per, the age for Collinder 359 is likely to be older. Assuming a factor of ~ 1.6 between the age from the turn-off main-sequence and the lithium test as suggested by Jeffries & Naylor (2001), the value of age for Collinder 359 would go up to 100 Myr. In this study, we will consider the mean value of the two ages, namely 80 Myr. The lithium test is obviously needed in Collinder 359 to constrain further the age of the cluster.

Based on the present data available for the cluster, we conclude that Collinder 359 has an age estimate comparable to the α Per cluster in the range 60–100 Myr.

4.5.3 The distance of the cluster

Finally, we present a distance estimate for Collinder 359 using the proper motion information available from the UCAC2 catalogue. We have cross-correlated the optically-selected cluster member candidates from the CFH12K optical survey with the UCAC2 catalogue (Zacharias et al. 2003), using matching radii of four times the dispersion value of $0.553''$ and $0.320''$ in right ascension and declination, respectively. A total of 472 objects (open circles in Figure 4.12) were common to both catalogues between $I = 11.6$ and 15.1 mag, representing about 70 % of the whole optical candidate list within this magnitude range. The UCAC2 catalogue includes only the objects with proper motion information so that the 30 % of objects lacking could be explained by the incompleteness of the UCAC2 catalogue.

We have already mentioned the large field contamination at magnitudes brighter than $I = 15$. To minimise this contamination, we have selected from the vector point diagram (left panel in Figure 4.12) proper motion candidates located within a circle centred on the motion of 67 Oph (0.41 and -8.22 mas/yr; Perryman et al. 1997). The radius of the circle, chosen equal to 3.5 mas/yr in both directions, corresponds to the dispersion of the probable cluster members selected by Kharchenko et al. (2004, personal communication; open squares in Figure 4.2) to derive a distance of 650 pc and an age of 30 Myr for Collinder 359. The method employed by Kharchenko to extract members and determine the cluster is as follows. First, objects are selected from their location within the cluster. Second, the proper motion is used to define the most probable members. Third, the selected members are plotted in a colour-magnitude diagram to derive age, distance, and reddening. Finally, this procedure is iterated until the best fit is achieved. The dispersion of the open circles in Figure 4.12 is mostly due to the error on the UCAC2 proper motion measurements (± 6 mas/yr), which is larger than the internal dispersion of the cluster. This dispersion indicates also that the sample of candidates is contaminated by field stars, as discussed previously. We have extracted 142 proper motion candidates (filled circles in Figure 4.12) within the circle defined above. Those objects are plotted as open triangles in the $(I, I-z)$ colour-magnitude diagram (Figure 4.6) and in the $(I-z, I-K)$ CCD (Figure 4.9).

The right panel of Figure 4.12 displays the $(I, I-z)$ colour-magnitude diagram for the optically-selected cluster member candidates in Collinder 359 with proper motion information from the Zacharias et al. (2003) catalogue. The best fit to the lower envelope of the cluster sequence (filled circles in Figure 4.12) is obtained for a distance of 500 pc and an age of 80 Myr (solid line in Figure 4.12). Other ages such as 30 Myr and 50 Myr appear too young for the cluster sequence as they tend to predict redder colours than those observed in the $I = 14-15$ magnitude range. Ages older than 80 Myr could also be possible, implying smaller distances. Note that the distance can be larger by about 50 pc if we take into account a mean extinction of 0.2 mag along the line of

sight of the cluster.

The sequence of proper motion candidates (filled circles in Figure 4.12) is about 0.1–0.2 mag wide. The reddest objects at bright magnitudes are likely field stars, effect not excluded due to the low galactic latitude of the cluster. We could also expect the presence of a binary sequence widening the cluster sequence.

The distance and age estimates from proper motion and photometry are certainly more reliable than turn-off main-sequence fitting technique based on a single high-mass star, 67 Oph. Furthermore, our estimate relies on a larger sample of cluster candidates than the former estimates from Van't-Veer (1980) and Ruciński (1987). Therefore, **we would favour a mean age of 80 Myr with an uncertainty of 20 Myr and distances of 500 ± 100 pc for Collinder 359.**

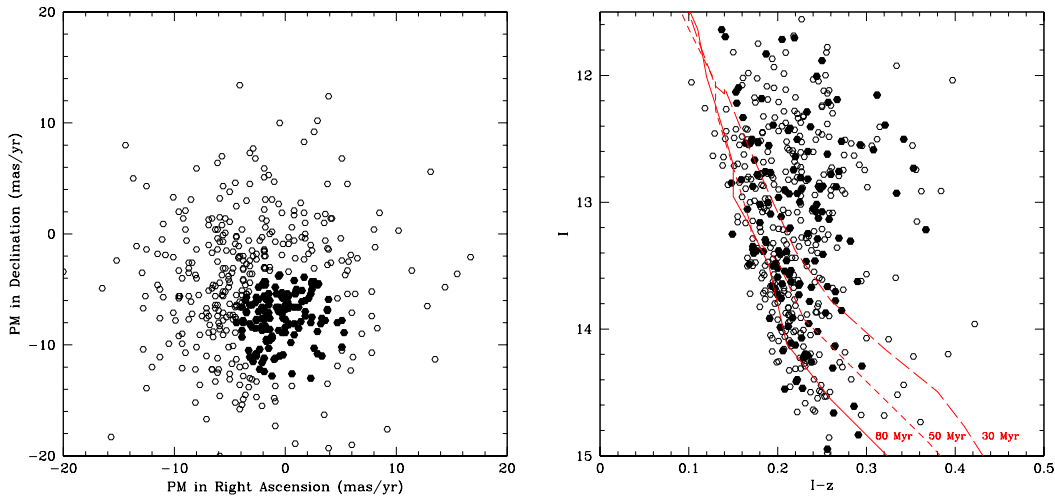


Figure 4.12: *Left panel:* Vector point diagram for optically-selected candidates common to the Zacharias et al. (2003) catalogue (open circles), including the ones with proper motion consistent with the cluster (filled circles). *Right panel:* ($I, I-z$) colour-magnitude diagram for the selected proper motion candidates. Filled and open circles have the same meaning as for the left panel. The solid, dashed, and long dashed lines correspond to the NextGen 80, 50, and 30 Myr isochrones, respectively (Baraffe et al. 1998). The lower envelope of the filled circles is best fit by a distance of 500 pc and an age of 80 Myr.

4.5.4 The cluster luminosity function

According to the results presented in the previous sections (§ 4.5.1–§ 4.5.3), we will assume a mean age of 80 Myr and a distance of 500 pc (distance modulus of 8.5 mag) for Collinder 359 to derive the cluster luminosity function (Figure 4.13 and Table 4.13). We remind that the uncertainty on the age and the distance of the cluster are 20 Myr and 100 pc, respectively. Nevertheless, we will address the issue regarding the influence of the age and the distance on the shape of the cluster luminosity function. We will consider here *only* the probable (Y+) cluster member candidates in

Collinder 359 from the results of the optical and the near-infrared photometry. We did not apply any selection based on proper motion measurements.

We have employed two approaches to derive the cluster luminosity function. The first approach consisted in counting the number of stars per bin of 0.5 mag (open squares in Figure 4.13). The second approach “smoothed” the luminosity function to better characterise the faint end, i.e. we have counted the number of stars per interval of 1.0 magnitude with steps of 0.5 magnitude (filled circles in Figure 4.13). Both methods yielded similar cluster luminosity functions.

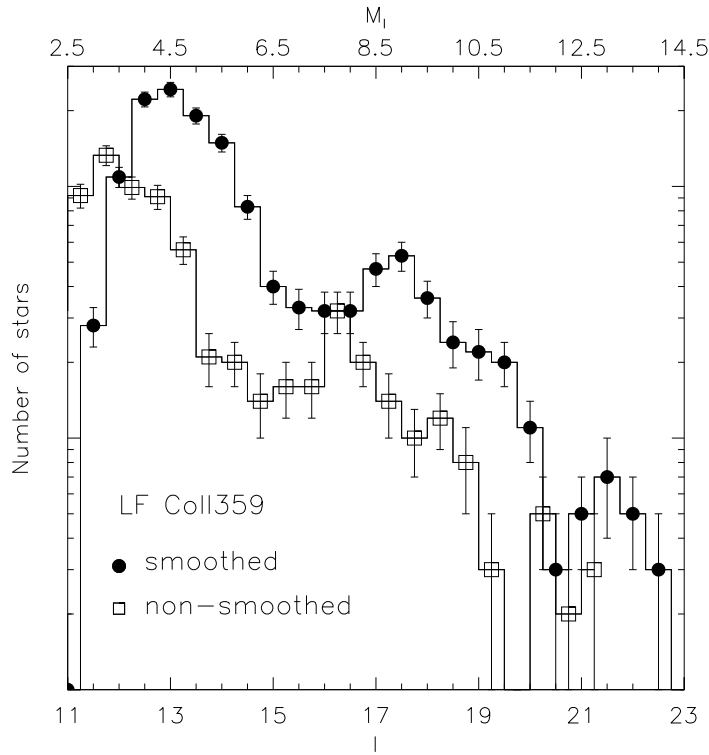


Figure 4.13: The cluster luminosity function assuming an age of 80 Myr and a distance of 500 pc for Collinder 359. The open squares represent the number of stars per bin of 0.5 magnitude whereas the filled circles indicate the number of stars in a 1.0 magnitude bin by step of 0.5 magnitudes. Poisson errors associated to the cluster luminosity function are indicated by vertical lines. Table 4.13 provides the number of stars per magnitude bin for the smoothed luminosity function.

Several features seen in the cluster luminosity function (Figure 4.13) are described below.

- A peak at $I = 12.5\text{--}13.0$ mag corresponding to approximately $1.0 M_{\odot}$ at an age of 80 Myr and a distance of 500 pc. The decline at brighter ($I \geq 12.5$) magnitudes reflects the incompleteness of the optical survey in that magnitude range caused by the saturation of the short exposures. The cross-correlation between the optically-selected cluster member candidates and the UCAC2 catalogue (Zacharias et al. 2003) indicates that a large number of objects have proper motions consistent with membership (Figure 4.12). However, the dispersion in the vector point diagram confirms a significant contamination by field stars difficult to

quantify at this stage.

- A peak at $I = 17.0\text{--}17.5$ mag ($M_I = 8.5\text{--}9.0$ mag) corresponding to masses of approximately $0.30 M_\odot$. A comparable peak is seen at $M_I = 11$ mag in NGC2516 (Jeffries et al. 2001), while this feature is detected at $M_I = 9$ mag in M35 (Barrado y Navascués et al. 2001) and $M_I = 10$ mag in α Per (Barrado y Navascués et al. 2002). This peak does not occur at the same absolute magnitude in all clusters, implying that it may be age dependent. This feature may correspond to the H₂-convection peak identified by Kroupa et al. (1990, 1993) in the luminosity function of nearby field stars but this hypothesis should be further investigated.
- A dip at $I = 20.0\text{--}20.5$ mag ($M \sim 0.070 M_\odot$) is clearly detected in the colour-magnitude diagram (Figure 4.6) well above our completeness limit. This feature is comparable to the gap seen in the α Per luminosity function at $M_I = 12.5$ mag (Barrado y Navascués et al. 2002). This dip is detected both in the field (Reid & Cruz 2002) and in young clusters, including σ Orionis (Béjar et al. 2001), the Trapezium Cluster (Lucas & Roche 2000), IC348 (Luhman 1999), the Pleiades (Jameson et al. 2002), and IC 2391 (Barrado y Navascués et al. 2001a). Despite the difference in age between the regions mentioned above, Jameson et al. (2002) argued that this gap is universal as it occurs consistently at the same spectral types. This feature might originate from the sharp fall in the luminosity-mass relation due to the formation of large dust grains at low temperatures around spectral types M7–M8 (Jameson et al. 2002). Considering the intrinsic colours versus spectral types given in Table 7 in Luhman et al. (2003b), a M7 dwarf has a $I-z = 0.98$ (no extinction is taken into account for this estimate). The observed dip in the colour-magnitude diagram for Collinder 359 occurs at $I-z = 0.85\text{--}1.00$ mag. However, IC348 is younger than Collinder 359, yielding hotter effective temperature at a given spectral type. Taking into account the uncertainties on the photometry (± 0.05 mag) and on the spectral type determination (half a subclass error), it is possible that the gap in the luminosity function is caused by the deficit of M7–M8 dwarfs.

4.6 The mass function of Collinder 359

4.6.1 The mass-magnitude relation

To transform the luminosity function of Collinder 359 into a mass function, we have used the NextGen and Dusty models from the Lyon group. For a given age and mass, the evolutionary models predict optical ($VRIz$) and near-infrared (JHK) absolute magnitudes. The I and z magnitudes were specifically computed for the CFH12K filters and we will use them to derive the mass function. We have merged both isochrone files to create a magnitude-mass relationship from 1.4 down to $0.010 M_\odot$. The NextGen isochrones are used for effective temperatures higher than 2500 K, corresponding to masses of $0.050 M_\odot$ at 80 Myr ($M_I \sim 13.0$ mag). These isochrones are completed by the Dusty models for lower masses down to $20 M_{Jup}$ ($M_I \sim 19.1$ mag at 80 Myr). The useful range of the merged isochrones in the course of our study of Collinder 359 is $1.3\text{--}0.030 M_\odot$.

The NextGen and Dusty models include the treatment of the atmospheres in contrast to other evolutionary models, such as those of D'Antona & Mazzitelli (1994), which assume grey atmospheres. These assumptions generally lead to higher effective temperatures and luminosities at a

Table 4.13: Number of stars per magnitude bin (luminosity function) and number of stars per mass bin in M_{\odot} (mass function) in Collinder 359, assuming a distance of 500 pc and an age of 80 Myr for the cluster. The luminosity function was transformed into a mass function using the NextGen and Dusty evolutionary models for masses higher and lower than $50 M_{\text{Jup}}$, respectively. The uncertainties quoted for the luminosity function are Poisson errors (square root of the number of stars per magnitude bin). The transformation of the luminosity function into a mass function was achieved by dividing the number of objects per magnitude bin by the difference of the upper and lower mass limit of the bin.

Mag bin	Mid-mass (M_{\odot})	Nb per mag bin	Nb per mass (M_{\odot})
11.0–12.0	1.390	28 ± 5	86 ± 15
11.5–12.5	1.241	109 ± 10	409 ± 37
12.0–13.0	1.124	222 ± 15	1002 ± 67
12.5–13.5	1.020	243 ± 16	1216 ± 80
13.0–14.0	0.924	191 ± 14	1073 ± 78
13.5–14.5	0.842	149 ± 12	876 ± 70
14.0–15.0	0.754	83 ± 9	468 ± 50
14.5–15.5	0.664	40 ± 6	277 ± 41
15.0–16.0	0.609	33 ± 6	283 ± 51
15.5–16.5	0.548	32 ± 6	233 ± 43
16.0–17.0	0.472	32 ± 6	190 ± 35
16.5–17.5	0.380	47 ± 7	256 ± 38
17.0–18.0	0.290	53 ± 7	326 ± 43
17.5–18.5	0.217	36 ± 6	291 ± 48
18.0–19.0	0.166	24 ± 5	272 ± 56
18.5–19.5	0.129	22 ± 5	348 ± 79
19.0–20.0	0.103	20 ± 4	439 ± 87
19.5–20.5	0.084	11 ± 3	328 ± 89
20.0–21.0	0.069	3 ± 2	120 ± 80
20.5–21.5	0.059	5 ± 2	210 ± 84
21.0–22.0	0.046	7 ± 3	378 ± 162
21.5–22.5	0.040	5 ± 2	574 ± 229
22.0–23.0	0.037	3 ± 2	446 ± 297

given mass. Furthermore, the treatment of the atmospheres predicts absolute magnitudes in various passbands, hence avoiding the use of bolometric corrections which remain highly uncertain for young open clusters. The models of Burrows et al. (2001) include non-gray atmospheres but are valid for masses lower than $0.1 M_{\odot}$, not low enough for our study. Finally, the Dusty models include the treatment of dust settling which affects the temperatures and observed colours of low-mass stars and brown dwarfs. The influence of the dust settling at the L/T transition around 1300 K for field objects has been proven and observed. The same effect will take place at earlier spectral types (late-M and early-L) in pre-main-sequence clusters due to the younger ages. The knowledge of opacity line lists for species such as TiO and VO, which are responsible for the shape of M dwarf spectra, is of prime importance to reproduce the observed colours of young cluster members.

Moreover, the evolutionary models from the Lyon group have been extensively used to estimate mass functions in open clusters, including the Pleiades (Martín et al. 1998; Dobbie et al. 2002;

Moraux et al. 2003), α Per (Barrado y Navascués et al. 2002), and M35 (Barrado y Navascués et al. 2001), and star-forming regions such as Taurus (Briceño et al. 2002) and IC348 (Luhman et al. 2003b). The NextGen and Dusty models have been the most successful evolutionary models in predicting coeval ages for the different components of the young multiple system GG Tau (White et al. 1999). Furthermore, different models from various groups had little effect on the mass function in α Per (Barrado y Navascués et al. 2002) and M35 (Barrado y Navascués et al. 2001). Finally, the mass estimates from evolutionary models appear generally underestimated by 5 to 20 % for main-sequence stars and by up to 50 % for pre-main-sequence stars (Hillenbrand & White 2004).

4.6.2 The cluster mass function

We have converted the cluster luminosity function into a mass function using the evolutionary models from the Lyon group (Baraffe et al. 1998; Chabrier et al. 2000b). The number of objects per unit of mass (dN/dM) is obtained by dividing the number of objects per magnitude bin (ΔN) by the difference between the upper and lower limits of the bin in mass ($\Delta M = M_2 - M_1$). The uncertainty is computed from the Poisson uncertainties of the luminosity function. For example, the magnitude range $I = 12\text{--}13$ mag corresponds to a mass range of $M = 1.241\text{--}1.020 M_{\odot}$. The number of objects per unit of mass and its uncertainty (Table 4.13) is given by:

$$\frac{dN}{dM} = \frac{\Delta N}{\Delta M} = \frac{222}{1.241 - 1.020} \pm \frac{\sqrt{222}}{1.241 - 1.020} = 1002 \pm 67$$

The mean mass and the number of stars per mass bin are given in Table 4.13. The mass function is plotted as filled circles in Figure 4.14. We will express the cluster mass function throughout this section as the mass spectrum (α represents the slope of the mass spectrum), namely:

$$\frac{dN}{dM} \propto M^{-\alpha}$$

The best linear fit to the cluster mass spectra, assuming an age of 80 Myr and a distance of 500 pc for Collinder 359, is obtained for $\alpha = 0.30$ (solid line in Figure 4.14).

Three major features are seen in the cluster mass function and described below:

- A peak at about $1 M_{\odot}$ which is not real due to the large field contamination observed in this range. Additional observations are needed to estimate the level of contamination in the $0.7\text{--}1.3 M_{\odot}$ mass range, at the distance and age of the cluster.
- A slow rise in the cluster mass function from $0.6 M_{\odot}$ down to our completeness limit at about $0.040 M_{\odot}$. The power law index α appears flatter than the Pleiades estimates.
- A dip in the mass function occurs around $0.070 M_{\odot}$ and is likely due to the dearth of M7–M8 objects. This gap is detected in the field (Reid & Cruz 2002) and in six open clusters, including the Pleiades (Jameson et al. 2002) and α Per (Barrado y Navascués et al. 2002). This argument is validated by the intrinsic colours of M7 dwarfs as defined by Luhman et al. (2003b) in the case of the IC348 cluster (see discussion in previous section).

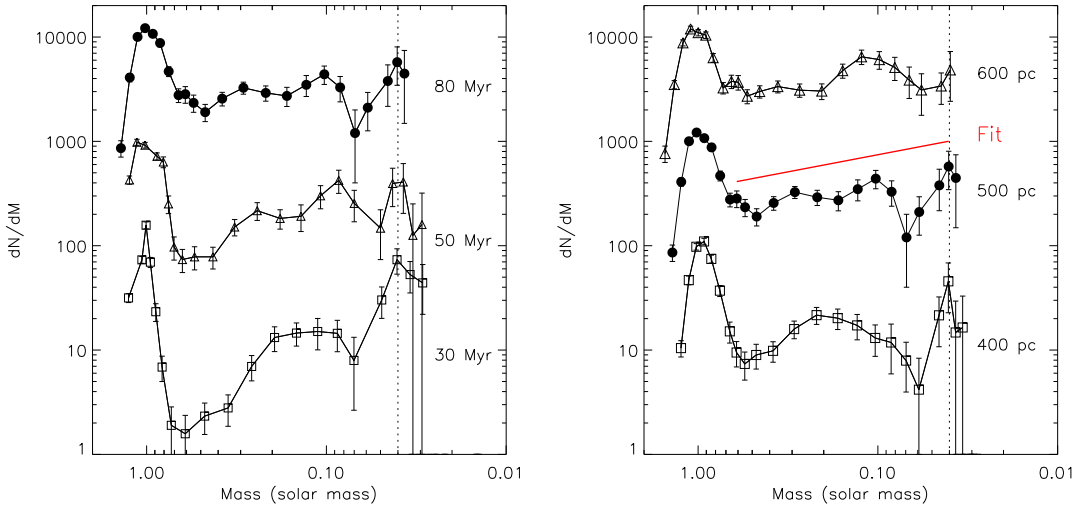


Figure 4.14: Mass function for Collinder 359. Filled circles represent the cluster mass function, assuming a distance of 500 pc and an age of 80 Myr for Collinder 359. *Left panel:* Influence of the age on the mass function for 30 Myr (open squares), 50 Myr (open triangles), and 80 Myr (filled circles). The slope of the mass function gets steeper for younger ages. *Right panel:* Influence of the distance on the mass function for 400 pc (open squares), 500 pc (filled circles), and 600 pc (open triangles), assuming an age of 80 Myr. The distance appears to have little influence on the slope of the mass function. The vertical dotted line represents the completeness of the CFH12K optical survey at $I = 22$, corresponding to a mass of $0.040 M_{\odot}$ at the assumed age and distance for the cluster. The three mass functions are offset for clarity.

Table 4.14: Dependence of the power law index α with distance and age in Collinder 359. We have used linear fits to estimate the slope of the mass spectrum, assuming different (distance, age) combinations for the cluster. The three ages are 30, 50, and 80 Myr assuming a distance of 500 pc. The three distances are 400, 500, and 600 pc, assuming a mean age of 80 Myr.

Age	Distance	Mass range	Power law index
80 Myr	400 pc	$M = 0.55 - 0.035 M_{\odot}$	$\alpha = 0.35 \pm 0.15$
	500 pc	$M = 0.61 - 0.040 M_{\odot}$	$\alpha = 0.30 \pm 0.10$
	600 pc	$M = 0.65 - 0.044 M_{\odot}$	$\alpha = 0.25 \pm 0.10$
50 Myr	400 pc	$M = 0.43 - 0.030 M_{\odot}$	$\alpha = 0.60 \pm 0.15$
	500 pc	$M = 0.54 - 0.030 M_{\odot}$	$\alpha = 0.45 \pm 0.10$
	600 pc	$M = 0.62 - 0.032 M_{\odot}$	$\alpha = 0.45 \pm 0.10$
30 Myr	400 pc	$M = 0.60 - 0.030 M_{\odot}$	$\alpha = 1.0 \pm 0.2$
	500 pc	$M = 0.70 - 0.030 M_{\odot}$	$\alpha = 1.0 \pm 0.2$
	600 pc	$M = 0.58 - 0.030 M_{\odot}$	$\alpha = 0.5 \pm 0.1$

We have investigated the influence of the age and the distance on the cluster mass spectrum. In the left panel in Figure 4.14, we have plotted the mass spectrum in Collinder 359 for three ages,

including 30 Myr (open squares), 50 Myr (open triangles), and 80 Myr (filled circles), assuming a distance of 500 pc. In the right panel in Figure 4.14, we have plotted the mass spectrum for three distances, including 400 pc (open squares), 500 pc (filled circles), and 600 pc (open triangles), assuming an age of 80 Myr.

We have used linear fits to estimate the slopes for each (distance, age) combination (Table 4.14). The change in distance (± 100 pc) seems to have little influence on the power law index α , independent of the assumed age. On the contrary, the slope of the mass spectrum tends to increase with younger ages, ranging from $\alpha = 0.3$ at 80 Myr to $\alpha = 1.0$ at 30 Myr. The gap observed around $0.070 M_{\odot}$ persists independent of the (distance, age) combination, implying that it is likely a real feature.

As the age of Collinder 359 is likely between 60 and 100 Myr and the distance 500 ± 100 pc, we conclude that the best fit to the cluster mass spectrum is obtained for a power law index $\alpha = 0.30 \pm 0.20$ over the mass range $0.60\text{--}0.04 M_{\odot}$.

4.6.3 Uncertainties on the cluster mass function

The derivation of the cluster mass function is, in theory, a straightforward process. Based on the selected cluster members, we count the number of stars per magnitude bins to create a luminosity function. To transform the luminosity function into a mass function, we apply a magnitude-mass relationship provided by evolutionary models. For a given age and a given mass, the evolutionary models provide luminosities and effective temperatures. However, in practice, the cluster mass function determination is hampered by multiple factors sometimes difficult to quantify.

1. The largest uncertainty resides in the distance of Collinder 359. Larger and smaller distances will shift objects towards higher and lower masses, respectively. We have assumed a distance of 500 pc for Collinder 359 and shown that distances spanning 400–600 pc have little influence on the overall shape of the mass function.
2. The second uncertainty concerns the age of Collinder 359. Older and younger ages will shift the objects towards higher and lower masses, respectively, with a tendency to increase the slope of the mass spectrum at younger ages.
3. Some objects might have escaped detection within the 1.6 square degree area surveyed in Collinder 359. Despite the good cosmetics of the CFH12K camera, some bona-fide cluster members might lie on a bad column or have their photometry affected by bad pixels. Similarly, bright stars hamper the detection of nearby faint cluster members. This effect is likely to be random. If the bias is larger towards fainter objects, α may have to be increased. Our ability of detecting substellar objects is affected by the fact that the luminosity of brown dwarfs decreases with age (de la Fuente Marcos & de la Fuente Marcos 2000).
4. A large number of faint ($I \geq 17$ mag) cluster member candidates are still lacking near-infrared photometry. Furthermore, optical spectroscopy is required to ascertain the membership of the selected candidates. As an example, the contamination was estimated at $\sim 25\text{--}40\%$ for low-mass stars and brown dwarfs in the Pleiades (Bouvier et al. 1998; Martín et al. 2000a; Moraux et al. 2001), and in α Per (Barrado y Navascués et al. 2002). We expect a comparable level of contamination in Collinder 359 due to its intermediate galactic latitude. If the contamination is larger in the brown dwarf regime than for low-mass stars, α may have to be decreased.

5. According to estimates from Kharchenko et al. (2004, personal communication), we have mainly focused on the cluster corona. If Collinder 359 is indeed a cluster younger than the Pleiades, the mass segregation and evaporation of brown dwarfs should be less than 10 %, assuming an homogeneous distribution of substellar objects across the cluster (de la Fuente Marcos & de la Fuente Marcos 2000). In contrast, if the cluster is older than the estimates presented here and if dynamical evolution has already taken place, the number of very low-mass stars and brown dwarfs detected in the surveyed area has been well overestimated. The α index may have to be increased according to the amount of brown dwarfs which have escaped the cluster.
6. We have used the magnitude-mass relationship from the Lyon group and combined the NextGen and Dusty models to infer a mass function from 1.3 to $0.040 M_{\odot}$. Other evolutionary models assume grey atmospheres (e.g. D'Antona & Mazzitelli 1994) and tend to predict higher effective temperatures and luminosities so α would have to be decreased. However, Barrado y Navascués et al. (2001, 2002) have shown that various evolutionary models had little influence on the α Per and M35 mass functions. A thorough comparison of a large sample of stars with different evolutionary tracks by Hillenbrand & White (2004) indicates that masses of main-sequence and pre-main-sequence objects are underestimated. The effect on the shape of the mass spectrum is difficult to assess in that case.
7. We have neglected the effect of unresolved binaries. For example, a brown dwarf in the Pleiades, PPI15 (Rebolo et al. 1995) was resolved into a spectroscopic binary brown dwarf (Basri & Martín 1999a). The influence of unresolved binaries in open clusters was quantified by Kroupa (2001), implying that the power law index α should be increased by about 0.5 over the $1.0-0.1 M_{\odot}$ mass range. Martín et al. (2000a) failed to detect companions in Pleiades brown dwarf candidates with separations wider than 27 AU at the distance of the cluster, suggesting that the binary frequency of brown dwarfs is not much larger than for M dwarfs and has little effect on the shape of the mass function. If the binary correction is important at low masses (for example if a large number of M dwarfs are binaries), α may have to be increased.
8. A possible age spread in the cluster was not considered throughout this study. Spectroscopic confirmation is required to place the cluster members in the HR diagram in order to estimate this effect.

To summarise, large uncertainties remain regarding the mass function in Collinder 359 which led us to consider a conservative error on the slope of the cluster mass function i.e. $\alpha = 0.3 \pm 0.2$ over the $0.6-0.04 M_{\odot}$ mass range.

4.6.4 Comparison with other young clusters

We have compared the mass function for Collinder 359 with estimates available in the literature for other young open clusters and star-forming regions. Figure 4.15 compares the mass function for Collinder 359 (filled circles) with α Per (Barrado y Navascués et al. 2002), M35 (Barrado y Navascués et al. 2001), and various estimates of the Pleiades mass spectrum (Bouvier et al. 1998; Martín et al. 1998; Dobbie et al. 2002; Tej et al. 2002).

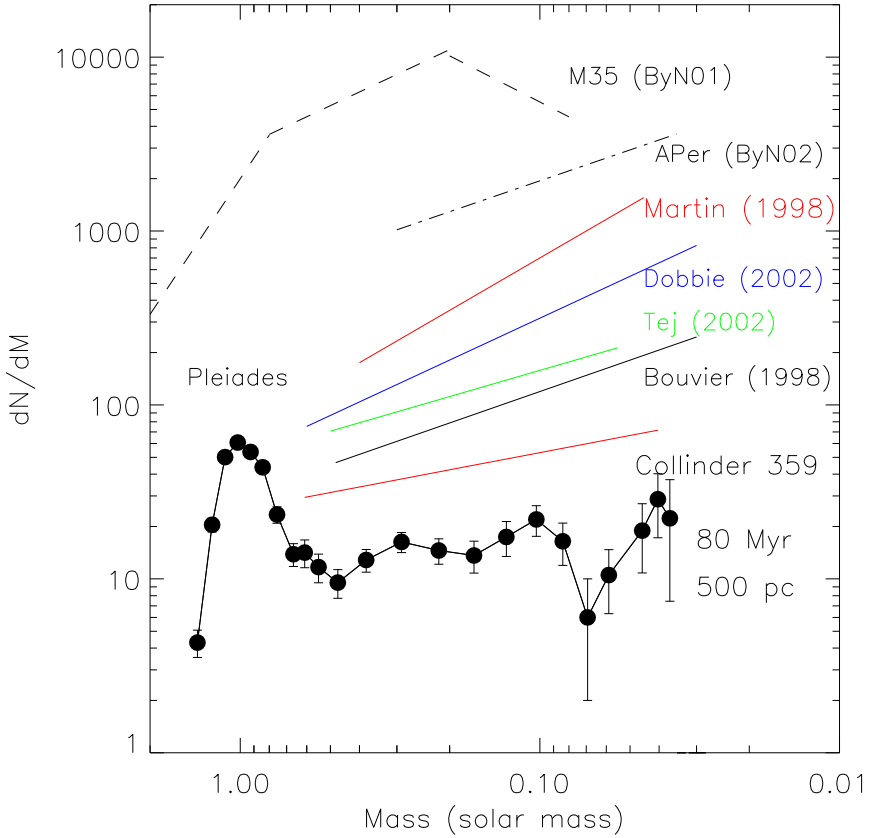


Figure 4.15: Comparison of the mas spectrum for Collinder 359 (filled circles with solid line) with other open clusters, including α Per (dot-dashed line; Barrado y Navascués et al. 2002), M35 (dashed line; Barrado y Navascués et al. 2001), and the Pleiades (Martín et al. 1998; Bouvier et al. 1998; Dobbie et al. 2002; Tej et al. 2002). The best linear fit to the cluster mass spectrum (red line) appears flatter than the Pleiades over the $0.55\text{--}0.035 M_\odot$ mass range. The peak at $\sim 1 M_\odot$ is not a real feature but the outcome of a large contamination at higher masses.

Across the stellar/substellar boundary, the power law indices estimated in the Pleiades by various groups were generally in good agreement within the errors with $\alpha=0.5\text{--}1.0$ in the $0.40\text{--}0.045 M_\odot$ mass range (Figure 4.15; Table 1.1 in Chapter 1).

Barrado y Navascués et al. (2002) has inferred a comparable mass function for the α Per cluster with $\alpha=0.59\pm0.05$ from 0.30 to $0.035 M_\odot$ (Figure 4.15; Chapter 3).

Concerning M35, the mass spectrum was approximated by a three-segment power law over the $6\text{--}0.08 M_\odot$ mass range (Figure 4.15; Barrado y Navascués et al. 2001).

The mass spectrum derived for Collinder 359 is overall consistent within the uncertainties with various estimates in open cluster and star-forming regions. Our result appear however flatter than the Pleiades and α Per estimates (Figure 4.15) although they might be considered in agreement within the error bars (0.1 and 0.2 for the Pleiades and Collinder 359, respectively).

Compared to other well-studied regions mentioned above, our estimate is solely based on optical and near-infrared photometric selection. The next step is to obtain low-resolution spectroscopy for all selected cluster member candidates in Collinder 359 to verify the validity of the mass function and the various observed dips and gaps. If confirmed, the gap at $0.070 M_{\odot}$ combined with the search for the lithium depletion boundary would add strong constraints on the age and the distance of the cluster and confirm the present estimates.

4.7 Conclusions of the survey in Collinder 359 and perspectives

We have presented in this chapter the first deep optical wide-field imaging survey complemented with near-infrared follow-up observations of the young open cluster Collinder 359. We have surveyed 1.6 square degrees in the cluster in the I and z filters down to detection and completeness limits of 22.0 and 24.0 with the CFH12K on the Canada-France-Hawaii 3.6-m telescope. Based on their location in the optical ($I, I-z$) colour-magnitude diagram, we have extracted a total of 1033 cluster member candidates in Collinder 359 spanning $1.3-0.040 M_{\odot}$, assuming a distance of 650 pc and an age of 80 Myr. We have cross-correlated the optically-selected candidates with the 2MASS database for objects brighter than $I = 17.0$ to weed out contaminating field stars. Further K' -band photometry has been obtained for a subsample of 39 faint cluster candidates to probe the contamination at and below the stellar/substellar boundary.

By comparing the location of the brightest cluster member, 67 Oph, with solar metallicity isochrones including moderate overshoot, we have derived an age of 60 ± 20 Myr for Collinder 359. The comparison of the NextGen evolutionary models to the cluster candidates selected from their proper motion and colours yielded a mean age of 80 Myr with an uncertainty of 20 Myr and a distance of 500 ± 100 pc. The age is larger than previous estimates in the literature, whereas the distance is within the uncertainties of former determinations but based on a larger number of objects. Hence, Collinder 359 is probably not a pre-main-sequence cluster (10–50 Myr) as thought earlier but likely coeval with α Per. The question set in § 4.1 regarding the test of pre-main-sequence evolutionary tracks with clusters 10–50 Myr old might not be solved with the study of Collinder 359.

Finally, we have derived luminosity and mass functions for Collinder 359 using the NextGen and Dusty models from the Lyon group. Despite the uncertainties inherent to photometric surveys in open clusters, we have reported a dip in the luminosity and mass functions located at $I = 20.5$ (corresponding to a mass of $70 M_{Jup}$) assuming a mean age of 80 Myr and a distance of 500 pc) likely caused by the dearth of M7–M8 dwarfs observed in the solar neighbourhood and young clusters. The best fit to the slope of the mass function, when expressed as the mass spectrum is $\alpha = 0.30 \pm 0.20$ over the $0.55-0.035 M_{\odot}$ mass range. The derived slope is flatter than estimates in the Pleiades and in the α Per clusters although they are consistent within the uncertainties. Spectroscopy is needed to verify the results presented in this chapter as our work is solely based on photometry. Our study do not provide a convincing evidence for a variable mass spectrum in open clusters.

The detailed study of Collinder 359 constitutes a first step towards the determination of an unbiased mass function in a previously unstudied young open cluster. Follow-up observations of the selected cluster member candidates in Collinder 359 are required to ascertain their membership,

including near-infrared imaging and optical spectroscopy. We have been granted observing time with several telescopes and instruments within the framework of the CFHT Key Programme to pursue our investigation of Collinder 359 and other pre-main-sequence clusters. The time schedule and the observations are divided as follows:

CFHT/CFHTIR	4 nights (30 May–03 June 2004)	Near-infrared imaging
Calar Alto 2.2-m/MAGIC	4 nights (10–13 June 2004)	Near-infrared imaging
WHT/AF2/WYFFOS	6 nights (18–24 June 2004)	Multi-object spectroscopy
TNG/DOLORES	3 nights (19–21 June 2004)	Optical spectroscopy

Near-infrared imaging will be obtained for the remaining faint ($I \geq 17.0$) cluster member candidates in Collinder 359 to probe the contamination by field stars at and below the hydrogen-burning limit. Low-resolution ($R \sim 600$) optical (6000–10000 Å) spectroscopy will provide spectral classification, gravity measurements, and determination of the level of chromospheric activity, which, together, will allow us to further constrain the membership of cluster candidates.

Longer term observations are foreseen to enlarge our study of Collinder 359. For example, higher resolution optical spectroscopy of the bright cluster members will provide radial and rotational velocities to study the dependence of these parameters with mass and age. Additionally, the inner square degree area in Collinder 359 remains to be surveyed to confirm the results presented in this chapter. Finally, objects brighter than $I \sim 12.0$ and thus more massive than $\sim 1 M_{\odot}$ should be investigated to derive a complete mass function from higher mass stars down to brown dwarfs.

Chapter 5

Outlook and future work for cluster membership

The surveys in α Per and Collinder 359 presented in this thesis are aimed at investigating the stellar and substellar IMF and its dependence with place and time. The α Per cluster has been much more targeted than Collinder 359 in the past. In α Per, we have presented spectroscopic assessment of some low-mass members. In Collinder 359, we have extracted a list of cluster member candidates down into the substellar regime based on their optical colours. Follow-up observations, including near-infrared imaging and optical spectroscopy are, however, required to ascertain the membership of photometrically-selected candidates and obtain a list of genuine members. The survey in Collinder 359 is part of a larger photometric programme aimed at investigating the dependence of the IMF with place and time as well as the properties of stars and brown dwarfs as a function of time.

We will discuss in this chapter the different phases necessary in the study of young open clusters with an emphasis on the remaining projects and future plans for the α Per and Collinder 359 open clusters. This procedure is extended to other open clusters as well. This chapter is structured as follows. The various possibilities offered by large-scale catalogues to study an open cluster as a whole entity are presented in § 5.1. The selection of proper motion candidates in open clusters is described in § 5.2. The near-infrared follow-up imaging of optically-selected cluster member candidates for membership assessment is detailed in § 5.3. The wealth of information provided by the optical spectroscopy to derive spectral types and investigate chromospheric activity, gravity, age, radial and rotational velocities of cluster member candidates is emphasised in § 5.4. Low-resolution near-infrared spectroscopy of cluster candidates is discussed in § 5.5. The identification of X-ray counterparts to photometrically-selected member candidates to ascertain their membership is presented in § 5.6. The issues regarding the binary fraction as a function of mass (§ 5.7) and the variability of cluster members (§ 5.8) are discussed as well.

5.1 Full coverage of a cluster

A survey of an open cluster as a whole entity provides insights on its extent and its dynamical evolution. The distribution of members across the cluster is a key parameter to probe a possible mass segregation. However, up to now, hardly any open cluster has been fully observed down to the brown dwarf regime mostly because of its large extent on the sky. Photographic plates at different epochs represent valuable tools to identify cluster members over large areas via proper motion. This technique is generally limited to the stellar content of open clusters and can reach down to the hydrogen-burning limit in a young nearby open clusters like the Pleiades (Hambly

et al. 1999). Large-scale sky surveys, including 2MASS, the SuperCOSMOS Sky Surveys, and the Guide Star Catalog provide additional photometry and proper motion for stellar members in numerous open clusters. The combination of these databases can serve as a starting point to deeper surveys dedicated to low-mass stars and brown dwarfs in a limited area in clusters.

Recently, Tej et al. (2002) proposed a pure statistical approach using nearby control fields to estimate the field contamination towards three clusters: the Pleiades, IC348, and σ Orionis. This method combined optical and near-infrared magnitudes from the Guide Star Catalog and 2MASS surveys. The cluster luminosity functions were corrected for the number of field stars in the same magnitude range over the same area. The inferred mass functions agreed within the uncertainties with estimates from deep surveys over a similar mass range. Optical spectroscopy of the selected objects would verify whether or not the level of contamination was correctly estimated. The main drawback of this method is the assumption of an age and a distance, parameters fairly well constrained for the three clusters under study but poorly known for the large majority of clusters.

Early studies in the α Per cluster made use of the Palomar photographic plates to extract member candidates over the entire cluster on the basis of their proper motion (Heckmann et al. 1956; Stauffer et al. 1985, 1989b; Prosser 1992). This selection extended to $V = 19$ mag, corresponding to $I \sim 16$ mag and spectral type of M5. Multi-band photometry and optical spectroscopy were necessary to ascertain the membership of these proper motion candidates due to the low galactic latitude of α Per.

A deep wide-field optical (R, I) survey over 4.5 deg^2 was initiated in α Per to find members down into the substellar regime (Barrado y Navascués et al. 2002). The extension of this deep survey to the remaining area would allow us to study the distribution of stars and brown dwarfs in the cluster. Moreover, observations in the z -band are necessary to probe substellar objects down to the deuterium burning limit at $13 M_{\text{Jup}}$.

Despite the large field-of-view ($42' \times 28'$) of the CFH12K camera, we have only been able to survey 1.6 square degrees in Collinder 359, which amounts for 30–40 % of the total cluster area, assuming a corona radius as derived by Kharchenko et al. (2004; personal communication). Two additional projects aiming at a full coverage of Collinder 359 from high-mass stars down into the substellar regime would provide an estimate of the mass function over the whole cluster area.

First, a complementary survey to the CFH12K optical study should be undertaken in the cluster centre in the I and z filters down to a completeness limit of 24.0 to infer a mass function over the whole area. The full coverage of the inner degree in Collinder 359 can be achieved in one night with 4 MegaCam pointings, for example. The MegaCam wide-field camera has superseded the CFH12K camera on the CFHT and offers a one square degree field-of-view with a spatial scale of $0.187''/\text{pixel}$.

The CFHT Key Programme focused on the low-mass end of the mass function skipping the study of high-mass members ($M \geq 1.3 M_{\odot}$) in Collinder 359. Optical and infrared photometry of stars with spectral types B to G could be derived from previous sky surveys such as 2MASS, SSS, and GSC. Subsequent spectroscopy for membership assessment is mandatory but could be conducted with small telescopes.

5.2 Proper motion

Proper motion surveys represent a powerful discriminant to identify members in open clusters and should be considered as the primary step to define a stellar sequence in new clusters prior to any deep photometric survey. The extraction of member candidates is optimally achieved for high galactic latitude open clusters with significant motion compared to field stars due to the lower contamination. The best targets to apply this technique are the Pleiades (e.g. Hambly et al. 1999) and the Hyades (Reid 1992) because both are nearby and located at high galactic latitude. The large majority of clusters listed in the Open Cluster Database do not harbour a significant motion compared to field stars so that the extraction of candidate should solely rely on the colour selection. Some clusters remain nevertheless suitable targets as their proper motion are larger than Collinder 359.

Two major proper motion catalogues are currently fully available to undertake, as an initial step, the selection of member candidates in open clusters. First, the SuperCOSMOS Sky Surveys provides proper motions and optical magnitudes in three broad bands (B_J , R , and I) for objects as faint as $R=20$ with declinations south of $+2^\circ$. The photographic plates covering the whole northern sky are scanned and processed at the moment and should be released in the near future (N. Hambly, personal communication). Second, the UCAC2 catalogue (Zacharias et al. 2003) provides proper motions of over 48 million sources north of $+2^\circ$ and south of $+40^\circ$ in declination with an accuracy of ± 6 mas/yr. This catalogue should be combined with other databases such as 2MASS or DENIS as it is incomplete and does not provide a colour term. The future release of the Guide Star Catalog (version 2.3) will additionally provide proper motions and photometry in three passbands for objects down to $R=20$ in the northern hemisphere after scanning and processing of the Palomar Schmidt plates, complementing hence the SuperCOSMOS Sky Surveys database. A step forward will be achieved with the GAIA astrometric satellite, providing highly accurate positions, proper motions and distances as well as radial velocities for stars few orders of magnitudes fainter than the *Hipparcos* detection limit.

Concerning α Per, proper motions revealed hundreds of cluster members down to $V=19.0$ mag (Prosser 1992) using Palomar Schmidt plates spanning an epoch difference of about 50 years. The motion of the α Per cluster is smaller than the Pleiades, on the order of $+23$ and -25 mas/yr (Robichon et al. 1999), rendering proper motion surveys less efficient. Colour selection and optical spectroscopy are, consequently, mandatory to weed out contaminating objects due to the low galactic latitude of the cluster ($b=-7^\circ$).

We have combined the wide-field optical survey implemented with the CFH12K camera with proper motion measurements from the UCAC2 catalogue (Zacharias et al. 2003) to infer new age and distance estimates for Collinder 359 (Chapter 4) despite the small cluster motion with respect to field stars. The vector point diagram (see Figure 4.12 for details) of the optically-selected candidates in Collinder 359 exhibits a shift in declination of about 8 mas/yr, suggesting that a large fraction of objects are, indeed, bona-fide cluster members. The same technique could be applied to clusters with comparable motion to Collinder 359 by combining the UCAC2 catalogue with all-sky surveys such as 2MASS, GSC, or DENIS.

5.3 Near-infrared imaging of cluster member candidates

The first steps in the study of young (10–200 Myr) open clusters consist in colour selection (Section 5.1) and/or proper motion (Section 5.2) of member candidates. This initial sample of candidates remains nevertheless polluted by galaxies, distant giants, and field dwarfs, harbouring colours similar to young pre-main-sequence objects. The contamination in the low-mass and brown dwarf regimes was estimated to be 25–40 % in the Pleiades (Bouvier et al. 1998; Martín et al. 2000a; Moraux et al. 2001) and in α Per (Barrado y Navascués et al. 2002).

Near-infrared photometry is a useful tool to weed out contaminating objects from cluster member candidates due to the large optical-to-infrared colour baseline. Evolutionary tracks predict bluer optical-to-infrared colours by 1.0 to 1.5 mag for field dwarfs compared to young pre-main-sequence objects (Chabrier et al. 2000b). The J and K -band follow-up observations of optically-selected cluster members have proven very efficient at eliminating field stars and background giants in the Pleiades (Zapatero Osorio et al. 1997a; Pinfield et al. 2000), α Per (Barrado y Navascués et al. 2002; Chapter 3), IC2391 (Barrado y Navascués et al. 2001a), and σ Orionis (Béjar et al. 2001). However, the use of I and K filters as primary selection for cluster member candidates in the α Per cluster turned out to be less efficient than the (R , I) or (I , Z) surveys due to the ability of the K -band to probe larger distances (Chapter 3).

The use of catalogues with proper motion and photometric measurements, including Super-COSMOS Sky Surveys and the Guide Star Catalog will provide initial samples of cluster member candidates in numerous unstudied open clusters. Additional infrared photometry from the DENIS and 2MASS surveys will weed out contaminating objects down to low-mass stars and possibly brown dwarfs, depending on the distance and age of the selected clusters. The extraction of lists of members in a large number of open clusters can be achieved with current archival data as described in this section and the previous ones. The main goal of this extensive work would be the study of the dependence of the mass function on place and time.

Future deep infrared large-scale surveys, including UKIDSS¹, WIRCam², and VISTA³ will probe young substellar objects over large areas. For example, the UKIDSS dedicated survey of galactic open clusters aims at surveying 1400 square degrees in JHK in 10 open clusters and star-forming regions down to $K = 18.7$, including 79 deg² in the Pleiades, 50 deg² in α Per, and 0.8 deg² in IC4665.

We have used near-infrared photometry to refine the list of optically-selected member candidates in Collinder 359 and reject contaminating field dwarfs and background giants. All candidates brighter than $I = 17$ had a counterpart in the 2MASS database, hence providing J , H , and K magnitudes. We have attempted to probe the contamination down to a mass of about $0.4 M_{\odot}$, assuming a distance of 500 pc and an age of 80 Myr for Collinder 359. Near-infrared photometry turned out to be inefficient in this mass range due to the small difference in $I-K$ colours between field stars and young cluster members. The large contamination observed at magnitudes brighter than $I = 15$ remain to be studied via another method.

A step forward consists in obtaining near-infrared pointing observations of fainter ($I \geq 17.0$) cluster member candidates in Collinder 359. We have already presented the results of a K -band

¹<http://www.ukidss.org/>

²<http://www.cfht.hawaii.edu/News/Projects/WIRCam/New/>

³<http://www.roe.ac.uk/atc/projects/vista/science/>

imaging of a subsample of about 40 optically-selected candidates in Collinder 359 (§ 4.4). We have been granted a total of 8 nights in June 2004 to pursue the infrared follow-up of candidates in three pre-main-sequence clusters observed within the framework of the CFHT Key Programme, including Collinder 359. The observations are divided into 4 nights with the infrared camera (CFHTIR) on the CFH 3.6-m telescope (30 May–02 June 2004) and 4 nights with the MAGIC camera on the Calar Alto 2.2-m telescope (10–13 June 2004). A total of 110 cluster member candidates in Collinder 359 spanning $I = 17.0\text{--}22.0$ lack near-infrared photometry, at distance of 500 pc and an age of 80 Myr. We will likely observe all remaining candidates in Collinder 359 with the nights granted on both telescopes. Note that the UKIRT WFCAM amera used for the UKIDSS project will be available for open proposals, offering an opportunity to include Collinder 359.

5.4 Optical spectroscopy of cluster member candidates

The next step in the study of open clusters consists in obtaining optical spectroscopy of photometrically-selected cluster member candidates to further ascertain their membership. Optical spectroscopy is a key step because it can provide spectral types, chromospheric activity, surface gravity measurements, lithium abundances, and radial and rotational velocities for each candidate. Many criteria described here to assess the membership of candidates have been applied to the α Per cluster (Chapter 3) and are foreseen in Collinder 359.

5.4.1 Spectral classification

The primary aim of the optical spectroscopy is to provide spectral classification for all cluster member candidates to verify their membership. Several spectral indices are available in the literature to estimate the spectral types of low-mass objects with an accuracy of half a subclass or better. The most reliable indices for field late-K and M dwarfs are listed in Table 1.2 in Chapter 1. These indices were specifically defined to estimate the effective temperature of old nearby dwarfs. Although the gravity influences the computation of these indices (Luhman 2000) is poorly known, they are nevertheless used to classify very low-mass stars and brown dwarfs in clusters. Evolutionary tracks are then used to estimate their mass, assuming an age and a distance for the cluster.

In Chapter 3 , we presented moderate-resolution spectroscopy of photometrically-selected cluster members in α Per conducted with the Twin spectrograph on the Calar Alto 3.5-m telescope. Combining spectral indices and comparison with template spectra of known dwarfs observed with the same instrument setup, we have inferred a spectral sequence in agreement with the photometric measurements in the $0.40\text{--}0.12 M_{\odot}$ mass range.

Optical spectroscopy of cluster member candidates in Collinder 359 will constrain the age and the distance of the cluster. The correlation between magnitudes and spectral types will constrain the distance of the cluster. The presence or absence of lithium in absorption at 6708 \AA will set upper limits on the age of the cluster. If the age and the distance estimates for Collinder 359 are correct, the stellar/substellar boundary at $0.075 M_{\odot}$ will occur at a spectral type of M6.5, according to evolutionary models (Baraffe et al. 1998).

5.4.2 Chromospheric activity

Optical spectroscopy provides access to the H α emission line at 6563 Å. The strength of the H α line reflects the level of chromospheric activity in young pre-main-sequence stars and provides an additional criterion for membership assessment. The detection of H α is a key step in the study of open clusters and has been already applied to the Pleiades (Martín et al. 1996), α Per (Chapter 3), IC2391 (Barrado y Navascués et al. 2001a), and σ Orionis (Barrado y Navascués et al. 2001b; Zapatero Osorio et al. 2002). A major drawback of the H α emission line is its variability observed both in young cluster members (Mohanty & Basri 2003) and in the field (e.g. Martín et al. 1999), producing flares with large equivalent widths.

In Chapter 3, we described the results of spectroscopic follow-up observations of all probable cluster member candidates in α Per extracted by Barrado y Navascués et al. (2002) in the 0.40–0.12 M $_{\odot}$ mass range. All objects exhibit H α in emission with equivalent widths ranging from 4 to 15 Å, in agreement with previous studies in the cluster (Zapatero Osorio et al. 1996; Prosser 1992, 1994). The detection of H α in photometrically-selected cluster members adds strong support to the belief that these candidates are members of the cluster although similar level of chromospheric activity is observed in field M dwarfs.

We will obtain low-resolution optical spectroscopy for numerous candidates in Collinder 359 to ascertain their membership and study the evolution of the chromospheric activity with mass. The procedure applied to the α Per cluster will be generalised to Collinder 359.

5.4.3 Surface gravity

Measurements of gravity-sensitive features, including the K I and Na I doublets at 7665/7699 Å and 8183/8195 Å, respectively, can be extracted from optical spectroscopy. A young pre-main-sequence object has lower surface gravity than field stars of similar spectral type, and hence, weaker K I and Na I equivalent widths ($\log(g) = 3.5\text{--}4.5$ versus $5.0\text{--}5.5$). The distinction between pre-main-sequence objects and giants is straightforward due to the extremely low surface gravity of the latter ($\log(g) \sim 0$). The study of stars and brown dwarfs in the solar neighbourhood, in open clusters, and in star-forming regions will provide a two-dimensional spectral classification based on both temperature and surface gravity.

In Chapter 3, we presented surface gravity measurements for a sample of low-mass stars in the α Per cluster. The equivalent widths of the K I and Na I doublets of cluster member candidates in α Per were generally weaker than old field dwarfs of similar spectral type observed within the framework of our proper motion survey (Chapter 2). This trend confirmed that those candidates are younger than nearby dwarfs and adds an additional criterion to spectral types and H α , hence supporting their membership.

A resolution of $R \sim 1000$ envisioned for the multi-fibre spectroscopy of cluster member candidates in Collinder 359 with the AF2/WYFFOS spectrograph will enable to deblend the K I and Na I doublets and provide surface gravity measurements over a large mass range. The results will be then compared to measurements in the α Per cluster (Chapter 3) and in the Pleiades (Martín et al. 1996). Moreover, modelling of the spectra of cluster member candidates in Collinder 359 with the latest atmosphere models (Allard et al. 2001) will allow us to determine the surface gravity with an uncertainty of ± 0.5 dex as well as effective temperature estimates.

5.4.4 Lithium depletion boundary

The presence of the lithium absorption line at 6708 Å is important for two reasons. First, the study of a variety of clusters will help understand the evolution of lithium with age as well as the role of mixing in stellar atmospheres. Second, the lithium absorption line is a key spectral feature used to date pre-main-sequence open clusters (Rebolo et al. 1992). This approach has been widely used in recent years to infer cluster ages, as in the Pleiades (Stauffer et al. 1998), α Per (Stauffer et al. 1999), IC 2391 (Barrado y Navascués et al. 1999), and NGC 2547 (Oliveira et al. 2003). The details of the lithium test applied in α Per are provided in Section 3.2. Collinder 359 is an interesting new target with an age similar to α Per.

Observations of cool, young, pre-main-sequence stars suggest that undepleted lithium will produce a saturated equivalent width of about 0.6 Å (Zapatero Osorio et al. 2002). Theoretical curves of growth predict that a star depleted by a factor of 100 from its initial lithium abundance will still have an equivalent width of ~ 0.3 Å with lines disappearing rapidly for lower abundances (Pavlenko et al. 1995). Evolutionary models (D'Antona & Mazzitelli 1994; Baraffe et al. 1998) predict a change in the lithium abundance over an interval of 0.2 mag in luminosity.

The lithium depletion boundary in Collinder 359 should be located around $I = 20$, assuming an age of 80 Myr and a distance of 500 pc for the cluster (Chapter 4). A 8-m class telescope is required to achieve equivalent width measurements as accurate as 0.1–0.2 Å at this faintness limit in order to refine the age of Collinder 359. The models from Burrows et al. (2001) predict that at 80 Myr, a $0.07 M_{\odot}$ has retained all its lithium whereas a $0.09 M_{\odot}$ object has depleted it all. However, if Collinder 359 is 30 Myr old (Wielen 1971), the lithium depletion boundary would occur more than one magnitude brighter at a mass of approximately $0.15 M_{\odot}$.

5.4.5 Rotational velocities

The main motivation for measuring rotational velocities in young open clusters is to determine the distribution of $v \sin(i)$ versus spectral type.

Studies carried out in the Pleiades (Stauffer et al. 1994a), α Per (Prosser 1994; Randich et al. 1996), IC2602 (Randich et al. 1995), and IC2391 (Stauffer et al. 1997) improved significantly our knowledge regarding the distribution of rotational velocities in open clusters over a large interval in age. A complete survey in Collinder 359 could be compared to those results to complete the sequence of ages. However, if Collinder 359 is younger than predicted in Chapter 4 (e.g. 30 Myr), its rotational velocity properties should be comparable to those observed in the pre-main-sequence clusters IC2602 and IC2391.

The measurements of rotational velocities require high-resolution optical spectroscopy. The NaID doublet at 5880–5900 Å provide the best discriminant of rapid rotators with rotational velocities larger 100 km s^{-1} (Stauffer et al. 1997). The general method to measure rotational velocities consists of artificially broadening a well-known standard star until the best match to the target spectrum is achieved (Hartmann et al. 1986).

5.4.6 Radial velocities

The last membership criterion for cluster candidates available from optical spectroscopy is the radial velocity. This obviously requires that the motion of the cluster is significantly different from field stars. For example, radial velocities are not of great use in the Pleiades as the mean

cluster motion ($v_{rad} = 5.9 \text{ km s}^{-1}$; Roswick et al. 1992) is comparable to the motion of field stars along that line of sight but a powerful discriminant in α Per ($v_{rad} = -2 \text{ km s}^{-1}$; Prosser 1994). No measurements are available in Collinder 359 but high-resolution optical spectroscopy can be obtained for the brightest members with a small telescope in order to estimate this component.

Radial velocity investigations require high-resolution optical spectroscopy as well as standard stars with high accurate radial measurements. Several strong iron and calcium lines are available in the wavelength ranges 6410–6495 Å, 7860–7980 Å, 8040–8160 Å, and 8230–8350 Å to derive radial velocities.

The determination of the radial velocities of members in Collinder 359, in addition to their proper motions, will allow us to explore the full space motion of the cluster. To date, some 40000 stars in the Galaxy have radial velocity measurements. To improve the statistics, the RAdial Velocity Experiment (RAVE)⁴ is an ambitious program aiming at measuring radial velocities and metallicities of about 50 million stars down to $V = 16$ mag. A complementary project will be undertaken with the future astrometric space mission GAIA for fainter objects. These databases will represent a major breakthrough to study the space motion of large numbers of stars, some of them belonging to open clusters such as α Per and Collinder 359.

5.4.7 Planned spectroscopic observations in Collinder 359

We have been granted follow-up observations to pursue the study the stellar and substellar mass functions in young clusters within the framework of the CFHT Key Programme. Two observing runs will take place in June 2004 to obtain low-resolution optical spectroscopy of cluster member candidates in open clusters and star-forming regions, including Collinder 359.

First, low-resolution ($R \sim 1000$) multi-fibre (150 fibres) optical (5500–8500 Å) spectroscopy of cluster member candidates in three pre-main-sequence clusters (Collinder 359, IC4665, and Steph 1) and in Serpens will be carried out on 18–26 June 2004 with the AF2/WYFFOS spectrograph mounted on the William Herschel Telescope in La Palma. The WYFFOS spectrograph is equipped with a 1024×1024 pixel camera with a spatial scale of 3 Å/pixel, yielding a field-of-view of approximately $40'$, comparable to the CFH12K camera.

Second, low-resolution ($R \sim 600$) optical (4470–10360 Å) long-slit spectroscopy of individual cluster member candidates in Collinder 359 will be conducted with the DOLORES spectrograph on the Telescopio Nazionale Galileo in La Palma on 19–21 June 2004. The spectrograph is equipped with a 2048×2048 pixel camera with a spatial scale of 0.275 Å/pixel, yielding a field-of-view of $9.4' \times 9.4'$.

These combined spectroscopic observations will provide spectral types, chromospheric activity and surface gravity measurements for a complete sample of cluster member candidates in Collinder 359 down to the hydrogen-burning limit, assuming an age of 80 Myr and a distance of 500 pc for the cluster.

⁴More information can be obtained at this URL: <http://www.aip.de/RAVE/>

5.5 Near-infrared spectroscopy of cluster member candidates

We have explored in the previous section (§ 5.4) the wealth of information provided by optical spectroscopy, including spectral types, chromospheric activity, lithium, surface gravity, radial and rotational velocities. However, the faintness of the least massive cluster members renders optical observations less adequate to analyse their characteristics. Long integration times on large telescopes are, therefore, required to achieve sufficient signal-to-noise for spectral typing and other studies mentioned previously. As young pre-main-sequence objects emit most of their flux at $1\text{ }\mu\text{m}$ and beyond, near-infrared wavelengths are appealing to derive effective temperature and bolometric luminosities. For example, a 80 Myr old object with $I = 20$ has a $K \sim 16.5$ and $J-K \sim 1.0$.

Several near-infrared spectral indices, independent of the interstellar reddening observed in star-forming regions, have been specifically defined to classify young low-mass stars and brown dwarfs (Wilking et al. 1999; Martín 2000). Those indices have been applied to infer surface gravity and effective temperature in several regions, including ρ Ophiuchus (Wilking et al. 1999), the Trapezium Cluster (Lucas et al. 2001), σ Orionis (Béjar et al. 2001), IC348 (Najita, Tiede, & Carr 2000), Taurus (Itoh, Tamura, & Tokunaga 2002), and Serpens (Lodieu et al. 2002a).

Gorlova et al. (2003) compared high signal-to-noise low-resolution near-infrared spectra with the latest atmosphere models of Allard et al. (2001) to distinguish young pre-main-sequence objects from field dwarfs. Several features, including H₂ at $1.33\text{ }\mu\text{m}$, CO at $2.30\text{ }\mu\text{m}$, FeH at $1.20\text{ }\mu\text{m}$, K I at $1.25\text{ }\mu\text{m}$, Na I at $2.21\text{ }\mu\text{m}$, and Ca I at $2.26\text{ }\mu\text{m}$, represent valuable discriminants to separate both types of objects.

Optical spectroscopy will enable a detailed study of cluster members in Collinder 359 down to the hydrogen-burning limit or slightly lower ($I \sim 20$ and $M = 0.075\text{ M}_\odot$). The faintest candidates extracted from the wide-field optical survey in Collinder 359 would then need to be followed-up spectroscopically in the near-infrared to derive spectral types and surface gravity because of their large optical-to-infrared colours ($I-K = 3.5-4.5$ for $I = 20.0-22.0$). The task remains difficult for two reasons. First, the difference in surface gravity between cluster members (80 Myr) and field dwarfs (~ 1 Gyr) is on the order of the accuracy of the method developed by Gorlova et al. (2003). Second, long integration times are still necessary to achieve reasonable signal-to-noise for those objects even with large telescopes. For example, a signal-to-noise of about 10 is achieved in an hour for objects with $K = 17.5$ at a resolution of 750 using ISAAC VLT and assuming a slit width of $1''$ and an airmass of 1.2. This signal-to-noise is worse than the one obtained with the FOCAS instrument on the Subaru telescope, assuming comparable requirements. As a consequence, near-infrared spectroscopy of the faintest candidates does not appear more effective than optical spectroscopy in young open clusters. This approach remains nevertheless useful in star-forming regions where the extinction often hampers studies at optical wavelengths.

5.6 X-ray surveys of open clusters

Open clusters are important to study the time evolution of stars and probe the age-activity relationship. Systematic X-ray studies of open clusters began with the Einstein Observatory in the 1980s (e.g. Micela et al. 1988) and later with the ROSAT satellite. Large areas in open clusters within 200 pc and ages ranging from 30 Myr to 50 Gyr have been surveyed in the soft (0.1–0.4 keV) and in the hard (0.4–2.0 keV) bands. Surveys conducted in X-rays represent an excellent way to discriminate between young dwarfs and main-sequence solar-type stars due to the higher L_X/L_{bol}

ratio observed at young ages. In addition, this ratio is independent of the distance. As a consequence, follow-up X-ray observations can be an efficient way to ascertain the membership of low-mass candidates in young clusters, as the Pleiades (Stauffer et al. 1994a), α Per (Randich et al. 1996), IC2602 (Randich et al. 1995), and IC2391 (Patten & Simon 1993) than in older ones as the Hyades (Stern et al. 1995). Collinder 359 represents a new target to probe X-ray activity in a more distant cluster with an age intermediate between IC2391 and the Pleiades.

A large percentage ($\geq 80\%$) of F, G, K, and M dwarfs in α Per extracted from former proper motion and photometric surveys were detected as X-ray emitters using the ROSAT satellite (Randich et al. 1996; Prosser et al. 1996b). New candidates were revealed by X-ray observations as well and confirmed later on. The observations in α Per were in agreement with results from the Pleiades and other pre-main-sequence clusters, yielding the following conclusions:

1. The faster the rotation rate is, the higher is the X-ray luminosity.
2. The X-ray luminosity peaks at G dwarfs and declines towards M dwarfs.
3. The mean X-ray luminosity of F and G dwarfs is larger for younger objects while no difference with age is found for K and M dwarfs.

With the advent of the *XMM* and *Chandra* X-ray satellites providing higher sensitivity and better resolution, a new opportunity is offered to investigate the evolution of activity with mass and the relation between X-ray emission and period in late-type dwarfs. First, the sensitivity of *XMM* is thousand times better than the *ROSAT* satellite in the 0.5–2.0 kev energy range, allowing the detection of brown dwarfs in the Orion Nebula Cluster (Feigelson et al. 2002). Second, the *XMM* and *Chandra* spatial resolutions are on the order of or better than a few arcsec (typically 2–3 arcsec) and allow direct identification of the optical counterpart with little uncertainty. The *XMM* and *Chandra* fields-of-view of about $30'$ and $17' \times 17'$, respectively, are comparable to current fields-of-view in the optical but still require numerous pointings to identify all members within a large area.

Several surveys conducted with *Chandra* led to the detection of Pleiades members (Daniel et al. 2002), hundreds of pre-main-sequence stars belonging to the Orion Nebula Cluster (Feigelson et al. 2002), and two brown dwarfs in the ρ Ophiuchus cloud (Ozawa et al. 2004). Assuming an upper limit of 650 pc for the distance of Collinder 359, we would expect to detect a high percentage of F–M cluster members to derive the mass-activity relationship and compare it with previous works conducted in the Pleiades (Stauffer et al. 1994a), α Per (Randich et al. 1996), IC2602 (Randich et al. 1995), and IC2391 (Patten & Simon 1993).

5.7 Binarity of cluster members

The binary fraction as a function of mass is an important issue to determine the IMF in the field and in young clusters and to address the issue of the formation of stars and brown dwarfs. How do unresolved binaries affect the mass function? Do brown dwarfs have similar binary properties as stars? How do brown dwarfs form? Several studies have shed some light on those matters. Using the latest observational surveys dedicated to the binarity of field G, K, and M stars, Kroupa (2001) concluded that the power law index α is underestimated by up to 0.5 if unresolved binaries are not corrected for. In addition, Delgado-Donate et al. (2004) found that the substellar IMF is more

sensitive to the initial conditions than the stellar mass function. Concerning the origin(s) of brown dwarfs, recent observational surveys concluded that binary brown dwarfs have different properties than stars (Section 1.5.1; Figure 1.6), in agreement with N-body simulations conducted by Kroupa & Bouvier (2003a).

Multiplicity among low-mass nearby systems appears smaller than for higher mass stars. Furthermore, low-mass stars and brown dwarfs seem to form tight systems and favour equal-mass binaries (Figure 1.6). Surveys in the Pleiades are suggestive of similarities between the low-mass objects in the Pleiades and their older counterparts in the solar neighbourhood. First, a high-resolution imaging survey of 13 Pleiades brown dwarfs has revealed two brown dwarf binaries with separation in the range 7–12 AU and mass ratios larger than 0.7 (Martín et al. 2003). Second, a proportion of $28 \pm 4\%$ binary systems was found among G and K dwarfs belonging to the Pleiades cluster over the projected separation range 26–580 AU and magnitude difference of $\Delta K \leq 4$ mag (Bouvier et al. 1997). The implications of these results are two-fold. First, the binary properties of stars do not extend in the substellar regime, implying that brown dwarfs form via a different mechanism which could be an early ejection from multiple systems (Reipurth & Clarke 2001; Kroupa & Bouvier 2003a). Second, young cluster members seem to have similar binary characteristics as their older field counterparts, suggesting a minor probability of binary disruption with age (Kroupa & Bouvier 2003b).

The binary fraction in the α Per cluster has been investigated as well. Patience et al. (2002) conducted speckle and high-resolution imaging of 109 α Per cluster members brighter than 12.3 in the K -band. Speckle imaging resolved 10 systems as binaries out of 109 members whereas the high-resolution imaging revealed 17 binaries and one quadruple system of the 33 members. Patience et al. (2002) concluded that the companion-star fraction is 0.09 ± 0.03 for α Per over the projected separation range 26–581 AU and magnitude difference $\Delta K \leq 4$ mag. A high-resolution imaging program of eight very low-mass stars and brown dwarf candidates in α Per, implemented with the *Hubble Space Telescope*, failed to detect multiple systems, suggesting that brown dwarf binaries wider than 12 AU are less frequent than 9 % (Martín et al. 2003). The results obtained in α Per are consistent with those in the Pleiades and in the field, hence confirming the previous implications.

To study the dependence of the binary fraction with mass in Collinder 359, a new program to search for companions should be initiated in the near future after assessing the membership of all photometric candidates. This project should be extended to the other pre-main-sequence clusters (IC4665, Stephenson 1, NGC 2232, and Collinder 70) surveyed within the framework of the CFHT Key Programme to investigate possible variations among clusters and the dependence on age. Ground-based adaptive optics and high-resolution imaging from space are the most common techniques to detect companions over a wide range of separations. Ultimately, the knowledge of the binary fraction over the whole mass range will allow us to correct the cluster IMF for binarity and address the issue of the origin of field stars and brown dwarfs.

5.8 Variability of cluster members

Variability monitoring of low-mass stars and brown dwarfs over several days or months have been conducted in the field and in clusters. The modulation of their light curve can originate from multiple phenomena, including surface inhomogeneities, magnetic star spots, flaring or eclipses

due to an unseen companion. The variability as a result of clouds or spots at the surface of a star or a substellar object is not well understood. Larger sample of objects and longer monitoring surveys should be undertaken to determine the variability as function of mass and age as well as the role of clouds on the atmospheres.

Variability of order of few percent in the has been reported in ultracool field dwarfs over timescales ranging from few hours to few days at optical and near-infrared wavelengths (Bailer-Jones & Mundt 1999, 2001; Clarke et al. 2002; Koen 2003).

Terndrup et al. (1999) found variability in two objects among a sample of eight low-mass stars and brown dwarfs belonging to the Pleiades. Bailer-Jones & Mundt (2001) failed to detect small amplitude variability in objects with spectral types M6–M9 in the Pleiades and σ Ori, respectively. Zapatero Osorio et al. (2003) reported low level variability in a young brown dwarf in σ Orionis. Herbst et al. (2001) concluded that essentially all members of the Orion Nebula Cluster are variable.

The young open clusters, α Per and Collinder 359 as well as the other pre-main-sequence clusters observed within the framework of the CFHT Key Programme, are well-suited for long-term variability monitoring of low-mass stars and brown dwarfs with a 2-m class telescope. The project should be started in α Per and Collinder 359 after spectroscopic assessment of all photometrically-selected cluster members. A monitoring program in Collinder 359 would require a wide-field camera on a small telescope to include several members in one field. For example, one CFH12K field-of-view could be targeted over several nights with repeated short (2 sec), medium (30 sec), and long (300 sec) exposures in the I -band to study variability down into the brown dwarf regime. The large number of reference stars in the wide-field images would enable the detection of low amplitude variations whereas the monitoring over several nights would detect variations from few hours to few days.

Conclusions and perspectives

In this work, we described the outcome of surveys dedicated to low-mass stars and brown dwarfs, including older ones in the solar neighbourhood and younger ones in two open clusters, α Per and Collinder 359. Here, we briefly summarise the main results of each study as well as the perspectives and future work. We will also discuss the implications of our work in a broader context.

Chapter 2 dealt with a proper motion survey in the southern sky ($\delta \leq -33^\circ$), aimed at finding nearby low-mass stars and brown dwarfs. The candidates were selected on the basis of their proper motion ($\mu \geq 0.2''/\text{yr}$) from overlapping regions of the United Kingdom Schmidt Telescope photographic plates taken in three passbands (B_J , R , and I) and at different epochs. The selection made use of the 2MASS and SuperCOSMOS Sky Surveys databases as well. We described the results of follow-up optical and near-infrared spectroscopy for about 70 objects and uncovered 6 subdwarfs, 10 early-M dwarfs, 48 late-M dwarfs, four L dwarfs, and a binary T dwarf. All four L dwarfs are within 50 pc as well as the majority of M dwarfs. Among the sample of ultracool dwarfs, three discoveries should be emphasised:

1. We reported the discovery of two bright late-M dwarfs with spectral types M7.5 and M8 at a distance of 8.0 and 6.4 pc, respectively. Those objects represent an important addition to the volume within 10 parsecs of the Sun. These two M dwarfs also constitute bona-fide new targets to search for substellar companions using high-resolution imaging and extrasolar planets with future space missions.
2. We discovered an active M8.5 dwarf as a wide companion to the M4/DA binary system LHS4039/LHS4040 at a distance of about 20 pc. One of the two optical spectra taken three years apart revealed a large H α emission line and a strong blue continuum shortwards of 7500 Å. The spectrum of this active M8.5 dwarf resembles the spectrum of LHS2397a, which has a tight brown dwarf companion at a separation of about 3 AU. High-resolution imaging of the M8.5 dwarf from the ground or from space is required to verify its binary status.
3. We discovered the closest and brightest binary T dwarf, ε Indi Ba,Bb, as wide companion to the K5V star ε Indi A located at a distance of 3.626 parsecs to the Sun. High angular resolution spectroscopy enabled us to classify ε Indi Ba and ε Indi Bb as T1 and T6 dwarfs with masses of $47 \pm 10 M_{\text{Jup}}$ and $28 \pm 7 M_{\text{Jup}}$, respectively, assuming an age of 0.8–2.0 Gyr. The mean separation of both components in July 2003 was $0.732 \pm 0.002''$, translating into a physical projected separation of 2.65 ± 0.01 AU at the distance of the system. The ε Indi B system represents an important addition to the 5-pc sample. Subsequent observations of this

bright and close binary brown dwarf will undoubtedly provide new insights on our knowledge of substellar objects. On the one hand, the separation and brightness of the ε Indi B system will allow high quality and high resolution spectroscopy from 0.6 to $5.0\mu\text{m}$ to improve the atmospheric models of brown dwarfs. On the other hand, the small separation of the ε Indi B system offers the opportunity to derive dynamical masses of brown dwarfs over a timescale of about 15 years to test evolutionary models in the substellar regime.

Our proper motion survey constitutes an alternative approach to the photometric surveys, whose primary selection criterion is based on the optical and/or infrared colours. The efficiency of our technique has been demonstrated by the discovery of several L dwarfs and the closest binary T dwarf to the Sun. Our method remains nevertheless neither volume nor magnitude limited; the only limitation being the depth in magnitudes of the photographic plates. Our survey complements the multiple searches dedicated to the search for very low-mass stars and brown dwarfs.

Chapter 3 presented the outcome of a wide-field near-infrared survey of a 0.7 square degree area in the α Per cluster reaching 0.040 M_\odot . Combining optical (R_c and I_c) and near-infrared (K') photometry with colour-magnitude and colour-colour diagram analysis, we have extracted 37 new probable cluster members, 18 in common with the previous study by Barrado y Navascués et al. (2002). Four objects are new brown dwarf candidates belonging to the cluster. Follow-up optical spectroscopy is, however, still required to verify the genuine membership of these photometric candidates.

We have also described the results of moderate-resolution optical spectroscopy for 29 cluster member candidates in α Per selected by Barrado y Navascués et al. (2002). All probable candidates, spanning $I = 15.0\text{--}17.0$ mag ($M \sim 0.40\text{--}0.12\text{ M}_\odot$) have spectral types, chromospheric activity, and gravity measurements consistent with membership. The remaining objects, previously classified as possible members and non-members of the cluster, were definitively rejected as cluster members based on their optical spectra. The derived cluster mass spectrum, approximated by a power law of index $\alpha = 0.59$, is very similar to the Pleiades mass function over the mass range $0.50\text{--}0.035\text{ M}_\odot$. Optical spectroscopy of four new infrared-selected candidates in α Per allowed us to reject them as cluster members, suggesting that optical-to-infrared colours represent a less efficient technique than optical (R, I) selection to extract members in a low galactic latitude open cluster.

Future projects to extend the coverage of the α Per cluster and probe lower mass brown dwarfs include:

- Optical spectroscopy of the remaining probable member candidates selected by Barrado y Navascués et al. (2002) and of the new infrared-selected candidates is required to ascertain their membership.
- A z -band survey of the 4.5 square degree area covered in the R and I filters to probe lower mass brown dwarfs belonging to α Per.
- Extend the coverage of the α Per cluster to the remaining non-surveyed area using the (R, I) or (I, z) optical filters to unearth new cluster members, including brown dwarfs.
- A high-resolution imaging program with ground-based or space facilities to search for companions around cluster members to compare the multiplicity fractions in clusters and in the field.

Chapter 4 dealt with a deep wide-field optical (I , z) survey covering 1.6 square degree in the young open cluster Collinder 359 down to a completeness limit of about $0.040 M_{\odot}$. From the optical (I , $I-z$) colour-magnitude diagram, we have extracted a total of 1033 cluster member candidates spanning $1.3-0.04 M_{\odot}$ up to a distance of 650 pc and an age of 80 Myr. However, the number of candidates falls down to approximately 400 if we consider objects massive than $0.6 M_{\odot}$ due to the large field contamination observed at bright magnitudes.

We presented near-infrared photometry for about 80 % of the optically-selected candidates, most of them having a counterpart in the 2MASS survey. We have additionally obtained K' -band photometry for 39 optically-selected candidates. Our optical data combined with proper motion measurements suggests that the mean distance of the cluster is 500 ± 100 pc with an age in the range 50–80 Myr, estimates larger than the distance of 250 pc and the age of 30 Myr quoted in the literature.

We derived the cluster luminosity function as well as the cluster mass function, using the NextGen (Baraffe et al. 1998) and Dusty (Chabrier et al. 2000b) models from the Lyon group. Several features were visible in the cluster luminosity function. First, a peak at bright magnitudes, not real and due to the large contamination by nearby field dwarfs expected in this magnitude range. Optical spectroscopy is required to refine the list of cluster at masses above $0.6 M_{\odot}$. Second, a peak at $I = 17.0-17.5$ was clearly detected and comparable to those seen in other open clusters but at a different absolute magnitude. Finally, a dip was seen at $I = 20.5$, most likely caused by the dearth of M7–M8 dwarfs observed both in the field and in young clusters. This dip in the luminosity function is responsible for the gap in the mass function at $70 M_{Jup}$, at the age and distance inferred for the cluster. The slope of the cluster mass spectrum over the mass range $0.55-0.035 M_{\odot}$ is $\alpha = 0.3 \pm 0.2$. The derived slope is flatter than estimates in Pleiades-like clusters with the caveat that our work is solely based on photometry.

This detailed photometric survey of the young open cluster Collinder 359 represents a first step towards a more accurate determination of the distance and age of the cluster and thereafter its mass function. A large number of follow-up observations are required before achieving that goal, some of them already having been granted observing time, including:

1. Near-infrared imaging of the remaining 250 optically-selected cluster member candidates in the magnitude range $I = 17.0-22.0$ to weed out contaminating objects. This project has been granted a total of 8 nights, split into 4 nights with the instrument MAGIC on the Calar Alto 2.2-m telescope and the infrared camera on the Canada-France-Hawaii telescope.
2. Optical spectroscopy of cluster candidates to ascertain their membership. Optical spectroscopy provides important additional criteria to confirm the membership, including spectral types, chromospheric activity, gravity, lithium, radial, and rotational velocities. Six nights have been granted with the AF2/WYFFOS multi-fibre spectrograph on the William Herschel telescope as well as three nights with the DOLORES spectrograph on the Telescopio Nazionale di Galileo in June 2004 to carry out low-resolution optical spectroscopy of the selected cluster candidates.

Collinder 359 was surveyed within the framework of the CFHT Key Programme as a pre-main-sequence open cluster along with four others. Optical spectroscopy of the photometrically-selected cluster member candidates will add further constraints to their membership and allow us to address the issues of the universality of the IMF and its variation with the environment.

Subsequent observations are foreseen to better understand the star and brown dwarf properties in young clusters. We plan to carry out the following observations:

- Extend the (I, z) coverage within the inner degree of the Collinder 359 core with MegaCam to derive a complete mass function over the whole cluster area.
- X-ray observations of cluster members with *XMM* and/or *Chandra* to study the age-activity relationship in young open clusters.
- High-resolution imaging of cluster members using adaptive optics on the ground in order to investigate the binary properties of the cluster.
- Long-term photometric monitoring of the cluster members to address the issue regarding the dependence of variability with mass.

Beyond α Per and Collinder 359, the major benefits of young clusters are the limited dynamical evolution and the large span in mass. A large number of open clusters listed in the Open Cluster Database have uncertain distances and ages because they originate from a small number of bright stars. The combination of photometry and proper motions available in large-scale sky surveys would help us refine those two crucial parameters prior to subsequent deep optical programs dedicated to very low-mass stars and brown dwarfs.

The current uncertainties on the mass function are too large at present to infer the original number of stars formed per unit of time in a given cluster and thus, provide important diagnostics on the birth and evolution of the stellar and substellar contents of the Galaxy. The ideal targets to address these issues would be pre-main-sequence (10–50 Myr) nearby ($d \leq 500$ pc) clusters at high galactic latitude with significant proper motion with regard to field stars to minimise the contamination.

The ultimate goal in the study of the IMF consists in answering the question of whether or not it is universal or if it depends on place, time, and metallicity. This issue was a major driver for the CFHT Key Programme and we hope to provide some hints after the spectroscopic results of large samples of low-mass stars and brown dwarfs in star-forming regions and pre-main-sequence open clusters and in the Hyades. Future space missions such as the JWST will allow us, on the one hand, to probe planetary-mass objects in star-forming clusters in order to investigate the role of the fragmentation limit on the shape of the mass function, and on the other hand, to study more distant clusters down into the substellar regime.

Ten years ago, the discovery of the first two unambiguous brown dwarfs triggered a revival of interest in the quest for substellar objects. Our knowledge of these objects straddling the realms of stars and planets has increased dramatically with the discovery of hundreds of brown dwarfs isolated in the field, as companions to stars, and in young clusters. The current techniques are capable of addressing some pressing issues within the next ten years. First, the emergence of low-mass binaries will allow the derivation of the dynamical mass of a brown dwarf in order to test the evolutionary tracks in the substellar domain. Second, new facilities such as SIRTF and ALMA will constrain the sizes and the masses of disks around nascent brown dwarfs to better understand their formation mechanism. Finally, deep surveys conducted in young clusters in a variety of environments will offer additional insights on the dependence of the IMF on time, place, and metallicity.

Bibliography

- Abt, H. A. & Cardona, O. 1983, *ApJ*, 272, 182
- Ackerman, A. S. & Marley, M. S. 2001, *ApJ*, 556, 872
- Alcock, C., Allsman, R. A., Alves, D. R., Axelrod, T. S., Becker, A. C., Bennett, D. P., Cook, K. H., Drake, A. J., Freeman, K. C., Geha, M., Griest, K., Keller, S. C., Lehner, M. J., Marshall, S. L., Minniti, D., Nelson, C. A., Peterson, B. A., Popowski, P., Pratt, M. R., Quinn, P. J., Stubbs, C. W., Sutherland, W., Tomaney, A. B., Vandehei, T., & Welch, D. 2001, *Nat*, 414, 617
- Allard, F., Hauschildt, P. H., Alexander, D. R., Tamai, A., & Schweitzer, A. 2001, *ApJ*, 556, 357
- An, J. H., Evans, N. W., Kerins, E., Baillon, P., Calchi Novati, S., Carr, B. J., Crézé, M., Giraud-Héraud, Y., Gould, A., Hewett, P., Jetzer, P., Kaplan, J., Paulin-Henriksson, S., Smartt, S. J., Tsapras, Y., & Valls-Gabaud, D. 2004, *ApJ*, 601, 845
- Apai, D., Pascucci, I., Henning, T., Sterzik, M. F., Klein, R., Semenov, D., Günther, E., & Stecklum, B. 2002, *ApJL*, 573, L115
- Armitage, P. J. & Bonnell, I. A. 2002, *MNRAS*, 330, L11
- Aspin, C., Sandell, G., & Russell, A. P. G. 1994, *A&AS*, 106, 165
- Béjar, V. J. S., Martín, E. L., Zapatero Osorio, M. R., Rebolo, R., Barrado y Navascués, D., Bailer-Jones, C. A. L., Mundt, R., Baraffe, I., Chabrier, C., & Allard, F. 2001, *ApJ*, 556, 830
- Béjar, V. J. S., Zapatero Osorio, M. R., & Rebolo, R. 1999, *ApJ*, 521, 671
- Bailer-Jones, C. A. L. & Mundt, R. 1999, *A&A*, 348, 800
- . 2001, *A&A*, 367, 218
- Bailes, M., Lyne, A. G., & Shemar, S. L. 1991, *Nat*, 352, 311
- Baraffe, I., Chabrier, G., Allard, F., & Hauschildt, P. H. 1997, *A&A*, 327, 1054
- . 1998, *A&A*, 337, 403
- . 2002, *A&A*, 382, 563
- Barrado y Navascués, D., Bouvier, J., Stauffer, J. R., Lodieu, N., & McCaughean, M. J. 2002, *A&A*, 395, 813

- Barrado y Navascués, D. & Martín, E. L. 2003, AJ, 126, 2997
- Barrado y Navascués, D., Stauffer, J. R., Briceño, C., Patten, B., Hambly, N. C., & Adams, J. D. 2001a, ApJS, 134, 103
- Barrado y Navascués, D., Stauffer, J. R., & Patten, B. M. 1999, ApJL, 522, L53
- Barrado y Navascués, D., Zapatero Osorio, M. R., Béjar, V. J. S., Rebolo, R., Martín, E. L., Mundt, R., & Bailer-Jones, C. A. L. 2001b, A&A, 377, L9
- Barrado y Navascués, D., Stauffer, J. R., Bouvier, J., & Martín, E. L. 2001, ApJ, 546, 1006
- Basri, G., Marcy, G. W., & Graham, J. R. 1996, ApJ, 458, 600
- Basri, G. & Martín, E. L. 1999a, AJ, 118, 2460
- . 1999b, ApJ, 510, 266
- Basri, G., Mohanty, S., Allard, F., Hauschildt, P. H., Delfosse, X., Martín, E. L., Forveille, T., & Goldman, B. 2000, ApJ, 538, 363
- Bate, M. R., Bonnell, I. A., & Bromm, V. 2002, MNRAS, 332, L65
- Baumgardt, H., Dettbarn, C., & Wielen, R. 2000, A&AS, 146, 251
- Becker, W. & Fenkart, R. 1971, A&AS, 4, 241
- Becklin, E. E. & Zuckerman, B. 1988, Nat, 336, 656
- Beichman, C. A., Chester, T. J., Skrutskie, M., Low, F. J., & Gillett, F. 1998, PASP, 110, 480
- Bertin, E. & Arnouts, S. 1996, A&AS, 117, 393
- Bessell, M. S. 1991, AJ, 101, 662
- Bizenberger, P., McCaughrean, M. J., Birk, C., Thompson, D., & Storz, C. 1998, in Proc. SPIE Vol. 3354, p. 825–832, Infrared Astronomical Instrumentation, Albert M. Fowler; ed., 825–832
- Blanco, V. M., Demers, S., Douglass, G. G., & Fitzgerald, M. P. 1968, Publications of the U.S. Naval Observatory Second Series, 21
- Boesgaard, A. M. & Friel, E. D. 1990, ApJ, 351, 467
- Boeshaar, P. C. 1976, Ph.D. Thesis, Ohio State Univ., Columbus
- Boffin, H. M. J., Watkins, S. J., Bhattal, A. S., Francis, N., & Whitworth, A. P. 1998, MNRAS, 300, 1189
- Bontemps, S., André, P., Kaas, A. A., Nordh, L., Olofsson, G., Huldtgren, M., Abergel, A., Blommaert, J., Boulanger, F., Burgdorf, M., Cesarsky, C. J., Cesarsky, D., Copet, E., Davies, J., Falgarone, E., Lagache, G., Montmerle, T., Péault, M., Persi, P., Prusti, T., Puget, J. L., & Sibille, F. 2001, A&A, 372, 173
- Boss, A. P. 1998, ApJ, 503, 923

- . 2000, ApJL, 536, L101
- . 2001, ApJL, 551, L167
- Boulanger, F., Bronfman, L., Dame, T. M., & Thaddeus, P. 1998, A&A, 332, 273
- Bouvier, J., Rigaut, F., & Nadeau, D. 1997, A&A, 323, 139
- Bouvier, J., Stauffer, J. R., Martín, E. L., Barrado y Navascues, D., Wallace, B., & Bejar, V. J. S. 1998, A&A, 336, 490
- Bouy, H., Brandner, W., Martín, E. L., Delfosse, X., Allard, F., & Basri, G. 2003, AJ, 126, 1526
- Briceño, C., Hartmann, L., Stauffer, J., & Martín, E. 1998, AJ, 115, 2074
- Briceño, C., Luhman, K. L., Hartmann, L., Stauffer, J. R., & Kirkpatrick, J. D. 2002, ApJ, 580, 317
- Burgasser, A. J., Geballe, T. R., Golimowski, D. A., Leggett, S. K., Kirkpatrick, J. D., Knapp, G. R., & Fan, X. 2003a, in IAU Symposium 211, “Brown dwarfs”, ed. E. L. Martín (San Francisco: ASP), p 377
- Burgasser, A. J., Kirkpatrick, J. D., Brown, M. E., Reid, I. N., Burrows, A., Liebert, J., Matthews, K., Gizis, J. E., Dahn, C. C., Monet, D. G., Cutri, R. M., & Skrutskie, M. F. 2002, ApJ, 564, 421
- Burgasser, A. J., Kirkpatrick, J. D., Brown, M. E., Reid, I. N., Gizis, J. E., Dahn, C. C., Monet, D. G., Beichman, C. A., Liebert, J., Cutri, R. M., & Skrutskie, M. F. 1999, ApJL, 522, L65
- Burgasser, A. J., Kirkpatrick, J. D., Cutri, R. M., McCallon, H., Kopan, G., Gizis, J. E., Liebert, J., Reid, I. N., Brown, M. E., Monet, D. G., Dahn, C. C., Beichman, C. A., & Skrutskie, M. F. 2000a, ApJL, 531, L57
- Burgasser, A. J., Kirkpatrick, J. D., Reid, I. N., Brown, M. E., Miskey, C. L., & Gizis, J. E. 2003b, ApJ, 586, 512
- Burgasser, A. J., McElwain, M. W., & Kirkpatrick, J. D. 2003c, AJ, 126, 2487
- Burgasser, A. J., Wilson, J. C., Kirkpatrick, J. D., Skrutskie, M. F., Colombo, M. R., Enos, A. T., Smith, J. D., Henderson, C. P., Gizis, J. E., Brown, M. E., & Houck, J. R. 2000b, AJ, 120, 1100
- Burrows, A., Hubbard, W. B., Lunine, J. I., & Liebert, J. 2001, Reviews of Modern Physics, 73, 719
- Burrows, A., Marley, M., Hubbard, W. B., Lunine, J. I., Guillot, T., Saumon, D., Freedman, R., Sudarsky, D., & Sharp, C. 1997, ApJ, 491, 856
- Butler, R. P., Marcy, G. W., Vogt, S. S., Fischer, D. A., Henry, G. W., Laughlin, G., & Wright, J. T. 2003, ApJ, 582, 455
- Cambresy, L., Copet, E., Epchtein, N., de Batz, B., Borsenberger, J., Fouque, P., Kimeswenger, S., & Tiphene, D. 1998, A&A, 338, 977

- Chabrier, G. 2003, PASP, 115, 763
- Chabrier, G. & Baraffe, I. 2000, ARA&A, 38, 337
- Chabrier, G., Baraffe, I., Allard, F., & Hauschildt, P. 2000a, ApJL, 542, L119
- . 2000b, ApJ, 542, 464
- Clarke, F. J., Tinney, C. G., & Covey, K. R. 2002, MNRAS, 332, 361
- Close, L. M., Potter, D., Brandner, W., Lloyd-Hart, M., Liebert, J., Burrows, A., & Siegler, N. 2002a, ApJ, 566, 1095
- Close, L. M., Siegler, N., Freed, M., & Biller, B. 2003, ApJ, 587, 407
- Close, L. M., Siegler, N., Potter, D., Brandner, W., & Liebert, J. 2002b, ApJL, 567, L53
- Cochran, W. D. & Hatzes, A. P. 1994, *Astrophys. Space. Sci.*, 212, 281
- Collinder, P. 1931, *Annals of the Observatory of Lund*, 2, 1
- Comerón, F., Neuhäuser, R., & Kaas, A. A. 2000, A&A, 359, 269
- Comerón, F., Pasquali, A., Rodighiero, G., Stanishev, V., De Filippis, E., López Martí, B., Gálvez Ortiz, M. C., Stankov, A., & Gredel, R. 2002, A&A, 389, 874
- Comerón, F., Rieke, G. H., Burrows, A., & Rieke, M. J. 1993, ApJ, 416, 185
- Comerón, F., Rieke, G. H., & Neuhäuser, R. 1999, A&A, 343, 477
- Cossburn, M. R., Hodgkin, S. T., Jameson, R. F., & Pinfield, D. J. 1997, MNRAS, 288, L23
- Cruz, K. L. & Reid, I. N. 2002, AJ, 123, 2828
- Cruz, K. L., Reid, I. N., Liebert, J., Kirkpatrick, J. D., & Lowrance, P. J. 2003, AJ, 126, 2421
- Cuby, J. G., Saracco, P., Moorwood, A. F. M., D'Odorico, S., Lidman, C., Comerón, F., & Spyromilio, J. 1999, A&A, 349, L41
- Cushing, M. C., Tokunaga, A. T., & Kobayashi, N. 2000, AJ, 119, 3019
- Dahn, C. C., Harris, H. C., Vrba, F. J., Guetter, H. H., Canzian, B., Henden, A. A., Levine, S. E., Luginbuhl, C. B., Monet, A. K. B., Monet, D. G., Pier, J. R., Stone, R. C., Walker, R. L., Burgasser, A. J., Gizis, J. E., Kirkpatrick, J. D., Liebert, J., & Reid, I. N. 2002, AJ, 124, 1170
- Dame, T. M., Hartmann, D., & Thaddeus, P. 2001, ApJ, 547, 792
- Daniel, K. J., Linsky, J. L., & Gagné, M. 2002, ApJ, 578, 486
- D'Antona, F. & Mazzitelli, I. 1994, ApJS, 90, 467
- de la Fuente Marcos, R. & de la Fuente Marcos, C. 2000, *Astrophys. Space. Sci.*, 271, 127
- de Zeeuw, P. T., Hoogerwerf, R., de Bruijne, J. H. J., Brown, A. G. A., & Blaauw, A. 1999, AJ, 117, 354

- Delfosse, X., Forveille, T., Martín, E. L., Guibert, J., Borsenberger, J., Crifo, F., Alard, C., Epchtein, N., Fouqué, P., Simon, G., & Tajahmady, F. 2001, A&A, 366, L13
- Delfosse, X., Tinney, C. G., Forveille, T., Epchtein, N., Bertin, E., Borsenberger, J., Copet, E., de Batz, B., Fouque, P., Kimeswenger, S., Le Bertre, T., Lacombe, F., Rouan, D., & Tiphene, D. 1997, A&A, 327, L25
- Delfosse, X., Tinney, C. G., Forveille, T., Epchtein, N., Borsenberger, J., Fouqué, P., Kimeswenger, S., & Tiphène, D. 1999, A&AS, 135, 41
- Delgado-Donate, E. J., Clarke, C. J., & Bate, M. R. 2003, MNRAS, 342, 926
- . 2004, MNRAS, 347, 759
- Dobbie, P. D., Kenyon, F., Jameson, R. F., Hodgkin, S. T., Pinfield, D. J., & Osborne, S. L. 2002, MNRAS, 335, 687
- Duquennoy, A. & Mayor, M. 1991, A&A, 248, 485
- Els, S. G., Sterzik, M. F., Marchis, F., Pantin, E., Endl, M., & Kürster, M. 2001, A&A, 370, L1
- Epchtein, N., de Batz, B., Capoani, L., Chevallier, L., Copet, E., Fouqué, P., Lacombe, F., Le Bertre, T., Pau, S., Rouan, D., & 38 coauthors. 1997, The Messenger, 87, 27
- Fan, X., Knapp, G. R., Strauss, M. A., Gunn, J. E., Lupton, R. H., Ivezić, Ž., Rockosi, C. M., Yanny, B., Kent, S., Schneider, D. P., 30 coauthors, & The SDSS Collaboration. 2000, AJ, 119, 928
- Fegley, B. J. & Lodders, K. 1996, ApJL, 472, L37
- Feigelson, E. D., Broos, P., Gaffney, J. A., Garmire, G., Hillenbrand, L. A., Pravdo, S. H., Townsley, L., & Tsuboi, Y. 2002, ApJ, 574, 258
- Fischer, D. A. & Marcy, G. W. 1992, ApJ, 396, 178
- Fredrick, L. W. 1956, AJ, 61, 437
- Freed, M., Close, L. M., & Siegler, N. 2003, ApJ, 584, 453
- Fukugita, M., Ichikawa, T., Gunn, J. E., Doi, M., Shimasaku, K., & Schneider, D. P. 1996, AJ, 111, 1748
- Gómez, M. & Kenyon, S. J. 2001, AJ, 121, 974
- Geballe, T. R., Knapp, G. R., Leggett, S. K., Fan, X., Golimowski, D. A., Anderson, S., Brinkmann, J., Csabai, I., Gunn, J. E., Hawley, S. L., & 19 coauthors. 2002, ApJ, 564, 466
- Girardi, L., Bertelli, G., Bressan, A., Chiosi, C., Groenewegen, M. A. T., Marigo, P., Salasnich, B., & Weiss, A. 2002, A&A, 391, 195
- Gizis, J. E. 1997, AJ, 113, 806

- Gizis, J. E., Kirkpatrick, J. D., Burgasser, A., Reid, I. N., Monet, D. G., Liebert, J., & Wilson, J. C. 2001a, ApJL, 551, L163
- Gizis, J. E., Kirkpatrick, J. D., & Wilson, J. C. 2001b, AJ, 121, 2185
- Gizis, J. E., Monet, D. G., Reid, I. N., Kirkpatrick, J. D., Liebert, J., & Williams, R. J. 2000, AJ, 120, 1085
- Gizis, J. E. & Reid, I. N. 1997, PASP, 109, 849
- . 1999, AJ, 117, 508
- Gizis, J. E., Reid, I. N., & Hawley, S. L. 2002, AJ, 123, 3356
- Gizis, J. E., Reid, I. N., Knapp, G. R., Liebert, J., Kirkpatrick, J. D., Koerner, D. W., & Burgasser, A. J. 2003, AJ, 125, 3302
- Gliese, W. & Jahreiss, H. 1995, Nearby Stars, Preliminary 3rd Version, 5070
- Goldman, B., Delfosse, X., Forveille, T., Afonso, C., Alard, C., Albert, J. N., Andersen, J., Ansari, R., Aubourg, É., 40 coauthors, & The EROS Collaboration. 1999, A&A, 351, L5
- Golimowski, D. A., Burrows, C. J., Kulkarni, S. R., Oppenheimer, B. R., & Brukardt, R. A. 1998, AJ, 115, 2579
- Gorlova, N. I., Meyer, M. R., Rieke, G. H., & Liebert, J. 2003, ApJ, 593, 1074
- Goto, M., Kobayashi, N., Terada, H., Gaessler, W., Kanzawa, T., Takami, H., Takato, N., Hayano, Y., Kamata, Y., Iye, M., Saint-Jacques, D. J., Tokunaga, A. T., Potter, D., & Cushing, M. 2002, ApJL, 567, L59
- Greene, T. P. & Lada, C. J. 1996, AJ, 112, 2184
- Halbwachs, J. L., Arenou, F., Mayor, M., Udry, S., & Queloz, D. 2000, A&A, 355, 581
- Hambly, N. C., Hawkins, M. R. S., & Jameson, R. F. 1993, A&AS, 100, 607
- Hambly, N. C., Hodgkin, S. T., Cossburn, M. R., & Jameson, R. F. 1999, MNRAS, 303, 835
- Hamuy, M., Walker, A. R., Suntzeff, N. B., Gigoux, P., Heathcote, S. R., & Phillips, M. M. 1992, PASP, 104, 533
- Hartmann, L., Hewett, R., Stahler, S., & Mathieu, R. D. 1986, ApJ, 309, 275
- Hawley, S. L., Covey, K. R., Knapp, G. R., Golimowski, D. A., Fan, X., Anderson, S. F., Gunn, J. E., Harris, H. C., Ivezić, Ž., Long, G. M., & 22 coauthors. 2002, AJ, 123, 3409
- Hawley, S. L., Gizis, J. E., & Reid, I. N. 1996, AJ, 112, 2799
- Hayashi, M. & Nakano, S. 1963, Progr. Theor. Phys., 30, 460
- Heckmann, O., Dieckvoss, W., & Kox, H. 1956, AN, 283, 109

- Henry, T., Franz, O., Wasserman, L., Benedict, G. F., Shelus, P., Ianna, P., Kirkpatrick, J. D., & McCarthy, D. 1997, Bull. AAS, 29, 1278
- Henry, T. J. & McCarthy, D. W. 1990, ApJ, 350, 334
- Henry, T. J., Walkowicz, L. M., Barto, T. C., & Golimowski, D. A. 2002, AJ, 123, 2002
- Herbig, G. H. 1998, ApJ, 497, 736
- Herbig, G. H. & Terndrup, D. M. 1986, ApJ, 307, 609
- Herbst, W., Bailer-Jones, C. A. L., & Mundt, R. 2001, ApJL, 554, L197
- Hillenbrand, L. A. 1997, AJ, 113, 1733
- Hillenbrand, L. A. & Carpenter, J. M. 2000, ApJ, 540, 236
- Hillenbrand, L. A., Strom, S. E., Calvet, N., Merrill, K. M., Gatley, I., Makidon, R. B., Meyer, M. R., & Skrutskie, M. F. 1998, AJ, 116, 1816
- Hillenbrand, L. A. & White, R. J. 2004, ApJ, 604, 741
- Hinz, J. L., McCarthy, D. W., Simons, D. A., Henry, T. J., Kirkpatrick, J. D., & McGuire, P. C. 2002, AJ, 123, 2027
- Hodgkin, S. T., Jameson, R. F., & Steele, I. A. 1995, MNRAS, 274, 869
- Hoyle, F. 1953, ApJ, 118, 513
- Humphreys, R. M. 1970, AJ, 75, 602
- Hunt, L. K., Mannucci, F., Testi, L., Migliorini, S., Stanga, R. M., Baffa, C., Lisi, F., & Vanzi, L. 1998, ApJ, 115, 2594
- Irwin, M., McMahon, R. G., & Reid, I. N. 1991, MNRAS, 252, 61P
- Itoh, Y., Tamura, M., & Tokunaga, A. T. 2002, PASJ, 54, 561
- Jameson, R. F., Dobbie, P. D., Hodgkin, S. T., & Pinfield, D. J. 2002, MNRAS, 335, 853
- Jayawardhana, R., Ardila, D. R., Stelzer, B., & Haisch, K. E. 2003a, AJ, 126, 1515
- Jayawardhana, R., Mohanty, S., & Basri, G. 2002, ApJL, 578, L141
- . 2003b, ApJ, 592, 282
- Jeffries, R. D. & Naylor, T. 2001, in ASP Conf. Ser. 243: From Darkness to Light: Origin and Evolution of Young Stellar Clusters, eds. T. Montmerle & P. André (San Francisco), p 633
- Jeffries, R. D., Thurston, M. R., & Hambly, N. C. 2001, A&A, 375, 863
- Johnson, H. L. & Morgan, W. W. 1953, ApJ, 117, 313
- Jones, B. F. 1973, A&AS, 9, 313

- Jones, B. F. & Walker, M. F. 1988, AJ, 95, 1755
- Kendall, T. R., Mauron, N., Azzopardi, M., & Gigoyan, K. 2003, A&A, 403, 929
- Kenworthy, M., Hofmann, K., Close, L., Hinz, P., Mamajek, E., Schertl, D., Weigelt, G., Angel, R., Balega, Y. Y., Hinz, J., & Rieke, G. 2001, ApJL, 554, L67
- Kirkpatrick, J. D., Allard, F., Bida, T., Zuckerman, B., Becklin, E. E., Chabrier, G., & Baraffe, I. 1999a, ApJ, 519, 834
- Kirkpatrick, J. D., Beichman, C. A., & Skrutskie, M. F. 1997, ApJ, 476, 311
- Kirkpatrick, J. D., Henry, T. J., & McCarthy, D. W. 1991, ApJS, 77, 417
- Kirkpatrick, J. D., Reid, I. N., Liebert, J., Cutri, R. M., Nelson, B., Beichman, C. A., Dahn, C. C., Monet, D. G., Gizis, J. E., & Skrutskie, M. F. 1999b, ApJ, 519, 802
- Kirkpatrick, J. D., Reid, I. N., Liebert, J., Gizis, J. E., Burgasser, A. J., Monet, D. G., Dahn, C. C., Nelson, B., & Williams, R. J. 2000, AJ, 120, 447
- Klein, R., Apai, D., Pascucci, I., Henning, T., & Waters, L. B. F. M. 2003, ApJL, 593, L57
- Klessen, R. S. 2001, ApJ, 556, 837
- Koen, C. 2003, MNRAS, 346, 473
- Koerner, D. W., Kirkpatrick, J. D., McElwain, M. W., & Bonaventura, N. R. 1999, ApJL, 526, L25
- Kroupa, P. 2001, MNRAS, 322, 231
- . 2002, Science, 295, 82
- Kroupa, P., Aarseth, S., & Hurley, J. 2001, MNRAS, 321, 699
- Kroupa, P. & Bouvier, J. 2003a, MNRAS, 346, 369
- . 2003b, MNRAS, 346, 343
- Kroupa, P., Bouvier, J., Duchêne, G., & Moraux, E. 2003, MNRAS, 346, 354
- Kroupa, P., Tout, C. A., & Gilmore, G. 1990, MNRAS, 244, 76
- . 1993, MNRAS, 262, 545
- Kumar, S. S. 1963, ApJ, 137, 1121
- Lépine, S., Rich, R. M., & Shara, M. M. 2003a, ApJL, 591, L49
- . 2003b, AJ, 125, 1598
- Lépine, S., Shara, M. M., & Rich, R. M. 2002, AJ, 124, 1190
- Lachaume, R., Dominik, C., Lanz, T., & Habing, H. J. 1999, A&A, 348, 897

- Lada, E. A. & Lada, C. J. 1995, AJ, 109, 1682
- Landolt, A. U. 1992, AJ, 104, 340
- Lane, B. F., Zapatero Osorio, M. R., Britton, M. C., Martín, E. L., & Kulkarni, S. R. 2001, ApJ, 560, 390
- Latham, D. W., Stefanik, R. P., Mazeh, T., Mayor, M., & Burki, G. 1989, Nat, 339, 38
- Lee, T. A. 1968, ApJ, 152, 913
- Leggett, S. K. 1992, ApJS, 82, 351
- Leggett, S. K., Geballe, T. R., Fan, X., Schneider, D. P., Gunn, J. E., Lupton, R. H., Knapp, G. R., Strauss, M. A., McDaniel, A., Golimowski, D. A., & 25 coauthors. 2000, ApJL, 536, L35
- Li, Z. 2002, ApJL, 574, L159
- Liebert, J., Kirkpatrick, J. D., Reid, I. N., & Fisher, M. D. 1999, ApJ, 519, 345
- Lin, D. N. C., Laughlin, G., Bodenheimer, P., & Rozyczka, M. 1998, Science, 281, 2025
- Liu, M. C., Fischer, D. A., Graham, J. R., Lloyd, J. P., Marcy, G. W., & Butler, R. P. 2002a, ApJ, 571, 519
- Liu, M. C., Najita, J., & Tokunaga, A. T. 2003, ApJ, 585, 372
- Liu, M. C., Wainscoat, R., Martín, E. L., Barris, B., & Tonry, J. 2002b, ApJL, 568, L107
- Lodieu, N., Caux, E., Monin, J.-L., & Klotz, A. 2002a, A&A, 383, L15
- Lodieu, N., McCaughrean, M., Bouvier, J., Barrado y Navascués, D., & Stauffer, J. R. 2003, in IAU Symposium 211, “Brown dwarfs”, ed. E. L. Martín (San Francisco: ASP), p 179–180
- Lodieu, N., Scholz, R.-D., & McCaughrean, M. J. 2002b, A&A, 389, L20
- Loktin, A. V. & Beshenov, G. V. 2001, Astronomy Letters, 27, 386
- Low, C. & Lynden-Bell, D. 1976, MNRAS, 176, 367
- Lucas, P. W. & Roche, P. F. 2000, MNRAS, 314, 858
- Lucas, P. W., Roche, P. F., Allard, F., & Hauschildt, P. H. 2001, MNRAS, 326, 695
- Luhman, K. L. 1999, ApJ, 525, 466
- . 2000, ApJ, 544, 1044
- . 2001, ApJ, 560, 287
- Luhman, K. L., Briceño, C., Stauffer, J. R., Hartmann, L., Barrado y Navascués, D., & Caldwell, N. 2003a, ApJ, 590, 348
- Luhman, K. L. & Rieke, G. H. 1999, ApJ, 525, 440

- Luhman, K. L., Rieke, G. H., Young, E. T., Cotera, A. S., Chen, H., Rieke, M. J., Schneider, G., & Thompson, R. I. 2000, ApJ, 540, 1016
- Luhman, K. L., Stauffer, J. R., Muench, A. A., Rieke, G. H., Lada, E. A., Bouvier, J., & Lada, C. J. 2003b, ApJ, 593, 1093
- Luyten, W. J. 1979, LHS catalogue. A catalogue of stars with proper motions exceeding 0"5 annually (Minneapolis: University of Minnesota, 1979, 2nd ed.)
- . 1980, NLTT catalogue. Vol.3: 0 deg. to -10 deg. (Minneapolis: University of Minnesota, 1980)
- Mac Low, M. M. & Klessen, R. S. 2004, Reviews of Modern Physics, 76, 125
- Marcy, G. W. & Butler, R. P. 1992, PASP, 104, 270
- . 2000, PASP, 112, 137
- Marcy, G. W., Butler, R. P., Vogt, S. S., Fischer, D., & Liu, M. C. 1999, ApJ, 520, 239
- Martín, E. L. 1997, A&A, 321, 492
- Martín, E. L. 2000, in In “Very Low-mass Stars and Brown Dwarfs”, ed. R. Rebolo and M. R. Zapatero-Osorio (Cambridge University Press, UK), p 119
- Martín, E. L., Barrado y Navascués, D., Baraffe, I., Bouy, H., & Dahm, S. 2003, ApJ, 594, 525
- Martín, E. L., Basri, G., Delfosse, X., & Forveille, T. 1997, A&A, 327, L29
- Martín, E. L., Basri, G., & Zapatero Osorio, M. R. 1999, AJ, 118, 1005
- Martín, E. L., Brandner, W., & Basri, G. 1999a, Science, 283, 1718
- Martín, E. L., Brandner, W., Bouvier, J., Luhman, K. L., Stauffer, J., Basri, G., Zapatero Osorio, M. R., & Barrado y Navascués, D. 2000a, ApJ, 543, 299
- Martín, E. L., Delfosse, X., Basri, G., Goldman, B., Forveille, T., & Zapatero Osorio, M. R. 1999b, AJ, 118, 2466
- Martín, E. L., Delfosse, X., & Guieu, S. 2004, AJ, 127, 449
- Martín, E. L., Koresko, C. D., Kulkarni, S. R., Lane, B. F., & Wizinowich, P. L. 2000b, ApJL, 529, L37
- Martín, E. L., Rebolo, R., & Zapatero-Osorio, M. R. 1996, ApJ, 469, 706
- Martín, E. L., Zapatero Osorio, M. R., Barrado y Navascués, D., Béjar, V. J. S., & Rebolo, R. 2001, ApJL, 558, L117
- Martín, E. L., Zapatero Osorio, M. R., & Rebolo, R. 1998, in ASP Conf. Ser. 134: “Brown Dwarfs and Extrasolar Planets”, eds. R. Rebolo, E. L. Martín, and M. R. Zapatero Osorio, p 507
- Massey, P. & Gronwall, C. 1990, ApJ, 358, 344

- Mayor, M., Duquennoy, A., Halbwachs, J.-L., & Mermilliod, J.-C. 1992, in ASP Conf. Ser. 32: IAU Colloq. 135: Complementary Approaches to Double and Multiple Star Research, eds. McAlister and W. I. Hartkopf, p 73
- Mayor, M. & Queloz, D. 1995, *Nat*, 378, 355
- Mazeh, T., Latham, D. W., & Stefanik, R. P. 1996, *ApJ*, 466, 415
- Mazzei, P. & Pigatto, L. 1988, *A&A*, 193, 148
- McCaughrean, M., Zinnecker, H., Andersen, M., Meeus, G., & Lodieu, N. 2002a, *The Messenger*, 109, 28
- McCaughrean, M. J., Close, L. M., Scholz, R.-D., Lenzen, R., Biller, B., Brandner, W., Hartung, M., & Lodieu, N. 2004, *A&A*, 413, 1029
- McCaughrean, M. J. & O'Dell, C. R. 1996, *AJ*, 111, 1977
- McCaughrean, M. J., Scholz, R.-D., & Lodieu, N. 2002b, *A&A*, 390, L27
- McCaughrean, M. J. & Stauffer, J. R. 1994, *AJ*, 108, 1382
- McDonald, J. M. & Clarke, C. J. 1993, *MNRAS*, 262, 800
- McMillan, R. S., Moore, T. L., Perry, M. L., & Smith, P. H. 1994, *Astrophys. Space. Sci.*, 212, 271
- Melotte, P. J. 1915, *Mem. R. Astron. Soc.*, 60, 175
- Mermilliod, J. C. 1981, *A&A*, 97, 235
- Meusinger, H., Schilbach, E., & Souchay, J. 1996, *A&A*, 312, 833
- Micela, G., Sciortino, S., Vaiana, G. S., Schmitt, J. H. M. M., Stern, R. A., Harnden, F. R., & Rosner, R. 1988, *ApJ*, 325, 798
- Miller, G. E. & Scalo, J. M. 1979, *ApJS*, 41, 513
- Mitchell, R. I. 1960, *ApJ*, 132, 68
- Mohanty, S. & Basri, G. 2003, *ApJ*, 583, 451
- Monet, D. B. A., Canzian, B., Dahn, C., Guetter, H., Harris, H., Henden, A., Levine, S., Luginbuhl, C., Monet, A. K. B., Rhodes, A., Riepe, B., Sell, S., Stone, R., Vrba, F., & Walker, R. 1998, *The USNO-A2.0 Catalogue*, 1252
- Monet, D. G., Levine, S. E., Canzian, B., Ables, H. D., Bird, A. R., Dahn, C. C., Guetter, H. H., Harris, H. C., Henden, A. A., Leggett, S. K., Levison, H. F., Luginbuhl, C. B., Martini, J., Monet, A. K. B., Munn, J. A., Pier, J. R., Rhodes, A. R., Riepe, B., Sell, S., Stone, R. C., Vrba, F. J., Walker, R. L., Westerhout, G., Brucato, R. J., Reid, I. N., Schoening, W., Hartley, M., Read, M. A., & Tritton, S. B. 2003, *AJ*, 125, 984

- Moorwood, A. F. M. & Spyromilio, J. 1997, in The Early Universe with the VLT, Eds by J. Bergeron, Berlin Springer, p 21
- Moraux, E., Bouvier, J., & Stauffer, J. R. 2001, A&A, 367, 211
- Moraux, E., Bouvier, J., Stauffer, J. R., & Cuillandre, J.-C. 2003, A&A, 400, 891
- Morgan, W. W., Keenan, P. C., & Kellman, E. 1943, An atlas of stellar spectra, with an outline of spectral classification (Chicago, Ill., The University of Chicago press)
- Muench, A. A., Lada, E. A., Lada, C. J., & Alves, J. 2002, ApJ, 573, 366
- Muench, A. A., Lada, E. A., Lada, C. J., Elston, R. J., Alves, J. F., Horrobin, M., Huard, T. H., Levine, J. L., Raines, S. N., & Román-Zúñiga, C. 2003, AJ, 125, 2029
- Munari, U., Dallaporta, S., Siviero, A., Soubiran, C., Fiorucci, M., & Girard, P. 2004, A&A, 418, L31
- Muzerolle, J., Hillenbrand, L., Calvet, N., Briceño, C., & Hartmann, L. 2003, ApJ, 592, 266
- Najita, J. R., Tiede, G. P., & Carr, J. S. 2000, ApJ, 541, 977
- Nakajima, T., Oppenheimer, B. R., Kulkarni, S. R., Golimowski, D. A., Matthews, K., & Durrrance, S. T. 1995, Nat, 378, 463
- Nakajima, Y., Tamura, M., Oasa, Y., & Nakajima, T. 2000, AJ, 119, 873
- Natta, A. & Testi, L. 2001, A&A, 376, L22
- Natta, A., Testi, L., Comerón, F., Oliva, E., D'Antona, F., Baffa, C., Comoretto, G., & Gennari, S. 2002, A&A, 393, 597
- Neuhäuser, R. & Comeron, F. 1998, Science, 282, 83
- Noll, K. S., Geballe, T. R., & Marley, M. S. 1997, ApJL, 489, L87
- Oliveira, J. M., Jeffries, R. D., Devey, C. R., Barrado y Navascués, D., Naylor, T., Stauffer, J. R., & Totten, E. J. 2003, MNRAS, 342, 651
- Oliveira, J. M., Jeffries, R. D., Kenyon, M. J., Thompson, S. A., & Naylor, T. 2002, A&A, 382, L22
- Oppenheimer, B. R., Golimowski, D. A., Kulkarni, S. R., Matthews, K., Nakajima, T., Creech-Eakman, M., & Durrance, S. T. 2001, AJ, 121, 2189
- Oppenheimer, B. R., Kulkarni, S. R., Matthews, K., & Nakajima, T. 1995, Science, 270, 1478
- Oswalt, T. D., Hintzen, P. M., & Luyten, W. J. 1988, ApJS, 66, 391
- Ozawa, H., Gross, N., & Montmerle, T. 2004, ArXiv Astrophysics e-prints, astro-ph/0407241
- Paczynski, B. 1986, ApJ, 304, 1
- Padoan, P. & Nordlund, Å. 2002, ApJ, 576, 870

- Palla, F. & Stahler, S. W. 1993, *ApJ*, 418, 414
- Papaloizou, J. C. B. & Terquem, C. 2001, *MNRAS*, 325, 221
- Patience, J., Ghez, A. M., Reid, I. N., & Matthews, K. 2002, *AJ*, 123, 1570
- Patten, B. M. & Pavlovsky, C. M. 1999, *PASP*, 111, 210
- Patten, B. M. & Simon, T. 1993, *ApJL*, 415, L123
- Pavlenko, Y. V., Rebolo, R., Martín, E. L., & Garcia Lopez, R. J. 1995, *A&A*, 303, 807
- Perryman, M. A. C., Lindegren, L., Kovalevsky, J., Hoeg, E., Bastian, U., Bernacca, P. L., Crézé, M., Donati, F., Grenon, M., van Leeuwen, F., van der Marel, H., Mignard, F., Murray, C. A., Le Poole, R. S., Schrijver, H., Turon, C., Arenou, F., Froeschlé, M., & Petersen, C. S. 1997, *A&A*, 323, L49
- Persi, P., Marenzi, A. R., Olofsson, G., Kaas, A. A., Nordh, L., Huldtgren, M., Abergel, A., André, P., Bontemps, S., Boulanger, F., Burgdorf, M., Casali, M. M., Cesarsky, C. J., Copet, E., Davies, J., Falgarone, E., Montmerle, T., Perault, M., Prusti, T., Puget, J. L., & Sibille, F. 2000, *A&A*, 357, 219
- Pickles, A. J. 1998, *PASP*, 110, 863
- Pinfield, D. J., Hodgkin, S. T., Jameson, R. F., Cossburn, M. R., Hambly, N. C., & Devereux, N. 2000, *MNRAS*, 313, 347
- Pinfield, D. J., Jameson, R. F., & Hodgkin, S. T. 1998, *MNRAS*, 299, 955
- Pinsonneault, M. H., Stauffer, J., Soderblom, D. R., King, J. R., & Hanson, R. B. 1998, *ApJ*, 504, 170
- Pokorny, R. S., Jones, H. R. A., & Hambly, N. C. 2003, *A&A*, 397, 575
- Potter, D., Martín, E. L., Cushing, M. C., Baudoz, P., Brandner, W., Guyon, O., & Neuhäuser, R. 2002, *ApJL*, 567, L133
- Prosser, C. F. 1992, *AJ*, 103, 488
- . 1994, *AJ*, 107, 1422
- Prosser, C. F., Randich, S., & Stauffer, J. R. 1996a, *AJ*, 112, 649
- Prosser, C. F., Randich, S., Stauffer, J. R., Schmitt, J. H. M. M., & Simon, T. 1996b, *AJ*, 112, 1570
- Prosser, C. P. & Randich, S. 1998, *AN*, 319, 201
- Prosser, C. P., Randich, S., & Simon, T. 1998, *AN*, 319, 215
- Queloz, D. 2002, in ASP Conf. Ser. 269: The Evolving Sun and its Influence on Planetary Environments, eds B. Montesinos, A. Gimenez, and E. F. Guinan (San Francisco, Astronomical Society of the Pacific), p 189

- Randich, S., Pallavicini, R., Meola, G., Stauffer, J. R., & Balachandran, S. C. 2001, A&A, 372, 862
- Randich, S., Schmitt, J. H. M. M., Prosser, C. F., & Stauffer, J. R. 1995, A&A, 300, 134
—. 1996, A&A, 305, 785
- Rebolo, R., Martín, E. L., & Magazzù, A. 1992, ApJL, 389, L83
- Rebolo, R., Zapatero Osorio, M. R., Madruga, S., Bejar, V. J. S., Arribas, S., & Licandro, J. 1998, Science, 282, 1309
- Rebolo, R., Zapatero-Osorio, M. R., & Martín, E. L. 1995, Nat, 377, 129
- Rees, M. J. 1976, MNRAS, 176, 483
- Reid, I. N., Burgasser, A. J., Cruz, K. L., Kirkpatrick, J. D., & Gizis, J. E. 2001a, AJ, 121, 1710
- Reid, I. N. & Cruz, K. L. 2002, AJ, 123, 2806
- Reid, I. N., Cruz, K. L., Laurie, S. P., Liebert, J., Dahn, C. C., Harris, H. C., Guetter, H. H., Stone, R. C., Canzian, B., Luginbuhl, C. B., Levine, S. E., Monet, A. K. B., & Monet, D. G. 2003, AJ, 125, 354
- Reid, I. N. & Gizis, J. E. 1997a, AJ, 113, 2246
—. 1997b, AJ, 114, 1992
- Reid, I. N., Gizis, J. E., & Hawley, S. L. 2002a, AJ, 124, 2721
- Reid, I. N., Gizis, J. E., Kirkpatrick, J. D., & Koerner, D. W. 2001b, AJ, 121, 489
- Reid, I. N., Hawley, S. L., & Gizis, J. E. 1995, AJ, 110, 1838
- Reid, I. N., Kilkenny, D., & Cruz, K. L. 2002b, AJ, 123, 2822
- Reid, I. N., Kirkpatrick, J. D., Liebert, J., Burrows, A., Gizis, J. E., Burgasser, A., Dahn, C. C., Monet, D., Cutri, R., Beichman, C. A., & Skrutskie, M. 1999, ApJ, 521, 613
- Reid, N. 1992, MNRAS, 257, 257
- Reid, N. & Gilmore, G. 1982, MNRAS, 201, 73
- Reipurth, B. & Clarke, C. 2001, AJ, 122, 432
- Rieke, G. H. & Lebofsky, M. J. 1985, ApJ, 288, 618
- Rieke, G. H. & Rieke, M. J. 1990, ApJL, 362, L21
- Robichon, N., Arenou, F., Mermilliod, J.-C., & Turon, C. 1999, A&A, 345, 471
- Rosvick, J. M., Mermilliod, J.-C., & Mayor, M. 1992, A&A, 255, 130
- Ruciński, S. M. 1980, Acta Astronomica, 30, 373

- . 1987, PASP, 99, 487
- Ruiz, M. T., Leggett, S. K., & Allard, F. 1997, ApJL, 491, L107
- Ruiz, M. T., Wischnjewsky, M., Rojo, P. M., & Gonzalez, L. E. 2001, ApJS, 133, 119
- Sahade, J. & Berón Dàvila, F. 1963, Annales d'Astrophysique, 26, 153
- Sahade, J. & Frieboes, H. 1960, PASP, 72, 52
- Salim, S., Lépine, S., Rich, R. M., & Shara, M. M. 2003, ApJL, 586, L149
- Salpeter, E. E. 1955, ApJ, 121, 161
- Saumon, D., Geballe, T. R., Leggett, S. K., Marley, M. S., Freedman, R. S., Lodders, K., Fegley, B., & Sengupta, S. K. 2000, ApJ, 541, 374
- Scalo, J. M. 1986, Fundamentals of Cosmic Physics, 11, 1
- Schneider, D. P., Knapp, G. R., Hawley, S. L., Covey, K. R., Fan, X., Ramsey, L. W., Richards, G. T., Strauss, M. A., Gunn, J. E., Hill, G. J., & 14 coauthors. 2002, AJ, 123, 458
- Scholz, R.-D., Irwin, M., Ibata, R., Jahreiß, H., & Malkov, O. Y. 2000, A&A, 353, 958
- Scholz, R.-D., Lodieu, N., Ibata, R., Bienaymé, O., Irwin, M., McCaughrean, M. J., & Schwone, A. 2004, MNRAS, 347, 685
- Scholz, R.-D., McCaughrean, M. J., Lodieu, N., & Kuhlbrot, B. 2003, A&A, 398, L29
- Scholz, R.-D. & Meusinger, H. 2002, MNRAS, 336, L49
- Scholz, R.-D., Szokoly, G. P., Andersen, M., Ibata, R., & Irwin, M. J. 2002, ApJ, 565, 539
- Schroeder, D. J., Golimowski, D. A., Brukardt, R. A., Burrows, C. J., Caldwell, J. J., Fastie, W. G., Ford, H. C., Hesman, B., Kletskin, I., Krist, J. E., Royle, P., & Zubrowski, R. A. 2000, AJ, 119, 906
- Schweitzer, A., Gisis, J. E., Hauschildt, P. H., Allard, F., & Reid, I. N. 2001, ApJ, 555, 368
- Schweitzer, A., Scholz, R.-D., Stauffer, J., Irwin, M., & McCaughrean, M. J. 1999, A&A, 350, L62
- Siess, L., Dufour, E., & Forestini, M. 2000, A&A, 358, 593
- Simons, D. A., Henry, T. J., & Kirkpatrick, J. D. 1996, AJ, 112, 2238
- Skrutskie, M. F., Schneider, S. E., Stiening, R., Strom, S. E., Weinberg, M. D., Beichman, C., Chester, T., Cutri, R., Lonsdale, C., Elias, J., Elston, R., Capps, R., Carpenter, J., Huchra, J., Liebert, J., Monet, D., Price, S., & Seitzer, P. 1997, in ASSL Vol. 210: The Impact of Large Scale Near-IR Sky Surveys, eds. F. Garzon et al., Dordrecht: Kluwer Academic Publishing Company, p 25
- Slesnick, C. L., Hillenbrand, L. A., & Carpenter, J. M. 2004, ApJ, 610, 1045

- Smith, V. V., Tsuji, T., Hinkle, K. H., Cunha, K., Blum, R. D., Valenti, J. A., Ridgway, S. T., Joyce, R. R., & Bernath, P. 2003, ApJL, 599, L107
- Stauffer, J., Hartmann, L. W., Jones, B. F., & McNamara, B. R. 1989a, ApJ, 342, 285
- Stauffer, J. R., Barrado y Navascués, D., Bouvier, J., Lodieu, N., & McCaughrean, M. 2003, in IAU Symposium 211, “Brown dwarfs”, ed. E. L. Martín (San Francisco: ASP), p 163–170
- Stauffer, J. R., Barrado y Navascués, D., Bouvier, J., Morrison, H. L., Harding, P., Luhman, K. L., Stanke, T., McCaughrean, M., Terndrup, D. M., Allen, L., & Assouad, P. 1999, ApJ, 527, 219
- Stauffer, J. R., Caillault, J.-P., Gagne, M., Prosser, C. F., & Hartmann, L. W. 1994a, ApJS, 91, 625
- Stauffer, J. R., Hartmann, L. W., Burnham, J. N., & Jones, B. F. 1985, ApJ, 289, 247
- Stauffer, J. R., Hartmann, L. W., & Jones, B. F. 1989b, ApJ, 346, 160
- Stauffer, J. R., Hartmann, L. W., Prosser, C. F., Randich, S., Balachandran, S., Patten, B. M., Simon, T., & Giampapa, M. 1997, ApJ, 479, 776
- Stauffer, J. R., Liebert, J., Giampapa, M., Macintosh, B., Reid, N., & Hamilton, D. 1994b, AJ, 108, 160
- Stauffer, J. R., Schultz, G., & Kirkpatrick, J. D. 1998, ApJL, 499, 219
- Stephens, D. C. & Leggett, S. K. 2004, PASP, 116, 9
- Stern, R. A., Schmitt, J. H. M. M., & Kahabka, P. T. 1995, ApJ, 448, 683
- Sterzik, M. F. & Durisen, R. H. 2003, A&A, 400, 1031
- Strauss, M. A., Fan, X., Gunn, J. E., Leggett, S. K., Geballe, T. R., Pier, J. R., Lupton, R. H., Knapp, G. R., Annis, J., Brinkmann, J., & 19 coauthors. 1999, ApJL, 522, L61
- Tarter, J. C. 1976, Bull. AAS, 8, 517
- Tej, A., Sahu, K. C., C. T., & Ashok, N. M. 2002, ApJ, 578, 523
- Terndrup, D. M., Krishnamurthi, A., Pinsonneault, M. H., & Stauffer, J. R. 1999, AJ, 118, 1814
- Testi, L., D’Antona, F., Ghinassi, F., Licandro, J., Magazzù, A., Maiolino, R., Mannucci, F., Marconi, A., Nagar, N., Natta, A., & Oliva, E. 2001, ApJL, 552, L147
- Testi, L., Natta, A., Oliva, E., D’Antona, F., Comeron, F., Baffa, C., Comoretto, G., & Gennari, S. 2002, ApJL, 571, L155
- Thorstensen, J. R. & Kirkpatrick, J. D. 2003, PASP, 115, 1207
- Tinney, C. G. 1998, MNRAS, 296, L42
- Tinney, C. G., Delfosse, X., & Forveille, T. 1997, ApJL, 490, L95
- Tinney, C. G., Delfosse, X., Forveille, T., & Allard, F. 1998, A&A, 338, 1066

- Tinney, C. G. & Reid, I. N. 1998, MNRAS, 301, 1031
- Tinney, C. G., Reid, I. N., & Mould, J. R. 1993, ApJ, 414, 254
- Tokovinin, A. A., Duquennoy, A., Halbwachs, J.-L., & Mayor, M. 1994, A&A, 282, 831
- Tokunaga, A. T. & Kobayashi, N. 1999, AJ, 117, 1010
- Trumpler, R. J. 1930, Lick Observatory Bulletin, 420, 154
- Tsuji, T. 2002, ApJ, 575, 264
- Tsvetanov, Z. I., Golimowski, D. A., Zheng, W., Geballe, T. R., Leggett, S. K., Ford, H. C., Davidsen, A. F., Uomoto, A., Fan, X., Knapp, G. R., & 16 coauthors. 2000, ApJL, 531, L61
- Udry, S., Mayor, M., Naef, D., Pepe, F., Queloz, D., Santos, N. C., & Burnet, M. 2002, A&A, 390, 267
- van Dokkum, P. G. 2001, PASP, 113, 1420
- van Leeuwen, F. 1999, A&A, 341, L71
- Van't-Veer, F. 1980, Acta Astronomica, 30, 381
- Voges, W., Aschenbach, B., Boller, T., Bräuninger, H., Briel, U., Burkert, W., Dennerl, K., Enghausen, J., Gruber, R., Haberl, F., Hartner, G., Hasinger, G., Kürster, M., Pfeffermann, E., Pietsch, W., Predehl, P., Rosso, C., Schmitt, J. H. M. M., Trümper, J., & Zimmermann, H. U. 1999, A&A, 349, 389
- Vogt, S. S., Marcy, G. W., Butler, R. P., & Apps, K. 2000, ApJ, 536, 902
- Volk, K., Blum, R., Walker, G., & Puxley, P. 2003, in International Astronomical Union Circular, 2
- Vuong, M. H., Cambrésy, L., & Epcstein, N. 2001, A&A, 379, 208
- Vuong, M. H., Montmerle, T., Grosso, N., Feigelson, E. D., Verstraete, L., & Ozawa, H. 2003, A&A, 408, 581
- Walter, F. M., Vrba, F. J., Mathieu, R. D., Brown, A., & Myers, P. C. 1994, AJ, 107, 692
- Watkins, S. J., Bhattacharjee, A. S., Boffin, H. M. J., Francis, N., & Whitworth, A. P. 1998a, MNRAS, 300, 1205
- . 1998b, MNRAS, 300, 1214
- White, R. J. & Basri, G. 2003, ApJ, 582, 1109
- White, R. J., Ghez, A. M., Reid, I. N., & Schultz, G. 1999, ApJ, 520, 811
- Wichmann, R., Bastian, U., Krautter, J., Jankovics, I., & Rucinski, S. M. 1998, MNRAS, 301, L39
- Wielen, R. 1971, A&A, 13, 309

- Wielen, R., Jahreiß, H., & Krüger, R. 1983, in IAU Colloq. 76: Nearby Stars and the Stellar Luminosity Function, eds. AG. Davis Philip, A.R. Upgren, L. Davis Press,, p 163–170
- Wilking, B. A., Greene, T. P., & Meyer, M. R. 1999, AJ, 117, 469
- Wilking, B. A., Meyer, M. R., Greene, T. P., Mikhail, A., & Carlson, G. 2004, AJ, 127, 1131
- Wilson, J. C., Miller, N. A., Gizis, J. E., Skrutskie, M. F., Houck, J. R., Kirkpatrick, J. D., Bur-gasser, A. J., & Monet, D. G. 2003, in IAU Symposium 211, “Brown dwarfs”, ed. E. L. Martín (San Francisco: ASP), 197
- Wolszczan, A. & Frail, D. A. 1992, Nat, 355, 145
- Wroblewski, H. & Costa, E. 1999, A&AS, 139, 25
- . 2000, A&AS, 142, 369
- . 2001, A&A, 367, 725
- Wroblewski, H. & Torres, C. 1989, A&AS, 78, 231
- . 1992, A&AS, 92, 449
- . 1994, A&AS, 105, 179
- . 1995, A&AS, 110, 27
- . 1996, A&AS, 115, 481
- . 1997, A&AS, 122, 447
- . 1998, A&AS, 128, 457
- York, D. G., Adelman, J., Anderson, J. E., Anderson, S. F., Annis, J., Bahcall, N. A., Bakken, J. A., Barkhouser, R., Bastian, S., Berman, E., & 134 coauthors. 2000, AJ, 120, 1579
- Zacharias, N., Urban, S. E., Zacharias, M. I., Wycoff, G. L., Hall, D. M., Germain, M. E., Hold-enried, E. R., & Winter, L. 2003, UCAC2 Catalogue, 1289, 0
- Zapatero Osorio, M. R., Béjar, V. J. S., Martín, E. L., Rebolo, R., Barrado y Navascués, D., Bailer-Jones, C. A. L., & Mundt, R. 2000, Science, 290, 103
- Zapatero Osorio, M. R., Béjar, V. J. S., Pavlenko, Y., Rebolo, R., Allende Prieto, C., Martín, E. L., & García López, R. J. 2002, A&A, 384, 937
- Zapatero Osorio, M. R., Caballero, J. A., Béjar, V. J. S., & Rebolo, R. 2003, A&A, 408, 663
- Zapatero Osorio, M. R., Martin, E. L., & Rebolo, R. 1997a, A&A, 323, 105
- Zapatero Osorio, M. R., Rebolo, R., & Martin, E. L. 1997b, A&A, 317, 164
- Zapatero Osorio, M. R., Rebolo, R., Martín, E. L., Basri, G., Magazzù, A., Hodgkin, S. T., Jame-son, R. F., & Cossburn, M. R. 1997c, ApJL, 491, L81

- Zapatero Osorio, M. R., Rebolo, R., Martín, E. L., & Garcia Lopez, R. J. 1996, A&A, 305, 519
- Zapatero Osorio, M. R., Rebolo, R., Martín, E. L., Hodgkin, S. T., Cossburn, M. R., Magazzù, A., Steele, I. A., & Jameson, R. F. 1999, A&AS, 134, 537
- Zucker, S. & Mazeh, T. 2001, ApJ, 562, 549

Appendices

Appendix A

Spectroscopy for southern sky proper motion objects

This appendix presents the results of the southern sky proper motion survey initiated by Scholz et al. (2000). The target selection was made by Ralf-Dieter Scholz, while I have reduced and analysed the optical and near-infrared photometric and spectroscopic observations (Chapter 2).

This appendix contains tables with the coordinates, proper motions, magnitudes, spectral indices, spectral types and distance estimates for all proper motion objects spectroscopically followed-up to date, along with their optical and/or near-infrared spectra. Some comparison stars with well-determined spectral types were also observed spectroscopically with the same telescope/instrument configuration such as LHS517 (M3.5), 2MASSW J0952219–192431 (M7.0), LP647-13 (M7.5), LP775-31 (M8.0), LP655-13 (M9.0), BRI B0021–0214 (M9.5), and Kelu 1 (L2.0) to compare to our targets.

- Table A.1 contains 67 proper motion candidates followed-up spectroscopically except the ε Indi B system. Column 1: Name of the object, Columns 2 and 3: coordinates in J2000, Column 4: Epoch, Columns 5 to 8: proper motion expressed in milli arcsec per year with the errors. The ^a and ^b exponents indicate that the object is also found in the proper motion catalogues of Pokorny, Jones, & Hambly (2003) and B1.0 catalogue (Monet et al. 2003), respectively.
- Table A.2 contains 67 proper motion candidates followed-up spectroscopically except the ε Indi B system. Three template objects are included for comparison purposes, namely BRI B0021–0214, LP944-20, and Kelu 1. Column 1: Name of the object, Columns 2–7: B_J , R , I , J , H , K_s magnitudes from the SuperCosmos Sky Surveys and 2MASS databases, Column 8 gives the final spectral type of each target and Column 9 provides an estimate of the distance based on the spectral type.
- Table A.3 lists the values of the spectral indices ($H\alpha$, TiO5, VO-a, and PC3) and the derived spectral types for 52 objects. The final spectral types are also given. Equivalent widths (in Å) of the gravity-sensitive K I and Na I doublets are also provided in columns 12 and 13.
- Figure A.1 shows the consistency of the optical indices from Martín et al. (1999b) and Kirkpatrick et al. (1999b) for the spectral classification of the red proper motion objects.
- Figure A.2 displays the optical (6000–10000 Å) spectra obtained with VLT/FORS1 and ESO 3.6-m/EFOSC2 for 10 early-M dwarfs with spectral types earlier than M5.

- Figure A.3 shows the optical (6000–10000 Å) spectra obtained with ESO 3.6-m/EFOSC2 for a sample of 34 M dwarfs with spectral types ranging from M5.5 to M8.5.
- Figure A.4 displays near-infrared (1.0–2.5 μm) spectra obtained with VLT/ISAAC and NTT/SofI for objects with or without optical spectroscopy. Objects whose spectral type are in square brackets have been spectroscopically observed *only* in the near-infrared (11), the objects with spectral types in parentheses were classified from the optical schemes (13).

Table A.1: List of the 67 red proper motion objects selected in the course of the Southern Sky proper motion survey (Section 2.4). Coordinates, epochs, and proper motions of each target are listed.

Targets	Coordinates (J2000)		Epoch	Proper Motions			
	R.A.	Declination		μ_α	μ_δ	σ_{μ_α}	σ_{μ_δ}
SSSPM J0006–2157 ^{a,b}	00:05:48.46	−21:57:19.7	1999.60	+721	−128	7	2
SSSPM J0027–5402 ^b	00:27:23.43	−54:01:46.1	1999.80	+415	+41	18	4
SSSPM J0030–3427 ^a	00:30:10.23	−34:26:55.5	2000.72	−102	−279	7	2
LP 645–52 ^b	00:35:41.68	−03:21:30.8	1998.71	+428	−84	3	1
SSSPM J0109–5101 ^b	01:09:01.50	−51:00:49.4	1999.81	+209	+86	2	7
SSSPM J0109–4955 ^b	01:09:09.18	−49:54:53.2	1999.81	+86	+128	9	8
SSSPM J0124–4240 ^{a,b}	01:23:59.05	−42:40:07.3	2000.63	−145	−229	4	7
SSSPM J0125–6546	01:24:49.63	−65:46:33.6	1999.90	+98	+82	7	8
SSSPM J0134–6315	01:33:32.44	−63:14:41.8	1999.90	+77	−81	8	9
LP 769–14 ^{a,b}	01:59:17.41	−17:30:08.7	2000.81	−119	−145	3	6
SSSPM J0204–3633 ^{a,b}	02:04:22.13	−36:32:30.8	2000.72	+216	−59	9	26
APMPM J0207–3722 ^{a,b}	02:07:14.08	−37:21:50.2	2000.72	+422	+134	2	6
SSSPM J0215–4804 ^{a,b}	02:14:48.14	−48:04:25.3	2000.01	+118	−332	9	5
SSSPM J0219–1939	02:19:28.07	−19:38:41.6	2000.89	+195	−174	4	5
SSSPM J0222–5412	02:21:54.94	−54:12:05.4	1999.82	+107	−14	7	8
SSSPM J0231–4122	02:31:22.25	−41:21:50.7	1999.66	+301	−127	4	28
SSSPM J0306–3648 ^{a,b}	03:06:11.59	−36:47:52.8	2000.00	−180	−670	9	8
SSSPM J0327–4236 ^b	03:26:32.78	−42:36:08.3	2000.77	+286	−22	25	28
LP 888–18 ^{a,b}	03:31:30.25	−30:42:38.8	1999.94	+40	−392	5	6
LP 775–31 ^b	04:35:16.12	−16:06:57.4	1998.90	+156	+315	3	4
LP 655–48 ^b	04:40:23.33	−05:30:07.9	2001.79	+339	+126	2	2
SSSPM J0500–5406 ^{a,b}	05:00:15.77	−54:06:27.3	1999.84	+207	−1022	9	2
SSSPM J0511–4606	05:11:01.63	−46:06:01.5	1999.77	+53	+121	9	6
ESO 207–61	07:07:53.27	−49:00:50.3	2000.15	−34	+401	14	8
SSSPM J0829–1309 ^b	08:28:34.11	−13:09:20.1	2001.28	−593	+14	6	7
LP 314–67 ^b	09:48:05.16	26:24:18.9	1999.07	−143	−438	13	2
LP 614–35 ^b	12:07:51.63	00:52:32.0	1999.07	−188	−11	2	4
APMPM J1222–2452 ^b	12:22:26.55	−24:52:15.8	1998.50	−442	+96	12	4
APMPM J1251–2121 ^b	12:50:52.65	−21:21:13.6	2000.20	+435	−349	4	3
CE 303 ^b	13:09:21.85	−23:30:35.0	1998.32	+8	−376	9	2
CE 352 ^b	13:40:38.77	−30:32:02.7	2000.23	−335	−103	7	4
LP 859–1 ^b	15:04:16.21	−23:55:56.4	1998.48	−339	−85	14	3
LHS 3141B ^b	15:59:37.99	−22:26:12.8	1999.32	+193	−538	8	21
SSSPM J1926–4311	19:26:08.59	−43:10:56.3	1999.53	−167	−1072	15	20
SSSPM J1930–4311 ^b	19:29:40.99	−43:10:36.8	2000.63	−19	−865	11	8
APMPM J1957–4216 ^b	19:56:57.61	−42:16:23.5	2000.57	+149	−1017	4	6
SSSPM J2003–4433 ^b	20:02:52.08	−44:33:03.6	1999.62	−17	−894	11	13
LP 815–21 ^b	20:28:04.52	−18:18:57.5	1998.44	−105	−175	5	6
SSSPM J2033–6919 ^b	20:32:32.91	−69:18:59.1	2000.43	+228	−459	10	5
APMPM J2036–4936 ^b	20:35:49.96	−49:36:07.7	1999.71	−86	−416	4	8
SSSPM J2052–4759 ^b	20:52:28.08	−47:58:44.2	1999.78	−7	−435	5	7
SSSPM J2059–8018	20:59:02.19	−80:17:36.9	2000.66	+361	−46	6	29
SSSPM J2101–5110	21:01:29.49	−51:10:02.9	1999.64	+69	−123	7	16
[HB88] M18 ^b	21:18:31.74	−45:05:52.2	1999.71	+388	−475	14	15
[HB88] M12 ^b	21:31:14.14	−42:24:14.3	1999.63	+48	−71	6	9

Table A.1: continued

Targets	Coordinates (J2000)		Epoch	Proper Motions			
	R.A.	Declination		μ_α	μ_δ	σ_{μ_α}	σ_{μ_δ}
LP 819-9 ^b	21:59:30.91	-15:54:16.5	2000.78	+0	-283	2	4
SSSPM J2229-6931 ^b	22:29:23.65	-69:30:56.9	2000.58	+47	-217	9	10
LDS4980 B ^b	22:35:58.17	07:57:13.9	2000.59	-112	-208	2	6
LDS4980 A ^b	22:36:00.63	07:56:03.5	2000.59	-103	-210	9	2
SSSPM J2240-4253 ^b	22:40:26.97	-42:53:18.4	2000.73	-35	-539	27	9
SSSPM J2257-5208	22:57:31.68	-52:08:26.3	1999.82	+57	+113	11	16
SSSPM J2258-4639	22:57:49.26	-46:38:44.5	2000.73	-185	+197	11	4
SSSPM J2307-5009 ^b	23:06:58.76	-50:08:58.9	1999.84	+452	+25	10	6
SSSPM J2310-1759	23:10:18.46	-17:59:09.0	1998.50	-23	-271	36	24
SSSPM J2319-4919 ^b	23:18:46.14	-49:19:18.0	2000.50	+216	-16	9	3
SSSPM J2322-6358	23:22:05.69	-63:57:58.0	1999.88	+121	-19	11	5
APMPM J2330-4737	23:30:16.12	-47:36:45.9	2000.79	-578	-983	2	2
APMPM J2331-2750 ^b	23:31:21.74	-27:49:50.0	1999.44	+85	+753	4	3
SSSPM J2335-6913 ^b	23:35:19.59	-69:13:17.0	2000.76	+66	-168	10	3
APMPM J2344-2906	23:43:31.98	-29:06:27.1	1998.85	+331	-217	10	6
SSSPM J2345-6810 ^b	23:44:57.97	-68:09:39.8	2000.77	+206	-81	11	4
APMPM J2347-3154 ^b	23:46:54.71	-31:53:53.2	1998.95	+424	-408	3	4
SSSPM J2352-2538 ^a	23:51:50.44	-25:37:36.6	1999.60	+354	+193	9	8
SSSPM J2353-4123 ^b	23:53:01.41	-41:23:24.6	1999.70	+130	+0	20	8
APMPM J2354-3316 ^{a,b}	23:54:09.28	-33:16:26.6	1999.57	-326	-389	8	13
SSSPM J2356-3426 ^{a,b}	23:56:10.81	-34:26:04.4	1999.57	+70	-301	9	5
SSSPM J2400-2008	23:59:57.62	-20:07:39.4	1998.61	+402	-511	29	10

Table A.2: List of the 67 red proper motion objects selected in the course of the Southern Sky proper motion survey (Section 2.4) with their optical and near-infrared magnitudes, spectral types (4 ≡ M4, 5 ≡ M5, 12 ≡ L2, etc . . .), and estimated distances (in parsecs).

Targets	B_J	R_{SSS}	I_{SSS}	J	H	K_s	SpT	Distance
SSSPM J0006–2157	22.56	19.41	16.21	13.27	12.62	12.20	8.5	25.0 ± 3.0
BRI B0021–0214	21.76	18.17	14.95	11.99	11.08	10.54	9.5	11.9 ± 1.4
SSSPM J0027–5402	19.15	18.06	14.70	12.36	11.72	11.34	7.0	20.8 ± 2.5
SSSPM J0030–3427	22.12	19.20	16.39	13.86	13.19	12.79	9.0	30.4 ± 3.6
LP 645–52	20.26	17.88	15.54	13.75	13.28	12.99	5.0	54.1 ± 6.5
SSSPM J0109–5101	21.19	18.21	14.81	12.23	11.54	11.09	8.0	16.8 ± 2.0
SSSPM J0109–4955	22.32	19.40	15.98	13.55	12.88	12.45	8.0	30.8 ± 3.7
SSSPM J0124–4240	22.16	19.35	16.17	13.15	12.47	12.04	10.5	17.3 ± 2.1
SSSPM J0125–6546	22.70	19.49	16.46	14.43	13.81	13.46	7.0	54.0 ± 6.5
SSSPM J0134–6315	22.11	19.01	15.97	14.51	14.02	13.70	8.0	47.9 ± 5.7
LP 769–14	21.15	18.63	16.44	14.61	13.96	13.70	4.5	86.9 ± 10.4
SSSPM J0204–3633		19.96	15.77	13.27	12.60	12.19	7.5	29.3 ± 3.5
APMPM J0207–3722	20.79	18.10	14.91	12.44	11.83	11.38	7.0	21.6 ± 2.6
SSSPM J0215–4804	22.20	19.14	16.17	13.56	12.96	12.52	8.0	30.9 ± 3.7
SSSPM J0219–1939		20.06	17.47	14.11	13.34	12.91	11.0	24.9 ± 3.0
SSSPM J0222–5412		20.30	17.08	13.90	13.22	12.66	9.0	30.9 ± 3.7
SSSPM J0231–4122		20.10	17.03	13.85	13.27	12.89	8.5	32.7 ± 3.9
SSSPM J0306–3648	20.55	17.67	13.80	11.69	11.07	10.63	8.0	13.1 ± 1.6
SSSPM J0327–4236		20.53	16.92	14.22	13.61	13.21	8.5	38.8 ± 4.7
LP 888–18	19.91	17.21	13.59	11.36	10.70	10.26	8.0	11.2 ± 1.3
LP 944–20	20.24	16.84	13.29	10.73	10.02	9.55	9.5	8.4 ± 1.0
LP 775–31	18.85	16.34	12.35	10.41	9.78	9.35	8.0	7.3 ± 0.9
LP 655–48	18.85	16.50	13.17	10.66	9.99	9.55	7.5	8.8 ± 1.1
SSSPM J0500–5406	20.10	17.31	15.56	14.44	14.12	13.97	esdM6	60.0 ± 15.0
SSSPM J0511–4606		19.97	17.01	13.89	13.19	12.71	8.5	33.3 ± 4.0
ESO 207–61		19.48	16.17	13.23	12.54	12.10	8.5	24.6 ± 2.9
SSSPM J0829–1309	22.58	18.84	16.01	12.80	11.85	11.30	12.0	11.6 ± 1.4
LP 314–67		18.03		15.59	15.03	14.85	sdM3.5	151.0 ± 15.0
LP 614–35	20.92	18.35	17.40	16.15	15.50	15.30	esdM0.5	102.0 ± 12.2
APMPM J1222–2452	21.17	18.70	16.13	14.33	13.85	13.49	5.0	103.0 ± 15.0
APMPM J1251–2121	19.40	17.03	13.64	11.16	10.55	10.13	7.0	12.0 ± 1.4
Kelu 1		19.58	17.11	13.41	12.39	11.75	12.0	15.4 ± 1.8
CE 303	20.41	17.83	14.52	11.78	11.08	10.67	8.0	13.6 ± 1.6
CE 352	20.58	18.26	17.23	15.70	15.27	15.04	esdM3	151.0 ± 15.0
LP 859–1	20.26	17.82	14.66	12.01	11.38	11.03	7.5	16.4 ± 2.0
LHS 3141B	21.65	19.41	16.34	13.61	13.12	12.84	7.0	37.0 ± 4.4
SSSPM J1926–4311	18.75	16.69	13.65	11.94	11.42	11.12	5.0	23.5 ± 2.8
SSSPM J1930–4311	21.08	18.42	16.31	14.79	14.23	14.09	edM5.5	44.0 ± 15.0
APMPM J1957–4216	19.39	17.32	14.53	12.38	11.99	11.66	5.0	28.8 ± 3.5
SSSPM J2003–4433		19.33	16.08	13.53	12.99	12.59	8.0	30.5 ± 3.7
LP 815–21	20.38	18.11	17.45	16.10	15.91	15.28	8.0	325.0 ± 15.0
SSSPM J2033–6919	22.59	19.75	16.42	13.64	12.98	12.58	8.0	32.1 ± 3.9
APMPM J2036–4936	21.17	18.75	16.34	14.62	14.16	13.75	4.5	87.3 ± 10.5
SSSPM J2052–4759	21.67	18.82	15.55	12.94	12.29	11.88	8.0	23.2 ± 2.8
SSSPM J2059–8018		20.50	16.91	14.28	13.69	13.41	7.5	46.6 ± 5.6
SSSPM J2101–5110		20.27	17.09	15.13	14.41	14.09	5.5	94.4 ± 11.3

Table A.2: continued

Targets	B_J	R_{SSS}	I_{SSS}	J	H	K_s	SpT	Distance
[HB88] M18	22.36	19.41	16.41	13.43	12.77	12.37	8.5	26.9 ± 3.2
[HB88] M12	21.27	18.63	16.46	14.52	13.92	13.57	4.5	83.4 ± 10.0
LP 819-9	20.80	18.47	16.50	15.07	14.59	14.31	4.0	116.2 ± 13.9
SSSPM J2229–6931		19.83	16.97	14.47	13.76	13.35	10.0	34.4 ± 4.1
LDS4980 B		18.35		15.05	14.53	14.25	3.5	124.5 ± 14.9
LDS4980 A		17.54		14.65	14.26	13.86	4.0	95.8 ± 11.5
SSSPM J2240–4253		19.67	16.53	13.76	13.19	12.80	8.0	33.9 ± 4.1
SSSPM J2257–5208		20.20	17.33	14.93	14.37	14.00	7.0	68.0 ± 8.2
SSSPM J2258–4639		19.81	16.43	13.61	12.93	12.60	8.5	29.3 ± 3.5
SSSPM J2307–5009	22.80	19.70	16.72	13.39	12.70	12.24	9.0	24.4 ± 2.9
SSSPM J2310–1759		20.52	17.68	14.38	13.58	12.97	9.5	35.7 ± 4.3
SSSPM J2319–4919	22.12	19.25	16.22	13.76	13.07	12.68	8.0	33.9 ± 4.1
SSSPM J2322–6358		19.54	16.48	14.26	13.65	13.20	7.5	46.2 ± 5.5
APMPM J2330–4737	19.38	16.79	13.29	11.23	10.64	10.28	6.0	14.5 ± 1.7
APMPM J2331–2750	20.42	17.89	14.41	11.65	11.06	10.65	7.5	13.9 ± 1.7
SSSPM J2335–6913	22.25	19.29	16.46	13.92	13.25	12.90	7.0	42.7 ± 5.1
APMPM J2344–2906	21.12	18.64	15.34	13.26	12.75	12.43	6.5	34.1 ± 4.1
SSSPM J2345–6810	22.26	19.49	16.39	13.98	13.36	12.96	7.0	43.9 ± 5.3
APMPM J2347–3154	22.51	19.49	15.91	13.28	12.68	12.20	8.0	27.2 ± 3.3
SSSPM J2352–2538	21.73	18.70	15.27	12.47	11.73	11.27	9.0	16.0 ± 1.9
SSSPM J2353–4123	22.23	19.08	16.89	14.39	13.73	13.33	6.0	62.1 ± 7.4
APMPM J2354–3316	22.20	19.30	16.57	13.05	12.36	11.88	8.0	24.5 ± 2.9
SSSPM J2356–3426	22.21	19.18	16.15	12.95	12.38	11.97	9.0	20.0 ± 2.4
SSSPM J2400–2008		20.29	17.45	14.38	13.62	13.25	9.5	35.7 ± 4.3

Table A.3: Values of spectral indices and spectral types (4 \equiv M4, 5 \equiv M5, 12 \equiv L2, etc ...) of 52 proper motion objects with optical spectroscopy (Section 2.4).

Name	H α	EW(H α)	TiO5	VO-a	PC3	SpT _{Tri05}	SpT _{VO-a}	SpT _{Pc3}	\langle SpT \rangle	Final SpT	KI	Na I
APMPM J1222–2452	0.87	0.0	0.29	2.04	1.25	5.11	5.18	4.80	5.03	5.0	10.3/7.3	6.5
CE 303	1.46	6.8	0.26	2.32	1.77	7.68	8.13	7.70	7.84	8.0	10.5/6.6	6.5
APMPM J1251–2121	1.11	2.6	0.24	2.27	1.61	7.57	7.61	6.90	7.36	7.0	12.6/9.9	5.9
LDS4980 B	0.99	0.6	0.38	1.98	1.12	4.14	4.58	3.90	4.21	4.0	4.0/2.5	6.0
LHS 3141B	1.25	4.8	0.12	2.06	1.65	6.96	6.87	7.10	6.98	7.0	19.8/14.5	9.2
LP 769-14	1.14	2.5	0.34	2.02	1.20	4.59	4.99	4.50	4.70	4.5	6.5/4.8	6.5
APMPM J2330–4737	1.29	5.6	0.20	2.14	1.50	6.01	6.24	6.30	6.18	6.0	14.2/10.4	7.3
APMPM J0207–3722	1.51	6.7	0.21	2.26	1.64	7.41	7.45	7.10	7.32	7.0	10.9/8.2	5.1
LP 859-1	0.97	0.2	0.00	2.23	1.70	0.00	7.14	7.40	4.85	7.5	11.6/9.9	6.2
APMPM J2344–2906	0.97	3.0	0.12	2.16	1.53	6.90	6.44	6.50	6.61	6.5	15.7/11.0	7.6
[HB88] M12	1.56	6.6	0.28	2.04	1.19	5.20	5.21	4.40	4.94	4.5	6.3/3.5	5.8
LP 645-52	0.92	0.2	0.31	2.00	1.28	4.82	4.71	5.00	4.84	5.0	3.8/2.0	5.6
LP 819-9	0.94	0.0	0.38	2.01	1.13	4.07	4.81	4.00	4.29	4.0	4.6/3.1	5.5
APMPM J2036–4936	0.86	0.0	0.29	2.02	1.14	5.05	4.96	4.00	4.67	4.5	0.00/0.0	0.0
LDS4980 A	0.93	0.0	0.44	1.98	1.02	3.43	4.52	3.10	3.68	3.5	2.4/1.7	4.3
APMPM J2331–2750	1.30	5.1	0.18	2.14	1.85	6.25	6.19	8.10	6.84	7.5	12.8/9.5	8.8
LP655-48	1.65	10.0	0.28	2.18	1.71	7.83	6.68	7.40	7.30	7.5	9.9/8.9	6.5
SSSPM J0204–3633	1.53	10.8	0.25	2.25	1.70	7.65	7.42	7.40	7.49	7.5	11.1/11.2	7.5
SSSPM J2322–6358	1.60	11.2	0.24	2.16	1.68	7.60	6.44	7.30	7.11	7.5	11.4/11.0	7.5
SSSPM J2059–8018	0.87	0.2	0.13	2.12	1.90	6.76	6.05	8.30	7.03	7.5	15.3/13.3	9.9
SSSPM J2310–1759	1.55	0.0	0.52	2.28	2.27	9.17	10.69	9.50	9.79	9.5	7.2/6.2	5.7
SSSPM J2335–6913	1.30	6.1	0.26	2.17	1.56	7.68	6.57	6.70	6.98	7.0	9.5/7.3	7.2
SSSPM J0306–3648	0.98	0.5	0.22	2.24	1.92	7.49	7.28	8.40	7.72	8.0	12.6/11.0	7.7
LP 888-18	1.54	11.0	0.26	2.26	1.82	7.72	7.48	7.90	7.70	8.0	12.6/11.1	8.4
SSSPM J2033–6919	0.98	1.0	0.21	2.28	1.80	7.44	7.71	7.90	7.68	8.0	11.9/10.3	7.8
APMPM J2347–3154	1.09	5.6	0.26	2.32	1.92	7.71	8.13	8.40	8.08	8.0	9.1/9.1	6.6

Table A.3: continued

Name	H α	EW(H α)	TiO5	VO-a	PC3	SpT _{Tri5}	SpT _{VO-a}	<SpT _{C3} >	Final SpT	KI	Na I
SSSPM J2352–2538	1.42	6.0	0.42	2.17	2.22	8.62	6.58	9.40	8.20	9.0	12.9/9.3
SSSPM J0006–2157	1.01	1.9	0.28	2.29	1.98	7.78	7.79	8.60	8.06	8.5	7.1/4.6
SSSPM J0219–1939	0.94	0.0	0.95	2.29	3.02	11.62	10.63	11.70	11.32	11.0	22.5/10.3
LP775-31	1.10	3.7	0.25	2.21	1.79	7.65	6.90	7.80	7.45	8.0	14.1/11.7
SSSPM J2003–4433	0.83	0.0	0.20	2.13	1.73	6.10	6.10	7.50	6.57	8.0	13.6/13.0
SSSPM J1926–4311	0.91	0.0	0.30	2.02	1.23	4.93	4.94	4.70	4.86	5.0	8.3/4.9
SSSPM J2052–4759	1.48	12.1	0.30	2.33	1.85	7.94	8.25	8.00	8.06	8.0	8.6/5.8
SSSPM J0109–5101	1.32	13.3	0.33	2.29	2.00	8.08	7.83	8.60	8.17	8.5	8.7/7.6
[HB88] M18	1.04	0.0	0.36	2.38	1.91	8.28	8.75	8.30	8.44	8.5	6.3/5.7
SSSPM J2353–4123	1.23	2.1	0.26	2.20	1.39	7.69	6.90	5.70	6.76	6.0	6.4/4.9
SSSPM J0327–4236	0.93	0.0	0.25	2.23	2.13	7.65	7.13	9.10	7.96	8.5	12.8/7.0
SSSPM J2240–4253	1.24	7.1	0.25	2.26	1.77	7.66	7.46	7.70	7.61	8.0	11.2/11.2
APMPM J1957–4216	0.97	0.0	0.26	2.02	1.27	5.36	5.01	4.90	5.09	5.0	8.3/5.8
SSSPM J2307–5009	1.32	2.0	0.51	2.33	2.27	9.13	8.26	9.50	8.96	9.0	5.7/5.5
SSSPM J0027–5402	1.95	14.5	0.28	2.21	1.50	7.80	6.99	6.30	7.03	7.0	8.9/6.7
ESO 207-61	1.17	2.8	0.31	2.32	1.97	7.99	8.13	8.50	8.20	8.5	11.3/12.2
SSSPM J0231–4122	0.78	0.0	0.41	2.27	2.19	8.57	7.56	9.30	8.48	8.5	15.7/14.9
SSSPM J0511–4606	0.80	0.0	0.31	2.48	2.00	7.99	9.30	8.70	8.66	8.5	9.0/7.1
SSSPM J2258–4639	0.83	0.0	0.23	2.18	2.43	7.53	6.65	9.80	7.99	8.5	7.0/3.9
SSSPM J0222–5412	1.06	0.0	0.43	2.64	2.16	8.68	8.14	9.20	8.67	9.0	7.7/5.0
SSSPM J2101–5110	1.21	7.1	0.30	2.13	1.34	4.98	6.10	5.40	5.49	5.5	1.4/7.4
SSSPM J2257–5208	1.01	2.6	0.20	2.14	1.47	6.08	6.21	6.20	6.17	7.0	11.3/9.5
SSSPM J0829–1309	1.00	0.0	1.01	2.03	2.75	11.94	12.43	11.50	11.96	12.0	20.9/11.0
SSSPM J2345–6810	1.03	0.0	0.24	2.20	1.50	7.58	6.89	6.30	6.92	7.0	9.9/6.9
SSSPM J2400–2008	1.05	0.0	0.61	2.48	2.31	9.70	9.75	9.60	9.68	9.5	0.00/0.0
SSSPM J2356–3426	0.94	0.0	0.43	2.31	2.17	8.65	8.06	9.20	8.64	9.0	10.1/6.8

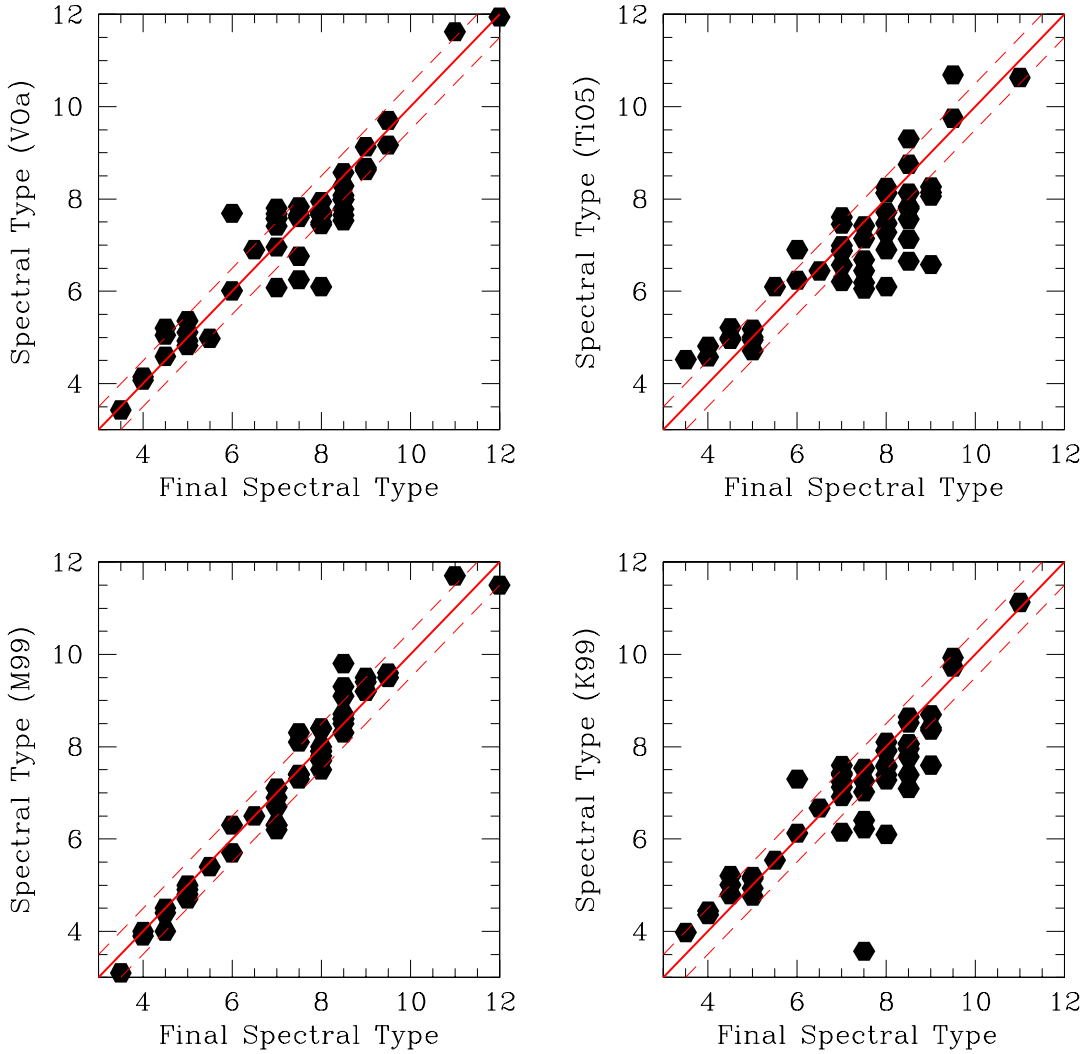


Figure A.1: Consistency of the optical indices from Martín et al. (1999b) and Kirkpatrick et al. (1999b) for the spectral classification of the red proper motion objects. The solid line indicates identical spectral types whereas the dashed lines indicate an uncertainty of half a subclass.

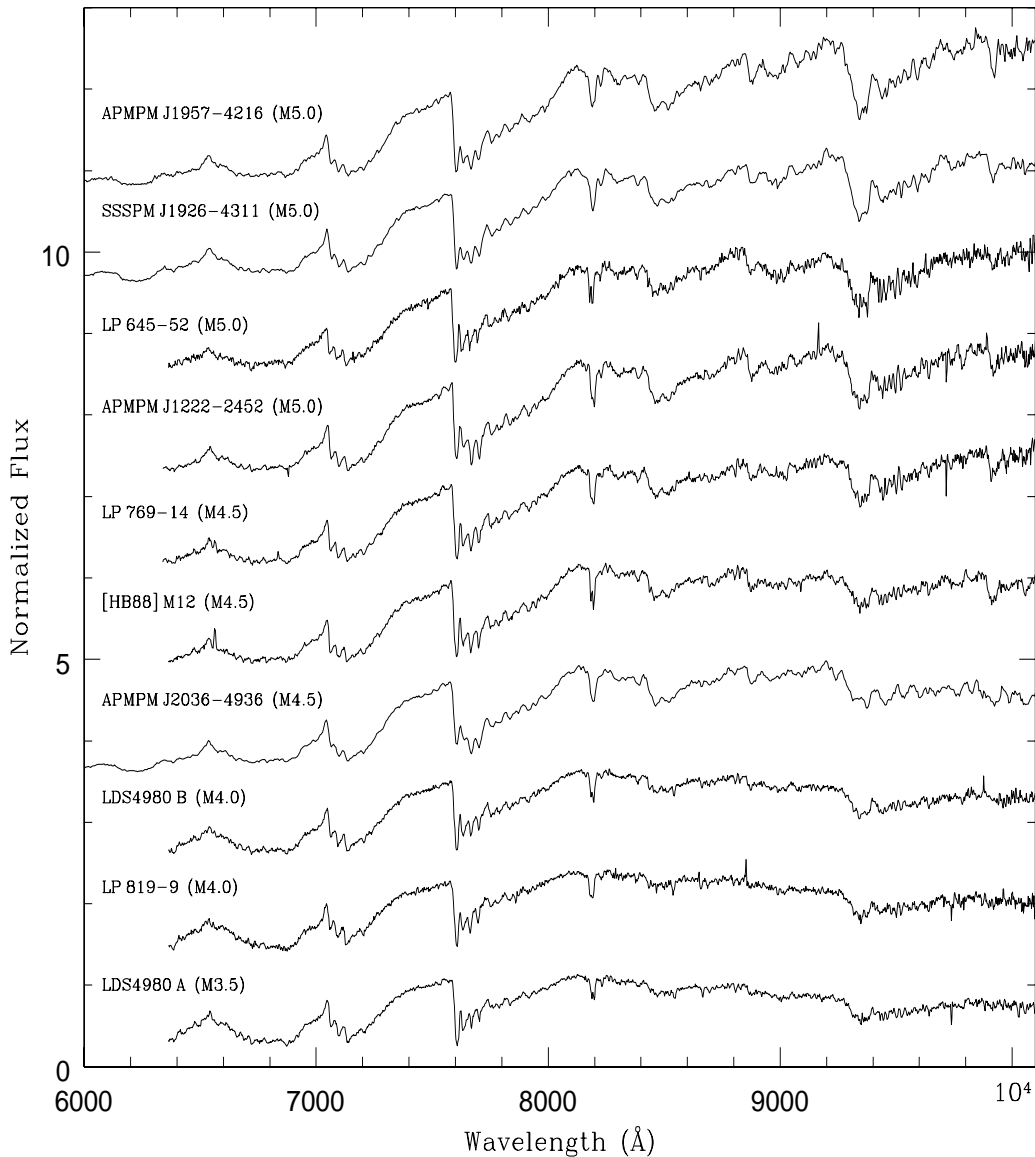


Figure A.2: Low-resolution spectra of 10 objects discovered in the course of our proper motion survey in the southern sky. Spectral types, are earlier or equal than M5.0, are derived according to the Kirkpatrick et al. (1999b) and Martín et al. (1999b)) classification schemes and direct comparison with template spectra. From bottom to top are LDS4980 A (M3.5), LP 819-9 (M4.0), LDS4980 B (M4.0), APMPM J2036-4936 (M4.5), [HB88] M12 (M4.5), LP 769-14 (M4.5), APMPM J1222-2452 (M5.0), LP 645-52 (M5.0), SSSPM J1926-4311 (M5.0), and APMPM J1957-4216 (M5.0). The uncertainty on the spectral type is typically half a subclass. An arbitrary constant has been added to separate the spectra in intensity.

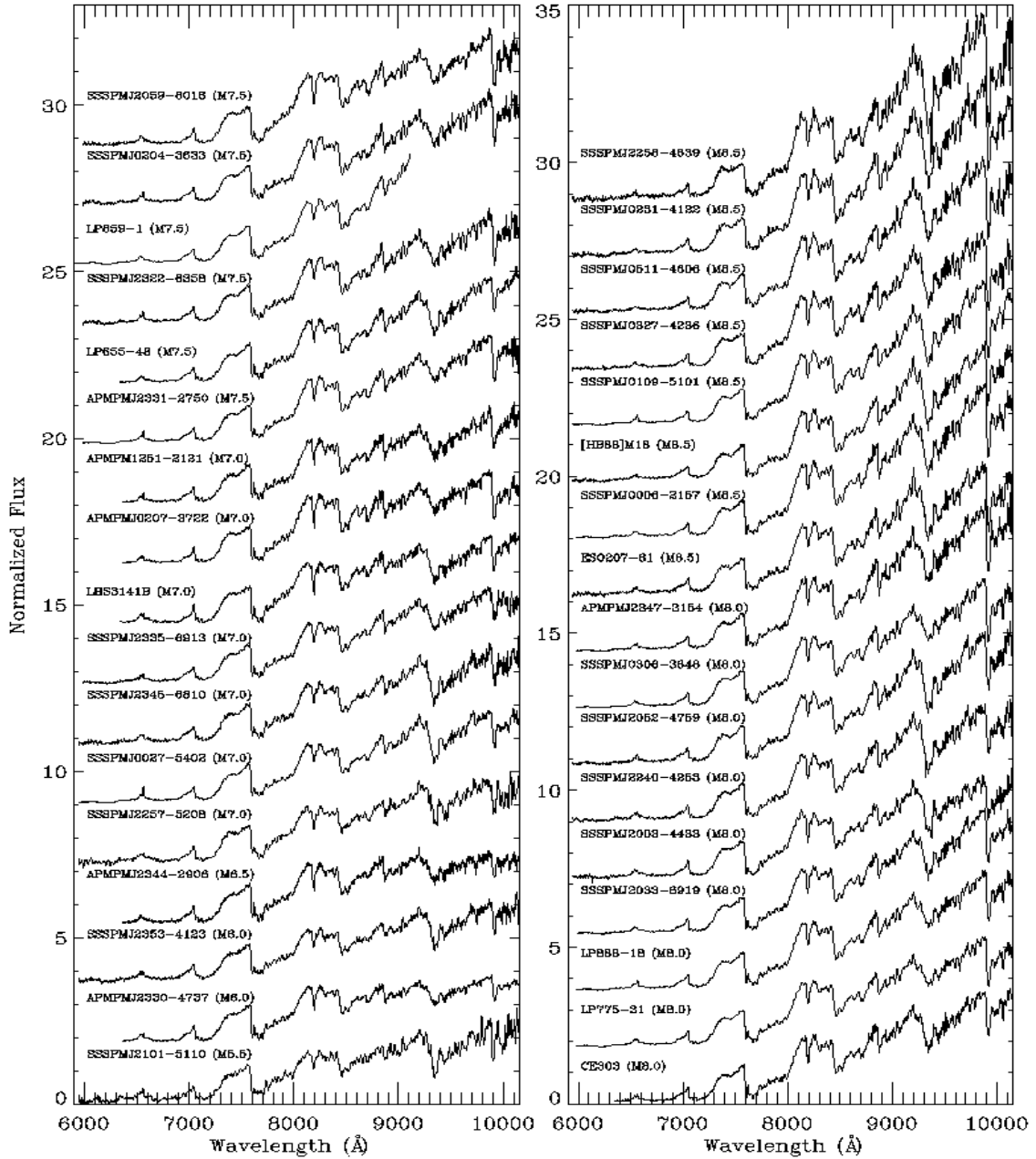


Figure A.3: Low-resolution spectra of 34 proper motion objects discovered in the course of our proper motion survey in the southern sky. These object were observed with the VLT/FORS1 and ESO 3.6m/EFOSC2 instruments and are ordered by increasing spectral types from M5.5 up to M8.5, assigned according to the Kirkpatrick et al. (1999b) and Martín et al. (1999b) classification schemes and direct comparison with template spectra. The uncertainty on the spectral type is typically half a subclass. An arbitrary constant has been added to separate the spectra in intensity. No telluric absorption correction has been applied to the optical spectra.

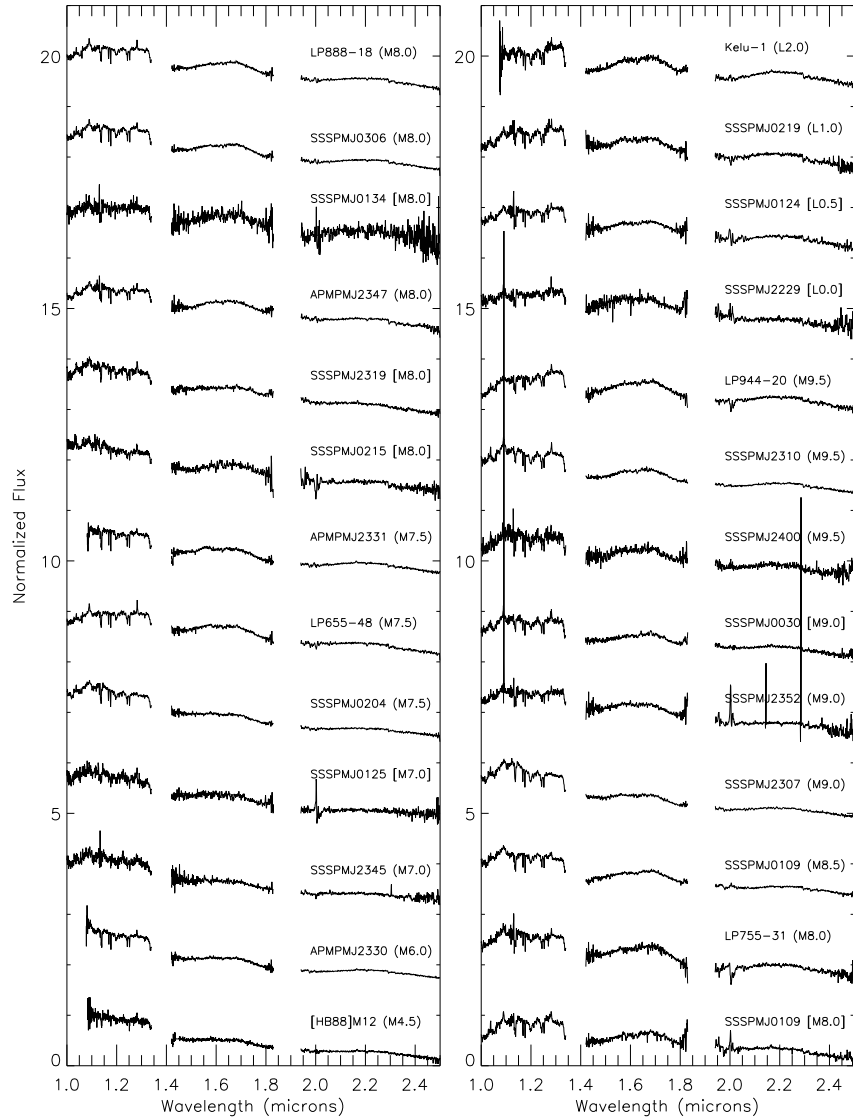


Figure A.4: Infrared spectra of a subsample of 26 proper motion targets from our proper motion survey observed with the VLT/ISAAC instrument in the case of [HB88] M12, APMPM J2330–4737 and APMPM J2331–2750 and with the NTT/SofI camera for the others. Objects whose spectral type are in square brackets have been spectroscopically observed *only* in the near-infrared (7), the objects with spectral types in parentheses were classified from the optical schemes (19). Spectral types attributed to SSSPM J0125–6546, SSSPM J0215–4804, SSSPM J2319–4919, SSSPM J0134–6315, SSSPM J0030–3427, SSSPM J2229–6931, and SSSPM J0124–4240 are M7.0, M8.0, M8.0, M9.0, L0.0, L0.5, respectively, with, at least, an uncertainty of a subclass. LP944-20 and Kelu 1 are included as templates for comparison purposes. An arbitrary constant has been added to separate the spectra in intensity. Telluric absorption bands around 1.3 and 1.9 μm have been removed for clarity.

Appendix B

Table of cluster members in the open cluster Collinder 359

The final list of cluster member candidates, provided in this appendix, contains a total of 1033 candidates ranging from $I = 12.0$ to $I = 22.5$ over 1.6 square degree area surveyed in Collinder 359. The whole sample of candidates is provided here as paper version. The different tables including candidates selected from the various (distance, age) combinations will be available on CD-ROMs or on request. The columns of Table B.1 provides the following information:

- Column 1 gives the name of the target according to the IAU convention. We used the name Coll359 J to refer to Collinder 359 followed by the coordinate in J2000.
- Columns 2 and 3 provide the field-of-view where the candidate is located and the number assigned during the extraction of the photometry.
- Column 4 provides the type of exposure (Short, Medium, and/or Long) from which the candidate was extracted.
- Columns 5 and 6 list the right ascension (in hours) and declination (in degrees) of the objects extracted from the CFH12K images (in J2000).
- Columns 7–12 give the optical (I and z) and the near-infrared (J , H , and K_s) magnitudes. The objects are ordered by decreasing I magnitudes. The near-infrared magnitudes are extracted from the 2MASS database.
- Columns 13 and 14 list the proper motion measurements extracted from the USNO CCD Astrograph Catalog (Zacharias et al. 2003).
- Column 15 gives the flag assign by the SExtractor package to the object. A flag of 0 indicates a good detection. A flag of 1 indicates that the object has neighbour bright and close enough to affect the automatic photometry. A flag of 2 indicates that the object was originally blended with another one, and a flag of 4 indicates that one pixel of the object is saturated or close to.
- Column 16 provides an update of the membership status of the candidate after considering the near-infrared follow-up. The Y+ stands for probable members, Y? for possible members, and NM for non-members.

Table B.1: List of all 1033 optically-selected cluster member candidates in Collinder 359.
Objects are ordered by increasing right ascension.

Numb	Coll359 J...	FOV	ID	Exp	RA	Dec	<i>I</i>	<i>J</i>	<i>H</i>	<i>K_s</i>	μ_{α}	μ_{α}	Flag	M?
1	Cr359 J175453+023353	D00	1469	S	17:54:53.20	02:33:53.6	11.537	11.326	0.291	10.197	9.457	—	—	2 Y+
2	Cr359 J175455+023128	D00	4569	M	17:54:55.60	02:31:28.8	14.045	13.894	0.246	12.649	11.904	11.744	—	2 Y+
3	Cr359 J175456+023748	D00	2228	M	17:54:56.95	02:37:48.2	19.771	19.171	0.696	—	—	—	—	0 Y+
4	Cr359 J175458+023758	D00	841	S	17:54:58.57	02:37:58.5	11.934	11.795	0.218	10.832	10.258	10.115	—	2 Y+
5	Cr359 J175458+021734	D06	271	SML	17:54:58.75	02:17:34.6	17.347	17.730	—	—	15.026	—	0 Y?	
6	Cr359 J175504+023318	D00	3923	M	17:55:04.95	02:33:18.8	16.133	15.718	0.510	14.363	13.708	13.446	—	0 Y+
7	Cr359 J175506+021710	D06	576	ML	17:55:06.60	02:17:10.5	19.556	18.704	0.947	—	—	15.874	—	0 Y?
8	Cr359 J175507+022403	D06	5613	L	17:55:07.79	02:24:03.2	22.480	21.320	1.170	—	—	—	—	3 Y+
9	Cr359 J175517+024026	D00	449	S	17:55:17.51	02:40:26.5	12.334	12.092	0.323	10.790	9.982	9.703	—	0 Y+
10	Cr359 J175523+024136	D01	1222	L	17:55:23.61	02:41:36.4	18.664	18.082	0.591	—	—	—	—	2 Y+
11	Cr359 J175526+023235	D01	7226	L	17:55:26.40	02:32:36.0	17.973	17.432	0.552	—	—	—	—	2 Y+
12	Cr359 J175530+022134	D07	993	SML	17:55:30.59	02:21:35.0	16.685	16.186	0.579	14.689	13.989	13.761	—	0 Y+
13	Cr359 J175554+023745	D02	2345	M	17:55:54.17	02:37:45.5	18.797	18.256	0.636	—	—	—	—	3 Y+
14	Cr359 J175557+024128	D02	1242	L	17:55:57.27	02:41:28.3	21.694	20.812	0.893	—	—	—	—	1 Y+
15	Cr359 J175603+021558	D08	234	M	17:56:03.19	02:15:58.9	18.395	17.866	0.624	—	—	—	—	0 Y+
16	Cr359 J175608+021917	D08	732	S	17:56:08.52	02:19:17.2	11.935	11.800	0.214	10.629	9.813	9.649	—	0 Y+
17	Cr359 J175610+023307	D02	6858	L	17:56:10.40	02:33:07.2	21.216	20.228	0.999	—	—	—	—	3 Y+
18	Cr359 J175611+022227	D08	2996	ML	17:56:11.10	02:22:27.6	18.979	18.417	0.657	—	—	—	—	0 Y+
19	Cr359 J175612+032619	C06	246	S	17:56:12.26	03:26:19.5	14.382	14.091	0.251	13.314	12.688	12.581	—	0 Y+
20	Cr359 J175612+032541	C06	107	S	17:56:12.45	03:25:41.8	13.059	12.857	0.161	12.266	11.878	11.767	—	0 Y+
21	Cr359 J175612+032744	C06	1353	ML	17:56:12.67	03:27:44.4	20.081	19.371	0.750	—	—	—	—	0 Y+
22	Cr359 J175613+033349	C06	1718	S	17:56:13.41	03:33:49.2	13.578	13.359	0.179	12.685	12.150	12.026	—	3 Y+
23	Cr359 J175613+032907	C06	762	S	17:56:13.62	03:29:07.7	13.228	13.018	0.170	12.280	11.730	11.609	—	0 Y+
24	Cr359 J175614+032646	C06	300	S	17:56:14.47	03:26:46.2	12.564	12.292	0.232	11.490	10.843	10.689	—	0 Y+
25	Cr359 J175615+032652	C06	358	SML	17:56:15.29	03:26:52.1	15.478	15.074	0.364	14.100	13.393	13.212	—	0 Y+
26	Cr359 J175615+032457	C06	1	S	17:56:15.33	03:24:57.0	14.277	14.021	0.216	13.379	12.804	12.825	—	0 Y+
27	Cr359 J175615+034347	C00	1853	S	17:56:15.36	03:43:47.7	15.670	15.247	0.383	14.195	13.524	13.316	—	2 Y+
28	Cr359 J175615+033215	C06	5563	L	17:56:15.80	03:32:15.6	18.720	18.105	0.645	—	—	—	—	2 Y+
29	Cr359 J175615+034544	C00	5815	L	17:56:15.80	03:45:44.2	19.407	18.754	0.683	—	—	—	—	2 Y+
30	Cr359 J175616+032753	C06	2331	L	17:56:16.08	03:27:53.9	19.777	19.093	0.714	—	—	—	—	0 Y+
31	Cr359 J175616+034050	C00	2701	S	17:56:16.62	03:40:50.9	13.046	12.723	0.283	11.953	11.258	11.166	—	2 Y+
32	Cr359 J175616+033022	C06	1016	SML	17:56:16.66	03:30:22.3	14.936	14.443	0.453	13.432	12.819	12.569	—	0 Y+
33	Cr359 J175617+034451	C00	1557	S	17:56:17.01	03:44:51.3	11.861	11.532	0.289	10.656	9.918	9.740	—	0 Y+
34	Cr359 J175617+021559	D09	249	M	17:56:17.04	02:15:59.7	20.330	19.633	0.792	—	—	—	—	0 Y+
35	Cr359 J175617+035136	C00	467	M	17:56:17.26	03:51:36.4	17.782	17.269	0.553	—	—	—	—	3 Y+
36	Cr359 J175617+035136	C00	827	L	17:56:17.26	03:51:36.7	17.750	17.204	0.576	—	—	—	—	3 Y+
37	Cr359 J175618+032840	C06	675	S	17:56:18.11	03:28:40.8	12.885	12.694	0.151	12.003	11.461	11.384	—	0 Y+
38	Cr359 J175618+032625	C06	245	S	17:56:18.19	03:26:25.2	11.957	11.561	0.356	10.646	10.019	9.787	—	0 Y+
39	Cr359 J175619+021826	D09	1251	ML	17:56:19.08	02:18:26.3	18.372	17.849	0.617	—	—	—	—	0 Y+
40	Cr359 J175619+032456	C06	11	SM	17:56:19.20	03:24:56.6	15.254	14.938	0.276	14.196	13.548	13.418	—	0 Y+

Table B.1: continued

Numb	Coll359 J...	FOV	ID	RA	Exp	Dec	I	H	K_s	μ_α	μ_α	Flag	M?	
41	C359 J175619+033345	C06	1712	S	1756:19:65	03:33:45.7	13.274	13.069	0.165	12.364	11.756	-	2	
42	C359 J175619+034134	C00	9483	L	1756:19:90	03:41:34.9	18.313	17.717	0.626	-	-	-	3	
43	C359 J175620+033729	C06	2339	S	1756:20:38	03:37:29.2	14.523	14.266	0.217	13.423	12.717	12.529	0	
44	C359 J175621+033204	C06	1363	S	1756:21:18	03:32:04.2	14.473	14.223	0.210	13.351	12.667	12.559	0	
45	C359 J175621+033935	C00	2401	S	1756:21:61	03:39:35.4	14.032	13.802	0.190	13.146	12.566	12.468	0	
46	C359 J175621+033712	C06	2098	S	1756:21:75	03:37:12.6	13.076	12.807	0.159	12.076	11.397	11.316	0	
47	C359 J175622+034048	C00	2672	SM	1756:22:10	03:40:48.2	15.922	15.404	0.479	14.057	13.784	13.589	0	
48	C359 J175622+033143	C06	1283	S	1756:22:11	03:31:43.4	14.158	13.768	0.350	12.805	12.155	11.894	0	
49	C359 J175623+034253	C00	2029	S	1756:23:43	03:42:53.5	13.908	13.669	0.199	12.979	12.350	12.250	0	
50	C359 J175623+033616	C06	2460	S	1756:23:72	03:36:16.3	13.174	12.926	0.208	12.056	11.265	11.114	2	
51	C359 J175624+034636	C00	1207	S	1756:24:17	03:46:36.6	12.135	11.989	0.106	11.474	11.120	11.041	2	
52	C359 J175624+023822	D03	912	SM	1756:24:56	02:38:22.1	16.143	15.700	0.523	14.255	13.499	13.286	0	
53	C359 J175625+021708	D09	259	SM	1756:25:55	02:17:08.1	15.155	14.835	0.399	13.542	12.893	12.709	0	
54	C359 J175625+021531	D09	1	S	1756:25:80	02:15:31.8	13.193	13.013	0.261	11.883	11.194	11.038	2	
55	C359 J175626+021820	D09	2141	L	1756:26:36	02:18:20.1	21.854	20.976	0.888	-	-	-	3	
56	C359 J175626+021532	D09	2	S	1756:26:48	02:15:32.2	11.812	11.669	0.223	10.623	9.906	9.906	2	
57	C359 J175626+021532	D09	1813	S	1756:28:11	03:43:45.9	12.638	12.407	0.191	11.687	11.128	10.963	0	
58	C359 J175628+035145	C00	143	S	1756:28:14	03:51:45.8	18.253	12.507	0.278	11.603	10.834	10.650	0	
59	C359 J175628+033446	C06	1921	S	1756:28:33	03:34:46.8	12.008	11.865	0.103	11.178	10.730	10.686	2	
60	C359 J175628+034721	C00	1073	S	1756:28:66	03:47:21.3	14.697	14.409	0.248	13.600	12.896	12.774	0	
61	C359 J175629+034440	C00	1622	S	1756:29:27	03:44:40.0	13.387	13.072	0.274	12.217	11.503	11.317	0	
62	C359 J175628+034345	C00	5500	ML	1756:29:37	02:32:04.0	19.561	18.864	0.792	-	-	-	0	
63	C359 J175631+032737	C06	503	S	1756:31:07	03:27:37.1	13.289	13.004	0.245	12.161	11.545	11.399	-11.3	
64	C359 J175632+035001	C00	467	S	1756:32:05	03:50:01.6	12.516	12.241	0.235	11.418	10.758	10.637	0	
65	C359 J175633+032646	C06	351	S	1756:33:90	03:26:46.9	14.049	13.817	0.192	12.878	12.122	11.963	-8.8	
66	C359 J175633+034544	C00	1382	S	1756:33:90	03:45:44.2	11.909	11.635	0.233	10.779	10.057	9.870	0	
67	C359 J175634+032952	C00	2506	S	1756:34:57	03:39:52.3	13.557	13.320	0.197	12.558	11.922	11.840	-	
68	C359 J175635+021727	D09	888	ML	1756:36:00	02:17:27.9	20.207	19.484	0.817	-	-	-	0	
69	C359 J175636+032550	D03	606	172	S	1756:36:31	03:25:50.3	14.111	13.856	0.215	13.038	12.437	12.284	-5.4
70	C359 J175636+032456	C06	102	M	1756:36:53	03:24:56.3	18.445	17.909	0.576	-	-	-	0	
71	C359 J175637+024026	D03	477	S	1756:37:46	02:40:26.5	11.704	11.565	0.219	10.482	9.751	9.630	-6.4	
72	C359 J175637+023913	D03	1693	M	1756:37:58	02:39:13.8	14.496	14.332	0.259	13.189	12.491	12.333	-2.1	
73	C359 J175638+021933	D09	3120	L	1756:38:74	02:19:33.9	18.078	17.541	0.547	-	-	-	3	
74	C359 J175638+021934	D09	684	S	1756:38:74	02:19:34.1	18.157	17.597	0.639	-	-	-	0	
75	C359 J175639+021626	D09	464	M	1756:39:26	02:16:26.0	20.524	19.811	0.808	-	-	-	0	
76	C359 J175639+034231	C00	8578	L	1756:39:78	03:42:31.5	17.752	16.535	1.248	-	-	-	4	
77	C359 J175640+032958	C07	4463	L	1756:40:32	03:29:58.6	17.364	16.819	0.575	-	-	-	3	
78	C359 J175643+024020	D03	534	S	1756:43:10	02:40:20.1	14.635	14.327	0.587	13.064	12.389	12.083	2	
79	C359 J175643+034231	C01	7843	L	1756:43:10	03:42:31.9	21.532	20.699	0.863	-	-	-	0	
80	C359 J175643+022980	D09	4553	M	1756:43:32	02:28:40.9	16.227	15.839	0.484	14.511	13.922	13.636	2	
81	C359 J175644+034125	C01	6336	M	1756:44:11	03:41:25.8	15.278	14.946	0.372	13.827	13.285	13.015	2	
82	C359 J175644+023545	D03	5263	L	1756:44:50	03:35:45.3	19.477	18.812	0.675	-	-	-	0	

Table B.1: continued

Numb	Coll359 J...	FOV	ID	RA	Dec	<i>I</i>	<i>z</i>	<i>L-z</i>	<i>J</i>	<i>H</i>	<i>K_s</i>	μ_{α}	μ_{α}	Flag	M?
83	Cr359 J175645+033948	C01	2577	S	17:56:45.14	03:39:48.6	16.474	15.986	0.448	14.909	14.388	—	—	—	Y+
84	Cr359 J175646+034104	C01	2573	SM	17:56:46.13	03:41:04.3	15.976	15.501	0.435	14.436	13.823	13.560	—	—	0 Y+
85	Cr359 J175647+032622	C07	385	S	17:56:47.06	03:26:22.2	12.280	12.021	0.219	11.114	10.383	10.254	-3.0	-1.5	0 Y+
86	Cr359 J175647+033637	C07	6144	ML	17:56:47.06	03:36:37.6	19.612	18.830	0.822	—	—	—	—	—	3 Y+
87	Cr359 J175648+032649	C07	1088	ML	17:56:48.08	03:26:49.6	19.676	18.676	0.693	—	—	—	—	—	3 Y+
88	Cr359 J175648+021525	D10	1	S	17:56:48.73	02:15:25.0	12.295	12.097	0.278	10.958	10.203	10.049	—	—	2 Y+
89	Cr359 J175648+024244	D04	20	S	17:56:48.91	02:42:44.3	12.121	11.949	0.252	10.761	10.020	9.824	-6.8	-8.2	0 Y+
90	Cr359 J175650+034715	C01	1200	S	17:56:50.93	03:47:15.3	12.797	12.603	0.154	11.899	11.357	11.280	—	—	0 Y+
91	Cr359 J175650+034941	C01	620	S	17:56:50.93	03:49:41.3	12.358	12.121	0.197	11.357	10.726	10.619	—	—	0 Y+
92	Cr359 J175651+032749	C07	730	S	17:56:51.03	03:27:49.1	13.721	13.512	0.169	12.707	12.065	11.931	-8.7	-2.6	0 Y+
93	Cr359 J175651+035227	C01	50	S	17:56:51.61	03:52:27.6	14.505	14.203	0.262	13.452	12.777	12.703	—	—	0 Y+
94	Cr359 J175652+033841	C01	9725	L	17:56:52.01	03:38:41.2	19.599	18.861	0.768	—	—	—	—	—	3 Y+
95	Cr359 J175652+034816	C01	962	S	17:56:52.31	03:48:16.1	13.364	13.171	0.153	12.517	11.973	11.880	—	—	0 Y+
96	Cr359 J175652+034422	C01	1802	S	17:56:52.61	03:44:22.9	12.189	12.006	0.143	11.299	10.716	10.645	—	—	0 Y+
97	Cr359 J175652+022512	D10	1737	S	17:56:52.83	02:25:12.6	12.608	12.608	0.384	11.202	10.257	9.975	-3.2	-2.9	0 Y+
98	Cr359 J175653+022300	D10	1335	S	17:56:53.08	02:23:00.3	11.982	11.858	0.207	10.761	10.148	10.041	3.8	4.5	2 Y+
99	Cr359 J175653+035002	C01	533	S	17:56:53.34	03:50:02.9	12.271	12.038	0.193	11.262	10.648	10.535	—	—	2 Y+
100	Cr359 J175654+022515	D10	1742	S	17:56:54.40	02:25:15.5	11.884	11.714	0.250	10.510	9.721	9.550	-2.9	-11.5	2 Y+
101	Cr359 J175654+032755	C07	760	S	17:56:54.53	03:27:55.5	13.835	13.583	0.212	12.681	12.013	11.887	-9.3	-12.1	0 Y+
102	Cr359 J175655+033932	C01	2404	S	17:56:55.44	03:39:32.4	13.060	12.814	0.206	11.975	11.312	11.136	-6.6	1.4	0 Y+
103	Cr359 J175655+032813	C07	830	SML	17:56:55.83	03:28:13.2	18.084	17.500	0.544	—	—	—	—	—	0 Y+
104	Cr359 J175657+032740	C07	702	S	17:56:57.08	03:27:40.2	14.066	13.807	0.220	12.838	12.058	11.920	—	—	2 Y+
105	Cr359 J175657+022532	D10	1797	S	17:56:57.28	02:25:32.8	12.038	11.720	0.397	10.332	9.417	9.131	-1.9	-1.4	0 Y+
106	Cr359 J175657+034947	C01	612	S	17:56:57.33	03:49:48.0	14.171	13.938	0.193	13.189	12.656	12.511	—	—	0 Y+
107	Cr359 J175657+035159	C01	347	L	17:56:57.83	03:51:59.9	19.780	19.097	0.714	—	—	—	—	—	2 Y+
108	Cr359 J175658+021609	D10	379	ML	17:56:58.79	02:16:09.5	17.228	16.749	0.573	—	—	—	—	—	0 Y+
109	Cr359 J175700+035225	C01	3	S	17:57:00.39	03:52:25.6	12.035	11.883	0.111	11.397	11.189	11.099	—	—	2 Y+
110	Cr359 J175700+033639	C07	2545	SM	17:57:00.75	03:36:39.2	15.906	15.426	0.439	14.352	13.760	13.492	—	—	0 Y+
111	Cr359 J175700+034818	C01	917	S	17:57:00.97	03:48:18.6	12.324	12.103	0.182	11.321	10.659	10.564	—	—	2 Y+
112	Cr359 J175701+034606	C01	1427	S	17:57:01.06	03:46:06.6	13.424	13.044	0.339	12.086	11.481	11.221	—	—	2 Y+
113	Cr359 J175701+035222	C01	68	M	17:57:01.17	03:52:22.1	18.269	17.747	0.563	—	—	—	—	—	0 Y+
114	Cr359 J175701+035128	C01	263	S	17:57:01.90	03:51:28.6	14.149	13.899	0.210	13.147	12.514	12.431	—	—	0 Y+
115	Cr359 J175701+023436	D04	1516	S	17:57:01.97	02:34:36.2	17.897	17.281	0.697	—	—	—	—	—	0 Y+
116	Cr359 J175702+033537	C07	9039	L	17:57:02.06	03:35:37.9	21.341	20.329	1.041	—	—	—	—	—	0 Y+
117	Cr359 J175703+034533	C01	1560	S	17:57:03.21	03:45:33.1	12.882	12.636	0.206	11.722	11.047	10.893	—	—	0 Y+
118	Cr359 J175704+033103	C07	1362	S	17:57:04.24	03:31:03.6	12.055	11.913	0.103	—	—	—	-6.3	-6.7	2 Y+
119	Cr359 J175704+032442	C07	1	S	17:57:05.43	03:24:42.1	13.572	13.319	0.213	12.415	11.725	11.609	-3.9	-8.7	2 Y+
120	Cr359 J175706+034235	C01	2168	S	17:57:06.80	03:42:35.8	12.499	12.318	0.141	11.533	10.918	10.800	-3.2	4.5	0 Y+
121	Cr359 J175708+032452	C08	160	SM	17:57:08.01	03:24:52.2	14.948	14.667	0.241	13.896	13.314	13.136	—	—	0 Y+
122	Cr359 J175708+032512	C08	227	S	17:57:08.68	03:25:12.5	13.756	13.524	0.192	12.891	12.470	12.374	—	—	2 Y+
123	Cr359 J175708+032940	C08	1238	S	17:57:08.88	03:29:40.6	13.574	13.350	0.185	12.593	11.989	11.882	-7.1	-7.1	0 Y+
124	Cr359 J175709+033203	C08	1859	SM	17:57:09.16	03:32:03.7	16.728	16.175	0.513	15.132	14.446	14.225	—	—	0 Y+

Table B.1: continued

Numb	Coll359 J... J175709+023927	FOV	ID	RA	Dec	<i>I</i>	<i>z</i>	<i>J-z</i>	<i>H</i>	<i>K_s</i>	μ_{α}	μ_{α}	Flag	M?
125	Cr359 J175710+023927	D04	566	S	17:57:09.32	02:39:27.9	11.737	10.909	0.908	8.881	-9.6	-9.2	2	Y+
126	Cr359 J175710+024030	D04	1155	M	17:57:10.47	02:40:30.8	15.555	15.255	0.415	13.972	13.267	12.974	-	3 Y+
127	Cr359 J175710+033729	C08	2690	S	17:57:10.60	03:37:30.0	14.789	14.404	0.346	13.488	12.855	12.561	-	0 Y+
128	Cr359 J175710+034228	C02	5208	M	17:57:10.74	03:42:28.8	17.762	17.265	0.536	-	-	-	0	Y+
129	Cr359 J175710+023529	D04	3509	M	17:57:10.89	02:35:29.9	15.263	15.005	0.353	13.707	13.142	12.852	-	0 Y+
130	Cr359 J175711+033407	C08	2327	S	17:57:11.09	03:34:07.9	12.746	12.408	0.298	11.397	10.524	10.349	-11.0	0.9
131	Cr359 J175711+032658	C08	592	S	17:57:11.37	03:26:58.8	12.503	12.151	0.312	11.178	10.359	10.110	3.8	-2.8
132	Cr359 J175711+034243	C02	1955	S	17:57:11.37	03:42:43.7	12.644	12.466	0.139	11.692	11.171	11.053	-4.4	-0.2
133	Cr359 J175711+023104	D04	5554	M	17:57:11.67	02:31:04.8	16.641	16.243	0.493	14.792	14.168	13.973	-	0 Y+
134	Cr359 J175711+022241	D10	1277	S	17:57:11.81	02:22:41.5	11.687	11.548	0.218	10.469	9.869	9.702	5.7	-2.5
135	Cr359 J175711+035210	C02	36	S	17:57:11.91	03:52:10.6	14.248	13.998	0.210	13.250	12.706	12.606	-	0 Y+
136	Cr359 J175713+033052	C08	1516	S	17:57:13.34	03:30:52.9	12.775	12.546	0.189	11.807	11.224	11.104	2.6	9.2
137	Cr359 J175713+034838	C02	757	S	17:57:13.75	03:48:38.8	14.443	14.154	0.249	13.226	12.424	12.270	-5.9	-0.7
138	Cr359 J175714+035032	C02	382	S	17:57:14.22	03:50:32.7	18.144	17.495	0.610	-	-	-	-	0 Y+
139	Cr359 J175714+035131	C02	485	ML	17:57:14.98	03:51:31.1	18.589	18.929	0.699	-	-	-	-	0 Y+
140	Cr359 J175715+032557	C08	393	S	17:57:15.78	03:25:57.8	13.461	13.211	0.210	12.450	11.849	11.740	2.6	-4.3
141	Cr359 J175713+034947	C02	502	S	17:57:16.40	03:49:47.7	13.702	13.458	0.204	12.672	12.117	11.923	-	0 Y+
142	Cr359 J175716+035136	C02	136	S	17:57:16.41	03:51:36.0	13.684	13.461	0.184	12.734	12.194	12.125	-	0 Y+
143	Cr359 J175716+021516	D11	53	M	17:57:16.62	02:15:17.0	19.199	18.657	0.637	-	-	-	-	0 Y+
144	Cr359 J175716+035009	C02	421	S	17:57:16.82	03:50:09.7	13.467	13.260	0.167	12.562	12.047	11.979	-	0 Y+
145	Cr359 J175717+034730	C02	2517	ML	17:57:17.08	03:47:30.1	19.314	18.563	0.790	-	-	-	-	3 Y+
146	Cr359 J175717+032802	C08	835	S	17:57:17.42	03:28:02.3	13.278	13.011	0.227	12.234	11.530	11.434	-11.1	-0.5
147	Cr359 J175717+035202	C02	222	M	17:57:17.71	03:52:02.1	19.652	18.999	0.693	-	-	-	-	0 Y+
148	Cr359 J175717+032815	C08	896	S	17:57:17.90	03:28:15.3	12.520	12.208	0.272	11.282	10.530	10.307	-2.1	-4.6
149	Cr359 J175717+034754	C02	937	S	17:57:17.99	03:47:54.8	17.974	17.399	0.534	-	-	-	-	0 Y+
150	Cr359 J175717+021835	D11	483	S	17:57:18.15	02:18:35.3	11.716	11.591	0.205	10.385	9.705	9.523	-2.6	-7.8
151	Cr359 J175719+022336	D11	1304	S	17:57:19.07	02:23:36.2	12.213	12.036	0.257	10.718	9.847	9.686	0.8	-8.1
152	Cr359 J175719+033414	C08	2379	S	17:57:19.23	03:34:14.4	13.459	13.266	0.154	12.533	11.986	11.872	-	0 Y+
153	Cr359 J175721+032640	C08	551	S	17:57:21.04	03:26:40.8	14.262	14.023	0.199	13.320	12.725	12.684	-6.5	-4.6
154	Cr359 J175721+032906	C08	2305	M	17:57:21.43	03:29:06.1	18.624	18.035	0.629	-	-	-	-	3 Y+
155	Cr359 J175721+033501	C08	2566	S	17:57:21.58	03:35:01.6	12.552	12.308	0.204	11.459	10.749	10.610	-	2 Y+
156	Cr359 J175724+034026	C02	2489	S	17:57:24.92	03:40:26.8	13.925	13.684	0.200	12.824	12.104	11.972	-8.5	3.1
157	Cr359 J175725+033117	C08	1676	SML	17:57:25.33	03:31:17.1	18.442	17.638	0.763	-	15.744	-	-	Y?
158	Cr359 J175725+024235	D05	170	M	17:57:25.47	02:42:35.9	15.368	15.100	0.363	13.839	13.186	12.940	-	2 Y+
159	Cr359 J175725+034307	C02	1878	S	17:57:25.82	03:43:07.4	13.252	13.063	0.149	12.294	11.711	11.630	1.0	-5.0
160	Cr359 J175726+030500	C08	1529	S	17:57:26.18	03:30:50.9	13.386	13.181	0.165	12.499	11.946	11.814	-	0 Y+
161	Cr359 J175725+033134	C08	1697	S	17:57:27.02	03:31:34.8	12.493	12.302	0.151	11.579	11.008	10.916	-3.9	-15.4
162	Cr359 J175727+034840	C02	730	S	17:57:27.45	03:48:40.7	13.113	12.918	0.155	12.211	11.675	11.549	0.6	0 Y+
163	Cr359 J175728+032848	C08	1075	S	17:57:28.45	03:28:48.6	14.976	14.687	0.249	-	-	-	-	Y+
164	Cr359 J175728+033036	C08	1509	SM	17:57:28.76	03:30:36.4	18.140	17.442	0.658	-	-	-	-	2 Y?
165	Cr359 J175729+032433	C08	82	M	17:57:29.26	03:24:33.4	18.249	17.747	0.543	-	-	-	-	0 Y+
166	Cr359 J175730+034102	C02	6520	M	17:57:30.01	03:41:02.8	15.627	15.320	0.347	14.342	13.661	13.493	-	2 Y+

Table B.1: continued

Numb	Coll359 J...	FOV	ID	Exp	RA	Dec	<i>I</i>	<i>L-z</i>	<i>J</i>	<i>H</i>	<i>K_s</i>	μ_{α}	μ_{α}	Flag	M?
167	Cr359 J175730+034026	C02	2515	S	17:57:30.72	03:40:26.4	12.713	12.522	0.151	11.718	11.087	0.3	-0.9	2	Y+
168	Cr359 J175731+034911	C02	607	S	17:57:31.21	03:49:11.2	12.406	12.129	0.237	11.229	10.450	-1.4	-6.0	0	Y+
169	Cr359 J175731+021853	D11	553	S	17:57:31.68	02:18:53.0	13.597	13.390	0.287	12.105	11.243	11.025	-	2	Y+
170	Cr359 J175731+033426	C08	2439	S	17:57:31.95	03:34:26.5	13.307	12.985	0.282	11.988	11.110	10.905	-1.7	-5.8	0
171	Cr359 J175733+034513	C02	3647	M	17:57:33.64	03:45:13.8	17.297	16.806	0.531	-	-	-	-	0	Y+
172	Cr359 J175733+034632	C02	1173	S	17:57:33.99	03:46:32.1	12.950	12.684	0.226	11.763	11.005	10.825	-5.1	-10.2	0
173	Cr359 J175734+034051	C02	2524	S	17:57:34.63	03:40:51.4	12.845	12.648	0.157	11.830	11.152	11.067	-1.0	4.7	2
174	Cr359 J175735+035150	C02	101	S	17:57:35.94	03:51:50.2	17.780	17.221	0.519	-	-	-	-	0	Y+
175	Cr359 J175736+032545	C09	716	M	17:57:36.72	03:25:45.2	20.025	19.330	0.735	-	-	-	-	3	Y+
176	Cr359 J175737+024153	D05	558	M	17:57:37.91	02:41:53.9	20.087	19.366	0.816	-	-	-	-	0	Y+
177	Cr359 J175738+033145	C09	1616	S	17:57:38.22	03:31:45.1	13.438	13.232	0.166	12.502	11.901	11.787	0.8	1.7	0
178	Cr359 J175739+032507	C09	157	SM	17:57:39.36	03:25:07.3	16.179	15.686	0.453	14.695	14.038	13.887	-	0	Y+
179	Cr359 J175739+032751	C09	707	S	17:57:39.61	03:27:51.0	12.919	12.669	0.210	11.864	11.242	11.078	1.7	1.9	2
180	Cr359 J175740+034815	C03	1031	S	17:57:40.16	03:48:15.4	13.501	13.289	0.172	12.544	11.982	11.839	-5.0	3.8	2
181	Cr359 J175741+032555	C09	306	S	17:57:41.04	03:25:55.3	14.007	13.739	0.229	13.014	12.389	12.281	-1.5	5.3	0
182	Cr359 J175741+032537	C09	247	S	17:57:41.54	03:25:37.2	14.226	13.958	0.229	-	-	-	-0.2	-5.8	0
183	Cr359 J175741+035039	C03	406	S	17:57:41.59	03:50:39.8	14.023	13.765	0.218	12.950	12.321	12.160	-5.0	1.1	2
184	Cr359 J175741+032459	C09	126	SM	17:57:41.73	03:24:59.5	14.835	14.504	0.291	13.761	13.087	12.945	0.5	-9.8	0
185	Cr359 J175743+032524	C09	951	L	17:57:43.07	03:25:24.5	21.625	20.771	0.884	-	-	-	-	0	Y+
186	Cr359 J175743+032953	C09	1239	SML	17:57:43.69	03:29:53.3	17.600	17.009	0.552	-	-	-	-	0	Y+
187	Cr359 J175743+032533	C09	245	S	17:57:43.75	03:25:33.8	15.168	14.619	0.509	13.557	12.855	12.635	-	3	Y+
188	Cr359 J175744+032433	C09	33	SM	17:57:44.10	03:24:33.1	15.396	15.027	0.330	14.228	13.569	13.348	-	0	Y+
189	Cr359 J175744+034935	C03	1567	ML	17:57:44.40	03:49:36.0	18.684	18.053	0.671	-	-	-	-	0	Y+
190	Cr359 J175744+033536	C09	2886	S	17:57:44.42	03:35:36.0	12.904	12.656	0.208	11.801	11.094	10.924	-1.5	-5.4	2
191	Cr359 J175744+033536	C09	33	S	17:57:44.42	03:35:36.0	17.994	17.399	0.555	-	-	-	-	0	Y+
192	Cr359 J175746+032456	C09	830	SM	17:57:46.14	03:28:10.2	16.073	15.600	0.452	14.651	14.074	13.728	-	0	Y+
193	Cr359 J175747+033457	C09	2327	S	17:57:47.78	03:34:57.4	12.425	12.232	0.153	11.467	10.875	10.762	-6.6	-4.9	0
194	Cr359 J175748+033547	C09	2859	S	17:57:48.13	03:35:47.7	12.668	12.454	0.174	11.713	11.071	10.952	5.1	-10.2	0
195	Cr359 J175748+034931	C03	696	S	17:57:48.39	03:49:31.7	12.483	12.282	0.160	11.540	11.004	10.887	4.1	-2.6	0
196	Cr359 J175748+034734	C03	1190	S	17:57:48.71	03:47:34.1	12.849	12.661	0.148	11.971	11.420	11.322	-1.4	-9.6	2
197	Cr359 J175748+034344	C03	2167	S	17:57:48.84	03:43:44.5	12.862	12.678	0.144	11.919	11.306	11.157	-6.1	0.4	0
198	Cr359 J175750+032747	C09	1820	ML	17:57:50.07	03:27:47.7	19.077	18.405	0.712	-	-	-	-	0	Y+
199	Cr359 J175752+032458	C09	352	ML	17:57:52.13	03:24:58.7	19.801	19.117	0.724	-	-	-	-	0	Y+
200	Cr359 J175752+033103	C09	1487	S	17:57:52.16	03:31:03.7	16.796	16.267	0.490	15.120	14.422	14.204	-	3	Y+
201	Cr359 J175753+035107	C03	267	S	17:57:53.28	03:51:07.7	13.409	13.173	0.196	12.497	11.995	11.864	-4.2	-2.2	0
202	Cr359 J175753+032640	C09	1202	M	17:57:53.45	03:26:40.5	17.970	17.426	0.584	-	-	-	-	0	Y+
203	Cr359 J175753+032815	C09	860	SM	17:57:53.47	03:28:15.6	16.136	15.549	0.547	14.447	13.742	13.472	-	0	Y+
204	Cr359 J175753+032821	C09	2088	M	17:57:53.52	03:28:21.6	19.464	18.721	0.782	-	-	-	-	0	Y+
205	Cr359 J175753+032436	C09	26	S	17:57:53.72	03:24:36.5	12.587	12.239	0.308	11.377	10.695	10.497	0.0	-8.9	0
206	Cr359 J175754+034523	C03	1743	S	17:57:54.08	03:45:24.0	14.306	14.052	0.213	13.153	12.402	12.216	-	2	Y+
207	Cr359 J175756+033154	C09	1677	S	17:57:56.58	03:31:54.6	13.349	13.137	0.172	12.359	11.786	11.666	0.8	-6.6	0
208	Cr359 J175757+034832	C03	926	S	17:57:57.64	03:48:32.5	12.548	12.351	0.157	11.604	10.952	10.840	3.9	12.4	0

Table B.1: continued

Numb	Coll359 J...:	FOV	ID	RA	Dec	<i>I</i>	<i>J</i>	<i>H</i>	<i>K_s</i>	μ_{α}	μ_{α}	Flag	M?	
209	Cr359 J175800+033133	C09	1578	S	17:58:00.06	03:31:33.5	12.628	12.313	0.275	11.405	10.570	-5.7	2 Y+	
210	Cr359 J175800+032520	C09	178	S	17:58:00.26	03:25:20.2	12.237	11.937	0.260	11.116	10.521	-3.5	2 Y+	
211	Cr359 J175800+034821	C03	960	S	17:58:00.54	03:48:21.0	12.401	12.156	0.205	11.287	10.561	-8.7	0 Y+	
212	Cr359 J175801+032442	C09	83	S	17:58:01.31	03:24:42.2	14.980	14.684	0.256	13.991	13.498	-4.1	-13.6 0 Y+	
213	Cr359 J175801+035045	C03	338	S	17:58:01.52	03:50:45.6	12.420	12.219	0.19	11.564	10.866	-8.0	5.9 0 Y+	
214	Cr359 J175802+032936	C09	1149	S	17:58:02.09	03:29:36.3	13.960	13.498	0.422	12.508	11.875	11.636	1.4 2.8 2 Y+	
215	Cr359 J175803+035005	C03	573	SM	17:58:03.02	03:50:05.0	15.786	15.327	0.419	14.377	13.675	13.480	-	- 0 Y+
216	Cr359 J175803+033059	C09	1455	S	17:58:03.06	03:30:59.7	13.679	13.442	0.197	12.702	12.075	11.975	0.8 -4.2 0 Y+	
217	Cr359 J175803+032751	C09	788	SM	17:58:03.61	03:27:51.1	17.307	16.676	0.591	-	-	-	- 0 Y+	
218	Cr359 J175803+035116	C03	257	SML	17:58:03.66	03:51:17.0	18.211	17.518	0.653	-	-	-	- 0 Y+	
219	Cr359 J175803+034702	C03	1314	S	17:58:03.94	03:47:02.6	13.556	13.333	0.183	12.555	11.919	11.811	0.9 -2.2 2 Y+	
220	Cr359 J175803+035024	C03	442	S	17:58:04.00	03:50:24.7	13.731	13.520	0.171	13.268	12.995	12.877	-	- 2 NM
221	Cr359 J175804+034923	C03	719	S	17:58:04.12	03:49:23.2	12.875	12.589	0.246	11.678	10.860	10.752	-2.1 -7.6 0 Y+	
222	Cr359 J175804+032747	C09	3033	L	17:58:04.70	03:27:47.2	19.496	18.784	0.742	-	-	-	- 3 Y+	
223	Cr359 J175804+034759	C03	1098	S	17:58:04.92	03:47:59.1	14.913	14.607	0.266	13.743	13.028	12.872	-	- 0 Y+
224	Cr359 J175805+035029	C03	1280	L	17:58:05.16	03:50:29.2	22.248	21.259	1.020	-	-	-	- 3 Y+	
225	Cr359 J175805+035024	C03	1206	S	17:58:05.74	03:47:35.7	17.491	16.920	0.531	-	-	-	- 0 Y+	
226	Cr359 J175806+032545	C10	271	S	17:58:06.55	03:25:45.4	12.537	12.214	0.283	11.295	10.512	10.288	4.2 1.4 0 Y+	
227	Cr359 J175807+032603	C10	353	S	17:58:07.44	03:26:03.8	14.073	13.839	0.194	13.140	12.647	12.470	-5.6 -9.1 0 Y+	
228	Cr359 J175807+032737	C10	685	S	17:58:07.48	03:27:37.4	13.475	13.265	0.170	12.591	12.121	11.981	-20.0 -3.4 0 Y+	
229	Cr359 J175809+033351	C10	2141	S	17:58:09.06	03:53:51.4	13.198	12.978	0.180	12.171	11.586	11.414	-8.7 -3.5 0 Y+	
230	Cr359 J175809+033726	C10	2498	S	17:58:09.07	03:37:26.1	12.624	12.422	0.162	11.631	11.050	10.913	-1.9 5.9 0 Y+	
231	Cr359 J175809+032535	C10	250	S	17:58:09.26	03:25:35.3	14.049	13.784	0.225	13.040	12.456	12.277	-	- 0 Y+
232	Cr359 J175809+033224	C10	1790	S	17:58:09.76	03:32:24.4	13.071	12.792	0.239	11.907	11.163	10.981	-4.1 -2.0 0 Y+	
233	Cr359 J175810+032846	C10	954	S	17:58:10.03	03:28:46.1	16.056	15.345	0.672	14.037	13.534	13.180	-	- 0 Y+
234	Cr359 J175810+032606	C10	401	S	17:58:10.75	03:26:06.4	17.241	16.693	0.508	-	-	-	- 0 Y+	
235	Cr359 J175812+032812	C10	840	SM	17:58:12.36	03:28:12.8	16.246	15.734	0.472	14.657	14.010	13.756	-	- 0 Y+
236	Cr359 J175812+032952	C10	1150	S	17:58:12.43	03:29:52.3	12.505	12.300	0.166	11.624	11.127	11.030	-21.1 -2.9 0 Y+	
237	Cr359 J175814+032539	C10	280	S	17:58:14.21	03:25:39.3	14.609	14.283	0.286	13.463	12.713	12.606	-3.6 -6.0 0 Y+	
238	Cr359 J175814+032443	C10	78	S	17:58:14.22	03:24:43.4	13.799	13.513	0.246	12.810	12.260	12.107	-6.1 -6.4 0 Y+	
239	Cr359 J175814+033641	C10	2657	S	17:58:14.54	03:36:41.7	12.823	12.624	0.159	11.902	11.386	11.246	1.5 -6.1 0 Y+	
240	Cr359 J175815+035125	C04	145	SM	17:58:15.86	03:51:25.4	16.329	15.706	0.582	14.458	13.959	13.583	-	- 0 Y+
241	Cr359 J175816+034816	C04	782	S	17:58:16.67	03:48:16.3	13.489	13.281	0.168	12.467	11.862	11.714	3.2 -8.1 0 Y+	
242	Cr359 J175816+032515	C10	192	S	17:58:16.71	03:25:15.9	14.450	14.153	0.258	13.344	12.749	12.578	-	- 0 Y+
243	Cr359 J175817+033957	C04	2637	S	17:58:17.01	03:39:57.8	15.120	14.663	0.417	13.613	13.032	12.778	-	- 0 Y+
244	Cr359 J175817+033920	C04	2507	S	17:58:17.07	03:39:20.6	14.825	14.377	0.408	13.242	12.598	12.348	-	- 0 Y+
245	Cr359 J175818+032444	C10	89	S	17:58:18.78	03:24:44.1	14.241	13.972	0.229	13.263	12.651	12.589	-5.3 -8.7 0 Y+	
246	Cr359 J175819+032515	C10	191	S	17:58:19.15	03:25:15.1	14.396	14.115	0.241	13.385	12.753	12.603	-8.0 -10.2 0 Y+	
247	Cr359 J175819+033516	C10	2972	S	17:58:19.69	03:35:16.1	12.335	12.137	0.158	11.417	10.909	10.802	-	- 0 Y+
248	Cr359 J175819+033106	C10	1501	SM	17:58:19.92	03:31:06.8	16.973	16.454	0.479	15.337	14.716	14.203	-	- 0 Y+
249	Cr359 J175819+033253	C10	1926	S	17:58:19.97	03:32:53.2	14.255	14.014	0.201	13.201	12.578	12.470	-9.6 2.0 0 Y+	
250	Cr359 J175821+033148	C10	1659	S	17:58:21.49	03:31:48.5	14.396	14.073	0.283	13.118	12.311	12.114	-3.6 -4.6 0 Y+	

Table B.1: continued

Numb	Coll359 J...	FOV	ID	RA	Dec	<i>I</i>	<i>L-z</i>	<i>J</i>	<i>H</i>	<i>K_s</i>	μ_{α}	μ_{α}	Flag	M?
251	Cr359 J175821+033356	C10	2190	S	17:58:21.62	03:33:57.0	14.659	14.407	0.213	13.640	-12.973	12.778	—	2 Y+
252	Cr359 J175822+033251	C10	1900	S	17:58:22.17	03:32:51.3	12.507	12.224	0.243	11.336	10.652	10.420	-12.5	-1.4 0 Y+
253	Cr359 J175823+032504	C10	151	S	17:58:23.62	03:25:04.5	13.503	12.230	0.233	12.018	11.907	11.907	-11.0	0 Y+
254	Cr359 J175823+033341	C10	2122	S	17:58:23.69	03:33:42.0	13.161	12.940	0.180	12.264	11.682	11.565	-1.7	-5.9 0 Y+
255	Cr359 J175824+033735	C10	2491	S	17:58:24.22	03:37:35.6	14.447	14.088	0.319	13.196	12.473	12.261	—	— 0 Y+
256	Cr359 J175824+035034	C04	296	S	17:58:24.34	03:50:34.4	13.164	12.960	0.164	12.175	11.589	11.482	-3.5	-5.4 0 Y+
257	Cr359 J175824+034036	C04	2755	S	17:58:24.90	03:40:36.0	12.549	12.342	0.167	11.510	10.827	10.682	-3.5	3.0 0 Y+
258	Cr359 J175824+033600	C10	2748	S	17:58:24.97	03:36:01.0	12.958	12.758	0.160	12.104	11.565	11.459	-7.5	-7.4 0 Y+
259	Cr359 J175825+035151	C04	37	S	17:58:25.28	03:51:51.9	14.644	14.340	0.264	13.510	12.711	12.583	—	— 0 Y+
260	Cr359 J175825+032455	C10	121	S	17:58:25.61	03:24:55.4	13.671	13.394	0.238	12.711	12.129	12.048	-2.4	-7.0 0 Y+
261	Cr359 J175826+033203	C10	1702	S	17:58:26.01	03:32:04.0	12.820	12.615	0.165	11.983	11.448	11.330	-12.5	4.3 0 Y+
262	Cr359 J175826+032622	C10	454	S	17:58:26.88	03:26:22.1	14.906	14.587	0.279	13.827	13.153	13.009	—	— 0 Y+
263	Cr359 J175827+033525	C10	2895	S	17:58:27.85	03:35:25.5	12.875	12.573	0.263	11.661	10.889	10.680	-6.6	-1.7 0 Y+
264	Cr359 J175828+034238	C04	8153	L	17:58:28.63	03:42:38.0	20.349	20.343	1.037	—	—	—	—	— 0 Y+
265	Cr359 J175829+033313	C10	2046	S	17:58:29.97	03:33:13.6	16.340	15.851	0.449	14.802	14.141	13.907	—	— 2 Y+
266	Cr359 J175830+033440	C10	2351	S	17:58:30.29	03:34:40.1	14.455	14.201	0.214	13.462	12.823	12.686	-1.7	1.2 0 Y+
267	Cr359 J175830+032705	C10	595	S	17:58:30.40	03:27:05.3	14.703	14.435	0.228	13.720	13.127	12.969	—	— 0 Y+
268	Cr359 J175830+032414	C10	24	ML	17:58:30.72	03:24:14.8	19.842	19.185	0.697	—	—	—	—	— 0 Y+
269	Cr359 J175830+033746	C10	10446	L	17:58:30.95	03:37:47.0	22.142	21.227	0.945	—	—	—	—	— 3 Y+
270	Cr359 J175831+033537	C10	2893	S	17:58:31.38	03:35:37.6	12.634	12.467	0.127	11.907	11.565	11.463	-12.6	-5.6 2 Y+
271	Cr359 J175832+033650	C10	2612	S	17:58:32.53	03:36:50.6	14.177	13.943	0.194	13.252	12.646	12.522	-3.3	-13.8 0 Y+
272	Cr359 J175833+032419	C04	3179	M	17:58:33.54	03:46:19.7	17.148	16.697	0.491	—	—	—	—	— 2 Y+
273	Cr359 J175833+032656	C11	518	S	17:58:33.95	03:26:56.5	15.007	14.660	0.307	11.947	11.187	11.015	-5.6	-0.1 0 Y+
274	Cr359 J175834+033617	C11	2369	S	17:58:34.72	03:36:17.9	13.047	12.823	0.185	—	—	—	—	— 3 Y+
275	Cr359 J175835+033146	C11	3779	M	17:58:35.45	03:31:46.2	18.511	17.980	0.571	—	—	—	—	— 3 Y+
276	Cr359 J175836+032509	C11	205	S	17:58:36.95	03:25:09.7	17.074	16.510	0.524	—	—	—	—	— 0 Y+
277	Cr359 J175836+032820	C11	799	S	17:58:36.98	03:28:20.1	14.257	13.977	0.241	13.038	12.247	12.038	-8.7	-5.6 0 Y+
278	Cr359 J175837+033119	C11	1433	S	17:58:37.13	03:31:19.3	14.701	14.432	0.229	13.543	12.836	12.670	—	— 0 Y+
279	Cr359 J175839+032412	C11	11	S	17:58:39.58	03:24:12.0	14.531	14.236	0.255	13.486	12.919	12.798	-0.5	10.0 0 Y+
280	Cr359 J175840+032557	C11	329	S	17:58:40.25	03:25:58.0	13.373	13.161	0.172	12.382	11.843	11.701	-1.9	-6.9 0 Y+
281	Cr359 J175843+032522	C11	556	M	17:58:43.76	03:25:22.1	18.541	17.991	0.590	—	—	—	—	— 0 Y+
282	Cr359 J175843+034324	C05	2236	SM	17:58:43.84	03:43:24.8	15.464	15.040	0.384	14.034	13.352	13.183	—	— 0 Y+
283	Cr359 J175844+032613	C11	943	M	17:58:44.49	03:26:13.6	16.440	16.034	0.446	14.938	14.222	13.980	—	— 0 Y+
284	Cr359 J175844+032416	C11	14	M	17:58:44.50	03:24:16.9	15.145	14.918	0.267	14.115	13.491	13.341	—	— 0 Y+
285	Cr359 J175845+035153	C05	179	S	17:58:45.04	03:51:53.3	14.889	14.606	0.243	13.824	13.222	13.135	—	— 0 Y+
286	Cr359 J175845+035134	C05	308	ML	17:58:45.59	03:51:34.2	20.442	19.560	0.922	—	—	—	—	— 1 Y+
287	Cr359 J175845+033317	C11	1813	S	17:58:45.90	03:33:18.0	13.825	13.605	0.180	12.811	12.177	12.031	-4.7	-3.1 0 Y+
288	Cr359 J175846+033007	C11	1183	S	17:58:46.18	03:30:07.6	13.639	13.428	0.171	12.579	11.980	11.830	—	— 2 Y+
289	Cr359 J175847+032805	C11	743	S	17:58:47.34	03:28:05.7	13.229	12.948	0.241	11.976	11.191	10.980	-5.6	-0.7 0 Y+
290	Cr359 J175847+035047	C05	410	S	17:58:47.53	03:50:47.0	12.288	12.015	0.233	11.149	10.507	10.312	-3.5	-5.7 2 Y+
291	Cr359 J175848+035117	C05	314	S	17:58:48.15	03:51:17.1	14.410	14.153	0.217	13.410	12.785	12.717	—	— 0 Y+
292	Cr359 J175849+032645	C11	470	S	17:58:49.32	03:26:45.6	12.771	12.549	0.182	11.739	11.056	10.927	-4.1	-13.4 2 Y+

Table B.1: continued

Numb	Coll359 J...:	FOV	ID	RA	Dec	<i>I</i>	<i>J</i>	<i>H</i>	<i>K_s</i>	μ_{α}	μ_{α}	Flag	M?	
293	Cr359 J175850+034524	C05	1649	S	17:58:50.64	03:45:24.7	12.801	12.553	0.208	11.738	11.150	—	2 Y+	
294	Cr359 J175851+033339	C11	1892	S	17:58:51.26	03:33:39.2	13.622	13.288	0.294	12.235	11.338	-0.3	-1.9 0 Y+	
295	Cr359 J175851+032329	C11	1710	SM	17:58:51.45	03:32:39.5	15.813	15.289	0.485	14.162	13.538	-	- 0 Y+	
296	Cr359 J175852+033359	C11	1971	S	17:58:52.28	03:33:59.6	17.857	17.124	0.693	—	15.158	-	- 0 Y?	
297	Cr359 J175852+032412	C11	6	S	17:58:52.53	03:24:12.7	14.447	14.195	0.212	13.411	12.875	-	- 3 Y+	
298	Cr359 J175852+032759	C11	724	S	17:58:52.61	03:27:59.8	12.454	12.231	0.183	11.430	10.831	-9.2	-1.4 0 Y+	
299	Cr359 J175852+032411	C11	7	S	17:58:52.83	03:24:11.1	13.135	12.843	0.252	12.019	11.385	-	- 2 Y+	
300	Cr359 J175852+032830	C11	834	S	17:58:52.87	03:28:30.8	13.158	12.963	0.155	12.242	11.697	7.8	-10.7 2 Y+	
301	Cr359 J175853+035034	C05	511	S	17:58:53.37	03:50:34.5	17.761	17.164	0.556	—	—	-	0 Y+	
302	Cr359 J175853+032914	C11	2514	ML	17:58:53.86	03:29:14.4	18.779	18.165	0.654	—	—	-	0 Y+	
303	Cr359 J175854+032418	C11	3	S	17:58:54.12	03:24:18.1	13.558	13.292	0.226	12.492	11.927	-	- 0 Y+	
304	Cr359 J175856+032709	C11	566	S	17:58:56.04	03:27:09.2	13.949	13.697	0.212	12.835	12.133	-1.9	-3.0 0 Y+	
305	Cr359 J175856+032920	C11	1027	S	17:58:56.06	03:29:20.5	13.916	13.685	0.191	12.909	12.248	12.089	-1.2 -12.8 0 Y+	
306	Cr359 J175856+032411	C11	5	S	17:58:56.82	03:24:11.6	12.300	12.014	0.246	—	—	-	0 Y+	
307	Cr359 J175857+033859	C05	6160	M	17:58:57.14	03:38:59.6	18.698	18.055	0.683	—	—	-	0 Y+	
308	Cr359 J175858+032533	C11	264	S	17:58:58.46	03:25:33.7	13.504	13.298	0.166	12.561	12.004	11.900	-2.3 -0.6 0 Y+	
309	Cr359 J175859+035015	C05	516	S	17:58:59.27	03:50:15.4	13.358	13.145	0.172	—	—	-	2 Y+	
310	Cr359 J175900+032417	C11	2	S	17:59:00.12	03:24:17.8	12.440	12.167	0.233	—	—	-	0 Y+	
311	Cr359 J175900+033227	C11	1639	S	17:59:00.91	03:32:27.2	13.256	12.959	0.257	12.061	11.093	-6.1	-1.4 0 Y+	
312	Cr359 J175942+015528	A06	92	S	17:59:42.58	01:55:28.1	14.140	13.915	0.225	—	—	-	0 Y+	
313	Cr359 J175943+015858	A06	746	S	17:59:43.56	01:58:58.5	13.878	13.663	0.216	12.917	12.279	12.188	-5.1 -4.1 0 Y+	
314	Cr359 J175944+020805	A06	2073	S	17:59:44.26	02:08:05.4	16.797	16.275	0.522	15.072	14.531	14.259	-	0 Y+
315	Cr359 J175945+020310	A06	1603	S	17:59:45.10	02:03:10.1	12.191	11.924	0.267	10.986	10.206	10.042	-0.3 -5.3 0 Y+	
316	Cr359 J175945+021632	A00	1260	S	17:59:45.72	02:16:32.9	13.446	13.251	0.195	12.488	11.927	11.802	-1.8 -2.0 0 Y+	
317	Cr359 J175946+021204	A00	2252	S	17:59:46.36	02:12:04.2	13.912	13.686	0.226	12.729	12.126	11.958	4.7 -11.9 2 Y+	
318	Cr359 J175946+020712	A06	2409	S	17:59:46.55	02:07:12.7	13.822	13.577	0.245	12.767	12.070	11.899	-1.9 -3.1 0 Y+	
319	Cr359 J175946+021748	A00	1008	S	17:59:46.78	02:17:48.2	14.209	13.974	0.234	13.092	12.371	12.207	-2.1 -8.3 0 Y+	
320	Cr359 J175947+020755	A06	2230	S	17:59:47.73	02:07:55.6	12.931	12.708	0.222	11.926	11.259	11.151	2.9 -8.8 2 Y+	
321	Cr359 J175948+021120	A00	2775	S	17:59:48.11	02:11:20.3	12.847	12.600	0.247	11.689	10.939	10.756	-2.9 -2.0 0 Y+	
322	Cr359 J175950+021314	A00	2007	SM	17:59:50.22	02:13:14.7	15.509	15.081	0.428	14.043	13.352	13.121	-	0 Y+
323	Cr359 J175950+021810	A00	949	S	17:59:50.50	02:18:10.7	17.131	16.607	0.524	—	—	-	0 Y+	
324	Cr359 J175950+021810	A00	3832	L	17:59:50.50	02:18:10.7	17.181	16.689	0.582	—	—	-	3 Y+	
325	Cr359 J175951+015839	A06	675	S	17:59:51.09	01:58:39.4	13.536	13.321	0.215	12.485	11.888	11.696	-	0 Y+
326	Cr359 J175951+022045	A00	374	S	17:59:51.85	02:20:45.2	15.925	15.463	0.462	14.474	13.635	13.400	-	0 Y+
327	Cr359 J175952+021255	A00	2036	S	17:59:52.13	02:12:55.9	12.503	12.161	0.342	11.062	10.129	9.887	-3.9 -9.3 0 Y+	
328	Cr359 J175952+020936	A00	2328	S	17:59:52.31	02:09:36.7	11.819	11.563	0.255	10.569	9.801	9.620	-3.8 -4.2 2 Y+	
329	Cr359 J175953+020459	A06	1963	S	17:59:53.01	02:04:59.6	12.046	11.800	0.246	10.947	10.202	10.061	-1.3 2 Y+	
330	Cr359 J175954+021536	A00	1472	S	17:59:54.37	02:15:36.1	14.308	14.046	0.262	13.223	12.514	12.269	5.1 -7.8 0 Y+	
331	Cr359 J175955+021044	A00	2642	S	17:59:55.49	02:10:44.5	12.429	12.210	0.219	11.321	10.577	10.383	7.8 -5.2 0 Y+	
332	Cr359 J175956+021044	A06	110	S	17:59:56.36	01:55:29.9	13.287	13.048	0.239	12.305	11.677	11.541	-	0 Y+
333	Cr359 J175957+020601	A06	2594	S	17:59:57.17	02:06:01.5	16.042	15.525	0.518	—	—	-	3 Y+	
334	Cr359 J175957+020038	A06	1088	S	17:59:57.30	02:00:38.9	13.380	13.142	0.238	12.211	11.449	11.278	-6.0 -12.2 0 Y+	

Table B.1: continued

Numb	Coll359 J...	FOV	ID	RA	Dec	<i>I</i>	<i>L-z</i>	<i>J</i>	<i>H</i>	<i>K_s</i>	μ_{α}	μ_{α}	Flag	M?
335	Cr359 J175957+020816	A06	2068	S	17:59:57.64	02:08:16.7	12.032	11.792	10.961	10.085	-0.3	1.9	2	Y+
336	Cr359 J175957+015522	A06	88	S	17:59:57.85	01:55:22.9	13.541	13.264	12.372	11.693	11.486	—	0	Y+
337	Cr359 J175958+021727	A00	1049	S	17:59:58.92	02:17:27.2	12.799	12.619	11.232	11.104	-11.3	-11.1	0	Y+
338	Cr359 J175959+022111	A00	259	S	17:59:59.00	02:21:11.5	14.020	13.775	12.964	12.262	12.140	-0.8	-5.4	0
339	Cr359 J175959+020540	A06	2175	S	17:59:59.23	02:05:40.7	13.467	13.235	12.322	11.742	11.607	-1.9	-7.7	0
340	Cr359 J175959+022122	A00	233	S	17:59:59.47	02:21:22.7	14.300	14.027	12.733	13.153	12.433	12.247	-8.1	0
341	Cr359 J180000+022159	A00	95	S	18:00:00.65	02:21:59.6	17.484	16.843	0.641	—	14.934	—	—	0
342	Cr359 J180000+020016	A06	1020	S	18:00:00.97	02:00:16.9	12.600	12.365	11.515	10.814	10.661	-0.3	-7.2	0
343	Cr359 J180002+020939	A00	2435	S	18:00:02.19	02:09:39.7	12.176	12.002	11.174	11.136	10.514	10.364	-5.9	8.6
344	Cr359 J180002+021322	A00	1912	S	18:00:02.61	02:13:22.1	12.872	12.689	11.84	11.219	11.041	-4.4	-5.5	0
345	Cr359 J180003+020158	A06	1340	S	18:00:03.42	02:01:58.1	12.098	11.902	11.96	11.085	10.474	10.333	-5.6	-3.1
346	Cr359 J180003+020606	A06	2556	S	18:00:03.80	02:06:06.6	15.464	15.133	0.331	14.245	13.471	13.259	—	0
347	Cr359 J180004+021633	A00	1239	S	18:00:04.05	02:16:33.8	13.076	12.826	0.250	11.839	11.004	10.823	-1.2	-9.4
348	Cr359 J180004+022210	A00	201	M	18:00:04.86	02:22:10.2	18.674	17.776	1.008	—	14.895	—	—	3
349	Cr359 J180005+020734	A06	2157	S	18:00:05.55	02:07:34.7	12.374	12.165	0.209	11.319	10.724	10.550	-5.9	1.5
350	Cr359 J180005+015733	A06	511	S	18:00:05.96	01:57:33.2	15.690	15.308	0.382	14.287	13.582	13.390	—	0
351	Cr359 J180008+020413	A06	1829	S	18:00:08.08	02:04:13.7	12.113	11.904	0.209	11.049	10.438	10.296	-9.0	2.1
352	Cr359 J180009+022228	A00	9	SM	18:00:09.18	02:22:28.3	16.664	15.995	0.669	14.852	14.165	13.862	—	0
353	Cr359 J180009+022152	A00	153	S	18:00:09.45	02:21:52.7	17.246	16.688	0.557	—	14.842	—	—	3
354	Cr359 J180010+020508	A07	2243	S	18:00:10.51	02:05:08.4	12.553	12.363	0.190	11.544	10.923	10.802	-1.8	-4.6
355	Cr359 J180010+015705	A07	524	SM	18:00:10.54	01:57:05.9	14.878	14.606	0.271	13.711	13.041	12.820	—	0
356	Cr359 J180011+020008	A07	1162	S	18:00:11.62	02:00:08.5	12.323	12.139	0.184	11.403	10.866	10.752	-1.8	0.6
357	Cr359 J180011+020350	A07	1948	S	18:00:11.82	02:03:50.3	12.897	12.671	0.227	11.812	11.066	10.897	-1.8	-8.3
358	Cr359 J180013+015703	A07	525	S	18:00:13.17	01:57:03.5	16.612	16.112	0.500	14.970	14.361	14.023	—	2
359	Cr359 J180013+020637	A07	2616	S	18:00:13.28	02:06:37.1	12.760	12.550	0.209	11.757	11.073	10.955	3.6	-0.6
360	Cr359 J180014+020523	A07	2774	S	18:00:14.91	02:05:23.7	15.709	15.309	0.399	14.314	13.560	13.295	—	0
361	Cr359 J180015+022201	A01	218	S	18:00:15.28	02:22:01.7	17.517	16.994	0.523	—	—	—	—	0
362	Cr359 J180016+021905	A01	840	S	18:00:16.62	02:19:05.7	12.934	12.721	0.213	11.860	11.190	11.059	-0.2	-5.6
363	Cr359 J180016+020314	A07	1826	S	18:00:16.90	02:03:14.5	13.590	13.390	0.200	12.635	11.967	11.879	-1.5	-6.4
364	Cr359 J180017+020113	A07	1387	S	18:00:17.21	02:01:13.5	12.213	12.038	0.175	11.302	10.717	10.642	-9.5	-5.6
365	Cr359 J180017+015801	A07	710	S	18:00:17.38	01:58:01.5	13.838	13.613	0.225	12.765	12.060	11.842	—	2
366	Cr359 J180018+015729	A07	623	SM	18:00:18.24	01:57:29.8	15.775	15.374	0.401	14.355	13.696	13.369	—	0
367	Cr359 J180018+022210	A01	122	S	18:00:18.47	02:22:10.7	12.593	12.376	0.217	11.586	10.982	10.846	2.9	10.2
368	Cr359 J180019+015957	A07	1141	S	18:00:19.04	01:59:57.4	13.726	13.509	0.217	12.684	11.954	11.837	—	0
369	Cr359 J180019+021515	A01	1703	S	18:00:19.16	02:15:16.0	12.808	12.612	0.195	11.759	11.041	10.950	-5.9	-14.6
370	Cr359 J180019+015926	A07	982	S	18:00:19.28	01:59:26.6	12.020	11.859	0.161	11.154	10.633	10.515	-4.4	2.5
371	Cr359 J180021+021240	A01	2287	S	18:00:21.78	02:12:40.4	14.221	13.987	0.235	13.136	12.390	12.190	8.5	1.9
372	Cr359 J180022+021436	A01	3978	ML	18:00:22.07	02:14:36.2	19.007	18.277	0.846	—	15.657	—	—	0
373	Cr359 J180022+021430	A01	1861	S	18:00:22.90	02:14:30.2	12.007	11.763	0.244	10.767	10.020	9.795	-1.5	-5.4
374	Cr359 J180025+021018	A01	2630	S	18:00:25.06	02:10:18.4	12.219	12.065	0.154	11.193	10.495	10.396	5.3	0
375	Cr359 J180025+020757	A07	2326	S	18:00:25.79	02:07:57.9	12.617	12.400	0.217	11.511	10.820	10.643	-3.8	-2.0
376	Cr359 J180026+022000	A01	663	SML	18:00:26.45	02:20:00.1	17.535	16.904	0.631	—	—	—	—	2

Table B.1: continued

Numb	Coll359 J...	FOV	ID	RA	Dec	<i>I</i>	<i>J</i>	<i>H</i>	<i>K_s</i>	μ_{α}	μ_{α}	Flag	M?
377	Cr359 J180027+015500	A07	125	S	18:00:27.93	01:55:00.3	12.981	12.801	11.416	—	—	2	Y+
378	Cr359 J180028+021656	A01	1312	S	18:00:28.84	02:16:56.0	13.674	13.455	12.539	11.780	11.622	-0.9	Y+
379	Cr359 J180031+021446	A01	1791	S	18:00:31.14	02:14:46.2	12.023	11.846	10.956	10.313	10.120	2.1	Y+
380	Cr359 J180032+021449	A01	1787	S	18:00:32.09	02:14:49.3	12.801	12.633	11.667	11.178	11.001	-4.4	Y+
381	Cr359 J180032+021940	A01	715	SM	18:00:32.36	02:19:40.6	14.974	14.597	13.633	12.862	12.627	—	Y+
382	Cr359 J180032+020711	A07	2501	S	18:00:32.82	02:07:11.3	17.752	17.148	16.604	—	15.438	—	Y?
383	Cr359 J180033+015501	A07	128	S	18:00:33.91	01:55:01.1	12.404	12.213	11.90	11.431	10.822	10.696	Y+
384	Cr359 J180033+021605	A01	1484	S	18:00:33.93	02:16:05.8	11.981	11.814	11.667	10.991	10.394	10.261	Y+
385	Cr359 J180034+021839	A01	933	S	18:00:34.82	02:18:39.1	13.521	13.321	12.502	11.842	11.740	11.78	Y+
386	Cr359 J180034+021458	A01	1752	S	18:00:34.98	02:14:58.5	12.803	12.581	11.602	10.782	10.649	-3.8	Y+
387	Cr359 J180037+020648	A07	2569	S	18:00:37.29	02:06:48.2	13.954	13.606	12.685	12.041	11.847	—	Y+
388	Cr359 J180040+015507	A08	217	SML	18:00:40.20	01:55:07.7	17.226	16.653	15.73	—	—	—	Y+
389	Cr359 J180041+022052	A02	325	SML	18:00:41.16	02:20:52.4	17.572	16.975	15.97	—	—	—	Y+
390	Cr359 J180042+022009	A02	1721	L	18:00:42.90	02:20:09.4	21.487	20.639	19.938	—	—	—	Y+
391	Cr359 J180043+022001	A02	490	SM	18:00:43.54	02:20:01.1	16.700	16.203	15.497	15.133	14.259	14.090	Y+
392	Cr359 J180043+015817	A08	911	S	18:00:43.74	01:58:17.2	13.162	12.740	12.422	11.833	11.206	10.944	Y+
393	Cr359 J180043+020733	A08	2750	S	18:00:43.98	02:07:33.7	13.577	13.356	12.222	12.619	11.957	11.839	Y+
394	Cr359 J180044+015500	A08	180	S	18:00:44.44	01:55:00.6	13.849	13.579	12.70	12.799	12.127	12.031	Y+
395	Cr359 J180045+015748	A08	774	S	18:00:45.29	01:57:48.3	12.535	12.371	11.64	11.892	11.497	11.458	Y+
396	Cr359 J180045+020257	A08	2038	S	18:00:45.70	02:02:57.1	17.465	16.933	15.33	—	14.913	—	Y+
397	Cr359 J180045+020911	A02	2375	S	18:00:45.85	02:09:11.5	12.504	12.333	11.71	11.418	10.722	10.609	Y+
398	Cr359 J180046+015606	A08	425	S	18:00:46.62	01:56:06.1	14.130	13.865	12.65	13.124	12.506	12.360	Y+
399	Cr359 J180046+015708	A08	655	S	18:00:46.76	01:57:09.0	13.867	13.624	12.43	12.417	12.356	3.5	Y+
400	Cr359 J180048+021412	A02	4121	M	18:00:48.19	02:14:12.7	14.445	14.318	13.237	13.267	12.576	12.413	Y+
401	Cr359 J180048+015702	A08	643	S	18:00:48.25	01:57:02.6	14.138	13.909	12.29	13.290	12.754	12.619	Y+
402	Cr359 J180048+015451	A08	166	S	18:00:48.68	01:54:51.6	16.035	15.570	14.65	14.748	14.198	13.855	Y+
403	Cr359 J180048+015514	A08	896	L	18:00:48.94	01:55:14.7	19.495	18.861	17.24	—	—	—	Y+
404	Cr359 J180049+020152	A08	1731	S	18:00:49.05	02:01:52.3	13.126	12.880	12.246	12.125	11.507	11.386	Y+
405	Cr359 J180049+015617	A08	494	S	18:00:49.62	01:56:17.6	14.532	14.279	12.53	13.036	12.866	12.125	Y+
406	Cr359 J180050+021026	A02	2645	S	18:00:50.95	02:10:26.4	12.174	12.034	11.40	11.147	10.564	10.428	Y+
407	Cr359 J180051+020028	A08	1395	S	18:00:51.41	02:00:28.2	12.553	12.201	11.352	11.253	10.377	10.201	Y+
408	Cr359 J180051+021854	A02	703	SM	18:00:51.42	02:18:54.6	15.061	14.729	13.332	13.779	13.136	12.945	Y+
409	Cr359 J180052+015829	A08	945	S	18:00:52.78	01:58:29.3	12.705	12.413	12.92	11.604	10.850	10.685	Y+
410	Cr359 J180052+020628	A08	2763	S	18:00:52.82	02:06:28.3	12.929	12.595	13.34	11.612	10.768	10.556	Y+
411	Cr359 J180053+015806	A08	858	S	18:00:53.18	01:58:06.5	11.818	11.668	11.150	11.218	10.873	10.784	Y+
412	Cr359 J180053+015940	A08	1230	S	18:00:53.20	01:59:40.2	13.597	13.350	12.447	12.639	12.027	11.926	Y+
413	Cr359 J180053+015956	A08	1280	S	18:00:53.66	01:59:56.0	13.612	13.387	12.25	12.689	12.144	12.011	Y+
414	Cr359 J180054+015728	A08	713	S	18:00:54.30	01:57:28.7	11.778	11.522	12.056	10.797	10.226	10.107	Y+
415	Cr359 J180054+020339	A08	4947	ML	18:00:54.60	02:03:39.9	18.562	18.028	16.44	—	—	—	Y+
416	Cr359 J180055+020718	A08	2603	S	18:00:55.69	02:07:18.8	13.555	13.259	12.96	12.335	11.507	11.294	Y+
417	Cr359 J180055+020258	A08	2051	SM	18:00:55.86	02:02:58.9	15.418	14.926	14.092	13.952	13.408	13.119	Y+
418	Cr359 J180056+020733	A08	2755	S	18:00:56.89	02:07:53.3	13.025	12.773	12.253	11.942	11.227	11.147	Y+

Table B.1: continued

Numb	Coll359 I...	FOV	ID	RA	Dec	<i>I</i>	<i>z</i>	<i>L-z</i>	<i>J</i>	<i>H</i>	<i>K_s</i>	μ_{α}	μ_{α}	Flag	M?	
419	Cr359 J180057+021441	A02	1586	S	18:00:57.00	02:14:41.4	11.640	11.503	0.137	10.648	9.938	0.3	-6.7	0	Y+	
420	Cr359 J180057+020705	A08	2670	S	18:00:57.11	02:07:05.1	14.222	13.986	0.236	13.187	12.557	12.400	-	-	0	Y+
421	Cr359 J180057+020009	A08	1348	S	18:00:57.24	02:00:09.3	13.614	13.390	0.223	12.720	12.205	12.028	-1.9	-1.6	2	Y+
422	Cr359 J180057+020332	A08	2148	S	18:00:57.50	02:03:32.9	12.238	11.989	0.250	11.222	10.596	10.439	-13.7	5.0	0	Y+
423	Cr359 J180057+015858	A08	1080	S	18:00:57.79	01:58:58.5	14.662	14.399	0.263	13.732	13.071	13.000	-0.5	-11.0	0	Y+
424	Cr359 J180057+015940	A08	1254	S	18:00:57.85	01:59:40.4	16.450	15.943	0.507	15.116	14.402	14.249	-	-	0	Y?
425	Cr359 J180058+020444	A08	2465	S	18:00:58.38	02:04:44.9	13.631	13.414	0.217	12.696	12.068	11.948	-3.8	-3.2	0	Y+
426	Cr359 J180100+021532	A02	3479	M	18:01:00.27	02:15:32.4	16.254	15.891	0.472	14.683	14.088	13.814	-	-	2	Y+
427	Cr359 J180100+015606	A08	424	S	18:01:00.57	01:56:06.7	12.548	12.254	0.293	11.484	10.730	10.580	-2.7	-8.5	0	Y+
428	Cr359 J180101+015503	A08	221	SM	18:01:01.00	01:55:03.1	17.049	16.403	0.646	-	-	-	-	-	0	Y+
429	Cr359 J180101+015519	A08	301	S	18:01:01.22	01:55:19.1	18.097	17.481	0.616	-	-	-	-	-	0	Y+
430	Cr359 J180102+015529	A08	343	S	18:01:02.48	01:55:29.8	17.518	16.922	0.596	-	-	-	-	-	0	Y+
431	Cr359 J180102+020238	A08	1953	S	18:01:02.80	02:02:38.7	13.654	13.429	0.224	12.703	12.138	11.996	-3.0	-6.4	0	Y+
432	Cr359 J180103+021357	A02	1766	S	18:01:03.64	02:13:57.8	11.695	11.554	0.141	10.692	10.091	9.973	-2.7	-10.9	0	Y+
433	Cr359 J180105+022206	A02	30	S	18:01:05.31	02:22:06.2	13.037	12.856	0.181	12.104	11.523	11.442	0.6	-13.7	0	Y+
434	Cr359 J180105+015803	A08	887	S	18:01:05.33	01:58:03.5	14.263	13.993	0.270	13.287	12.602	12.510	-11.0	-5.7	0	Y+
435	Cr359 J180105+021641	A02	1156	S	18:01:05.79	02:16:41.6	12.267	12.126	0.142	11.306	10.697	10.600	-6.3	-13.3	2	Y+
436	Cr359 J180106+022009	A02	408	SM	18:01:06.80	02:20:09.2	14.817	14.437	0.379	13.344	12.597	12.396	-	-	0	Y+
437	Cr359 J180107+020527	A09	3073	S	18:01:07.87	02:05:27.1	13.574	13.356	0.218	12.361	11.574	11.416	-0.9	-17.3	0	Y+
438	Cr359 J180109+020255	A09	1985	S	18:01:09.92	02:02:55.0	15.218	14.860	0.357	13.872	13.262	13.050	-	-	2	Y+
439	Cr359 J180110+015745	A09	753	S	18:01:10.57	01:57:45.3	13.018	12.792	0.226	11.969	11.298	11.144	-5.6	-7.8	2	Y+
440	Cr359 J180111+020044	A09	1430	S	18:01:11.04	02:00:44.1	11.934	11.737	0.196	10.939	10.336	10.208	-5.0	-4.4	0	Y+
441	Cr359 J180111+020956	A03	6644	M	18:01:11.68	02:09:56.3	19.824	19.222	0.712	-	-	-	-	-	0	Y+
442	Cr359 J180112+033644	B06	2623	S	18:01:12.28	03:36:44.1	18.107	17.466	0.691	-	-	-	-	-	0	Y+
443	Cr359 J180113+033101	B06	1286	S	18:01:13.13	03:31:01.3	12.641	12.471	0.220	11.745	11.169	11.013	-1.4	-8.6	2	Y+
444	Cr359 J180113+034756	B00	989	S	18:01:13.75	03:47:56.8	13.247	13.063	0.234	12.207	11.575	11.397	2.3	-13.0	0	Y+
445	Cr359 J180113+021256	A03	2284	S	18:01:13.84	02:12:56.0	11.869	11.674	0.194	10.859	10.122	9.958	-6.9	0.8	0	Y+
446	Cr359 J180114+034155	B00	9500	L	18:01:14.13	03:41:55.1	22.318	21.358	0.021	-	-	-	-	-	0	Y+
447	Cr359 J180114+033442	B06	2194	SM	18:01:14.64	03:34:42.1	14.721	14.437	0.334	13.560	12.887	12.691	-	-	0	Y+
448	Cr359 J180115+033501	B06	5098	M	18:01:15.97	03:35:01.6	16.741	16.327	0.475	15.265	14.497	14.127	-	-	0	Y+
449	Cr359 J180116+015507	A09	141	S	18:01:16.16	01:55:07.6	12.632	12.347	0.286	11.479	10.833	10.658	0.3	-0.3	2	Y+
450	Cr359 J180116+020705	A09	2727	S	18:01:16.17	02:07:05.3	12.519	12.341	0.178	11.474	10.843	10.711	-0.9	-0.7	2	Y+
451	Cr359 J180116+034218	B00	2296	S	18:01:16.67	03:42:18.1	13.690	13.467	0.274	12.538	11.805	11.592	-1.8	3.1	0	Y+
452	Cr359 J180116+035112	B00	235	S	18:01:16.72	03:51:12.4	11.820	11.662	0.209	10.849	10.236	10.144	-4.7	-1.6	0	Y+
453	Cr359 J180117+032540	B06	131	S	18:01:17.61	03:25:40.3	13.153	12.846	0.357	11.796	10.858	10.603	15.5	-3.6	0	Y+
454	Cr359 J180117+015818	A09	869	S	18:01:17.62	01:58:18.9	11.749	11.571	0.178	10.901	10.344	10.287	2.4	-1.5	0	Y+
455	Cr359 J180117+034004	B00	2521	S	18:01:17.72	03:40:04.9	12.783	12.581	0.252	11.638	10.948	10.736	9.2	-17.6	2	Y+
456	Cr359 J180117+020412	A09	2305	S	18:01:17.77	02:04:12.5	13.210	13.009	0.201	12.198	11.520	11.379	-6.1	-11.2	0	Y+
457	Cr359 J180117+021057	A03	3338	S	18:01:17.77	02:10:58.0	12.327	12.098	0.229	11.130	10.335	10.161	-7.7	-9.1	0	Y+
458	Cr359 J180118+032501	B06	2	S	18:01:18.68	03:25:01.1	12.747	12.523	0.274	11.767	11.143	10.996	-12.8	-6.7	0	Y+
459	Cr359 J180120+021826	A03	928	S	18:01:20.44	02:18:26.5	12.405	12.089	0.315	10.992	10.070	9.841	-4.8	-3.5	0	Y+
460	Cr359 J180120+015558	A09	350	S	18:01:20.55	01:55:58.2	14.047	13.810	0.237	13.125	12.534	12.424	-6.3	-6.4	0	Y+

Table B.1: continued

Numb	Coll359 J...	FOV	ID	RA	Dec	<i>I</i>	<i>J</i>	<i>H</i>	<i>K_s</i>	μ_{α}	μ_{δ}	Flag	M?
461	Cr359 J180120+020130	A09	1604	S	18:01:20.81	02:01:30.1	12.317	0.243	11.183	10.425	—	—	2 Y+
462	Cr359 J180121+0121958	A03	1244	M	18:01:21.02	02:19:58.8	15.918	15.482	14.308	13.561	13.343	—	3 Y+
463	Cr359 J180121+015613	A09	411	S	18:01:21.51	01:56:13.1	13.885	13.652	0.233	12.879	12.191	12.099	-3.8 -2.4 0 Y+
464	Cr359 J180122+022210	A03	1	S	18:01:22.08	02:22:10.5	12.882	12.581	0.301	11.733	10.923	10.758	-6.3 -5.6 2 Y+
465	Cr359 J180122+015924	A09	1153	S	18:01:22.50	01:59:24.6	13.438	13.222	0.216	12.496	11.859	11.774	-5.6 4.3 0 Y+
466	Cr359 J180122+034137	B00	2988	S	18:01:22.67	03:41:37.3	13.461	13.063	0.448	12.056	11.453	11.270	— — 0 Y+
467	Cr359 J180123+021935	A03	680	S	18:01:23.25	02:19:35.2	18.211	17.619	0.592	—	—	—	— 0 Y+
468	Cr359 J180123+034536	B00	1493	S	18:01:23.42	03:45:36.2	12.392	12.247	0.195	11.467	10.907	10.743	-0.9 -11.2 0 Y+
469	Cr359 J180123+033017	B06	2712	M	18:01:23.86	03:30:17.9	16.763	16.349	0.474	15.299	14.563	14.258	— — 0 Y+
470	Cr359 J180124+015453	A09	145	S	18:01:24.94	01:54:53.9	17.962	17.414	0.548	—	—	—	— 0 Y+
471	Cr359 J180125+022118	A03	199	S	18:01:25.59	02:21:18.8	12.806	12.580	0.226	11.889	11.259	11.161	0.2 0.2 0 Y+
472	Cr359 J180125+020220	A09	1822	S	18:01:25.92	02:02:20.2	12.621	12.365	0.256	11.501	10.748	10.548	-3.2 -8.1 0 Y+
473	Cr359 J180126+020120	A09	1580	S	18:01:26.23	02:01:20.4	12.283	12.075	0.207	11.272	10.685	10.547	-6.9 -7.4 0 Y+
474	Cr359 J180126+021311	A03	2283	SM	18:01:26.40	02:13:11.2	15.172	14.866	0.306	13.878	13.290	12.966	— — 0 Y+
475	Cr359 J180126+022027	A03	408	S	18:01:26.44	02:20:27.7	12.863	12.681	0.182	11.998	11.423	11.327	-6.0 -6.9 0 Y+
476	Cr359 J180127+020035	A09	1465	SM	18:01:27.21	02:00:35.9	16.236	15.752	0.485	14.713	13.987	13.710	— — 0 Y+
477	Cr359 J180128+015708	A09	606	S	18:01:28.00	01:57:08.8	12.268	12.013	0.255	11.202	10.537	10.351	— — 0 Y+
478	Cr359 J180128+022038	A03	355	S	18:01:28.58	02:20:38.9	12.337	12.114	0.223	11.315	10.669	10.542	-6.9 -5.1 0 Y+
479	Cr359 J180129+021605	A03	1509	S	18:01:29.02	02:16:05.9	12.183	12.001	0.182	11.229	10.622	10.424	-2.6 -5.7 0 Y+
480	Cr359 J180129+035103	B00	263	S	18:01:29.76	03:51:03.4	12.332	12.184	0.197	11.377	10.868	10.692	-3.3 -0.6 2 Y+
481	Cr359 J180130+015759	A09	867	S	18:01:30.19	01:57:59.8	17.411	16.864	0.547	—	—	—	— 0 Y+
482	Cr359 J180130+015759	A09	867	S	18:01:30.19	01:57:59.8	17.411	16.864	0.547	—	—	—	— 0 Y+
483	Cr359 J180130+033423	B06	2132	S	18:01:30.77	03:34:23.5	13.463	13.271	0.242	12.359	11.609	11.410	0.3 -5.6 0 Y+
484	Cr359 J180131+015620	A09	426	S	18:01:31.23	01:56:20.1	12.299	12.038	0.262	11.203	10.530	10.331	-9.6 -5.8 2 Y+
485	Cr359 J180131+033207	B06	1589	S	18:01:31.92	03:32:07.6	12.249	12.049	0.250	11.113	10.353	10.217	-11.5 -4.6 0 Y+
486	Cr359 J180132+021929	A03	644	S	18:01:32.42	02:19:29.7	13.410	13.207	0.203	12.439	11.840	11.669	3.9 -5.9 2 Y+
487	Cr359 J180134+020239	A09	1913	S	18:01:34.34	02:02:39.5	12.304	12.080	0.224	11.236	10.655	10.426	— — 2 Y+
488	Cr359 J180135+033245	B06	1727	S	18:01:35.98	03:32:45.0	12.099	12.099	0.207	11.248	10.569	10.422	— — 0 Y+
489	Cr359 J180136+032837	B06	820	SM	18:01:36.36	03:28:38.0	14.285	14.555	0.348	13.583	12.907	12.652	— — 0 Y+
490	Cr359 J180136+032459	B06	36	S	18:01:36.55	03:24:60.0	13.854	13.633	0.272	12.733	12.004	11.817	1.4 -7.9 2 Y+
491	Cr359 J180136+015932	A10	1148	S	18:01:36.67	01:59:32.7	12.174	11.954	0.220	11.214	10.563	10.469	-2.9 7.7 0 Y+
492	Cr359 J180137+020948	A04	6771	M	18:01:37.12	02:09:48.6	20.326	19.622	0.815	—	—	—	— 3 Y+
493	Cr359 J180137+021813	A04	841	S	18:01:37.95	02:18:14.0	12.210	12.009	0.201	11.032	10.232	10.059	3.6 1.8 0 Y+
494	Cr359 J180137+035021	B00	426	S	18:01:37.98	03:50:21.6	12.575	12.415	0.211	11.541	10.866	10.729	-5.4 0.1 0 Y+
495	Cr359 J180138+033257	B06	1811	SM	18:01:38.60	03:32:58.0	15.564	15.217	0.398	14.249	13.607	13.356	— — 0 Y+
496	Cr359 J180139+015805	A10	871	S	18:01:39.18	01:58:05.2	16.322	15.838	0.484	14.875	14.149	13.946	— — 0 Y+
497	Cr359 J180139+035009	B00	1163	M	18:01:39.37	03:50:09.4	18.576	18.050	0.586	—	—	—	— 0 Y+
498	Cr359 J180140+020641	A10	2773	S	18:01:40.62	02:06:41.6	13.437	13.237	0.200	12.512	11.870	11.837	-4.5 -0.9 2 Y+
499	Cr359 J180141+020525	A10	3010	S	18:01:41.50	02:05:25.4	12.118	11.860	0.258	10.979	10.221	10.016	-7.8 -5.5 2 Y+
500	Cr359 J180141+032446	B07	41	SM	18:01:41.57	03:24:46.8	15.533	15.124	0.459	14.229	13.544	13.182	— — 0 Y+
501	Cr359 J180141+021841	A04	752	S	18:01:41.59	02:18:41.3	12.776	12.593	0.183	11.699	10.993	10.819	-1.9 -2.0 0 Y+
502	Cr359 J180142+020400	A10	2261	SM	18:01:42.88	02:04:00.2	14.216	13.863	0.353	13.037	12.282	12.050	-44.7 16.8 0 Y+

Table B.1: continued

Numb	Coll359 J...	FOV	ID	RA	Dec	<i>I</i>	<i>L-z</i>	<i>J</i>	<i>H</i>	<i>K_s</i>	μ_{α}	μ_{α}	Flag	M?
503	Cr359 J180142+032658	B07	1122	M	18:01:42.93	03:26:58.5	14.929	14.682	0.307	13.767	13.003	12.860	—	2 Y+
504	Cr359 J180143+033921	B01	2750	S	18:01:43.12	03:39:21.8	15.147	14.836	0.361	13.828	13.164	13.015	—	0 Y+
505	Cr359 J180143+032907	B07	1059	S	18:01:43.75	03:29:07.9	12.607	12.431	0.226	11.622	10.976	10.855	-5.1	-3.8 0 Y+
506	Cr359 J180144+021026	A04	2885	S	18:01:44.31	02:10:26.5	13.777	13.513	0.265	12.569	11.896	11.663	0.8	-9.1 0 Y+
507	Cr359 J180144+021555	A04	1358	S	18:01:44.61	02:15:55.2	11.831	11.644	0.187	10.767	10.009	9.843	-0.3	-5.7 0 Y+
508	Cr359 J180144+021432	A04	1664	S	18:01:44.64	02:14:32.2	12.097	11.941	0.156	11.511	10.373	10.373	2.6	-10.3 0 Y+
509	Cr359 J180144+034550	B01	3430	ML	18:01:44.99	03:45:50.7	19.414	18.768	0.706	—	—	—	—	3 Y+
510	Cr359 J180145+020007	A10	1334	S	18:01:45.01	02:00:07.7	13.400	13.155	0.245	12.352	11.661	11.553	-4.1	-15.8 2 Y+
511	Cr359 J180145+034655	B01	1449	SM	18:01:45.35	03:46:55.4	15.602	15.219	0.433	14.163	13.450	13.226	—	2 Y+
512	Cr359 J180145+032755	B07	763	S	18:01:45.95	03:27:55.3	12.723	12.546	0.226	11.773	11.007	10.915	-6.1	-0.4 0 Y+
513	Cr359 J180146+020633	A10	2762	S	18:01:46.24	02:06:33.9	13.730	13.526	0.204	12.792	12.244	12.156	-5.3	-7.5 0 Y+
514	Cr359 J180146+020200	A10	1758	S	18:01:46.42	02:02:00.0	12.478	12.253	0.225	11.512	10.878	10.785	-3.6	-11.9 0 Y+
515	Cr359 J180147+032650	B07	565	SM	18:01:47.21	03:26:50.1	17.998	17.356	0.692	—	—	15.651	—	0 Y+
516	Cr359 J180149+015608	A10	393	S	18:01:49.14	01:56:08.1	12.899	12.698	0.201	12.157	11.712	11.588	-4.2	-1.1 0 Y+
517	Cr359 J180149+035214	B01	165	M	18:01:49.15	03:52:14.5	19.095	18.502	0.653	—	—	—	—	0 Y+
518	Cr359 J180150+020518	A10	3061	S	18:01:50.48	02:05:18.5	15.063	14.721	0.342	13.871	13.129	12.949	—	— 0 Y+
519	Cr359 J180150+015449	A10	130	S	18:01:50.73	01:54:49.8	15.107	14.734	0.373	13.947	13.224	13.011	—	— 0 Y+
520	Cr359 J180150+035023	B01	508	S	18:01:50.94	03:50:23.4	13.051	12.861	0.240	12.069	11.406	11.312	-3.9	-6.6 2 Y+
521	Cr359 J180151+020923	A04	2691	S	18:01:51.28	02:09:23.1	13.161	12.866	0.295	11.950	11.289	11.095	—	— 0 Y+
522	Cr359 J180151+034559	B01	1629	S	18:01:51.71	03:45:59.8	12.879	12.662	0.266	11.714	10.962	10.799	-1.7	-9.5 2 Y+
523	Cr359 J180152+022137	A04	104	S	18:01:52.07	02:21:37.9	14.546	14.301	0.245	13.457	12.702	12.494	10.2	0.3 0 Y+
524	Cr359 J180152+020011	A10	5642	L	18:01:52.92	02:00:11.4	19.603	18.879	0.814	—	—	—	—	3 Y+
525	Cr359 J180153+015855	A10	1063	S	18:01:53.05	01:58:55.8	12.522	12.311	0.210	11.692	11.204	11.118	-9.6	-31.1 0 Y+
526	Cr359 J180153+020150	A10	1757	S	18:01:53.48	02:01:50.5	13.774	13.544	0.230	12.848	12.244	12.118	—	— 0 Y+
527	Cr359 J180153+020406	A10	2283	S	18:01:53.52	02:04:06.7	13.383	13.181	0.201	12.569	11.981	11.883	-1.2	-9.4 0 Y+
528	Cr359 J180154+022027	A04	328	S	18:01:54.20	02:20:27.5	12.332	12.172	0.161	11.364	10.693	10.582	-1.8	-5.8 2 Y+
529	Cr359 J180154+034043	B01	3090	S	18:01:54.48	03:40:43.5	12.435	12.272	0.212	11.462	10.844	10.682	-0.6	-6.6 0 Y+
530	Cr359 J180154+015624	A10	450	S	18:01:54.55	01:56:24.6	12.383	12.127	0.256	11.460	10.805	10.653	-10.1	-2.1 0 Y+
531	Cr359 J180154+020916	A04	2664	S	18:01:54.57	02:09:16.8	12.579	12.426	0.153	11.600	10.973	10.860	—	0 Y+
532	Cr359 J180155+015945	A10	1260	S	18:01:55.41	01:59:45.6	13.411	13.160	0.251	12.459	11.801	11.667	-0.6	-8.7 0 Y+
533	Cr359 J180155+015549	A10	350	S	18:01:55.74	01:55:49.3	13.957	13.722	0.235	13.055	12.488	12.366	-3.5	-7.0 0 Y+
534	Cr359 J180156+015723	A10	711	S	18:01:56.16	01:57:23.6	13.811	13.504	0.307	12.749	12.093	11.882	—	— 0 Y+
535	Cr359 J180156+021827	A04	770	S	18:01:56.19	02:18:27.8	12.943	12.700	0.242	11.749	10.909	10.717	-4.4	-0.3 0 Y+
536	Cr359 J180156+022116	A04	143	S	18:01:56.30	02:21:16.1	12.860	12.664	0.196	11.877	11.249	11.064	8.3	-8.5 2 Y+
537	Cr359 J180156+015814	A10	916	S	18:01:56.44	01:58:44.4	14.846	14.496	0.350	13.717	13.026	12.815	—	— 3 Y+
538	Cr359 J180156+020115	A10	1620	S	18:01:56.73	02:01:15.5	13.017	12.773	0.244	12.053	11.415	11.291	-1.9	-11.2 0 Y+
539	Cr359 J180156+033447	B07	2524	S	18:01:56.94	03:34:47.5	17.040	16.500	0.590	15.158	14.487	14.134	—	— 0 Y+
540	Cr359 J180157+021305	A04	2008	S	18:01:57.93	02:13:05.0	11.792	11.578	0.214	10.661	9.974	9.718	—	— 2 Y+
541	Cr359 J180158+034410	B01	2109	S	18:01:58.13	03:44:10.5	12.439	12.289	0.201	11.407	10.746	10.628	-8.0	-4.0 0 Y+
542	Cr359 J180158+021354	A04	1822	S	18:01:58.18	02:13:54.7	12.684	12.500	0.184	11.659	11.042	10.878	-14.4	-4.8 0 Y+
543	Cr359 J180158+021307	A04	2004	S	18:01:58.36	02:13:07.0	12.783	12.599	0.184	11.754	11.122	10.945	—	— 2 Y+
544	Cr359 J180158+015812	A10	897	S	18:01:58.43	01:58:12.2	13.294	13.041	0.253	12.334	11.771	11.572	-3.8	-3.1 0 Y+

Table B.1: continued

Numb	Coll359 J... Cr359 J180158+033621	FOV B07	ID 6467	RA M	Dec 18:01:58.75	<i>I</i>	<i>J</i>	<i>H</i>	<i>K_s</i>	μ_{α}	μ_{α}	Flag	M?
545	Cr359 J180158+021856	A04	679	S	18:01:58.93	02:18:56.5	13.016	12.836	0.180	12.024	11.321	-1.7	-8.6
546	Cr359 J180159+020640	A10	2751	S	18:01:59.05	02:06:40.8	13.590	13.372	0.218	12.669	12.122	11.975	-
547	Cr359 J180159+022001	A04	428	S	18:01:59.38	02:20:01.4	12.427	12.261	0.166	11.464	10.842	10.665	5.6
548	Cr359 J180200+015609	A10	437	SM	18:02:00.19	01:56:09.6	16.060	15.541	0.518	14.602	13.878	13.648	-
549	Cr359 J180200+015609	A10	1649	S	18:02:00.29	03:45:53.0	12.712	12.541	0.222	11.637	10.982	10.768	-9.6
550	Cr359 J180200+034553	B01	1389	S	18:02:01.02	02:00:18.4	13.706	13.441	0.265	12.642	11.987	11.820	-3.3
551	Cr359 J180201+020018	A10	2162	S	18:02:02.08	02:03:48.3	11.924	11.590	0.334	10.676	9.816	9.627	-2.6
552	Cr359 J180202+020348	A10	743	L	18:02:02.47	02:21:09.0	22.045	21.150	0.985	-	-	-	-5.4
553	Cr359 J180202+022108	A04	1035	S	18:02:03.02	03:48:17.2	12.505	12.334	0.222	11.518	10.834	10.681	-
554	Cr359 J180203+034817	B01	6069	M	18:02:03.35	02:06:42.2	19.867	19.210	0.768	-	-	-	0
555	Cr359 J180203+020642	A10	73	S	18:02:04.16	01:54:33.6	13.625	13.335	0.290	12.475	11.727	11.562	-2.7
556	Cr359 J180204+015433	A11	197	S	18:02:04.18	01:55:05.5	13.730	13.505	0.224	12.716	12.204	11.963	-1.9
557	Cr359 J180204+015505	A11	2589	S	18:02:08.70	02:06:37.6	12.531	12.353	0.178	11.576	10.987	10.813	-0.5
558	Cr359 J180208+020637	A11	1180	L	18:02:11.02	01:55:14.1	20.761	19.984	0.868	-	-	-	-4.8
559	Cr359 J180211+015514	A11	2675	M	18:02:11.16	03:47:27.8	20.168	19.376	0.852	-	-	-	0
560	Cr359 J180211+034727	B02	3269	SM	18:02:11.38	03:35:47.8	16.851	16.347	0.554	15.172	14.688	14.191	-
561	Cr359 J180211+035457	B08	2273	S	18:02:11.48	02:13:20.0	11.999	11.746	0.254	10.700	9.783	9.583	-4.4
562	Cr359 J180211+021320	A05	916	S	18:02:12.12	02:18:41.8	11.558	11.331	0.227	10.368	9.576	9.350	-6.4
563	Cr359 J180212+021841	A05	1247	S	18:02:12.17	01:59:50.9	13.543	13.335	0.208	12.496	11.889	11.742	-6.0
564	Cr359 J180212+015950	A11	2060	ML	18:02:12.46	03:28:25.0	19.218	18.594	0.684	-	-	-	-8.5
565	Cr359 J180212+032825	B08	1928	S	18:02:12.79	02:02:50.3	15.559	15.215	0.344	14.266	13.597	13.416	-
566	Cr359 J180212+020250	A11	203	S	18:02:13.44	01:55:02.8	14.498	14.260	0.237	13.564	13.003	12.842	-9.6
567	Cr359 J180213+015502	A11	2943	S	18:02:13.59	02:05:03.6	14.549	14.243	0.306	13.355	12.643	12.426	-
568	Cr359 J180213+020503	A11	1014	SM	18:02:13.74	02:18:35.6	16.057	15.614	0.443	14.537	14.031	13.882	-
569	Cr359 J180213+021835	A05	246	S	18:02:14.50	01:55:15.3	14.292	13.996	0.295	13.110	12.327	12.212	-0.6
570	Cr359 J180214+015515	A11	4196	M	18:02:15.07	03:44:28.1	15.660	15.371	0.349	14.425	13.650	13.426	-
571	Cr359 J180215+034428	B02	2300	S	18:02:15.32	02:04:23.7	17.226	16.692	0.534	-	-	-	0
572	Cr359 J180215+020423	A11	1414	S	18:02:15.52	02:00:39.6	12.757	12.488	0.269	11.563	10.790	10.570	1.8
573	Cr359 J180215+020039	A11	3094	S	18:02:16.41	02:09:48.9	12.131	11.978	0.153	11.145	10.499	10.353	-3.3
574	Cr359 J180216+020948	A05	196	S	18:02:17.61	01:55:05.6	13.734	13.513	0.221	12.852	12.241	12.114	-
575	Cr359 J180217+015505	A11	3497	ML	18:02:20.97	02:00:37.5	19.663	18.959	0.813	-	-	-	0
576	Cr359 J180217+032436	B08	2	S	18:02:17.78	03:24:36.4	14.116	13.822	0.344	13.055	12.476	12.222	-
577	Cr359 J180218+034103	B02	3058	SM	18:02:18.38	03:41:03.0	15.684	15.307	0.428	14.175	13.703	13.370	-
578	Cr359 J180220+020052	A11	1501	S	18:02:20.13	02:00:52.4	17.121	16.553	0.568	-	-	-	0
579	Cr359 J180220+020037	A11	2283	S	18:02:23.27	02:04:26.3	12.759	12.573	0.186	11.783	11.165	11.033	0.9
580	Cr359 J180222+032935	B08	1344	SM	18:02:22.05	03:29:35.1	16.242	15.722	0.570	14.442	13.831	13.602	-
581	Cr359 J180222+032658	B08	618	S	18:02:22.56	03:26:58.4	12.155	11.893	0.312	10.892	10.120	9.916	-2.4
582	Cr359 J180223+020659	A11	2604	S	18:02:23.09	02:06:39.7	12.469	12.261	0.208	11.401	10.716	10.477	-
583	Cr359 J180223+020510	A11	10063	L	18:02:23.22	02:05:10.6	18.861	18.191	0.760	-	-	-	3
584	Cr359 J180223+020426	A11	2283	S	18:02:23.27	02:04:26.3	12.759	12.573	0.186	14.420	13.770	13.507	-5.4
585	Cr359 J180223+033027	B08	1588	SM	18:02:23.41	03:30:27.2	15.977	15.554	0.473	-	-	-	0
586	Cr359 J180223+015827	A11	3875	L	18:02:23.75	01:58:27.8	21.717	20.831	0.976	-	-	-	3

Table B.1: continued

Numb	Coll359 J...	FOV	ID	RA	Dec	<i>I</i>	<i>z</i>	<i>L-z</i>	<i>J</i>	<i>H</i>	<i>K_s</i>	μ_{α}	μ_{α}	Flag	M?	
587	Cr359 J180224+015758	A11	846	S	18:02:24.06	01:57:58.7	14.208	13.963	0.245	13.115	12.308	—	—	2	Y+	
588	Cr359 J180225+032822	B08	1031	S	18:02:25.39	03:28:22.5	12.303	12.131	0.222	11.245	10.575	10.396	-8.0	-1.4	0	Y+
589	Cr359 J180226+034655	B02	1320	S	18:02:26.43	03:46:56.0	16.890	0.618	—	—	—	—	—	—	0	Y+
590	Cr359 J180227+015818	A11	893	S	18:02:27.67	01:58:18.6	12.142	11.887	0.256	11.023	10.280	10.098	-3.9	-5.1	0	Y+
591	Cr359 J180229+035200	B02	64	S	18:02:29.29	03:52:00.8	13.212	13.012	0.250	12.236	11.519	11.421	1.7	-2.3	0	Y+
592	Cr359 J180229+034717	B02	1211	SM	18:02:29.84	03:47:17.4	15.268	14.915	0.404	13.920	13.346	13.090	—	—	0	Y+
593	Cr359 J180230+015723	A11	695	S	18:02:30.27	01:57:23.2	12.835	12.627	0.208	11.902	11.306	11.237	—	—	0	Y+
594	Cr359 J180230+020409	A11	2210	S	18:02:30.79	02:04:09.8	12.718	12.555	0.163	11.833	11.204	11.099	-7.1	-16.7	2	Y+
595	Cr359 J180231+034733	B02	1116	S	18:02:31.04	03:47:33.2	12.086	11.948	0.188	11.143	10.546	10.409	5.6	-3.3	3	Y+
596	Cr359 J180233+032736	B08	878	S	18:02:33.23	03:27:36.5	14.413	14.171	0.292	13.150	12.426	12.232	—	—	0	Y+
597	Cr359 J180233+034701	B02	4967	L	18:02:33.35	03:47:01.8	19.433	18.650	0.843	—	—	—	—	—	3	Y+
598	Cr359 J180233+034701	B02	2903	ML	18:02:33.35	03:47:01.9	19.394	18.645	0.809	—	—	—	—	—	0	Y+
599	Cr359 J180234+034528	B02	3680	M	18:02:34.54	03:45:28.5	19.152	18.577	0.635	—	—	—	—	—	3	Y+
600	Cr359 J180235+035103	B02	252	S	18:02:35.46	03:51:03.2	12.417	12.253	0.214	11.432	10.784	10.671	-1.2	-9.2	0	Y+
601	Cr359 J180240+033413	B09	5487	M	18:02:40.24	03:34:13.3	16.981	16.551	0.491	—	—	—	—	—	0	Y+
602	Cr359 J180240+033539	B09	3105	S	18:02:40.57	03:35:39.2	12.466	12.266	0.250	11.260	10.441	10.214	-8.5	-6.1	0	Y+
603	Cr359 J180242+034402	B03	4866	ML	18:02:42.53	03:44:02.8	18.275	17.766	0.569	—	—	—	—	—	0	Y+
604	Cr359 J180244+034456	B03	4339	ML	18:02:44.59	03:44:56.7	18.679	18.138	0.601	—	—	—	—	—	3	Y+
605	Cr359 J180245+034927	B03	809	S	18:02:45.32	03:49:27.4	12.948	12.738	0.260	11.876	11.137	10.994	-6.1	-2.5	0	Y+
606	Cr359 J180251+034835	B03	2115	M	18:02:51.28	03:48:35.4	16.725	16.312	0.473	—	—	—	—	—	3	Y+
607	Cr359 J180252+033030	B09	3357	M	18:02:52.37	03:30:30.1	14.694	14.466	0.288	13.610	12.907	12.704	—	—	0	Y+
608	Cr359 J180253+032656	B09	611	S	18:02:53.60	03:26:56.8	12.373	12.197	0.226	11.279	10.562	10.414	-3.0	-3.6	0	Y+
609	Cr359 J180253+035159	B03	44	S	18:02:53.69	03:51:59.8	12.906	12.683	0.273	11.928	11.209	11.088	-9.3	-4.0	0	Y+
610	Cr359 J180254+035027	B03	549	SM	18:02:54.42	03:50:27.1	15.761	15.377	0.434	14.452	13.773	13.509	—	—	0	Y+
611	Cr359 J180257+034942	B03	730	S	18:02:57.77	03:49:42.4	12.484	12.276	0.258	11.451	10.659	10.510	-5.0	-7.3	2	Y+
612	Cr359 J180259+035027	B03	555	SM	18:02:59.04	03:50:27.2	17.166	16.633	0.582	—	—	—	—	—	0	Y+
613	Cr359 J180259+033555	B09	6894	M	18:02:59.73	03:55:55.4	17.164	16.654	0.570	—	—	—	—	—	2	Y+
614	Cr359 J180303+032607	B09	985	M	18:03:03.57	03:26:07.8	14.856	14.638	0.258	13.752	12.956	12.800	-5.9	3.2	2	Y+
615	Cr359 J180305+035059	B03	1155	L	18:03:05.01	03:50:59.3	21.857	20.979	0.939	—	—	—	—	—	3	NM
616	Cr359 J180309+032632	B10	491	S	18:03:09.70	03:26:32.9	13.072	12.880	0.243	12.159	11.543	11.444	-0.3	-8.9	0	Y+
617	Cr359 J180310+032427	B10	47	SM	18:03:10.56	03:24:27.7	17.498	16.912	0.636	—	—	—	—	—	0	Y+
618	Cr359 J180311+033205	B10	1917	SM	18:03:11.52	03:32:05.9	14.697	14.315	0.432	13.327	12.736	12.438	—	—	0	Y+
619	Cr359 J180315+033059	B10	1662	S	18:03:15.50	03:30:60.0	12.556	12.311	0.295	11.427	10.647	10.445	-1.4	-3.0	0	Y+
620	Cr359 J180315+032636	B10	517	S	18:03:15.70	03:26:36.9	12.449	12.253	0.246	11.511	10.961	10.803	-2.1	-0.3	0	Y+
621	Cr359 J180318+034141	B04	2583	S	18:03:18.06	03:41:42.0	12.589	12.426	0.213	11.376	10.591	10.347	4.1	1.4	2	Y+
622	Cr359 J180319+032753	B10	3883	L	18:03:19.46	03:27:53.1	20.612	19.818	0.854	—	—	—	—	—	3	Y+
623	Cr359 J180323+033016	B10	1527	S	18:03:23.82	03:30:16.9	14.678	14.434	0.294	13.629	13.013	12.739	-4.5	4.6	0	Y+
624	Cr359 J180324+033207	B10	1956	S	18:03:24.26	03:32:07.9	13.610	13.410	0.250	12.626	12.008	11.835	-7.1	-7.6	0	Y+
625	Cr359 J180325+034003	B04	3046	SM	18:03:25.20	03:40:03.5	14.917	14.642	0.325	13.626	13.009	12.742	—	—	0	Y+
626	Cr359 J180332+033556	B10	3209	SM	18:03:32.25	03:35:56.6	14.733	14.421	0.361	13.506	12.831	12.601	8.0	0.4	0	Y+
627	Cr359 J180332+034326	B04	2183	SM	18:03:32.35	03:43:26.7	14.778	14.518	0.310	13.489	12.835	12.614	—	0	Y+	
628	Cr359 J180334+032556	B11	396	S	18:03:34.56	03:25:57.0	16.119	15.696	0.473	14.628	13.987	13.709	—	—	0	Y+

Table B.1: continued

Numb	Coll359 J...:	FOV	ID	RA	Dec	<i>I</i>	<i>J</i>	<i>H</i>	<i>K_s</i>	μ_{α}	μ_{α}	Flag	M?					
629	Cr359 J180334+032543	B11	340	S	18:03:34.73	03:25:43.9	14.682	14.413	0.320	13.546	12.818	-1.9	5.1	2	Y+			
630	Cr359 J180335+033344	B11	2246	SM	18:03:35.21	03:33:45.0	17.353	16.817	0.586	-	-	-	-	0	Y+			
631	Cr359 J180338+034813	B05	3734	L	18:03:38.29	03:48:13.5	20.242	19.490	0.812	-	-	-	-	1	Y+			
632	Cr359 J180340+034544	B05	1924	S	18:03:40.64	03:45:44.8	14.042	13.778	0.314	12.732	12.141	11.952	-	2	Y+			
633	Cr359 J180341+033421	B11	5375	M	18:03:41.16	03:34:21.1	16.623	16.202	0.481	15.093	14.494	14.281	-	3	Y+			
634	Cr359 J180342+032123	B11	7730	L	18:03:42.43	03:32:13.8	20.257	19.492	0.825	-	-	-	-	3	Y+			
635	Cr359 J180343+033137	B11	3969	M	18:03:43.45	03:31:38.0	17.720	17.166	0.614	-	-	-	-	2	Y?			
636	Cr359 J180347+033258	B11	4694	M	18:03:47.78	03:32:58.9	19.404	18.781	0.683	-	-	-	-	0	Y+			
637	Cr359 J180347+034805	B05	1203	S	18:03:47.91	03:48:05.2	12.780	12.570	0.260	11.571	10.803	10.603	-3.8	-8.0	0	Y+		
638	Cr359 J180349+032450	B11	148	S	18:03:49.31	03:24:50.4	12.635	12.412	0.273	11.452	10.783	10.610	-	0	Y+			
639	Cr359 J180351+032945	B11	2938	M	18:03:51.72	03:29:45.4	18.234	17.735	0.559	-	-	-	-	0	Y+			
640	Cr359 J180353+032450	B11	179	S	18:03:53.89	03:24:50.4	15.136	14.829	0.357	13.781	13.107	12.833	-	0	Y+			
641	Cr359 J180355+033133	B11	3940	M	18:03:55.98	03:31:33.6	17.781	17.299	0.542	-	-	-	-	3	Y+			
642	Cr359 J180357+032844	B11	1047	S	18:03:57.59	03:28:44.4	12.672	12.501	0.221	11.660	10.926	10.757	-	2	Y+			
643	Cr359 J180357+032705	B11	679	SM	18:03:57.61	03:27:05.8	15.049	14.705	0.393	13.764	13.045	12.783	-	0	Y+			
644	Cr359 J180401+033407	B11	9437	L	18:04:01.65	03:34:07.2	21.897	20.973	0.984	-	-	-	-	1	Y+			
645	Cr359 J180432+031617	E06	250	S	18:04:32.45	03:16:17.8	14.800	14.470	0.310	-	-	-	-	0	Y?			
646	Cr359 J180432+032706	E06	3290	S	18:04:32.53	03:27:06.6	15.140	14.734	0.386	13.856	13.217	12.985	-	0	Y+			
647	Cr359 J180432+031800	E06	679	S	18:04:32.70	03:18:00.9	13.873	13.598	0.254	12.954	12.335	12.238	1.5	-5.1	0	Y+		
648	Cr359 J180432+031713	E06	488	SM	18:04:32.99	03:17:13.1	17.155	16.394	0.741	-	-	-	-	0	Y+			
649	Cr359 J180433+032822	E06	3124	SM	18:04:33.39	03:28:22.7	17.734	17.108	0.606	-	-	-	-	0	Y+			
650	Cr359 J180433+032128	E06	1631	S	18:04:33.46	03:21:28.6	12.710	12.551	0.138	12.037	11.697	11.606	-3.8	-14.9	0	Y+		
651	Cr359 J180433+033912	E00	2364	M	18:04:33.65	03:39:12.5	18.331	17.828	0.572	-	-	-	-	0	Y+			
652	Cr359 J180434+033912	E00	1013	S	18:04:34.17	03:39:12.6	14.314	14.075	0.220	13.359	12.805	12.666	-7.1	-6.7	0	Y+		
653	Cr359 J180434+034156	E00	257	S	18:04:34.64	03:41:56.9	13.843	13.530	0.292	12.802	12.224	12.074	-	0	Y+			
654	Cr359 J180434+031556	E06	133	S	18:04:34.80	03:15:57.0	13.146	12.734	0.392	-	-	-	-	0	Y+			
655	Cr359 J180434+033834	E00	1183	S	18:04:34.99	03:38:34.7	13.333	13.104	0.210	12.468	11.927	11.787	-12.9	-3.5	0	Y+		
656	Cr359 J180435+034033	E00	627	S	18:04:35.22	03:40:33.9	13.402	13.209	0.173	12.733	12.442	12.303	-1.9	-4.3	0	Y+		
657	Cr359 J180435+033914	E00	973	S	18:04:35.33	03:39:14.1	12.664	12.404	0.240	11.649	11.023	10.872	-	0	Y+			
658	Cr359 J180435+032127	E06	3976	M	18:04:35.59	03:21:27.9	18.766	18.231	0.605	-	-	-	-	3	Y+			
659	Cr359 J180435+033659	E00	1662	S	18:04:35.87	03:36:59.1	13.868	13.604	0.244	12.989	12.441	12.390	-31.9	-5.5	0	Y+		
660	Cr359 J180436+033705	E00	1658	S	18:04:36.11	03:37:05.5	16.853	16.289	0.543	-	-	-	-	0	Y+			
661	Cr359 J180436+033705	E00	1658	SM	18:04:36.11	03:37:05.5	16.853	16.289	0.543	-	-	-	-	0	Y+			
662	Cr359 J180436+033020	E00	3377	S	18:04:36.91	03:30:20.6	14.184	13.888	0.276	13.136	12.464	12.349	13.1	5.6	2	Y+		
663	Cr359 J180437+033637	E00	1799	S	18:04:37.45	03:36:37.3	16.996	16.489	0.486	-	-	-	-	0	Y+			
664	Cr359 J180437+031900	E06	960	S	18:04:37.49	03:19:00.1	13.758	13.534	0.204	12.831	12.290	12.164	1.0	-5.2	0	Y+		
665	Cr359 J180437+033055	E00	3541	S	18:04:37.63	03:30:55.8	12.555	12.229	0.306	11.425	10.769	10.601	-9.0	0.4	0	Y+		
666	Cr359 J180438+034106	E00	482	S	18:04:38.40	03:41:06.5	13.767	13.528	0.219	12.853	12.276	12.163	-8.4	-7.2	0	Y+		
667	Cr359 J180439+033421	E00	8531	L	18:04:39.36	03:34:21.7	20.020	19.252	0.788	-	17.787	-	-	3	NM	3	Y+	
668	Cr359 J180439+032929	E00	3076	S	18:04:39.58	03:29:29.0	16.514	15.973	0.521	-	-	-	-	3	Y+	0	Y+	
669	Cr359 J180439+031611	E06	227	S	18:04:39.61	03:16:11.6	14.168	13.891	0.257	13.338	12.826	12.704	-	0	Y+	0	Y+	
670	Cr359 J180439+033041	E00	3462	S	18:04:39.84	03:30:41.8	13.887	13.654	0.213	13.016	12.487	12.369	-5.4	1.4	0	Y+	0	Y+

Table B.1: continued

Numb	Coll359 J...	FOV	ID	RA	Dec	<i>I</i>	<i>L-z</i>	<i>J</i>	<i>H</i>	<i>K_s</i>	μ_{α}	μ_{α}	Flag	M?		
671	Cr359 J1804439+031813	E06	741	S	18:04:39.93	03:18:13.8	14.070	13.823	0.227	13.114	12.497	-1.5	-10.3	2	Y+	
672	Cr359 J180440+032357	E06	2370	S	18:04:40.21	03:23:57.2	14.311	14.065	0.226	13.270	12.618	-8.9	-0.6	2	Y+	
673	Cr359 J180440+033115	E00	3645	S	18:04:40.49	03:31:15.6	14.585	14.333	0.231	13.584	12.908	-12.5	-13.9	0	Y+	
674	Cr359 J180440+032151	E06	1779	SM	18:04:40.50	03:21:51.3	15.355	14.967	0.368	14.125	13.469	13.159	—	0	Y+	
675	Cr359 J180441+033339	E00	2603	S	18:04:41.04	03:33:39.1	12.603	12.343	0.240	11.547	10.907	10.743	5.0	-0.4	0	Y+
676	Cr359 J180441+031540	E06	297	M	18:04:41.11	03:15:40.1	18.883	18.261	0.691	—	—	—	—	—	0	Y+
677	Cr359 J180441+034216	E00	140	S	18:04:41.43	03:42:16.2	12.589	12.326	0.243	11.698	11.157	11.060	—	—	2	Y+
678	Cr359 J180441+032636	E06	3558	S	18:04:41.62	03:26:36.6	12.972	12.766	0.186	12.085	11.505	11.397	-4.7	-7.7	0	Y+
679	Cr359 J180443+031531	E06	85	SM	18:04:43.04	03:15:31.7	16.992	16.415	0.557	15.407	14.670	14.445	—	—	0	Y+
680	Cr359 J180444+034206	E00	223	SM	18:04:44.00	03:42:06.4	15.761	15.284	0.457	14.362	13.790	13.480	—	—	0	Y+
681	Cr359 J180445+033814	E00	1283	S	18:04:45.70	03:38:14.6	13.728	13.508	0.200	12.781	12.167	12.045	3.8	-6.9	0	Y+
682	Cr359 J180445+033201	E00	3855	S	18:04:45.95	03:32:01.8	17.969	17.303	0.646	—	—	—	—	—	0	Y+
683	Cr359 J180445+033547	E00	2002	S	18:04:45.95	03:35:47.4	12.817	12.563	0.234	11.758	11.051	10.864	-1.4	-7.6	2	Y+
684	Cr359 J180446+031534	E06	71	S	18:04:46.16	03:15:34.0	13.954	13.683	0.251	13.169	12.794	12.657	—	—	0	Y?
685	Cr359 J180446+032329	E06	2281	SM	18:04:46.38	03:23:30.0	16.412	15.873	0.519	14.915	14.253	13.987	—	—	0	Y+
686	Cr359 J180446+031837	E06	864	S	18:04:46.52	03:18:37.3	14.033	13.787	0.226	13.025	12.324	12.216	-1.2	3.1	0	Y+
687	Cr359 J180447+031116	E00	3622	S	18:04:47.22	03:31:16.8	12.819	12.629	0.170	11.936	11.384	11.278	-21.5	8.9	2	Y+
688	Cr359 J180447+031640	E06	371	S	18:04:47.93	03:16:40.8	13.599	13.398	0.182	12.897	12.469	12.428	-8.4	-2.6	2	Y+
689	Cr359 J180448+032026	E06	1398	S	18:04:48.10	03:20:26.5	13.439	13.199	0.220	12.427	11.742	11.610	-5.9	-8.3	0	Y+
690	Cr359 J180448+034236	E00	98	S	18:04:48.49	03:42:36.2	18.251	17.624	0.606	—	—	—	—	—	3	Y+
691	Cr359 J180449+031945	E06	1191	S	18:04:49.27	03:19:45.5	12.727	12.446	0.261	11.575	10.790	10.604	-9.3	-9.0	2	Y+
692	Cr359 J180449+031655	E06	457	SM	18:04:49.66	03:16:55.9	17.709	17.139	0.551	—	—	—	—	—	0	Y+
693	Cr359 J180449+033342	E00	2653	SM	18:04:49.72	03:33:42.7	18.219	17.644	0.556	—	—	—	—	—	0	Y+
694	Cr359 J180450+033833	E00	1184	S	18:04:50.08	03:38:33.2	13.568	13.248	0.300	12.340	11.508	11.313	1.8	-0.4	0	Y+
695	Cr359 J180450+033136	E00	3697	S	18:04:50.24	03:31:36.8	14.756	14.439	0.297	13.640	12.892	12.654	—	—	0	Y+
696	Cr359 J180451+032004	E06	1294	S	18:04:51.64	03:20:04.6	13.085	12.807	0.258	11.928	11.132	10.935	-8.1	-3.7	0	Y+
697	Cr359 J180451+034039	E00	597	S	18:04:51.93	03:40:39.4	13.642	13.425	0.197	12.719	12.137	11.997	-5.1	-4.8	0	Y+
698	Cr359 J180453+031618	E06	752	M	18:04:53.16	03:16:18.0	18.361	17.848	0.583	—	—	—	—	—	3	Y+
699	Cr359 J180454+031557	E06	193	SM	18:04:54.99	03:15:57.3	14.947	14.671	0.256	14.031	13.481	13.247	3.0	-4.5	0	Y+
700	Cr359 J180455+033552	E00	1963	S	18:04:55.91	03:35:52.2	13.054	12.868	0.166	12.150	11.573	11.424	—	—	0	Y+
701	Cr359 J180457+031706	E06	468	S	18:04:57.28	03:17:06.7	12.785	12.599	0.166	12.050	11.576	11.470	—	—	0	Y+
702	Cr359 J180457+032112	E06	1634	SM	18:04:57.72	03:21:12.5	15.771	15.254	0.496	14.127	13.426	13.141	—	—	0	Y+
703	Cr359 J180458+032732	E06	3329	S	18:04:58.38	03:27:32.9	13.086	12.841	0.224	12.030	11.341	11.169	—	—	2	Y+
704	Cr359 J180458+033116	E00	7371	M	18:04:58.45	03:31:16.9	18.300	17.790	0.581	—	—	—	—	—	3	Y+
705	Cr359 J180458+033831	E00	2695	ML	18:04:58.45	03:38:31.9	20.532	19.741	0.861	—	—	—	—	—	0	Y+
706	Cr359 J180458+033335	E00	2634	S	18:04:58.76	03:33:35.1	13.384	13.188	0.176	12.495	11.955	11.814	2.1	-5.8	0	Y+
707	Cr359 J180459+034133	E00	358	SM	18:04:59.63	03:41:33.7	15.861	15.470	0.371	14.537	13.884	13.673	—	—	0	Y+
708	Cr359 J180459+033402	E00	2501	S	18:04:59.88	03:34:02.0	13.875	13.646	0.209	12.880	12.108	12.005	-20.8	-34.1	3	Y+
709	Cr359 J180502+031932	E07	1340	S	18:05:02.88	03:19:32.3	12.448	12.244	0.183	11.610	11.059	10.924	5.9	-12.3	2	Y+
710	Cr359 J180502+033842	E01	1243	S	18:05:02.99	03:38:42.7	13.336	12.943	0.243	12.277	11.548	11.451	2.6	-3.1	0	Y+
711	Cr359 J180503+034120	E01	514	S	18:05:03.67	03:41:20.7	13.077	12.874	0.183	12.317	11.832	11.708	-15.7	-18.3	2	Y+
712	Cr359 J180503+031506	E07	2	S	18:05:03.77	03:15:06.4	14.145	13.904	0.221	13.695	13.502	13.475	—	—	0	NM

Table B.1: continued

Numb	Coll359 J...:	FOV	ID	RA	Dec	<i>I</i>	<i>z</i>	<i>I-z</i>	<i>J</i>	<i>H</i>	<i>K_s</i>	μ_{α}	μ_{α}	Flag	M?	
713	Cr359 J180504+033243	E01	3023	S	18:05:04.14	03:32:43.5	13.114	12.890	0.204	12.176	11.592	2.4	-4.5	0	Y+	
714	Cr359 J180504+031509	E07	98	S	18:05:04.38	03:15:09.2	15.815	15.385	0.410	14.761	14.070	13.837	—	—	0	Y+
715	Cr359 J180506+031515	E07	126	S	18:05:06.31	03:15:15.4	15.469	15.132	0.317	14.579	14.019	13.795	—	—	0	NM
716	Cr359 J180506+032913	E01	3239	S	18:05:06.36	03:29:13.2	13.677	13.395	0.262	12.534	11.748	11.562	-3.9	-5.5	0	Y+
717	Cr359 J180506+031627	E07	475	S	18:05:06.48	03:16:27.8	13.894	13.624	0.250	12.874	12.268	12.100	-4.5	-6.6	0	Y+
718	Cr359 J180507+032109	E07	4088	M	18:05:07.23	03:21:09.9	15.959	15.631	0.398	14.605	13.913	13.618	—	—	3	Y+
719	Cr359 J180507+033026	E01	6863	M	18:05:07.44	03:30:26.9	16.536	16.139	0.467	—	—	—	—	—	2	Y+
720	Cr359 J180508+031525	E07	157	S	18:05:08.18	03:15:26.0	13.685	13.468	0.197	13.079	12.753	12.637	—	—	2	NM
721	Cr359 J180510+032957	E01	3329	S	18:05:10.76	03:29:57.7	12.892	12.697	0.175	11.980	11.431	11.310	-4.4	-6.5	0	Y+
722	Cr359 J180511+032221	E07	2225	SM	18:05:11.10	03:22:21.1	16.667	16.139	0.508	—	—	14.325	—	—	0	Y+
723	Cr359 J180511+031602	E07	366	S	18:05:11.42	03:16:02.2	14.263	14.030	0.213	13.472	12.927	12.780	—	—	0	Y+
724	Cr359 J180511+031930	E07	2946	M	18:05:11.49	03:19:30.8	19.173	18.581	0.662	—	—	—	—	—	3	Y+
725	Cr359 J180511+033652	E01	1813	S	18:05:11.89	03:36:52.9	14.654	14.412	0.222	13.617	12.965	12.823	-3.0	-13.1	0	Y+
726	Cr359 J180512+031658	E07	589	S	18:05:12.01	03:16:58.4	12.962	12.741	0.201	12.130	11.558	11.385	-2.1	-6.6	0	Y+
727	Cr359 J180512+033156	E01	7877	M	18:05:12.59	03:31:56.1	20.156	19.467	0.759	—	—	—	—	—	0	Y+
728	Cr359 J180513+033630	E01	1910	S	18:05:13.03	03:36:30.8	14.314	14.066	0.228	13.298	12.601	12.455	—	—	2	Y+
729	Cr359 J180513+031921	E07	1315	S	18:05:13.09	03:19:21.0	13.318	13.111	0.187	12.422	11.824	11.711	2.4	-4.3	2	Y+
730	Cr359 J180513+031622	E07	466	S	18:05:13.30	03:16:22.4	14.095	13.874	0.201	13.363	12.863	12.820	5.6	-5.4	0	Y+
731	Cr359 J180513+031533	E07	252	SML	18:05:13.61	03:15:33.4	17.586	16.932	0.634	—	—	—	—	—	0	Y+
732	Cr359 J180514+034219	E01	218	S	18:05:14.51	03:42:19.7	12.759	12.511	0.227	11.791	11.226	11.053	-4.5	-7.5	0	Y+
733	Cr359 J180515+031633	E07	525	SM	18:05:15.34	03:16:53.8	17.329	16.764	0.544	—	—	—	—	—	0	Y+
734	Cr359 J180515+031926	E07	1339	S	18:05:15.61	03:19:26.3	12.745	12.506	0.218	11.721	11.061	10.876	-3.2	-6.4	0	Y+
735	Cr359 J180515+034256	E01	32	M	18:05:15.61	03:42:56.8	19.446	18.753	0.763	—	—	—	—	—	0	Y+
736	Cr359 J180515+032048	E07	1761	S	18:05:15.81	03:20:48.5	14.022	13.797	0.205	13.069	12.360	12.227	-1.9	-1.5	0	Y+
737	Cr359 J180516+034110	E01	547	S	18:05:16.59	03:41:10.5	13.791	13.571	0.200	12.846	12.257	12.155	6.0	-7.1	2	Y+
738	Cr359 J180516+032036	E07	3671	M	18:05:16.85	03:20:56.6	19.630	19.018	0.682	—	—	—	—	—	0	NM
739	Cr359 J180517+032221	E07	2178	S	18:05:17.58	03:22:21.2	12.458	12.309	0.129	11.698	11.215	11.108	1.8	1.0	0	Y+
740	Cr359 J180518+033910	E01	1107	S	18:05:18.27	03:39:10.7	13.267	13.012	0.235	12.228	11.626	11.446	-6.1	-7.4	0	Y+
741	Cr359 J180519+034052	E01	1270	ML	18:05:19.99	03:40:52.3	19.461	18.779	0.752	—	—	—	—	—	0	Y+
742	Cr359 J180520+033116	E01	3714	S	18:05:20.17	03:31:16.3	14.927	14.601	0.306	13.769	13.073	12.892	—	—	0	Y+
743	Cr359 J180520+032213	E07	4232	M	18:05:20.36	03:21:23.9	18.166	17.625	0.611	—	—	—	—	—	0	Y?
744	Cr359 J180520+033817	E01	1404	S	18:05:20.52	03:58:17.3	17.269	16.717	0.532	—	—	—	—	—	0	Y+
745	Cr359 J180520+031558	E07	495	M	18:05:20.66	03:15:38.3	18.705	18.148	0.627	—	—	—	—	—	3	Y+
746	Cr359 J180520+033024	E01	6963	M	18:05:20.70	03:30:24.7	19.055	18.463	0.662	—	—	—	—	—	0	Y+
747	Cr359 J180520+032159	E07	2117	SM	18:05:20.74	03:21:59.1	15.963	15.545	0.398	14.584	13.956	13.653	—	—	0	Y+
748	Cr359 J180520+034229	E01	167	S	18:05:20.84	03:42:29.8	12.420	12.237	0.164	11.657	11.283	11.193	-10.1	-7.1	0	Y+
749	Cr359 J180520+033011	E01	3412	S	18:05:20.90	03:30:11.6	12.526	12.280	0.227	11.411	10.675	10.548	-1.0	0	Y+	
750	Cr359 J180522+033645	E01	1821	S	18:05:22.74	03:36:45.8	13.349	13.105	0.224	12.245	11.518	11.359	-4.5	-8.9	0	Y+
751	Cr359 J180522+033111	E01	3262	S	18:05:22.79	03:31:11.4	12.965	12.771	0.174	12.073	11.383	11.313	—	—	2	Y+
752	Cr359 J180523+031658	E07	1340	M	18:05:23.18	03:16:58.0	15.860	15.507	0.422	14.207	13.658	13.339	—	—	2	Y+
753	Cr359 J180525+034241	E01	3	S	18:05:25.14	03:42:41.9	12.698	12.523	0.155	12.031	11.688	11.616	-2.1	1.4	0	Y+
754	Cr359 J180525+034200	E01	688	L	18:05:25.45	03:42:00.8	20.860	19.976	0.903	—	—	—	—	—	3	Y+

Table B.1: continued

Numb	Coll359 J...	FOV	ID	RA	Dec	<i>I</i>	<i>z</i>	<i>L-z</i>	<i>J</i>	<i>H</i>	<i>K_s</i>	μ_{α}	μ_{α}	Flag	M?	
755	Cr359 J180526+031526	E07	201	S	18:05:26.11	03:15:27.0	14.059	13.730	0.309	12.997	12.288	—	—	0	Y+	
756	Cr359 J180528+031641	E08	1219	M	18:05:28.68	03:16:41.5	20.232	19.551	0.751	—	—	—	—	0	Y+	
757	Cr359 J180529+032050	E08	2055	S	18:05:29.22	03:20:50.0	16.644	16.161	0.462	13.411	12.746	12.610	1.8	0.0	Y+	
758	Cr359 J180529+032023	E08	1870	S	18:05:29.32	03:20:23.2	14.294	14.043	0.231	14.603	13.903	13.694	—	2	Y+	
759	Cr359 J180529+032721	E08	3652	S	18:05:29.74	03:27:21.6	15.892	15.497	0.375	14.729	14.099	13.819	—	0	Y+	
760	Cr359 J180529+032551	E08	4341	SM	18:05:29.76	03:25:51.7	16.097	15.664	0.413	10.911	11.041	10.911	1.7	3	Y+	
761	Cr359 J180529+033635	E02	1678	S	18:05:29.85	03:36:35.8	12.642	12.393	0.230	12.866	12.289	12.154	8.3	3	Y+	
762	Cr359 J180530+033943	E02	842	S	18:05:30.26	03:39:43.5	13.405	13.175	0.210	12.538	11.970	11.854	-5.6	0	Y+	
763	Cr359 J180530+034020	E02	672	S	18:05:30.46	03:40:20.7	14.326	14.093	0.213	13.348	12.758	12.720	-5.0	0	Y+	
764	Cr359 J180530+033615	E02	1768	S	18:05:30.68	03:36:15.6	12.440	12.279	0.142	11.765	11.384	11.310	-5.7	0	Y+	
765	Cr359 J180530+033636	E02	1694	S	18:05:30.82	03:36:36.7	13.830	13.598	0.212	12.413	12.06	12.057	6.4	2	Y+	
766	Cr359 J180531+033719	E02	1497	S	18:05:31.31	03:37:19.8	14.013	13.773	0.220	13.106	12.557	12.413	-6.9	0	Y+	
767	Cr359 J180532+033222	E02	2883	S	18:05:32.54	03:32:22.9	13.799	13.582	0.197	12.830	12.307	12.169	-5.9	0	Y+	
768	Cr359 J180533+034218	E02	459	M	18:05:33.70	03:42:18.6	18.626	18.081	0.615	—	—	—	—	3	Y+	
769	Cr359 J180534+034213	E02	100	S	18:05:34.09	03:42:13.9	12.893	12.709	0.164	12.193	11.781	11.702	-14.4	8.0	Y+	
770	Cr359 J180534+031741	E08	969	S	18:05:34.15	03:17:41.6	13.538	13.302	0.215	12.624	11.988	11.938	-3.0	-8.4	0	Y+
771	Cr359 J180535+032416	E08	9597	L	18:05:35.16	03:24:16.8	20.062	19.298	0.784	—	—	—	—	0	Y+	
772	Cr359 J180535+032941	E02	3069	S	18:05:35.29	03:29:41.3	13.570	13.355	0.196	12.636	12.065	11.962	-10.1	3.3	Y+	
773	Cr359 J180535+032949	E02	2951	S	18:05:35.33	03:29:49.3	18.102	17.534	0.547	—	—	—	—	0	Y+	
774	Cr359 J180535+032932	E02	3058	S	18:05:35.45	03:29:32.5	12.077	11.897	0.160	11.254	10.738	10.643	-13.4	-1.1	0	Y+
775	Cr359 J180535+032703	E08	3858	S	18:05:35.58	03:27:03.9	13.257	13.023	0.214	12.296	11.681	11.563	—	0	Y+	
776	Cr359 J180535+031622	E08	1077	M	18:05:35.65	03:16:22.6	19.238	18.655	0.653	—	—	—	—	3	Y+	
777	Cr359 J180535+033347	E02	5910	M	18:05:35.95	03:33:47.2	18.493	17.927	0.636	—	—	—	—	3	Y+	
778	Cr359 J180536+031533	E08	279	S	18:05:36.04	03:15:33.3	14.467	14.219	0.228	13.614	13.044	12.951	0.0	-8.4	2	Y+
779	Cr359 J180536+034101	E02	488	S	18:05:36.64	03:41:01.4	16.975	16.472	0.482	—	—	—	—	0	Y+	
780	Cr359 J180536+031627	E08	267	SM	18:05:36.72	03:15:27.2	15.072	14.766	0.286	14.058	13.439	13.368	-12.8	-10.4	0	Y+
781	Cr359 J180536+034119	E02	418	SM	18:05:36.78	03:41:19.4	16.993	16.409	0.564	—	—	—	—	0	Y+	
782	Cr359 J180536+034040	E02	541	S	18:05:36.88	03:40:40.2	12.392	12.050	0.321	11.088	10.283	10.067	-1.5	-7.1	0	Y+
783	Cr359 J180537+033854	E02	1087	S	18:05:37.30	03:38:54.8	18.052	17.474	0.558	—	—	—	—	3	Y+	
784	Cr359 J180537+033455	E02	2129	S	18:05:37.70	03:34:55.9	13.199	12.984	0.195	12.305	11.759	11.651	-3.9	-6.2	0	Y+
785	Cr359 J180537+034044	E02	551	S	18:05:37.74	03:40:44.7	14.414	14.173	0.221	13.473	12.940	12.751	-1.8	-7.0	0	Y+
786	Cr359 J180537+034127	E02	971	M	18:05:37.87	03:41:27.9	16.959	16.494	0.536	—	—	—	—	3	Y+	
787	Cr359 J180538+033358	E02	2460	S	18:05:38.16	03:33:58.3	17.841	17.273	0.548	—	—	—	—	0	Y+	
788	Cr359 J180538+034008	E02	722	S	18:05:38.17	03:40:08.6	14.194	13.937	0.237	13.232	12.600	12.464	5.1	-2.4	2	Y+
789	Cr359 J180538+034114	E02	413	S	18:05:38.50	03:41:14.1	13.700	13.474	0.207	12.835	12.344	12.240	-3.8	-12.8	2	Y+
790	Cr359 J180538+031735	E08	968	S	18:05:38.51	03:17:36.0	14.978	14.668	0.289	13.941	13.294	13.091	—	0	Y?	
791	Cr359 J180538+033654	E02	1618	S	18:05:38.69	03:36:54.4	14.015	13.787	0.209	13.089	12.490	12.363	-0.9	-15.1	0	Y+
792	Cr359 J180538+033036	E02	2981	S	18:05:38.73	03:30:36.2	13.643	13.398	0.225	12.620	11.968	11.826	-1.9	-5.6	0	Y+
793	Cr359 J180539+031649	E08	1329	M	18:05:39.57	03:16:49.2	19.241	18.634	0.677	—	—	—	—	3	Y+	
794	Cr359 J180541+032253	E08	2718	S	18:05:41.01	03:22:53.2	14.126	13.886	0.220	13.196	12.557	12.406	-4.4	-8.0	0	Y+
795	Cr359 J180541+032546	E08	4332	S	18:05:41.18	03:25:46.9	13.935	13.701	0.214	13.003	12.347	12.239	-5.3	-1.5	2	Y+
796	Cr359 J180541+031628	E08	619	S	18:05:41.62	03:16:28.5	14.498	14.229	0.249	13.566	12.970	12.883	-0.6	2.7	0	Y+

Table B.1: continued

Numb	Coll359 J...	FOV	ID	RA	Dec	<i>I</i>	<i>J</i>	<i>H</i>	<i>K_s</i>	μ_{α}	μ_{α}	Flag	M?
797	Cr359 J180541+032510	E08	3471	SM	18:05:41.80	03:25:10.7	15.394	14.945	0.429	14.019	13.406	—	Y+
798	Cr359 J180542+032619	E08	4167	S	18:05:42.30	03:26:19.1	13.210	12.977	0.213	12.239	11.650	-5.0	-12.6
799	Cr359 J180542+034128	E02	375	SM	18:05:42.60	03:41:28.9	17.276	16.708	0.548	—	—	-	Y+
800	Cr359 J180543+033915	E02	932	S	18:05:43.15	03:39:15.8	12.788	12.574	0.193	11.929	11.444	11.294	-4.7
801	Cr359 J180543+033319	E02	2606	S	18:05:43.78	03:33:19.5	13.296	13.090	0.186	12.418	11.891	11.746	-5.0
802	Cr359 J180543+031450	E08	102	M	18:05:43.86	03:14:50.9	16.865	16.428	0.507	—	—	-	Y+
803	Cr359 J180543+032236	E08	2608	S	18:05:43.92	03:22:36.7	13.324	13.109	0.195	12.445	11.888	11.789	-1.9
804	Cr359 J180544+031512	E08	191	S	18:05:44.96	03:15:12.8	14.081	13.736	0.325	13.022	12.355	12.286	0.4
805	Cr359 J180544+034210	E02	120	S	18:05:44.99	03:42:10.8	12.873	12.602	0.251	11.932	11.334	11.185	-3.5
806	Cr359 J180545+032146	E08	2374	S	18:05:45.30	03:21:46.3	13.868	13.654	0.194	13.058	12.493	12.387	-6.9
807	Cr359 J180545+032439	E08	3333	S	18:05:45.40	03:24:39.2	17.601	17.040	0.541	—	—	—	Y+
808	Cr359 J180545+033215	E02	2905	S	18:05:45.47	03:32:15.2	13.500	13.294	0.186	12.606	12.059	11.943	-11.5
809	Cr359 J180545+033138	E02	3677	S	18:05:45.48	03:31:38.5	17.380	16.820	0.540	—	—	-11.8	0
810	Cr359 J180546+033603	E02	1848	S	18:05:46.09	03:36:03.1	14.981	14.699	0.263	13.976	13.373	13.180	—
811	Cr359 J180546+034019	E02	662	S	18:05:46.27	03:40:19.6	14.635	14.375	0.240	13.739	13.057	13.034	1.0
812	Cr359 J180546+034151	E02	239	S	18:05:46.52	03:41:51.1	14.324	14.079	0.225	13.454	12.959	12.823	0
813	Cr359 J180546+034145	E02	2327	S	18:05:46.55	03:34:15.9	13.596	13.243	0.333	12.387	11.697	11.477	-9.3
814	Cr359 J180546+031942	E08	1649	S	18:05:46.98	03:19:42.0	13.979	13.747	0.212	13.122	12.550	12.451	0.3
815	Cr359 J180546+032444	E08	3315	S	18:05:47.04	03:24:44.7	13.203	12.968	0.214	12.238	11.580	11.502	0.0
816	Cr359 J180547+033148	E02	3707	S	18:05:47.08	03:31:48.8	17.996	17.428	0.547	—	—	—	Y+
817	Cr359 J180547+033727	E02	1430	S	18:05:47.15	03:37:28.0	12.822	12.590	0.212	11.892	11.330	11.198	5.4
818	Cr359 J180548+031454	E08	1	S	18:05:48.02	03:14:54.2	13.436	13.170	0.247	12.727	12.329	12.323	—
819	Cr359 J180548+034216	E02	130	S	18:05:48.02	03:42:16.2	18.137	17.393	0.724	—	—	—	Y+
820	Cr359 J180548+033619	E02	1774	SML	18:05:48.48	03:36:20.0	17.548	16.882	0.646	—	—	15.008	—
821	Cr359 J180549+031733	E08	953	S	18:05:49.49	03:17:33.7	14.487	14.220	0.247	13.570	12.898	12.806	4.7
822	Cr359 J180549+031922	E08	1557	S	18:05:49.64	03:19:22.7	13.772	13.508	0.244	12.798	12.143	12.044	-5.8
823	Cr359 J180549+031835	E08	1308	S	18:05:49.68	03:18:35.9	13.628	13.392	0.215	12.761	12.172	12.116	-7.0
824	Cr359 J180549+031530	E08	523	M	18:05:49.69	03:15:30.6	18.945	18.306	0.709	—	—	16.355	—
825	Cr359 J180550+033708	E02	1546	S	18:05:50.12	03:37:08.8	15.528	15.168	0.339	14.293	13.796	13.588	—
826	Cr359 J180550+033239	E02	2816	S	18:05:50.20	03:32:39.6	17.378	16.854	0.504	—	—	—	Y+
827	Cr359 J180550+033812	E02	1220	S	18:05:50.33	03:38:12.9	12.937	12.640	0.277	11.872	11.203	11.020	—
828	Cr359 J180551+033350	E02	2444	S	18:05:51.54	03:33:50.3	13.662	13.450	0.192	12.728	12.134	12.057	-1.8
829	Cr359 J180551+031550	E08	439	SML	18:05:51.99	03:15:50.6	17.778	17.056	0.702	—	—	15.471	—
830	Cr359 J180552+031837	E08	2594	M	18:05:52.26	03:18:37.9	19.456	18.761	0.765	—	—	—	2
831	Cr359 J180552+034240	E02	1	S	18:05:52.95	03:42:40.3	13.782	13.526	0.236	12.878	12.308	12.213	-3.2
832	Cr359 J180553+031502	E08	159	S	18:05:53.15	03:15:02.4	14.543	14.191	0.332	13.562	12.998	12.947	—
833	Cr359 J180553+033510	E02	2089	SM	18:05:53.59	03:55:10.6	17.044	16.531	0.493	—	—	14.743	—
834	Cr359 J180554+031521	E08	418	M	18:05:54.01	03:15:21.0	19.260	18.585	0.745	—	—	16.720	—
835	Cr359 J180554+032336	E08	2979	SM	18:05:54.11	03:23:36.5	16.572	16.035	0.518	15.010	14.308	14.097	—
836	Cr359 J180554+032047	E08	2084	S	18:05:54.36	03:20:47.8	17.456	16.868	0.568	—	—	—	3
837	Cr359 J180555+032253	E08	2766	S	18:05:55.11	03:22:53.5	17.472	16.920	0.532	—	—	—	0
838	Cr359 J180555+033310	E02	2632	S	18:05:55.20	03:33:10.8	13.697	13.492	0.186	12.837	12.326	12.172	-6.6

Table B.1: continued

Numb	Coll359 J...	FOV	ID	RA	Dec	<i>I</i>	<i>L-z</i>	<i>J</i>	<i>H</i>	<i>K_s</i>	μ_{α}	μ_{α}	Flag	M?
839	Cr359 J180555+031620	E08	566	S	18:05:55.47	03:16:20.4	12.791	12.292	0.479	11.398	10.771	—	—	2 Y+
840	Cr359 J180555+033228	E02	2827	S	18:05:55.86	03:32:28.9	13.661	13.447	0.194	12.671	12.117	11.967	4.7	-8.0 0 Y+
841	Cr359 J180556+032537	E08	11012	L	18:05:56.37	03:25:37.3	19.317	0.746	—	—	—	—	—	3 Y+
842	Cr359 J180556+032658	E08	3929	S	18:05:56.57	03:26:58.7	14.452	13.981	0.451	12.741	12.140	11.886	—	— 0 Y+
843	Cr359 J180558+033553	E03	2268	S	18:05:58.47	03:35:53.6	13.079	12.837	0.222	12.057	11.405	11.286	-1.9	— 0 Y+
844	Cr359 J180558+031614	E09	388	S	18:05:58.75	03:16:14.3	13.503	13.288	0.195	12.667	12.223	12.131	0.9	2.2 0 Y+
845	Cr359 J180559+033423	E03	2768	S	18:05:59.59	03:34:23.1	13.025	12.815	0.190	12.186	11.618	11.490	-5.9	-20.0 2 Y+
846	Cr359 J180600+031518	E09	75	S	18:06:00.03	03:15:18.4	12.509	12.213	0.276	11.444	10.835	10.724	-1.4	0.0 2 Y+
847	Cr359 J180600+032354	E09	2729	SM	18:06:00.06	03:23:54.8	15.967	15.443	0.504	14.432	13.700	13.465	—	— 0 Y+
848	Cr359 J180600+031606	E09	358	S	18:06:00.77	03:16:06.8	14.252	13.960	0.272	13.212	12.588	12.434	—	— 0 Y+
849	Cr359 J180600+034029	E03	732	S	18:06:00.95	03:40:29.6	14.060	13.832	0.208	13.162	12.655	12.487	3.5	-16.3 0 Y+
850	Cr359 J180600+031454	E09	140	M	18:06:00.97	03:14:54.1	19.271	18.690	0.651	—	—	—	—	— 0 Y+
851	Cr359 J180601+032713	E09	3534	S	18:06:01.77	03:27:13.4	14.955	14.631	0.304	13.763	13.105	12.864	—	— 2 Y+
852	Cr359 J180602+031523	E09	178	S	18:06:02.18	03:15:23.2	17.874	17.294	0.560	—	—	—	—	— 0 Y+
853	Cr359 J180602+033332	E03	3078	S	18:06:02.79	03:33:32.3	13.729	13.497	0.212	12.764	12.092	11.930	2.9	1.6 2 Y+
854	Cr359 J180603+031546	E09	241	S	18:06:03.05	03:15:46.4	13.295	13.057	0.218	12.422	11.924	11.763	-12.0	0 Y+
855	Cr359 J180603+031620	E09	463	SM	18:06:03.13	03:16:20.7	15.532	15.029	0.483	14.037	13.482	13.261	—	— 0 Y+
856	Cr359 J180604+033428	E03	2801	SML	18:06:04.22	03:34:28.1	17.910	17.315	0.575	—	—	—	—	— 0 Y+
857	Cr359 J180605+033304	E03	3261	S	18:06:05.37	03:33:04.8	14.171	13.946	0.206	13.258	12.650	12.467	2.9	1.6 2 Y+
858	Cr359 J180605+033236	E03	3405	S	18:06:05.99	03:32:36.7	12.832	12.580	0.232	11.766	11.071	10.848	-3.2	-4.4 0 Y+
859	Cr359 J180606+033921	E03	1110	SML	18:06:06.15	03:39:21.7	17.701	17.087	0.595	—	—	—	—	— 0 Y+
860	Cr359 J180606+031620	E09	952	S	18:06:06.55	03:18:05.5	13.084	12.852	0.212	12.100	11.507	11.349	-3.2	7.3 0 Y+
861	Cr359 J180606+033307	E03	3280	S	18:06:06.59	03:33:07.1	17.896	17.324	0.552	—	—	—	—	— 0 Y+
862	Cr359 J180607+031457	E09	188	M	18:06:07.10	03:14:57.1	19.184	18.593	0.660	—	—	—	—	— 0 Y+
863	Cr359 J180607+032229	E03	3444	S	18:06:07.24	03:52:29.4	12.971	12.761	0.190	12.068	11.475	11.353	3.9	-1.4 0 Y+
864	Cr359 J180607+033619	E03	2104	S	18:06:07.81	03:56:19.5	13.475	13.280	0.175	12.638	12.125	11.984	-2.6	-13.3 0 Y+
865	Cr359 J180608+034237	E03	1	SM	18:06:08.26	03:42:38.0	14.229	13.994	0.215	13.523	13.232	13.114	—	NM 0 Y+
866	Cr359 J180608+031700	E09	651	S	18:06:08.39	03:17:00.9	14.639	14.387	0.242	13.680	13.142	12.983	3.9	-19.3 0 Y+
867	Cr359 J180608+034222	E03	109	S	18:06:09.00	03:42:23.0	14.818	14.516	0.282	13.864	13.314	13.226	—	0 Y?
868	Cr359 J180609+033508	E03	2530	SM	18:06:09.54	03:55:08.8	16.020	15.612	0.388	14.683	14.015	13.742	—	— 0 Y+
869	Cr359 J180609+031520	E09	151	SM	18:06:09.62	03:15:20.4	15.206	14.764	0.422	13.896	13.273	13.019	—	— 0 Y+
870	Cr359 J180609+032433	E09	2898	S	18:06:09.76	03:24:33.5	13.388	13.158	0.210	13.386	11.702	11.480	-0.5	-3.7 0 Y+
871	Cr359 J180609+033437	E03	2680	S	18:06:09.81	03:34:37.2	13.764	13.558	0.186	12.857	12.266	12.132	-5.6	-5.2 0 Y+
872	Cr359 J180609+031451	E09	135	M	18:06:09.97	03:14:51.3	18.770	18.210	0.630	—	—	—	—	— 0 Y+
873	Cr359 J180610+032039	E09	1727	S	18:06:10.05	03:20:39.7	14.158	13.932	0.207	13.177	12.516	12.373	-9.9	-7.8 0 Y+
874	Cr359 J180610+033315	E03	3220	S	18:06:10.19	03:33:15.5	17.791	17.195	0.576	—	—	—	—	— 0 Y+
875	Cr359 J180610+032521	E09	3105	S	18:06:10.73	03:25:21.4	12.999	12.755	0.225	11.905	11.185	10.967	-2.3	-12.2 0 Y+
876	Cr359 J180611+031659	E09	611	S	18:06:11.20	03:16:59.2	12.913	12.531	0.362	11.580	10.759	10.484	-3.2	-13.0 2 Y+
877	Cr359 J180611+031510	E09	107	S	18:06:11.78	03:15:10.6	15.145	14.843	0.283	14.112	13.544	13.513	—	3 Y+
878	Cr359 J180612+031513	E09	129	S	18:06:12.09	03:15:13.3	15.739	15.360	0.359	14.581	13.992	13.767	—	2 Y+
879	Cr359 J180612+034208	E03	145	S	18:06:12.93	03:42:08.3	12.974	12.786	0.168	12.349	12.141	12.077	—	2 Y?
880	Cr359 J180613+034129	E03	884	ML	18:06:13.23	03:41:29.7	20.114	19.282	0.902	—	—	—	—	0 Y+

Table B.1: continued

Numb	Coll359 J...	FOV	ID	RA	Dec	<i>I</i>	<i>J</i>	<i>H</i>	<i>K_s</i>	μ_{α}	μ_{α}	Flag	M?
881	Cr359 J180613+034144	E03	287	S	18:06:13.35	03:41:44.8	14.440	14.078	0.342	13.278	12.412	6.9	-9.0
882	Cr359 J180613+032346	E09	2680	S	18:06:13.51	03:23:46.8	15.040	14.642	0.377	—	—	—	0 Y+
883	Cr359 J180614+031957	E09	1521	S	18:06:14.14	03:19:57.1	13.911	13.674	0.217	12.896	12.288	12.136	-0.2
884	Cr359 J180614+031444	E09	2	S	18:06:14.25	03:14:44.3	13.806	13.575	0.212	13.038	12.693	12.605	—
885	Cr359 J180614+032823	E09	3142	S	18:06:14.45	03:28:23.1	13.055	12.869	0.166	12.105	11.472	11.412	-0.2
886	Cr359 J180614+032637	E09	3654	S	18:06:14.60	03:26:37.1	13.388	13.184	0.184	12.451	11.825	11.671	-6.1
887	Cr359 J180615+032928	E03	3842	S	18:06:15.01	03:29:28.8	12.875	12.683	0.172	12.016	11.444	11.322	0 Y+
888	Cr359 J180615+031518	E09	172	S	18:06:15.04	03:15:18.5	18.370	17.556	0.794	—	—	—	0 Y+
889	Cr359 J180615+033542	E03	2303	S	18:06:15.56	03:35:42.7	14.202	13.936	0.247	13.181	12.441	12.257	-10.5
890	Cr359 J180615+033459	E03	2538	S	18:06:15.95	03:34:59.1	13.983	13.740	0.223	13.014	12.398	12.212	—
891	Cr359 J180616+032205	E09	4962	M	18:06:16.58	03:22:05.1	14.473	14.335	0.208	13.589	13.042	12.988	3.8
892	Cr359 J180616+033748	E03	1565	S	18:06:16.99	03:37:48.6	13.147	12.955	0.172	12.389	11.897	11.762	-27.7
893	Cr359 J180617+034159	E03	215	M	18:06:17.26	03:41:59.3	15.002	14.685	0.297	14.055	13.450	13.397	-4.4
894	Cr359 J180617+031543	E09	278	S	18:06:17.96	03:15:43.6	17.859	17.271	0.569	—	—	—	0 Y+
895	Cr359 J180618+032121	E09	1958	M	18:06:18.02	03:21:21.4	15.792	15.356	0.416	14.509	13.948	13.685	—
896	Cr359 J180618+031620	E09	496	S	18:06:18.15	03:16:20.7	18.096	17.283	0.794	—	—	—	0 Y+
897	Cr359 J180618+033555	E03	2238	S	18:06:18.34	03:35:55.3	13.889	13.657	0.212	12.927	12.229	12.130	-6.3
898	Cr359 J180619+034240	E03	6	S	18:06:19.21	03:42:40.6	14.154	13.813	0.321	13.267	12.852	12.760	0.4
899	Cr359 J180619+033231	E03	3416	S	18:06:19.28	03:32:31.9	12.837	12.598	0.219	11.832	11.169	11.008	0.8
900	Cr359 J180619+031556	E09	890	M	18:06:19.39	03:15:56.8	19.845	19.217	0.698	—	—	—	0 Y+
901	Cr359 J180619+033248	E03	3321	S	18:06:19.83	03:32:48.8	13.283	12.993	0.269	12.098	11.292	11.114	-10.9
902	Cr359 J180620+031628	E09	492	S	18:06:20.05	03:16:28.0	13.092	12.828	0.245	12.121	11.426	11.268	-1.4
903	Cr359 J180620+033009	E03	4063	S	18:06:20.05	03:30:10.0	13.678	13.450	0.207	12.768	12.120	11.959	-3.3
904	Cr359 J180620+031944	E09	1464	S	18:06:20.23	03:19:44.2	13.728	13.516	0.192	12.833	12.294	12.186	-15.5
905	Cr359 J180620+034041	E03	597	S	18:06:20.24	03:40:41.2	14.135	13.900	0.215	13.244	12.700	12.593	-6.5
906	Cr359 J180620+033711	E03	1771	S	18:06:20.46	03:37:11.1	13.362	13.165	0.177	12.564	12.051	11.948	-14.5
907	Cr359 J180620+033615	E03	2119	S	18:06:20.99	03:36:15.7	14.197	13.946	0.231	13.277	12.622	12.522	-3.0
908	Cr359 J180621+032815	E09	3837	S	18:06:21.86	03:28:15.5	16.159	15.683	0.456	14.592	14.018	13.641	0 Y+
909	Cr359 J180622+031804	E09	2386	M	18:06:22.10	03:18:04.6	16.389	16.010	0.449	—	—	—	0 Y+
910	Cr359 J180622+031635	E09	557	M	18:06:23.25	03:16:35.3	15.607	15.210	0.377	14.369	13.624	13.490	—
911	Cr359 J180624+032739	E09	3174	S	18:06:24.11	03:27:39.7	15.311	14.972	0.319	14.148	13.577	13.310	—
912	Cr359 J180624+033724	E03	1748	S	18:06:24.81	03:37:24.3	18.107	17.520	0.567	—	—	—	0 Y+
913	Cr359 J180625+034225	E03	30	S	18:06:25.51	03:42:25.1	13.288	13.041	0.227	12.620	12.282	12.231	—
914	Cr359 J180625+031846	E10	1202	S	18:06:25.82	03:18:46.8	12.537	12.348	0.169	11.702	11.179	11.103	-7.5
915	Cr359 J180626+034047	E03	546	S	18:06:26.18	03:40:47.7	12.878	12.612	0.247	11.909	11.177	11.032	-7.6
916	Cr359 J180626+033945	E03	2609	L	18:06:26.26	03:39:45.7	18.889	18.121	0.789	—	—	—	3 Y+
917	Cr359 J180627+031724	E10	795	S	18:06:27.47	03:17:25.0	12.756	12.477	0.259	11.668	10.945	10.758	-14.8
918	Cr359 J180627+031649	E10	597	S	18:06:27.64	03:16:49.0	12.259	12.120	0.118	11.672	11.372	11.349	-24.2
919	Cr359 J180628+033514	E04	2206	SM	18:06:28.04	03:35:14.6	15.428	15.064	0.344	14.194	13.511	13.322	—
920	Cr359 J180628+031958	E10	1614	SM	18:06:28.75	03:19:58.9	15.633	15.249	0.364	14.311	13.657	13.437	-2.6
921	Cr359 J180629+031900	E10	1292	S	18:06:29.76	03:19:00.3	12.743	12.367	0.356	11.394	10.524	10.325	-14.7
922	Cr359 J180630+031650	E10	561	S	18:06:30.37	03:16:50.8	13.233	13.031	0.181	12.420	11.907	11.811	-10.8

Table B.1: continued

Numb	Coll359 J...	FOV	ID	RA	Dec	<i>I</i>	<i>L-z</i>	<i>J</i>	<i>H</i>	<i>K_s</i>	μ_{α}	μ_{α}	Flag	M?
923	Cr359 J180631+033016	E04	3666	S	18:06:31.11	03:30:16.8	13.067	12.860	0.188	12.086	11.481	-3.2	0	Y+
924	Cr359 J180631+031500	E10	68	S	18:06:31.42	03:15:00.3	14.518	14.163	0.335	13.409	12.708	-5.0	-13.1	0
925	Cr359 J180631+031453	E10	159	ML	18:06:31.54	03:14:53.8	19.678	16.690	0.788	—	—	—	—	Y+
926	Cr359 J180632+031915	E10	1398	S	18:06:32.49	03:19:15.8	17.219	14.354	0.321	13.505	12.892	—	—	Y+
927	Cr359 J180632+033404	E04	2554	S	18:06:32.62	03:34:04.4	14.695	13.207	0.228	12.408	11.738	11.608	—	0
928	Cr359 J180633+033540	E04	2048	S	18:06:33.06	03:35:40.1	13.455	12.624	0.260	11.810	11.086	10.932	-6.1	2
929	Cr359 J180633+031648	E10	609	S	18:06:33.08	03:16:48.5	12.904	12.624	0.260	11.241	11.716	11.586	-12.5	2
930	Cr359 J180633+031923	E10	1396	S	18:06:33.36	03:19:23.6	12.988	12.793	0.174	11.241	11.716	0.9	-18.9	0
931	Cr359 J180634+032327	E10	2637	S	18:06:34.20	03:23:27.8	12.766	12.554	0.192	11.868	11.290	11.184	-2.3	0
932	Cr359 J180635+031500	E10	74	S	18:06:35.76	03:15:00.3	14.979	14.666	0.292	14.013	13.412	13.350	—	2
933	Cr359 J180636+032329	E10	2717	S	18:06:36.00	03:23:29.6	17.612	17.044	0.548	—	—	—	—	Y+
934	Cr359 J180636+034058	E04	403	S	18:06:36.91	03:40:58.0	12.602	12.393	0.189	11.665	11.025	-2.6	-2.3	2
935	Cr359 J180637+031535	E10	243	S	18:06:37.80	03:15:35.3	14.261	14.004	0.238	13.392	12.839	1.8	-7.4	0
936	Cr359 J180637+032226	E10	2336	S	18:06:37.86	03:22:26.6	13.286	13.094	0.172	12.525	12.016	11.912	-4.1	0
937	Cr359 J180637+033532	E04	2084	S	18:06:37.92	03:35:32.4	13.216	12.990	0.206	12.249	11.608	11.475	-9.0	-10.7
938	Cr359 J180638+031646	E10	594	S	18:06:38.51	03:16:46.5	13.683	13.450	0.213	—	—	—	—	3
939	Cr359 J180640+032329	E10	2669	S	18:06:40.11	03:23:29.0	13.548	13.287	0.241	12.465	11.693	11.537	-10.5	-9.9
940	Cr359 J180640+032206	E10	2236	S	18:06:40.44	03:22:06.2	14.079	13.855	0.203	13.176	12.594	12.504	—	2
941	Cr359 J180640+031859	E10	1289	S	18:06:40.97	03:18:59.2	12.412	12.262	0.129	11.826	11.459	11.445	—	0
942	Cr359 J180641+032451	E10	3044	S	18:06:41.12	03:24:51.2	12.794	12.596	0.178	11.946	11.342	11.255	-4.8	-11.7
943	Cr359 J180641+032526	E10	4208	S	18:06:41.33	03:25:26.0	14.227	13.982	0.225	13.259	12.542	12.399	-8.1	-15.2
944	Cr359 J180641+031716	E10	2907	L	18:06:41.34	03:17:16.7	21.511	20.648	0.883	—	—	—	—	3
945	Cr359 J180641+031510	E10	134	S	18:06:41.50	03:15:10.4	15.099	14.776	0.303	14.141	13.489	13.393	-1.7	0
946	Cr359 J180641+031844	E10	1240	S	18:06:41.59	03:18:44.2	14.198	13.786	0.392	12.919	12.253	12.027	6.0	-19.0
947	Cr359 J180643+032412	E10	2907	S	18:06:43.13	03:24:12.1	14.292	13.960	0.312	13.099	12.441	12.238	—	0
948	Cr359 J180643+032640	E10	12218	L	18:06:43.69	03:26:40.1	19.047	18.356	0.711	—	—	—	—	3
949	Cr359 J180644+031534	E10	233	S	18:06:44.01	03:15:34.3	12.932	12.637	0.276	11.986	11.433	11.332	-3.5	-20.4
950	Cr359 J180645+031442	E10	1	S	18:06:45.85	03:14:42.0	13.926	13.627	0.279	13.209	12.857	12.838	—	0
951	Cr359 J180645+031708	E10	774	SM	18:06:45.95	03:17:08.9	15.315	14.964	0.331	14.280	13.491	13.380	—	0
952	Cr359 J180646+034001	E04	2469	L	18:06:46.75	03:40:01.4	19.701	18.953	0.768	—	—	—	—	2
953	Cr359 J180647+032116	E10	2006	S	18:06:47.31	03:21:16.3	13.705	13.487	0.199	12.795	12.245	12.112	-4.2	-2.1
954	Cr359 J180647+031707	E10	719	S	18:06:47.61	03:17:07.4	12.190	11.981	0.189	11.414	10.972	10.901	-5.4	-3.1
955	Cr359 J180647+033809	E04	1260	S	18:06:47.83	03:38:10.0	14.881	14.538	0.323	13.709	12.980	12.800	—	2
956	Cr359 J180647+032926	E04	3418	S	18:06:48.00	03:29:26.6	13.718	13.514	0.184	12.896	12.308	12.209	-16.5	-4.9
957	Cr359 J180648+031554	E10	334	S	18:06:48.25	03:15:54.2	13.283	13.031	0.232	12.440	11.970	11.895	-7.8	0
958	Cr359 J180648+031602	E10	386	S	18:06:48.68	03:16:02.1	13.217	12.830	0.367	11.944	11.092	10.911	-3.8	-7.8
959	Cr359 J180649+033616	E04	1887	SM	18:06:49.07	03:36:16.3	17.677	17.100	0.556	—	—	—	—	0
960	Cr359 J180649+031920	E10	1448	SM	18:06:49.40	03:19:20.0	17.263	16.727	0.516	—	—	—	—	0
961	Cr359 J180650+031834	E10	1190	S	18:06:50.37	03:18:34.3	13.482	13.264	0.198	12.677	12.170	12.066	1.8	-7.0
962	Cr359 J180650+032040	E10	6319	L	18:06:50.37	03:20:40.2	22.281	21.342	0.959	—	—	—	—	3
963	Cr359 J180650+031800	E10	1025	S	18:06:50.44	03:18:00.9	13.665	13.388	0.256	12.617	11.917	-10.8	2	Y+
964	Cr359 J180651+031450	E10	175	M	18:06:51.07	03:14:50.7	19.093	18.506	0.657	—	—	—	—	2

Table B.1: continued

Numb	Coll359 J...	FOV	ID	RA	Dec	<i>I</i>	<i>J</i>	<i>H</i>	<i>K_s</i>	μ_{α}	μ_{α}	Flag	M?
965	Cr359 J180651+033213	E04	3123	S	18:06:51.25	03:32:13.7	16.096	15.653	0.422	14.744	14.016	—	2 Y+
966	Cr359 J180651+031514	E10	165	S	18:06:51.34	03:15:14.4	14.737	14.434	0.283	13.977	13.507	13.449	—
967	Cr359 J180651+034105	E04	356	S	18:06:51.40	03:41:05.6	13.816	13.576	0.220	12.936	12.348	-11.3	-5.0
968	Cr359 J180651+034012	E04	611	S	18:06:51.58	03:40:12.4	14.272	14.022	0.230	13.253	12.575	12.450	-2.2
969	Cr359 J180652+031449	E10	42	SM	18:06:52.21	03:14:49.2	14.942	14.667	0.254	—	—	—	0 NM
970	Cr359 J180653+032235	E10	2385	S	18:06:53.11	03:22:35.8	13.428	13.191	0.217	12.530	11.919	11.841	0 Y+
971	Cr359 J180653+034112	E04	1032	M	18:06:53.39	03:41:12.9	15.076	14.863	0.283	14.077	13.456	13.332	—
972	Cr359 J180654+034025	E04	523	S	18:06:54.02	03:40:25.4	13.644	13.419	0.205	12.774	12.260	12.127	3.3
973	Cr359 J180655+032601	E11	3264	S	18:06:55.22	03:26:01.8	13.684	13.457	0.207	12.853	12.251	12.182	—
974	Cr359 J180655+031551	E11	290	S	18:06:55.61	03:15:51.1	13.084	12.802	0.262	12.096	11.469	11.373	6.1 -11.1
975	Cr359 J180656+033222	E05	10305	L	18:06:56.14	03:32:22.4	21.026	19.714	1.332	—	—	—	2 Y+
976	Cr359 J180656+031829	E11	1041	SM	18:06:56.59	03:18:29.0	16.241	15.790	0.430	14.906	14.185	14.047	—
977	Cr359 J180656+032301	E11	2286	S	18:06:56.59	03:23:01.8	13.236	13.006	0.211	12.325	11.645	11.583	2.3 -1.0
978	Cr359 J180657+034026	E05	2197	L	18:06:57.34	03:40:26.9	19.336	18.368	0.988	—	—	16.962	—
979	Cr359 J180657+033223	E05	3577	S	18:06:57.49	03:32:23.8	12.515	12.313	0.181	11.622	11.028	10.969	-5.7 -5.5
980	Cr359 J180658+032849	E05	8301	M	18:06:58.16	03:28:49.6	15.458	15.388	0.499	14.837	13.583	13.583	—
981	Cr359 J180658+031850	E11	1091	S	18:06:58.23	03:18:50.1	12.069	12.069	0.229	11.263	10.588	10.396	-4.7 -10.1
982	Cr359 J180659+033709	E05	3806	M	18:06:59.72	03:37:09.4	16.011	15.668	0.413	14.652	14.050	13.854	—
983	Cr359 J180659+031523	E11	196	S	18:06:59.87	03:15:23.7	12.216	11.973	0.222	11.479	11.097	11.011	—
984	Cr359 J180659+034004	E05	882	S	18:06:59.96	03:40:04.3	13.358	13.146	0.192	12.464	11.887	11.717	-8.7 -7.7
985	Cr359 J180700+033537	E05	2465	S	18:07:00.97	03:35:37.8	18.331	17.741	0.569	—	—	—	0 Y+
986	Cr359 J180701+031543	E11	301	SM	18:07:01.18	03:15:43.4	17.034	16.404	0.610	15.317	14.706	14.302	—
987	Cr359 J180702+033219	E05	10242	L	18:07:02.57	03:32:19.8	22.175	21.072	1.123	—	—	18.308	—
988	Cr359 J180702+033610	E05	6320	L	18:07:02.87	03:36:10.9	21.376	20.306	1.090	—	—	—	0 Y?
989	Cr359 J180703+031547	E11	285	S	18:07:03.54	03:15:47.2	13.358	13.071	0.267	12.420	11.805	11.700	-6.5 -9.3
990	Cr359 J180703+031519	E11	558	M	18:07:03.97	03:15:19.9	19.090	18.441	0.718	—	—	—	0 Y+
991	Cr359 J180704+033223	E05	3586	S	18:07:04.10	03:32:23.1	13.470	13.261	0.189	12.567	11.945	11.847	—
992	Cr359 J180704+033741	E05	1695	S	18:07:04.81	03:37:41.9	13.093	12.882	0.192	12.126	11.501	11.362	-0.2 -0.9
993	Cr359 J180705+033241	E05	3508	S	18:07:05.03	03:32:41.5	13.135	12.857	0.258	11.995	11.188	11.008	-2.4 -5.9
994	Cr359 J180705+031621	E11	433	S	18:07:05.12	03:16:21.8	12.732	12.359	0.353	11.487	10.631	10.468	0.3 -8.2
995	Cr359 J180705+031818	E11	969	S	18:07:05.52	03:18:18.7	12.885	12.638	0.228	11.899	11.315	11.152	-7.2 0
996	Cr359 J180706+031910	E11	1211	S	18:07:06.12	03:19:10.6	12.896	12.628	0.248	11.840	11.102	10.935	1.7 -3.9
997	Cr359 J180706+031748	E11	2140	M	18:07:06.32	03:17:48.3	18.445	17.852	0.664	—	—	—	0 Y+
998	Cr359 J180706+032611	E11	3559	S	18:07:06.38	03:26:11.2	13.122	12.929	0.173	12.338	11.793	11.680	—
999	Cr359 J180708+032455	E11	2855	S	18:07:08.02	03:24:55.5	12.673	12.460	0.193	11.812	11.213	11.087	0.3 -3.4
1000	Cr359 J180708+031443	E11	44	S	18:07:08.29	03:14:43.7	13.460	13.245	0.195	12.889	12.593	12.552	—
1001	Cr359 J180708+033924	E05	1083	S	18:07:08.31	03:39:25.0	13.003	12.795	0.189	12.157	11.571	11.420	-1.8 -4.3
1002	Cr359 J180708+031851	E11	1130	S	18:07:08.36	03:18:51.5	14.045	13.826	0.199	13.134	12.574	12.447	—
1003	Cr359 J180708+031552	E11	338	S	18:07:08.45	03:15:52.9	14.398	14.155	0.222	13.526	12.900	12.834	0.0 -7.7
1004	Cr359 J180708+032037	E11	1632	S	18:07:08.85	03:20:37.0	13.320	13.066	0.234	12.319	11.670	11.524	6.3 -5.4
1005	Cr359 J180711+031534	E11	255	S	18:07:11.09	03:15:34.3	14.072	13.752	0.300	13.158	12.421	12.298	8.1 -1.2
1006	Cr359 J180711+032242	E11	2211	S	18:07:11.26	03:22:42.8	13.630	13.368	0.242	12.679	11.938	11.792	-13.6 2

Table B.1: continued

Numb	Coll359 J...	FOV	ID	RA	Dec	<i>I</i>	<i>L-z</i>	<i>J</i>	<i>H</i>	<i>K_s</i>	μ_{α}	μ_{α}	Flag	M?		
1007	Cr359 J180711+032228	E11	2125	S	18:07:11.78	03:22:28.6	13.143	12.897	0.226	12.215	11.582	0.8	2.1	0	Y+	
1008	Cr359 J180711+031457	E11	123	S	18:07:11.89	03:14:57.3	14.494	14.219	0.254	13.683	13.261	—	—	0	NM	
1009	Cr359 J180713+034133	E05	360	S	18:07:13.03	03:41:53.0	13.156	12.949	0.187	12.288	11.716	11.670	—	0	Y+	
1010	Cr359 J180713+034030	E05	708	S	18:07:13.16	03:40:30.3	14.104	13.879	0.205	13.280	12.686	12.647	—	0	Y+	
1011	Cr359 J180713+031820	E11	985	S	18:07:13.38	03:18:20.7	13.001	12.813	0.169	12.184	11.622	11.539	-5.6	-5.6	2	Y+
1012	Cr359 J180714+032408	E11	2672	S	18:07:14.04	03:24:08.7	15.788	15.317	0.451	—	—	—	—	0	Y+	
1013	Cr359 J180714+031613	E11	435	S	18:07:14.19	03:16:13.5	13.898	13.620	0.258	12.873	12.249	12.132	5.1	6.8	2	Y+
1014	Cr359 J180714+034128	E05	716	M	18:07:14.58	03:41:28.9	17.233	16.763	0.540	—	—	—	—	0	Y+	
1015	Cr359 J180714+031503	E11	149	S	18:07:14.63	03:15:03.6	14.406	13.766	0.620	12.717	12.123	11.842	—	0	Y+	
1016	Cr359 J180714+033640	E05	2015	S	18:07:14.66	03:36:40.7	12.793	12.504	0.269	11.659	10.849	10.667	-3.5	-2.7	2	Y+
1017	Cr359 J180715+031525	E11	244	S	18:07:15.12	03:15:25.9	15.020	14.736	0.264	14.102	13.472	13.291	—	—	2	Y+
1018	Cr359 J180715+031842	E11	2705	M	18:07:15.20	03:18:42.6	19.393	18.774	0.690	—	—	—	—	0	Y+	
1019	Cr359 J180715+031457	E11	342	M	18:07:15.92	03:14:57.8	19.592	18.870	0.793	—	—	—	—	0	Y+	
1020	Cr359 J180715+033612	E05	2151	S	18:07:15.95	03:36:12.9	12.782	12.585	0.177	11.971	11.382	11.302	-0.8	-6.6	0	Y+
1021	Cr359 J180716+031447	E11	66	S	18:07:16.02	03:14:47.7	14.389	14.076	0.292	—	—	—	—	2	Y+	
1022	Cr359 J180716+033704	E05	1882	S	18:07:16.19	03:37:04.4	13.626	13.411	0.195	12.736	12.112	12.020	13.5	-11.3	2	Y+
1023	Cr359 J180716+033631	E05	2122	S	18:07:16.62	03:36:31.6	15.540	15.185	0.335	14.376	13.709	13.527	—	—	3	Y+
1024	Cr359 J180716+031546	E11	306	S	18:07:16.70	03:15:46.6	14.139	13.855	0.264	13.184	12.589	12.449	2.9	-10.8	2	Y+
1025	Cr359 J180716+032115	E11	1825	S	18:07:16.85	03:21:15.5	13.986	13.763	0.203	13.103	12.496	12.393	1.2	-6.6	0	Y+
1026	Cr359 J180716+032337	E11	2512	S	18:07:16.87	03:23:37.8	14.644	14.403	0.221	13.711	13.041	12.988	—	—	0	Y+
1027	Cr359 J180717+031438	E11	116	M	18:07:17.12	03:14:38.5	18.654	18.128	0.596	—	—	—	—	0	Y+	
1028	Cr359 J180717+031451	E11	256	M	18:07:17.28	03:14:51.1	19.158	18.555	0.673	—	—	—	—	0	Y+	
1029	Cr359 J180718+031507	E11	177	SM	18:07:18.06	03:15:07.6	15.055	14.760	0.275	—	—	—	—	0	Y+	
1030	Cr359 J180718+031855	E11	1152	S	18:07:18.80	03:18:55.3	13.301	13.074	0.207	12.463	11.884	11.762	-6.6	-12.2	0	Y+
1031	Cr359 J180719+031442	E11	1	S	18:07:19.69	03:14:42.5	13.156	12.922	0.214	—	—	—	—	2	Y+	
1032	Cr359 J180720+032042	E11	1668	S	18:07:20.23	03:20:42.9	12.901	12.672	0.208	12.061	11.464	11.355	-5.2	0	Y+	
1033	Cr359 J180720+031916	E11	1297	SM	18:07:20.33	03:19:16.4	17.433	16.884	0.529	—	—	—	-3.3	—	0	Y+

Appendix C

Finding charts for candidate members of Collinder 359

This appendix contains finding charts of all 1033 cluster member candidates selected in Collinder 359 up to a distance of 650 pc and an age of 80 Myr.

We do not provide a finding chart per object but two finding charts per chip, yielding a total of 120 finding charts with a field-of-view of about $24' \times 22'$. North is up and East is left. To avoid overloading the paper version of this thesis, we have decided to save the finding charts on a CD-ROM. Only one example is provided in this appendix, for the top part of CCD00 in Field A.

We have used the long exposures to create finding charts in order to recognise each candidate on the image. Hence, candidates selected from the short and medium exposures appear saturated in the finding charts. Each object is marked with the field name (A–E), CCD number (00–11), and its ID number.

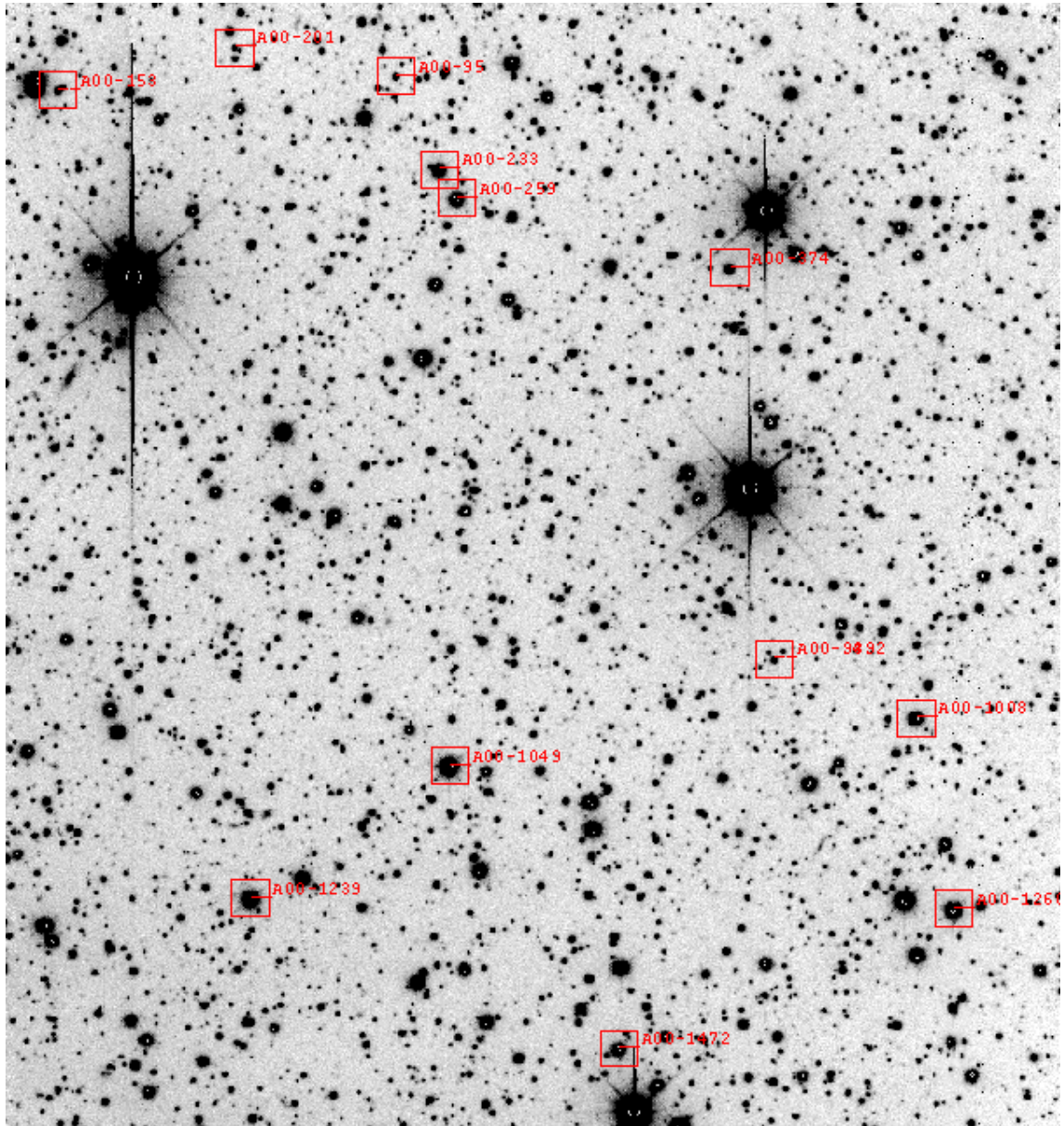


Figure C.1: Finding chart for candidates in CCD00 in Field A (top). The field-of-view is about $24' \times 22'$. North is up and East is left.

Appendix D

List of my publications

Refereed papers

1. Klotz, A., Caux, E., Monin, J.-L., **Lodieu, N.** 2004, accepted to A&A: Substellar objects in star-forming regions: A deep near-infrared survey of the Serpens cloud.
2. J. Greiner, J., Klose, J., Salvato, M., Zeh, A., Schwarz, R., Hartmann, D. H., Masetti, N., Stecklum, B., Lamer, G., **Lodieu, N.**, Scholz, R.-D., Sterken, C., Gorosabel, J., Burud, I., Rhoads, J., Mitrofanov, I., Litvak, M., Sanin, M., Grinkov, V., Andersen, M. I., Castro Ceron, J. M., Castro-Tirado, A.J., Fruchter, A., Fynbo, J.U., Hjorth, J., Kaper, L., Kouveliotou, C., Palazzi, E., Pian, E., Rol, E., Tanvir, N. R., Vreeswijk, P. M., Wijers, R. A. M. J., van den Heuvel, E.. GRB 011121: A collimated outflow into wind-blown surroundings, *ApJ*, 599:1223-1237, 2004.
3. McCaughrean, M. J., Close, L. M., Scholz, R.-D., Lenzen, R., Biller, B., Brandner, W., Hartung, W., & **Lodieu, N.**. Epsilon Indi Ba,Bb: the nearest binary brown dwarf. *A&A*, 413:1029-1036, 2004.
4. Scholz, R.-D., **Lodieu, N.**, Ibata, R., Irwin, M., McCaughrean, M. J., & Schwone, A.. An active M8.5 dwarf wide companion to the M4/DA binary LHS4039/LHS4040. *MNRAS*, 347:685-690, 2004.
5. Scholz, R.-D., McCaughrean, M. J., **Lodieu, N.**, & Kuhlbrot, B.. Epsilon Indi B: a new benchmark T dwarf. *A&A*, 398:29–32, 2003.
6. Barrado y Navascués, D., Bouvier, J., Stauffer, J. R., **Lodieu, N.**, & McCaughrean, M. J.. A substellar mass function for α Per. *A&A*, 395:813–821, 2002.
7. McCaughrean, M. J., Scholz, R.-D., & **Lodieu, N.**. Search for nearby stars among proper motion stars selected from optical-to-infrared photometry: two late M dwarfs within 10 pc. *A&A*, 390:27–30, 2002.
8. **Lodieu, N.**, Scholz, R.-D., & McCaughrean, M. J.. Discovery of three new L dwarfs in the Southern Sky. *A&A*, 389:20–23, 2002.
9. **Lodieu, N.**, Caux, E., Monin, J.-L., & Klotz, A.. Discovery of the first young brown dwarf in the Serpens. *A&A*, 383:15-18, 2002.

Conference proceedings

1. Monin, J.-L., Caux, E., Klotz, A., & **Lodieu, N.**. The first young brown dwarf in the Serpens cloud. In E. L. Martín, eds., *Brown Dwarfs*, IAU Symposium 211, pp83–86, 2003.
2. Stauffer, J. R., Barrado y Navascués, D., Bouvier, J., **Lodieu, N.**, & McCaughrean, M. J.. Brown dwarfs in the Alpha Persei cluster. In E. L. Martín, eds., *Brown Dwarfs*, IAU Symposium 211, pp163–170, 2003.
3. **Lodieu, N.**, McCaughrean, M. J., Barrado y Navascués, D., Bouvier, J., & Stauffer, J. R.. A search for brown dwarfs in the Alpha Persei cluster. In E. L. Martín, eds., *Brown Dwarfs*, IAU Symposium 211, pp179–180, 2003.

Others publications and articles

1. Scholz, R.-D., McCaughrean, M. J., **Lodieu, N.**, & Kuhlbrot, B.. Discovery of Nearest Known Brown Dwarf., ESO Press Release, 13 January 2003
2. McCaughrean, M. J., Zinnecker, H., Andersen, M., Meeus, G., & **Lodieu, N.**. Standing on the shoulder of a giant: ISAAC, Antu, and star formation. *ESO Messenger*, 109:28, 2002.
3. Greiner, J., Klose, S.; Zeh, A.; Lamer, G., Scholz, R.-D.; **Lodieu, N.**, van den Heuvel, E. P. J., Vreeswijk, P., Kaper, L., Castro-Tirado, A. J., and 10 co-authors. GRB 011121. *GCN*, 1166:1, 2001.
4. Greiner, J., Szokoly, G., Eisloeffel, J., Stecklum, B., Klose, S., Stanke, Th., **Lodieu, N.**, McCaughrean, M. J., Castro-Tirado, A. J.. H band observation of GRB 001212. *GCN*, 907:1, 2000.

AUTHOR: Nicolas Lodieu

TITLE: Surveys for low-mass stars and brown dwarfs:
Solar Neighbourhood and intermediate-age clusters Alpha Per and Collinder 359

THESIS ADVISORS: Dr. Emmanuel Caux & Prof. Dr. Mark McCaughrean

PLACE AND DATE OF THE DEFENCE: 07 July 2004 at 10h30
Salle de Conférences, CESR
9, Avenue du Colonel Roche
31400 Toulouse

ENGLISH SUMMARY

We describe results for surveys for low-mass stars and brown dwarfs, including older ones in the nearby field and younger ones in more distant clusters.

First, we present the outcome of a proper motion survey aimed at finding some of the nearest and coolest neighbours to the Sun. We have uncovered numerous ultracool dwarfs within 50 parsecs, including the closest brown dwarf binary.

Second, we focus on the substellar mass function in young open clusters. We have carried out a wide-field near-infrared survey of a 0.7 square degree region in the Alpha Per cluster, yielding new member candidates, including several brown dwarfs. We have also conducted an optical survey of a 1.6 square degree area in Collinder 359. New bona-fide members have been extracted from solar mass stars to brown dwarfs, yielding a revised distance and age for the cluster. The derived mass function continues rising into the substellar regime with a slope flatter than that estimated for Pleiades-like clusters.

KEYWORDS

Stars: low-mass stars, brown dwarfs

Stars: luminosity function, mass function

Solar Neighbourhood and individual clusters Alpha Per and Collinder 359

Techniques: photometric, spectroscopic

Techniques: optical, near-infrared

DISCIPLINE: Astrophysics

ADDRESS OF THE INSTITUTE: Astrophysikalisches Institut Potsdam
An der Sternwarte 16
D–14 482 Potsdam
Germany